Unclassified **NEA/CSNI/R(2005)5/VOL2**

Organisation de Coopération et de Développement Economiques
Organisation for Economic Co-operation and Development **06-Sep-2005**

English text only

NUCLEAR ENERGY AGENCY
COMMITTEE ON THE SAFETY OF NUCLEAR INSTALLATIONS

NEA/CSNI/R(2005)5/VOL2
Unclassified

INTERNATIONAL STANDARD PROBLEM NO. 48
CONTAINMENT CAPACITY

Appendices C to G

The complete document is only available in pfd format.

JT00188856

English text only

ORGANISATION FOR ECONOMIC CO-OPERATION AND DEVELOPMENT

Pursuant to Article 1 of the Convention signed in Paris on 14th December 1960, and which came into force on 30th September 1961, the Organisation for Economic Co-operation and Development (OECD) shall promote policies designed:

- to achieve the highest sustainable economic growth and employment and a rising standard of living in member countries, while maintaining financial stability, and thus to contribute to the development of the world economy;
- to contribute to sound economic expansion in member as well as non-member countries in the process of economic development; and
- to contribute to the expansion of world trade on a multilateral, non-discriminatory basis in accordance with international obligations.

The original member countries of the OECD are Austria, Belgium, Canada, Denmark, France, Germany, Greece, Iceland, Ireland, Italy, Luxembourg, the Netherlands, Norway, Portugal, Spain, Sweden, Switzerland, Turkey, the United Kingdom and the United States. The following countries became members subsequently through accession at the dates indicated hereafter: Japan (28th April 1964), Finland (28th January 1969), Australia (7th June 1971), New Zealand (29th May 1973), Mexico (18th May 1994), the Czech Republic (21st December 1995), Hungary (7th May 1996), Poland (22nd November 1996), Korea (12th December 1996) and the Slovak Republic (14 December 2000). The Commission of the European Communities takes part in the work of the OECD (Article 13 of the OECD Convention).

NUCLEAR ENERGY AGENCY

The OECD Nuclear Energy Agency (NEA) was established on 1st February 1958 under the name of the OEEC European Nuclear Energy Agency. It received its present designation on 20th April 1972, when Japan became its first non-European full member. NEA membership today consists of 28 OECD member countries: Australia, Austria, Belgium, Canada, the Czech Republic, Denmark, Finland, France, Germany, Greece, Hungary, Iceland, Ireland, Italy, Japan, Luxembourg, Mexico, the Netherlands, Norway, Portugal, Republic of Korea, the Slovak Republic, Spain, Sweden, Switzerland, Turkey, the United Kingdom and the United States. The Commission of the European Communities also takes part in the work of the Agency.

The mission of the NEA is:

- to assist its member countries in maintaining and further developing, through international co-operation, the scientific, technological and legal bases required for a safe, environmentally friendly and economical use of nuclear energy for peaceful purposes, as well as
- to provide authoritative assessments and to forge common understandings on key issues, as input to government decisions on nuclear energy policy and to broader OECD policy analyses in areas such as energy and sustainable development.

Specific areas of competence of the NEA include safety and regulation of nuclear activities, radioactive waste management, radiological protection, nuclear science, economic and technical analyses of the nuclear fuel cycle, nuclear law and liability, and public information. The NEA Data Bank provides nuclear data and computer program services for participating countries.

In these and related tasks, the NEA works in close collaboration with the International Atomic Energy Agency in Vienna, with which it has a Co-operation Agreement, as well as with other international organisations in the nuclear field.

COMMITTEE ON THE SAFETY OF NUCLEAR INSTALLATIONS

The NEA Committee on the Safety of Nuclear Installations (CSNI) is an international committee made up of senior scientists and engineers, with broad responsibilities for safety technology and research programmes, and representatives from regulatory authorities. It was set up in 1973 to develop and co-ordinate the activities of the NEA concerning the technical aspects of the design, construction and operation of nuclear installations insofar as they affect the safety of such installations.

The committee's purpose is to foster international co-operation in nuclear safety amongst the OECD member countries. The CSNI's main tasks are to exchange technical information and to promote collaboration between research, development, engineering and regulatory organisations; to review operating experience and the state of knowledge on selected topics of nuclear safety technology and safety assessment; to initiate and conduct programmes to overcome discrepancies, develop improvements and research consensus on technical issues; to promote the coordination of work that serve maintaining competence in the nuclear safety matters, including the establishment of joint undertakings.

The committee shall focus primarily on existing power reactors and other nuclear installations; it shall also consider the safety implications of scientific and technical developments of new reactor designs.

In implementing its programme, the CSNI establishes co-operative mechanisms with NEA's Committee on Nuclear Regulatory Activities (CNRA) responsible for the program of the Agency concerning the regulation, licensing and inspection of nuclear installations with regard to safety. It also co-operates with NEA's Committee on Radiation Protection and Public Health (CRPPH), NEA's Radioactive Waste Management Committee (RWMC) and NEA's Nuclear Science Committee (NSC) on matters of common interest.

Foreword

The International Standard Problem No.48- Containment Capacity report NEA/CSNI/R(2005)5 is divided into three Volumes:

While Volume 1 is the Synthesis Report, Volumes 2 and 3 contain the contributions of participating organizations for both phases 2 and 3.

Table of Contents

NEA/CSNI/R(2005)5/Volume 2
Appendix C: British Energy
Nuclear Installations Inspectorate/Health & Safety Executive
NNC Ltd.
Phase 2 ……..…..C-1 to C-78
Phase 3 ……...C-79 to C-162

Appendix D: Energoprojekt Praha, UJV Rez. Div.
Phase 2 ……...D-1 to D-18
Phase 3 ……D-19 to D-38

Appendix E: Fortum Nuclear Services Ltd.
Phase 2: No report available
Phase 3…….....E-1 to E-7

Appendix F: Gesellschaft für Anlagen und Reaktorsicherheit mbH
Phase 2 ……F-1 to F-24
Phase 3 ……..F-25 to F-66

Appendix G: Institut de Radioprotection et de Sûreté Nucléaire
Commissariat a l'Energie Atomique
Phase 2 ……...G-1 to G-84
Phase 3……..G-85 to G-86

NEA/CSNI/R(2005)5/Volume 3
Appendix H: Japan PCCV Research Group
Phase 2: No report available
Phase 3 ……...H-1 to H-52

Appendix I: Korea Atomic Energy Research Institute
Phase 2 ……..I-1 to I-26
Phase 3: No report available

Appendix J: Korea Power Engineering Company
Phase 2 …….J-1 to J-24
Phase 3 ……...J-25 to J-62

Appendix K: US Nuclear Regulatory Commission
Sandia National Laboratories
David Evans and Associates
Phase 2 ……...K-1 to K-66
Phase 3 …….K-67 to K-95

Appendix L: Scanscot Technology
Phase 2 and Phase 3 ……L-1 to L-159

Appendix C: British Energy
Nuclear Installations Inspectorate/Health & Safety Executive
NNC Ltd.

Phase 2: from C-1 to C-78
Phase 3: from C-79 to C-162

Page intentionally left blank

International Standard Problem on Containment Capacity (ISP- 48)

Nawal K Prinja BSc, MSc, PhD, FIMechE
James Curley BSc
Ian Sanders BEng
NNC Limited
Booths Hall
Knutsford
Cheshire
WA16 8QZ

Issue 02
April 2004

DOCUMENT ISSUE RECORD
(engineering documents)

Adding value through knowledge

Document Title :	International Standard Problem on Containment Capacity (ISP-48)
Project Reference:	C11248/TR/001

Purpose of Issue : For Information

Security Class : Unclassified

Issue	Description of Amendment	Originator/ Author	Checker	Approver	Date
01	Original Issue	J Curley	I Sanders	N Prinja	Jan 2004
02	Inclusion of FE model description and updated analysis results	J Curley	I Sanders	N Prinja	April 2004

Total number of pages:	Intro: (i)-(vi)	Text 1-23	Tables T1-T2	Figures F1-F43	Appendices N/A

Previous issues of this document shall be destroyed or marked **SUPERSEDED**

Distribution Graham Doughty (BE), Dave Shepherd (NII,HSE), M Hessheimer (SNL), Eric Mathet (OECD), JCU, NKP, Jobfile (J5646)

3050aOct99 Controlling procedure - QP11, QP40 DSC Ref

Contents

List of Tables iii

List of Figures iv

1 INTRODUCTION 1

2 TECHNICAL BACKGROUND 2

3 SCOPE 4
3.1 PHASE 1: DATA COLLECTION AND IDENTIFICATION. 4
3.2 PHASE 2: CALCULATION OF THE LIMIT STATE TEST (LST) PERFORMED AT SNL - MECHANICAL LOADING 4

4 ¼ SCALE PCCV FINITE ELEMENT MODEL 6
4.1 DESCRIPTION OF GLOBAL MODEL 6
4.2 CYLINDER WALL AND DOME 6
4.3 BASEMAT 6
4.4 THE CYLINDER WALL PENETRATIONS 7
4.5 THE POST-TENSIONING TENDONS 7
4.6 INTERNAL LINER AND LINER ANCHORAGE 7
4.7 CONCRETE REINFORCEMENTS 8
4.8 PCCV SUPPORT CONDITIONS 9

5 REVIEW OF TEST DATA 10
5.1 CONCRETE MATERIALS 10
5.2 TENDON / REBAR MATERIALS 11
5.3 VESSEL PRE-TENSIONING 11

6 MODEL UPDATE TO ABAQUS V6.4 13
6.1 CONCRETE MATERIAL MODEL 13
6.2 CHANGES TO MODEL PARAMETERS 14

7 LST ANALYSIS RESULTS 15
7.1 COMPARISON WITH TEST DATA – GLOBAL DISPLACEMENTS / STRAINS 15
7.2 CALCULATION OF LIMIT LOAD 16

8 ASSESSMENT OF RESULTS 17
8.1 ELASTIC RESPONSE OF VESSEL 17
8.2 ASSESSMENT OF CONCRETE CRACKING 17
8.3 ASSESSMENT OF LINER TEARING 18
8.4 ASSESSMENT OF TENDON RESPONSE 18

9 CONCLUSION 19

10 PROPOSALS FOR PHASE 3 20
10.1 ASSESSMENT OF FULL SIZE CONTAINMENTS 20
10.2 DEFINITION OF THERMAL LOADING 20
10.3 Creep Behaviour at Elevated Temperatures 21

11 REFERENCES 22

12 NOTATION 23
12.1 ABBREVIATIONS 23

List of Tables

Table 1 Original and updated Young's Modulus
Table 2 Original and updated Density
Table 3 Original and updated Poisson's Ratio
Table 4 Original and updated Compressive & Tensile Strength for cylinder wall
Table 5 Anchorage properties
Table 6 Material properties for the ABAQUS Version 6.4 analysis

List of Figures

Figure 1 Standard Output Locations
Figure 2 Finite Element Representation of the PCCV
Figure 3 Detail view of the PCCV dome model
Figure 4 The basemat model showing locations of global restraints
Figure 5 Detailed view of the equipment hatch penetration model
Figure 6 Detailed view of the airlock penetration model
Figure 7 Detailed view of the main steam and feed water penetration model
Figure 8 PCCV vertical tendons model
Figure 9 Equipment hatch penetration lining and cover plate
Figure 10 PCCV model supported on soil springs
Figure 11 Internal liner model, showing detail around the main steam and feedwater penetrations
Figure 12 Comparison of Test & Pre-test Vertical Tendon Loads
Figure 13 Comparison of Test & Pre-test Hoop Tendon Loads
Figure 14 Variation in tendon load due to friction and seating loss
Figure 15 Stress-Strain Tension Stiffening Relationship
Figure 16 Stress-Strain Compression Hardening Relationship
Figure 17 Location 1 Vertical Displacement
Figure 18 Location 2 Radial Displacement
Figure 19 Location 3 Radial Displacement
Figure 20 Location 4 Radial Displacement
Figure 21 Location 5 Radial Displacement
Figure 22 Location 6 Radial Displacement
Figure 23 Location 7 Radial Displacement
Figure 24 Location 8 Vertical Displacement
Figure 25 Location 9 Radial Displacement
Figure 26 Location 10 Vertical Displacement
Figure 27 Location 11 Vertical Displacement
Figure 28 Location 12 Radial Displacement
Figure 29 Location 13 Radial Displacement
Figure 30 Location 14 Radial Displacement
Figure 31 Location 15 Radial Displacement
Figure 32 Location 16 Meridional Rebar Strain
Figure 33 Location 17 Meridional Rebar Strain
Figure 34 Location 18 Meridional Rebar Strain
Figure 35 Location 19 Meridional Rebar Strain

Figure 36 Location 20 Meridional Rebar Strain
Figure 37 Location 21 Meridional Rebar Strain
Figure 38 Location 22 Hoop Rebar Strain
Figure 39 Location 23 Meridional Rebar Strain
Figure 40 Location 24 Hoop Rebar Strain
Figure 41 Location 25 Meridional Rebar Strain
Figure 42 Location 26 Meridional Rebar Strain
Figure 43 Location 27 Hoop Rebar Strain
Figure 44 Location 28 Meridional Rebar Strain
Figure 45 Location 29 Meridional Rebar Strain
Figure 46 Location 30 Meridional Rebar Strain
Figure 47 Location 31 Meridional Rebar Strain
Figure 48 Location 32 Hoop Rebar Strain
Figure 49 Location 33 Meridional Rebar Strain
Figure 50 Location 34 Meridional Liner Strain
Figure 51 Location 35 Meridional Liner Strain
Figure 52 Location 36 Meridional Liner Strain
Figure 53 Location 37 Hoop Liner Strain
Figure 54 Location 38 Meridional Liner Strain
Figure 55 Location 39 Hoop Liner Strain
Figure 56 Location 40 Meridional Liner Strain
Figure 57 Location 41 Hoop Liner Strain
Figure 58 Location 42 Meridional Liner Strain
Figure 59 Location 43 Meridional Liner Strain
Figure 60 Location 44 Hoop Liner Strain
Figure 61 Location 45 Hoop Liner Strain
Figure 62 Location 46 Hoop Liner Strain
Figure 63 Location 47 Radial Base Liner Strain
Figure 64 Location 48 Hairpin Tendon Strain
Figure 65 Location 49 Hairpin Tendon Strain
Figure 66 Location 50 Hoop Tendon Strain
Figure 67 Location 51 Hoop Tendon Strain
Figure 68 Location 52 Hoop Tendon Strain
Figure 69 Location 53 Hoop Tendon Strain
Figure 70 Location 54 Hairpin Tendon Force
Figure 71 Location 55 Hoop Tendon Force
Figure 72 Displaced shape using ANAMAT concrete material model @ 1.72MPa

Figure 73 Displaced shape using ABAQUS concrete material model @ 1.40MPa
Figure 74 Finite element model at junction of thin/thick liner plate
Figure 75 Equivalent plastic strain contour at junction of thin/thick liner plate
Figure 76 Equivalent plastic liner strains for ANAMAT analysis
Figure 77 Equivalent plastic liner strains for ABAQUS analysis
Figure 78 Limit Load Range
Figure 79 Contour plot showing concrete damage @ 0.66MPa
Figure 80 Displaced shape of cylinder showing butterfly mode @ 1.4MPa
Figure 81 Concrete acoustic monitoring system
Figure 82 Liner tears after LST
Figure 83 Vertical tendon axial load @1.48MPa

1 INTRODUCTION

At the June 2002 meeting of the Committee on the Safety of Nuclear Installations (CSNI), the proposal (Ref 1) for the International Standard Problem 48 (ISP48) on containment integrity was approved.

This report covers Phases 1 and 2 of the ISP 48 work done by NNC Limited under contract (C11248) from British Energy. NRC/NUPEC sponsored tests of the ¼ scale pre-stressed concrete containment vessel (PCCV) have been executed at Sandia National Laboratories (SNL) in USA. The Limit State Test (LST) executed during September 2000 was based on pneumatic pressurization of the vessel and achieved a maximum pressure of 1.3MPa (3.3 times the design pressure). The objectives of the ISP48 are to extend the understanding of capacities of actual containment structures based on the results of the PCCV LST and any other sources of available research.

Under contract to the United Kingdom Health and Safety Executive (HSE), NNC participated in the LST round robin exercise and completed the analysis (Ref 2) to predict the limit load of the vessel. Predictions from all the participants of the round robin were collated and published by SNL in August 2000 (Ref 3). The LST identified liner tearing as the mode of failure. Whilst there was no visible damage to the PCCV structure, the breach of the pressure boundary dictated the limit load due to the excessive leakage rate. It can be seen from Ref 3 that out of the total of 17 participants, the NNC/HSE model is one of only four that successfully predicted liner tearing as the failure mode. It was recognised at the international pre-test round robin meeting in October 1999 that the NNC/HSE model was one of the most sophisticated models. The NNC/HSE model was a full 3D global model, which took account of interaction between all the main structural features.

Following the pre-test round robin, NNC carried out the post-test analysis under HSE contract CE/GNSR/1 and the work was presented in Ref 4. This work consisted of a comparison between the FE analysis and the test results to give an assessment of the accuracy and reliability in predicting failure modes and limit loads of PCCV structures using finite element analysis. It also included analysis of the Structural Failure Mode Test (SFMT) executed in November 2001, in which hydraulic pressure was used to overpressurise the containment to total structural collapse. The results of the overpressurisation test have been published by SNL in Ref 5. The analysis carried out by NNC in Ref 4 predicted the failure location and the behaviour up to collapse with good accuracy.

All the test and the analysis work done to date has shown that leakage occurs before the burst pressure but in this study only the mechanical loading (gravity, prestress and internal pressure) was considered and thermal loading was ignored. In real containments, increase in internal pressure is associated with thermal loading. One of the aims of the ISP48 is to study the effects of accident temperatures and see if the onset of leakage is closer to the burst pressure in full size containments.

Technical background to the PCCV analysis work done under the international roundrobin is presented in section 2 and the scope of work for Phases 1 and 2 of the ISP48 project is give in section 3. A description of the finite element model is given in section 4. Review of the test data and subsequent changes to the FE model are presented in sections 5 and 6 respectively. The latest analysis results are given in section 7 followed by the assessment of results in section 8. The conclusions from this study are in section 9. Recommendations for the next Phase (3) work are made in section 10.

2 TECHNICAL BACKGROUND

The original LST test sponsored by the NRC/NUPEC attracted contributions from 17 participants from USA, Canada, France, Japan, Korea, UK, Spain, China, India and Russia who submitted their pre-test analysis results. 14 of these participants presented their results at the meeting held in October 1999 at Sandia Laboratories, USA. There was significant difference in the behaviour predicted by the participants. This was mainly due to the modelling approach, assumptions and interpretation of the design data. Many of the participants constructed global models of the PCCV reflecting their assumptions, to predict the limit load. Others made detailed models of local features like the penetrations and buttresses but did not have a full global model. The NNC/HSE model was the only full 3-D global model (see Ref 2) which had included sufficient details of all the important local features like the tendon layout, penetrations, buttresses, stressing gallery, soil foundation and the liner.

In Ref 2 the NNC/HSE model was analysed using version 5.8 of the ABAQUS general purpose FE code (Ref 6). It was found that the concrete material model in the 5.8 version of ABAQUS gave numerical problems and the global 3-D model could not be analysed beyond an internal pressure of 0.71 MPa. The analysis beyond 0.71MPa was completed by incorporating the ANACAP concrete material model routine supplied by ANATECH (Ref 7).

The main objective of the exercise was to predict the failure mode and the behaviour up to the limit load. The NNC/HSE model accurately predicted that the liner tearing would control the limit load. It also predicted accurately that the main structural components like the tendons and reinforcing bars would not fail before liner tearing. Whilst the failure mode was predicted accurately, there remained discrepancies between the history of the response recorded during the test and that predicted by the FE analysis. This could be because the model did not take account of the as-built conditions, which were investigated in the post-test analysis (Ref 4).

The test model had a design pressure, Pd, of 0.39Mpa and the Limit State Test (LST) achieved a pressure of 1.295MPa (3.3 Pd), which was well beyond the design basis. The test was limited because the vessel leak rates increased beyond the supply limit of the N_2 pressurization system. The overall PCCV structure remained substantially intact after the LST. The sponsors agreed to extend the test and SNL sealed the leaks and conducted the Structural Failure Mode Test (SFMT) by using a water pressurization system. The SFMT was conducted on 14 November 2001 and achieved its objective of causing global collapse of the PCCV structure, reaching a pressure of 1.423MPa (3.65 Pd).

The LST and SFMT data in conjunction with the pre-test and the post-test analyses show three stages of the structural response of the pressurized PCCV as it approaches its structural collapse load.

The first stage of predominantly elastic response can be predicted with very good accuracy using standard finite element technology. The second stage involving inelastic response with extensive concrete cracking required specialist concrete material models and detailed geometric representation of the main structural features. It is important to model the interaction between various structural elements to simulate load redistribution as some components yield or fail. Such local yielding or rupture may lead to loss of functionality or breach of pressure boundary. The third stage involving gross deformation leading to structural collapse required solution of a highly non-linear problem. Extensive concrete cracking, well beyond the tension stiffening range, occurs and requires robust constitutive models capable of simulating extensively cracked concrete. Provided such a specialist FE package is available, an experienced analyst can predict the collapse limit and failure mode with fair accuracy.

As part of the ISP48, additional information about the test has now been made available to the participants (Ref 5). For meaningful application of this research to real size containments, a number of issues like the effect of thermal loading and scaling remain to be resolved.

3 SCOPE

The full scope of the ISP48 is to perform a new stress analysis of the ¼ scale PCCV using the same models as for the post-test analysis (Ref 4), but incorporating thermal loading in addition to the mechanical loading. The existing FE results (from Refs 2 and 4) and the results from the new stress analysis will be compared with the test data to indicate the following:-

- Effect of accident temperatures on the containment capacity
- Would the onset of leakage be later and much closer to the burst pressure

The overall project comprises four phases of work as follows:

Phase 1: Data collection and identification

Phase 2: Calculation of the LST

Phase 3: Calculation of response to both thermal and mechanical loadings

Phase 4: Reporting workshop

This report addresses Phases 1 and 2 only, with recommendations for the way forward in phase 3. The scope of work for phases 1 and 2 covered by this report as follows:

3.1 PHASE 1: DATA COLLECTION AND IDENTIFICATION.

The purpose of this phase is to review construction and vessel load data collected by SNL during the LST/SFMT testing. Assessment includes reviewing the concrete, liner plate, tendon and rebar material properties and the tendon post-tensioning loads. This information has been issued to all ISP participants (Ref 5) who are to use the data for analysis. Necessary changes to the NNC model used in the previous analysis will be identified for the ISP.

It is also required that results are reported at the standard output locations used in the PCCV pretest round robin Figure 1. This will enable direct comparison between the analytical results of the participants. NNC has provided results at the 55 standard output locations in electronic format in an MS Excel spreadsheet.

3.2 PHASE 2: CALCULATION OF THE LIMIT STATE TEST (LST) PERFORMED AT SNL - MECHANICAL LOADING

This task requires updating of the FE model to take account of any new information from the Phase 1 review. The requirement is to analyse the LST (applying only the mechanical loads) to predict the extent of concrete cracking, liner tearing and tendon rupture. Comparison between the analytical and test results will be made. The peak sustainable load will also be calculated and compared with the test.

In the previous analysis work (Refs 2 and 4), the ANACAP routine supplied by ANATECH was used to remove some of the limitations of the ABAQUS version 5.8 concrete material model. Incorporation of this concrete model extended the range of pressure over which predictions could be made. A new concrete material model has been made available in the

latest release of ABAQUS version 6.4. It is proposed to use the latest concrete material model in ABAQUS v6.4 with the NNC's 3D global model to perform the LST analysis.

In this Phase, it is required of each participant to suggest a way forward for the following two topics: -

- Transposition to real size containments. This will include consideration of scaling issues.
- Definition of thermal loading for Phase 3.

4 ¼ SCALE PCCV FINITE ELEMENT MODEL

4.1 DESCRIPTION OF GLOBAL MODEL

Concrete components of the vessel are simulated with the ABAQUS eight-node solid element C3D8. The eight-node solid element is mathematically formulated such that it accommodates the inclusion of steel reinforcements. At a minority of locations, due to meshing requirements, six-node linear prism elements (C3D6) were used. Six-node prism elements do not support reinforcement capability. Within the cylinder, all solid elements are fully integrated, while the basemat and dome elements have reduced integration. Figure 2 shows the 3D global model of the PCCV model.

The origin of the FE model is at the centre of the top surface of the basemat. Directions 1, 2 and 3 are X, Y and Z respectively. X is along the 90^o azimuth, Y is vertical and Z is along the 180^o azimuth.

4.2 CYLINDER WALL AND DOME

The mesh density of the cylinder wall and dome in the circumferential direction was driven by the requirement to model the vertical post-tensioning tendons explicitly. Three elements were employed in the wall-thickness direction of the cylinder and dome. For the fully integrated elements, this gives a total of six integration points through the wall to provide adequate information in areas of high bending. To allow for the explicit representation of each vertical tendon, 184 solid elements were arranged around the circumference of the vessel. The resulting layout consists of a cylinder and dome wall mesh with elements at approximately 2 degree intervals in the circumferential direction.

The mesh density in the vertical direction was influenced by the specification of the hoop tendons in the concrete elements. The cylinder hoop tendons were arranged at vertical intervals of 112.7mm. The solid element nodes are meshed vertically to correspond with the spacing of the hoop tendons.

The height of the elements in the lower half of the dome is base on the vertical spacing of the dome hoop tendons. The dome elements are uniformly meshed up to a height of 14690mm, the location of the uppermost hoop tendon. The meshing of the dome in the hoop direction was dictated by the vertical plane of the tendons through the dome. In the dome apex region, a refined solid element mesh allows meshing of the vertical tendons where they intersect at the vessel crown. Figure 3 shows a detailed view of the model.

The buttresses at the 90^o and the 270^o azimuths are reinforced columns onto which the hoop tendons are anchored. The stiffness of the cylinder and the dome at the 90^o and 270^o azimuths is enhanced by the restraining effect of the buttresses. The reinforcement scheme of the buttresses comprises vertical, radial U bars and trim bars. Additional stiffening is provided by the steel plates at the tendon anchorage end-blocks. The buttresses and their reinforcement have been modelled explicitly.

4.3 BASEMAT

The basemat is a thick concrete reinforced slab supporting the vessel superstructure within which the vertical tendons are anchored. It is heavily reinforced at its top and bottom surfaces. The top surface reinforcement consists of a layer of hoop rebars sandwiched between two grids of radially spanning rebars. The bottom surface is reinforced with a rectangular grid of cross rebars. Additional reinforcement is provided in the vicinity of the tendon anchorage gallery. The flexural reinforcements were defined within each solid element. The basemat shear reinforcements were not modelled. Figure 4 shows a view of the basemat.

4.4 THE CYLINDER WALL PENETRATIONS

The cylinder wall penetrations and their immediate vicinity have been explicitly modelled. Structural features within the penetration area that are represented explicitly in the model are the enhanced reinforcement stiffening, thickened wall section (airlock and equipment hatch penetrations), steel plates lining the penetration cavity, the penetrations cover plates, the vertical and hoop tendons, internal vessel liner and the liner anchorage. The finite element meshes of the airlock, equipment hatch, main steam and feed water penetrations are shown in Figures 5, 6 and 7.

4.5 THE POST-TENSIONING TENDONS

The post-tensioning tendons have been modelled using two different approaches. The vertical tendons were modelled explicitly using the two-node, linear truss element T3D2. For each tendon, nodes have been generated coincident to the solid element concrete nodes along the tendon path. Typically, in the non-penetrated areas a vertical tendon consists of up to 220 elements, depending upon its location within the vessel. Each vertical tendon node lying within the cylinder of the vessel is constrained in the horizontal degrees of freedom (i.e. the X and Z directions) to the coincident concrete nodes. The vertical degree of freedom (Y) of tendon nodes within the cylinder were left unconstrained, allowing relative sliding of the tendons and concrete in the vertical direction. Within the cylinder, friction at the concrete/tendon interface is assumed to be negligible and has not been modelled. However, within the dome, the curved trajectory of the tendon causes appreciable friction at the concrete/tendon interface, resulting in a non-uniform variation of load in the tendon. Although interface behaviour has not been explicitly modelled, the non-uniform distribution of load in the vertical tendons over the dome is allowed for by constraining all coincident tendon and concrete nodal degrees of freedom. The vertical tendon mesh is shown in Figure 8

The hoop tendons are modelled as single rebars embedded within concrete elements. The concrete elements were defined such that an element edge lies along the path of the hoop tendon as this facilitated the placement of the hoop tendons with the elements. Each hoop tendon starts at one face of the buttress, completes a 360^{o} loop around the vessel and is anchored at the opposite face on the same buttress. Alternative tendons are anchored at opposite buttresses. Interface behaviour between the concrete and the tendon has not been modelled. Frictional loss in the hoop tendons is discussed in section 5.3.

4.6 INTERNAL LINER AND LINER ANCHORAGE

The thicker insert plates surrounding the main steam and feed water penetrations are simulated with the shell element S4R. The S4R element is a general purpose shell element

suitable for both 'thick and thin shell' applications. It accounts for finite membrane strains and allows for change in thickness. Therefore it is suitable for large strain analysis. An S4R element has 4 nodes and 6 DOF at each node. In order to try to keep the size of the model within manageable limit, it was decided to model the general area of the liner with membrane type M3D4R elements. These elements are reduced integration 4 noded membrane elements with only two in-plane DOFs. Such elements are suitable for thin plates which offer strength in the plane of the element and have negligible bending stiffness. The liner elements are meshed around nodes defined independently but coincide with adjacent concrete nodes. The internal liner mesh is shown in Figure 2. The meshes of the plate lining the equipment hatch penetration cavity are presented in Figure 9

The liner-to-concrete anchorage was modelled by connecting the liner node to the corresponding coincident concrete node with three linear spring elements at each node, representing the radial, hoop and axial anchorage plate stiffness. Given that the pitch of the horizontal and vertical liner anchorage plates is not uniform, no attempt was made to simulate the anchorage plates at their exact locations. The spring stiffness values given in Table 5 are derived from test results for the pull-out of anchorage plates in tensile and shear modes, Ref 5, as follows.

The pull-out and shear test reported in Ref 5 are based on tests conducted on a number of pre-stressed and non-pre-stressed liner/concrete anchorage arrangements. In this work, test results from the pre-stressed liner/concrete anchorage arrangements have been used to derive the stiffness of the anchorage. The liner strip, 300mm wide, and embedded in a block of concrete was loaded first by tension load and then by shear load. In each case the stiffness of the arrangement was computed. For each case the average measured values were used as the basis for calculating the equivalent anchorage spring stiffness. The measured tensile and shear stiffness are respectively 127ton/mm and 59ton/mm.

In the finite element model, the radial tensile anchorage stiffness is represented by 36 springs in the hoop direction. The equivalent tensile spring stiffness is computed as follows:

$$\text{Tensile spring stiffness} = \frac{127 \times 1000 \times 9.81 \times 2\pi \times 5376}{36 \times 300}$$

$$= 3.89 \times 10^6 \text{ N/mm}$$

There are 36 shear springs around the circumference of the vessel model. The shear spring stiffness is given as:

$$\text{Meridional/hoop spring stiffness} = \frac{59 \times 1000 \times 9.81 \times 2\pi \times 5376}{36 \times 300}$$

$$= 1.82 \times 10^6 \text{ N/mm}$$

4.7 CONCRETE REINFORCEMENTS

The grid of reinforcing bars in the vessel has been represented as rebar smeared within the parent solid elements. The orientation, cross-sectional area, spacing and material properties are taken from the construction drawings, Ref 9.

The duct-supporting steel frame construction is modelled as single rebars within the parent solid elements. The properties of the steel frame are given in Ref 9.

4.8 PCCV SUPPORT CONDITIONS

The basemat is constructed on a 150mm thick un-reinforced slab which itself is supported on an engineered sand and gravel subgrade. The soil stiffness was characterised as exhibiting a settlement of less than 25mm due to a bearing pressure of 35Ton/m^2, Ref 10.

The soil was represented using grounded spring elements (SPRING1). Each node on the bottom surface of the basemat was supported on a spring element, Figure 10. The spring stiffness was computed based on the influence area of each spring node.

The vessel was constrained to eliminate rigid body translations and rotations at four nodal positions on the top surface of the basemat in the horizontal degrees of freedom Figure 4

5 REVIEW OF TEST DATA

5.1 CONCRETE MATERIALS

A full review of the concrete material test data versus the original LST analysis was carried out. During this phase of the review, in the process of upgrading the input files from Version 5.8 to 6.4, it was decided that the model would now incorporate three different material models for each of the three main components of the PCCV global model. Therefore separate materials would be used for the cylinder, dome and basemat regions.

The concrete material properties that were assessed for review in the global model are: -

- Young's modulus
- Density
- Poisson's Ratio
- Compressive Strength
- Tensile Strength

Each property was assessed and an average selected for each region of the model.

5.1.1 Young's Modulus

Previously the model only used a single Young's modulus for all of the components. The new analysis has three Young's moduli specified as shown in Table 1.

From Table 1 it can be seen that the Young's modulus has increased for the dome component. However, it has decreased for the basemat and the cylinder components. The largest change is the decrease of approximately 8% for the cylinder.

5.1.2 Density

Once again three densities have been specified for the new analysis and are given in Table 2. The table of densities shows that there was a little difference between the values used in the original LST analysis and the actual test data, giving rise to a small decrease in mass.

5.1.3 Poisson's Ratio

The Poisson's ratio has increased quite considerably for all of the components of the global model. The increase in Poisson's ratio would give a marginal rise in displacements for the same vessel with the same internal pressure. The values used for Poisson's ratio are given in Table 3

5.1.4 Compressive & Tensile Strength

The compressive and tensile strengths of the concrete define the starting point for the non-linear portion of concrete material model. The non-linear portion of the concrete material model incorporates effects of tension stiffening, damaged plasticity and compression hardening. In the global model of the PCCV a non-linear material used is for the main cylinder wall and the dome. From the concrete test data the values in Table 4 were calculated.

These properties have been incorporated into the latest ABAQUS concrete material model, which is described in section 6.

5.2 TENDON / REBAR MATERIALS

The tendon and rebar materials in the global model were once again assessed during the SFMT analysis. A review of the data supplied in Ref 5 showed that the material properties were identical to those used for the SFMT therefore no modification to the material properties was required.

5.3 VESSEL PRE-TENSIONING

The load distribution within the tendons was non-uniform because of friction between the tendons and ducts. This was taken into account during the pre-test analysis by using the design values of the anchorage loads of 350kN and 471kN for the hoop and vertical tendons respectively. Variation in the tendon loads due to frictional loss was obtained by applying the following Equation 1.

$$P = P_{1,2}\, e^{(-\mu\beta - 0.001L)} \qquad \textbf{Equation 1}$$

Where

$P_{1,2}$ = Load at the tensioning end 1 or 2.

β = Change of angle from tensioning end.

P = Load at β from tensioning end.

μ = Friction Coefficient.

L = Length of Tendon.

Hydraulic jacks were used to tension the tendons to the desired load. They were then anchored at the buttresses and the base mat for the hoop and vertical tendons respectively. Each hoop tendon was modelled by 183 elements, and from the element nodal coordinate, the average change of angle from the anchorage was calculated. The same procedure was used for the vertical tendons, but only over the dome area. Friction losses for the vertical tendons in the wall region were assumed to be negligible.

A sample of the pre-loads for a selection of hoop and vertical tendons were measured at the time of the test. It was seen that the values observed before the test were not consistent with the design loads. The pre-loads specified in the pre-test analysis were up to 10% higher than the pre-load values in the test. The comparison is shown in Figure 12 and Figure 13 for vertical and horizontal tendons respectively. The tendon pre-load values within the input decks were then altered to simulate the test results taking into account the distribution of the load due to friction. Not all tendon values were measured, so the tendons for which there were known measured values were altered individually, and the intervening tendon loads were assigned an average value.

The equipment hatch, airlock and mainstream penetrations were modelled separately from the cylinder, so the areas where tendons passed through the penetrations were assigned an average value around that section of the tendon.

At the “Post-Test Meeting” it was confirmed that seating-loss of the tendons had a larger effect on the vessel than that initially calculated. The seating loss occurs when the tendons are initially tensioned and then released by the hydraulic jacks. The tendons contract slightly as they “settle in”. The pre-test analysis did not take into account this seating loss acting on the tendons and had assumed that the loss was negligible. Allowance for this was made in the post-test analysis and was assumed to act over a 90° segment (45° sections on each side of the buttress). The average seating loss of 24757N was taken from the PCCV test results, and was included in the calculations for the pre-loads. The modelling assumed that the seating loss was linear throughout the 90° segment. Figure 14 shows the variation in tendon load due to friction and the seating loss. The friction coefficient of 0.21 for the steel tendons was kept unchanged.

6 MODEL UPDATE TO ABAQUS V6.4

The PCCV global model was updated from ABAQUS Version 5.8 to the most recent version of 6.4. The main difference between the two versions of ABAQUS is the format in which the input files are created. . Using a utility included in version 6.4, the version 5.8 input files were reformatted for use with version 6.4. Once the conversion was completed the input files were checked against the original to check all the changes made had been implemented correctly.

6.1 CONCRETE MATERIAL MODEL

ABAQUS version 6.4 includes an improved concrete damaged plasticity model. It uses concepts of isotropic damaged elasticity in combination with isotropic tensile and compressive plasticity to represent the inelastic behaviour of concrete.

The parameters, which are required for definition of the concrete model, are as follows: -

- Tension stiffening
- Tension damage
- Compression damage (optional)
- Compression hardening

All of the above parameters are required, with the exception of the compression damage as little damage occurs during the pre-stressing of the vessel.

The concrete model is a continuum, plasticity based, damage model for concrete. It assumes that the two failure mechanisms are tensile cracking and compressive crushing.

The model assumes that the tensile cracking of the concrete is characterised by damaged plasticity. Under uniaxial tension the stress-strain response is linear until the failure stress is reached. It is at this point micro cracking of the concrete is initiated. Once beyond the failure stress the cracking of the concrete is represented by a strain softening approach.

6.1.1 Tension Stiffening

The tension stiffening option is used to model the interaction and load transfer between the concrete and the steel reinforcement. The tension stiffening can be simulated in ABAQUS either by a post failure stress-strain approach or by applying a fracture energy criterion.

The post failure stress-strain is defined as a yield stress versus a cracking strain or displacement. ABAQUS converts the cracking strain or displacement into plastic strain automatically. A reasonable estimate of tension stiffening for heavily reinforced concrete is to assume that the strain softening after failure reduces the stress linearly to zero at a total strain of about 10 times the initial cracking strain. This approach can be seen in Figure 15

The fracture energy approach uses an initial yield stress and a value for the fracture energy, which was available from the test data.

6.1.2 Tension & Compression Damage

The degree of tension and/or compression damage determines the amount of post cracking damage (or stiffness degradation). This also determines the amount of recovery that can take place in the concrete after unloading. This is defined by using a damage variable and a direct cracking strain or displacement.

6.1.3 Compression Hardening

This parameter is used to define the changes in compressive strength of the concrete as shown in Figure 16. The compression hardening is defined in terms of a stress versus a crushing strain. During uniaxial compression, the response is linear until the value of initial yield (σ_c). In the plastic regime the response is characterised by a stress hardening and then a strain softening approach that occurs after the ultimate stress (σ_{cu}) is reached.

6.2 CHANGES TO MODEL PARAMETERS

The properties for the linear portion of the concrete modelling, which includes the basemat and buttresses was updated in line with the material data provided in section 5.1.1 to 3.

The properties for the Non-Linear portion of the modelling (for the cylinder and dome), however, provided some problems. In order to be able to use the updated concrete model within ABAQUS Version 6.4, the material test data had to be reviewed in line with the new concrete material model.

Initial runs using the test data from Ref 5 produced convergence problems due to the initial onset of micro cracking and premature failure of the global model under tension. Therefore some sensitivity models were run in order to deduce a correct tensile material property that could be used in the global model.

The model built for testing the concrete properties was a solid cylindrical specimen of 150mm in diameter by 300mm long. A pressure was applied to one end of the cylinder with the other end being fixed in the axial degree of freedom. This put the concrete specimen under uniaxial tension.

The material properties, which give rise to the failure of the concrete within the global model, are the tension stiffening and the tension damage parameters. The tension stiffening can be controlled by various different means as stated previously. It can be controlled either by the fracture energy or by specifying the stress-strain or stress-displacement curves.

All three approaches for modelling the tension stiffening were considered and data implemented from the uniaxial tensile tests on the concrete specimens. Firstly the strain approach was adopted and this proved that failure of the concrete occurred too early due to the initial yield stress being too low and complete cracking of the concrete had occurred before 0.6MPa. With increased tensile strength at a value of 4.4 N/mm^2 the model ran much further before running into convergence problems.

Secondly the fracture energy approach was adopted and an average value from the material test data of 0.121 N/mm was used. This was checked against values from the CEB-FIP Model Code 1990 and was found to be a reasonable value if not a little too high for the

aggregate size (10mm) being used. The code gave a value of approximately 0.11 N/mm. The fracture energy approach once again produced convergence problems at a low pressure and complete failure occurred at approximately 0.5 MPa.

Finally the stress versus displacement approach was tested, again using data from the material tests. This approach gave complete failure of the concrete to be at around 0.52Mpa even with an increased yield of 4.4MPa.

The reason for the increased yield stress for the concrete was to take into account the effect of the steel rebar within the concrete, which would delay the initial onset of micro cracking.

The tension damage option as explained previously must be used in order to simulate the complete failure of the concrete. If this option is not used then as the concrete passes its ultimate stress and proceeds into the plastic region, it will continue behaving as a plastic material and not fail completely.

In conclusion to the sensitivity studies the tension stiffening was defined by the stress-strain approach. The compression hardening was also defined by the stress-strain approach.

Using the stress-strain approach gave the best results for comparison with the LST and the previous analysis using the ANAMAT concrete material model.

The final material properties used in the analysis are given in Table 6.

7 LST ANALYSIS RESULTS

The finite element model data as presented in Figures 17 to 71 have the initial values reset as to line up with the Limit State Test Results.

7.1 COMPARISON WITH TEST DATA – GLOBAL DISPLACEMENTS / STRAINS

Figures 17 to 71 are the comparison of the new ABAQUS 6.4 global model against the LST test data. As the concrete material model is relatively new, it was decided that the previous analysis using the ANAMAT concrete material model would also be included in this comparison.

The other reason for this is that after reviewing the data from both of these analyses, the final deformed shape is different. The model using the ABAQUS concrete material shows its maximum displacement at the equipment hatch location, whereas the ANAMAT material model shows it to be on the 0^o azimuth at an elevation of 7.73m. The location of maximum displacement as exhibited by the ANAMAT model agrees with the failure location of the SFMT test. The difference in location can be seen in Figures 72 and 73 for the ANAMAT and ABAQUS respectively. Even with the above differences, the ABAQUS V6.4 analysis gives a better agreement for the initial state of the model. This could be due to the updated elastic material properties that are the latest test data supplied. This is discussed further in section 8.1.

7.2 CALCULATION OF LIMIT LOAD

The limit load is determined by the inability of the vessel to retain pressure and this is dependent on the integrity of the steel liner. The steel liner has low ductility at the welded locations, where an average rupture strain of 22% was observed in the original tests performed on the liner material. More recent test data shows that the actual rupture strain was more likely to be in the region of 6%.

From the global model high localised strains were found to be present at the locations where junctions between thick insert plates and the thinner Liner plate. These are at the airlock and equipment hatch and main steam feed penetrations. The junction of the two plates at the equipment hatch was examined using a local 2D plate model as described in Ref 8 and the model mesh can be seen in Figure 74 and the plastic strains can be seen in Figure 75. The equivalent plastic strains can be seen in Figures 76 and 77 for the ANAMAT and the ABAQUS analyses respectively. Previously the model showed that a free field strain of 3% gave rise to an 11% strain at the thick/thin plate junction. Now with the test data showing the rupture strain to be 6% the strain in the free field only needs to reach 1.5%. Figure 78 shows the response of the liner at location 44 for the meridional strain. This gives a limit load range of approximately 1.2 to 1.4Mpa, which compared with the pressure of 2.5Pd (1.0Mpa) when substantial leakage was observed during the LST.

8 ASSESSMENT OF RESULTS

The primary objective of this phase of the ISP is to present the results from the LST analysis of the PCCV utilising the information presented in SNL's test report (Ref. 3). This ensures all participants in the ISP are using the same data. This section presents NNC's results. Comparisons are also made with the test data and results reported for the post-test analysis of the PCCV reported in reference C6635/TR/001.

8.1 ELASTIC RESPONSE OF VESSEL

Figures 17 to 31 present the displacement histories for locations 1 to 15 during the LST pressurisation. Comparing the test and analytical results highlights two facets of the vessel response.

At internal pressures up to 0.6MPa, the vessels response remains essentially elastic. At 0.6MPa concrete cracking is initiated (see. section 8.2) and an increasing non-linear response can be seen. The non-linear response increases up to the LST limit of 1.3MPa. This is caused by crack progression in the concrete and yielding in some regions of the steel liner as the pressure increases. The response of the vessel over the LST pressure range is predicted by both analysis models and is confirmed by the test. Complete failure of the vessel is not achieved.

As Figures 32 to 71 have been reset at the beginning of the test we cannot see the original offset between the two finite element models and the Limit State Test results. However, the ABAQUS v6.4 results demonstrate that at the beginning of vessel pressurisation the initial conditions obtained from the analysis correspond well with the test data. This is a significant improvement on the results predicted by the ANAMAT analysis. Previously, the difference in initial conditions between the test and ANAMAT results was attributed to shrinkage and creep effects in the concrete (Ref 4). These effects had not been fully captured in the analysis. However, the primary difference between the ANAMAT and the ABAQUS v6.4 analyses are the values of the concrete material elastic constants Young's modulus (E) and Poisson's ratio (ν), as discussed in section 5.1. This would indicate that the elastic properties have a significant influence on the initial conditions predicted by analysis, whilst also retaining the global elastic response of the vessel.

8.2 ASSESSMENT OF CONCRETE CRACKING

The ABAQUS 6.4 analysis confirms crack initiation in the concrete occurs at 0.6MPa. This is predominantly in the vertical direction and local to the intersection of the cylinder wall and buttresses. Figure 79 highlights the areas of damaged concrete from the analysis. As the vessel is pressurised, the inner surface of the wall experiences tension caused by local bending about the buttresses. The deformed shape of the cylinder, presented in Figure 80, highlights this. These analytical results are in close agreement with the test results. Figure 81 presents output from the acoustic monitoring system used for the LST test. This confirms a number of cracks are initiated local to the wall buttress at the 270^0 azimuth at a pressure of approximately 1.5 Pd (0.59MPa).

8.3 ASSESSMENT OF LINER TEARING

Section 7.2 highlights that liner tearing is initiated at the junction of the thick insert plates and steel liner local to the wall penetrations. Figure 77 shows the areas of high liner strain in these regions. The analysis estimates tearing in the pressure range 1.2 to 1.4MPa. The inspection results of the liner after the LST test presented in Figure 82, confirm the largest liner tear local to the equipment hatch penetration. However, tearing occurs at a pressure of 1.0MPa (2.5 Pd). The difference in the predicted and test pressures are attributed to variations inherent in the vessel construction. The analytical pressure calculated is based on a rupture strain of 6% for the welded liner. This is obtained from tensile tests of liner specimens conducted after the model testing (Ref 5). The number of specimens tested was limited and variations in the results obtained can be expected throughout the actual structure.

8.4 ASSESSMENT OF TENDON RESPONSE

Figure 83 presents a plot of the displaced shape of the PCCV vertical tendons at a pressure of 1.4MPa. This figure also presents the axial stress distribution in each tendon. As expected, it is observed that the tendon displacements follow the wall radial displacements. Also as would be expected, the highest loaded tendons occur in the free-field region adjacent to the 0^o azimuth. This is the location of the wall experiencing the largest radial displacements. An axial stress of approximately $1419N/mm^2$ is calculated for these tendons. This is less than the yield stress of $1741N/mm^2$. Stress concentrations are seen in the tendons surrounding the wall penetrations. This is due to the reduced length of these tendons in the analysis, which are restrained axially local to the openings.
Inspection of Figures 64 to 71 indicates that none of the vertical or horizontal tendons break during the LST.

9 CONCLUSION

Conclusions from the analysis of the LST, utilising the data supplied for the ISP are summarised as follows: -

(i) Catastrophic structural failure of the PCCV does not occur in the LST pressure range.

(ii) Excessive leakage rate due to liner tearing is predicted as the limiting fault for the test. Initiation of liner tearing is predicted in the range 1.2 to 1.4MPa.

(iii) The location of liner tear at the insert plate junction predicted by analysis is confirmed by LST.

(iv) Concrete cracking is first observed at a pressure of 0.6MPa on the inner surface of the cylinder walls, local to the buttresses.

(v) The values of elastic material constants used for analysis are influential in predicting initial conditions for the containment. This is demonstrated in the ABAQUS v6.4 analysis for which closer correlation with the test results is seen. Good correlation is also obtained for the linear/elastic range of the response.

(vi) Tendons do not yield during the LST.

(vii) The concrete material modelling facility in ABAQUS v6.4 now offers a viable package for analysis of failure modes in concrete structures.

10 PROPOSALS FOR PHASE 3

Two objectives are proposed for phase 3 of the ISP.

- To assess issues relating to the translation of the LST test results to a full size structure.
- Evaluate the effects of elevated temperatures on the failure mode and limit load of the containment.

The way forward is to be discussed at a meeting of the participants, scheduled for March 2004. Issues pertinent to those discussions are summarised in sections 10.1 and 10.2. Section 10.3 is specific to discussing creep issues at elevated temperatures.

10.1 ASSESSMENT OF FULL SIZE CONTAINMENTS

The LST results are all specific to the ¼ scale model. A fundamental issue associated with testing models is with what confidence can the failure mode obtained be expected to occur in full size containments.

It is important to recognise that some physical parameters, such as gravity and friction, cannot be scaled and may have a disproportionate effect on the results from the test. For example, preload losses in the tendons caused by friction interaction with the vessel wall are known to be significant. Friction is a physical constant so will losses in the test model be proportionally higher than for full size containments? Gravity is another physical constant. Are its effects more influential on the smaller test model or full size containments? How significant are the preload losses due to tendon anchorage at the seatings and how is this affected by scaling?

Fabrication issues relevant to construction may also affect the failure mode predicted. This is particularly applicable to the liner. The liner for the LST model is 3mm thick and welding such a thin plate is fraught with problems. For example, are the residual stresses and heat-affected zone disproportionately high compared to a full size vessel? Also, can construction tolerances be scaled and are those for the test model achievable in reality? In full size containments these issues may not be as significant and liner tearing may occur at higher pressures to that predicted by the test. This may result in a different initiating fault for the full size containment to that predicted by the model.

These parameters should be debated and conclusions drawn as to how the response of full size containments may be different.

10.2 DEFINITION OF THERMAL LOADING.

Common approaches for calculating thermal distributions using numerical analysis include nodal mapping of temperatures and heat transfer analysis. Both options provide a temperature profile throughout the structure for transient heating/cooling cycles and steady state conditions.

Nodal mapping requires the specification of a temperature at each node in the FE model. Temperatures are specified for the initial condition of the structure and the elevated condition at steady state or each increment of a transient. Thermal strains are calculated from the temperature differentials. The mapping is mesh sensitive and may not be directly

applicable to a pre-existing model. To alleviate this discrepancy, a post-processing routine would be required for interpolation of the temperatures to a model with a different mesh.

Heat transfer analysis offers a more generic approach. All aspects of thermal behaviour can be replicated, whether it is conduction, convection or radiation. A key aspect of this approach is that the analysis is not mesh dependant. The thermal behaviour is defined in terms of heat transfer coefficients, boundary temperatures and concentrated heat fluxes. For these reasons, heat transfer would be the preferred analysis method to adopt in Phase 3. However, it will require detailed definition of the thermal properties and thermal boundary conditions.

For any thermal cycle the inertias associated with the components of a PCCV will result in different responses at different times. The liner is a thin shell and will expand quickly in response to increasing temperature. It is therefore more susceptible to localised high compressive strains during the heat up phase. Thermal expansion of the liner may also delay liner rupture when internal pressure is applied. Peak temperatures are achieved at steady state. During the cool down phase the concrete is susceptible to cracking induced by tensile strains. The ISP meeting must therefore assess which aspect of the PCCV's response is considered important when defining the thermal analysis for Phase 3.

10.3 CREEP BEHAVIOUR AT ELEVATED TEMPERATURES

The results from the LST analysis indicate that the material elastic constants used for the analysis are a major influence on the initial conditions and linear response of the vessel. However, containments are required to withstand high temperature fault conditions. Under such conditions redistribution of stress due to creep behaviour in the concrete and steel components can be expected. This could influence the containments integrity at elevated temperatures.

11 REFERENCES

Ref Title

1 International Standard Problem on Containment Capacity (ISP48), Working Group on Ageing of Concrete Structures (IAGE/CONCRETE), CSNI Proposal, IAGEWG(2002)15, Rev 0, June 2002

2 HSE/NNC Pretest Analysis Report for ¼ Scale PCCV Model, NNC Report C5769/TR/002.

3 Pretest Round Robin Analysis of a Prestressed Concrete Containment Vessel, Sandia National Lab., NUREG/CR-6678, SANDE 00-1535, August 2000

4 HSE/NNC PCCV Round Robin Post Test Analysis, NNC Report C6635/TR/001, Issue 01, Dec 2002

5 Overpressurisation Test of a 1:4 Scale Prestress Concrete Containment Vessel Model, Sandia National Lab., NUREG/CR-6810, SAND2003-0840P, Project Report No. R-SN-P-010, March 2003

6 ABAQUS/Standard, ABAQUS/CAE, ABAQUS/Viewer, ABAQUS Inc., USA

7 ANACAP-ANATECH Concrete Analysis Program Users Guide, ANATECH Research Corp., USA

8 HSE/NNC Pretest Analysis Report for ¼ Scale PCCV Model, NNC Report C5769/TR/004.

9 Obayashi Corporation package of construction drawings of PCCV model

10 Sandia National Laboratory PCCV Design Package, Material Properties Report

12 NOTATION

α	Coefficient of thermal expansion
β	Azimuth angle
ε_0	Initial strain (creep + shrinkage)
ε	Strain
σ	Stress
σ_c	Compressive Yield Stress
σ_{cu}	Ultimate Compressive Yield Stress
σ_t	Tensile Yield Stress
μ	Coefficient of friction
E	Young's modulus
E_0	Initial Young's modulus
L	Length of tendon
P1, P2	Tension loads at the tensioning ends
Pd	Design pressure = 0.39MPa
T	Temperature

12.1 ABBREVIATIONS

FE	Finite Element
LST	Limit State Test
PCCV	Pre-stressed Concrete Containment Vessel
SFMT	Structural Failure Mode Test
SNL	Sandia National Laboratories

Table 1 Original and updated Young's Modulus

Component [Abaqus Version]	Young's modulus (N/mm^2)
All [V5.8] (original)	27950
Basemat [V6.4]	26973
Dome [V6.4]	28270
Cylinder [V6.4]	25831

Table 2 Original and updated Density

Component [Abaqus Version]	Density (tonne/mm^3)
All [V5.8] (original)	$2.21 * 10^{-9}$
Basemat [V6.4]	$2.19 * 10^{-9}$
Dome [V6.4]	$2.20 * 10^{-9}$
Cylinder [V6.4]	$2.14 * 10^{-9}$

Table 3 Original and updated Poisson's Ratio

Component [Abaqus Version]	Poisson's Ratio
All [V5.8] (original)	0.180
Basemat [V6.4]	0.214
Dome [V6.4]	0.217
Cylinder [V6.4]	0.218

Table 4 Original and updated Compressive & Tensile Strength for cylinder wall

Material Property [Abaqus Version]	Value (N/mm^2)
Compressive Strength [V5.8] (original)	24
Tensile Strength [V5.8] (original)	4.4
Compressive Strength [V6.4]	55.86
Tensile Strength [V6.4]	2.06

Table 5 Anchorage properties

Description of Spring	Stiffness (N/mm)
Liner tensile pull-out stiffness	3890000
Liner shear stiffness	1820000
Penetration lining anchor	581000

Table 6 Material properties for the ABAQUS Version 6.4 analysis

Material Property	Dome	Cylinder	Basemat
Young's Modulus (N/mm^2)	$2.8358 * 10^4$	$2.58 * 10^4$	$2.758 * 10^4$
Poisson's Ratio	0.217	0.218	0.214
Density ($tonne/mm^3$)	$2.258 * 10^{-9}$	$2.1458 * 10^{-9}$	$2.1958 * 10^{-9}$
Concrete Damaged Plasticity (dilation angle,,,,viscosity)	35.0,,,,0.001	35.0,,,,0.001	Not Used*
Concrete Compression hardening (yield stress, inelastic crushing strain)	42.4,0.00 59.64,0.00099	42.4,0.00 59.64,0.00099	Not Used*
Concrete Tension Stiffening (direct stress post cracking, direct strain)	4.4,0 0.04458,0.006058	4.4,0 0.04458,0.006058	Not Used*
Concrete Tension Damage (tensile damage variable, direct strain)	0,0 $0.99,6.058 * 10^{-3}$	0,0 $0.99,6.058 * 10^{-3}$	Not Used*

NB: Stress in MPa

* Items marked as Not Used are due to the material properties for these components being linear.

Figure 1 Standard Output Locations

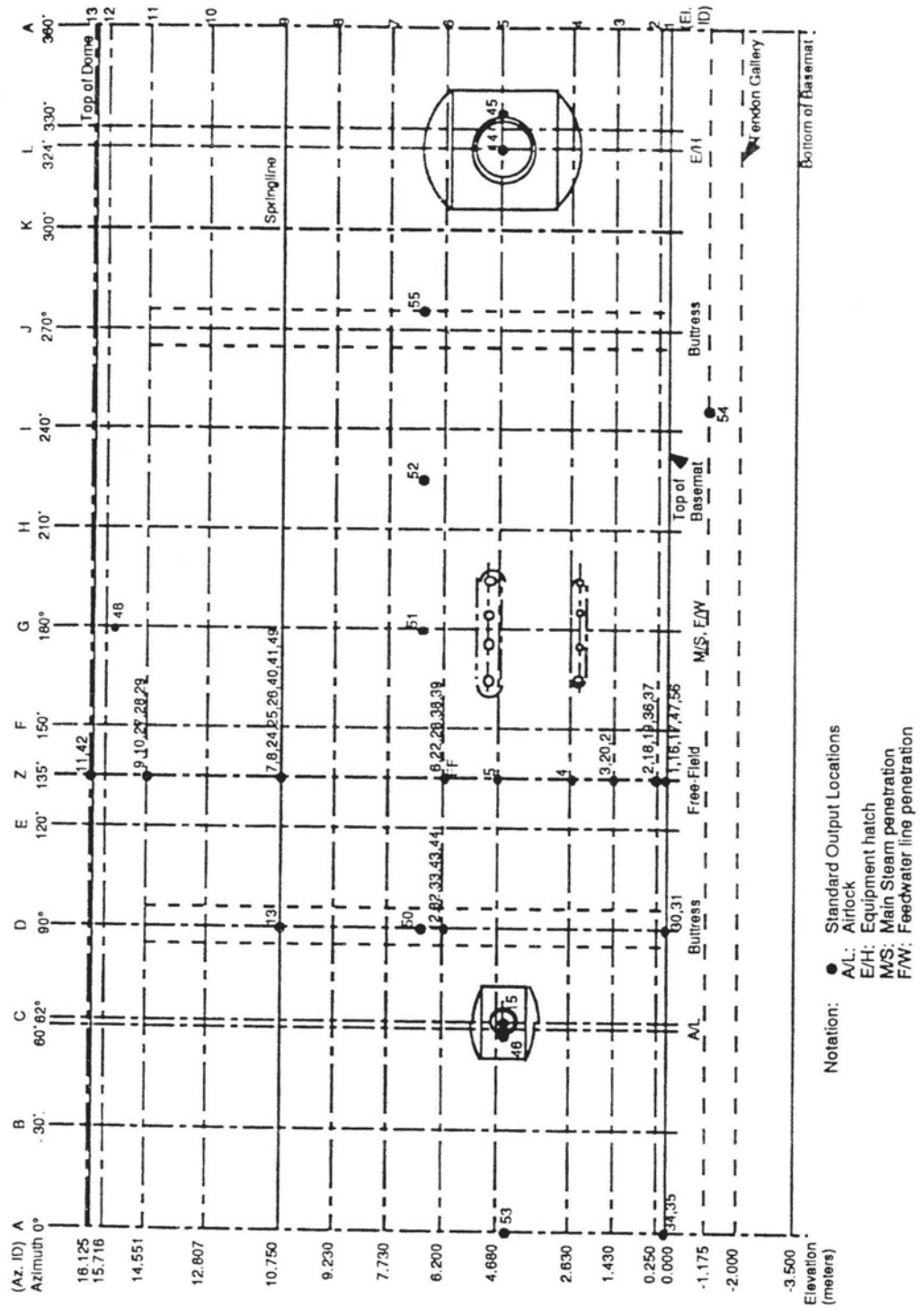

Figure 2 Finite Element Representation of the PCCV

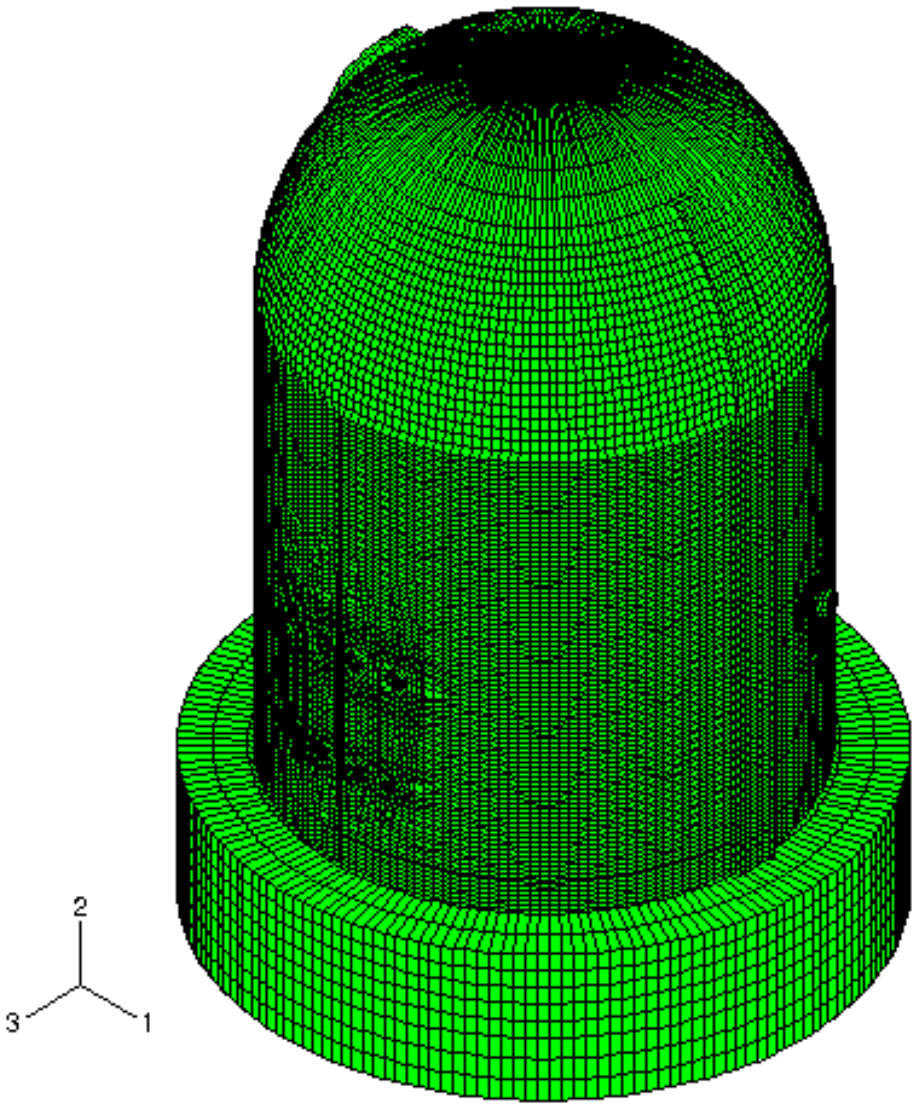

Figure 3 Detail view of the PCCV dome model

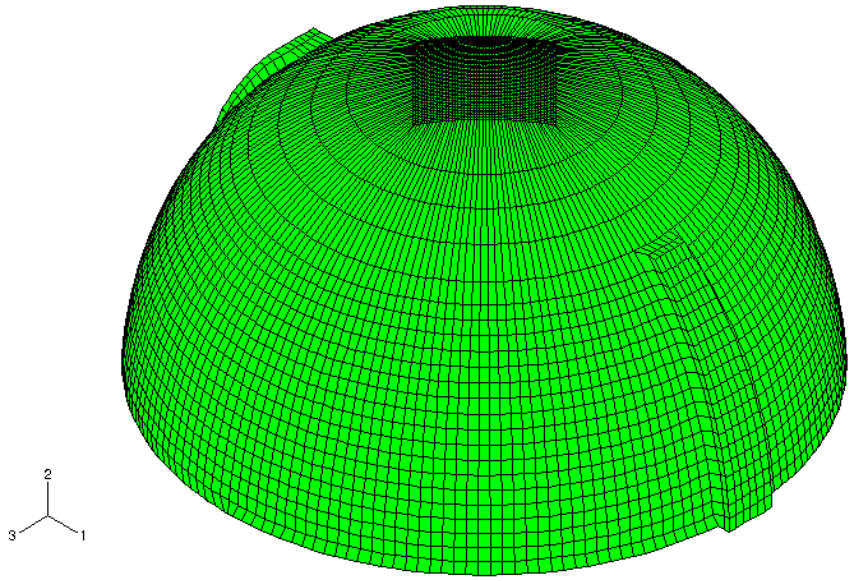

Figure 4 The basemat model showing locations of global restraints

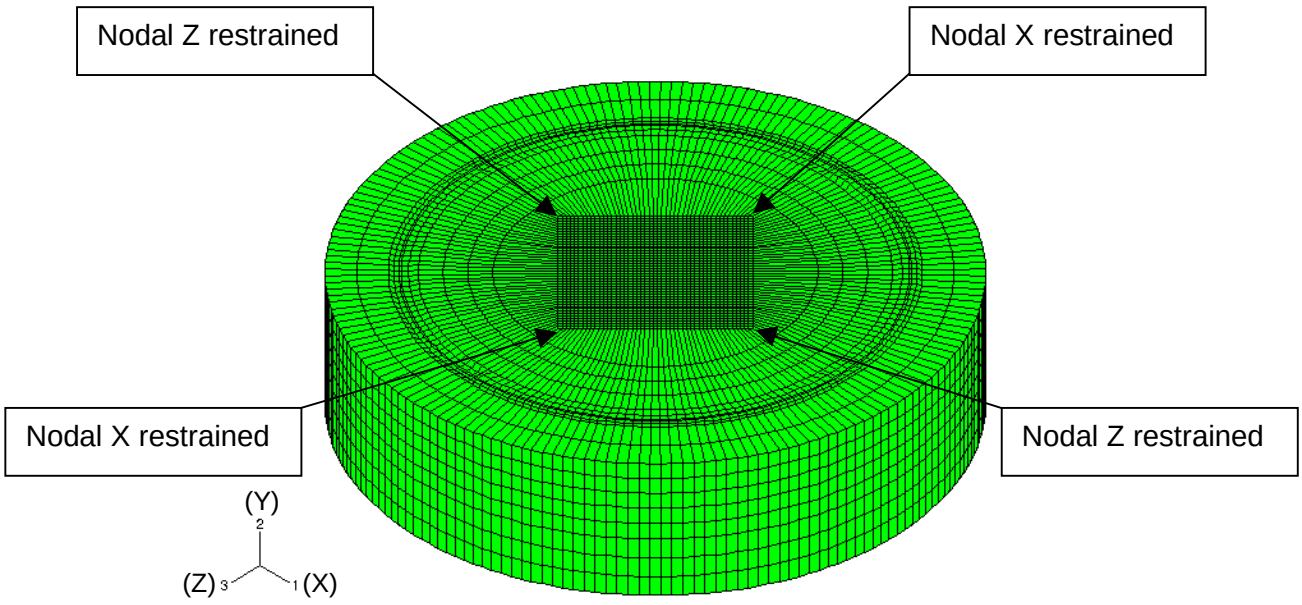

Figure 5 Detailed view of the equipment hatch penetration model

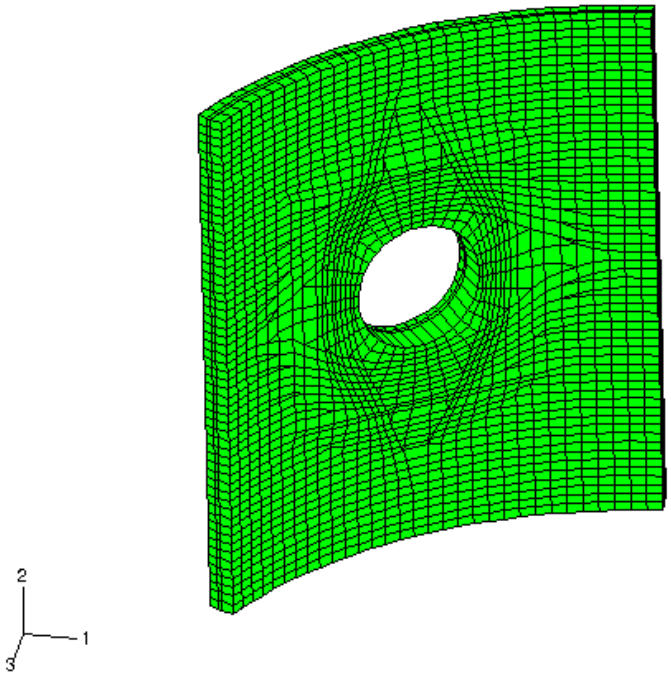

Figure 6 Detailed view of the airlock penetration model

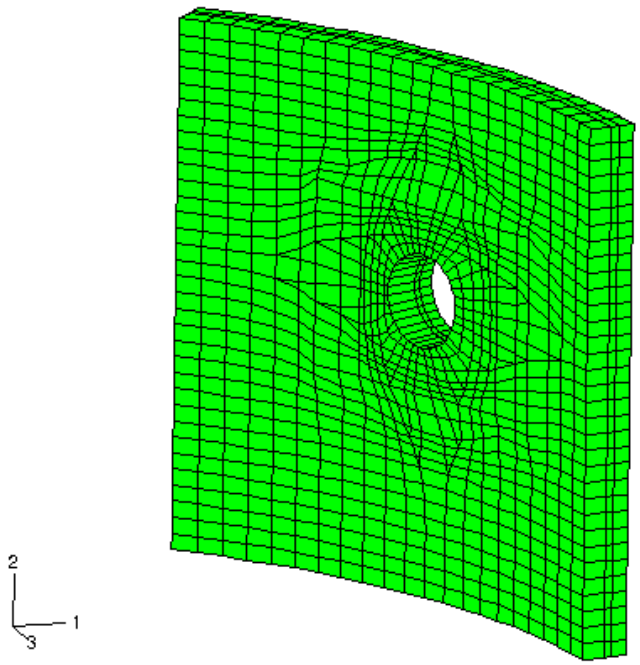

Figure 7 Detailed view of the main steam and feed water penetration model

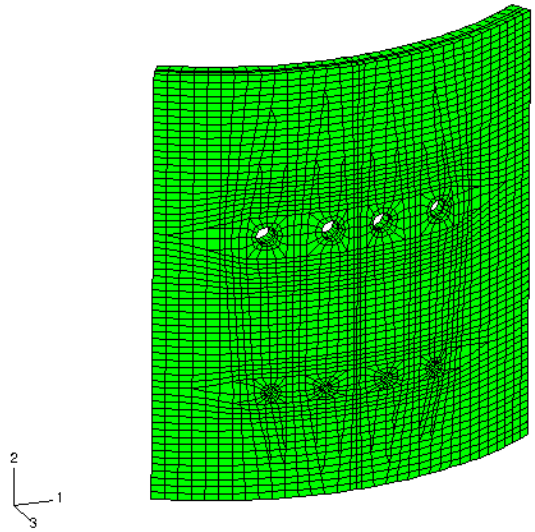

Figure 8 PCCV vertical tendons model

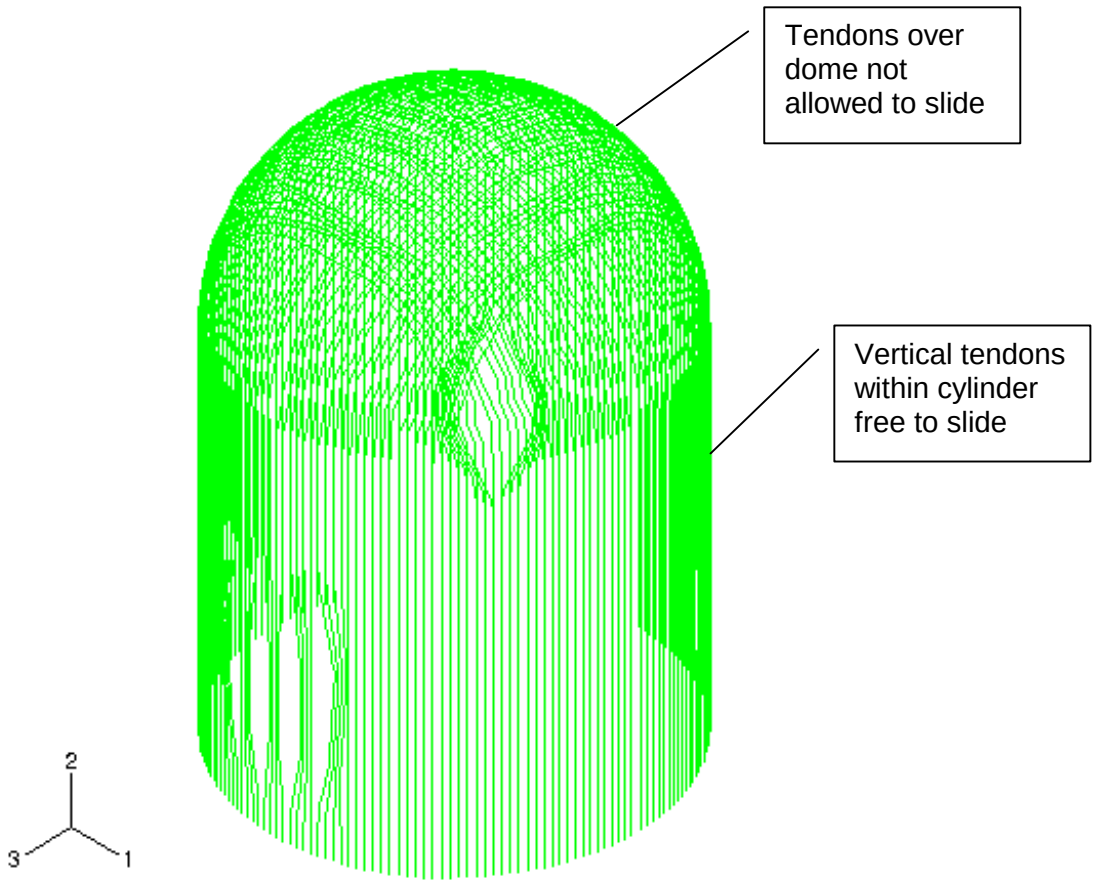

Figure 9 Equipment hatch penetration lining and cover plate

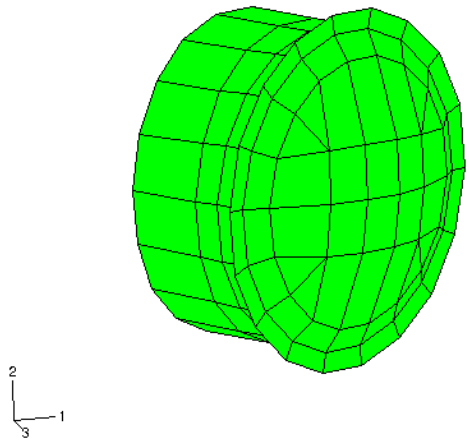

Figure 10 PCCV model supported on soil springs

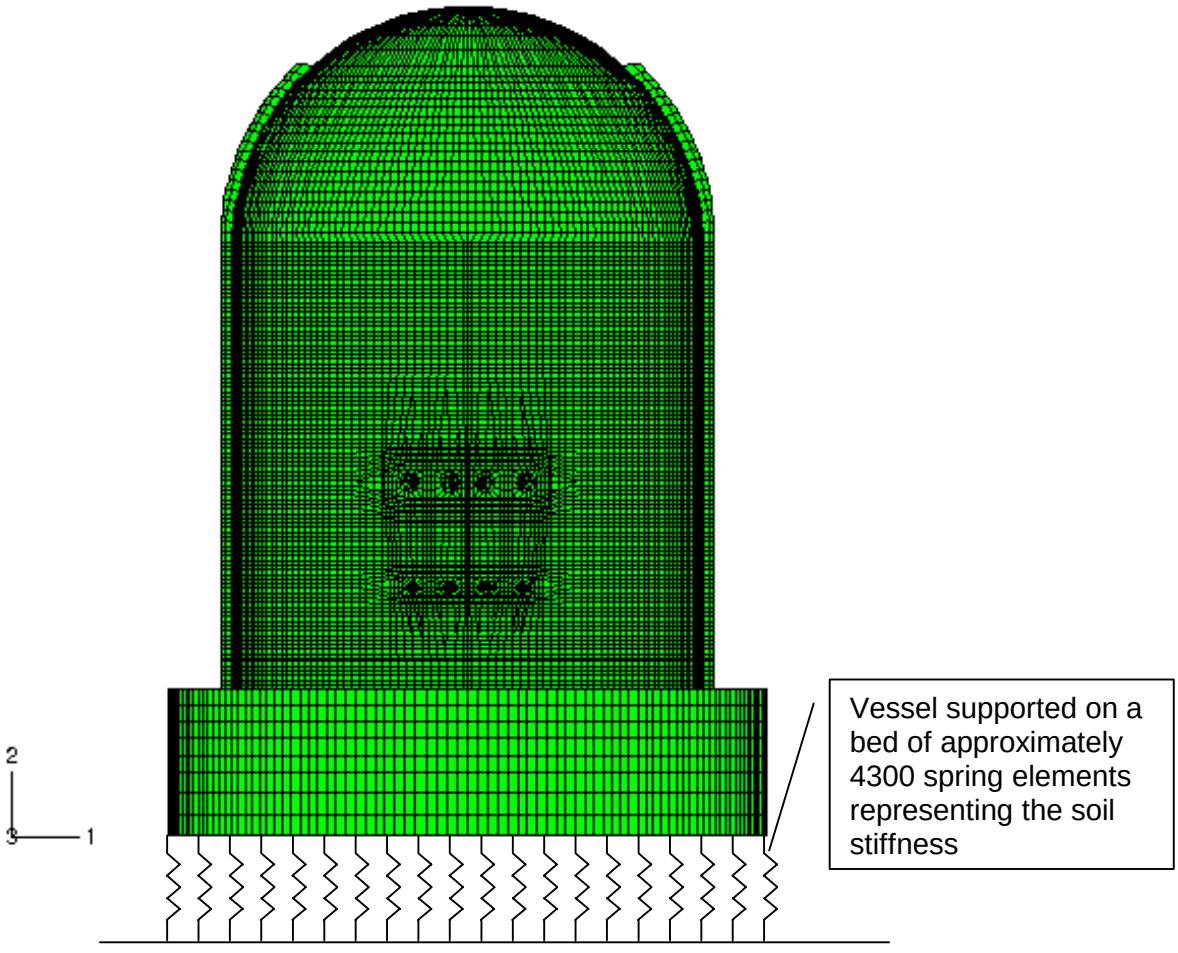

Figure 11 Internal liner model, showing detail around the main steam and feedwater penetrations

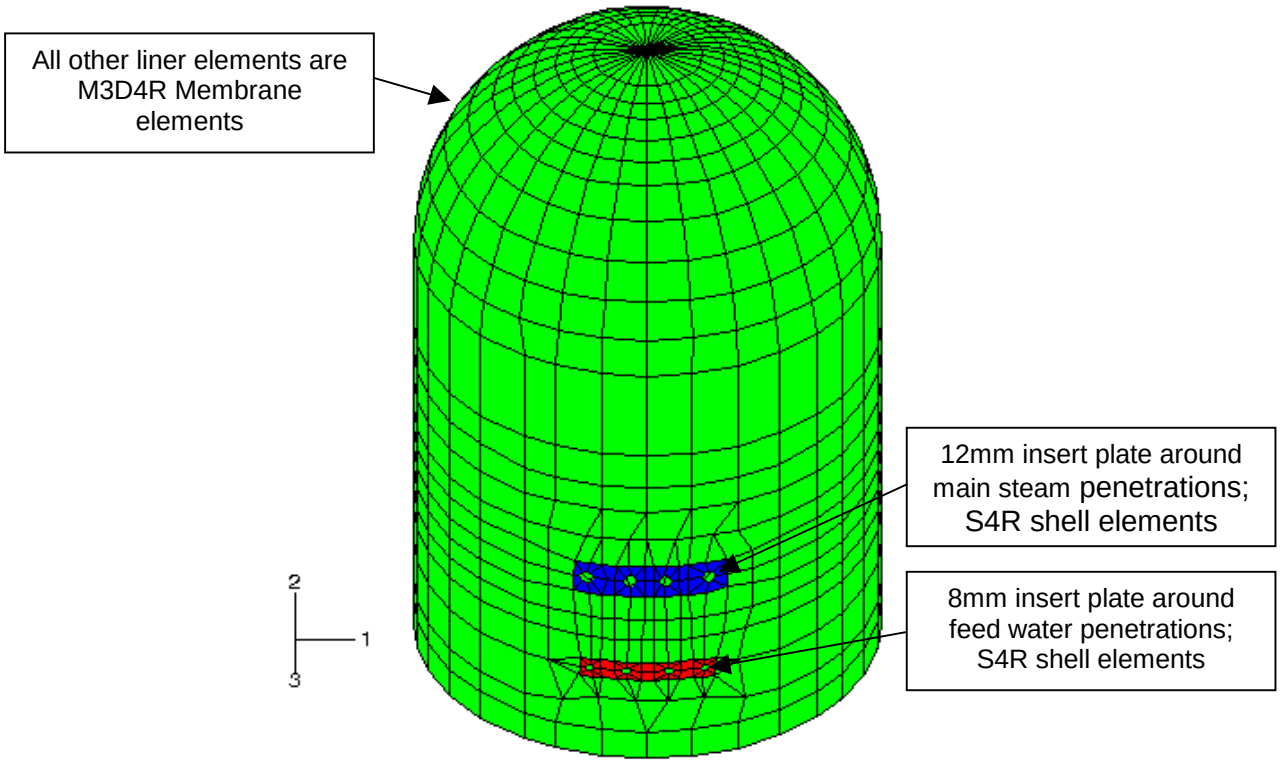

Figure 12 Comparison of Test & Pre-test Vertical Tendon Loads

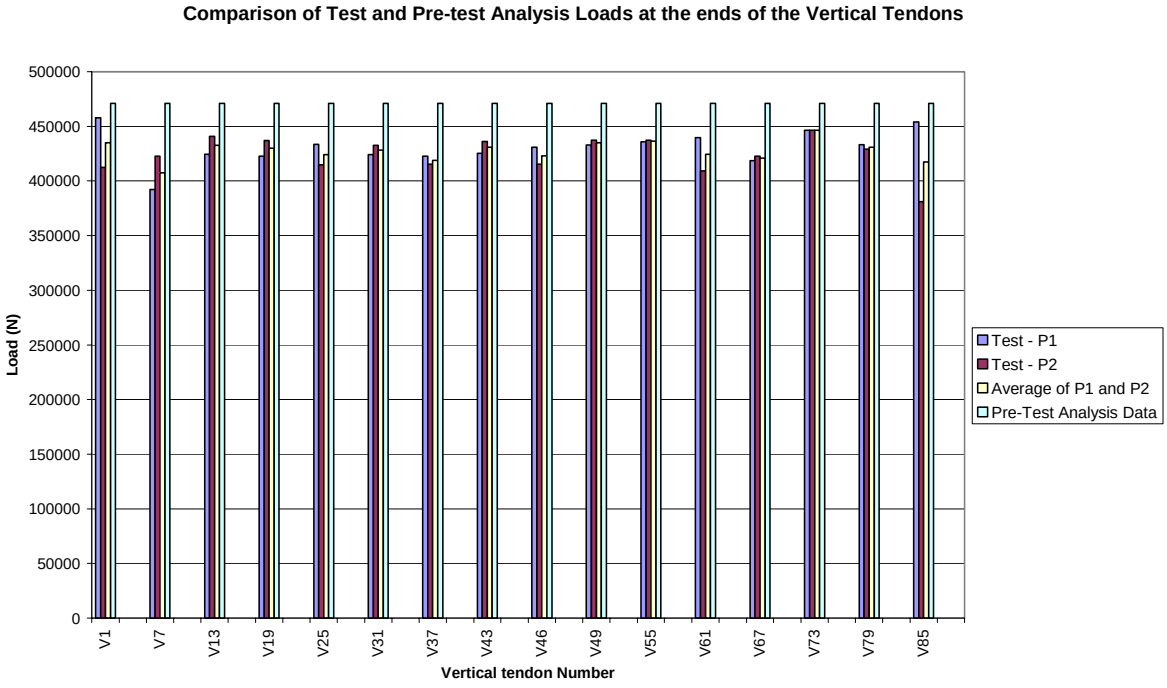

Figure 13 Comparison of Test & Pre-test Hoop Tendon Loads

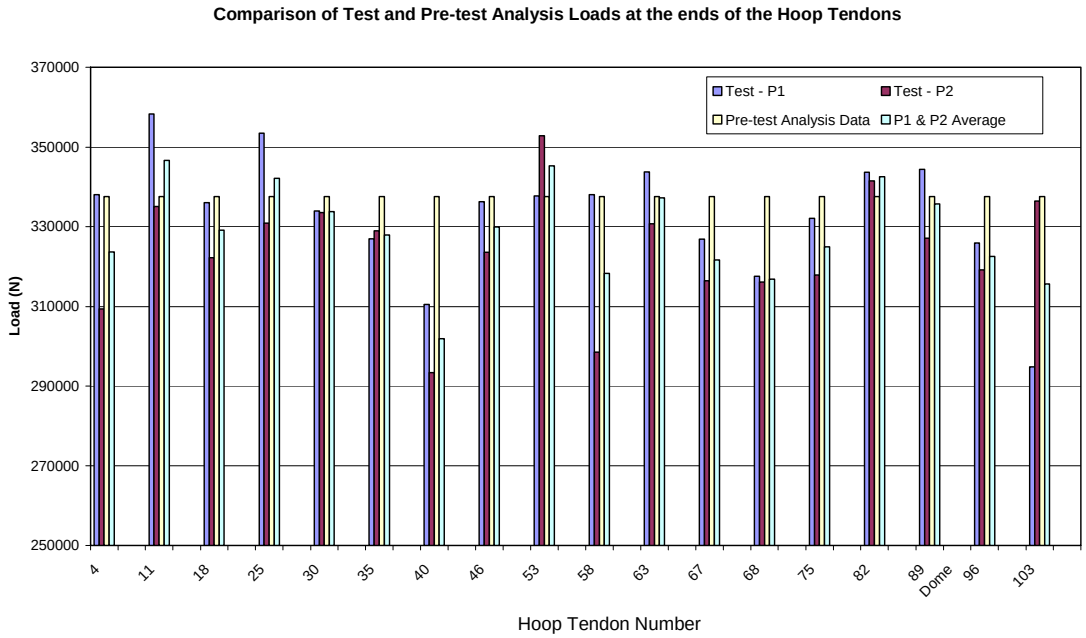

Figure 14 Variation in tendon load due to friction and seating loss

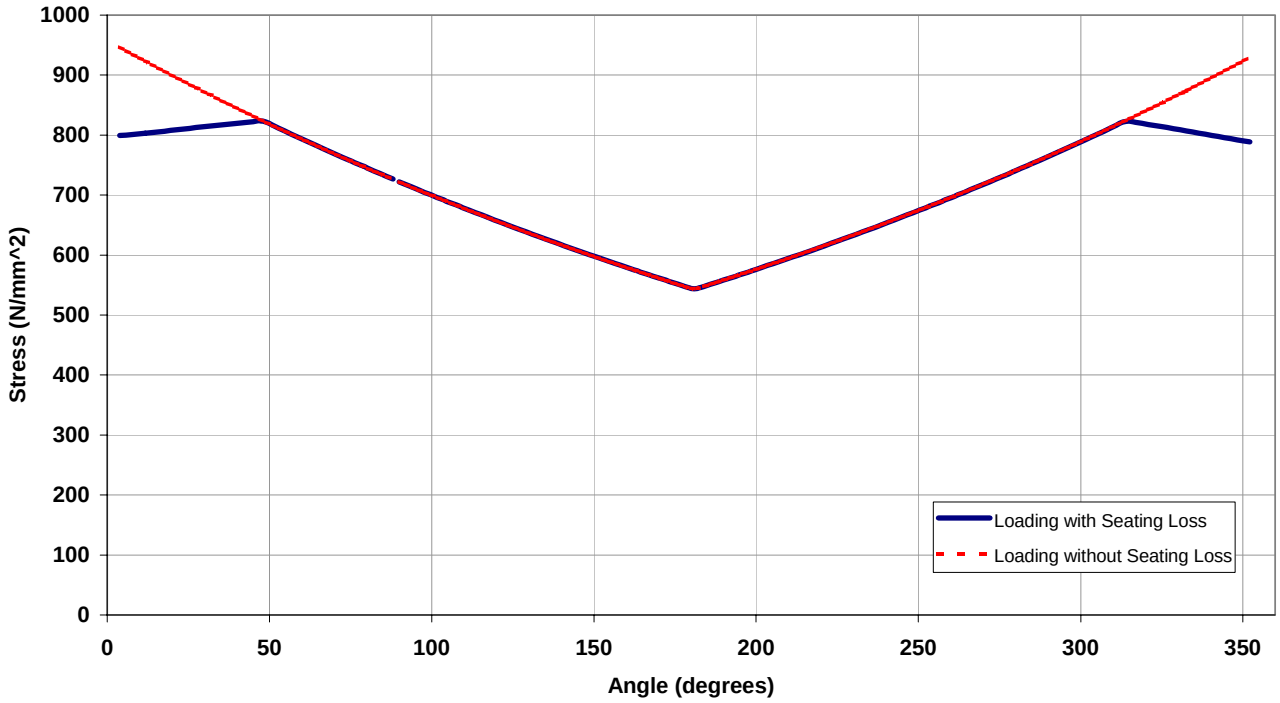

Figure 15 Stress-Strain Tension Stiffening Relationship

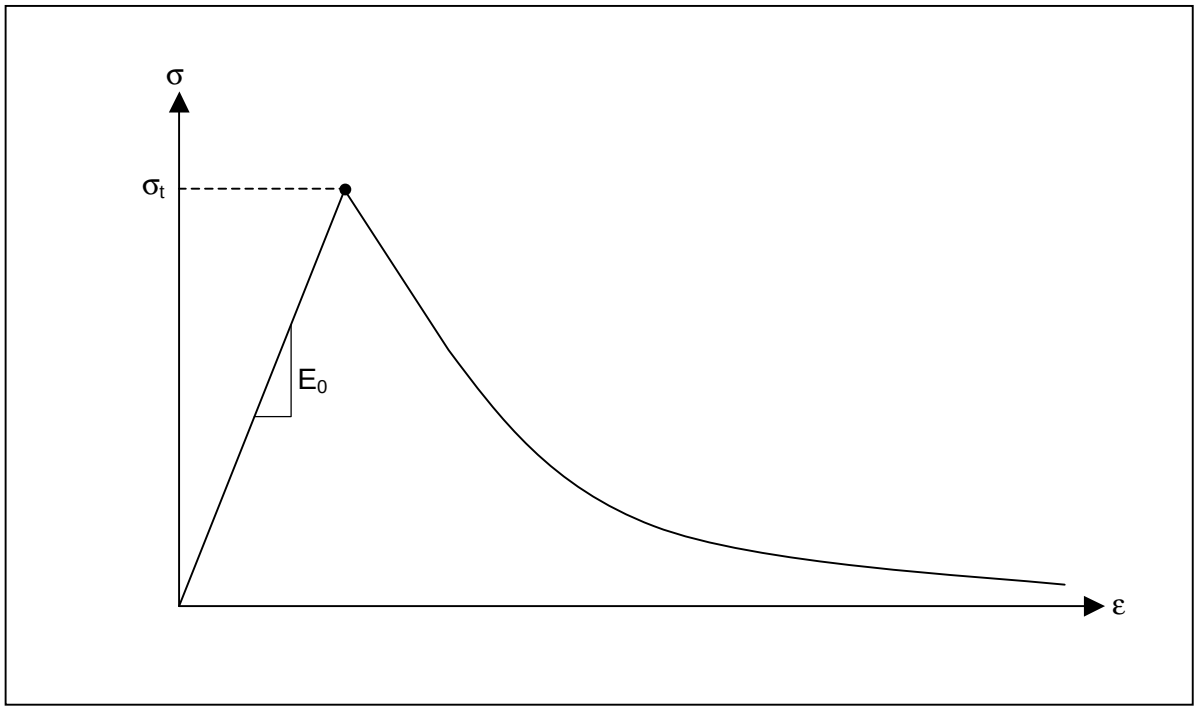

Figure 16 Stress-Strain Compression Hardening Relationship

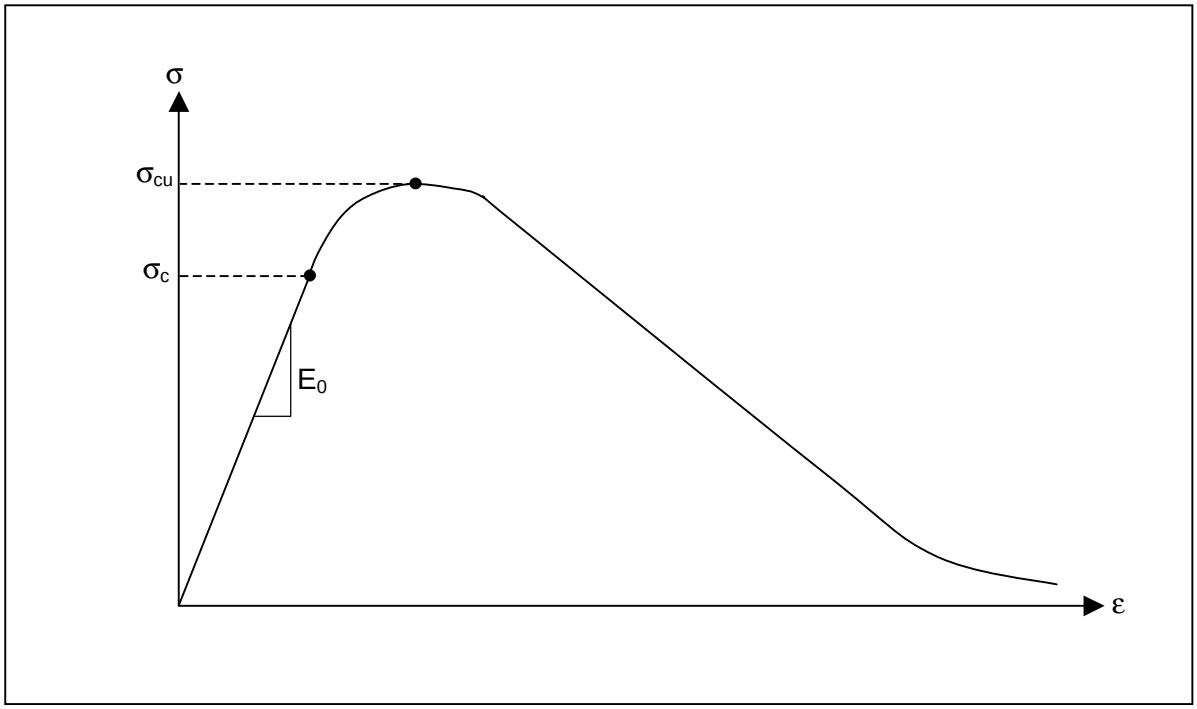

Figure 17 Location 1 Vertical Displacement

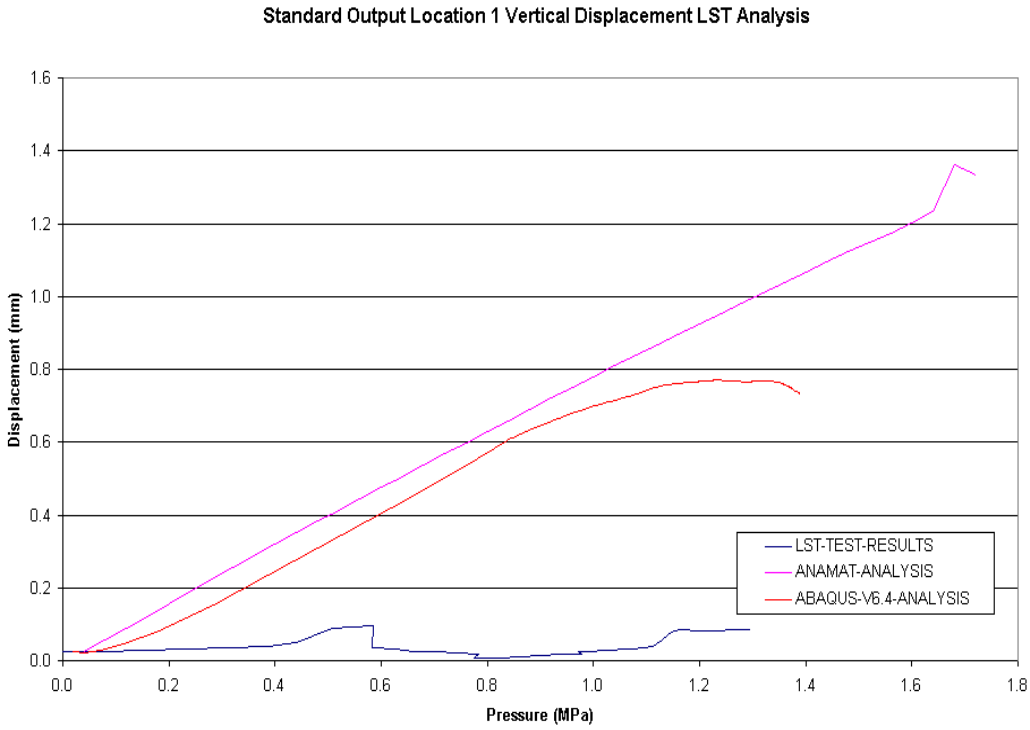

Figure 18 Location 2 Radial Displacement

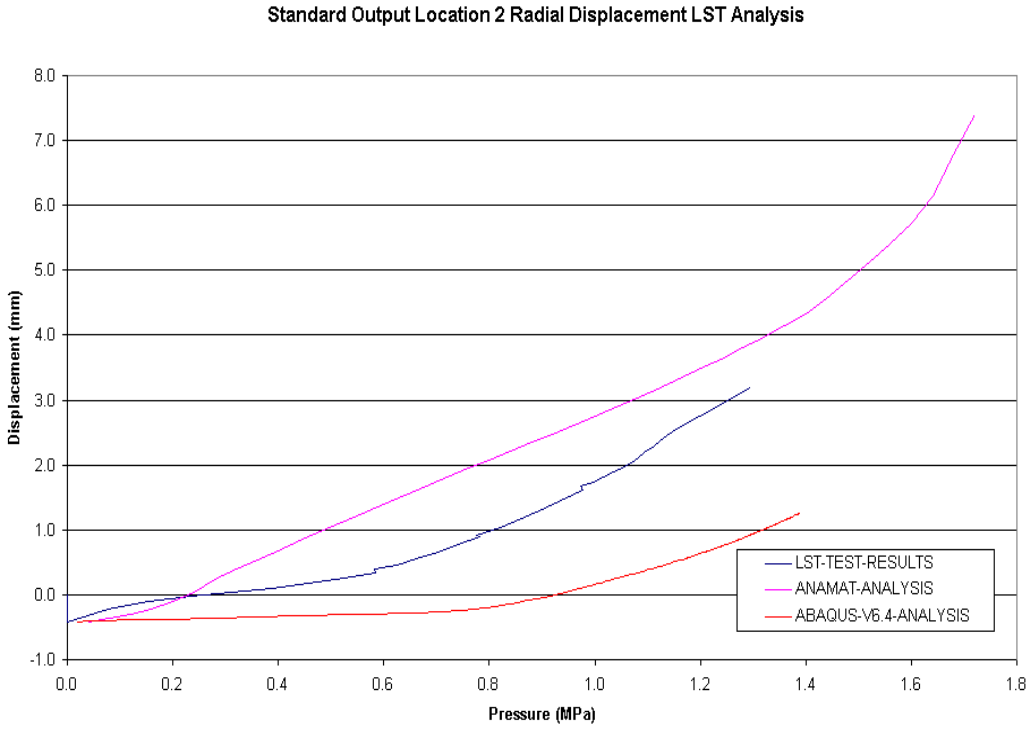

Figure 19 Location 3 Radial Displacement

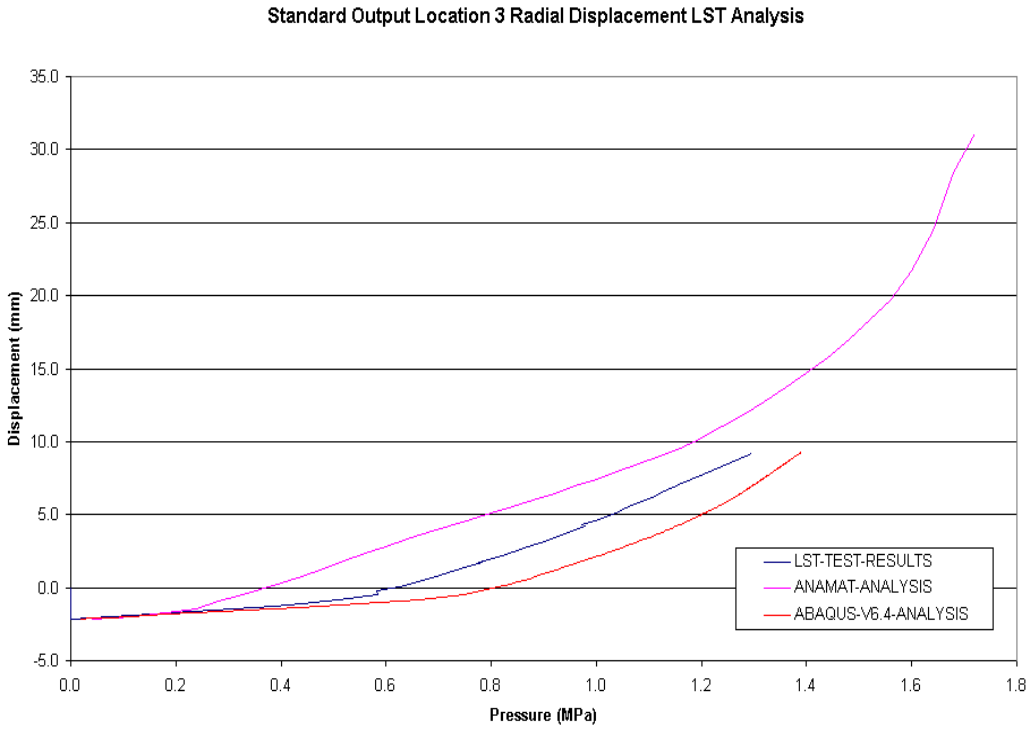

Figure 20 Location 4 Radial Displacement

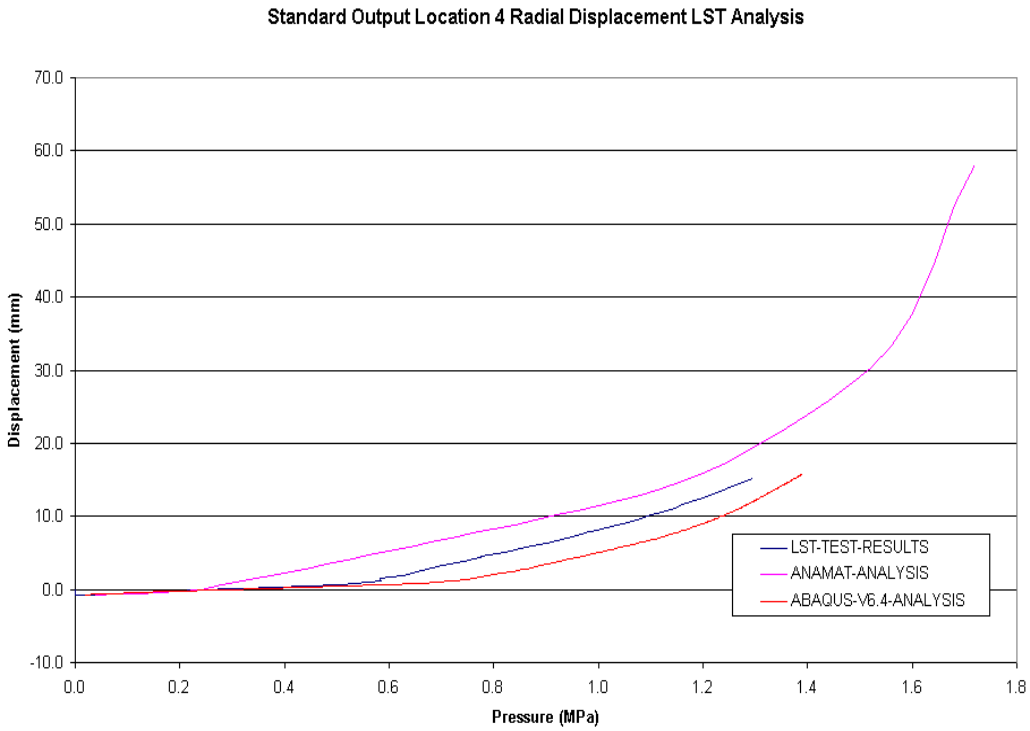

Figure 21 Location 5 Radial Displacement

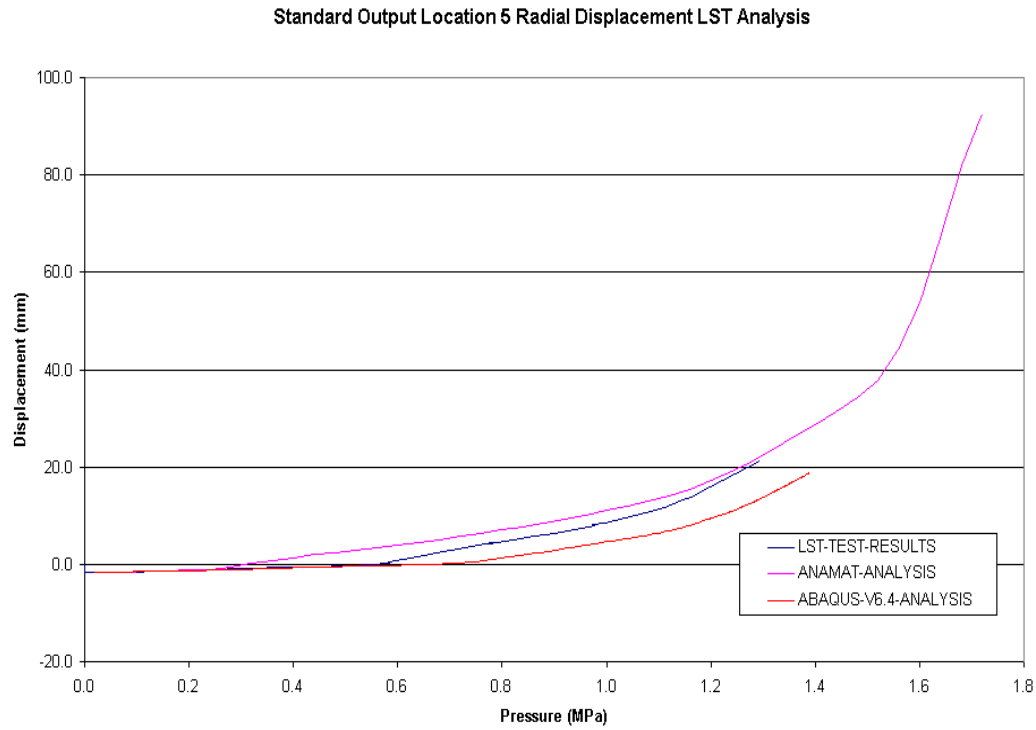

Figure 22 Location 6 Radial Displacement

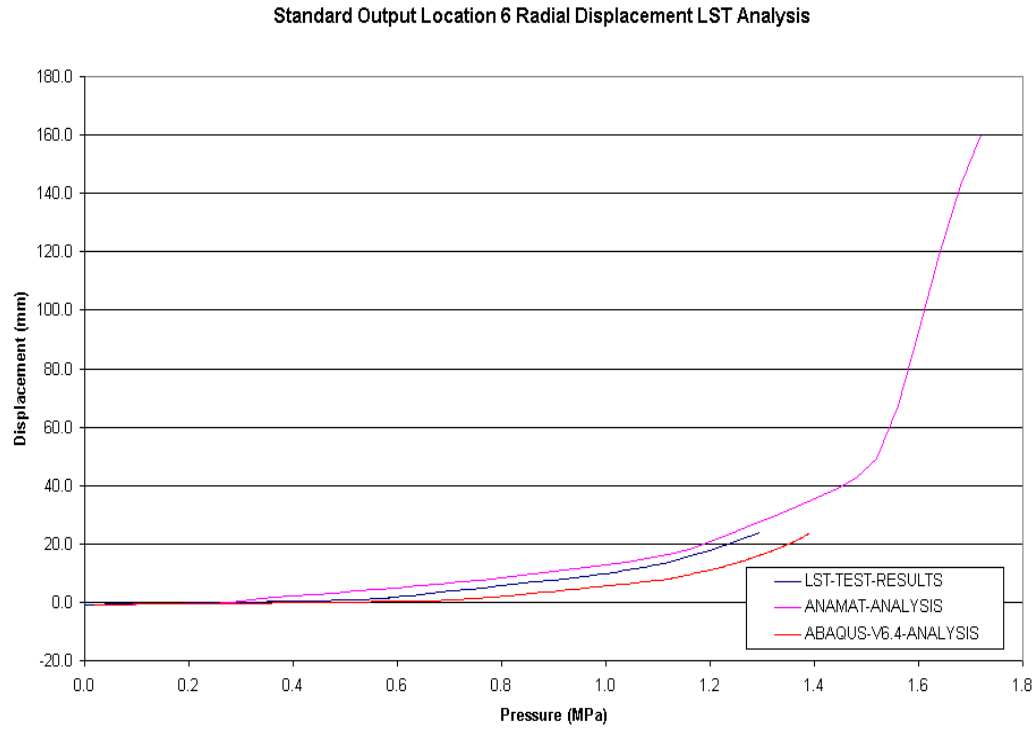

Figure 23 Location 7 Radial Displacement

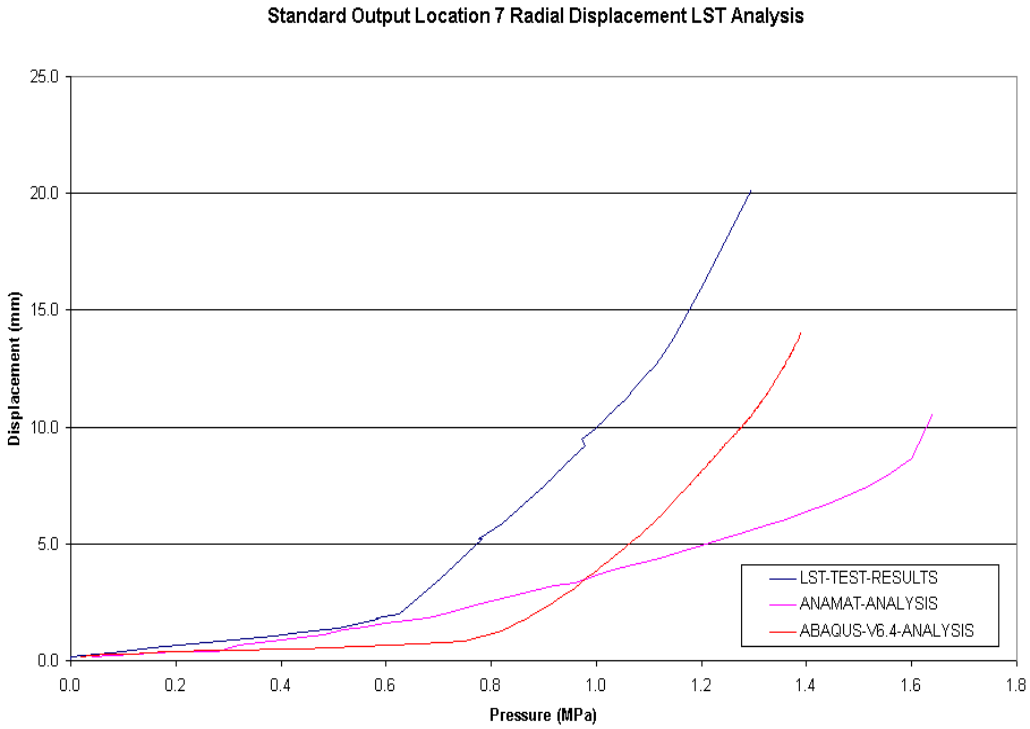

Figure 24 Location 8 Vertical Displacement

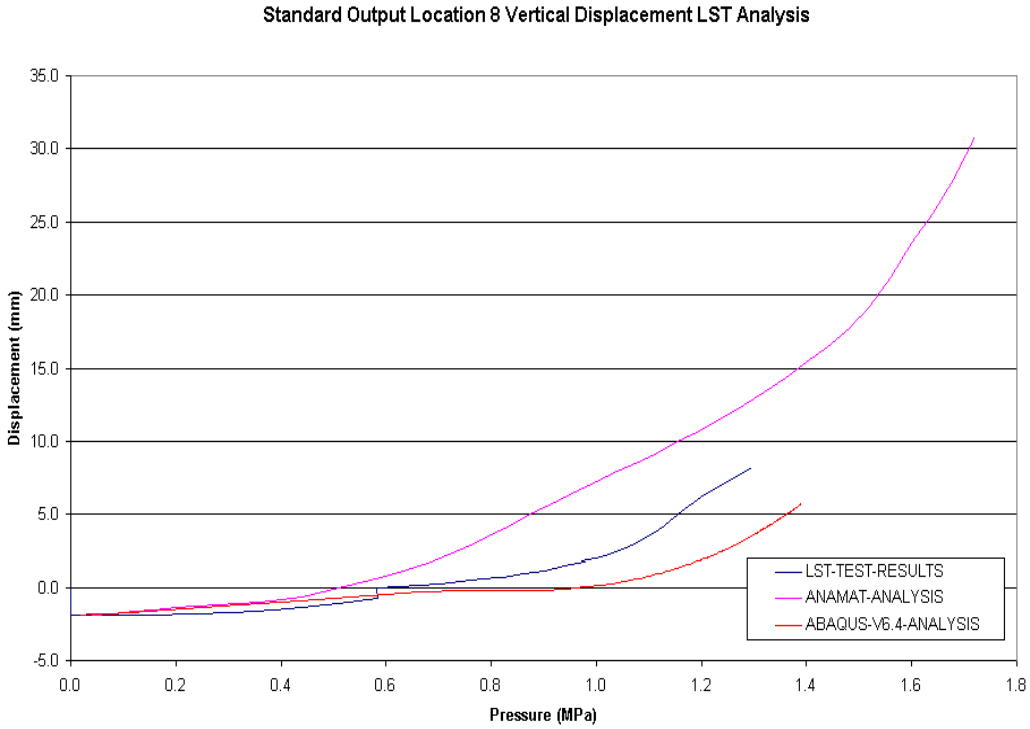

Figure 25 Location 9 Radial Displacement

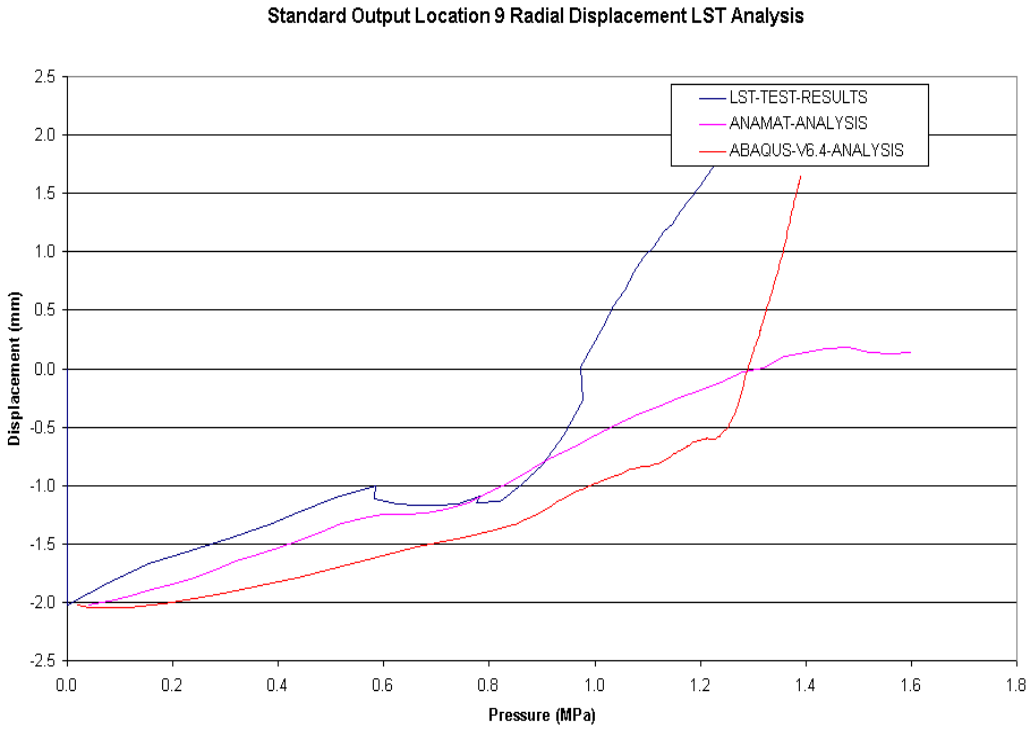

Figure 26 Location 10 Vertical Displacement

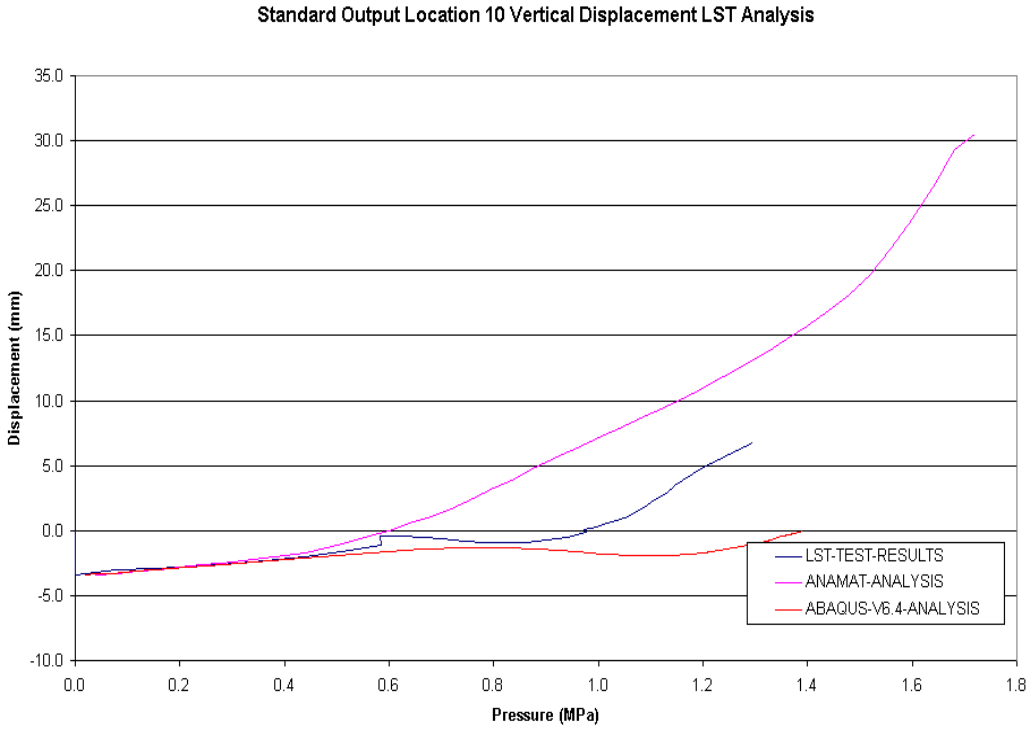

Figure 27 Location 11 Vertical Displacement

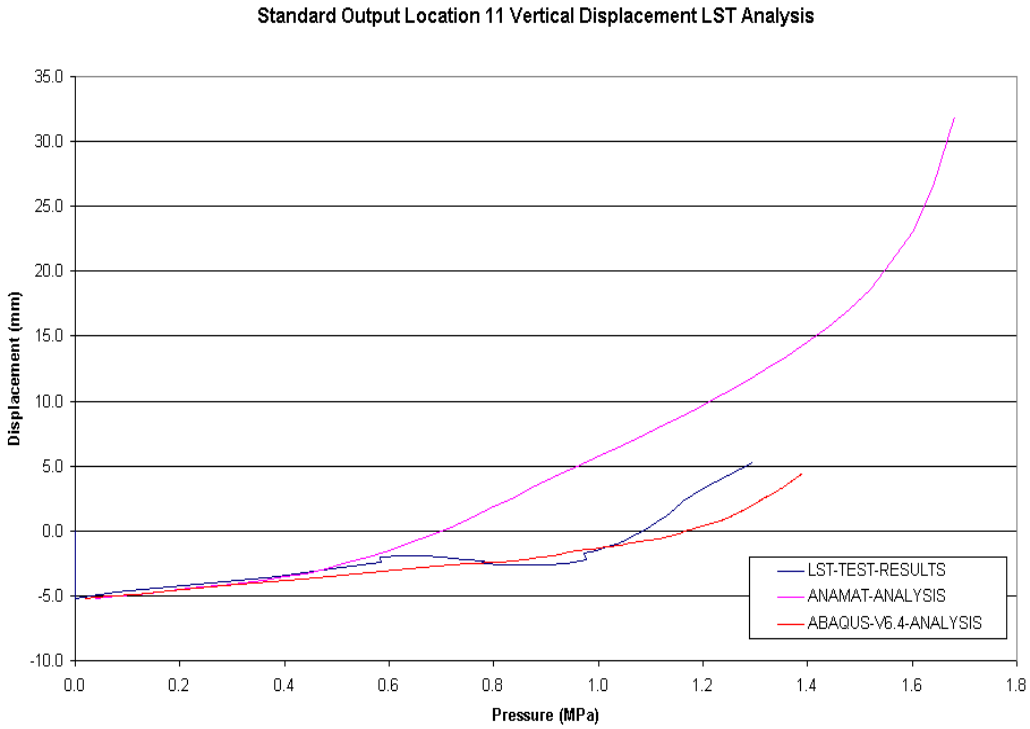

Figure 28 Location 12 Radial Displacement

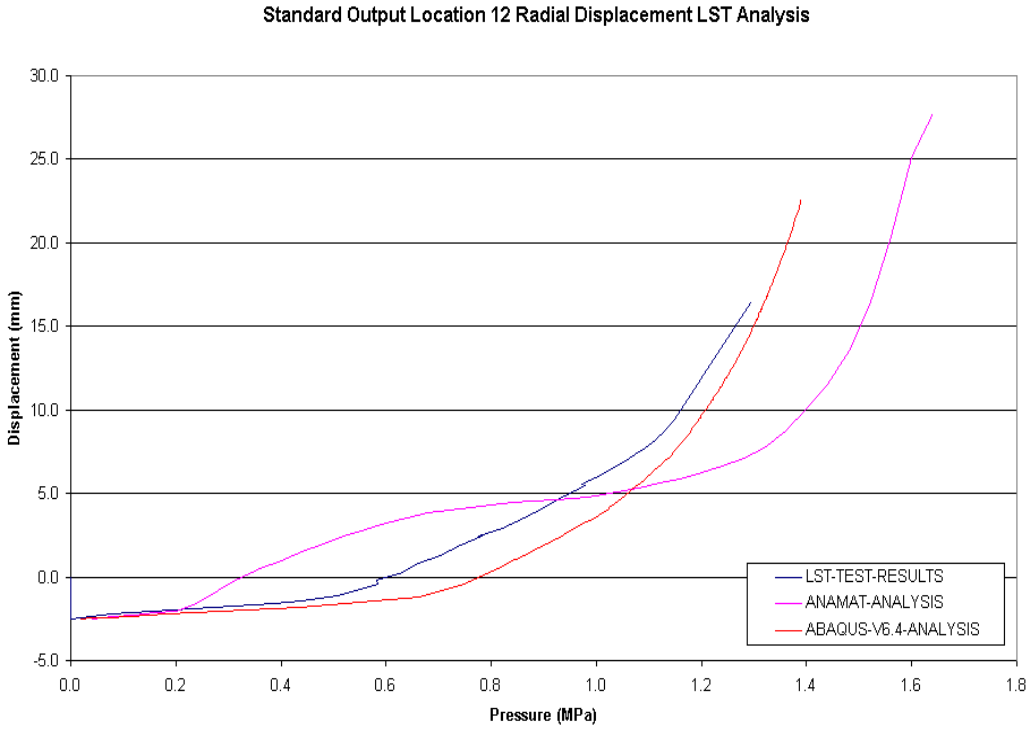

Figure 29 Location 13 Radial Displacement

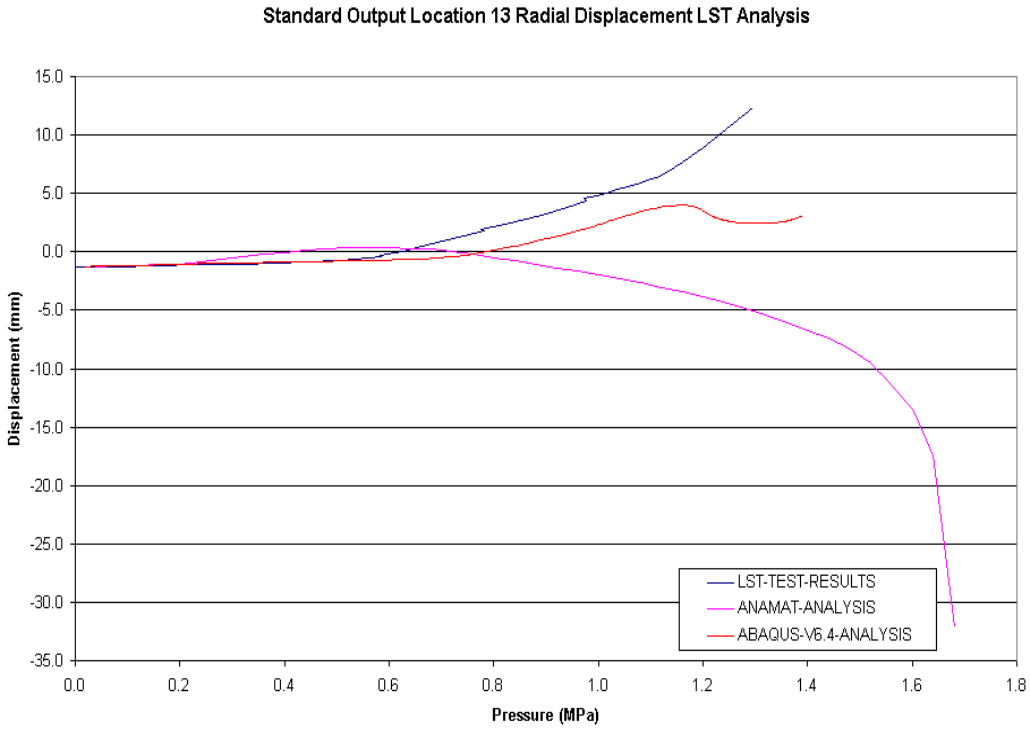

Figure 30 Location 14 Radial Displacement

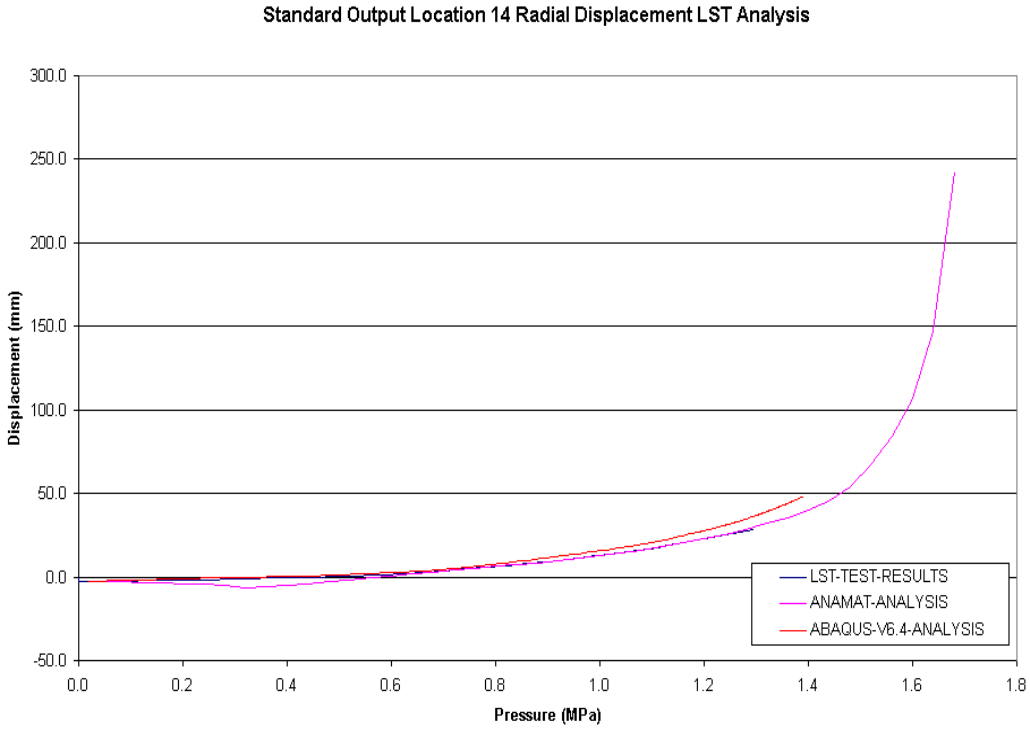

Figure 31 Location 15 Radial Displacement

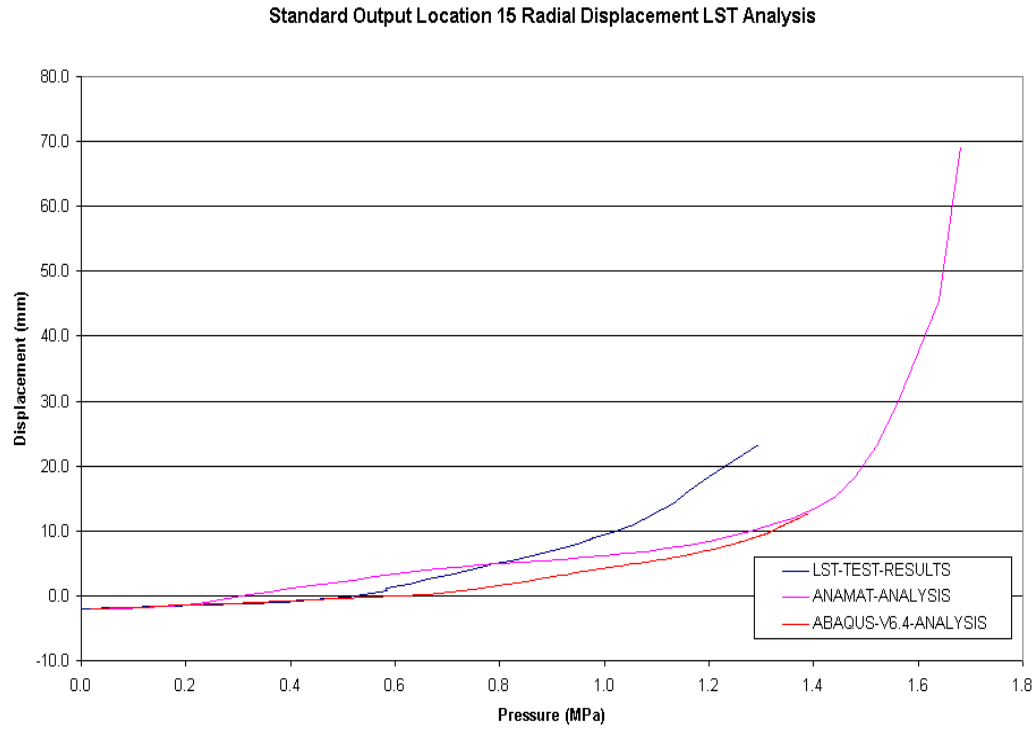

Figure 32 Location 16 Meridional Rebar Strain

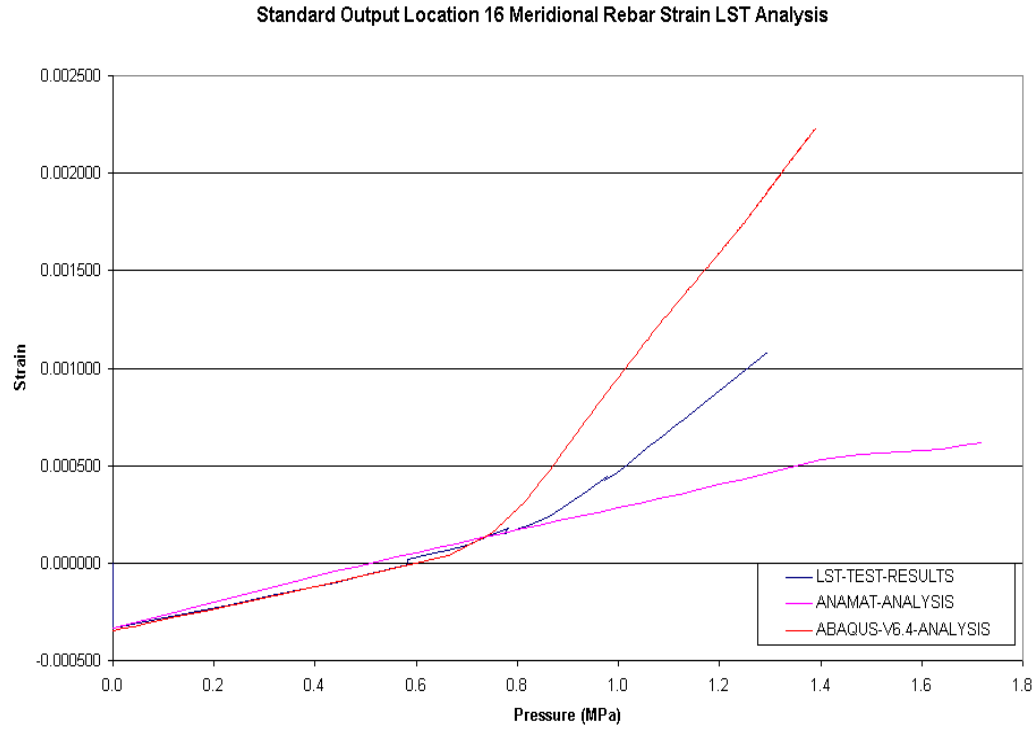

Figure 33 Location 17 Meridional Rebar Strain

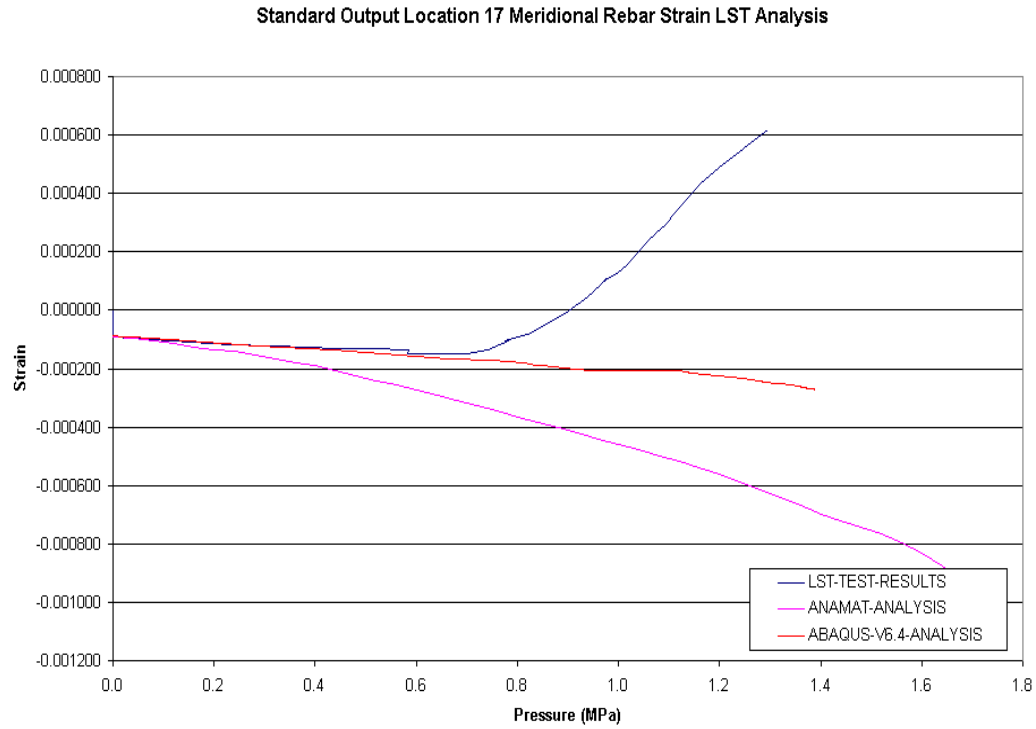

Figure 34 Location 18 Meridional Rebar Strain

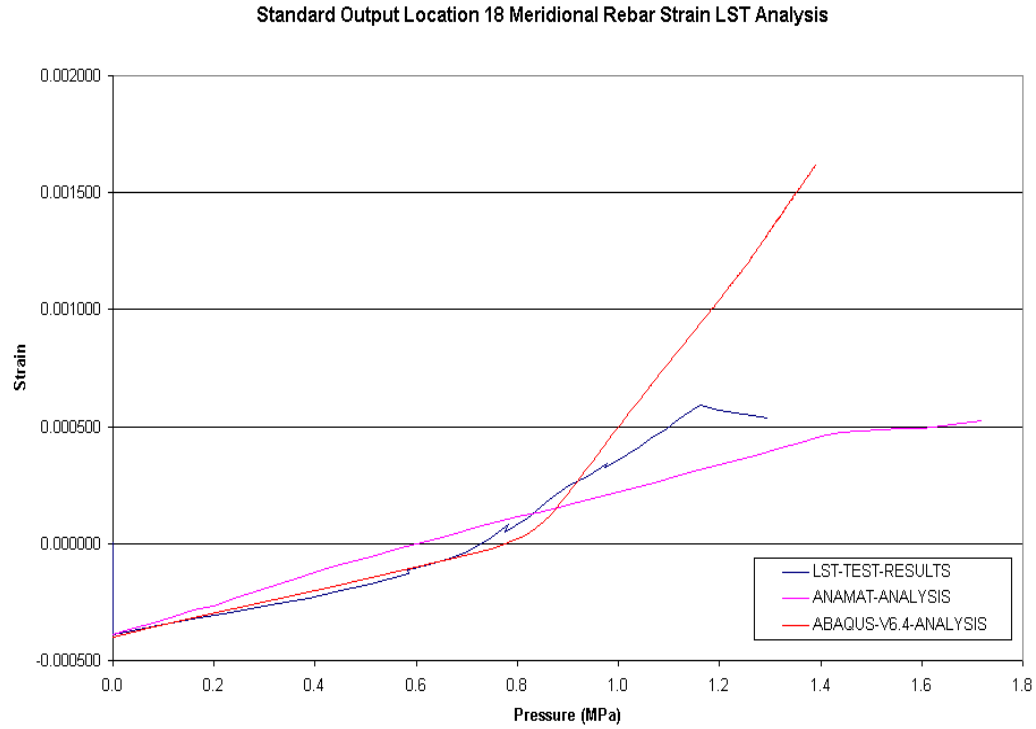

Figure 35 Location 19 Meridional Rebar Strain

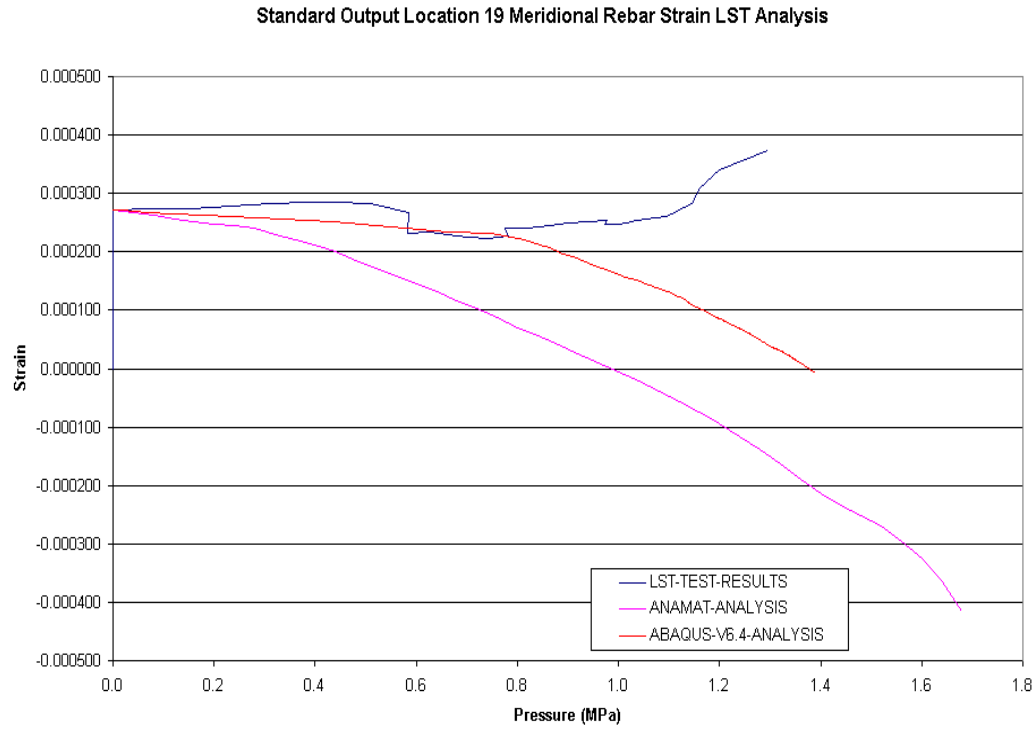

Figure 36 Location 20 Meridional Rebar Strain

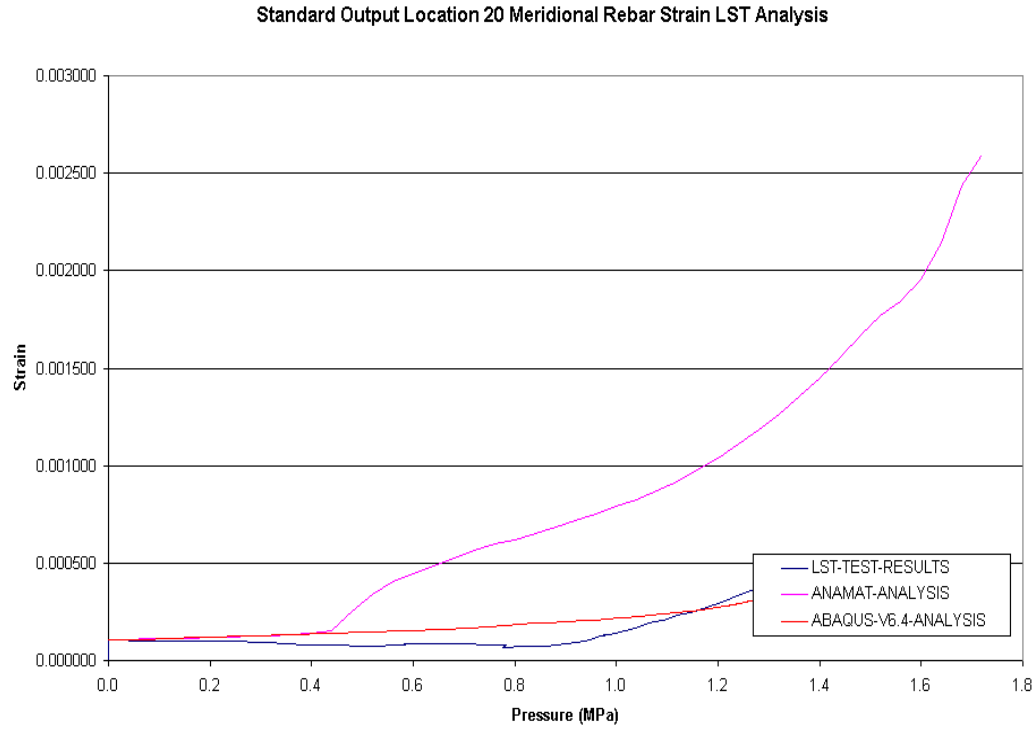

Figure 37 Location 21 Meridional Rebar Strain

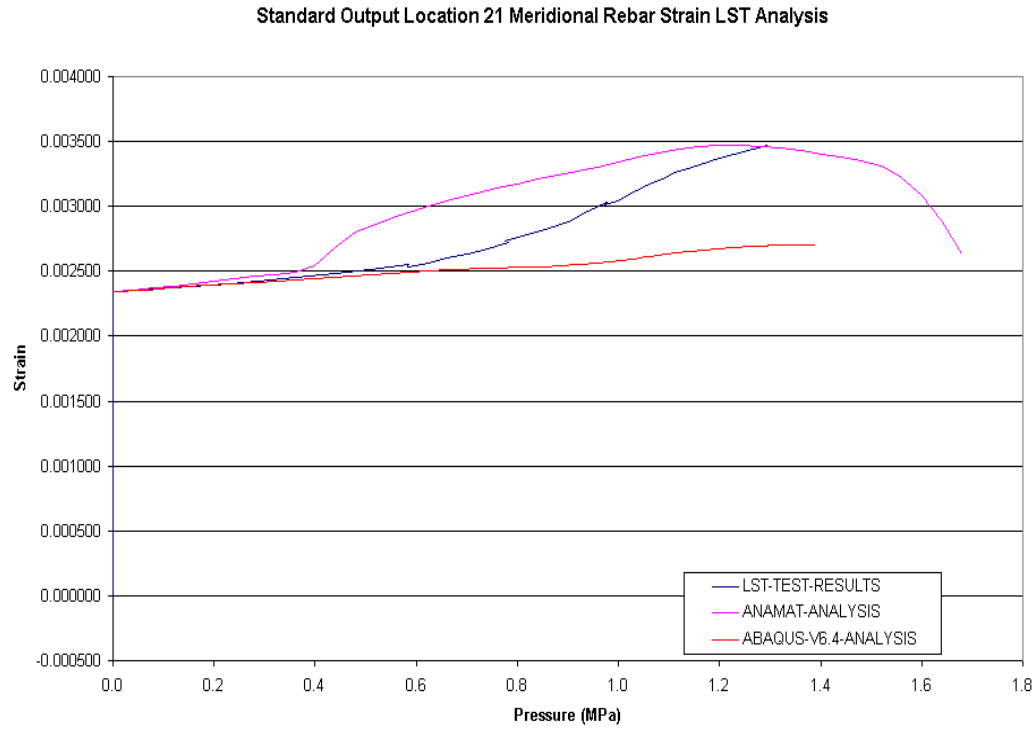

Figure 38 Location 22 Hoop Rebar Strain

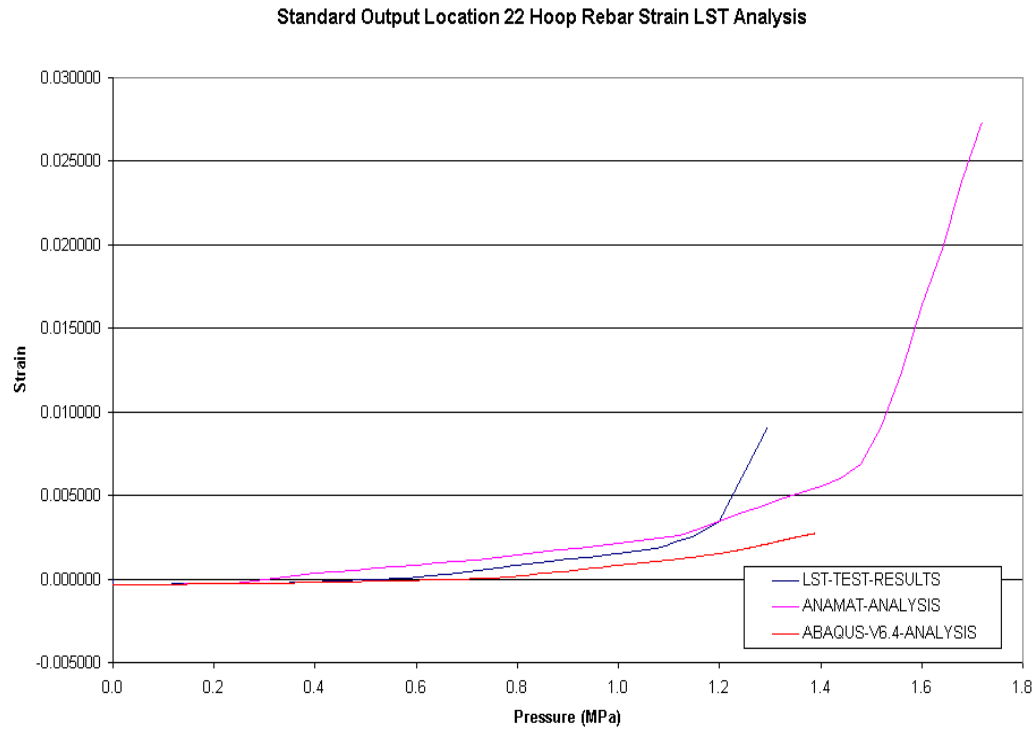

Figure 39 Location 23 Meridional Rebar Strain

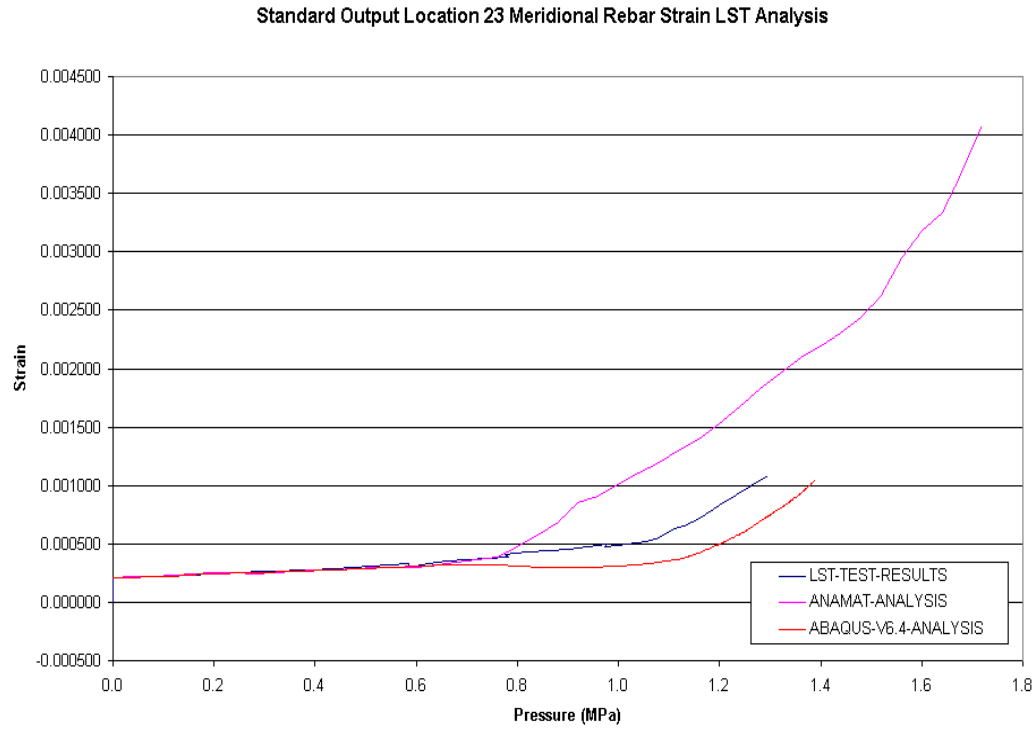

Figure 40 Location 24 Hoop Rebar Strain

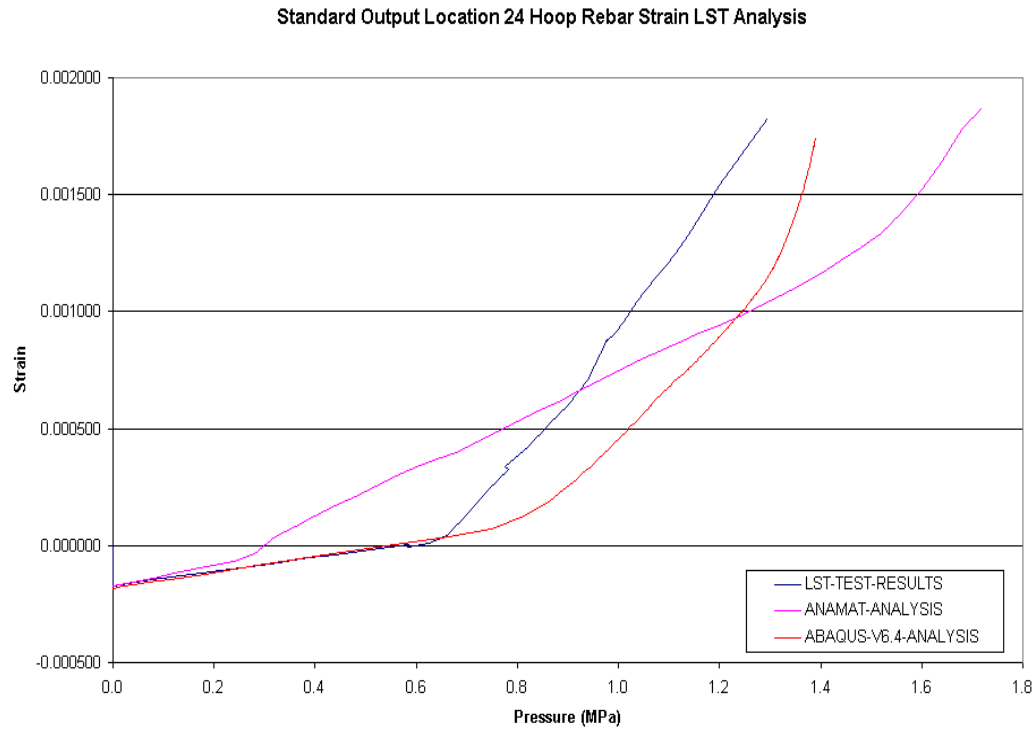

Figure 41 Location 25 Meridional Rebar Strain

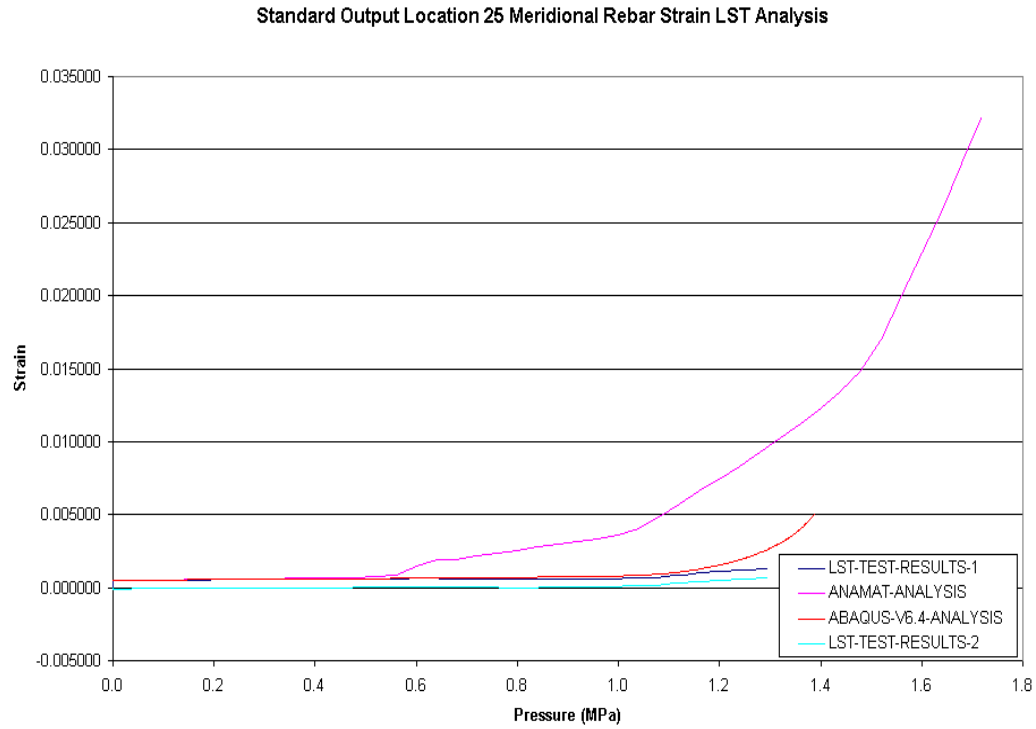

Figure 42 Location 26 Meridional Rebar Strain

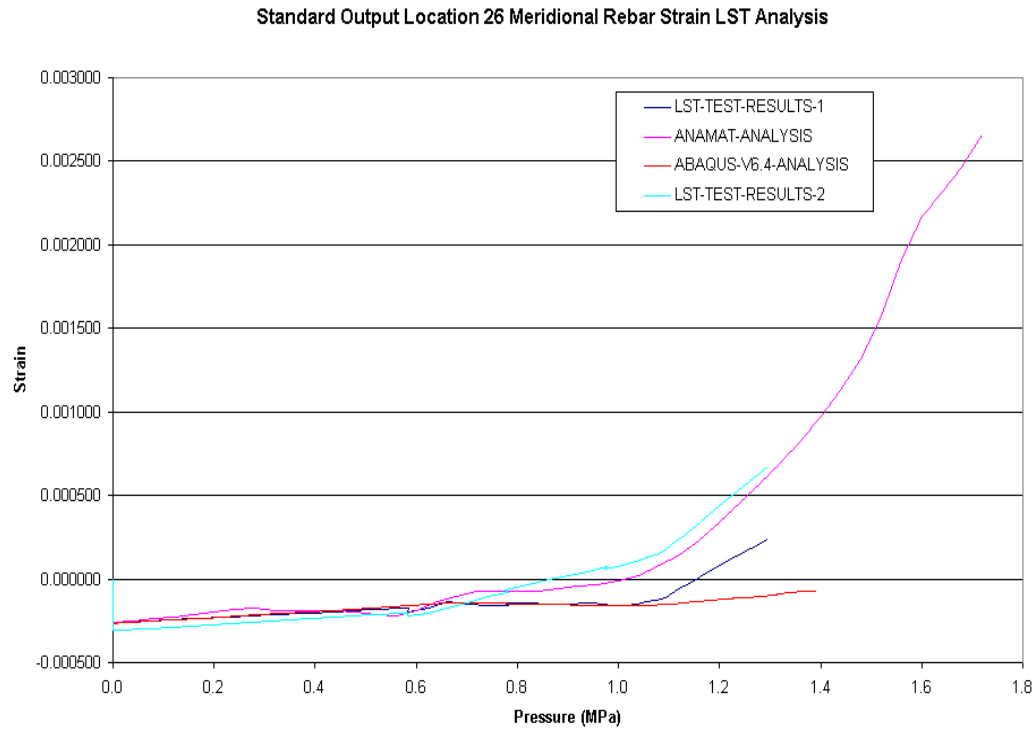

Figure 43 Location 27 Hoop Rebar Strain

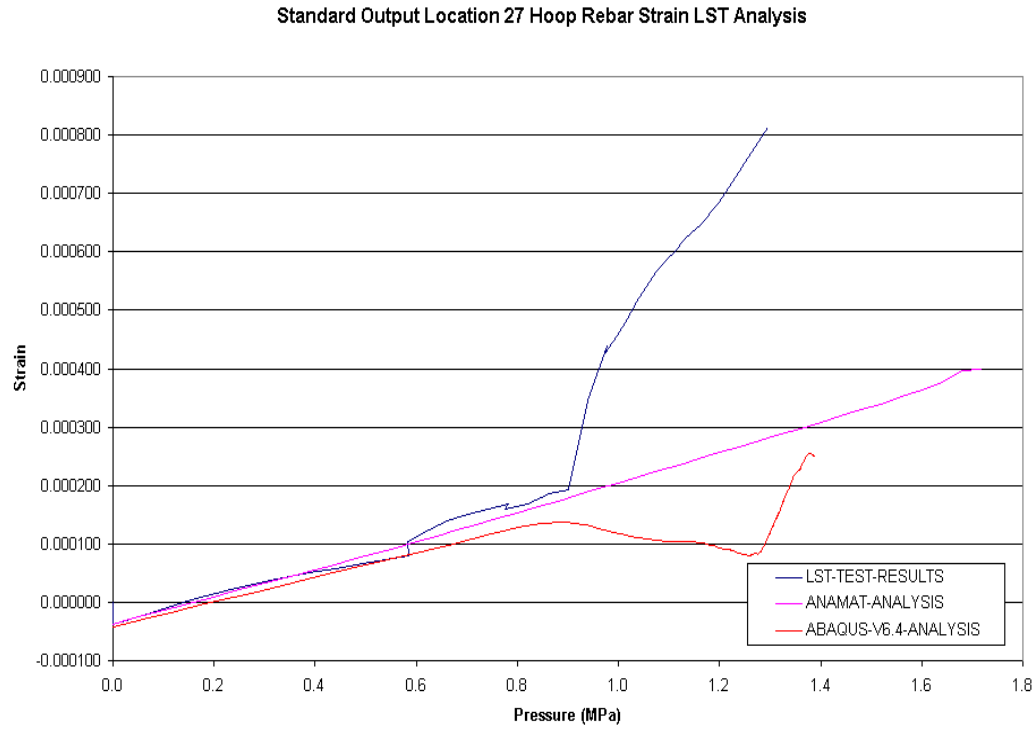

Figure 44 Location 28 Meridional Rebar Strain

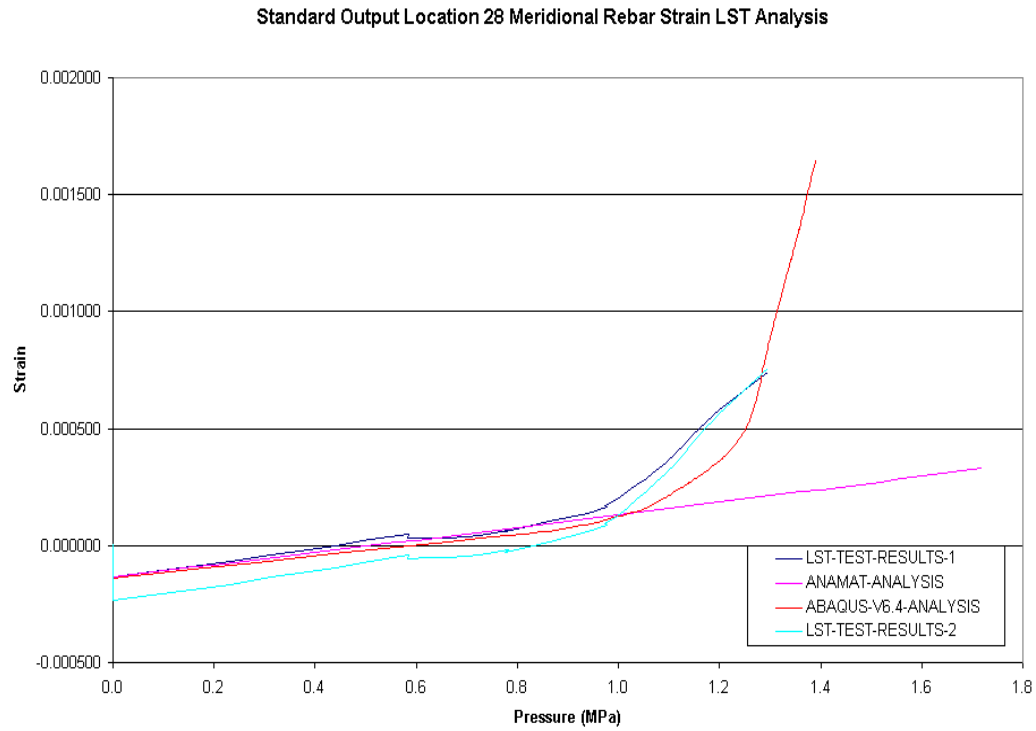

Figure 45 Location 29 Meridional Rebar Strain

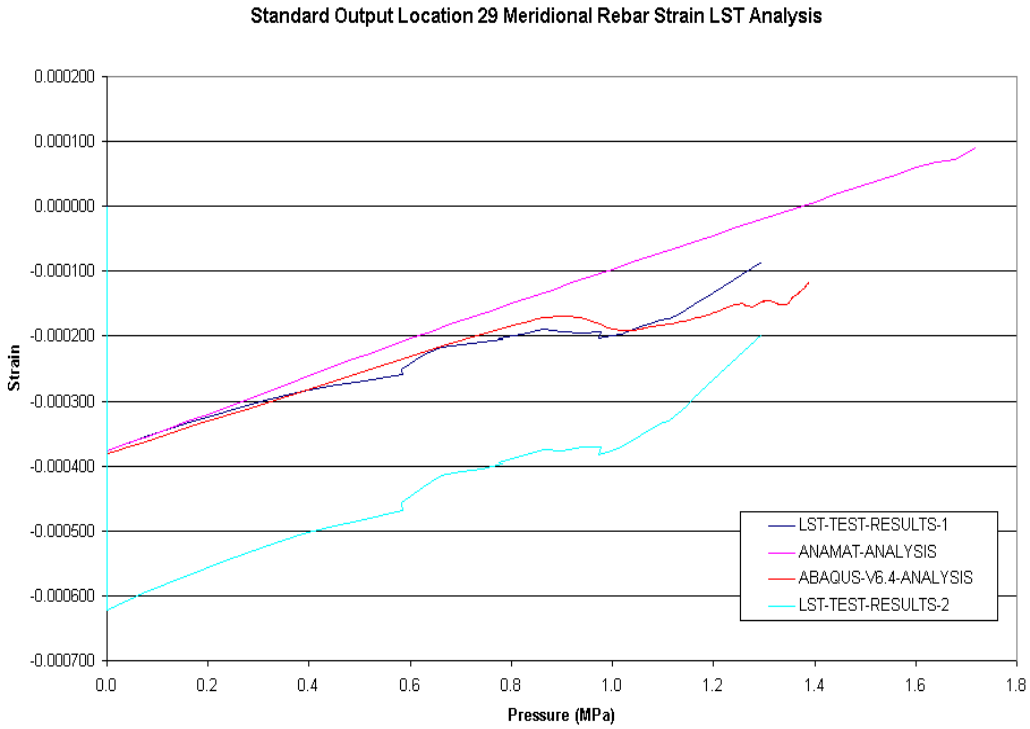

Figure 46 Location 30 Meridional Rebar Strain

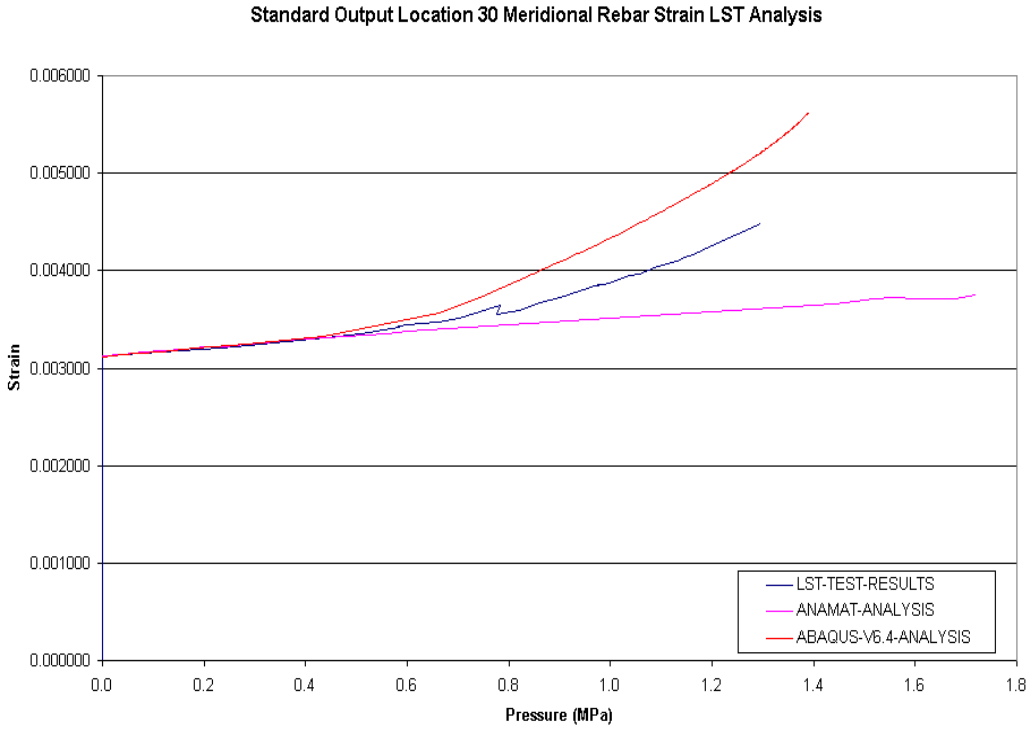

Figure 47 Location 31 Meridional Rebar Strain

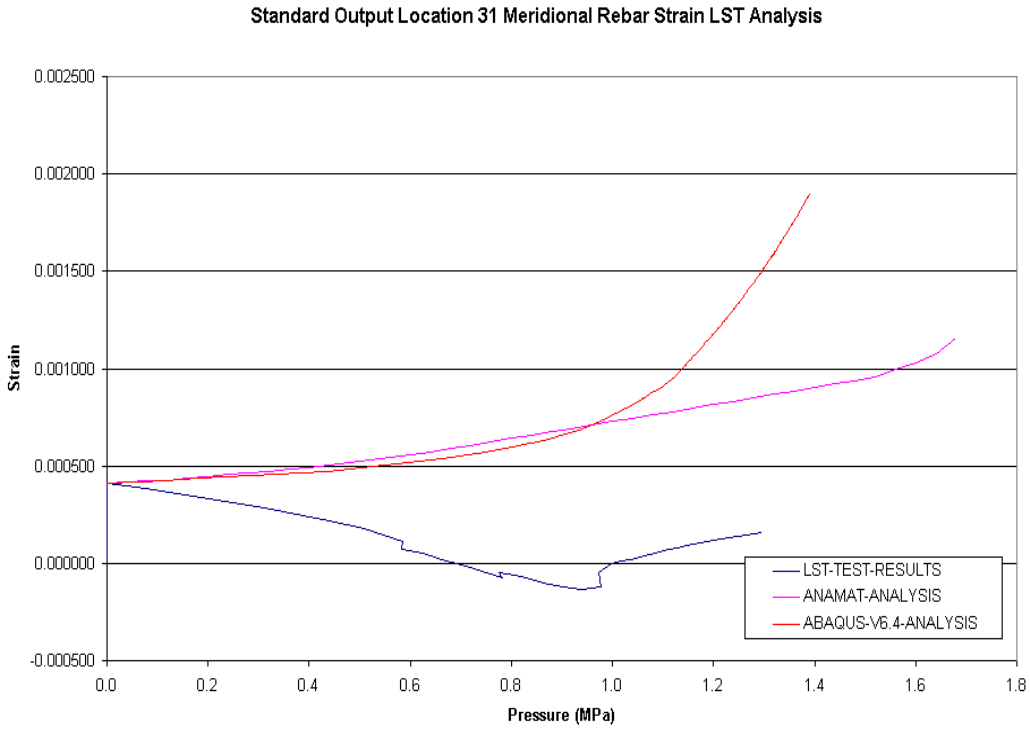

Figure 48 Location 32 Hoop Rebar Strain

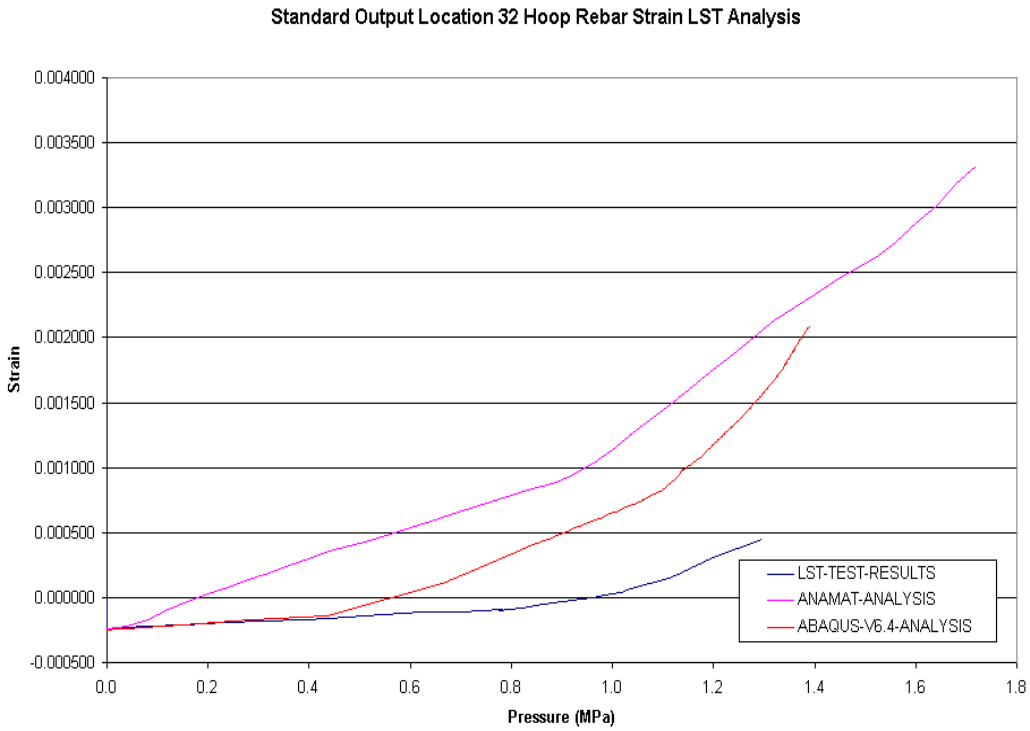

Figure 49 Location 33 Meridional Rebar Strain

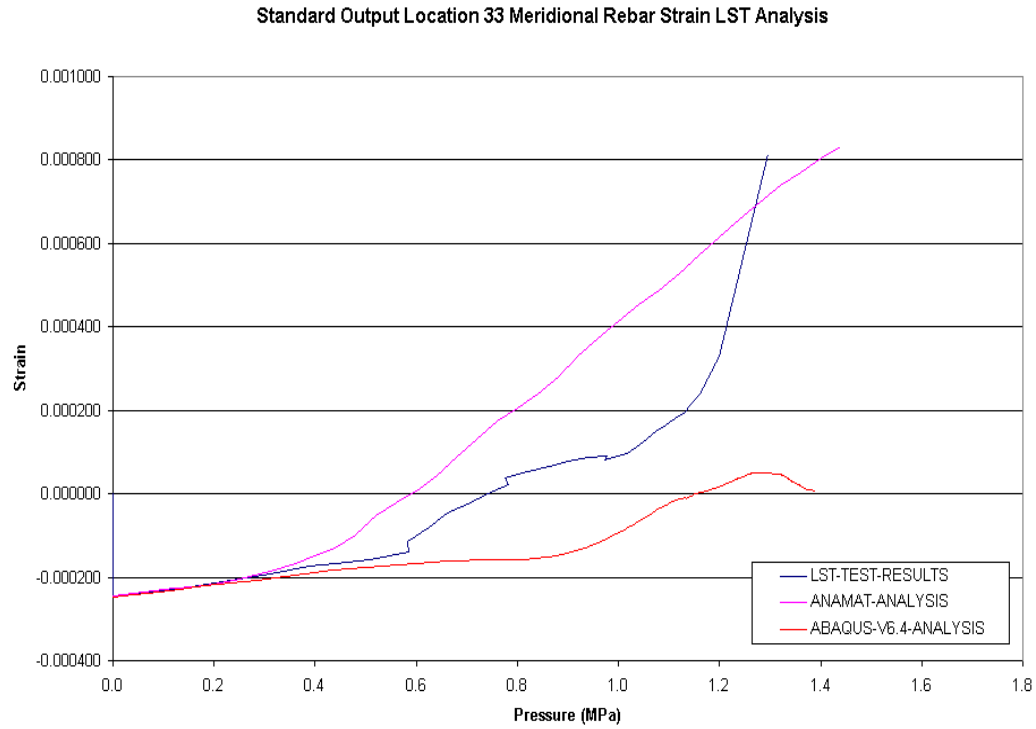

Figure 50 Location 34 Meridional Liner Strain

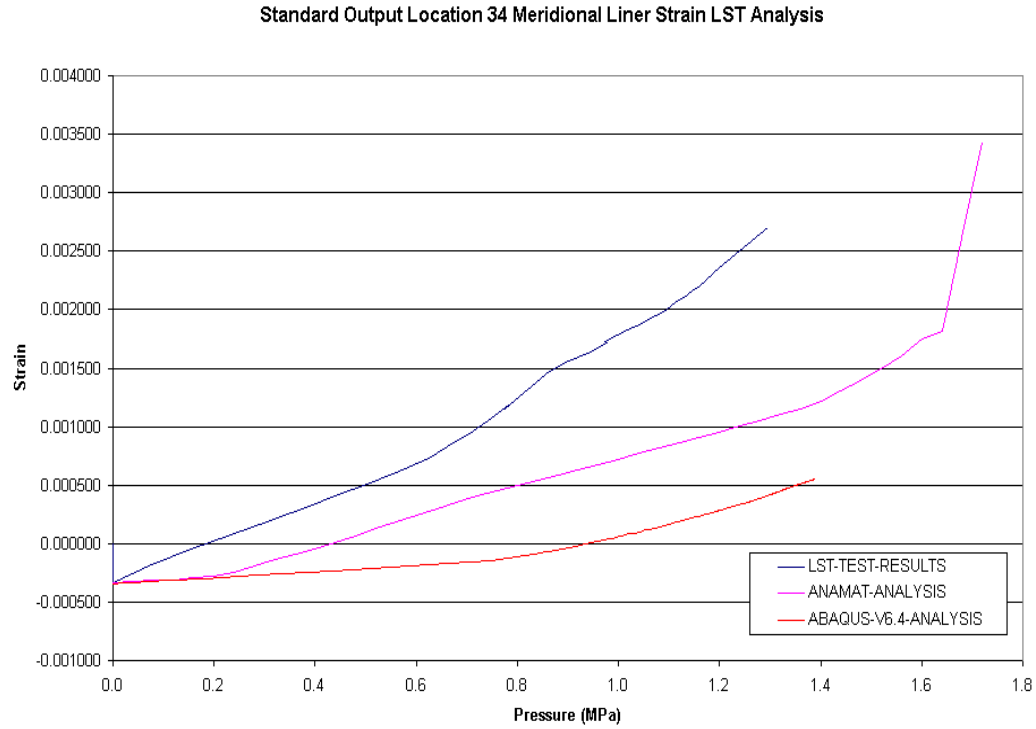

Figure 51 Location 35 Meridional Liner Strain

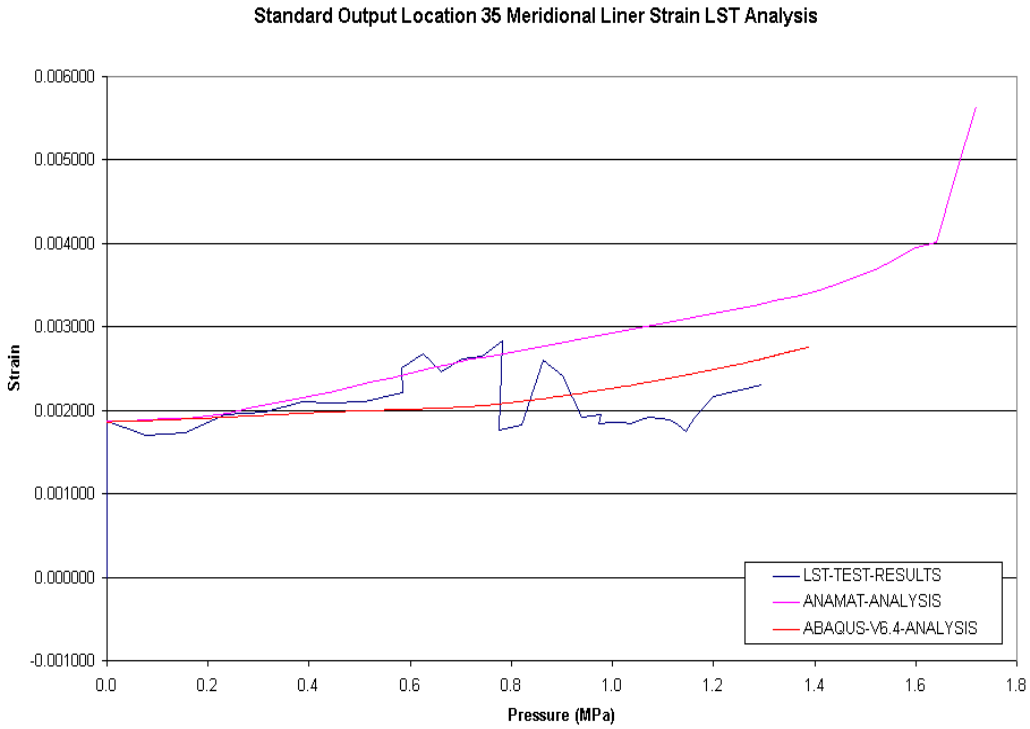

Figure 52 Location 36 Meridional Liner Strain

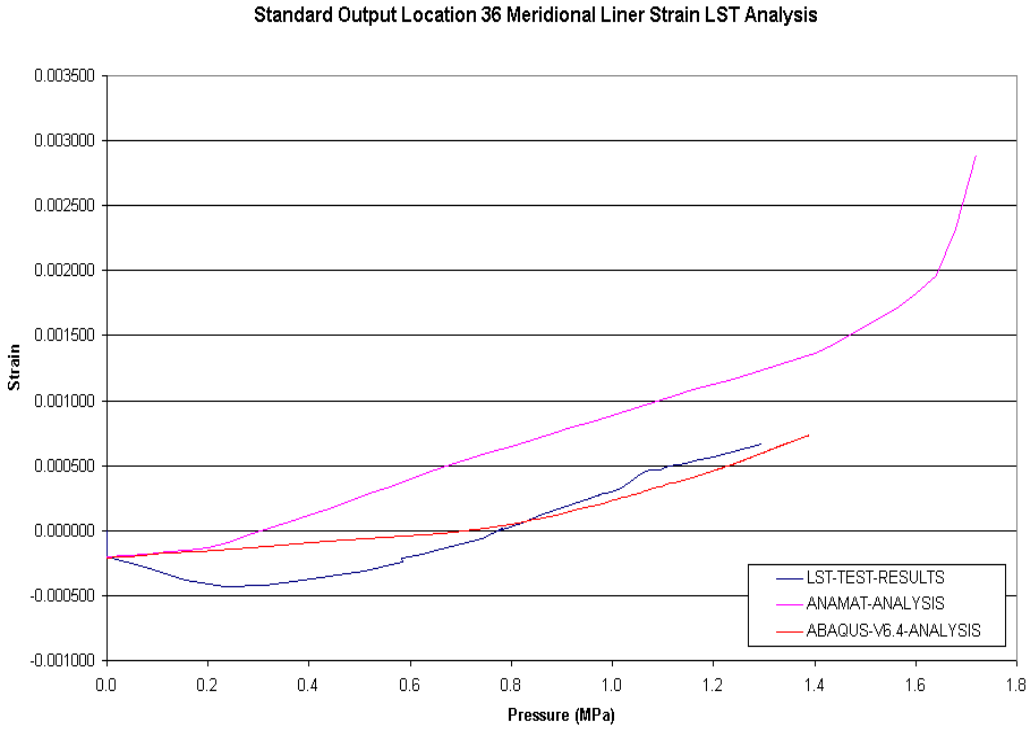

Figure 53 Location 37 Hoop Liner Strain

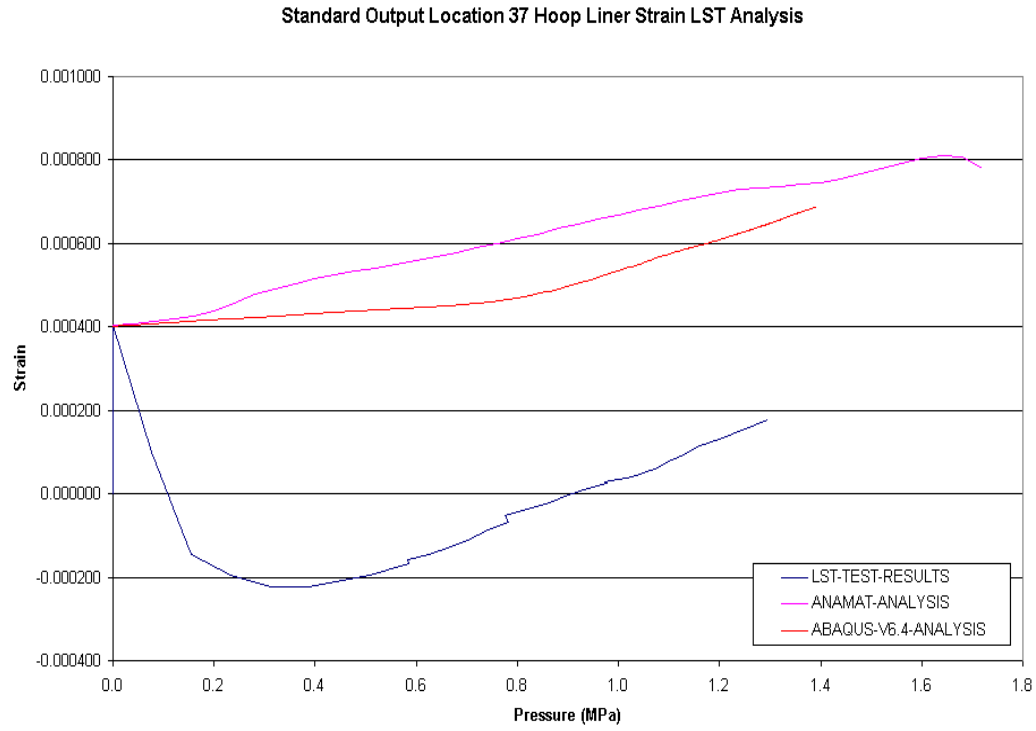

Figure 54 Location 38 Meridional Liner Strain

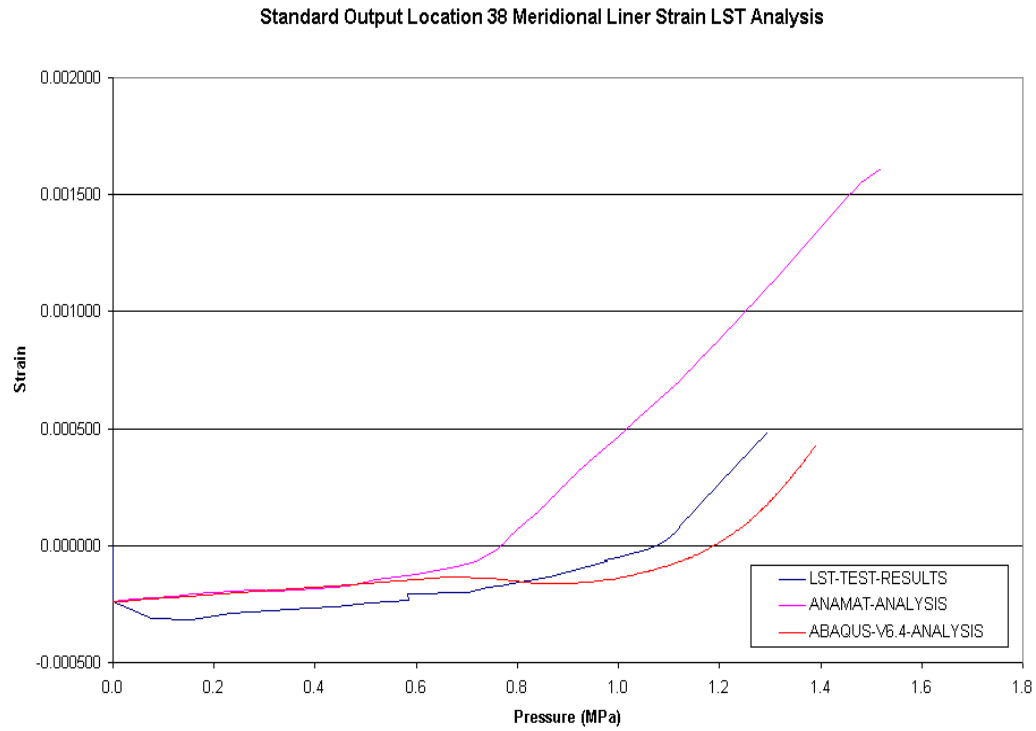

Figure 55 Location 39 Hoop Liner Strain

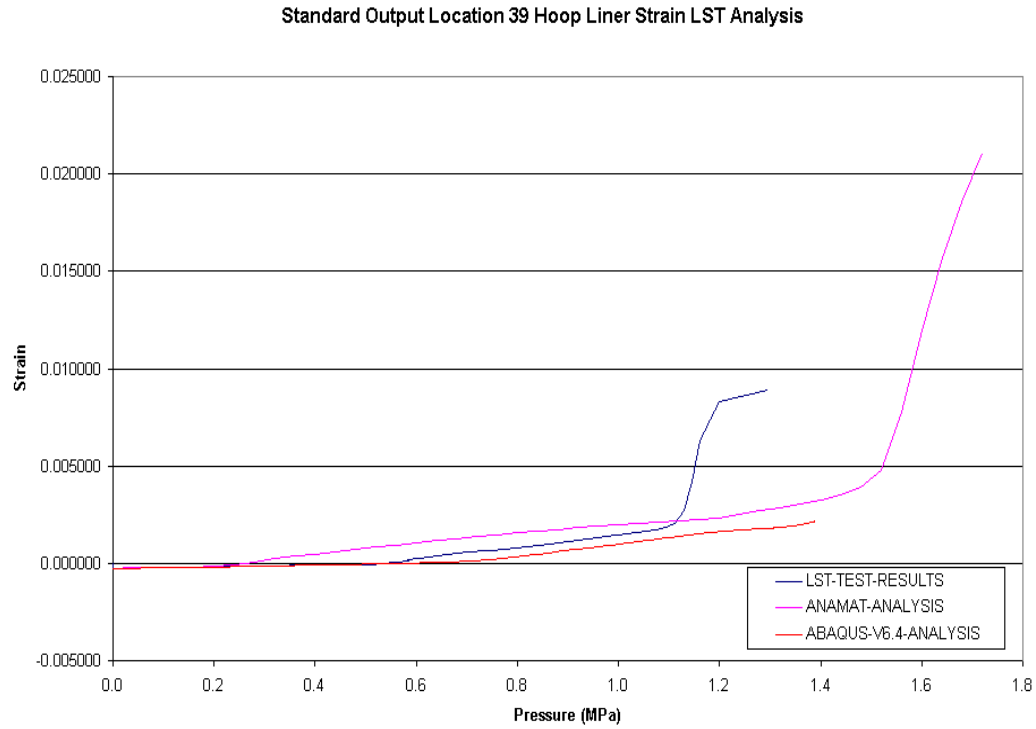

Figure 56 Location 40 Meridional Liner Strain

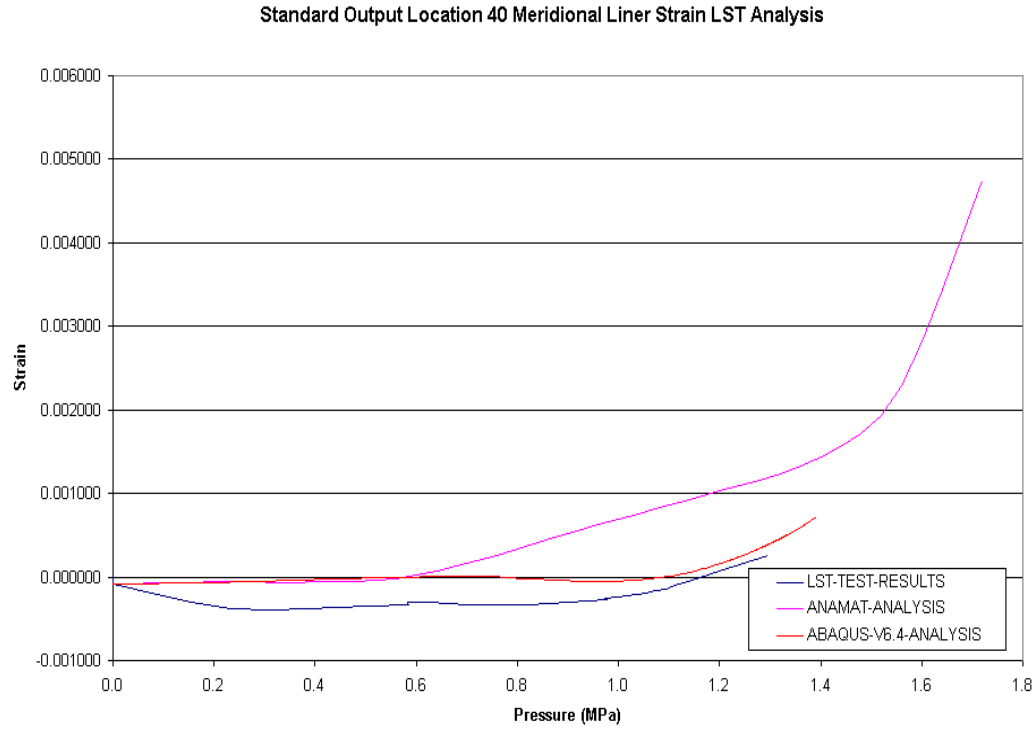

Figure 57 Location 41 Hoop Liner Strain

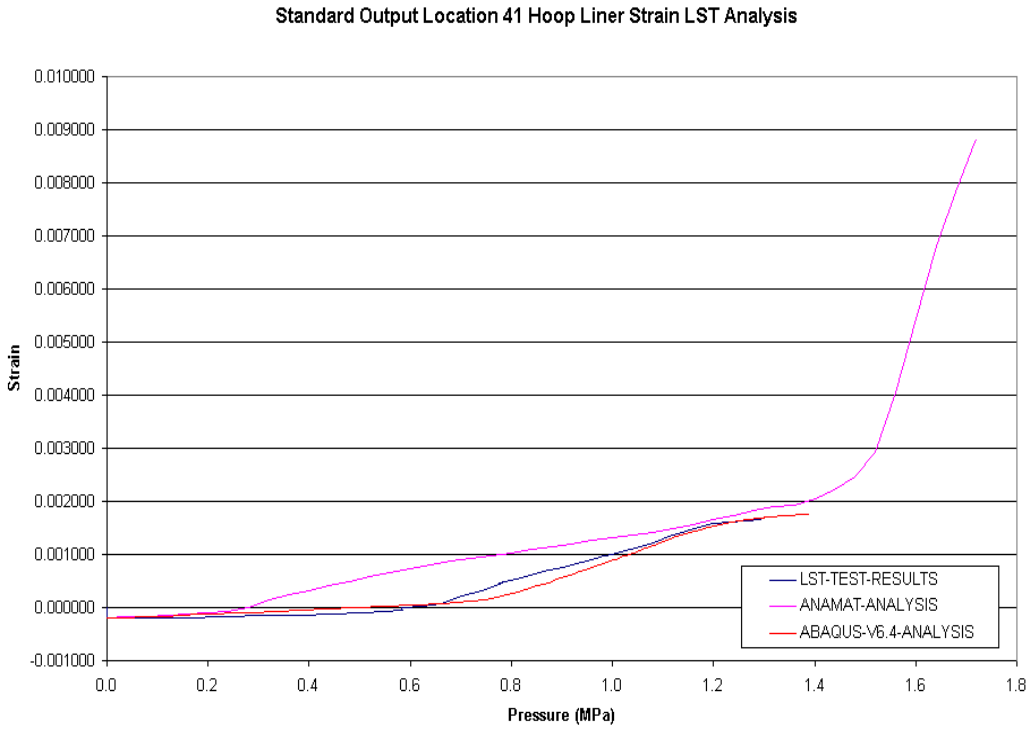

Figure 58 Location 42 Meridional Liner Strain

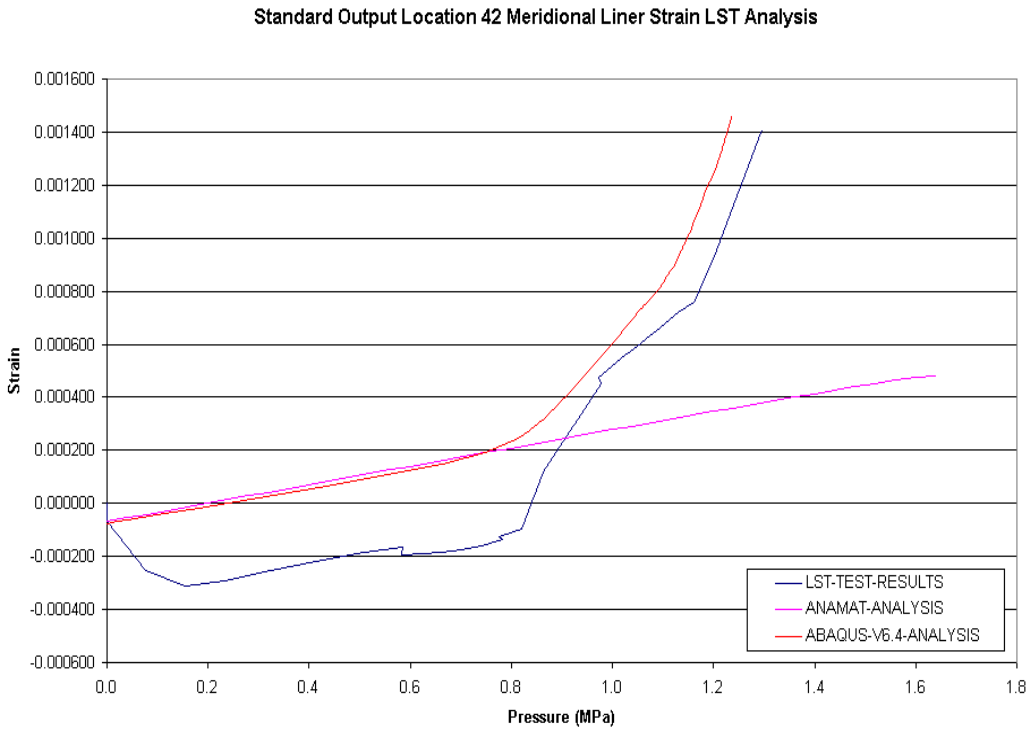

Figure 59 Location 43 Meridional Liner Strain

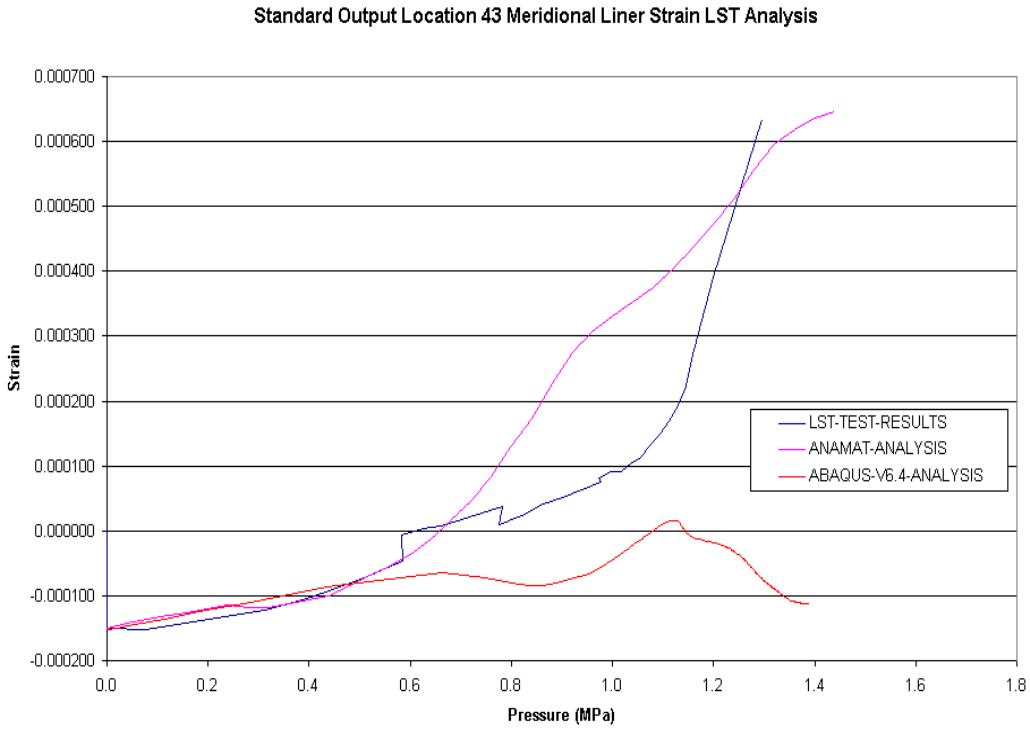

Figure 60 Location 44 Hoop Liner Strain

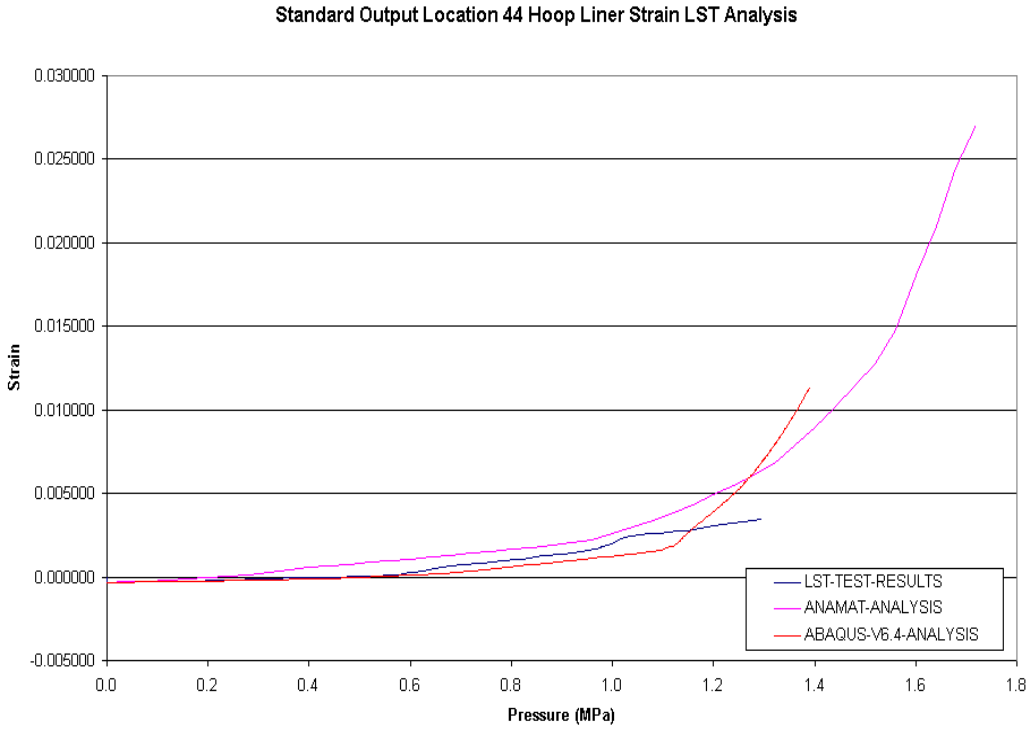

Figure 61 Location 45 Hoop Liner Strain

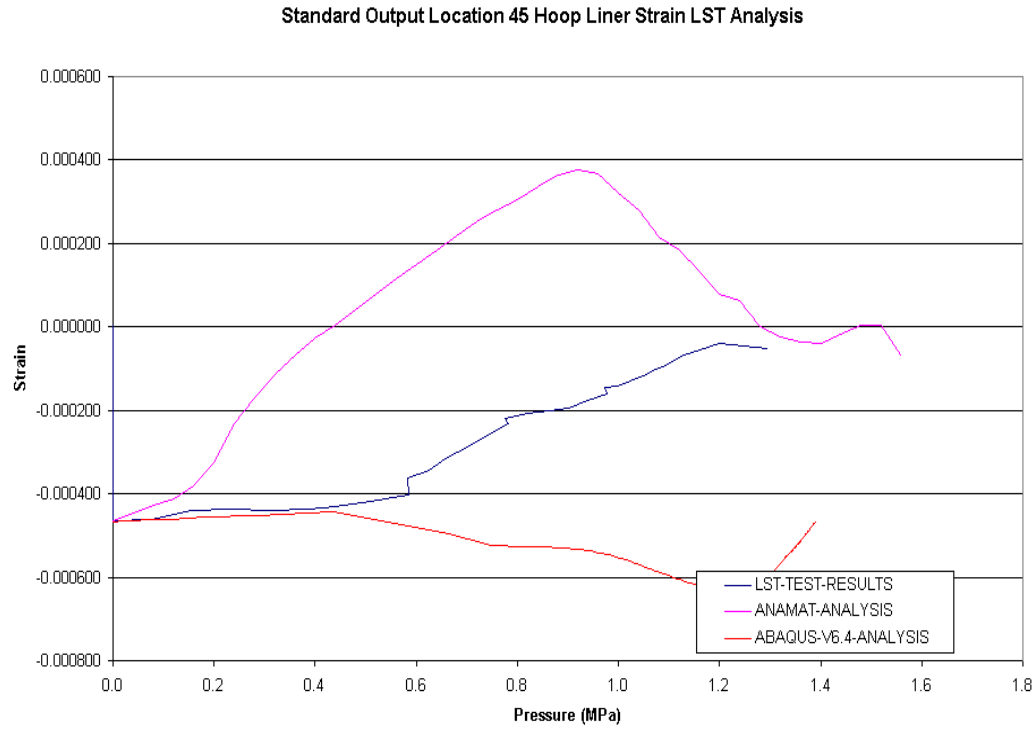

Figure 62 Location 46 Hoop Liner Strain

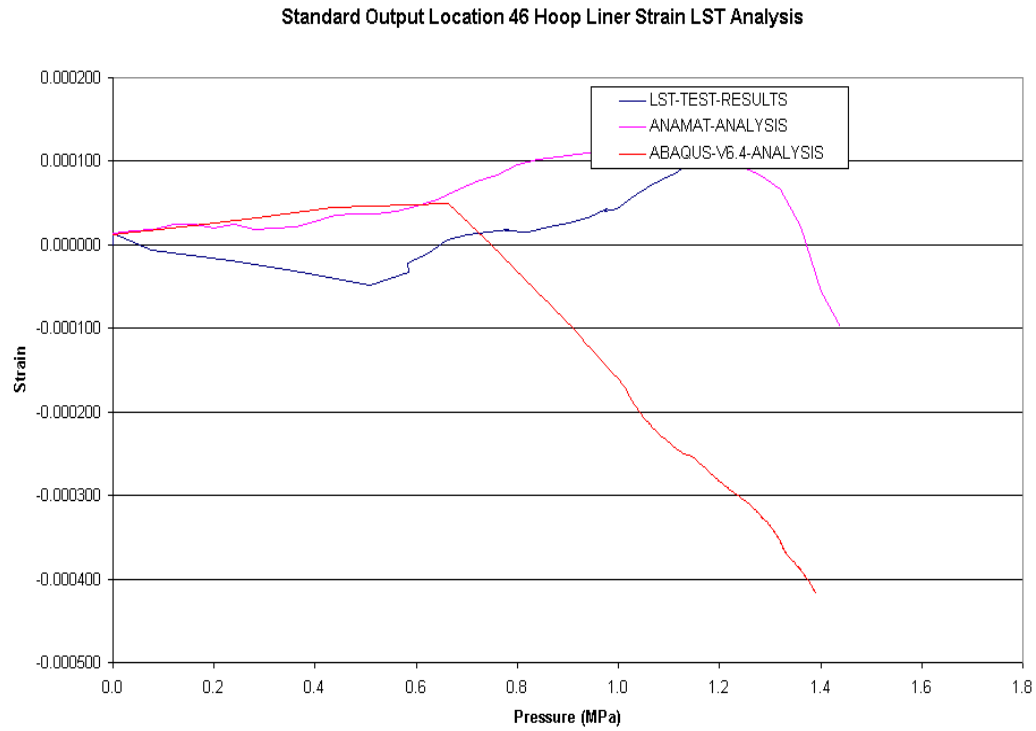

Figure 63 Location 47 Radial Base Liner Strain

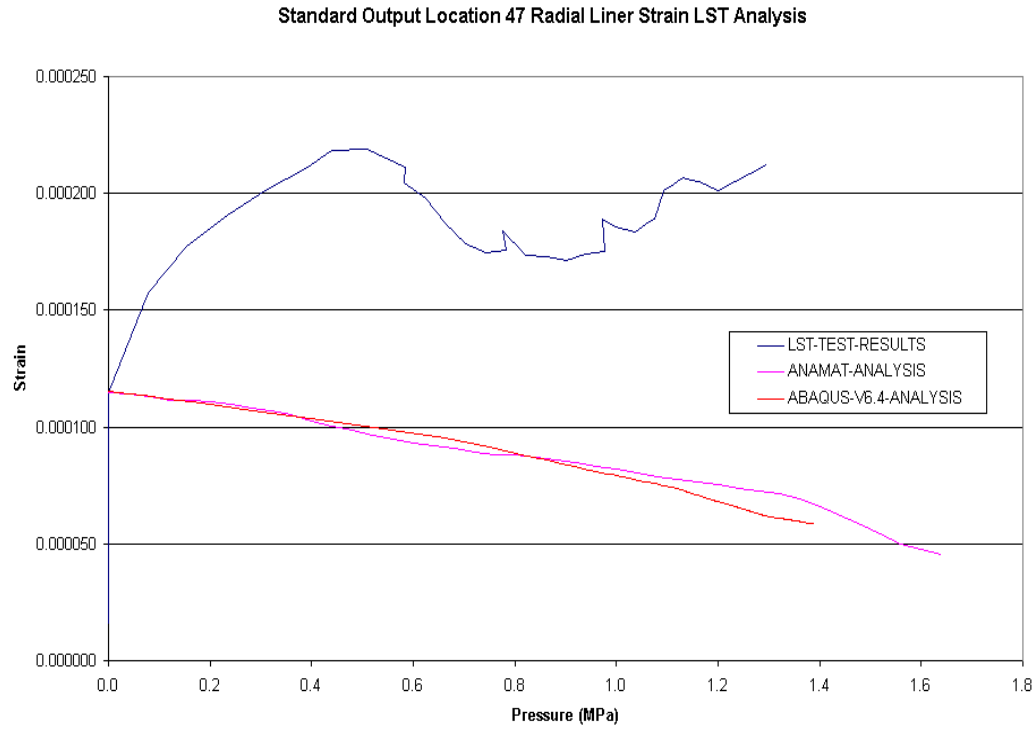

Figure 64 Location 48 Hairpin Tendon Strain

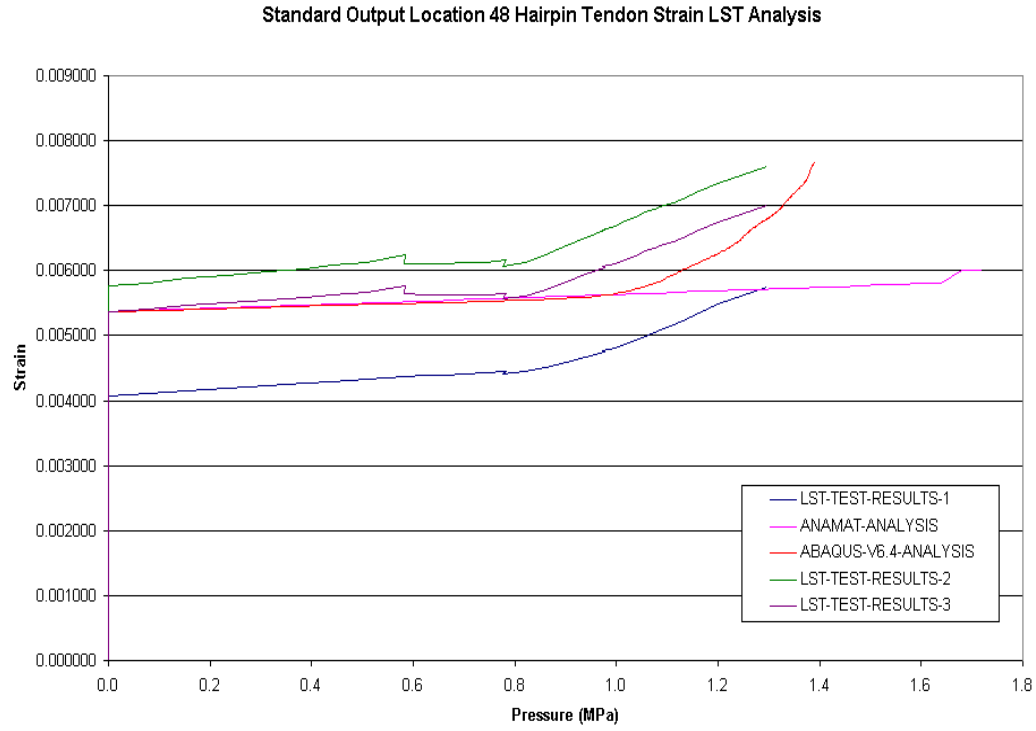

Figure 65 Location 49 Hairpin Tendon Strain

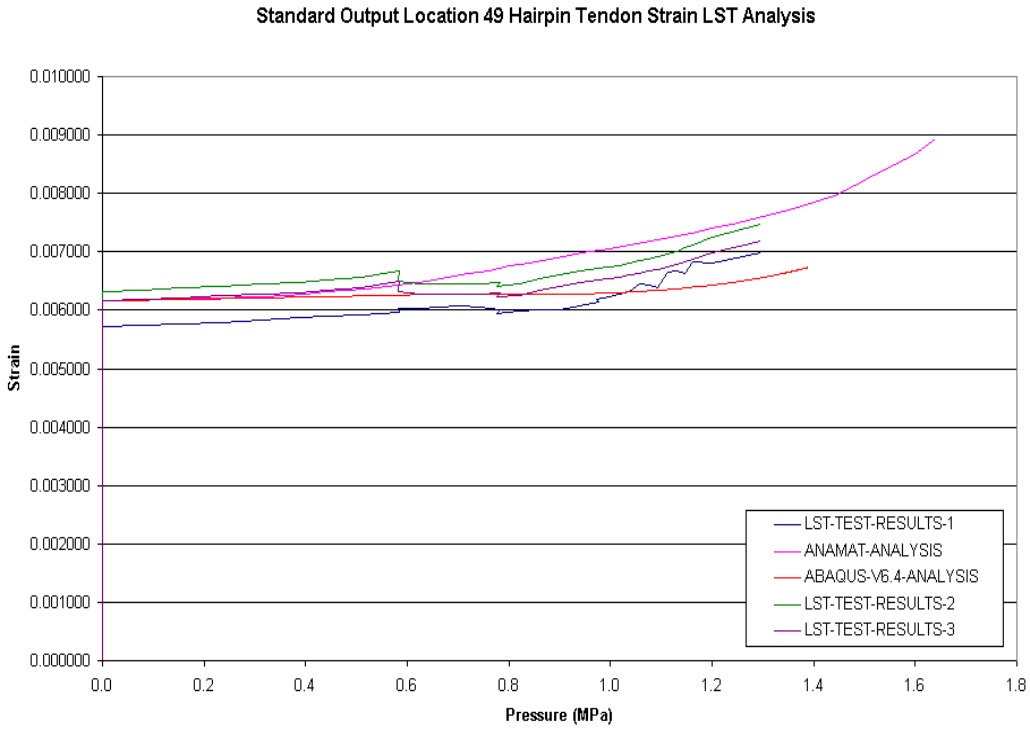

Figure 66 Location 50 Hoop Tendon Strain

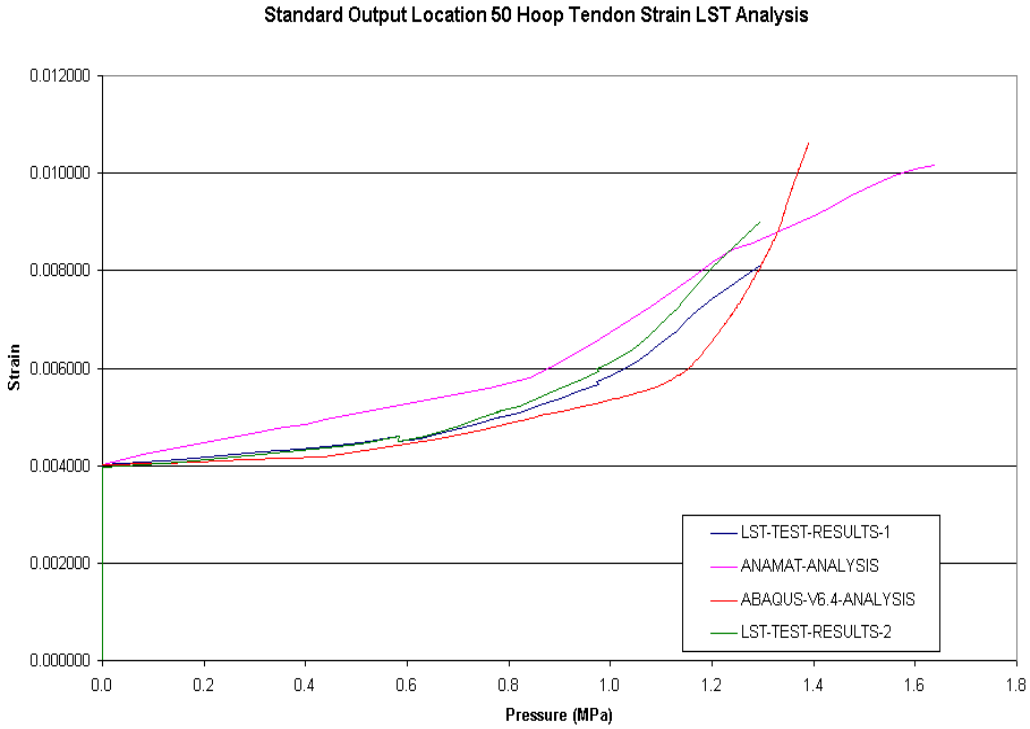

Figure 67 Location 51 Hoop Tendon Strain

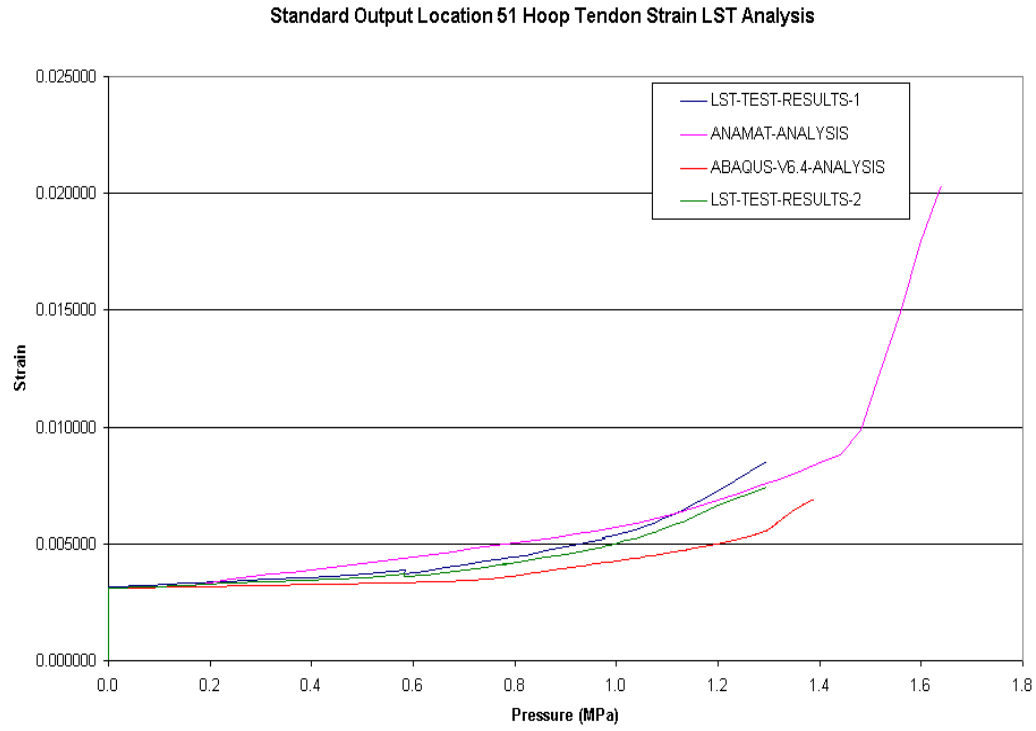

Figure 68 Location 52 Hoop Tendon Strain

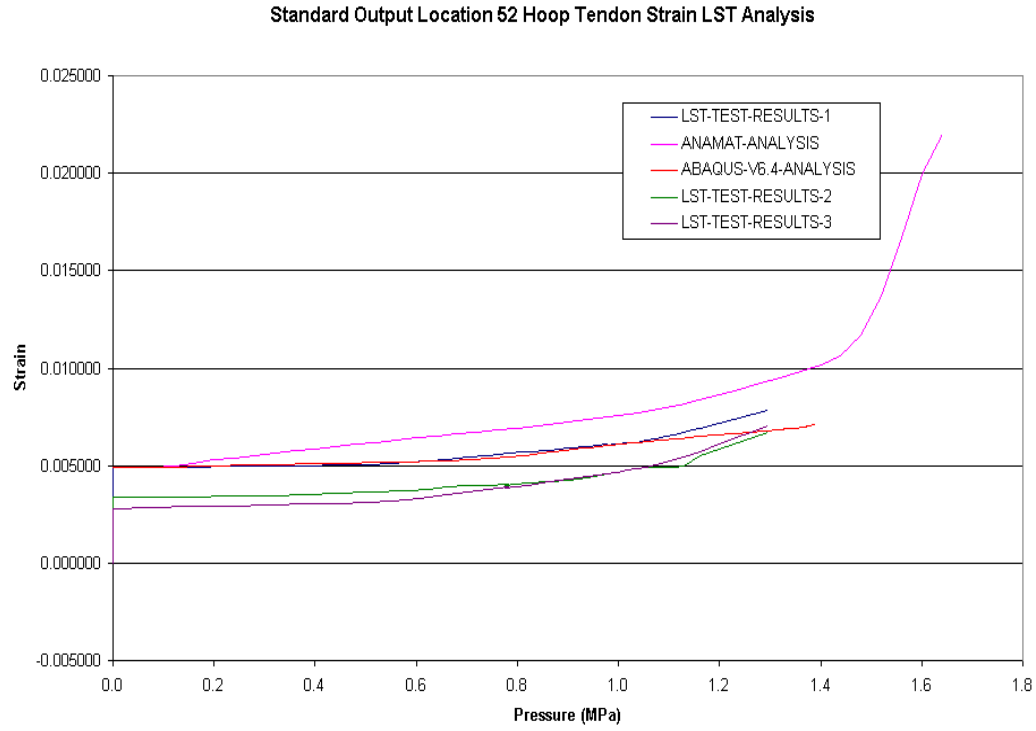

Figure 69 Location 53 Hoop Tendon Strain

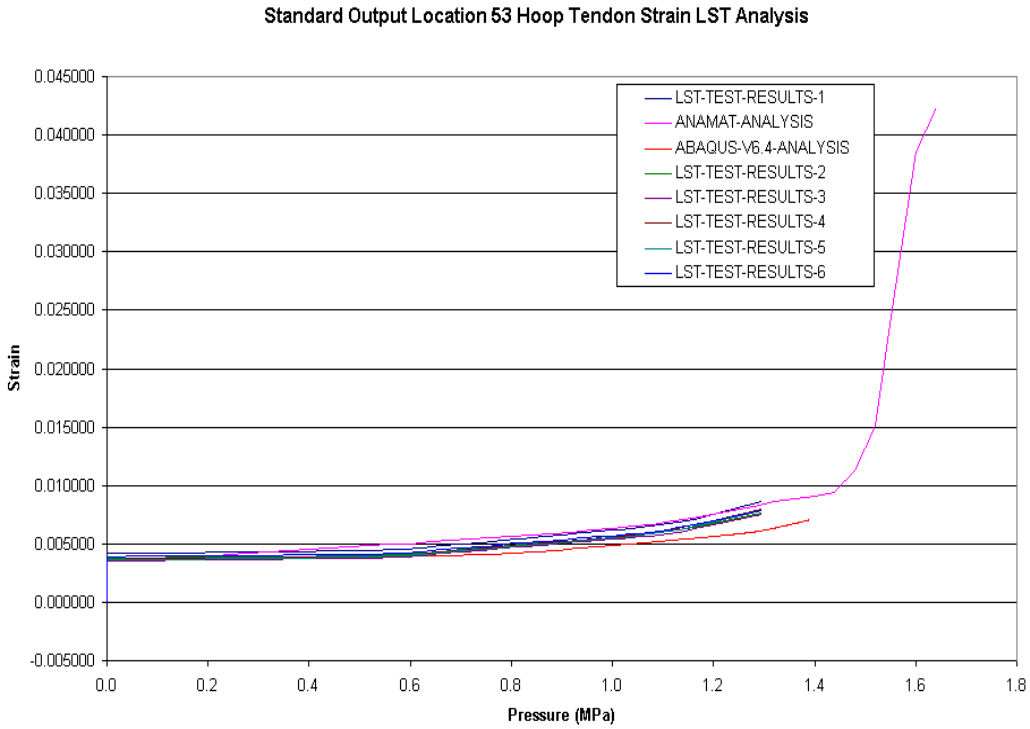

Figure 70 Location 54 Hairpin Tendon Force

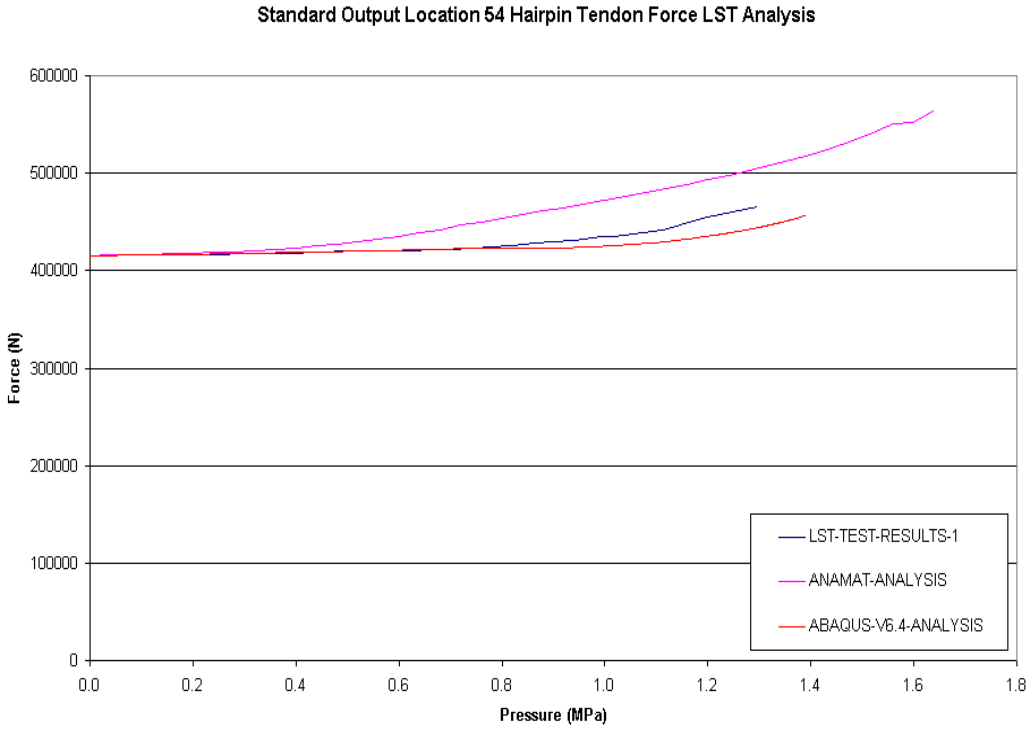

Figure 71 Location 55 Hoop Tendon Force

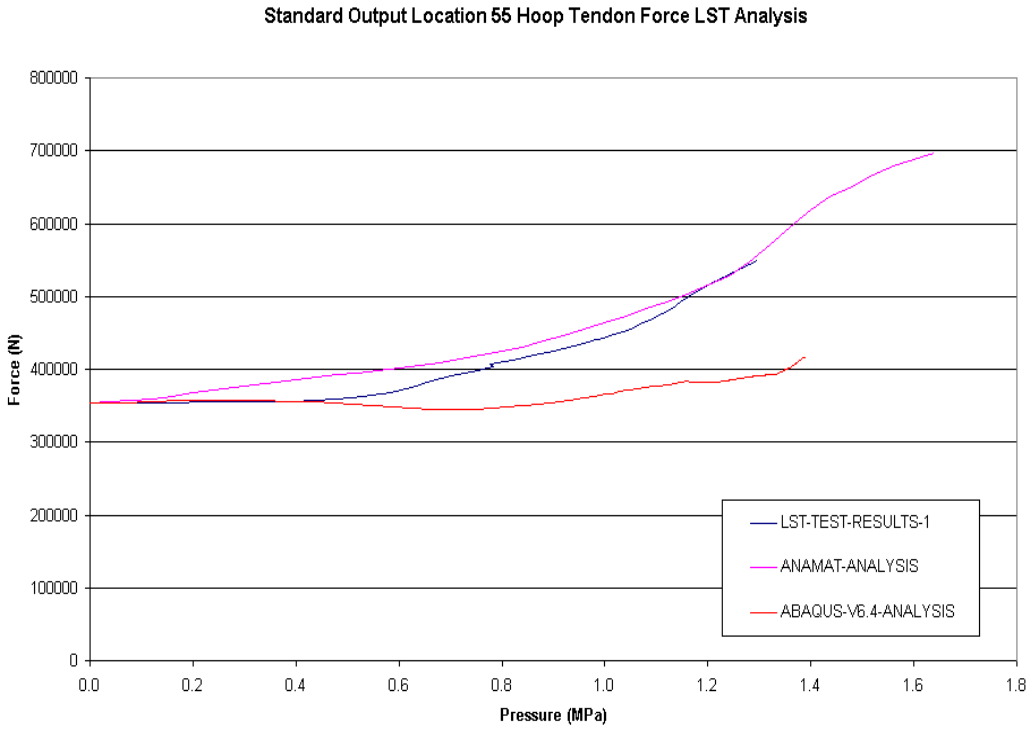

Figure 72 Displaced shape using ANAMAT concrete material model @ 1.72MPa

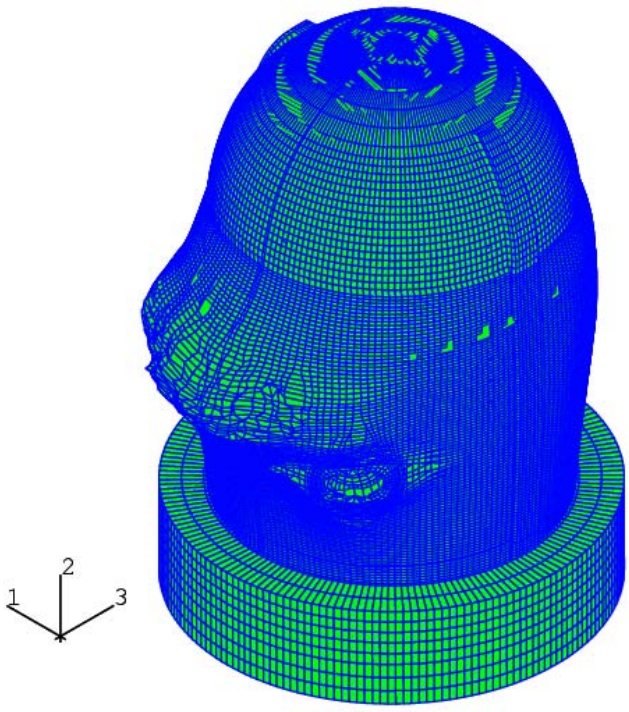

Figure 73 Displaced shape using ABAQUS concrete material model @ 1.40MPa

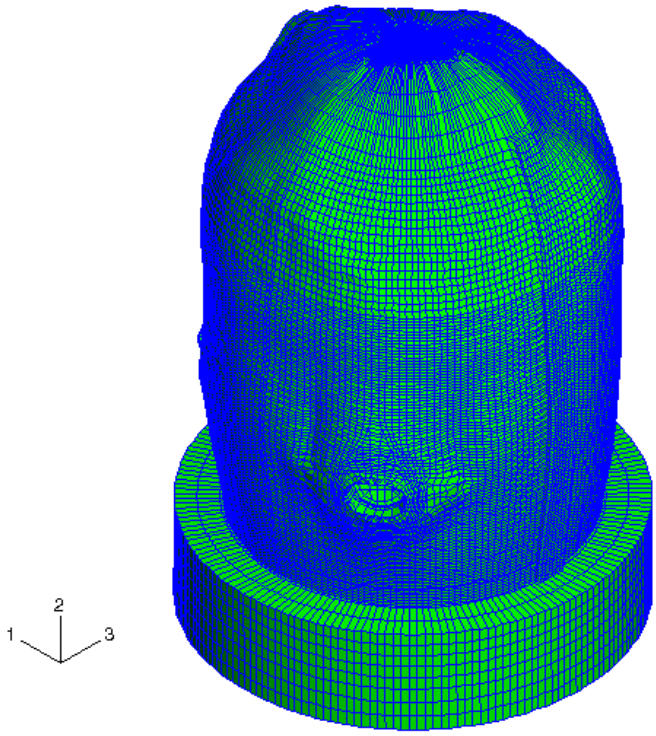

Figure 74 Finite element model at junction of thin/thick liner plate

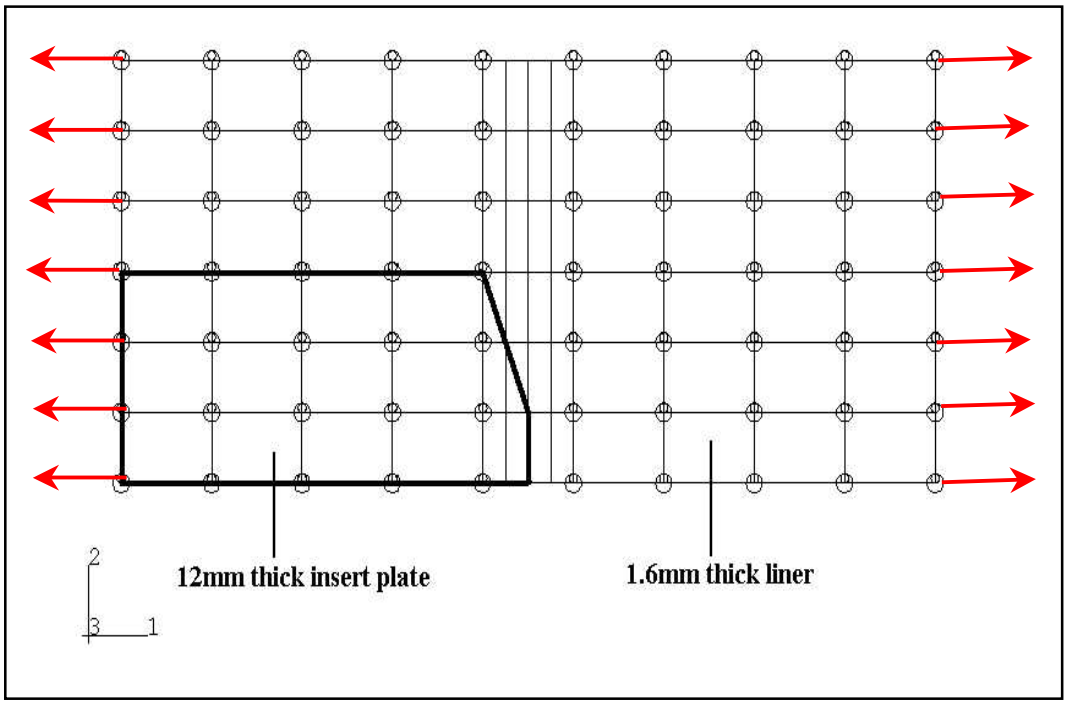

Figure 75 Equivalent plastic strain contour at junction of thin/thick liner plate

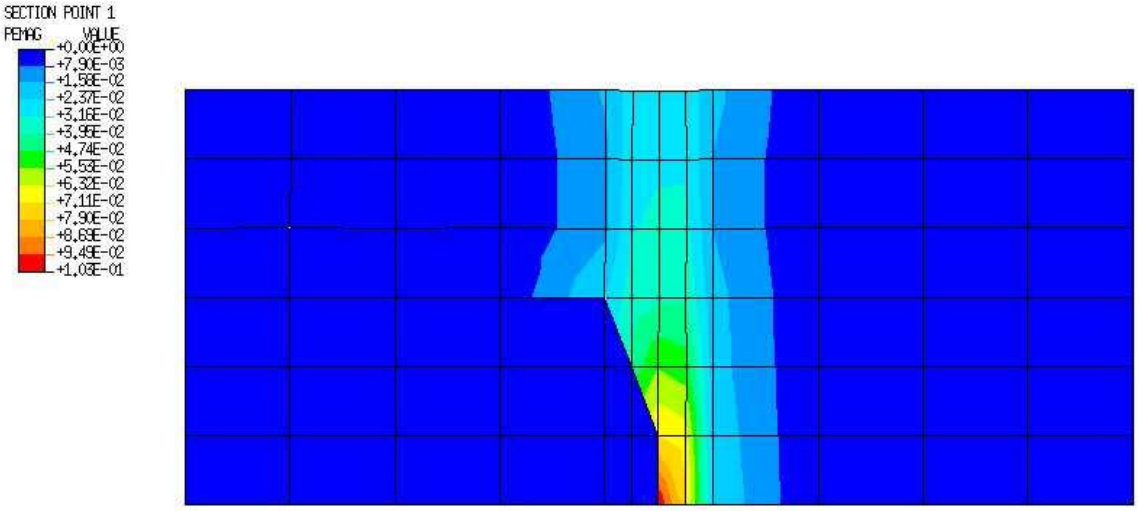

Figure 76 Equivalent plastic liner strains for ANAMAT analysis

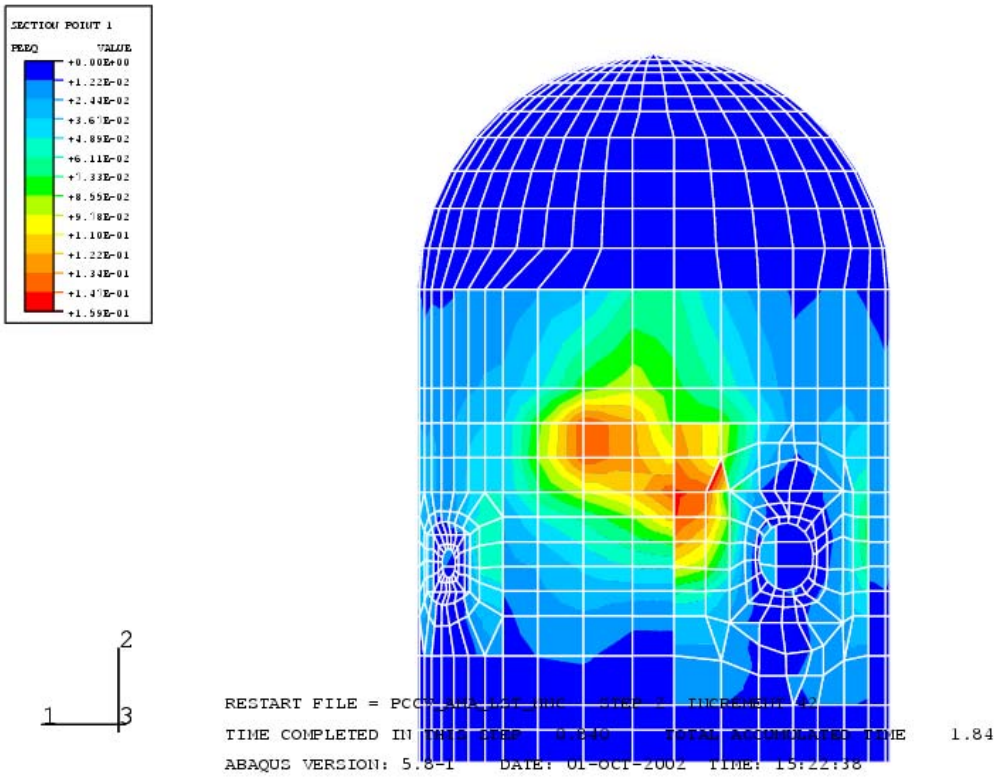

Figure 77 Equivalent plastic liner strains for ABAQUS analysis

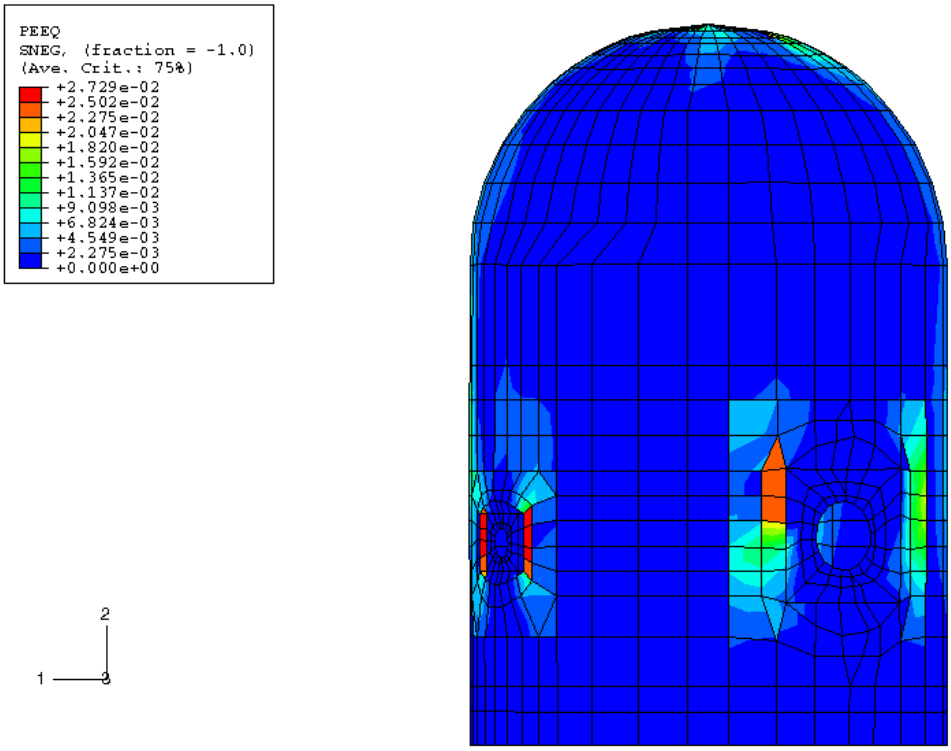

Figure 78 Limit Load Range

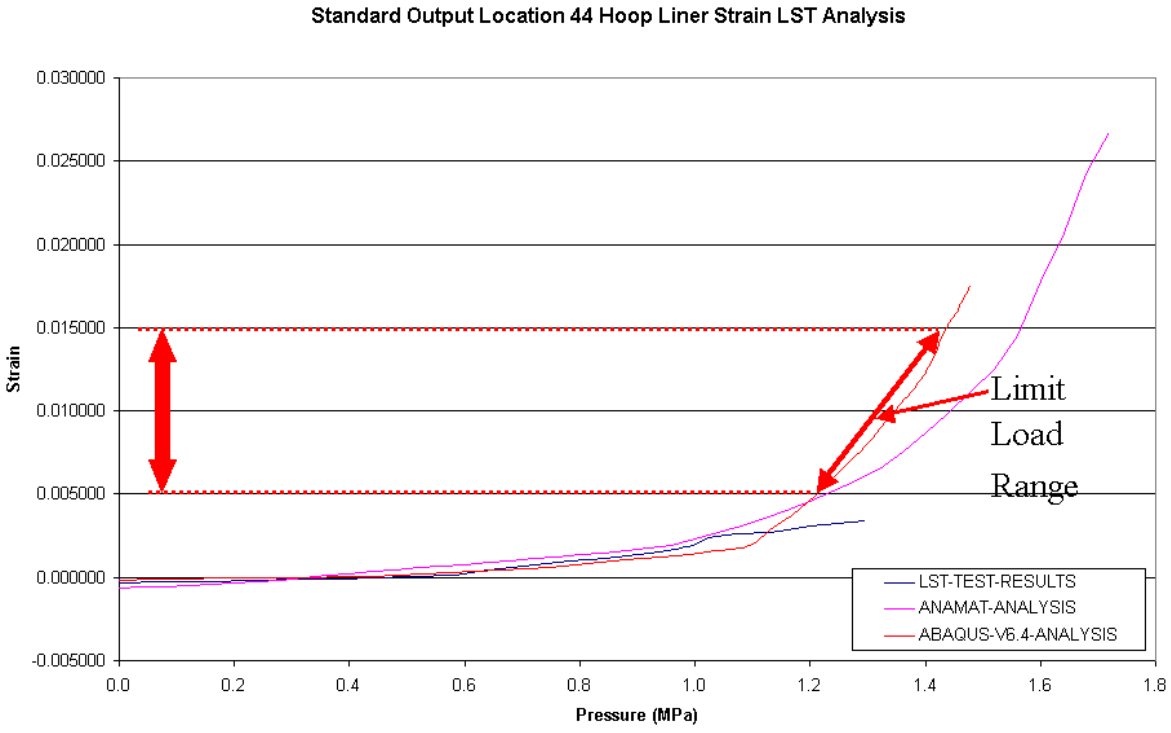

Figure 79 Contour plot showing concrete damage @ 0.66MPa

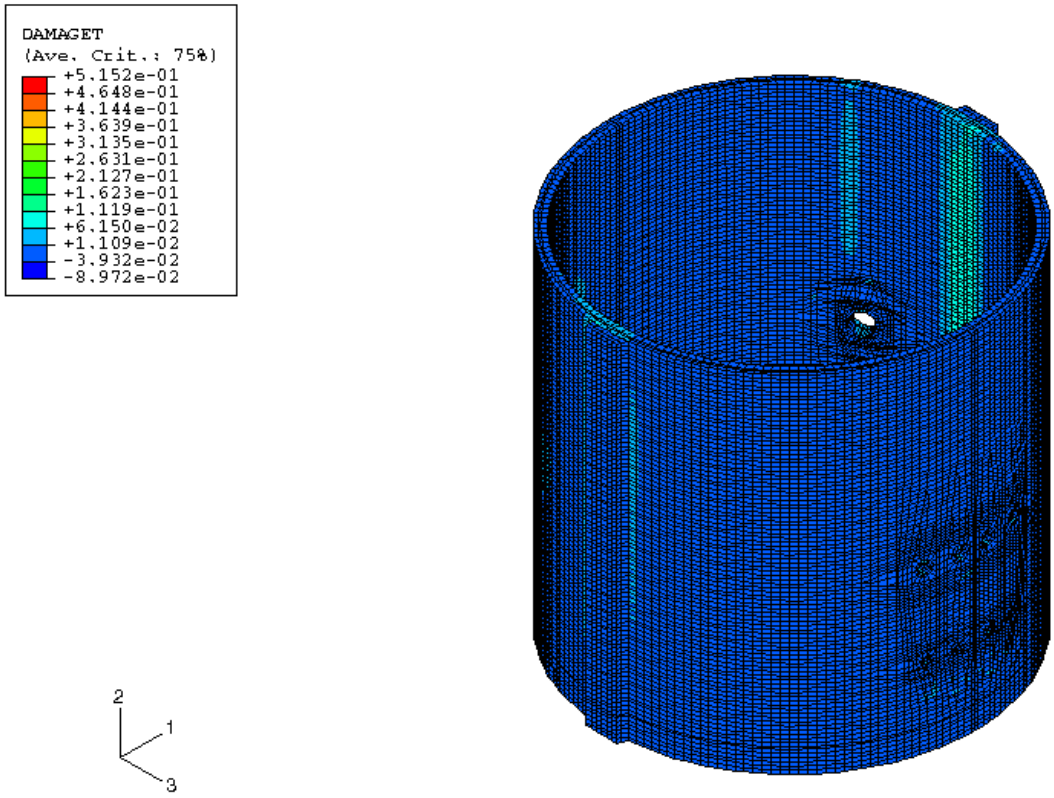

Figure 80 Displaced shape of cylinder showing butterfly mode @ 1.4MPa

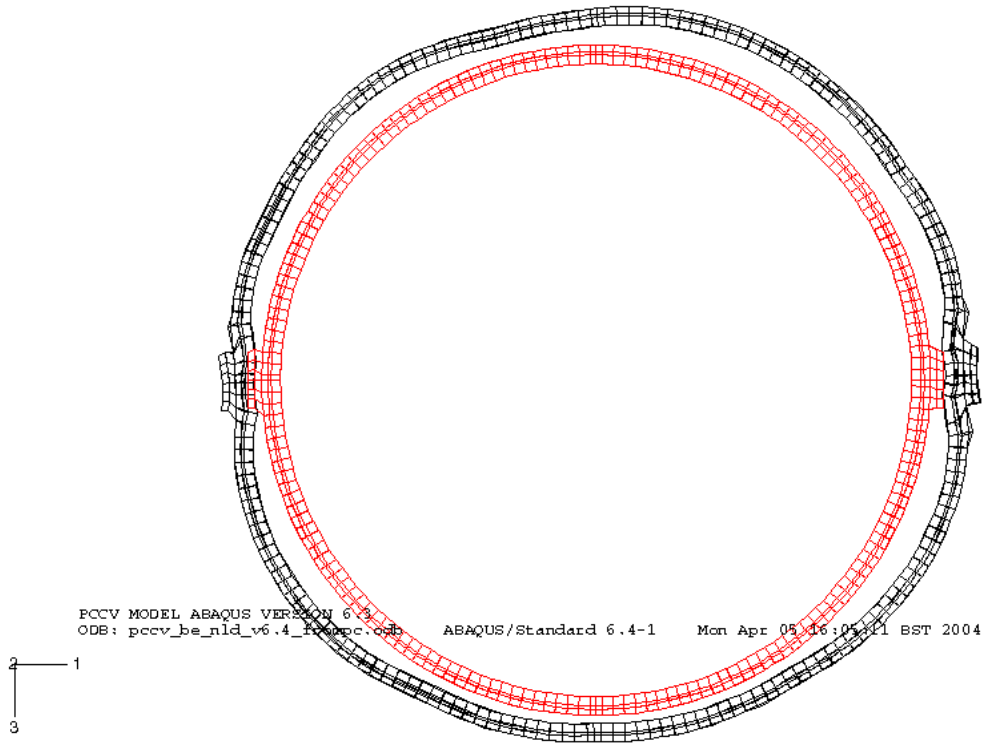

Figure 81 Concrete acoustic monitoring system

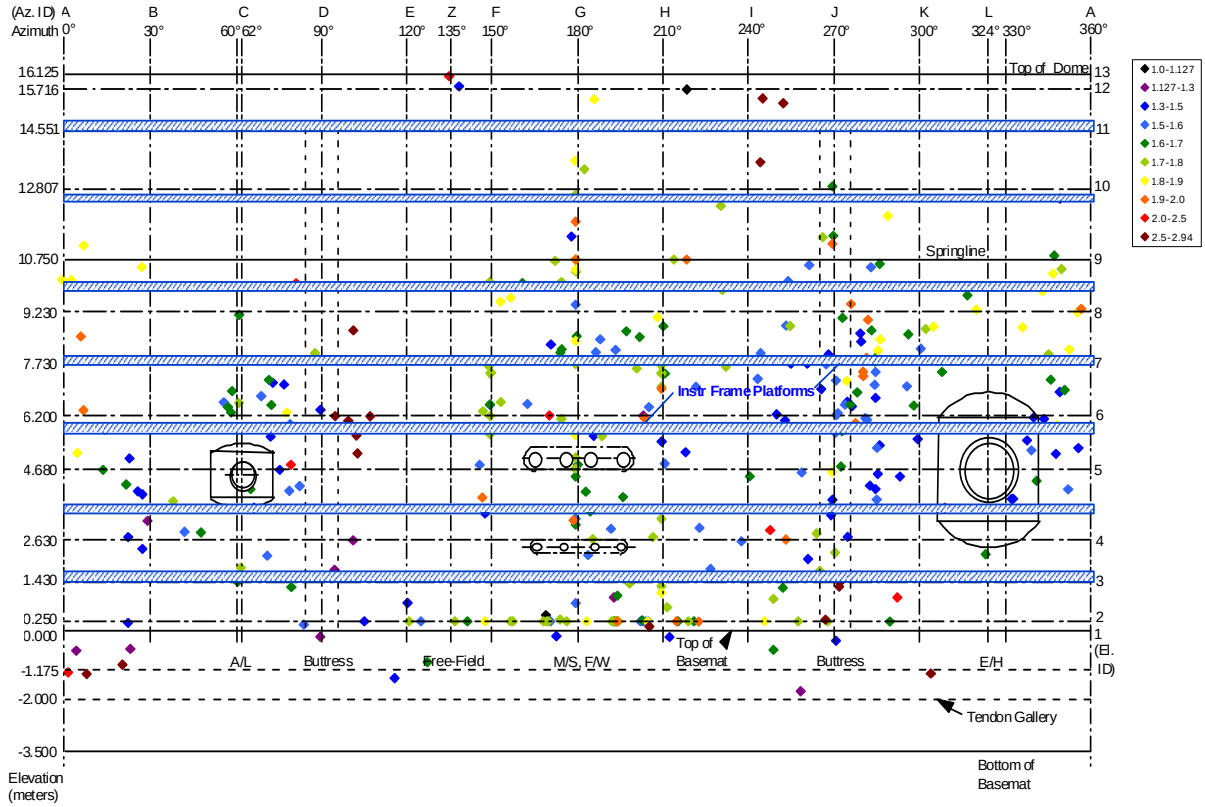

Figure 82 Liner tears after LST

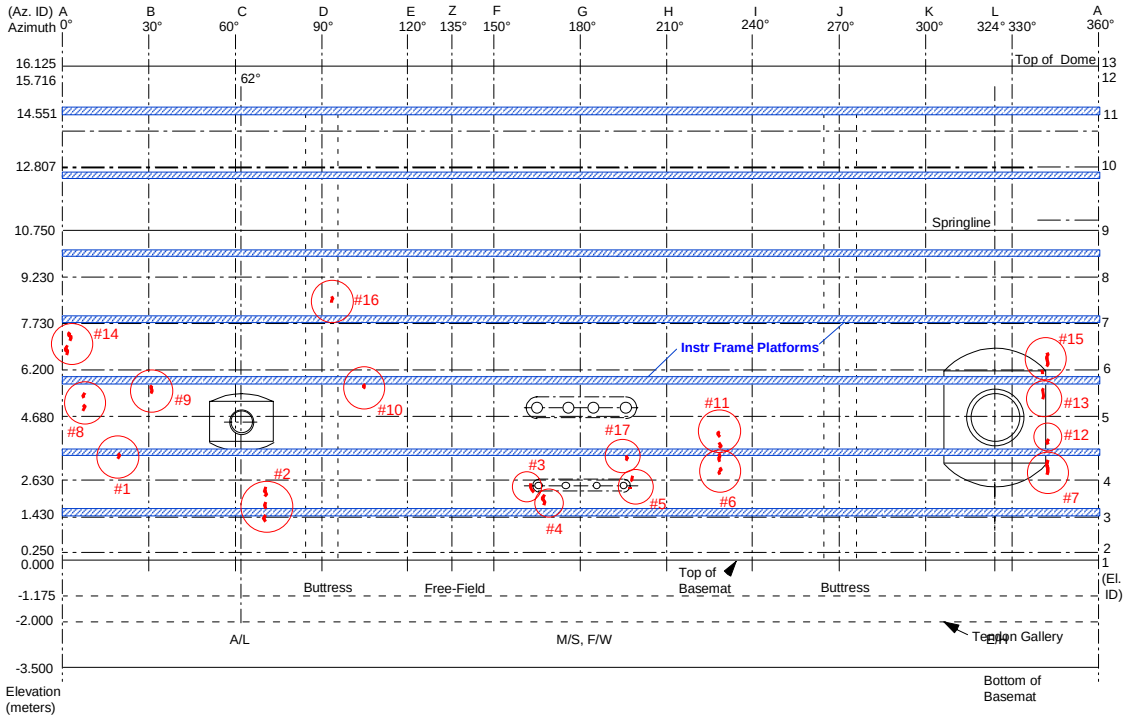

Figure 83 Vertical tendon axial load @1.4MPa

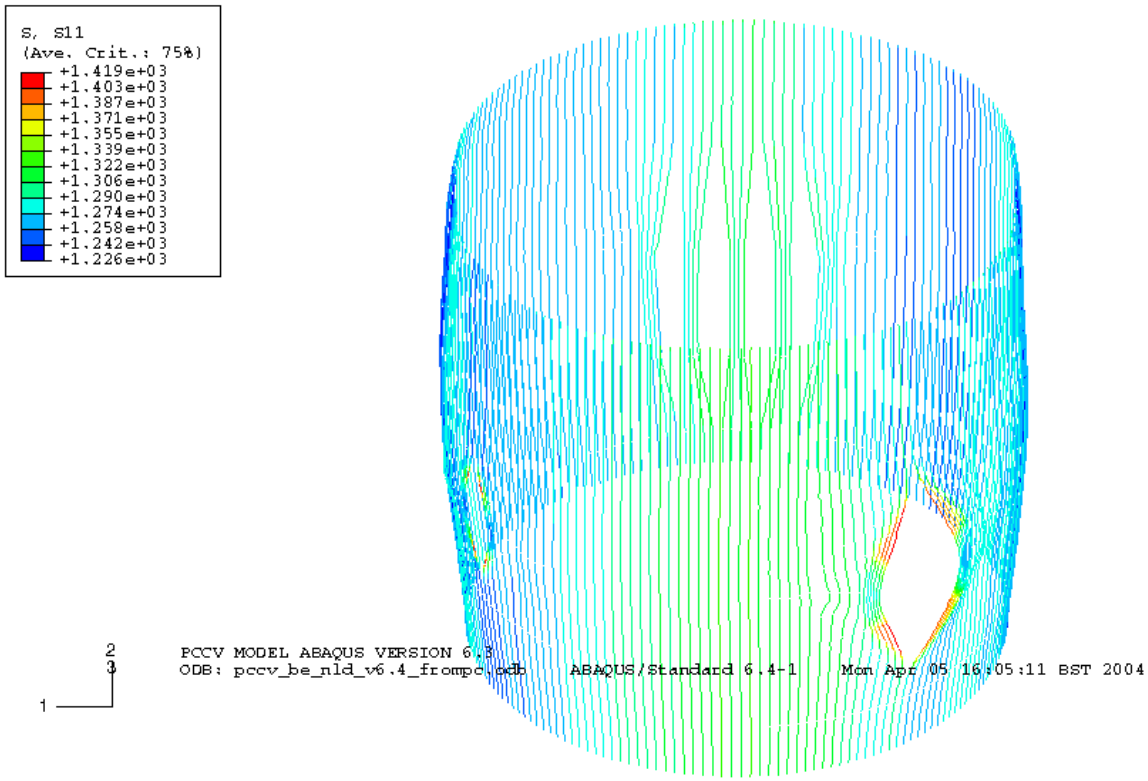

Page intentionally left blank

International Standard Problem on Containment Capacity (ISP- 48) Phase 3

Client: British Energy Generation (UK) Limited
Contract PPK/40099409/FKR

Nawal K Prinja BSc, MSc, PhD, FIMechE
James Curley BSc
NNC Limited
Booths Hall
Knutsford
Cheshire
WA16 8QZ

Customer Number: CE/PWR/6002
Document Number: 11248/TR/002 Issue 04
July 2005

CONFIDENTIALITY, INTELLECTUAL PROPERTY RIGHTS, AND DISCLAIMER STATEMENT

DISCLAIMER

DOCUMENT ISSUE RECORD
(engineering documents)

Adding value through knowledge

Document Title :	International Standard Problem on Containment Capacity (ISP–48) Phase 3
Project Reference:	11248/TR/002 (CE/PWR/6002)

Purpose of Issue : For Information

Security Class : Unclassified

Issue	Description of Amendment	Originator/ Author	Checker	Approver	Date
01	Original Issue	J Curley	N Prinja	N Prinja	Jan 2005
02	Revised to account for BE and HSE comments at review meeting of 15th March 2005 and ISP48 Workshop held 4-8 April 2005.	J Curley	N Prinja	N Prinja	April 2005
03	Revised to account for further internal review comments.	J Curley	N Prinja	N Prinja	June 2005
04	Report reformatted and Executive Summary added.	J Curley	N Prinja	N Prinja	July 2005

Total number of pages:	Intro: (i)-(xii)	Text 1-27	Tables T1-T3	Figures F1-F42	Appendices N/A

Previous issues of this document shall be destroyed or marked **SUPERSEDED**

Distribution: See Distribution List

3050aJan04 Controlling procedure – QP7, QP11, QP40

Distribution List

M W Johnston, British Energy, Peel Park	1 copy + electronic copy
G T Doughty, British Energy, Peel Park	1 copy + electronic copy
R A Ainsworth, British Energy, Barnwood	1 copy + electronic copy
D Barber, British Energy, Barnwood	Executive Summary
D W Twidale, HSE, Bootle	1 copy
D Shepherd, HSE, Bootle	1 copy + electronic copy
M Hatton, HSE	1 bound +1 unbound + electronic copy
J Llambias, NNC	Executive Summary
John Griffin, NNC	Executive Summary
N K Prinja, NNC	1 copy
J Curley, NNC	1 copy
Job File, J5646, NNC	1 copy + electronic copy (for EDMS)

CONTENTS

Distribution List iv

Executive Summary vii

LIST OF TABLES ix

LIST OF FIGURES x

1 INTRODUCTION 1

2 TECHNICAL BACKGROUND 3

3 SCOPE 5
3.1 Phase 3 Calculation of the Thermal Effects of Case 1 of ISP48 5
3.2 Transient Thermal Creep in Concrete 6
3.2.1 Theory 6

4 ¼ SCALE PCCV FINITE ELEMENT MODEL 8
4.1 Description of the Global Model 8
4.2 Cylinder Wall and Dome 8
4.3 Basemat 9
4.4 The Cylinder Wall Penetrations 9
4.5 The Post-Tensioning Tendons 9
4.5.1 Vessel Pre-Tensioning System 10
4.6 Internal Liner and Liner Anchorage 11
4.7 Concrete Reinforcements 11
4.8 PCCV Support Conditions 11

5 REVIEW OF THERMAL PROPERTIES SUPPLIED BY SNL 13
5.1 Thermal Property Data Supplied by SNL 13
5.2 Loading Data Supplied by SNL 13

6 MODELLING 14
6.1 Heat Transfer Modelling 14
6.1.1 Concrete Elements 14
6.1.2 Liner Elements 14
6.1.3 Tendons and Rebars 14
6.1.4 Material Properties 14
6.1.5 Boundary Conditions 14
6.1.6 Conduction Between Liner and Inner Concrete 15
6.1.7 Convection from Outer Concrete Surfaces 15
6.1.8 Loading 15
6.2 Stress Analysis Modelling 15
6.2.1 Loading 16
6.2.2 ANAMAT and ABAQUS 16

7 RESULTS 17
7.1 Heat Transfer Results 17
7.2 Stress Analysis Results 17

8 ASSESSMENT OF RESULTS 19
8.1 Thermal Deformation 19
8.2 Liner Assessment 19
8.3 Tendon Assessment 20

8.4 Thermal Transient Creep 21
8.5 Concrete Cracking 21
8.6 PCCV Failure Mode 22
9 COMPUTER FILES 23
10 CONCLUSIONS 25
11 REFERENCES 26
12 NOTATION AND ABBREVIATIONS 27

Executive Summary

NRC/NUPEC sponsored tests of the ¼ scale pre-stressed concrete containment vessel (PCCV) which have been executed at Sandia National Laboratories (SNL) in the USA. The Limit State Test (LST) executed during September 2000 was based on pneumatic pressurisation of the vessel and achieved a maximum pressure of 1.3MPa (3.3 times the design pressure). The objectives of the International Standard Problem (ISP48) project are to extend the understanding of capacities of actual containment structures based on the results of the PCCV LST and any other sources of available research.

NNC sponsored by HSE participated in the LST round robin exercise and completed the analysis to predict the limit load of the vessel. Predictions from all the participants of the round robin were collated and published by SNL in August 2000. The LST identified liner tearing as the mode of failure. Whilst there was no visible damage to the PCCV structure, the breach of the pressure boundary dictated the limit load due to excessive leakage rate. Out of the total 17 participants, the NNC/HSE model was one of only four that successfully predicted liner tearing as the mode of failure. It was recognised at the international pre-test round robin meeting in October 1999 that the NNC/HSE model was one of the most sophisticated 3D full global models, which took account of the interaction between all the main structural features.

All the previous test and analysis work done has shown that leakage occurs before the burst pressure but in these studies only the mechanical loading (gravity, prestress and internal pressure) was considered and thermal loading was ignored. In real containments, increase in internal pressure is associated with thermal loading. One of the aims of Phase 3 of the ISP48 project was to study the effects of accident temperatures and see if the onset of leakage is closer to the burst pressure in full size containments.

This reports presents the assessment of concrete containment capacity for phase 3 of the ISP 48 project. The mandatory load case for phase 3 (Case 1) involving saturated steam conditions was analysed by using a full 3D global model of the containment structure. Heat transfer and nonlinear stress analysis was conducted using version 6.4 of ABAQUS to study the influence of thermal loading on the containment capacity. In addition, the effects of Thermal Transient Creep (TTC) in concrete at elevated temperatures have been investigated using the equivalent modulus approach. It is concluded that the thermal straining of the liner results in rupture at approximately 1.25MPa, which is 14% higher than the rupture pressure of 1.1MPa obtained from the limit state test. The pressure required to induce tendon failure increases from 1.4MPa to approximately 1.50MPa. This is an increase of 7% compared to the limit state test. However, the modelling assumption of no sliding in the hoop tendons prevents load redistribution. Therefore, it can be concluded that in this case thermal loads do not change the pressure at tendon rupture. Inclusion of thermal loading and temperature dependent effect of TTC show that the margin between the liner rupture and the structural collapse decreases.

For the accident condition investigated, liner rupture is the initial failure mode. The design intent of liner rupture before catastrophic structural failure of the containment is maintained.

If the margin between tendon failure and liner rupture is defined as the ratio of vessel pressurisation required to cause the failures, the margin decreases from 1.27 for pressure only to 1.2 for pressure plus temperature loads.

LIST OF TABLES

Table 1 Results Summary for Case 1 (P+T) from Start of Fault at Standard Output Locations

Table 2 Anchorage properties

Table 3 Heat Transfer Material Properties

Table 4 Additional Stress Analysis Material Properties

Table 5 Summary of Results: Calculated Pressures (MPa) and Strains (%)

LIST OF FIGURES

Figure 1 Case 1 Pressure vs Time loading received from SNL
Figure 2(a) Case 1 Temperature vs Time loading received from SNL
Figure 2(b) Case 1 Temperature vs Pressure Loading
Figure 3 Finite Element Representation of the PCCV
Figure 4 Detail view of the PCCV dome model
Figure 5 The basemat model showing locations of global restraints
Figure 6 Detailed view of the equipment hatch penetration model
Figure 7 Detailed view of the airlock penetration model
Figure 8 Detailed view of the main steam and feed water penetration model
Figure 9 PCCV vertical tendons model
Figure 10 Equipment hatch penetration lining and cover plate
Figure 11 PCCV model supported on soil springs
Figure 12 Internal liner model, showing detail around the main steam and feedwater penetrations
Figure 13 Comparison of Test & Pre-test Vertical Tendon Loads
Figure 14 Comparison of Test & Pre-test Hoop Tendon Loads
Figure 15 Variation in tendon load due to friction and seating loss
Figure 16 Convection to free air vs. temperature
Figure 17 Nodal Temperature at Location 1
Figure 18 Nodal Temperature at Location 6
Figure 19 Nodal Temperature at Locations 7 & 8
Figure 20 Nodal Temperature at Location 11
Figure 21 Nodal Temperature at Location 12
Figure 22 Nodal Temperature at Location 13
Figure 23 Nodal Temperature at Location 14
Figure 24 Nodal Temperature at Location 18
Figure 25 Nodal Temperature at Location 19
Figure 26 Nodal Temperature at Locations 22 & 23
Figure 27 Nodal Temperature at Locations 32 & 33
Figure 28 Nodal Temperature at Locations 38 & 39
Figure 29 Nodal Temperature at Location 42
Figure 30 Nodal Temperature at Location 45
Figure 31 Nodal Temperature at Location 48
Figure 32 Nodal Temperature at Location 50
Figure 33 Nodal Temperature at Location 52

Figure 34 Nodal Temperature at Location 55
Figure 35 Temperature contour profile, vertical section through PCCV
Figure 36 Temperature contour profile at cylinder / basemat junction
Figure 37 Temperature contour profile through the cylinder wall
Figure 38 Stress Analysis Model – Location 1
Figure 39 Stress Analysis Model – Location 6
Figure 40 Stress Analysis Model – Location 7
Figure 41 Stress Analysis Model – Location 8
Figure 42 Stress Analysis Model – Location 11
Figure 43 Stress Analysis Model – Location 12
Figure 44 Stress Analysis Model – Location 13
Figure 45 Stress Analysis Model – Location 14
Figure 46 Stress Analysis Model – Location 18
Figure 47 Stress Analysis Model – Location 19
Figure 48 Stress Analysis Model – Location 22
Figure 49 Stress Analysis Model – Location 23
Figure 50 Stress Analysis Model – Location 32
Figure 51 Stress Analysis Model – Location 33
Figure 52 Stress Analysis Model – Location 38
Figure 53 Stress Analysis Model – Location 39
Figure 54 Stress Analysis Model – Location 42
Figure 55 Stress Analysis Model – Location 45
Figure 56 Stress Analysis Model – Location 48
Figure 57 Stress Analysis Model – Location 50
Figure 58 Stress Analysis Model – Location 52
Figure 69 Stress Analysis Model – Location 54
Figure 60 Stress Analysis Model – Location 55
Figure 61 Standard Output Location 39 Liner Hoop Mechanical Strain
Figure 62 Standard Output Location 39 Hoop Liner Mechanical Stress
Figure 63 Standard Output Location 53 Hoop Tendon Mechanical Strain
Figure 64 Equivalent Youngs Modulus for Simulating Transient Thermal Creep
Figure 65 Tendon Load Profile During Vessel Pressurisation and Heat-Up
Figure 66 Inner Cylinder Wall E11 Stain Distribution - Comparison Highlighting Effects of Thermal Transient Creep
Figure 67 Inner Cylinder Wall E33 Stain Distribution - Comparison Highlighting Effects of Thermal Transient Creep
Figure 68 Inner Cylinder Wall E22 (Axial) Stain Distribution - Comparison Highlighting Effects of Thermal Transient Creep

Figure 69 Deformation Comparison: E/H Elevation at 0.837 MPa Internal Pressure and 179^0 C Temperature

Figure 70 Deformation Comparison: 90-270^O Azimuth at 0.837 MPa Internal Pressure and 179^{o}C Temperature

Figure 71 Deformation Comparison: 0-180^o Azimuth at 0.837 MPa Internal Pressure and 179^o C Temperature

Figure 72 Liner Meridional Stress at Locations 36, 38 and 40

Figure 73 Hoop Stresses at Vessel Inner and Outer Surfaces, Wall Mid-Height

Figure 74 Meridional Stresses at Vessel Inner and Outer Surfaces, Wall Mid-Height

Figure 75 Hoop Stress Variation Thru Wall at 135^0 Azimuth and Cylinder Mid-Height

Figure 76 Meridional Stress Variation Thru Wall at 135^0 Azimuth and Cylinder Mid-Height

1 INTRODUCTION

At the June 2002 meeting of the Committee on the Safety of Nuclear Installations (CSNI), the proposal (Ref 1) for the International Standard Problem 48 (ISP 48) on containment integrity was approved. British Energy contracted NNC Limited (Contract Ref: PPK/40099409/FKR) to perform the ISP48 analysis work. Phases 1 and 2 of the project work were reported by NNC in Ref 2. This report covers Phase 3 of the ISP 48 work. The scope of these phases of work is described in section 3.

NRC/NUPEC sponsored tests of the ¼ scale pre-stressed concrete containment vessel (PCCV) which have been executed at Sandia National Laboratories (SNL) in the USA (Ref 3). The Limit State Test (LST) executed during September 2000 was based on pneumatic pressurisation of the vessel and achieved a maximum pressure of 1.3MPa (3.3 times the design pressure). The objectives of the ISP48 are to extend the understanding of capacities of actual containment structures based on the results of the PCCV LST and any other sources of available research.

Under contract to the United Kingdom Health and Safety Executive (HSE), NNC participated in the LST round robin exercise and completed the analysis (Ref 4) to predict the limit load of the vessel. Predictions from all the participants of the round robin were collated and published by SNL in August 2000 (Ref 5). The LST identified liner tearing as the mode of failure. Whilst there was no visible damage to the PCCV structure, the breach of the pressure boundary dictated the limit load due to excessive leakage rate. It can be seen from Ref 5 that out of the total 17 participants, the NNC/HSE model is one of only four that successfully predicted liner tearing as the mode of failure. It was recognised at the international pre-test round robin meeting in October 1999 that the NNC/HSE model was one of the most sophisticated models. The NNC/HSE model was a full 3D global model, which took account of the interaction between all the main structural features.

Following the pre-test round robin, NNC carried out the post-test analysis under HSE contract CE/GNSR/1 and the work was presented in Ref 6. This work consisted of a comparison between the FE analysis and the test results to give an assessment of the accuracy and reliability in predicting the failure modes and limit loads of PCCV structures using finite element analysis. It also included analysis of the Structural Failure Mode Test (SFMT) executed in November 2001, in which hydraulic pressure was used to over pressurise the containment to total structural collapse. The results of the over pressurisation test have been published by SNL in Ref 3. The analysis carried out in Ref 6 predicted the failure location and the behaviour up to collapse with good accuracy.

All the previous test and analysis work done has shown that leakage occurs before the burst pressure but in these studies only the mechanical loading (gravity, prestress and internal pressure) was considered and thermal loading was ignored. In real containments, increase in internal pressure is associated with thermal loading. One of the aims of Phase 3 of the ISP48 project is to study the effects of accident temperatures and see if the onset of leakage is closer to the burst pressure in full size containments.

The 2nd meeting of the ISP48 project held in Spain in March 2004, reviewed Phase 2 results and finalised the combination of mechanical and thermal loadings for Phase 3 (Ref 7). The mandatory Case 1 consists of applying saturated steam conditions as steady state static loading and recommended Case 2 simulates Station Blackout pressure and temperature transients. This work covers only Case 1 of Phase 3.

Technical background to the PCCV analysis work done under the international round robin is presented in section 2 and the scope of the work for Phase 3 of the ISP48 project is given in section 3. The scope and results for Phases 1 and 2 of the ISP48 project can be found in Ref 2. A description of the FE model is given in section 4. Review of the data provided for Phase 3 and changes to the FE models can be found in sections 5 and 6 respectively. The analysis results for phase 3 can be found in section7 followed by the assessment of results in section 8. The conclusions of this study are in section 9.

2 TECHNICAL BACKGROUND

The original LST test sponsored by the NRC/NUPEC attracted contributions from 17 participants from USA, Canada, France, Japan, Korea, UK, Spain, China, India and Russia who submitted their pre-test analysis results. 14 of these participants presented their results at the meeting held in October 1999 at Sandia Laboratories, USA. There was significant difference in the behaviour predicted by the participants. This was mainly due to the modelling approach, assumptions and interpretation of the design data. Many of the participants constructed global models of the PCCV reflecting their assumptions, to predict the limit load. Others made detailed models of local features such as the penetrations and buttresses but did not have a full global model. The NNC/HSE model was the only full 3-D global model (see Ref 4) which had included sufficient details of all the important local features like the tendon layout, penetrations, buttresses, stressing gallery, soil foundation and the liner.

In Ref 4 the NNC/HSE model was analysed using version 5.8 of the ABAQUS general purpose FE code (Ref 8). It was found that the concrete material model in the 5.8 version of ABAQUS gave numerical problems and the global 3-D model could not be analysed beyond an internal pressure of 0.71MPa. The analysis beyond 0.71MPa was completed by incorporating the ANACAP concrete material model routine supplied by ANATECH (Ref 9).

The main objective of the exercise was to predict the failure mode and the behaviour up to the pressure capability. The NNC/HSE model accurately predicted that the liner tearing would control the pressure capability. It also predicted accurately that the main structural components like the tendons and reinforcing bars would not fail before liner tearing. Whilst the failure mode was predicted accurately, there remained discrepancies between the history of the response recorded during the test and that predicted by the FE analysis. This was because the model did not take account of the as-built conditions, which were investigated in the post-test analysis (Ref 6).

The test model had a design pressure, Pd, of 0.39MPa and the Limit State Test (LST) achieved a pressure of 1.295MPa (3.3 Pd), which was well beyond the design basis. The test was limited because the vessel leak rates increased beyond the supply limit of the nitrogen pressurization system. The overall PCCV structure remained substantially intact after the LST. The sponsors agreed to extend the test and SNL sealed the leaks and conducted the Structural Failure Mode Test (SFMT) by using a water pressurization system. The SFMT was conducted on 14 November 2001 and achieved its objective of causing global collapse of the PCCV structure, reaching a pressure of 1.423MPa (3.65 Pd).
The LST and SFMT data in conjunction with the pre-test and the post-test analyses show three stages of the structural response of the pressurized PCCV as it approaches its structural collapse load.

The first stage of predominantly elastic response can be predicted with very good accuracy using standard finite element technology. The second stage involving inelastic response with extensive concrete cracking required specialist concrete material models and detailed geometric representation of the main structural features. It is important to model the interaction between various structural elements to simulate load redistribution as some components yield or fail. Such local yielding or rupture may lead to loss of functionality or breach of pressure boundary. The third stage involving gross deformation and structural collapse requires the solution of a highly non-linear problem. Extensive concrete cracking, well beyond the tension

stiffening range, occurs and requires robust constitutive models capable of simulating extensively cracked concrete. Provided such a specialist FE package is available, an experienced analyst can predict the collapse limit and failure mode with fair accuracy.

As part of the ISP48, additional information about the test was made available to the participants (Ref 3). The data supplied to the participants for Phase 1 of the ISP48 project for the main structural material properties was reviewed in Ref 2. After a review of the data the NNC global model was updated for Phase 2 of the ISP48 project. In addition to updating the material properties the global model was modified for analysis using the latest ABAQUS 6.4 code (Ref 10). The reason for this was the inclusion by ABAQUS of a new concrete material model. Details of the upgrading and inclusion of the new concrete material model within ABQUS is reported in Ref 2.

For Phase 3 of the ISP48 project data has been supplied to the participants on the thermal properties of the PCCV, including thermal conductivities, specific heat capacity and surface film coefficients. In addition to the thermal properties being supplied, pressure and temperature time histories were provided for loading the vessel.

3 SCOPE

The overall project comprises four phases of work as follows:

- Phase 1: Data collection and identification (already reported in Ref 2)
- Phase 2: Calculation of the LST using updated data reported in Ref 2
- Phase 3: Calculation of response to both thermal and mechanical loadings
- Phase 4: Reporting workshop

For Phase 3, two load cases (mandatory Case 1 and recommended Case 2) were specified in Ref 7. Case 1 is of particular interest for PCCV structures, which may be exposed to long-term thermal loading. This report addresses Phase 3 in which only the mandatory Case 1 has been analysed. Instead of Case 2, effort has been spent on analysing case 1 for the effects of transient thermal creep in concrete.
The full scope of Phase 3 of the ISP48 is to perform a new stress analysis of the ¼ scale PCCV using the same models as for the Phase 2 analysis (Ref 2), but incorporating thermal loading in addition to the mechanical loading. The existing FE results (from Refs 2, 4 and 6) and the results from the new stress analysis will be compared with the test data to indicate the following:-

- Effect of accident temperatures on the containment capacity
- Would the onset of leakage be later and much closer to the burst pressure

3.1 Phase 3 Calculation of the Thermal Effects of Case 1 of ISP48

This task requires calculation of the effects of accident temperatures upon the global model of the PCCV. Case 1 consists of applying saturated steam conditions as steady state static loading. This case considers the simulation of plant steady state conditions at normal operation, followed by a simplified loss of cooling accident in which temperatures increase to 200^{o}C and a pressure of 1.46MPa is achieved in 42 minutes. The loading of the vessel for Case 1 has been defined by SNL which specifies a linear increase in pressure and a non-linear increase in temperature as shown in Figures 1 and 2.

The analysis for Case 1 of Phase 3 requires the analysis of two models. Initially a heat transfer model is analysed followed by a stress analysis model.

The global model, as updated for Phase 2 of the ISP48 project is utilised for both analyses. The data supplied by SNL provided the participants with the choice of either performing their own heat transfer analysis or to use the thermal gradients through the wall thickness supplied by SNL. In this work, full heat transfer analysis is done.

In the previous analysis work (Refs 4 and 6), the ANACAP routine supplied by ANATECH was used to remove some of the limitations of the ABAQUS version 5.8 concrete material model. Incorporation of this concrete model extended the range of pressure over which predictions could be made. A new concrete material model is available in ABAQUS 6.4 that allows the analysis of extended pressure range.

It is also required that results are reported at the revised standard output locations as defined by the ISP48 project. A list of these revised locations can be found in Table 1. This will enable direct comparison between analytical results of the participants. NNC has provided results at all the 23 required locations.

3.2 Transient Thermal Creep in Concrete

Three forms of concrete creep have the potential to be accelerated by the effects of elevated temperatures. These are enhanced flow, delayed elastic, and transient thermal creep. Of these, transient thermal creep is considered to be by far the most significant component in mature concrete and this study will assess the effects for a PCCV under Case 1 loading.

Transient thermal creep can be defined as the strain in excess of the creep at a constant temperature and load, and can be expressed as a function of the change in temperature alone. Transient thermal creep only occurs when the concrete is heated beyond a temperature to which it has previously been exposed and, importantly, has been found to be irrecoverable.

Although the mechanisms which cause the development of transient creep strains are not fully understood, it is thought that between 100°C and 200°C, drying of the cement matrix is the most important factor, whilst at higher temperatures a change in the chemical structure of the cement matrix is the primary factor.

An approach for modelling this is to use what is known as an 'equivalent modulus approach'. This approach is adopted for the analysis because ABAQUS cannot facilitate the modelling of concrete cracking and creep simultaneously. Research data is available on the relationship between the temperature, stress level, level of TTC and the Young's modulus associated with these parameters. The relationship of Youngs Modulus with respect to concrete temperature used for the modelling is shown in Figure 64 for the dome, cylinder wall and basemat.

3.2.1 Theory

Ref 15 specifies the Transient Thermal Creep Law as follows;

$$S = a \times T^{n} \quad (1)$$

where
S = micro strain per unit stress
T = Temperature in degrees Celsius

And for concrete the constants are
a = 1.74×10^{-4}
n = 2.362

Equivalent Modulus Law;

$$E_T = \frac{E}{1 + (E \times S)} \quad (2)$$

where
E_T = Transient Modulus
E = Initial Modulus

Therefore;

$$E_T = \frac{E}{1 + (E \times a \times T^{n})} \quad (3)$$

The effects of basic mechanical creep have been neglected as this study is interested in the effects of temperature which are independent of time.

4 ¼ SCALE PCCV FINITE ELEMENT MODEL

4.1 Description of the Global Model

Concrete components of the vessel are simulated with the ABAQUS eight-node solid element C3D8. The eight-node solid element is mathematically formulated such that it accommodates the inclusion of steel reinforcements. At a minority of locations, due to meshing requirements, six-node linear prism elements (C3D6) were used. Six-node prism elements do not support reinforcement capability. Within the cylinder, all solid elements are fully integrated, while the basemat and dome elements have reduced integration. Figure 3 shows the 3D global model of the PCCV model.

The origin of the FE model is at the centre of the top surface of the basemat. Directions 1, 2 and 3 are X, Y and Z respectively. X is along the 90^{o} azimuth, Y is vertical and Z is along the 180^{o} azimuth.

4.2 Cylinder Wall and Dome

The mesh density of the cylinder wall and dome in the circumferential direction was driven by the requirement to model the vertical post-tensioning tendons explicitly. Three elements were employed in the wall-thickness direction of the cylinder and dome. For the fully integrated elements, this gives a total of six integration points through the wall to provide adequate information in areas of high bending. To allow for the explicit representation of each vertical tendon, 184 solid elements were arranged around the circumference of the vessel. The resulting layout consists of a cylinder and dome wall mesh with elements at approximately 2o intervals in the circumferential direction.

The mesh density in the vertical direction was influenced by the specification of the hoop tendons in the concrete elements. The cylinder hoop tendons were arranged at vertical intervals of 112.7mm. The solid element nodes are meshed vertically to correspond with the spacing of the hoop tendons.

The height of the elements in the lower half of the dome is base on the vertical spacing of the dome hoop tendons. The dome elements are uniformly meshed up to a height of 14690mm, the location of the uppermost hoop tendon. The meshing of the dome in the hoop direction was dictated by the vertical plane of the tendons through the dome. In the dome apex region, a refined solid element mesh allows meshing of the vertical tendons where they intersect at the vessel crown. Figure 4 shows a detailed view of the model.

The buttresses at the 90o and the 270o azimuths are reinforced columns onto which the hoop tendons are anchored. The stiffness of the cylinder and the dome at the 90o and 270o azimuths is enhanced by the restraining effect of the buttresses. The reinforcement scheme of the buttresses comprises vertical, radial U bars and trim bars. Additional stiffening is provided by the steel plates at the tendon anchorage end-blocks. The buttresses and their reinforcement have been modelled explicitly.

4.3 Basemat

The basemat is a thick concrete reinforced slab supporting the vessel superstructure within which the vertical tendons are anchored. It is heavily reinforced at its top and bottom surfaces. The top surface reinforcement consists of a layer of hoop rebars sandwiched between two grids of radially spanning rebars. The bottom surface is reinforced with a rectangular grid of cross rebars. Additional reinforcement is provided in the vicinity of the tendon anchorage gallery. The flexural reinforcements were defined within each solid element. The basemat shear reinforcements were not modelled. Figure 5 shows a view of the basemat.

4.4 The Cylinder Wall Penetrations

The cylinder wall penetrations and their immediate vicinity have been explicitly modelled. Structural features within the penetration area that are represented explicitly in the model are the enhanced reinforcement stiffening, thickened wall section (airlock and equipment hatch penetrations), steel plates lining the penetration cavity, the penetrations cover plates, the vertical and hoop tendons, internal vessel liner and the liner anchorage. The finite element meshes of the equipment hatch, airlock, main steam and feed water penetrations are shown in Figures 6, 7 and 8.

4.5 The Post-Tensioning Tendons

The post-tensioning tendons have been modelled using two different approaches. The vertical tendons were modelled explicitly using the two-node, linear truss element T3D2. For each tendon, nodes have been generated coincident to the solid element concrete nodes along the tendon path. Typically, in the non-penetrated areas a vertical tendon consists of up to 220 elements, depending upon its location within the vessel. Each vertical tendon node lying within the cylinder of the vessel is constrained in the horizontal degrees of freedom (i.e. the X and Z directions) to the coincident concrete nodes. The vertical degree of freedom (Y) of tendon nodes within the cylinder were left unconstrained, allowing relative sliding of the tendons and concrete in the vertical direction. Within the cylinder, friction at the concrete/tendon interface is assumed to be negligible and has not been modelled. However, within the dome, the curved trajectory of the tendon causes appreciable friction at the concrete/tendon interface, resulting in a non-uniform variation of load in the tendon. Although interface behaviour has not been explicitly modelled, the non-uniform distribution of load in the vertical tendons over the dome is allowed for by constraining all coincident tendon and concrete nodal degrees of freedom. The vertical tendon mesh is shown in Figure 9.

The hoop tendons are modelled as single rebars embedded within concrete elements. The concrete elements were defined such that an element edge lies along the path of the hoop tendon as this facilitated the placement of the hoop tendons with the elements. Each hoop tendon starts at one face of the buttress, completes a 360o loop around the vessel and is anchored at the opposite face on the same buttress. Alternative tendons are anchored at opposite buttresses. Interface behaviour between the concrete and the tendon has not been modelled. Frictional loss in the hoop tendons is discussed in the section below.

4.5.1 Vessel Pre-Tensioning System

The load distribution within the tendons was non-uniform because of friction between the tendons and ducts. This was taken into account during the pre-test analysis by using the design values of the anchorage loads of 350kN and 471kN for the hoop and vertical tendons respectively. Variation in the tendon loads due to frictional loss was obtained by applying the following Equation 4.

$$P = P_{1,2}\, e^{(-\mu\beta - 0.001L)} \qquad (4)$$

Where

$P_{1,2}$ = Load at the tensioning end 1 or 2.
β = Change of angle from tensioning end.
P = Load at β from tensioning end.
μ = Friction Coefficient.
L = Length of Tendon.

Hydraulic jacks were used to tension the tendons to the desired load. They were then anchored at the buttresses and the base mat for the hoop and vertical tendons respectively. Each hoop tendon was modelled by 183 elements, and from the element nodal coordinate, the average change of angle from the anchorage was calculated. The same procedure was used for the vertical tendons, but only over the dome area. Friction losses for the vertical tendons in the wall region were assumed to be negligible.

A sample of the pre-loads for a selection of hoop and vertical tendons were measured at the time of the test. It was seen that the values observed before the test were not consistent with the design loads. The pre-loads specified in the pre-test analysis were up to 10% higher than the pre-load values in the test. The comparison is shown in Figure 13 and Figure 14 for vertical and horizontal tendons respectively. The tendon pre-load values within the input decks were then altered to simulate the test results taking into account the distribution of the load due to friction. Not all tendon values were measured, so the tendons for which there were known measured values were altered individually, and the intervening tendon loads were assigned an average value.

The equipment hatch, airlock and mainstream penetrations were modelled separately from the cylinder, so the areas where tendons passed through the penetrations were assigned an average value around that section of the tendon. At the “Post-Test Meeting” it was confirmed that seating-loss of the tendons had a larger effect on the vessel than that initially calculated. The seating loss occurs when the tendons are initially tensioned and then released by the hydraulic jacks. The tendons contract slightly as they “settle in”. The pre-test analysis did not take into account this seating loss acting on the tendons and had assumed that the loss was negligible. Allowance for this was made in the post-test analysis and was assumed to act over a 90° segment (45° sections on each side of the buttress). The average seating loss of 24757N was taken from the PCCV test results, and was included in the calculations for the pre-loads. The modelling assumed that the seating loss was linear throughout the 90° segment. Figure 15 shows the variation in tendon load due to friction and the seating loss. The friction coefficient of 0.21 for the steel tendons was kept unchanged.

4.6 Internal Liner and Liner Anchorage

The thicker insert plates surrounding the main steam and feed water penetrations are simulated with the shell element S4R. The S4R element is a general purpose shell element suitable for both 'thick and thin shell' applications. It accounts for finite membrane strains and allows for change in thickness. Therefore it is suitable for large strain analysis. An S4R element has 4 nodes and 6 DOF at each node. In order to try to keep the size of the model within manageable limit, it was decided to model the general area of the liner with membrane type M3D4R elements. These elements are reduced integration 4 noded membrane elements with only two in-plane DOFs. Such elements are suitable for thin plates which offer strength in the plane of the element and have negligible bending stiffness. The liner elements are meshed around nodes defined independently but coincide with adjacent concrete nodes. The internal liner mesh is shown in Figure 12, where the meshes of the plate lining the main steam and feed water penetrations can also be seen.

The liner-to-concrete anchorage was modelled by connecting the liner node to the corresponding coincident concrete node with three linear spring elements at each node, representing the radial, hoop and axial anchorage plate stiffness. Given that the pitch of the horizontal and vertical liner anchorage plates is not uniform, no attempt was made to simulate the anchorage plates at their exact locations. The pull-out and shear test reported in Ref 3 are based on tests conducted on a number of pre-stressed and non-pre-stressed liner/concrete anchorage arrangements. In this work, test results from the pre-stressed liner/concrete anchorage arrangements have been used to derive the stiffness of the anchorage. The liner strip, 300mm wide, and embedded in a block of concrete was loaded first by tension load and then by shear load. In each case the stiffness of the arrangement was computed. For each case the average measured values were used as the basis for calculating the equivalent anchorage spring stiffness. In the finite element model, the radial tensile anchorage stiffness is represented by 36 springs in the hoop direction. The equivalent tensile spring stiffness is computed as 3.89 x 106 N/mm. There are also 36 shear springs around the circumference of the vessel model. The shear spring stiffness is 1.82 x 10^6 N/mm. The spring stiffness values are given in Table 2.

4.7 Concrete Reinforcements

The grid of reinforcing bars in the vessel has been represented as rebar smeared within the parent solid elements. The orientation, cross-sectional area, spacing and material properties are taken from the construction drawings, Ref 12.

The duct-supporting steel frame construction is modelled as single rebars within the parent solid elements. The properties of the steel frame are given in Ref 12.

4.8 PCCV Support Conditions

The basemat is constructed on a 150mm thick un-reinforced slab which itself is supported on an engineered sand and gravel subgrade. The soil stiffness was characterised as exhibiting a settlement of less than 25mm due to a bearing pressure of 35Ton/m2, Ref 12.

The soil was represented using grounded spring elements (SPRING1). Each node on the bottom surface of the basemat was supported on a spring element, Figure 11. The spring stiffness was computed based on the influence area of each spring node.

The vessel was constrained to eliminate rigid body translations and rotations at four nodal positions on the top surface of the basemat in the horizontal degrees of freedom as shown in Figure 5.

5 REVIEW OF THERMAL PROPERTIES SUPPLIED BY SNL

For phase 3 of the ISP48 project additional data was supplied by SNL. This additional data was for the thermal properties of the PCCV and details of the loading conditions for Cases 1 & 2.

Case 1 is a saturated steam condition case, which adds steady state temperatures to a the pressure loading.

Case 2 is an accident safety case, essentially a Station Blackout scenario with a hydrogen burn at about 4-1/2 hours into the event.

NNC have analysed the Case 1 scenario only.

5.1 Thermal Property Data Supplied by SNL

The additional data package from SNL provided thermal properties for the PCCV model, these included:-

- Surface film coefficients for convection to free air for the cylinder, dome & basemat.
- Surface film coefficients for conduction into the soil from the basemat.
- Specific heat capacity of the concrete.
- Thermal conductivity for the concrete.

Thermal conductivity and specific heat capacity properties used for analysis are presented in Table 3.

5.2 Loading Data Supplied by SNL

The temperature loading for Case 1 is a non-linear increase from 100^{o}C to 200^{o}C (Figure 2). The temperature loading was defined over a period of approximately 42 minutes, which was a pseudo time step as the heat transfer analysis is performed at steady state increments of temperature.

The pressure loading was a linear increase from 0MPa to 1.46MPa over the 42 minute pseudo time step (Figure 1). Note that the liner temperature had to be raised from ambient (assumed to be 20^{o}C) to 100^{o}C before this loading could be applied.

6 MODELLING

6.1 Heat Transfer Modelling

The global PCCV model that was used for Phases 1 & 2 was updated for heat transfer analysis. In order for the model to be used for heat transfer analysis some modifications were required. These are highlighted in the sections below.

6.1.1 Concrete Elements

All concrete solid elements were replaced with corresponding heat transfer DC3D8 and DC3D6 elements, these include both the full and reduced integration continuum elements. This is because there are no reduced integration heat transfer elements available for 8 node continuum elements.

6.1.2 Liner Elements

The Liner elements (which were M3D4 & M3D3 membrane elements) were replaced by S4 and S3 shell elements respectively. Even though the shell elements provide an in plane stiffness this was acceptable as the stiffness can be neglected for heat transfer analysis.

6.1.3 Tendons and Rebars

The vertical tendons were previously modelled using T3D2 truss elements, for heat transfer analysis the element type had to be modified to DC1D2 (1D solid) elements. These elements were then attached to the concrete using equations to couple the temperature degrees of freedom. The hoop tendons and rebars were previously modelled using the *REBAR command within ABAQUS. This type of element cannot be used during heat transfer and was omitted for the heat transfer analysis. However the nodal temperatures are applied to the rebars and tendons during the stress analysis.

6.1.4 Material Properties

All of the concrete and steel elements are assigned thermal properties. This includes

- Thermal Expansion Coefficient
- Specific Heat Capacity

Sandia National Laboratories (SNL) supplied the values for the thermal expansion coefficient and the specific heat capacities for the concrete, however standard values were used for the steel elements (Ref 14). These properties can be found in Table 3.

6.1.5 Boundary Conditions

Boundary conditions applied are as follows:-

- Sink Temperature of 25^{o}C outside the PCCV.
- Convection from the outer surfaces of the cylinder, dome and exposed sections of the basemat concrete to free air.
- Convection from the insulated bottom surface of the basemat to the soil.

6.1.6 Conduction Between Liner and Inner Concrete

To facilitate Conduction between the Liner and the concrete, surfaces were created on the outer surface of the liner and the inner surface of the concrete so that a gap conduction could be set up. Gap conductivity uses the two surfaces and a specified conductivity depending upon distance between the two surfaces. The conductivity was set as a perfect thermal contact. Therefore between the two surfaces the thermal conductivity was defined as being the same as the conductivity of steel irrespective of distance between the surfaces.

6.1.7 Convection from Outer Concrete Surfaces

Two separate regions were specified for the convection from the outer surface of the concrete. Firstly one region was defined for the dome, cylinder and exposed sections of the basemat (i.e. top and sides) to allow for standard convection. Secondly the base of the basemat was defined as a surface to simulate conduction from the basemat into the soil. The convection parameter from the outer surfaces were provided by SNL and are shown below:-

Convection to free air:

$$h = 4.80 * (\Delta T)^{1/3} \text{ W/mK} \qquad (5)$$

Convection into soil:

$$h = 0.0724 \text{ W/mK} \qquad (6)$$

A plot of the convection to free air vs temperature can be found in Figure 16.

Effects of radiation have been ignored.

6.1.8 Loading

The heat transfer analysis was completed in two steps. The first step was a steady state heat transfer step in which the liner temperature was raised from 20^{o}C to 100^{o}C.

The second step raised the liner temperature in accordance with the temperature profile provided by SNL. Loading was applied in pseudo time increments and a steady state solution was obtained at each increment up to the 42.23 minute pseudo time as defined in the original SNL heat transfer analysis. By performing the heat transfer analysis in this way the pressure loading can be run as a time history using steady state temperatures at each increment of pressure. The temperature loading can be seen in Figure 2.

6.2 Stress Analysis Modelling

The stress analysis model was taken from the original Phase 2 model and incorporated the thermal expansion coefficient option for the steel and concrete sections. The values for the thermal expansion coefficients can be found in Table 4. The stress analysis model has all of the rebars and tendons modelled.

6.2.1 Loading

The stress analysis model was loaded as follows:-

Step 1 – Application of prestressing
Step 2 – Increase model temperature from 20°C to 100°C steady state
Step 3 – Apply temperature and pressure loading as defined by SNL (Fig. 1)

Steps 2 & 3 of the stress analysis model read in the nodal temperatures from Steps 1 & 2 respectively from the heat transfer analysis and are applied at each increment as a steady state temperature.

6.2.2 ANAMAT and ABAQUS

The stress displacement analysis was initially planned to be performed using the concrete material models within the user subroutine ANAMAT (Ref 9). The reason for this was to be able to incorporate different thermal effects, such as transient thermal creep (TTC) and thermal degradation of the concrete.

After receiving the ANAMAT routine it was found that the thermal degradation model within the ANAMAT could not be used for the PCCV analysis as the model is based upon a specific concrete material for which the maximum compressive strength was 30MPa. The concrete used in construction of the PCCV has a compressive strength double this. When running the analysis with such a low compressive strength, singularities cause the analysis to stop during the prestressing step.

It was therefore decided to use the ABAQUS v6.4 (Ref 10) concrete material model for the Stress Displacement analysis. Compared to the ABAQUS v5.8 model available for previous PCCV analyses (Refs 4 and 6), version 6.4 provides an improved concrete damaged plasticity model. This model accounts for elastic stiffness degradation induced by plastic straining under tensile and compressive loading and also includes stiffness recovery effects under cyclic loading. The concrete material properties for this analysis were identical to the analysis performed for Phase 2 of the ISP48 analysis with the inclusion of the thermal expansion coefficient.

A limitation of the concrete modelling in ABAQUS v6.4 is that the effects of concrete fracture and creep cannot be combined to act together. Therefore, TTC was modelled using the effective modulus approach described earlier in section 3.2. However, it should be noted that this method os reducing the Young's modulus to take account of TTC can exaggerate the numerical convergence problems which can occur when stiffness is reduced due to extensive cracking in concrete. In this case, the analysis with TTC terminated at pressure of 0.89MPa.

7 RESULTS

7.1 Heat Transfer Results

Once the heat transfer analysis had been completed the nodal temperatures for the standard output locations for phase 3 were extracted and are presented in Figures 17 to 34. Some plots show two curves, these are the inside and outside nodal temperatures of the elements used in the Phase 2 analysis. Figure 35 shows the through thickness steady state temperature gradient at the end of heating (i.e. 42 minutes) and Figure 36 shows a closer view of the cylinder wall junction with the basemat. Influence of the thermal boundary conditions is visible in these plots. Because of the insulating properties of the soil, the base mat does not loose much heat and gets hotter compared to the walls which loose heat to the outside air.

Figure 37 shows the temperature contour through the cylinder wall thickness. A hand calculation for the validation of the heat transfer model was performed. This calculation was to validate the outer wall temperature under steady state loading. The hand calculation gave a good agreement with the finite element model. The FE model gave an outer wall temperature of 56.66^{o}C and the hand calculation gave 56.52^{o}C. The value provided by SNL was given as 53.5^{o}C. The slight difference between the analysis and the SNL data is due to a small difference in the material property data.

7.2 Stress Analysis Results

For the ISP 48 project the number of standard output locations have been reduced to 23 locations and a list of the locations with descriptions can be found in Table 1. For each location, results obtained from the following are plotted:

- LST test results (pressure only) from Ref 3.
- FE analysis pressure only.
- FE analysis pressure plus temperature.
- FE analysis pressure plus temperature with TTC.

The results are plotted against pressure which is related to temperature as shown in Figure 2(b).

The finite element model data as presented in Figures 38 to 60 have the initial values reset to line up with the Limit State Test results. These figures are a comparison of the Phase 3 results against the Phase 2 and the LST results at these locations.

The impact of Thermal Transient Creep is assessed by comparison of the component strain distributions in the inner ring of elements of the containment cylinder. This information is presented in Figures 66 to 68.

Comparisons of the vessels deformed shape due to pressure only, pressure with temperature and pressure with temperature including TTC are presented in Figures 69 to 71. Figure 69 presents a plan view at the height of the equipment hatch. Figures 70 and 71 present a meridional section through the vessel at the 90^{o} to 270^{o} azimuth and 0^{o} to 180^{o} azimuth respectively. In all cases the deformations are presented for a pressure of 0.837MPa and temperature of 179^{o}C.

To demonstrate the effects of thermal loading and vessel pressurisation in the liner, the liner hoop stress at location 39 is presented in Figure 62 for case 1 pressure only and pressure with temperature loadings. In the free field area, at azimuth 135^{o}, meridional (axial) stresses at inside liner surface at locations 36, 38 and 40 (at elevation 0.25m, 6.2m and 10.75m respectively) are presented in Figure 72 for pressure plus temperature loading.

The effects of thermal loading at mid-height to the vessel wall are highlighted by comparing pressure only and pressure with temperature results for case 1. Hoop and axial stress histories at the inner and outer surfaces of the wall are presented in Figures 73 and 74. Hoop and axial stress profiles through the wall are presented at pressures of 0.1MPa, 0.75MPa and 0.89MPa in Figures 75 and 76. These pressures approximate to the onset of cracking at the outer wall surface, the inner wall surface and the maximum pressure reached for the analysis including TTC effects.

8 ASSESSMENT OF RESULTS

8.1 Thermal Deformation

The influence of thermal loading on the structural behaviour can be appreciated from the deformed shape plots presented in Figures 69 to 71. The analysis increment with pressure of 0.837MPa and corresponding temperature of 179^{o}C was selected for comparing deformed shapes available for all three loading conditions involving for pressure, pressure plus temperature and TTC.

Figure 69 shows radial deformation comparison at the Equipment Hatch level. As expected the radial deformation under thermal loading is higher with the maximum deflection almost doubling at the Equipment Hatch.

Figures 70 and 71 show deformed shapes at two vertical sections (90^{o}– 270^{o} and 0^{o}–180^{o}). As expected the structure expands upwards lifting the apex of the dome by additional 15mm when thermal loading is applied. Also, upward bending (hogging) of the base slab occurs due to the temperature gradient. Under pressure only loading, the base slab top deflects down by 8.5mm but under combined thermal loading it lifts up by 6 to 7mm. The hogging of the base slab also causes increased bending at the wall/base junction.

8.2 Liner Assessment

The primary function of the steel liner is to act as the pressure boundary for the containment. Therefore it is important to know the pressure it can sustain before rupture. It is the design intent that liner rupture and pressure leakage occurs at levels below that required to cause catastrophic failure of the concrete containment structure. The limit state test (Ref. 3) demonstrated this design feature. Liner rupture was the first failure mode and the high leak rates seen ensured the concrete containment did not fail catastrophically.

The limit state test in Ref 3 did not consider the effects of accident temperature transients. Under such conditions, liner thermal expansion could influence the limit load before rupture. If liner thermal expansion is constrained by the concrete containment, compressive strains may be induced in the liner that increases the pressure required to cause rupture. From a design viewpoint, the concern is that the pressure required for liner rupture may increase thereby reducing the margin between liner rupture and structural failure of the vessel.

Figure 61 (for location 39) presents the mechanical strain (total strain – thermal strain) in the liner in the hoop direction midway up the cylinder wall, at the 135^{o} azimuth. This figure highlights the decreased strains that are calculated in the liner when the thermal loading is included. These are indicative of a compressive stress developed in the liner (see Figure 62) due to the differential thermal expansion between the liner and concrete wall. Assuming at vessel failure the liner strain at this location is the same as that observed during LST (0.0015), the data indicates that the rupture pressure increases by 0.15MPa to 1.25MPa when thermal expansion is included (see Figure 61). The results indicate that as expected, the liner is under compression initially due to the differential thermal expansion but begins to experience tensile stress at 0.9MPa, as shown in Figure 62. This leads to liner rupture at a pressure 14% higher than the rupture pressure when only pressure loading is applied.

Figure 62 shows that the initial compressive stress in the liner at location 39 increases from 50MPa to approximately 150MPa when thermal loading is applied. Also, Figure 72 indicates that in the meridional (axial) direction the liner remains under compression. It is recognised that such a compressive stress may lead to liner buckling. However, this failure mode can be ignored because the anchor spacing of the liner in the model was not scaled. It is three times bigger than the actual PCCV.

8.3 Tendon Assessment

Ultimate structural collapse of the PCCV test model was initiated by failure of hoop tendons located in the free field region, approximately mid-height to the cylinder wall. Tendon failures resulted in a loss of pre-load to the concrete in this region and a breach of the wall ensued. It is therefore important to assess if the application of accident temperatures reduces the pressure at which rupture of the tendons occurs. Two aspects are assessed.

The first aspect is the temperature of the tendons during the fault. A significant increase could lower the material yield strength. Figure 37 presents a profile of the temperature distribution through the cylinder wall of the vessel. This shows the peak fault temperature of 200^{o}C is transferred through the liner to the inner surface of the wall. However, the temperature quickly reduces through the wall thickness due to the insulating properties of the concrete. The hoop tendons are located in the wall, approximately 216mm from the inner surface. At this location the temperature approximates to a range between 100^{o}C to 130^{o}C and therefore is well below the level required to reduce the material yield strength. Figures 32, 33 and 34 present the thermal transient at locations close to the hoop tendons at mid height of the cylinder. These confirm the temperature range attained is between 100^{o}C and 130^{o}C.

The second aspect of vessel response considered is its global response when accident temperatures are included. Thermal expansion of the vessel could increase the prestress in the tendons and decrease the pressure required to cause rupture. Figure 63 presents the mechanical strain (total strain – thermal strain) histories for the hoop tendon located at an elevation of 4.57m, mid-way between the equipment and airlock hatches. This is the region of vessel rupture seen during the structural failure test. The figure highlights that at the vessel rupture pressure of 1.4MPa, a tendon strain of 0.0034 is induced when pressure only is applied. For the pressure plus temperature case, a tendon strain of 0.0034 equates to a pressure limit of 1.5Mpa when the calculated results are extrapolated. It indicates that at best the vessel capacity will increase by 7% but in reality no change in pressure at tendon rupture is expected. It should be noted that the tendon rupture pressure remains above the liner rupture pressure reported in section 8.1.

The load distribution along the hoop tendon at different stages of vessel pressurisation, during Case 1, is presented in Figure 65. This shows how the tendon loads redistribute as the vessel pressure increases. At the pre-stressing load, the tendon profile is as expected. High loads occur at the anchor points at the 90^{o} and 270^{o} azimuths. The loads then reduce to a minimum at the mid-length due to friction losses between the tendon and concrete wall. As the vessel pressure increases, the loads redistribute such that the maximum shifts to the mid-length of the tendon. This coincides with the tendon failures and containment breach at the 0^{o} azimuth during the LST. It is the vessels deformation that causes load concentration in the tendons and leads to tendon failure.

Whilst the analysis indicates a 7% increase in the vessel pressure at tendon rupture, it should be noted that the modelling assumption of no relative sliding between the hoop tendons and vessel wall prevents tendon load redistribution. Therefore, it can be concluded that the thermal loading in this case does not change the pressure at tendon rupture and is expected to be the same as that obtained for the pressure only case.

8.4 Thermal Transient Creep

For the thermal transient investigated, the impact of TTC on strain levels is shown to be small. Comparison of the inner wall strain distributions presented in Figures 66, 67 and 68 highlight there is very little change when TTC is simulated. The only noticeable change is highlighted in Figure 66. A nominal reduction is observed in the E11 (i.e. radial at this location) tensile strain at the top of the buttress on the 270^{o} azimuth. The level of TTC activity in concrete is temperature dependant. Creep initiation occurs at levels above 85^{o}C and activity increases with respect to temperatures in excess of this. However, for the fault transient investigated relatively low temperature distributions dominate, particularly through the thickness of the containment concrete boundary. Hence significant strain re-distribution is not witnessed.

The inclusion of TTC has an effect on vessel displacements. The effects are most pronounced for the radial displacements, as presented in Figures 39 and 43. TTC is simulated using an effective Young's modulus approach to reduce the material stiffness of the concrete. Thus the restraining effects of the pre-tensioning tendons become more dominant as the concrete stiffness reduces. The increasing dominance of the compressive pre-loading results in the reduced displacements calculated for the TTC analysis.

This investigation considers a fault transient based on a loss of cooling accident for a typical PWR containment. However, for British Advanced Gas-cooled Reactors (AGR), the pre-stressed concrete pressure vessels (PCPV) are expected to experience more elevated and sustained thermal transients. Thus TTC can be expected to be of more significance to the AGRs.

8.5 Concrete Cracking

Localised concrete cracking initiates at 0.6 MPa under pressure loading. To assess the effect of thermal loading on concrete cracking behaviour, Figures 73 and 74 present the hoop and meridional stress components in the concrete wall, mid-height to the cylinder. Comparisons are presented for the inner and outer surfaces of the wall. It is worth noting that tensile stress limits are reached earlier in the meridional direction. It can be seen that cracking is dominated by axial stresses in the wall.

For leakage, through wall cracking is important. For the pressure only case, crack initiation at mid-height occurs through the wall at approximately 0.75MPa due to axial stresses and at 1.1 MPa due to hoop stresses. However, with the inclusion of thermal loading the inside surface experiences additional compression due to the thermal expansion of the liner into the concrete and the outside surface experiences more tension. Cracking in the concrete occurs at approximately 0.1MPa at the outside surface. Through thickness stress distributions at pressures of 0.1MPa, 0.75MPa and 0.89MPa are shown in Figures 75 and 76. These clearly indicate that the through thickness stress distribution becomes more uniform as the loading is

increased whilst limiting the tensile stresses due to concrete cracking. It should be noted that for leakage, thru wall cracking must occur which is expected at approximately 0.8MPa at this location when thermal loading is added.

8.6 PCCV Failure Mode

The inclusion of thermal effects does not change the failure mode of the PCCV. Crack initiation in the concrete wall followed by liner rupture and then tendon failure remains the sequence of events leading to the ultimate failure of the vessel. Also the location of these failure events is the same for the pressure only and pressure with temperature cases. From this it can be concluded that vessel failure is primarily caused by discontinuities in the overall stiffness characteristics of the geometrically axisymmetric containment vessel. The design objective for such vessels should be to try an eliminate such discontinuities in the stiffness were possible.

For the load case investigated TTC has not been shown to be an important factor. This is because the thermal loading is limited to a maximum temperature of 200^{o}C. At higher temperatures TTC is expected to become a more significant effect in the vessels response.

9 COMPUTER FILES

Files relevant to the analyses presented in this report are retained on NNC's computing system as follows;

Pressure Only - Stress Analysis Input Files

Directory:
/net/nas01/users/ics/pccv/ISP48/Phase1-2/non_linear_dome

Main Input File	-	PCCV_BE_NLD_V6.4.inp
Airlock Penetration	-	airlock_v64.inp
Basemat	-	basemat_v64.inp
Vessel Cylinder wall	-	cylinder_v64.inp
Vessel Dome	-	dome_nl_v64.inp
Equipment Hatch	-	eqpt_v64.inp
Steel Liner	-	liner_v64.inp
Material Properties	-	material_props_v64.inp
Steam and Feedwater Penetrations	-	msfwt_v64.inp

Case 1 - Heat Transfer Analysis Input Files

Directory:
/net/fbc/analysis/ics/STEADY_STATE_AMPLITUDE

Main Input File	-	PCCV_HT_V6.4-SSAMP.inp
Airlock Penetration	-	airlock_v64_HT.inp
Basemat	-	basemat_v64_HT.inp
Vessel Cylinder wall	-	cylinder_v64_HT.inp
Vessel Dome	-	dome_nl_v64_HT.inp
Equipment Hatch	-	eqpt_v64_HT.inp
Steel Liner	-	liner_v64_HT.inp
Material Properties	-	material_props_v64_HT.inp
Steam and Feedwater Penetrations	-	msfwt_v64_HT.inp

Case 1 - Stress Analysis Input Files

Directory:
/net/nas01/users/ics/pccv/ISP48/Phase3/Stress_Displacement_Model/ABAQUS_NO CREEP

Main Input File	-	PCCV_SD_ABA_NOC_V6.4-r.inp
Airlock Penetration	-	airlock_v64.inp
Basemat	-	basemat_v64.inp
Vessel Cylinder wall	-	cylinder_v64.inp
Vessel Dome	-	dome_nl_v64.inp
Equipment Hatch	-	eqpt_v64.inp
Steel Liner	-	liner_v64.inp
Material Properties	-	mat_props_stress_displacement_ABA_v64.inp
Steam and Feedwater Penetrations	-	msfwt_v64.inp

Case 1 – Degraded Elastic Modulus Analysis Input Files

Directory:

/net/nas01/users/ics/pccv/ISP48/Phase3/Stress_Displacement_Model/TTC_SENSITIVITY_STUDIES/DEGRADING_E

Main Input File	-	PCCV_SD_ABA_DEGE1_V6.4.inp
Airlock Penetration	-	airlock_v64.inp
Basemat	-	basemat_v64.inp
Vessel Cylinder wall	-	cylinder_v64.inp
Vessel Dome	-	dome_nl_v64.inp
Equipment Hatch	-	eqpt_v64.inp
Steel Liner	-	liner_v64.inp
Material Properties	-	mat_props_SD-DEGE1.inp
Steam and Feedwater Penetrations	-	msfwt_v64.inp

Standards Output Location Results

Stress Analysis results presented within this report for the standard output locations are stored in the following MS Excel files:-

SDMR_Black & White.xls
Strains_39
NNC Stress Plots_SOL_34to42 Rev02

10 CONCLUSIONS

A summary of results under pressure only and under combined pressure plus temperature (Case 1) is given in Table 5. When the effects of accident temperatures on concrete containments are considered, the following conclusions can be made.

- The elevated temperatures induce significant thermal expansion of the steel liner. The thermal straining of the liner results in rupture at approximately 1.25MPa. This is 14% higher than the rupture pressure of 1.1MPa obtained from the mechanical loading of the limit state test.
- From the analysis results, the pressure required to induce tendon failure increases from 1.4MPa to approximately 1.50MPa. This is an increase of 7% compared to the limit state test. However, the modelling assumption of no sliding in the hoop tendons prevents load redistribution. Therefore, it can be concluded that in this case thermal loads do not change the pressure at tendon rupture.
- For the accident condition investigated, liner rupture is the initial failure mode. The design intent of liner rupture before catastrophic structural failure of the containment is maintained.
- If the margin between tendon failure and liner rupture is defined as the ratio of vessel pressurisation required to cause the failures, the margin decreases from 1.27 for pressure only to 1.2 for pressure plus temperature loads.
- With the addition of thermal loading compressive effects on the PCCV inner concrete wall are increased due to expansion of the liner. However cracking on the outside surface occurs earlier at 0.1MPa. Through wall cracking is expected at approximately 0.8MPa.
- The temperature dependent effect of TTC in concrete is simulated using an effective modulus approach. For the accident condition investigated TTC is shown to have a small effect on PCCV strain distributions, but reduced vessel displacements are witnessed.

11 REFERENCES

Ref Title

1 International Standard Problem on Containment Capacity (ISP48), Working Group on Ageing of Concrete Structures (IAGE/CONCRETE), CSNI Proposal, IAGEWG(2002)15, Rev 0, June 2002.

International Standard Problem on Containment Capacity (ISP-48) Phases 1 & 2 NNC Report C11248/TR/001 Issue 2 April 2004.

3 Overpressurisation Test of a 1:4 Scale Prestress Concrete Containment Vessel Model, Sandia National Lab., NUREG/CR-6810, SAND2003-0840P, Project Report No. R-SN-P-010, March 2003.

4 HSE/NNC Pretest Analysis Report for ¼ Scale PCCV Model, NNC Report C5769/TR/002.

5 Pretest Round Robin Analysis of a Prestressed Concrete Containment Vessel, Sandia National Lab., NUREG/CR-6678, SANDE 00-1535, August 2000.

6 HSE/NNC PCCV Round Robin Post Test Analysis, NNC Report C6635/TR/001, Issue 01, Dec 2002.

7 Summary Records of the 2nd meeting of the ISP48 Exercise on Containment Capacity. Madrid, Spain, 19 March 2004. OECD Nuclear Energy Agency IAGE-CONC/ISP48/(04)1. 2 April 2004.

8 ABAQUS/Standard Version 5.8, ABAQUS/CAE, ABAQUS/Viewer, ABAQUS Inc., USA.

9 ANACAP-ANATECH Concrete Analysis Program Users Guide, ANATECH Research Corp., USA.

10 ABAQUS/Standard Version 6.4, ABAQUS/CAE, ABAQUS/Viewer, ABAQUS Inc., USA.

11 HSE/NNC Pretest Analysis Report for ¼ Scale PCCV Model, NNC Report C5769/TR/004.

12 Obayashi Corporation package of construction drawings of PCCV model.

13 Sandia National Laboratory PCCV Design Package, Material Properties Report.

14 An Engineering Data Book – J R Calvert & R A Farrar 1999.

15 Structural Performance of PCPV's at Elevated Temperatures. Nuclear Electric plc, EWI-17275/R/008, December 1996.

12 NOTATION AND ABBREVIATIONS

α	Coefficient of thermal expansion
β	Azimuth angle
ε_0	Initial strain (creep + shrinkage)
ε	Strain
σ	Stress
μ	Coefficient of friction
E	Young's modulus
E_T	Transient Thermal Creep Young's modulus
L	Length of tendon
P1, P2	Tension loads at the tensioning ends
Pd	Design pressure = 0.39MPa
T	Temperature
h	Heat transfer film coefficient
s	Creep microstrain per unit stress

ABBREVIATIONS

FE	Finite Element
LST	Limit State Test
PCCV	Pre-stressed Concrete Containment Vessel
SFMT	Structural Failure Mode Test
SNL	Sandia National Laboratories
TTC	Transient Thermal Creep

Table 1 Results Summary for Case 1 (P+T) from Start of Fault at Standard Output Locations

***Results linearly extrapolated to 1.46 MPa**

Loc. #	Type	Orientation	Az. (deg)	Elev. (m)	Comment	General Location	Time 0 min, Pressure 0 MPa	Time 2.83 min, Pressure 0.10 MPa	Time 7.57 min, Pressure 0.26 MPa	Time 15.01 min, Pressure 0.52 MPa	Time 26.16 min, Pressure 0.90 MPa	Time 42.23 min, Pressure 1.46 MPa*
1	Displacement (mm)	Vertical	135	0.00	Outside Cylinder	Top of Basemat	0.0	0.22	0.46	0.80	1.20	1.66
6	Displacement (mm)	Radial	135	6.20	Inside Liner Surf	Cylinder Midheight	0.0	1.46	4.23	8.6	15.8	39.6
7	Displacement (mm)	Radial	135	10.75	Inside Liner Surf	Springline	0.0	0.83	1.86	3.36	6.15	40.0
8	Displacement (mm)	Vertical	135	10.75	Inside Liner Surf	Springline	0.0	1.86	4.01	6.9	9.99	22.7
11	Displacement (mm)	Vertical	135	16.13	Inside Liner Surf	Dome Apex	0.0	2.47	5.35	9.18	13.3	37.9
12	Displacement (mm)	Radial	90	6.20	Inside Liner Surf	Buttress Midheight	0.0	0.85	3.74	8.23	16.7	40.8
13	Displacement (mm)	Radial	90	10.75	Inside Liner Surf	Buttress Springline	0.0	0.81	1.59	2.55	4.07	-15.9
14	Displacement (mm)	Radial	324	4.675	Inside Liner Surf	E/H Centre	0.0	1.07	2.8	6.13	15.7	80.9
18	Rebar Strain (x E-3)	Meridional	135	0.25	Inner Rebar	Cylinder Base	0.0	0.16	0.37	0.66	1.12	2.43
19	Rebar Strain (xE-3)	Meridional	135	0.25	Outer Rebar	Cylinder Base	0.0	0.15	0.4	0.51	0.45	0.05
22	Rebar Strain (xE-3)	Hoop	135	6.20	Outer Rebar	Cylinder Midheight	0.0	0.16	0.41	0.81	1.59	3.95
23	Rebar Strain (xE-3)	Meridional	135	6.20	Outer Rebar	Cylinder Midheight	0.0	0.14	0.31	0.55	0.82	2.07
32	Rebar Strain (xE-3)	Hoop	90	6.20	Outer Rebar	Buttress Midheight	0.0	0.12	0.24	0.4	1.13	15.4
33	Rebar Strain (xE-3)	Meridional	90	6.20	Outer Rebar	Buttress Midheight	0.0	0.14	0.31	0.52	0.69	-1.21
38	Liner Strain (xE-3)	Meridional	135	6.20	Inside Liner Surf	Cylinder Midheight	0.0	0.14	0.31	0.54	0.76	1.8
39	Liner Strain (xE-3)	Hoop	135	6.20	Inside Liner Surf	Cylinder Midheight	0.0	0.19	0.42	0.78	1.5	3.4
42	Liner Strain (xE-3)	Meridional	135	16.13	Inside Liner Surf	Dome Apex	0.0	0.16	0.36	0.64	1.2	6.37
45	Liner Strain (xE-3)	Hoop	332	4.675	Inside Liner Surf	10mm from thick plate	0.0	0.15	0.32	0.49	0.7	1.25
48	Tendon Strain (xE-3)	Hairpin	180	15.60	Tendon – V37	Tendon Apex	0.0	0.17	0.37	0.62	0.94	8.3
50	Tendon Strain (xE-3)	Hoop	90	6.58	Tendon – H53	Mid Tendon	0.0	0.16	0.32	0.57	1.75	57.6
52	Tendon Strain (xE-3)	Hoop	280	6.58	Tendon – H53	Tendon near Buttress	0.0	0.19	0.44	0.8	1.34	1.97
54	Tendon Force (kN)	Hairpin	241	-1.16	Tendon – V37	Tendon Gallery	0.0	2.3	6.58	14.0	22.6	63.8
55	Tendon Force (kN)	Hoop	275	6.58	Tendon – H53	Buttress	0.0	0.0	1.06	5.5	13.2	-

Table 2 Anchorage properties

Description of Spring	Stiffness (N/mm)
Liner tensile pull-out stiffness	3890000
Liner shear stiffness	1820000
Penetration lining anchor	581000

Table 3 Heat Transfer Material Properties

Heat Transfer Property	Steel (Liner & Tendons)	Concrete
Conductivity (W/mmK)	50 (Ref 14)	1.0-1.6 (SNL)
Specific Heat Capacity (Nmm/tonneK)	$4.6*10^{8}$ (Ref 14)	$0.879*10^{9}$ (SNL)

Table 4 Additional Stress Analysis Material Properties

Heat Transfer Property	Steel (Liner & Tendons)	Concrete
Thermal Expansion (mm/mm^{o}C)	$10.8*10^{-6}$ (SNL)	$10*10^{-6}$ (SNL)

Table 5 Summary of Results: Calculated Pressures (MPa) and Strains (%)

Loading	Cracking Pressure (Type/Location)		Liner Yield in tension	Liner Tearing (Leakage)	Hoop Tendon Stress		Pressure @ Failure	Free Field Hoop Strain**	Max Radial Displacement***	Failure Mode
	Hoop	Meridional			Yield+	Rupture				
Pressure	0.6(1) 1.1(3)	0.6(1) 0.75(3)	0.75	1.1*	1.16	1.4 !	(a) 1.1 (b) 1.4	0.12%	38.8mm	(a) Liner tearing. (b) Hoop Tendon failure.
Pressure + Temperature	0.6(1) 0.1(2) 1.1(3)	0.6(1) 0.1(2) 0.8(3)	0.83	1.25 *	0.96	1.5 !	(a) 1.25 (b) 1.50	0.06%	49.4mm	(a) Liner tearing. (b) Hoop Tendon failure.
Pressure + Temperature with TTC	0.6(1) 0.1(2)	0.6(1) 0.1(2)	0.82	>0.9	-	-	-	-	-	
LST Test Results	0.59 (1)	-	-	0.98	1.02	-	(a) 0.98 (b) 1.295	0.17% -	28.30mm	(a) Liner Tearing, 1% mass/day leak. (b) Max. Pressure @ 1000% mass/day leak
SFMT Test Results	-	-	-	-	-	1.4	1.4	-	86mm	Structural collapse

* Liner strain of 0.17% reached at SOL39 when leak rate in LST reached 1% mass/day

! Hoop tendon strain of 0.34% at the maximum SFMT pressure in tendon H53

** Mechanical strains at SOL39 @0.98Mpa

*** Displacement at SOL 14 @1.295Mpa

+ Assumed yield strain of 0.2% obtained from tendon testing at SOL50

Concrete cracking type and location

1. Initial cracking at inside surface of the wall
2. Initial cracking at outside surface of the wall
3. Through wall cracking

Figure 1 Case 1 Pressure vs Time loading received from SNL

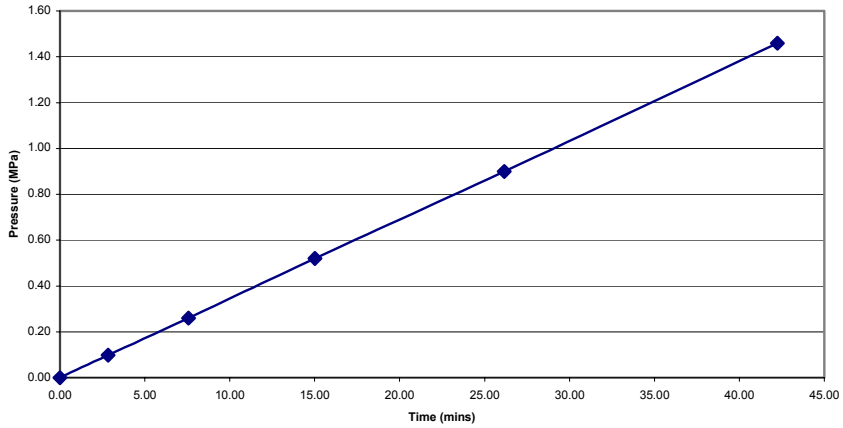

Figure 2(a) Case 1 Temperature vs Time loading received from SNL

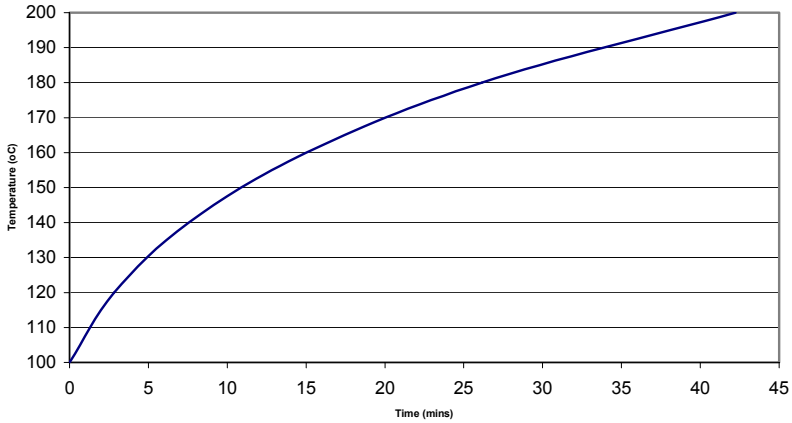

Figure 2(b) Case 1 Temperature vs Pressure Loading

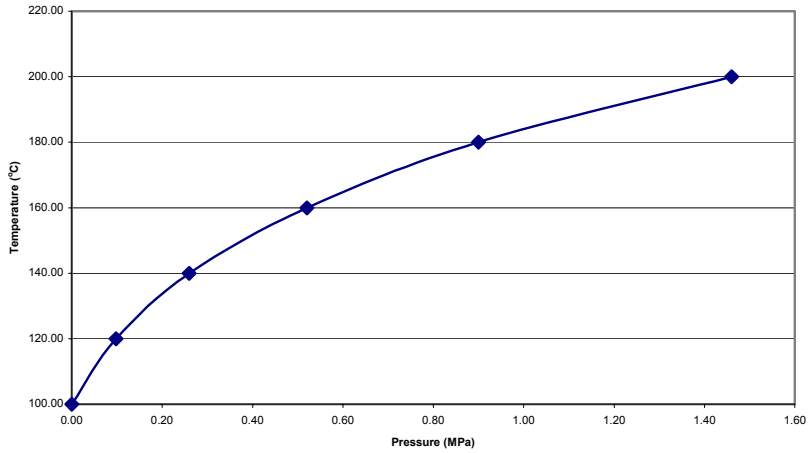

Figure 3 Finite Element Representation of the PCCV

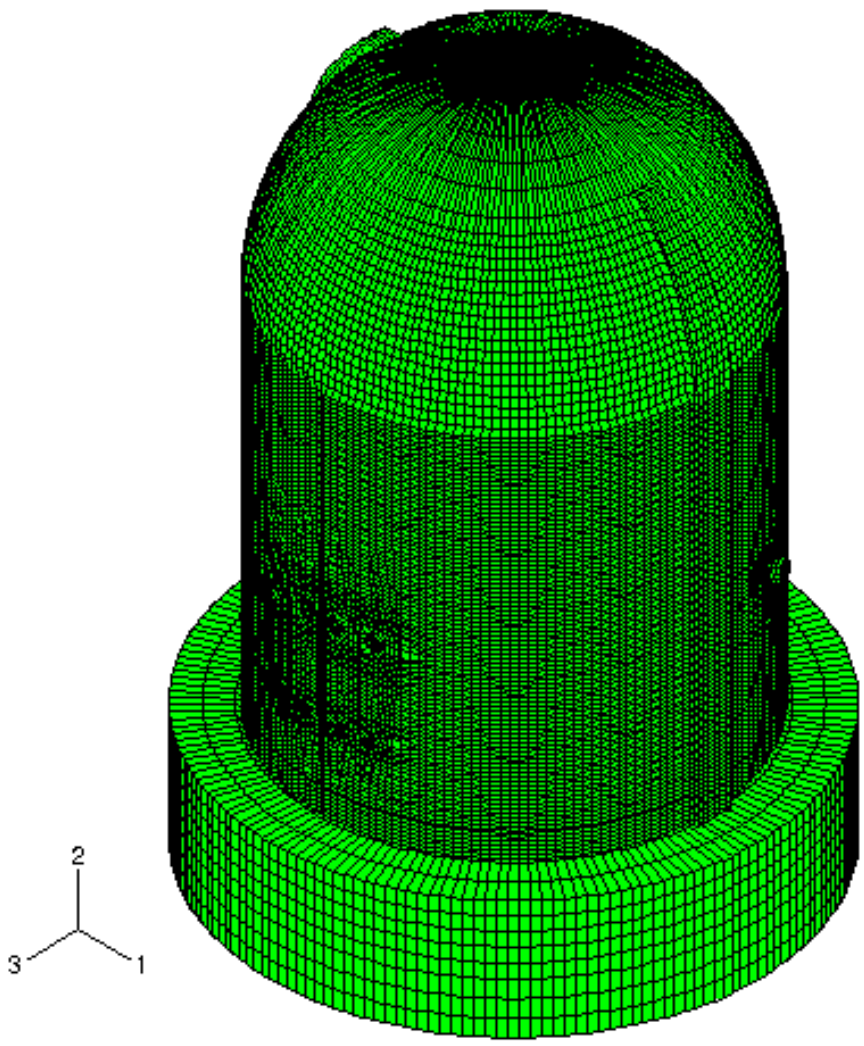

Figure 4 Detail view of the PCCV dome model

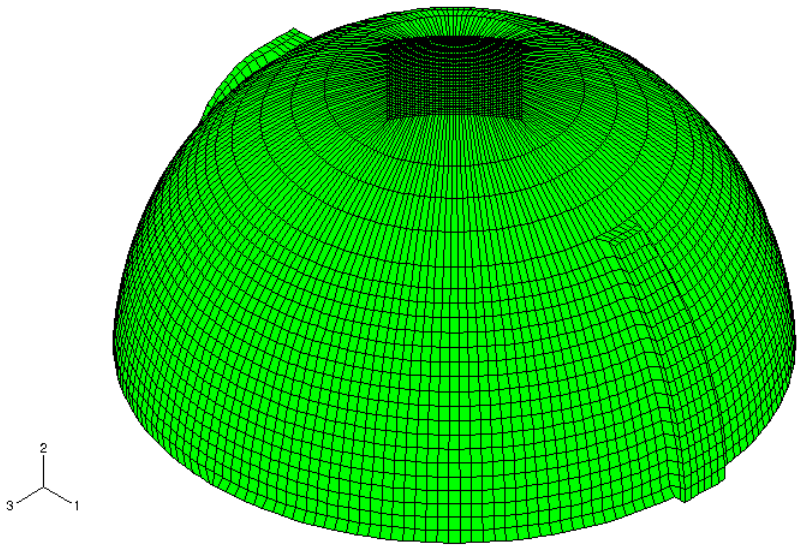

Figure 5 The basemat model showing locations of global restraints

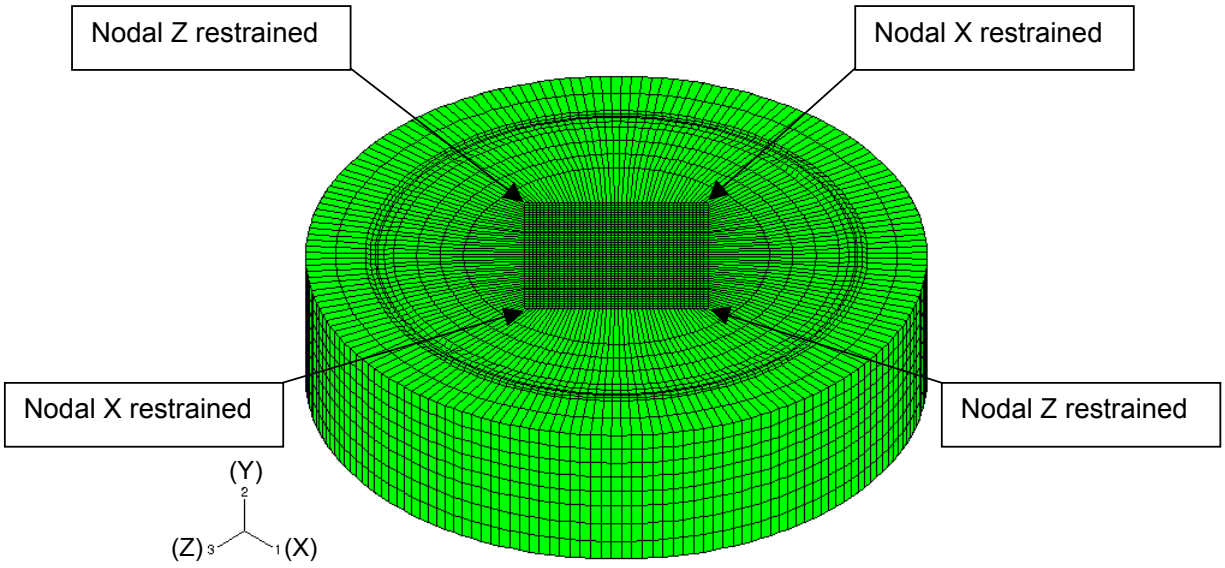

Figure 6 Detailed view of the equipment hatch penetration model

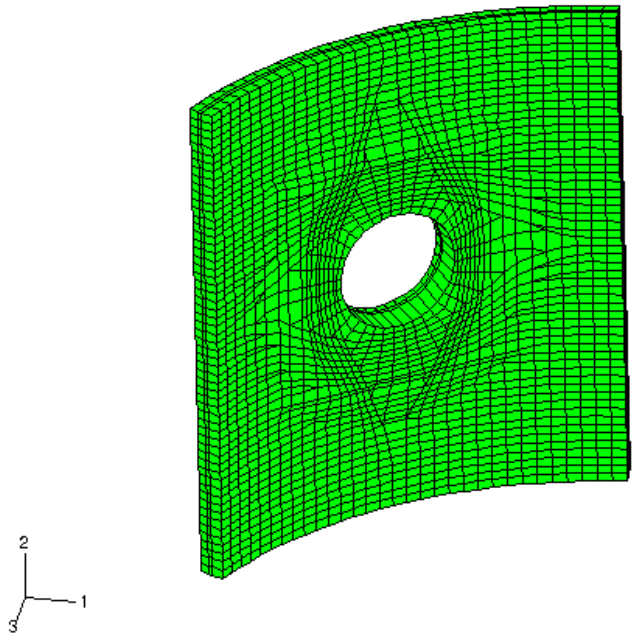

Figure 7 Detailed view of the airlock penetration model

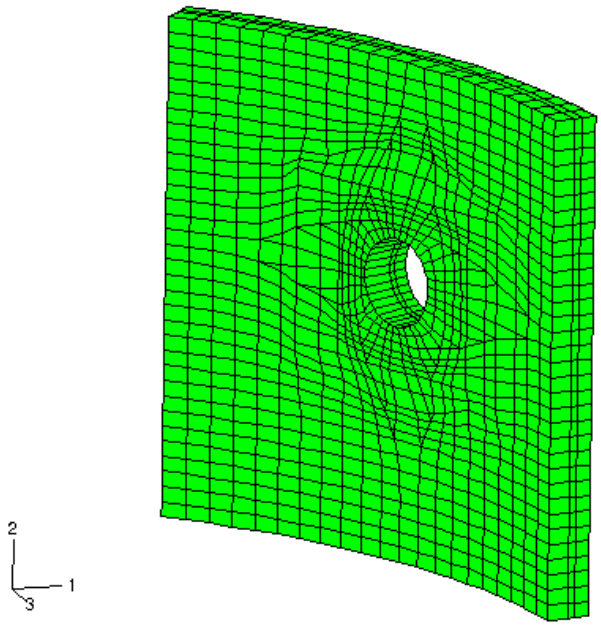

Figure 8 Detailed view of the main steam and feed water penetration model

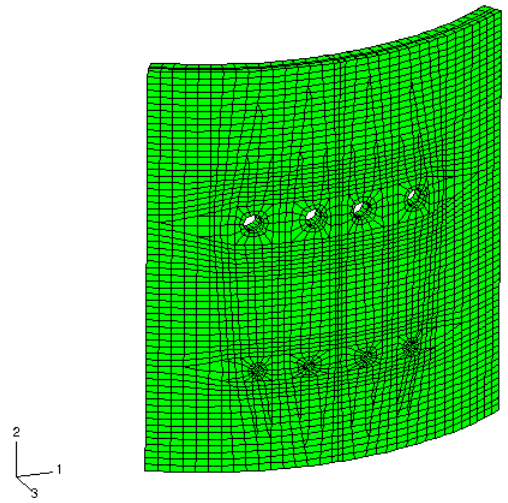

Figure 9 PCCV vertical tendons model

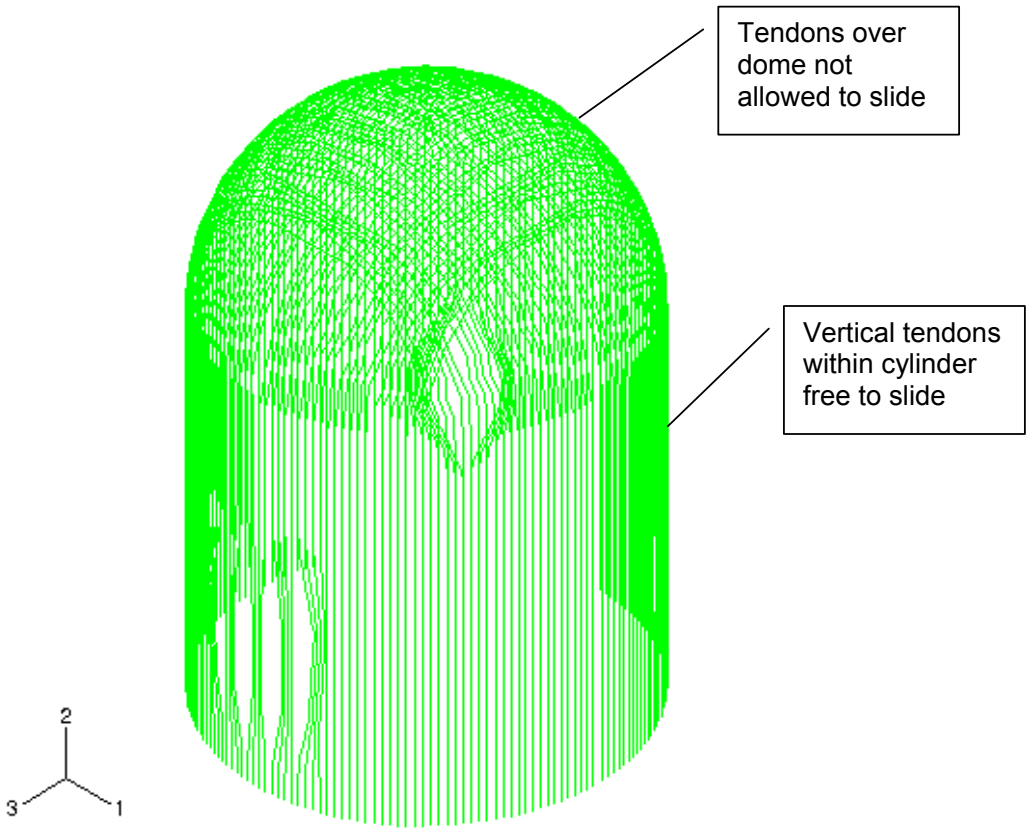

Figure 10 Equipment hatch penetration lining and cover plate

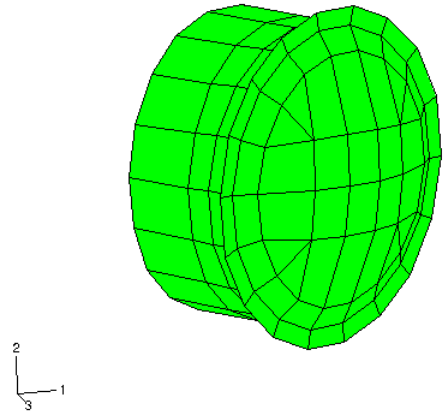

Figure 11 PCCV model supported on soil springs

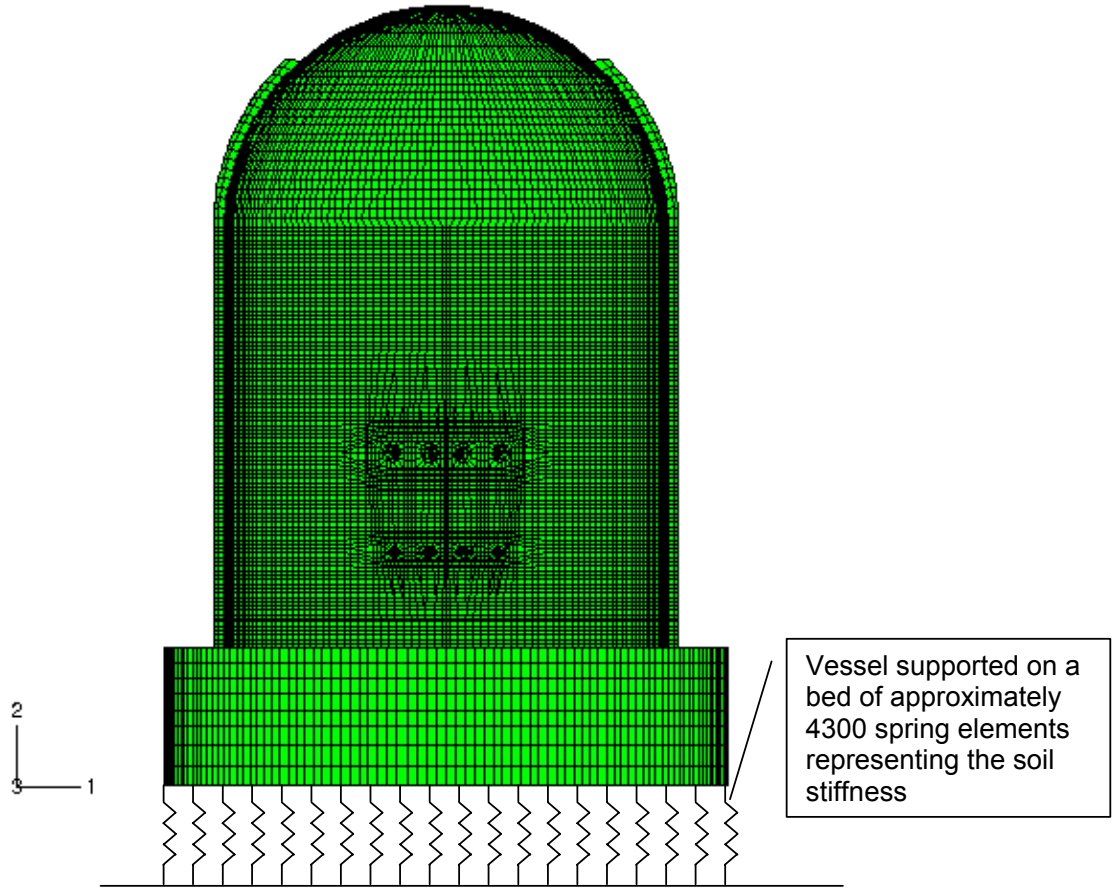

Figure 12 Internal liner model, showing detail around the main steam and feedwater penetrations

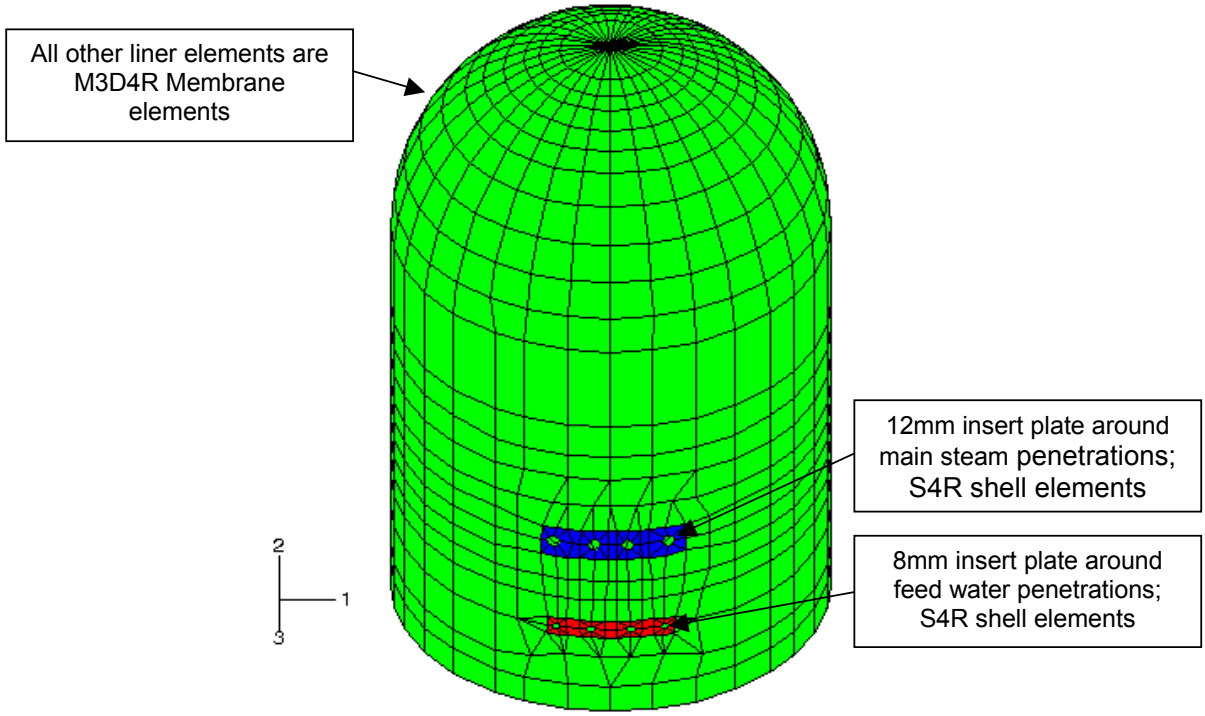

Figure 13 Comparison of Test & Pre-test Vertical Tendon Loads

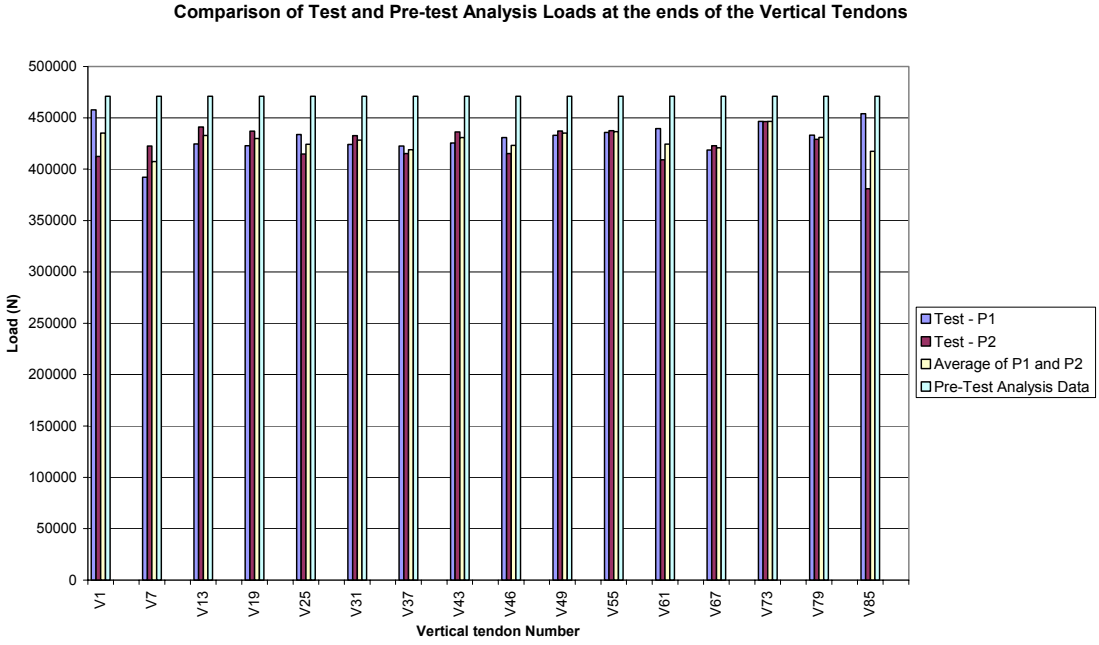

Figure 14 Comparison of Test & Pre-test Hoop Tendon Loads

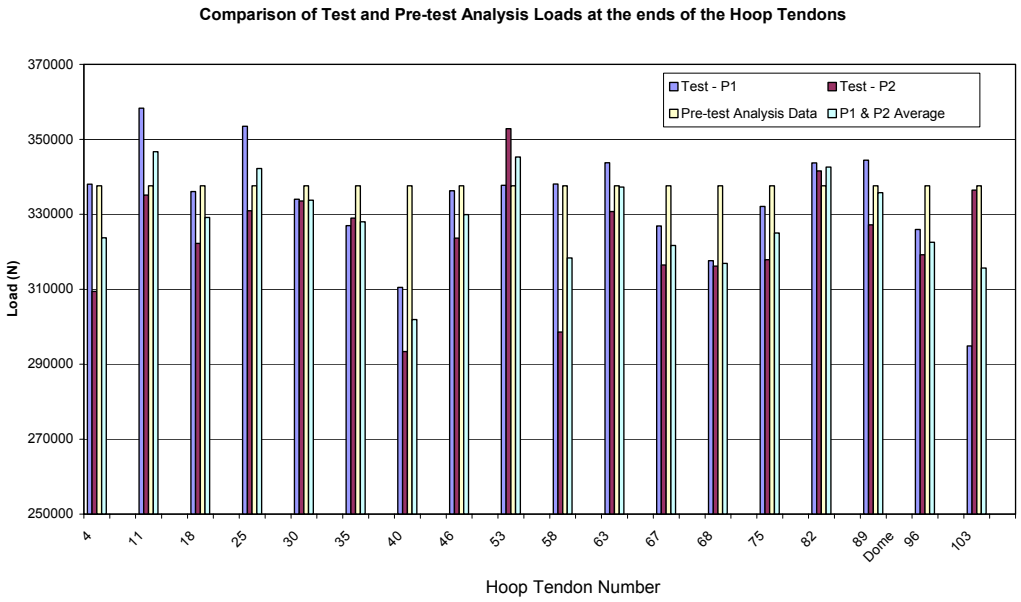

Figure 15 Variation in tendon load due to friction and seating loss

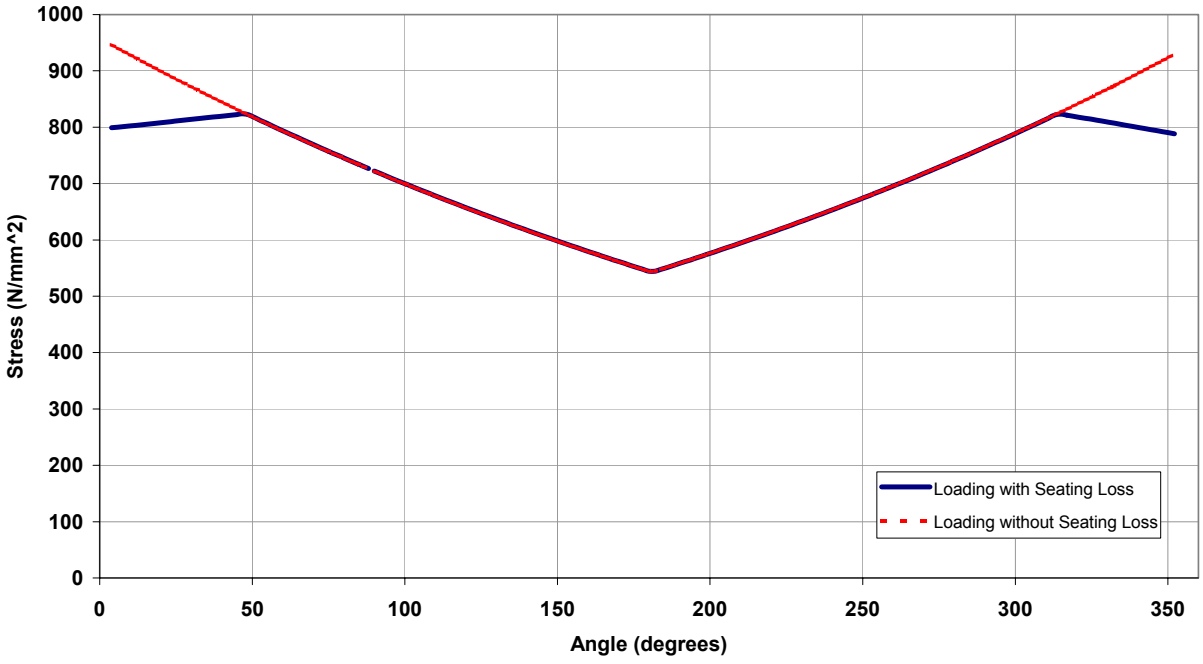

Figure 16 Convection to free air vs. temperature

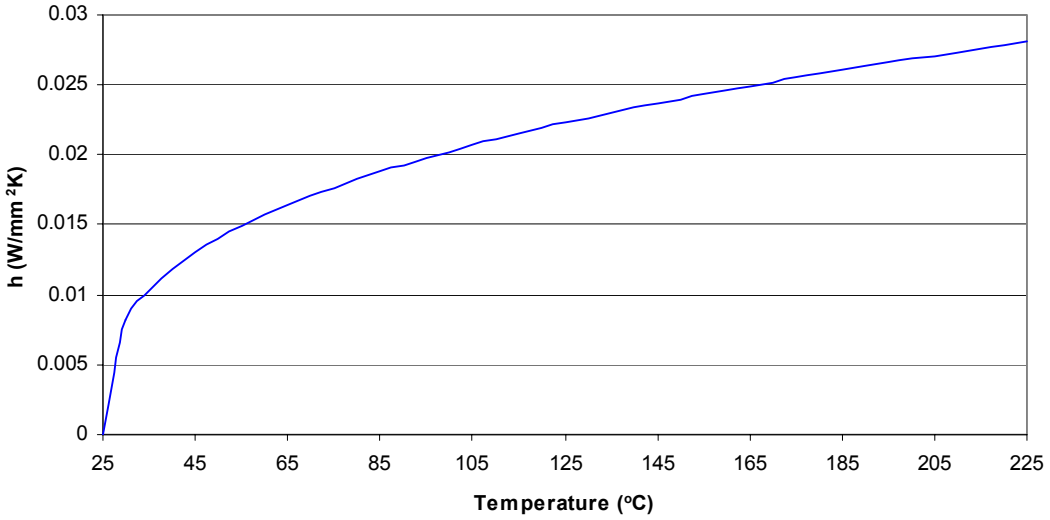

Figure 17 Nodal Temperature at Location 1

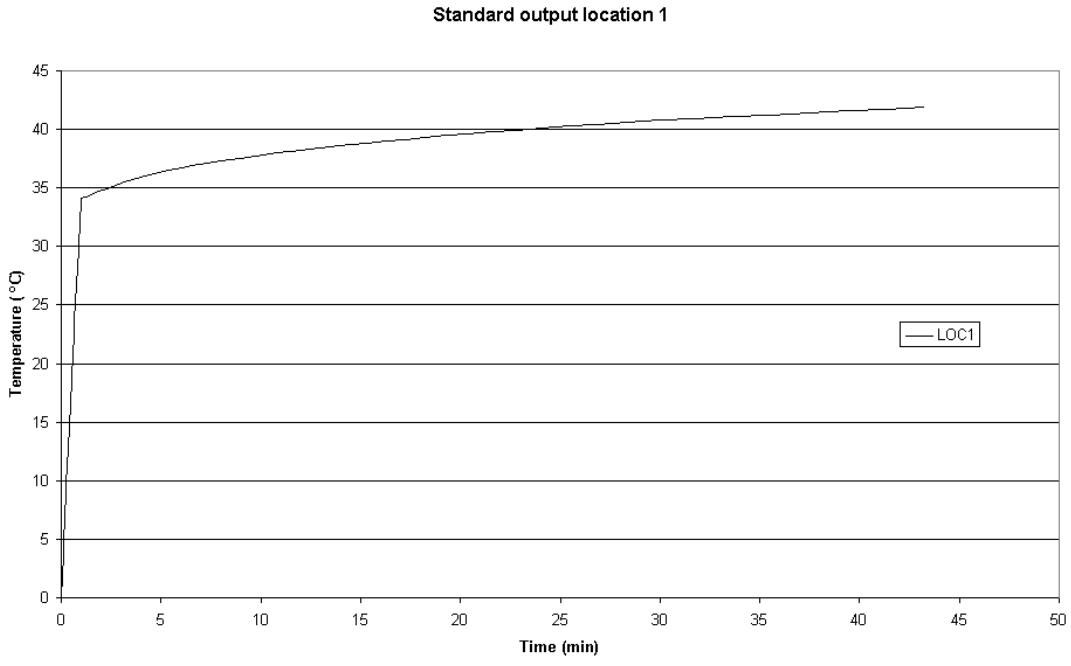

Figure 18 Nodal Temperature at Location 6

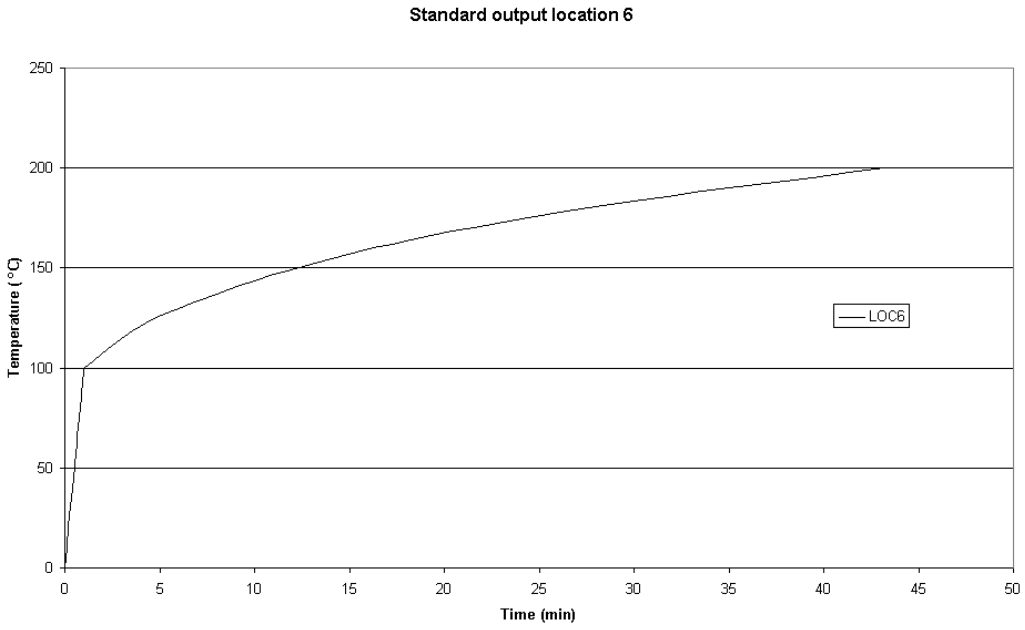

Figure 19 Nodal Temperature at Location 7 & 8

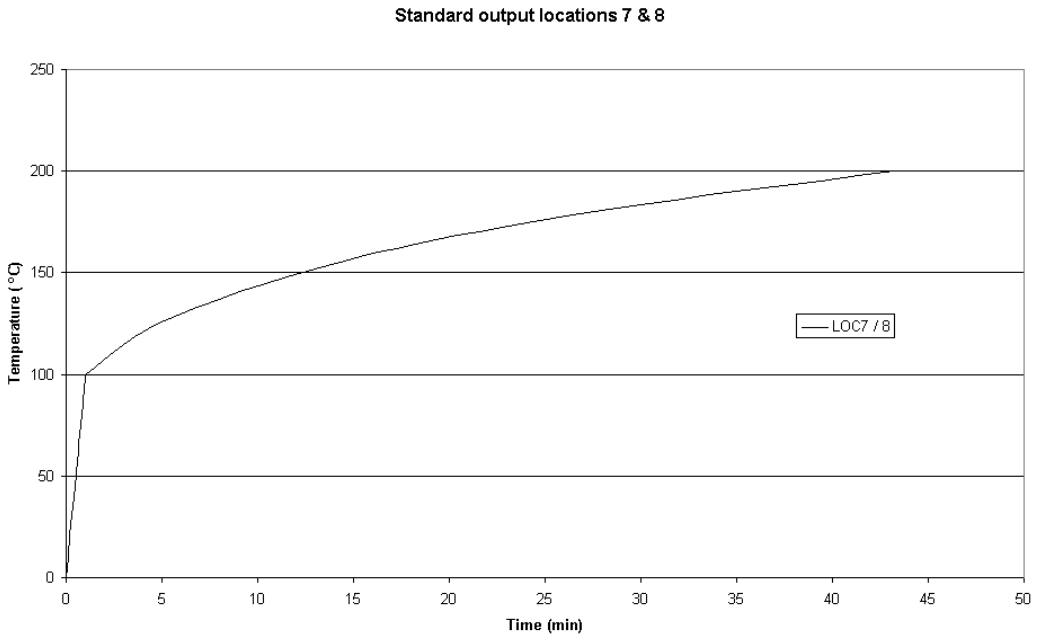

Figure 20 Nodal Temperature at Location 11

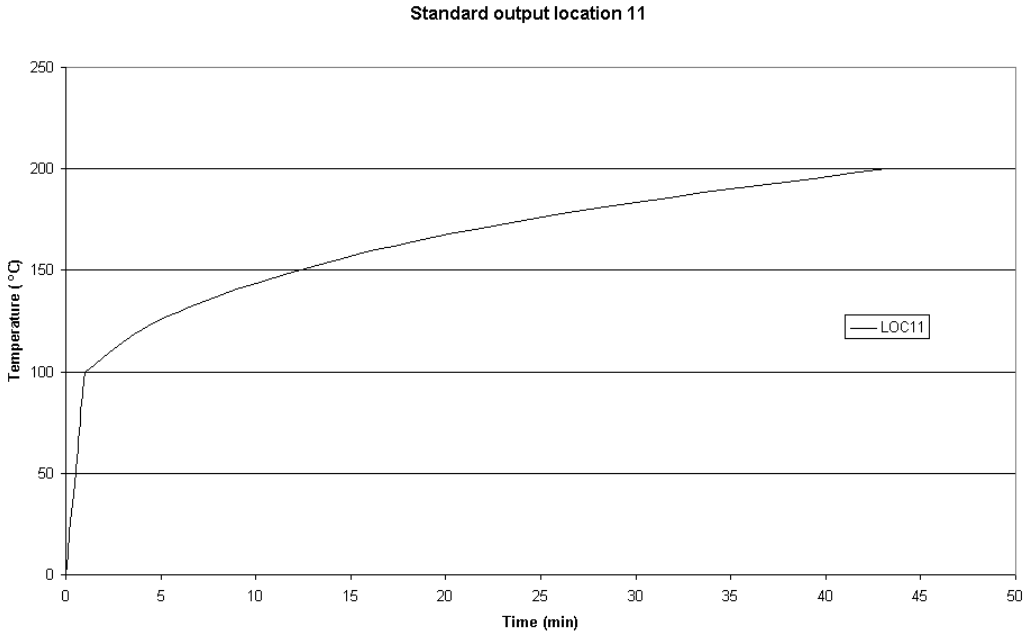

Figure 21 Nodal Temperature at Location 12

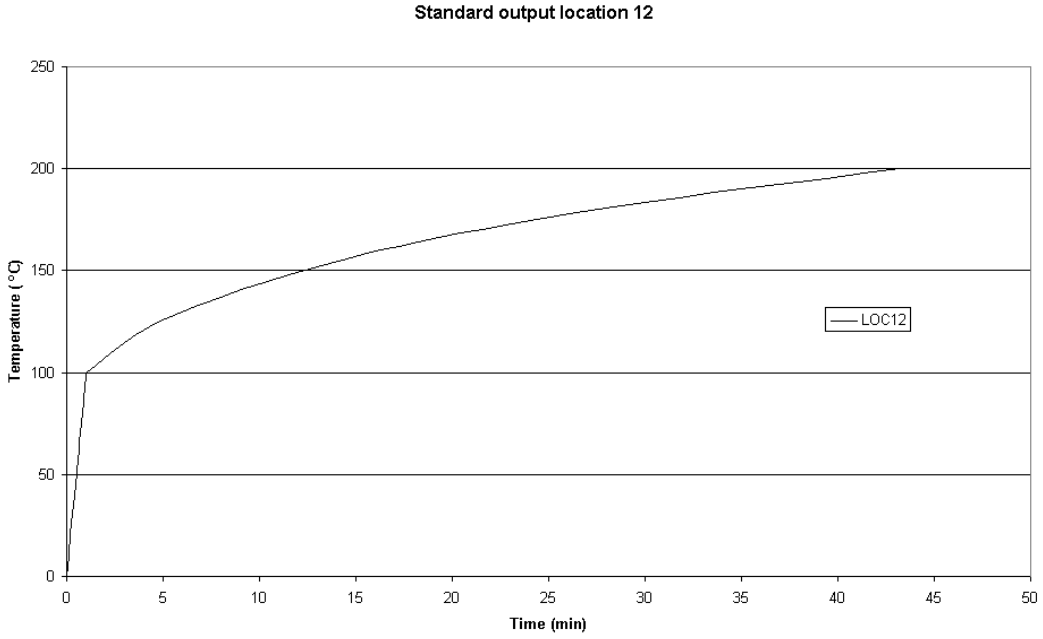

Figure 22 Nodal Temperature at Location 13

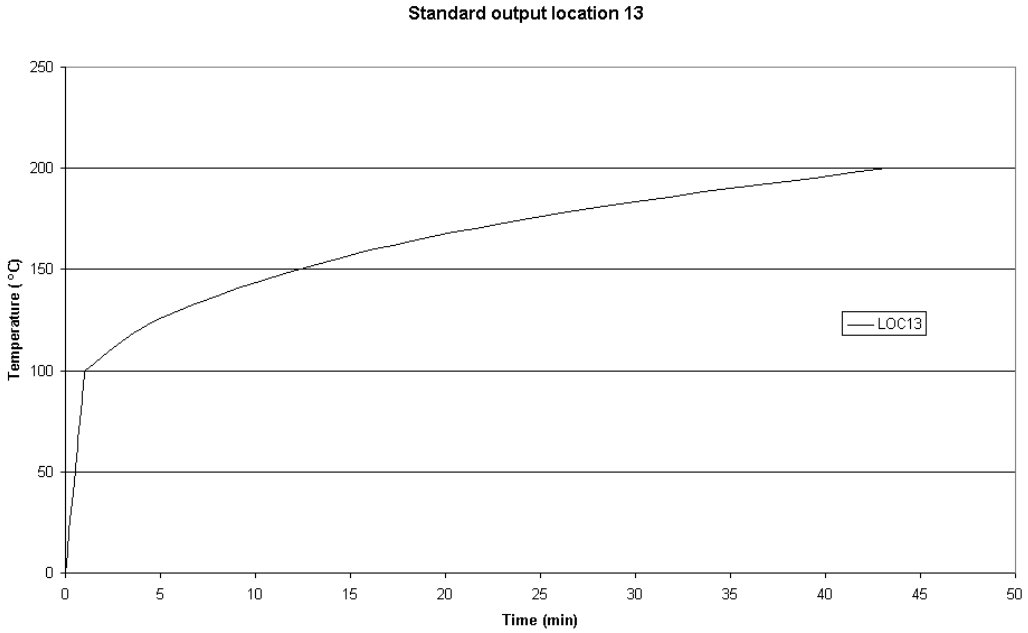

Figure 23 Nodal Temperature at Location 14

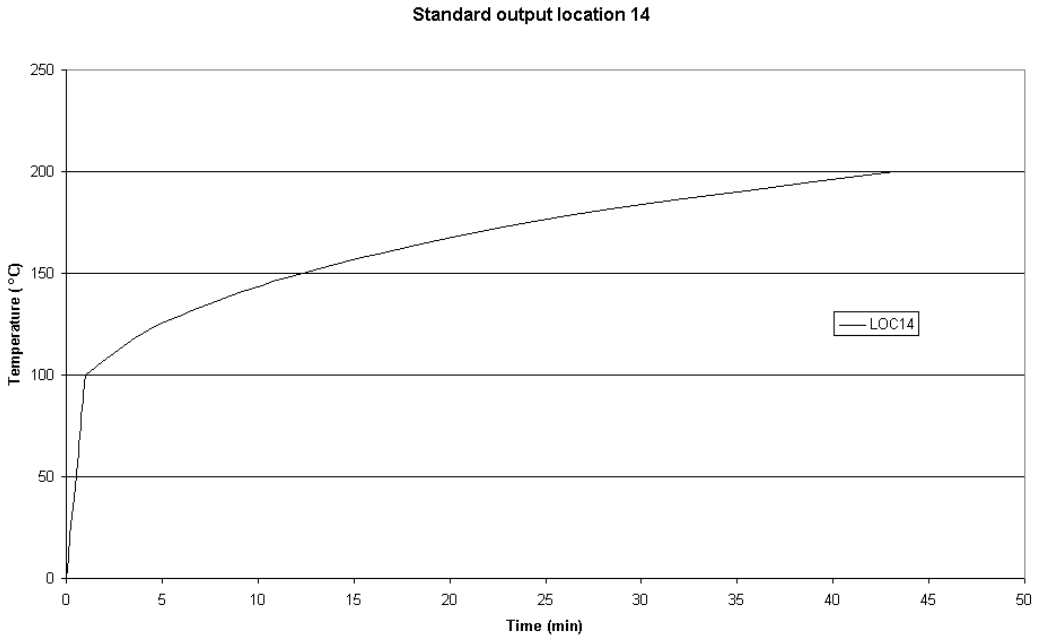

Figure 24 Nodal Temperature at Location 18

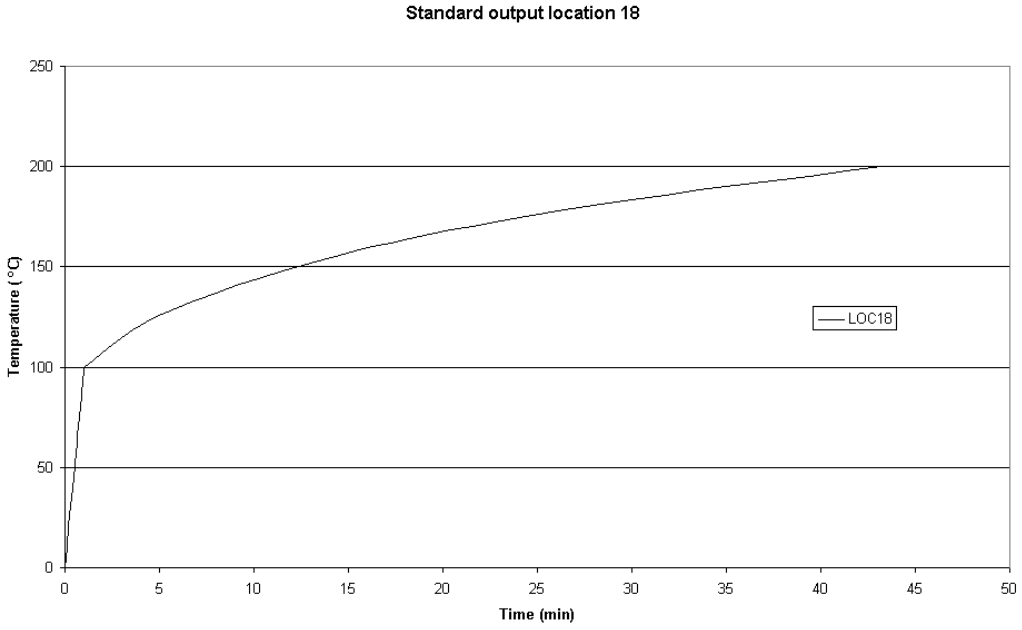

Figure 25 Nodal Temperature at Location 19

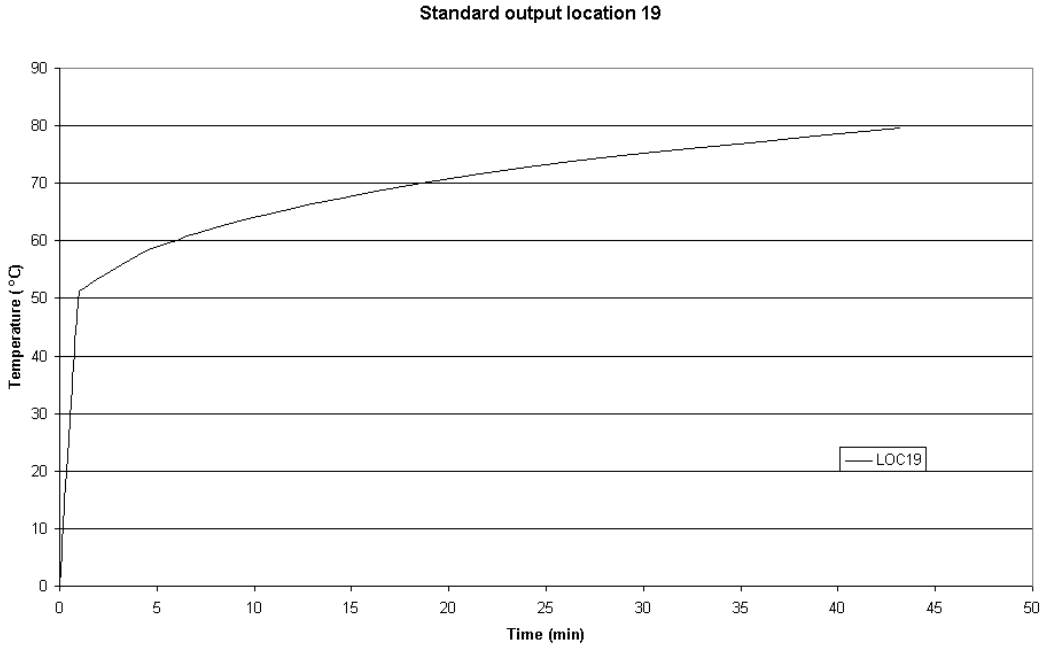

Figure 26 Nodal Temperature at Locations 22 and 23

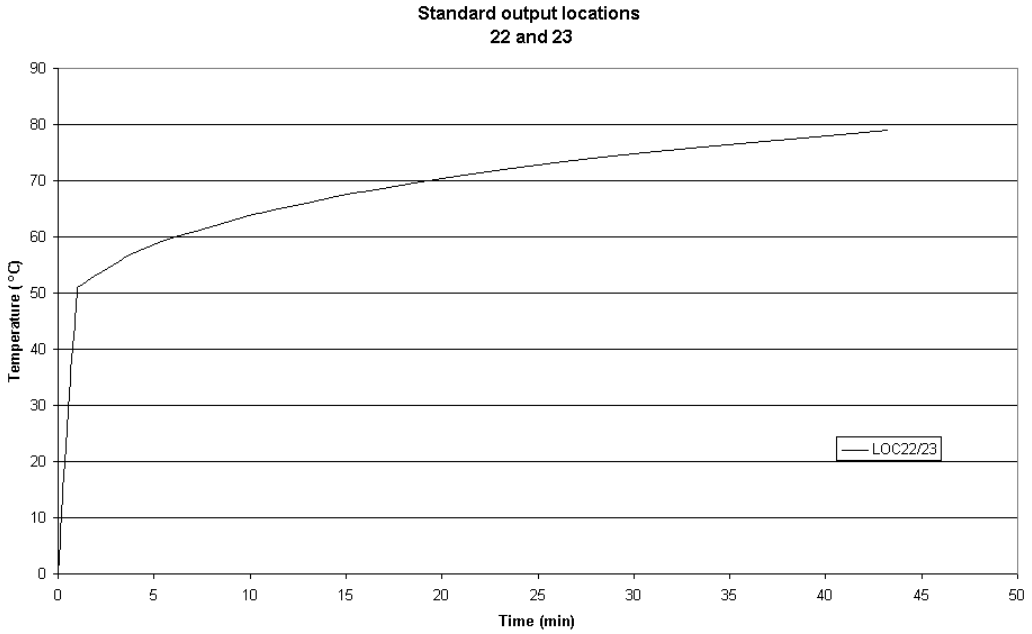

Figure 27 Nodal Temperature at Locations 32 and 33

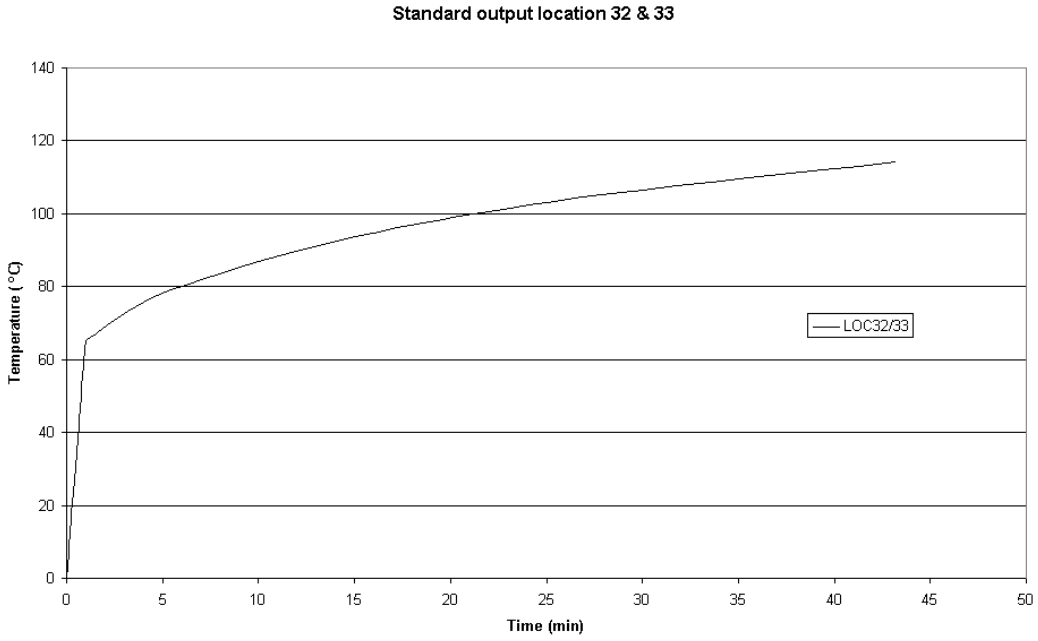

Figure 28 Nodal Temperature at Locations 38 & 39

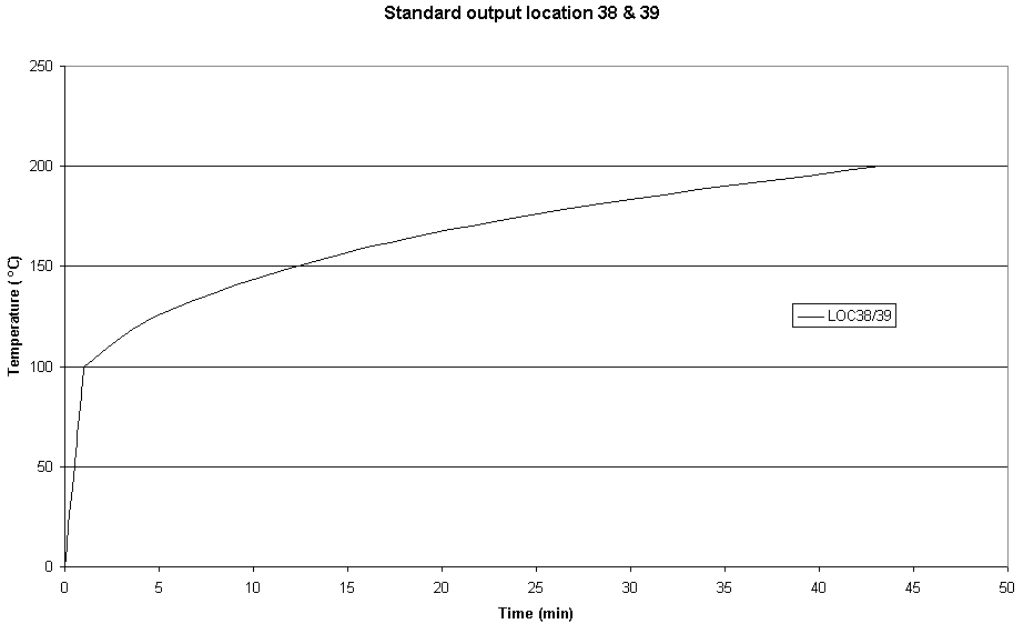

Figure 29 Nodal Temperature at Location 42

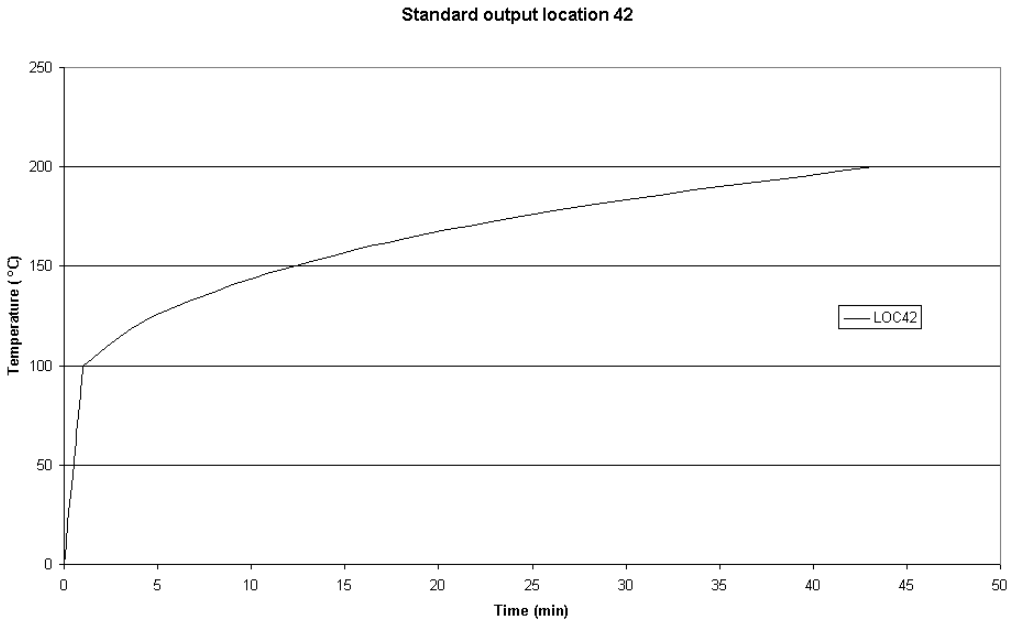

Figure 30 Nodal Temperature at Location 45

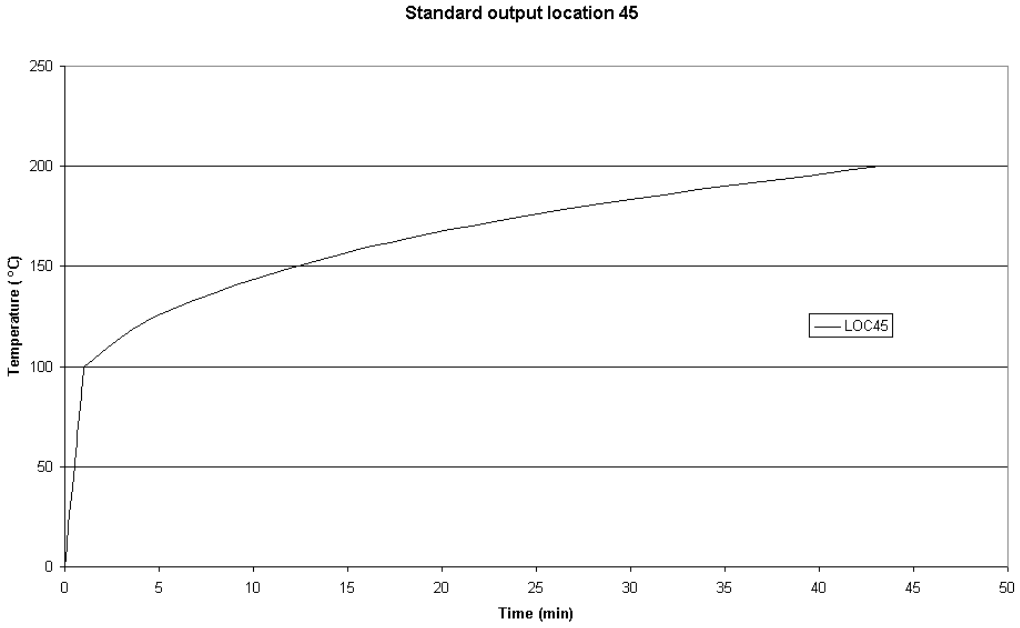

Figure 31 Nodal Temperature at Location 48

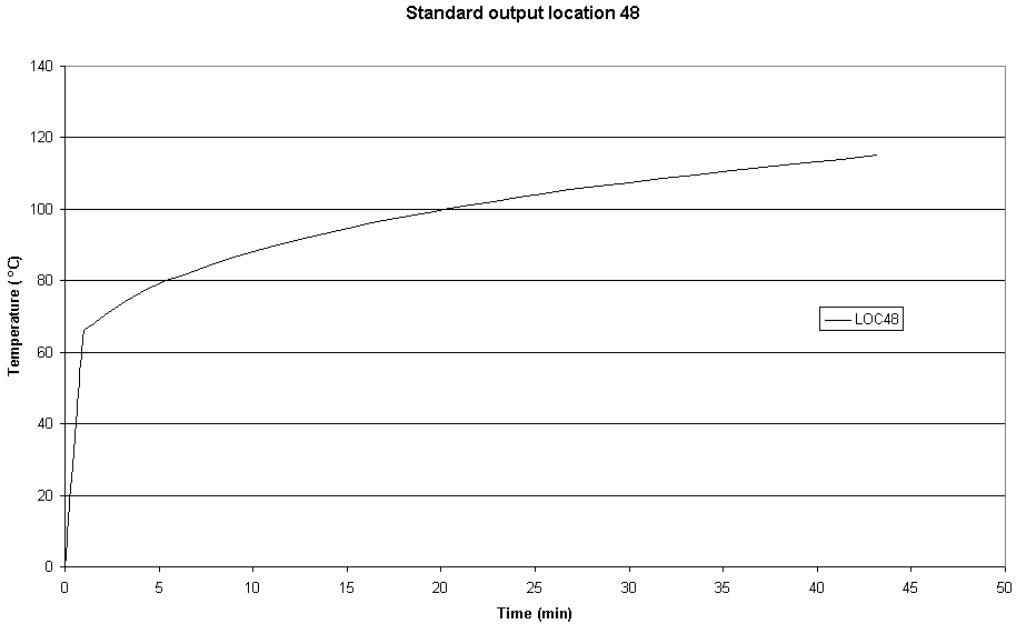

Figure 32 Nodal Temperature at Location 50

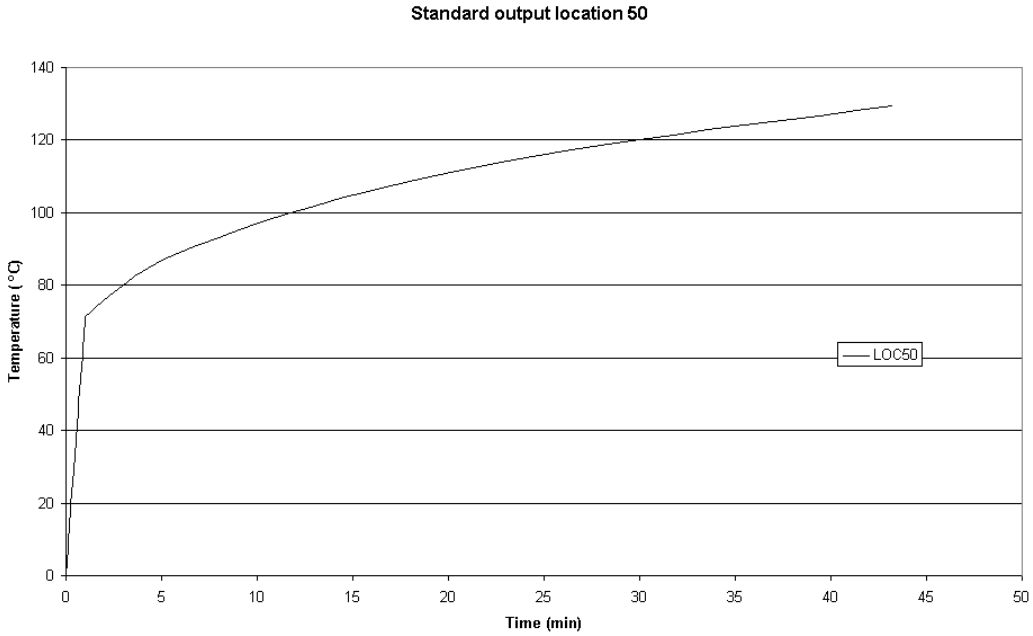

Figure 33 Nodal Temperature at Location 52

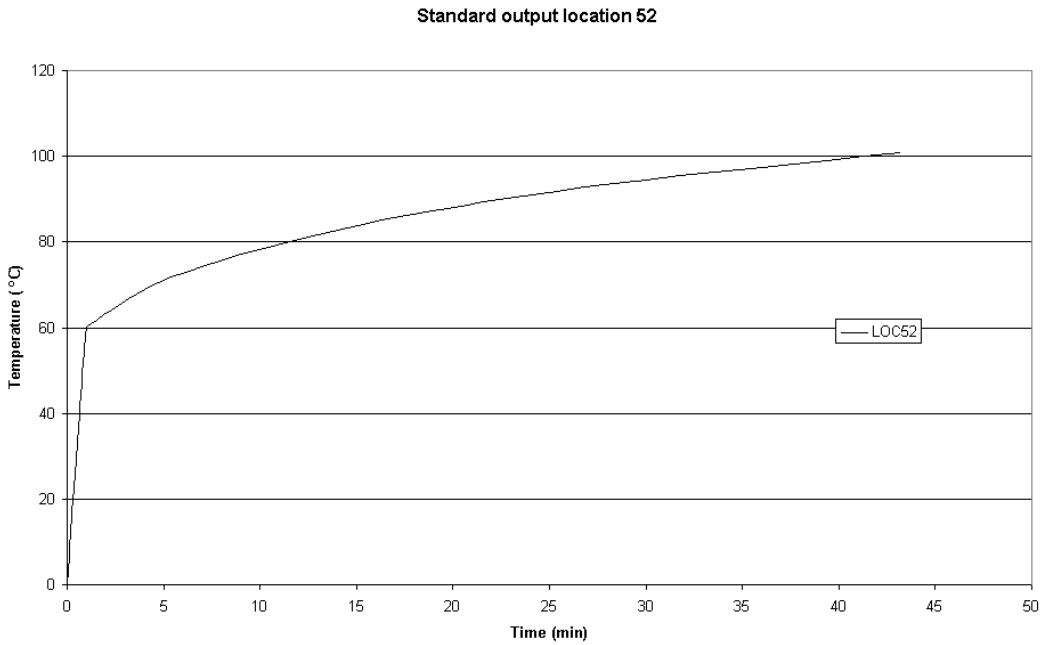

Figure 34 Nodal Temperature at Location 55

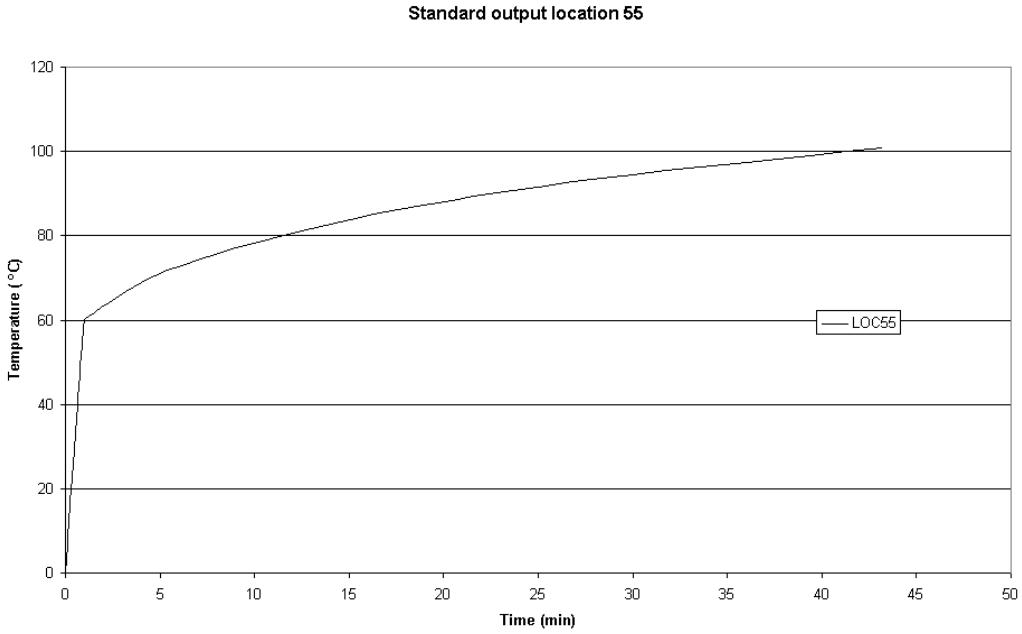

Figure 35 Temperature contour profile, vertical section through PCCV

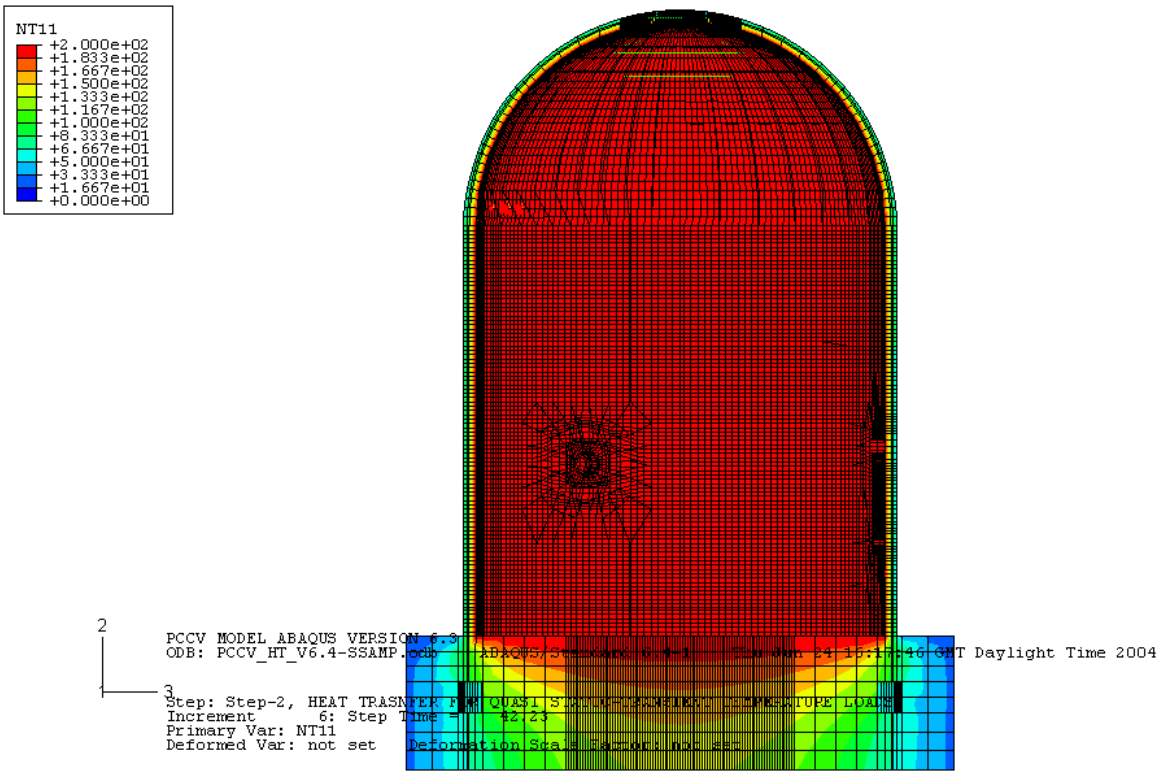

Figure 36 Temperature contour profile at cylinder / basemat junction

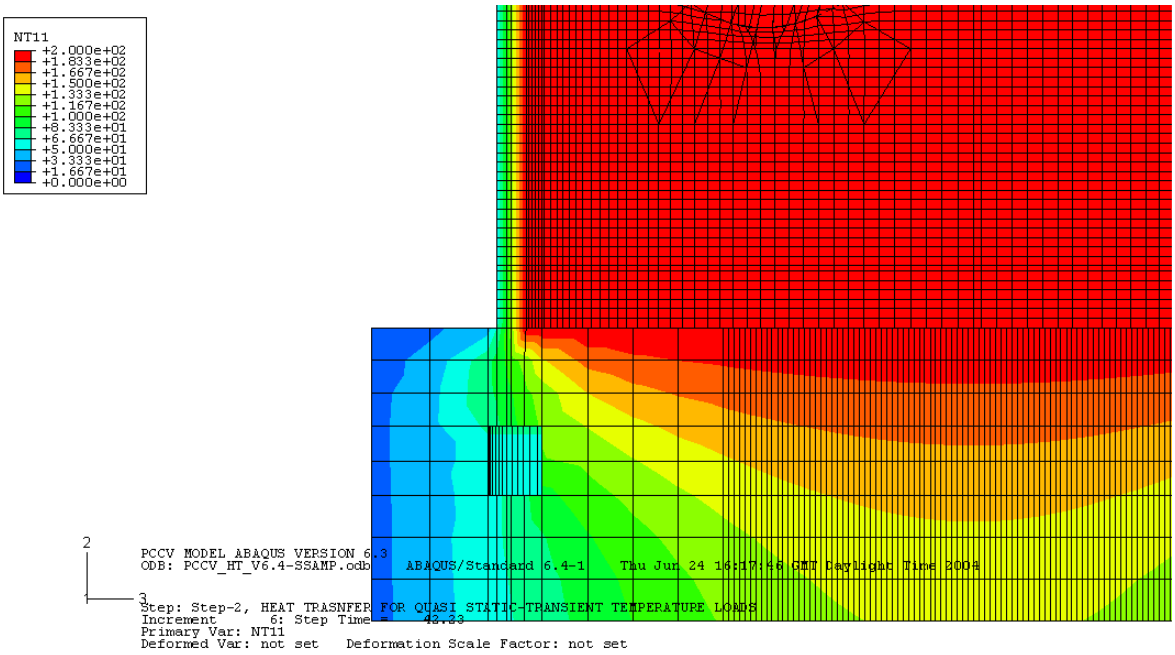

Figure 37 Temperature contour profile through the cylinder wall

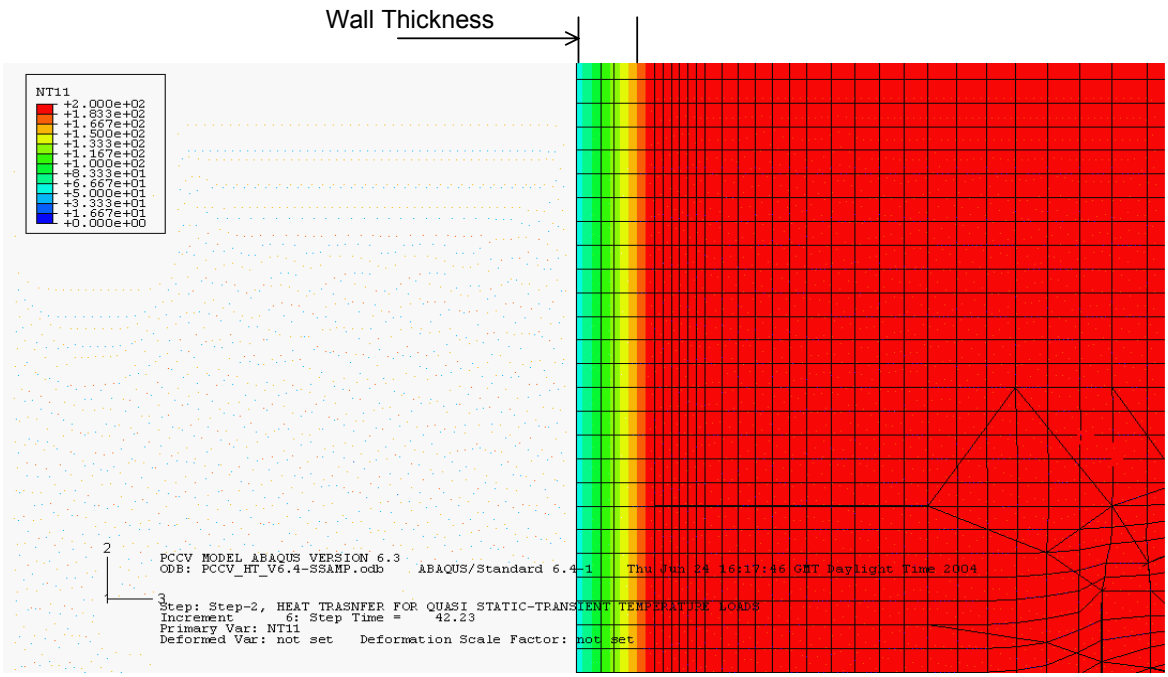

Figure 38 Stress Analysis Model – Location 1

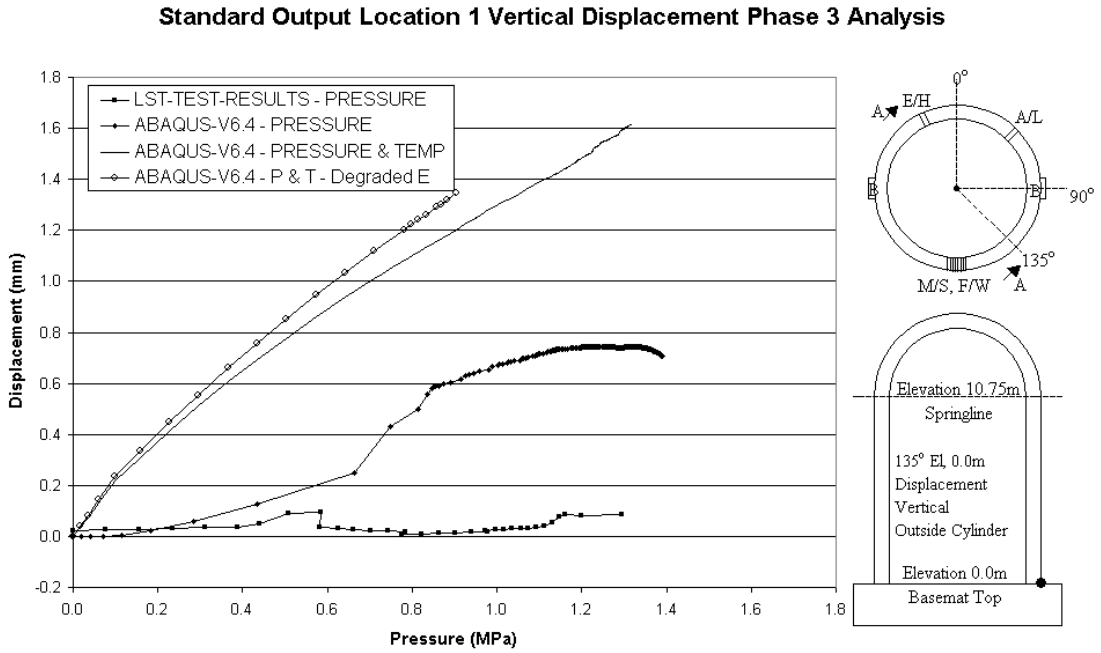

Figure 39 Stress Analysis Model – Location 6

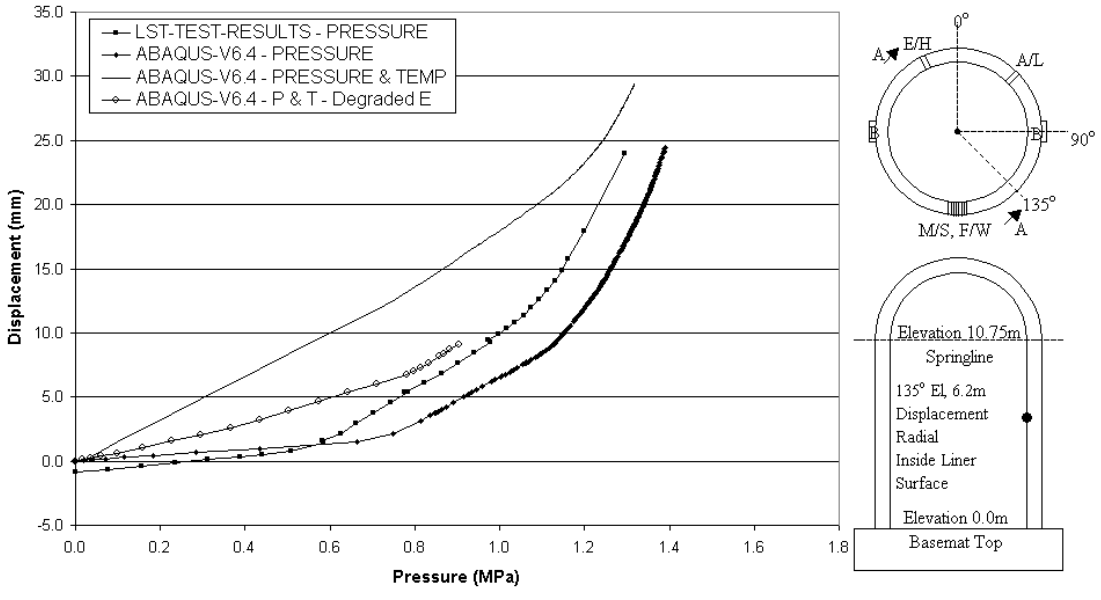

Figure 40 Stress Analysis Model – Location 7

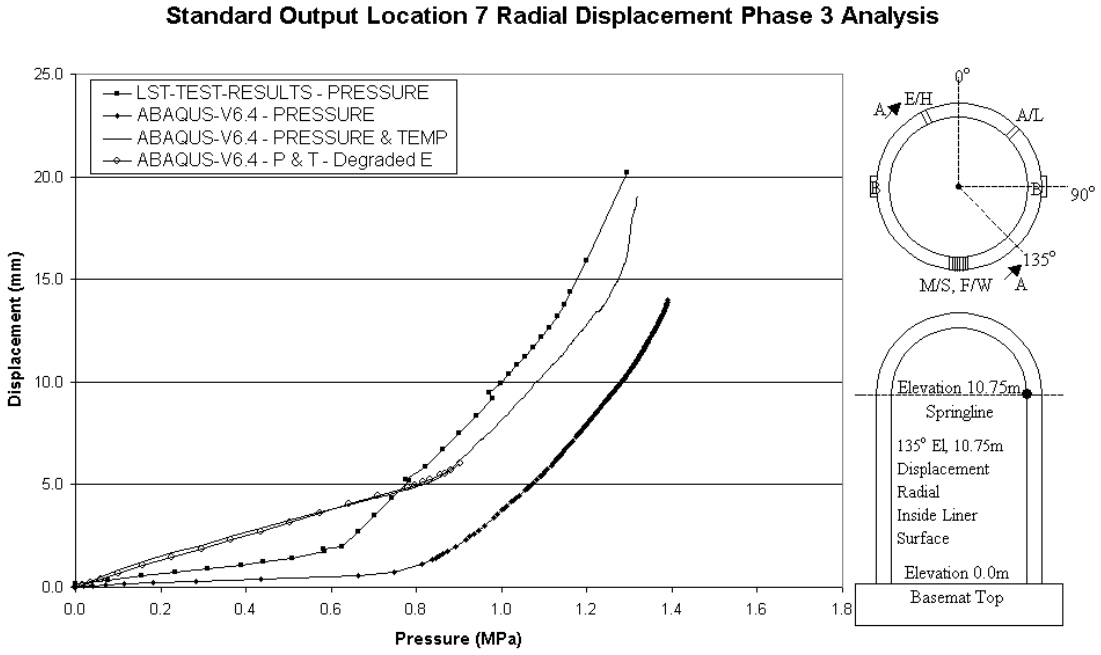

Figure 41 Stress Analysis Model – Location 8

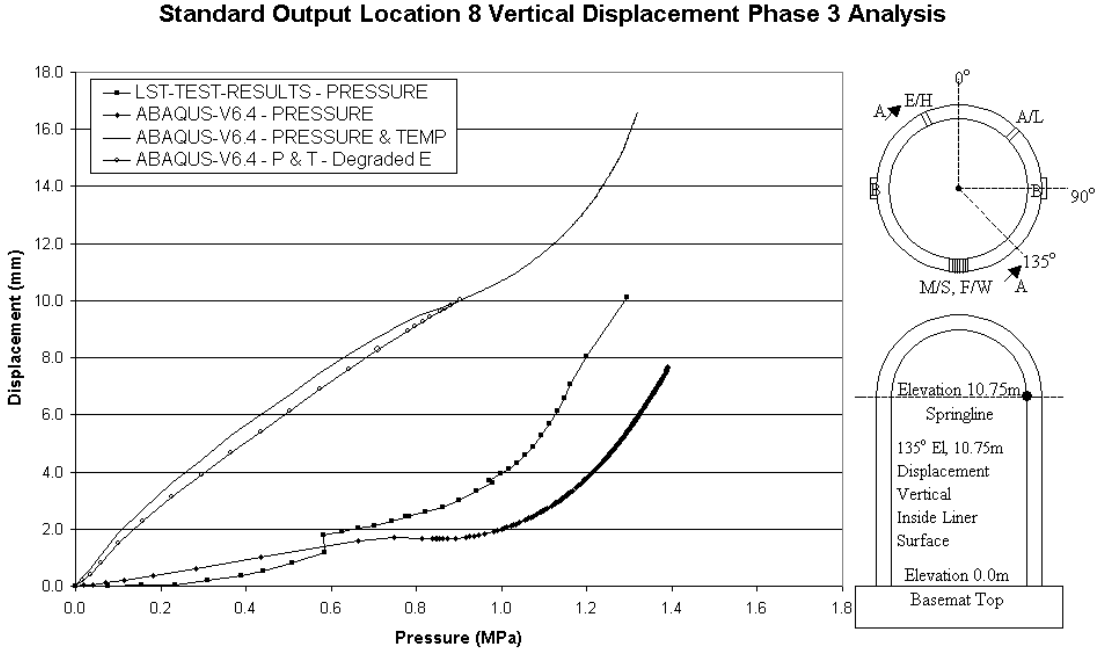

Figure 42 Stress Analysis Model – Location 11

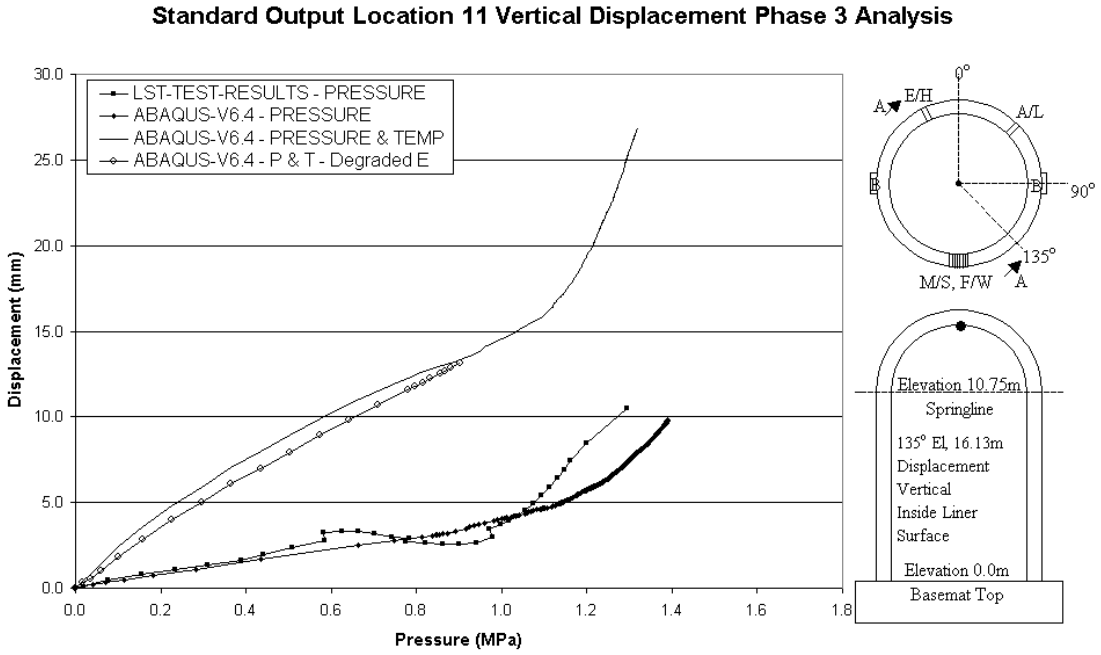

Figure 43 Stress Analysis Model – Location 12

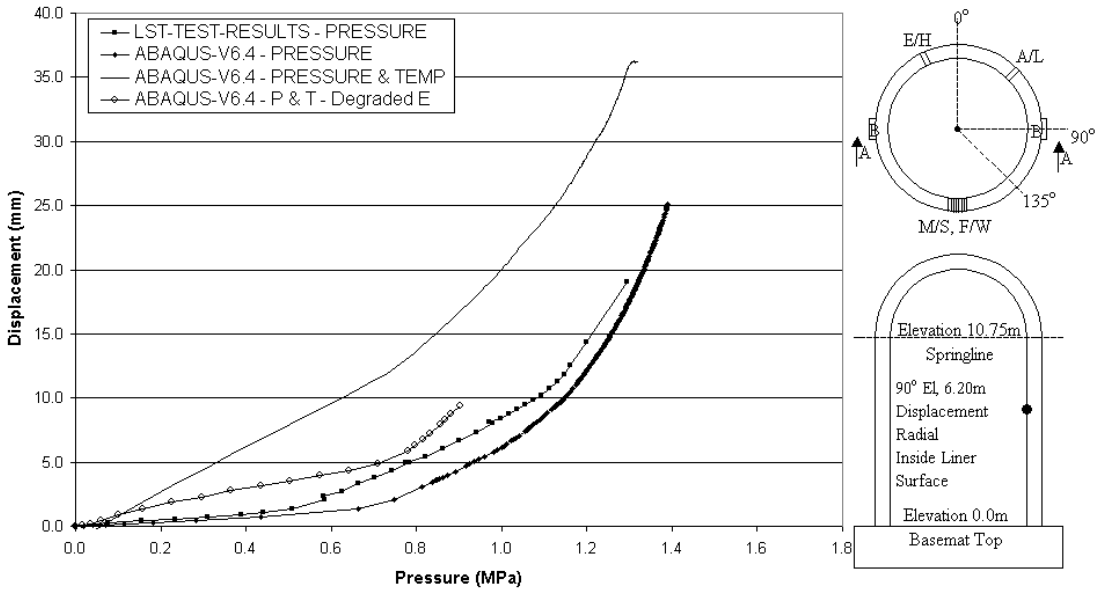

Figure 44 Stress Analysis Model – Location 13

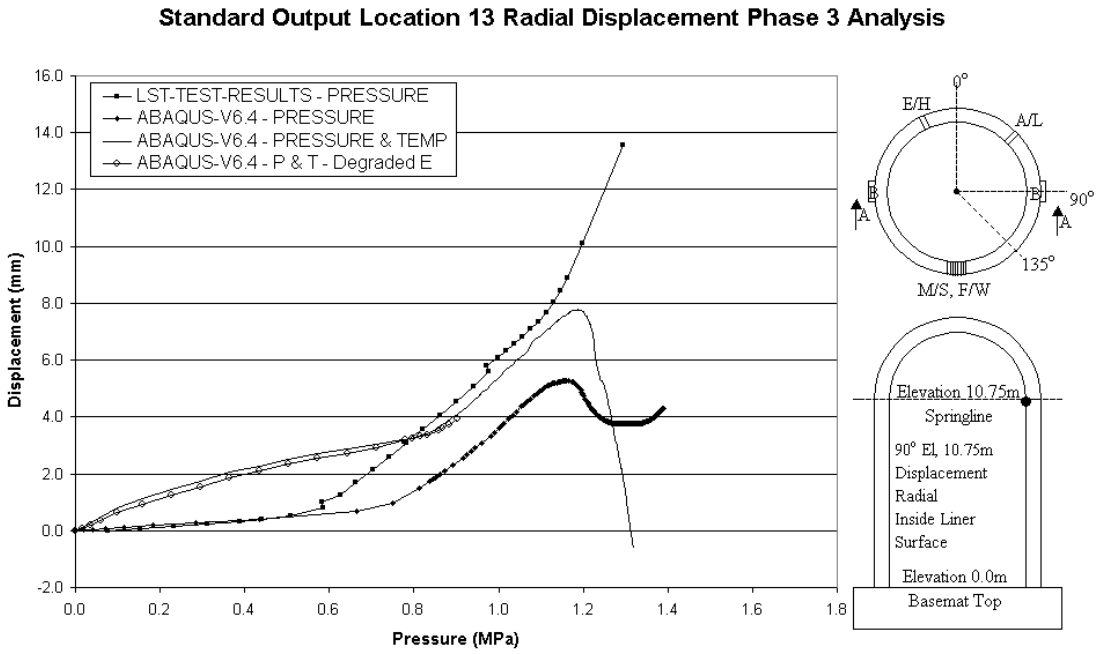

Figure 45 Stress Analysis Model – Location 14

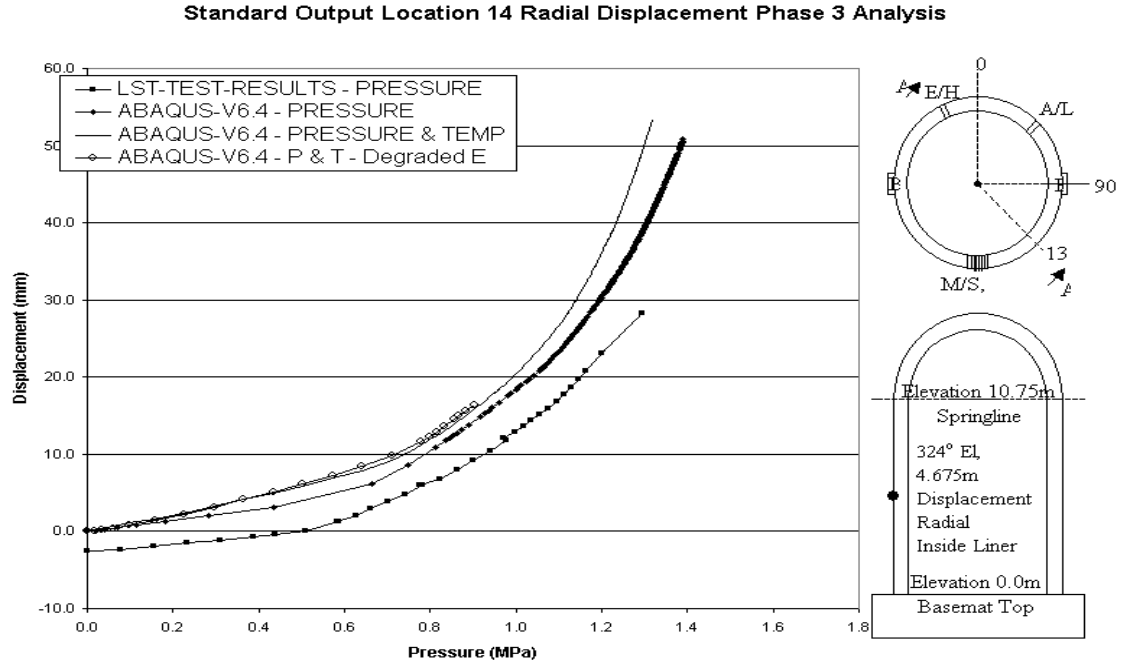

Figure 46 Stress Analysis Model – Location 18

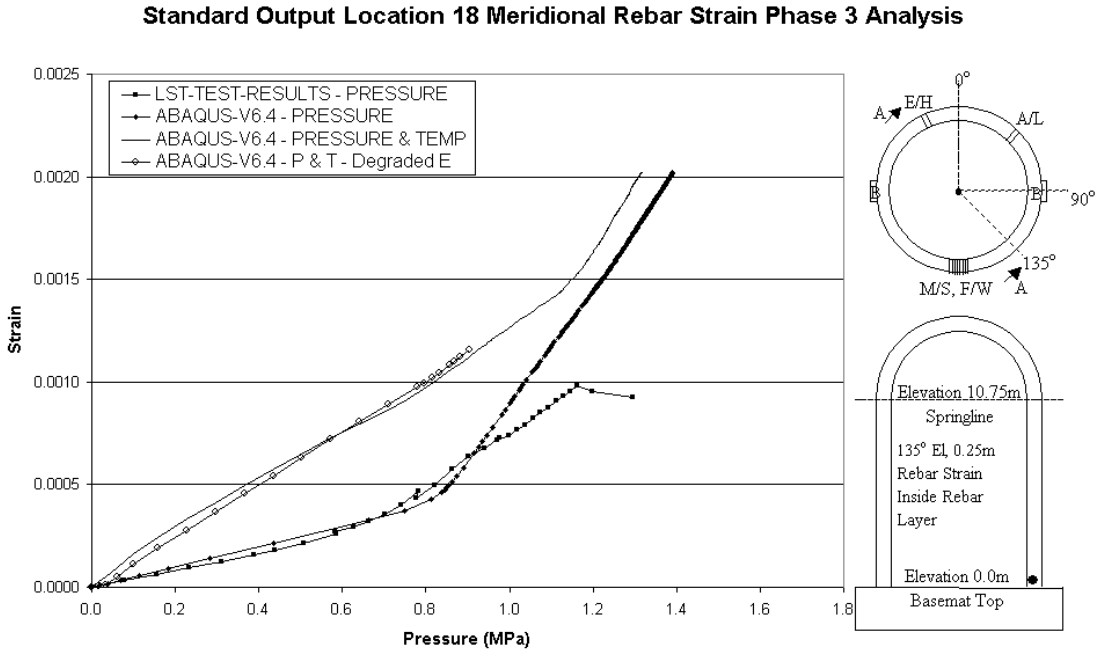

Figure 47 Stress Analysis Model – Location 19

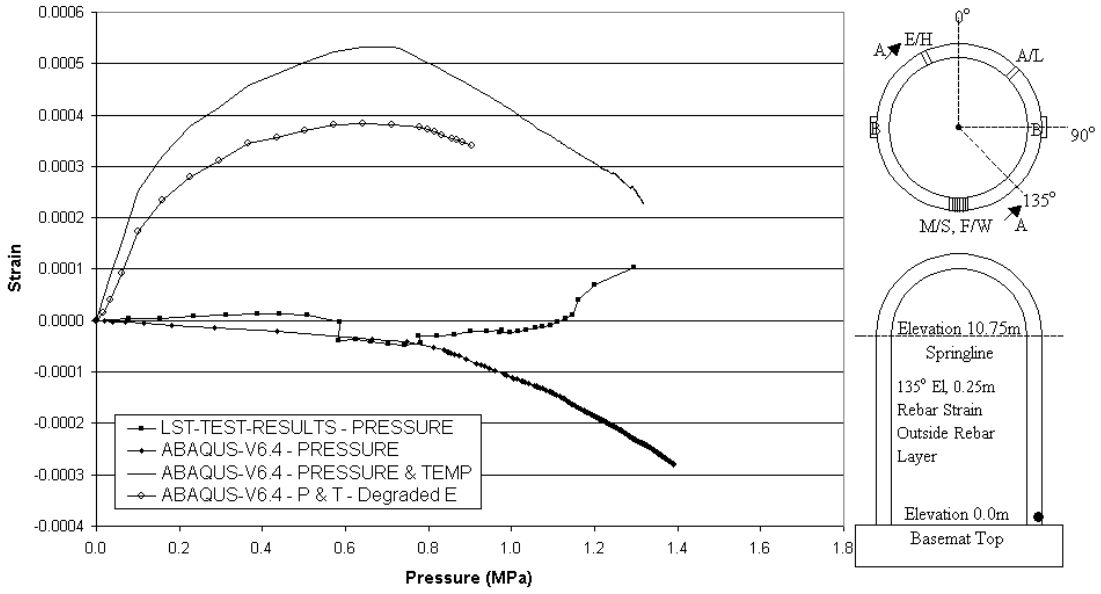

Figure 48 Stress Analysis Model – Location 22

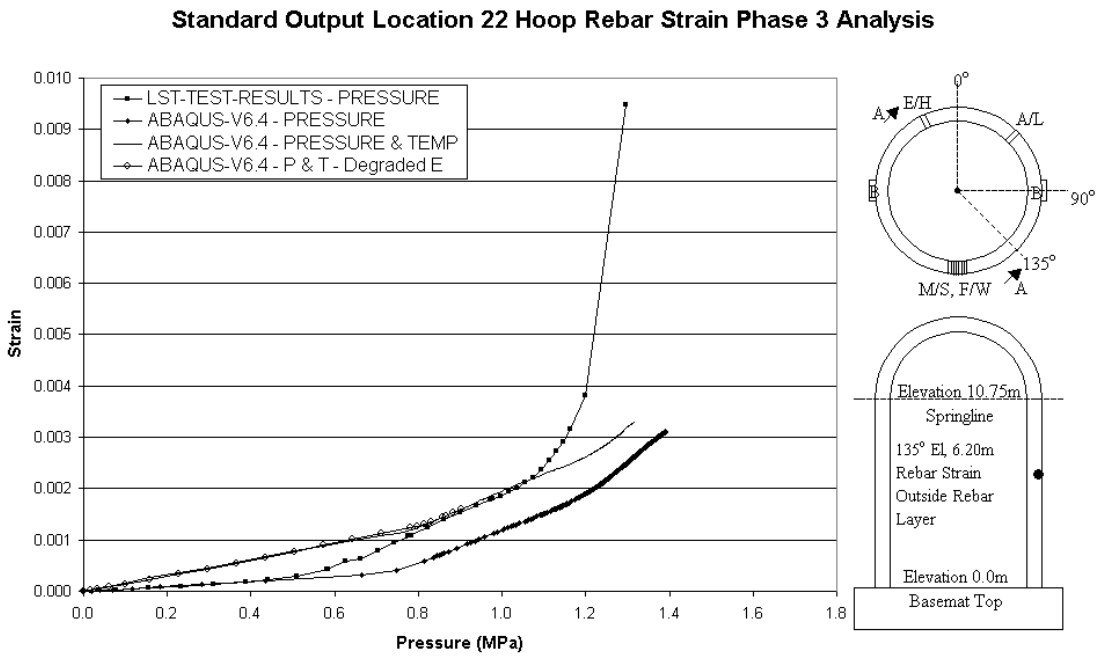

Figure 49 Stress Analysis Model – Location 23

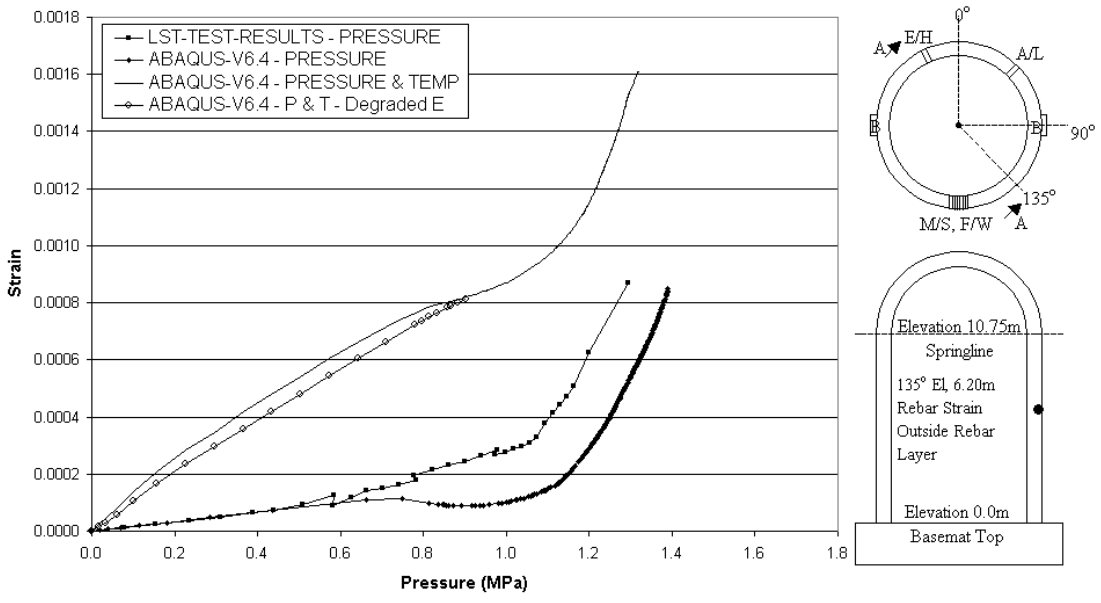

Figure 50 Stress Analysis Model – Location 32

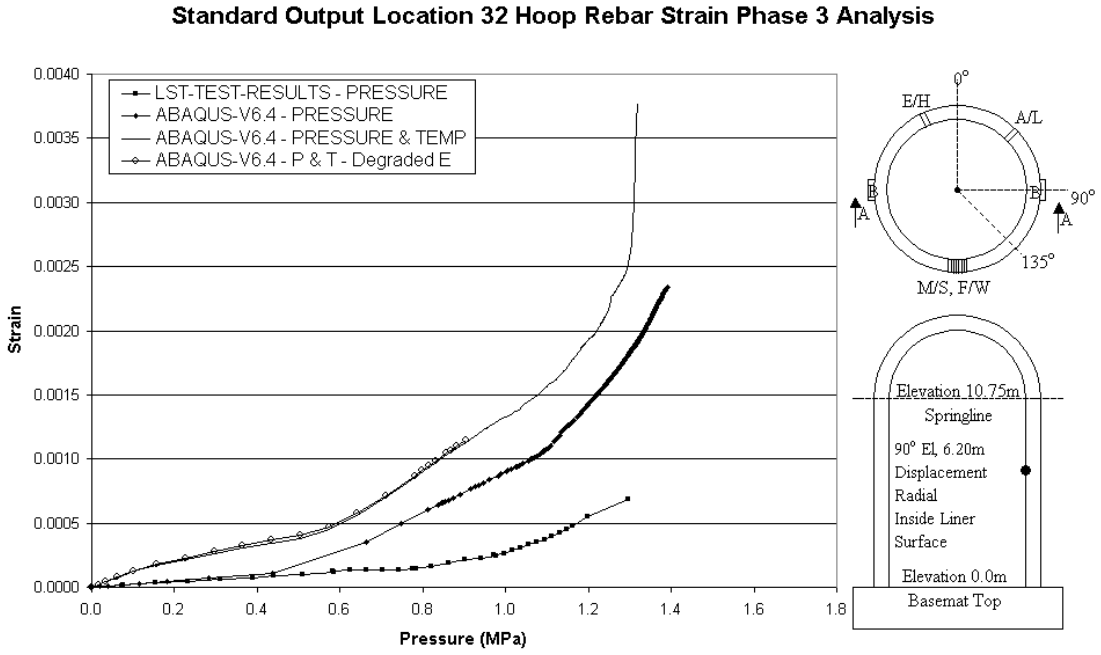

Figure 51 Stress Analysis Model – Location 33

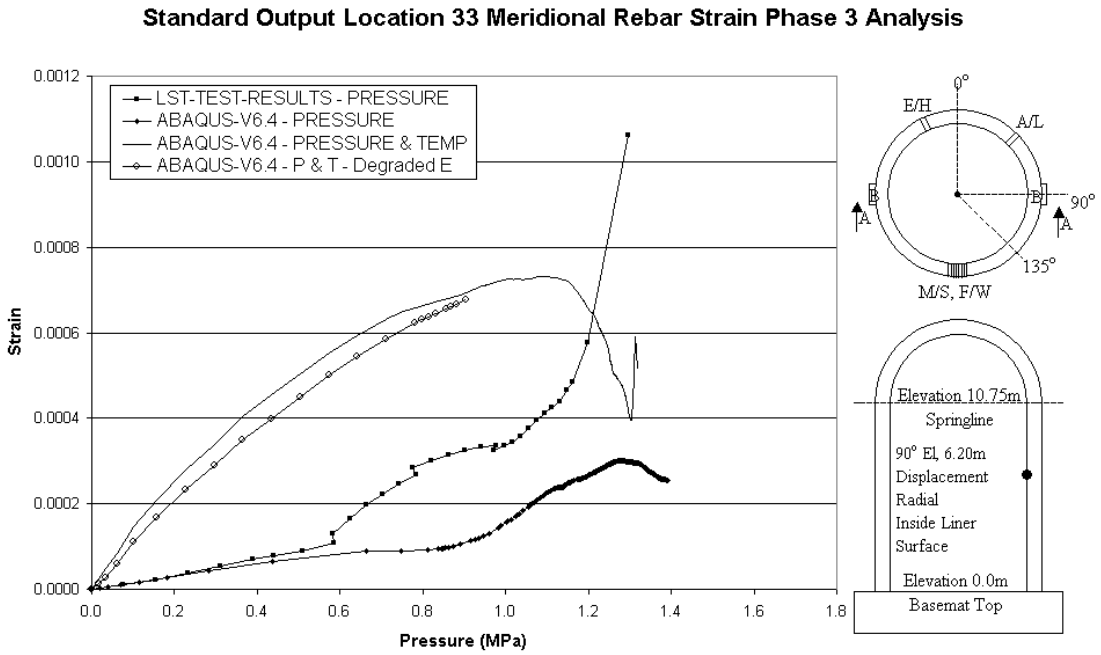

Figure 52 Stress Analysis Model – Location 38

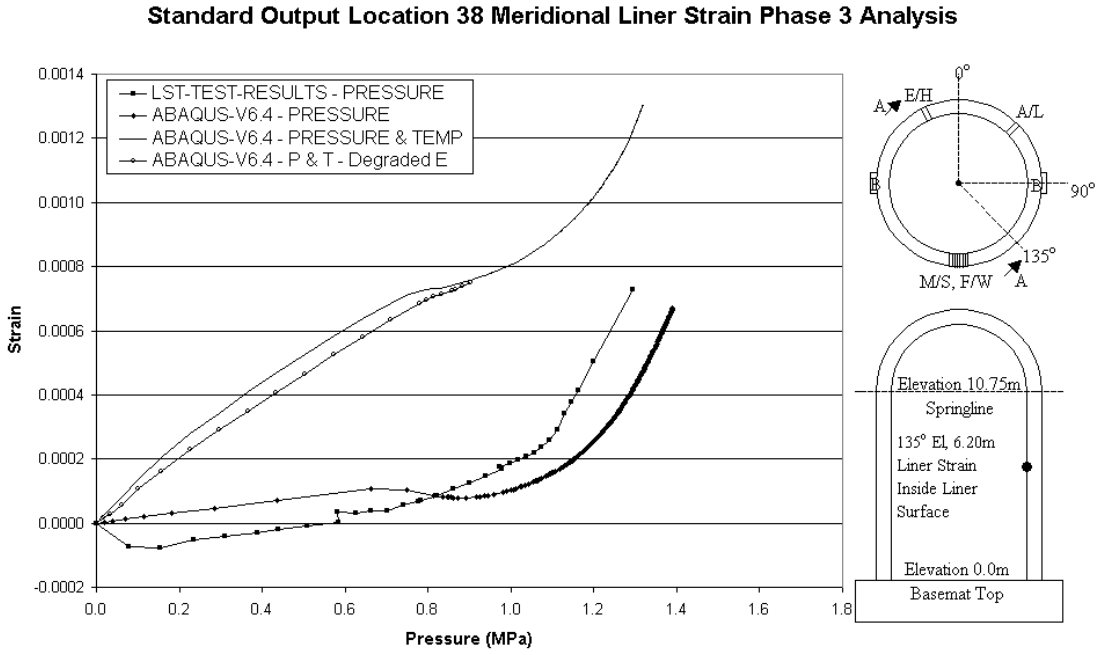

Figure 53 Stress Analysis Model – Location 39

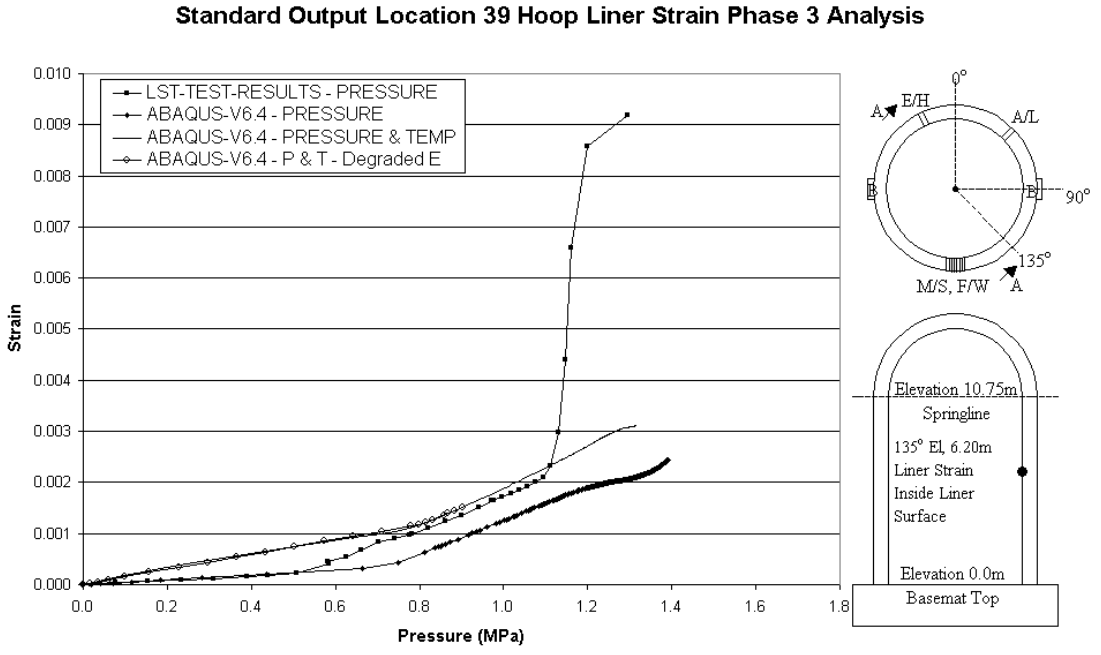

Figure 54 Stress Analysis Model – Location 42

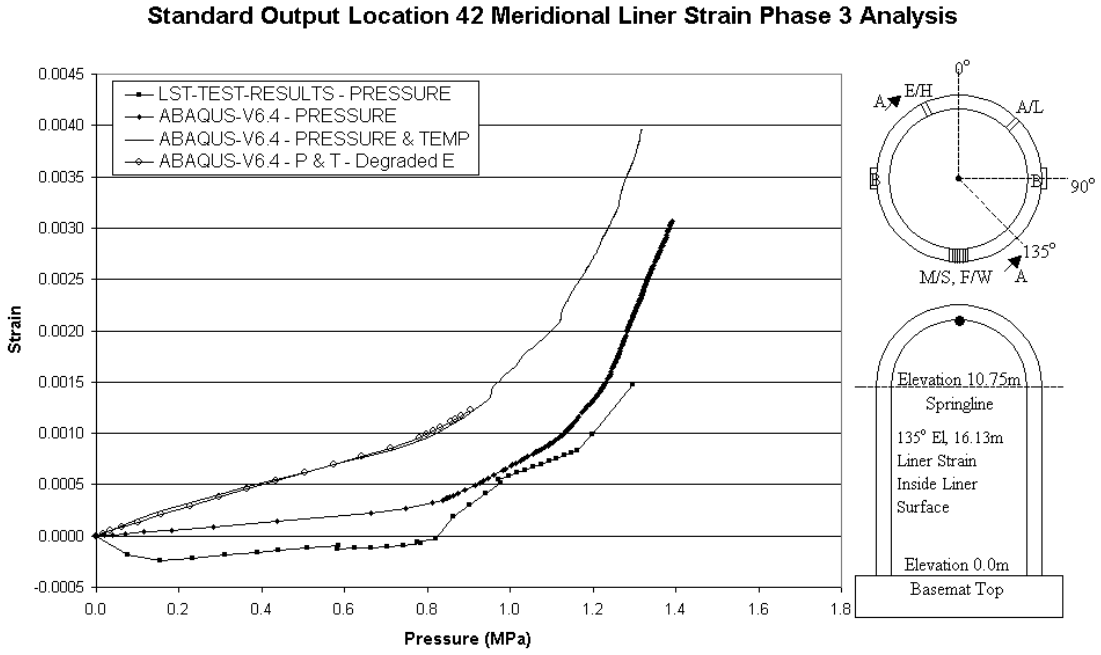

Figure 55 Stress Analysis Model – Location 45

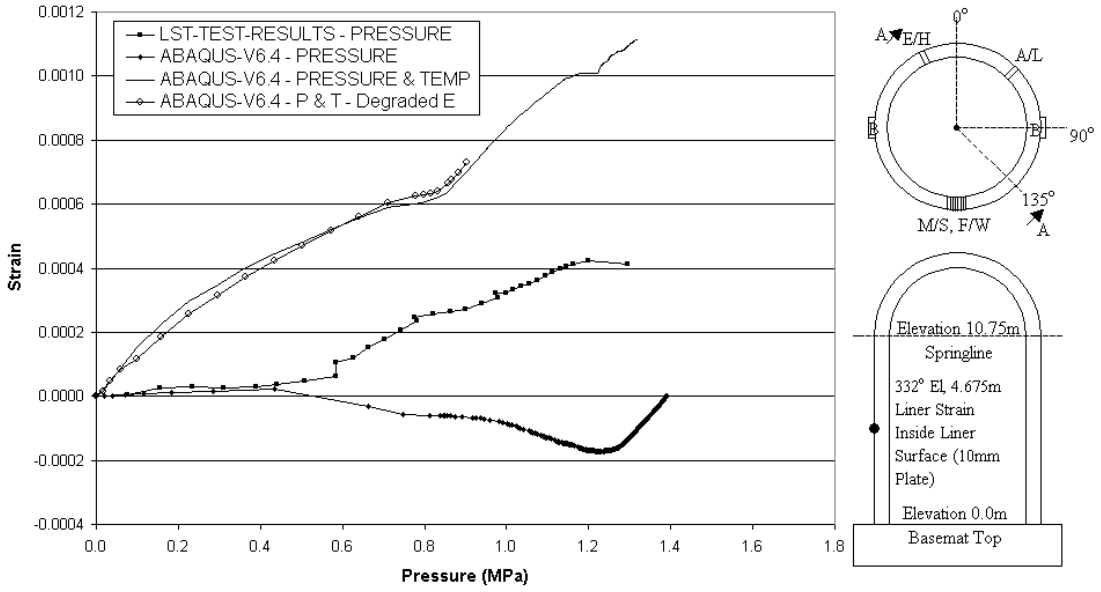

Figure 56 Stress Analysis Model – Location 48

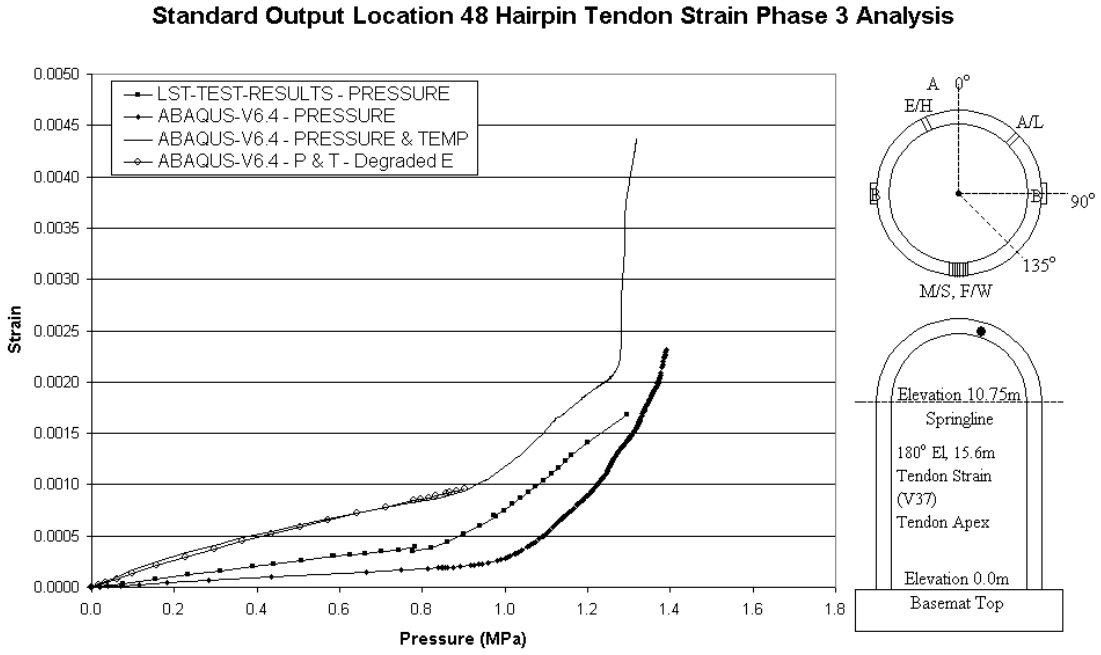

Figure 57 Stress Analysis Model – Location 50

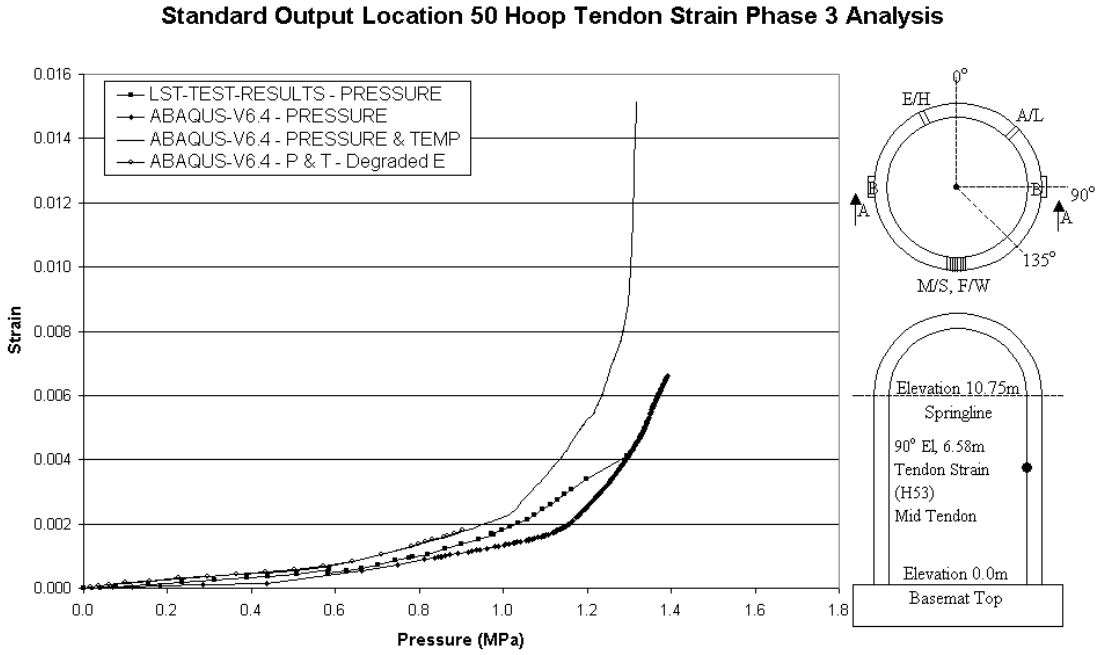

Figure 58 Stress Analysis Model – Location 52

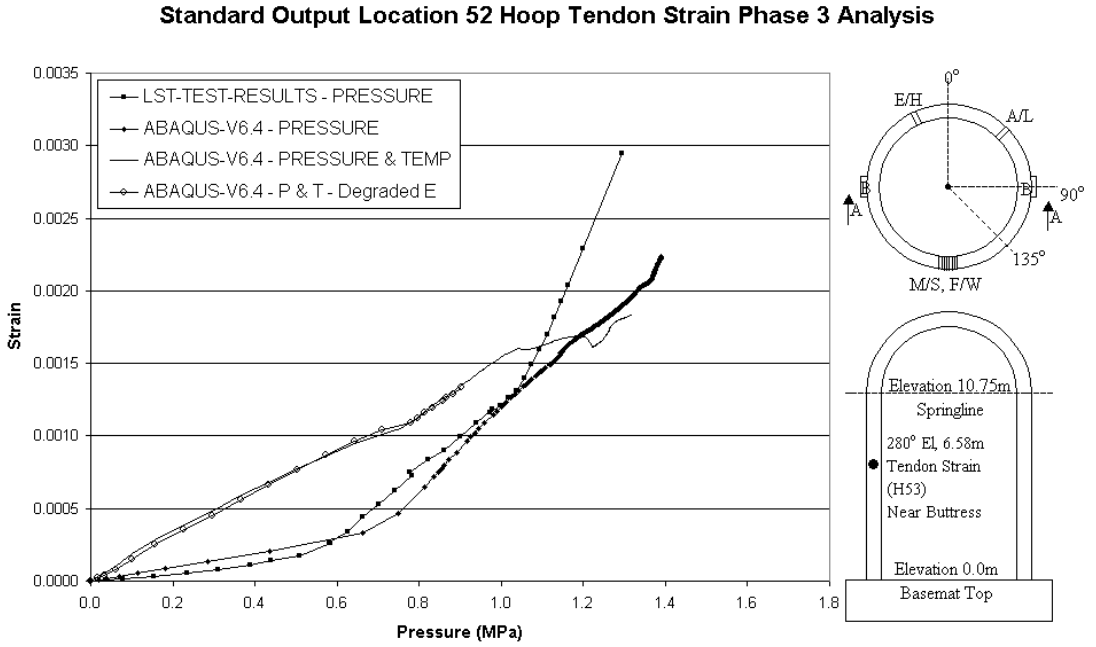

Figure 59 Stress Analysis Model – Location 54

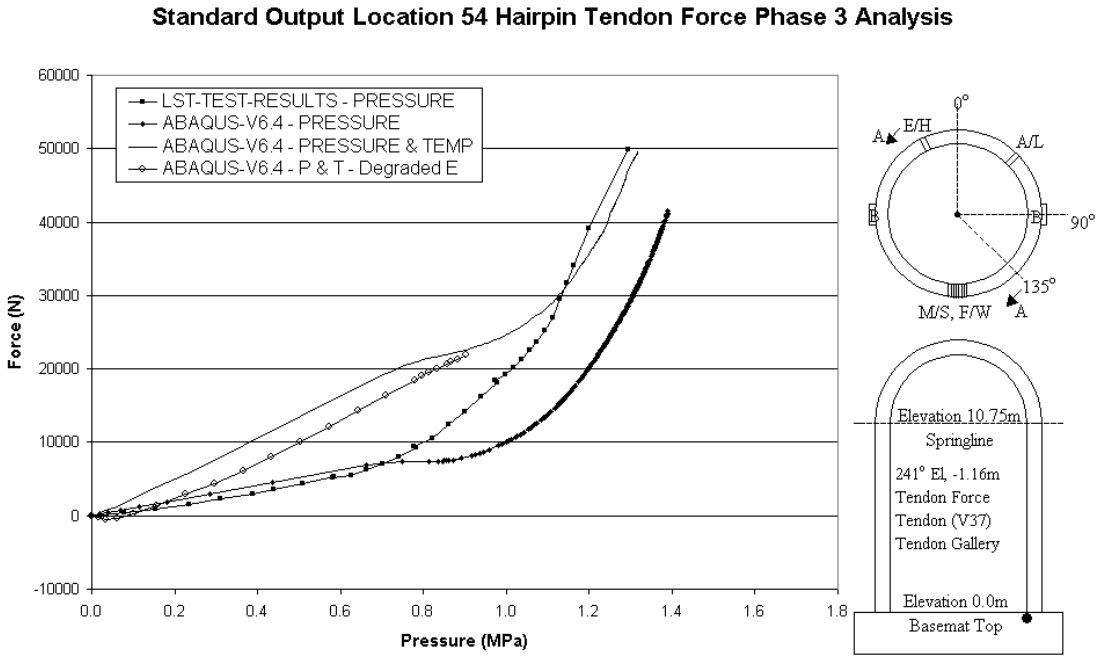

Figure 60 Stress Analysis Model – Location 55

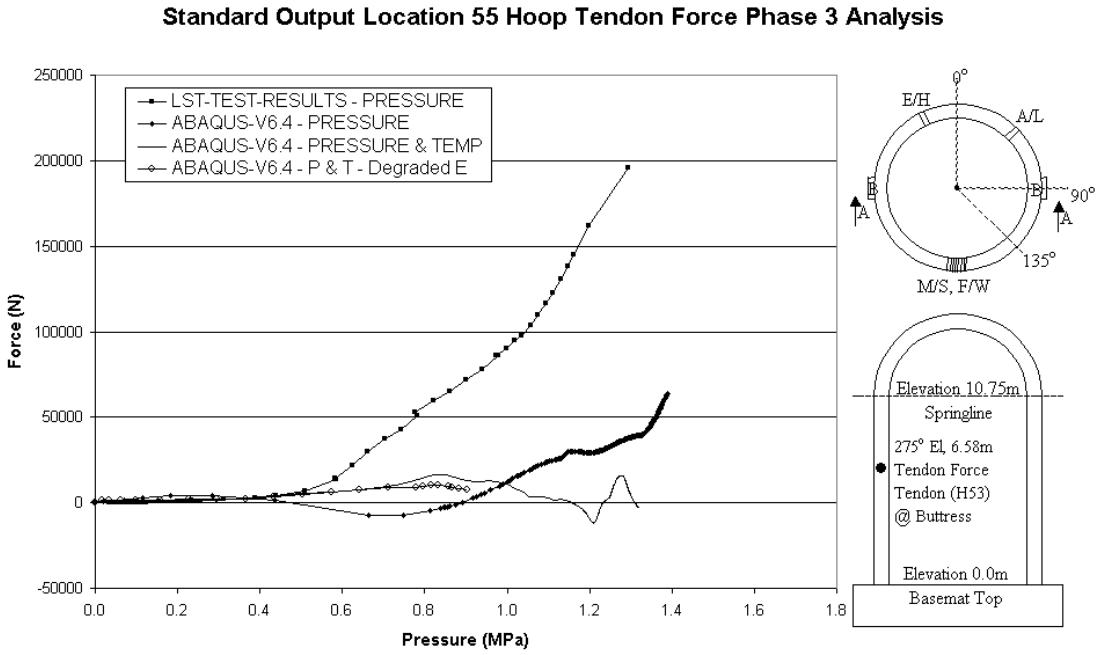

Figure 61 Standard Output Location 39 Liner Hoop Mechanical Strain

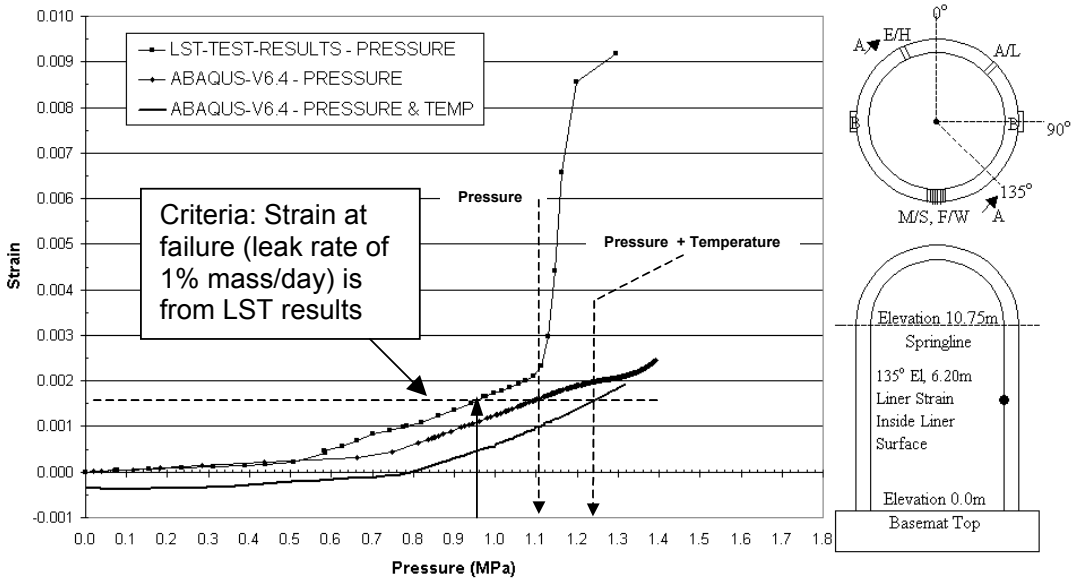

Figure 62 Standard Output Location 39 Hoop Liner Stress

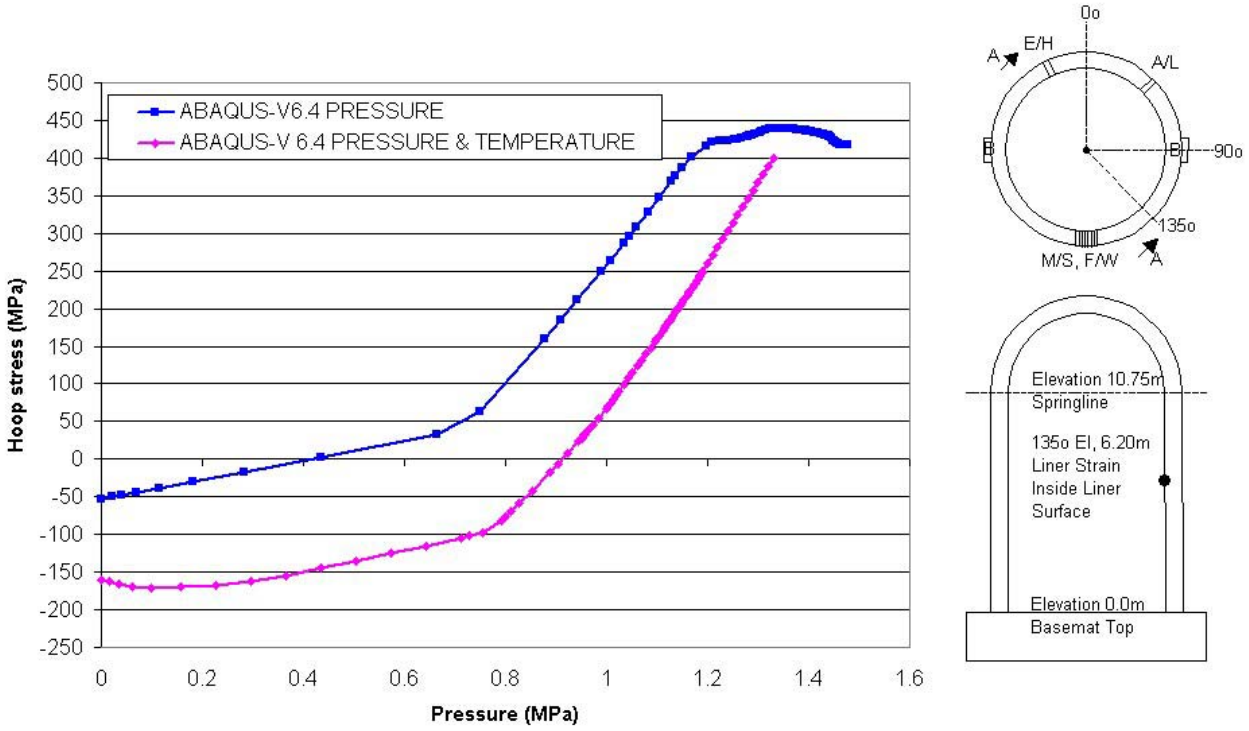

Figure 63 Standard Output Location 53 Hoop Tendon Mechanical Strain

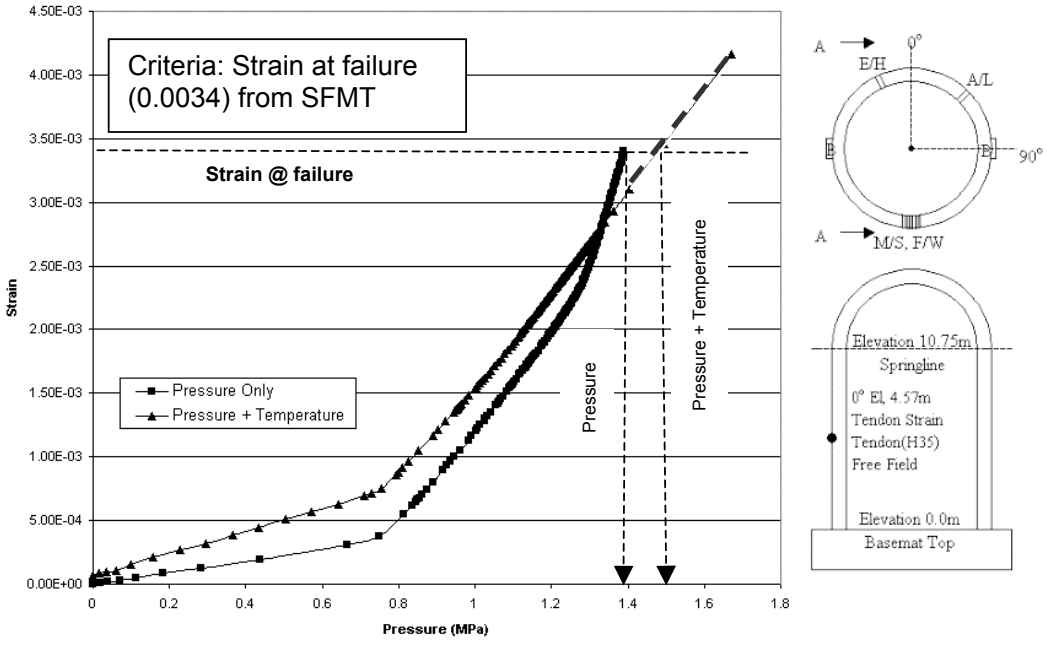

Figure 64 Equivalent Young's Modulus For Simulating Transient Thermal Creep

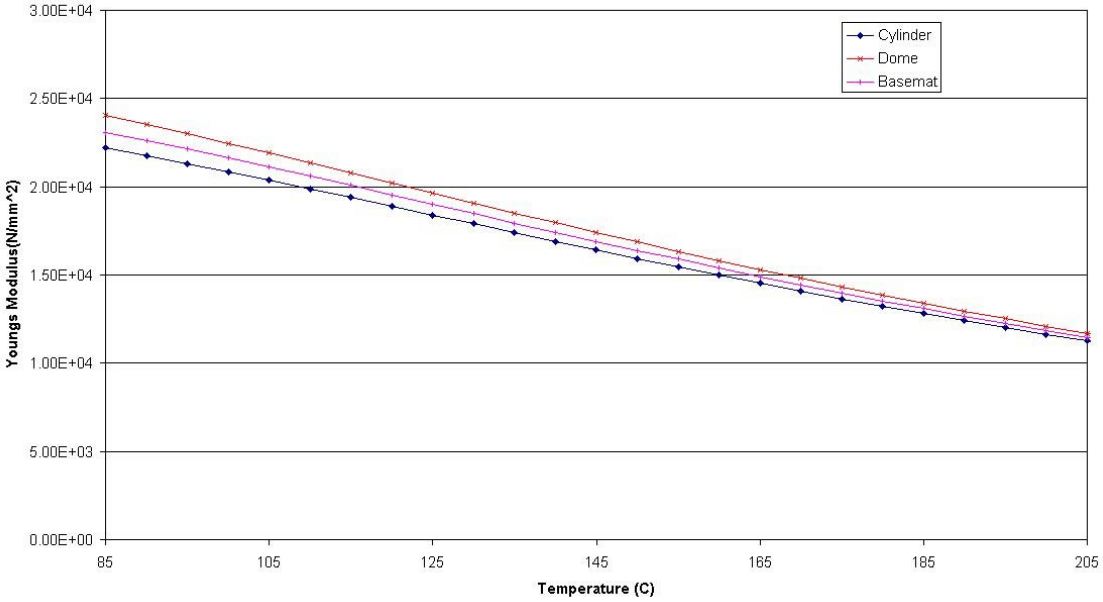

Figure 65 Tendon Load Profile During Vessel Pressurisation and Heat-Up

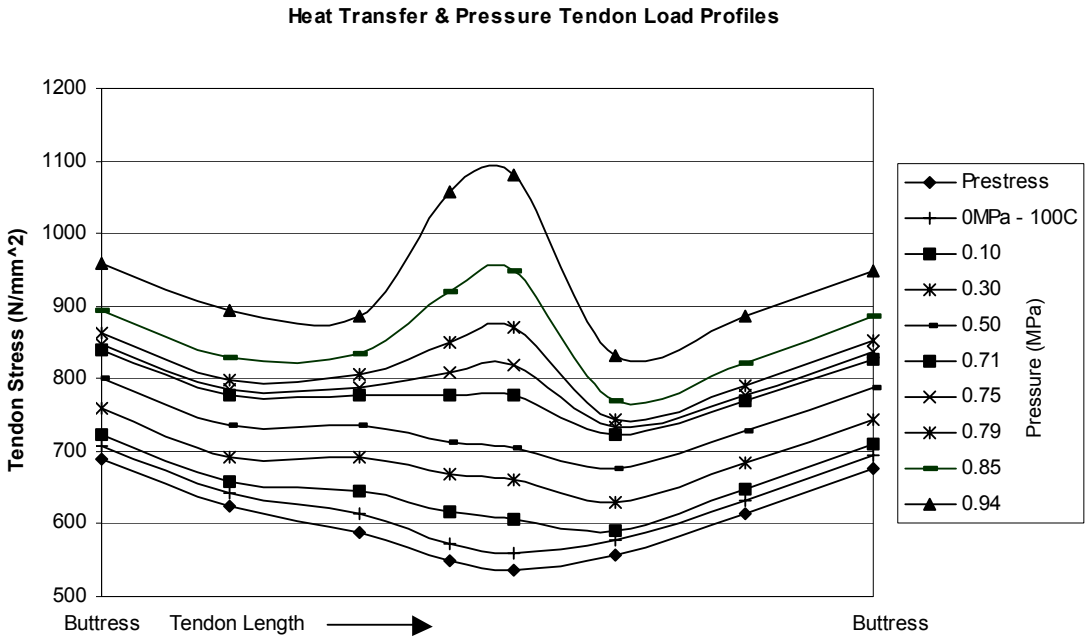

Figure 66 Inner Cylinder Wall E11 Stain Distribution - Comparison Highlighting Effects of Thermal Transient Creep

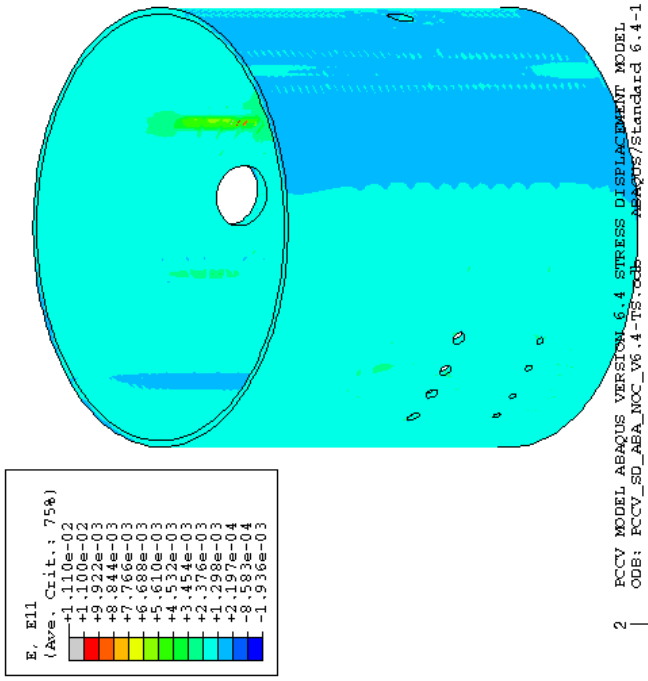

Thermal Transient Creep Not Simulated

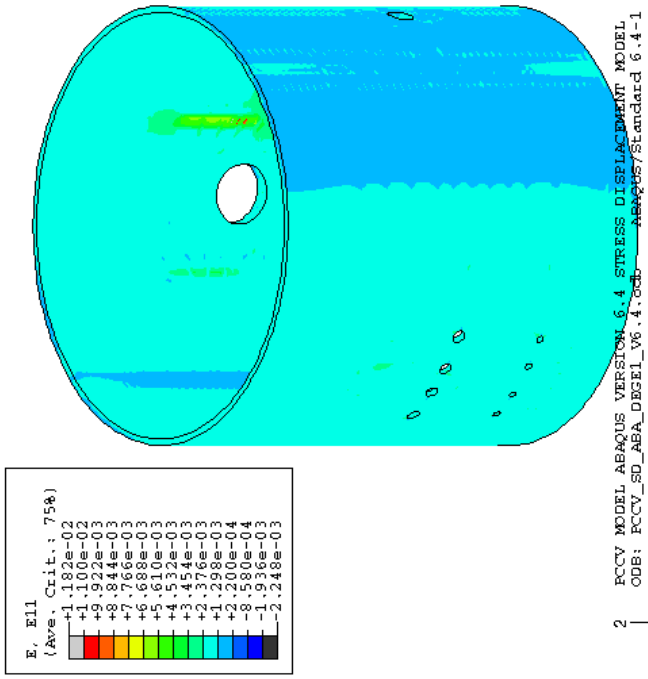

Thermal Transient Creep Simulated

Figure 67 Inner Cylinder Wall E33 Strain Distribution – Comparison Highlighting Effects of Thermal Transient Creep

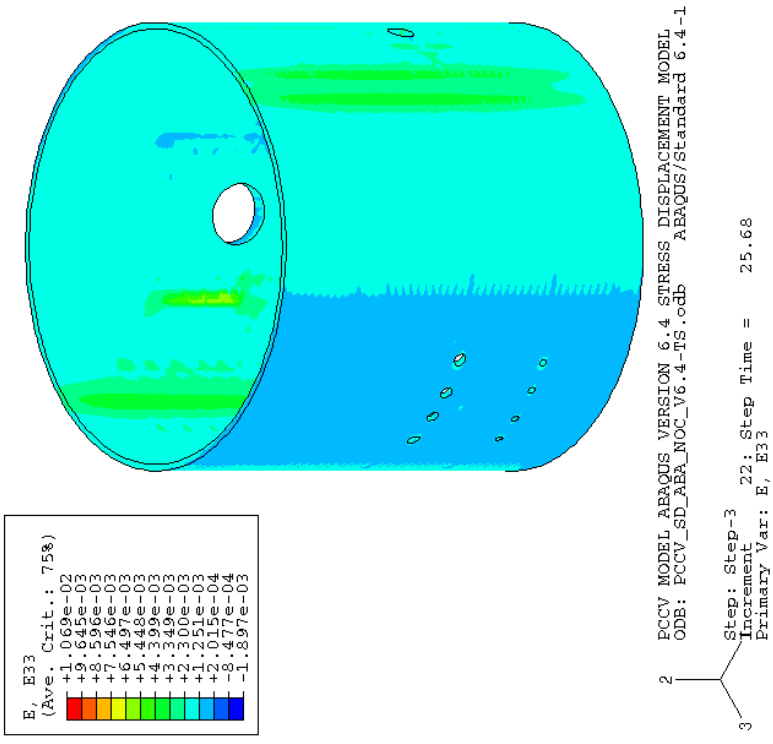

Thermal Transient Creep Not Simulated

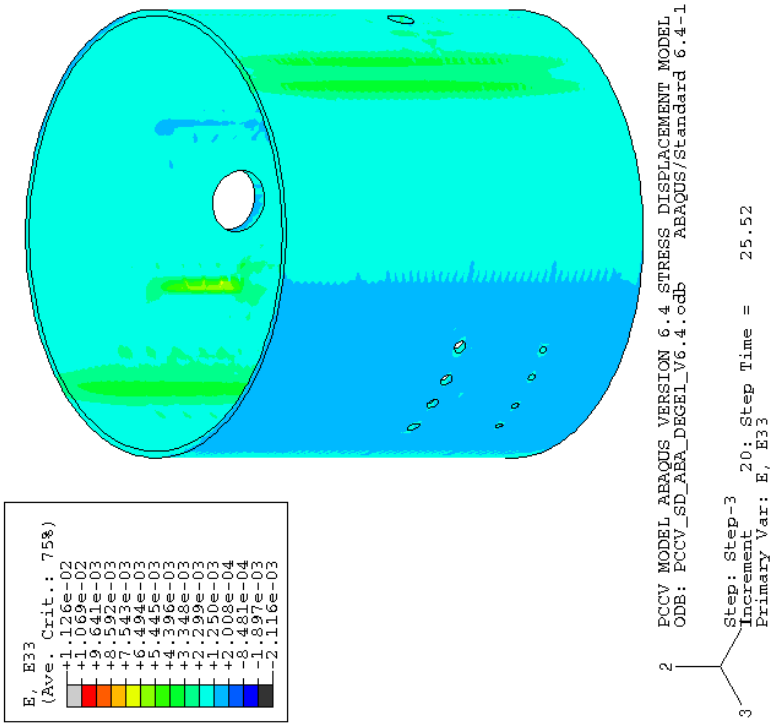

Thermal Transient Creep Simulated

Figure 68 Inner Cylinder Wall E22 (Axial) Strain Distribution – Comparison Highlighting Effects of Thermal Transient Creep

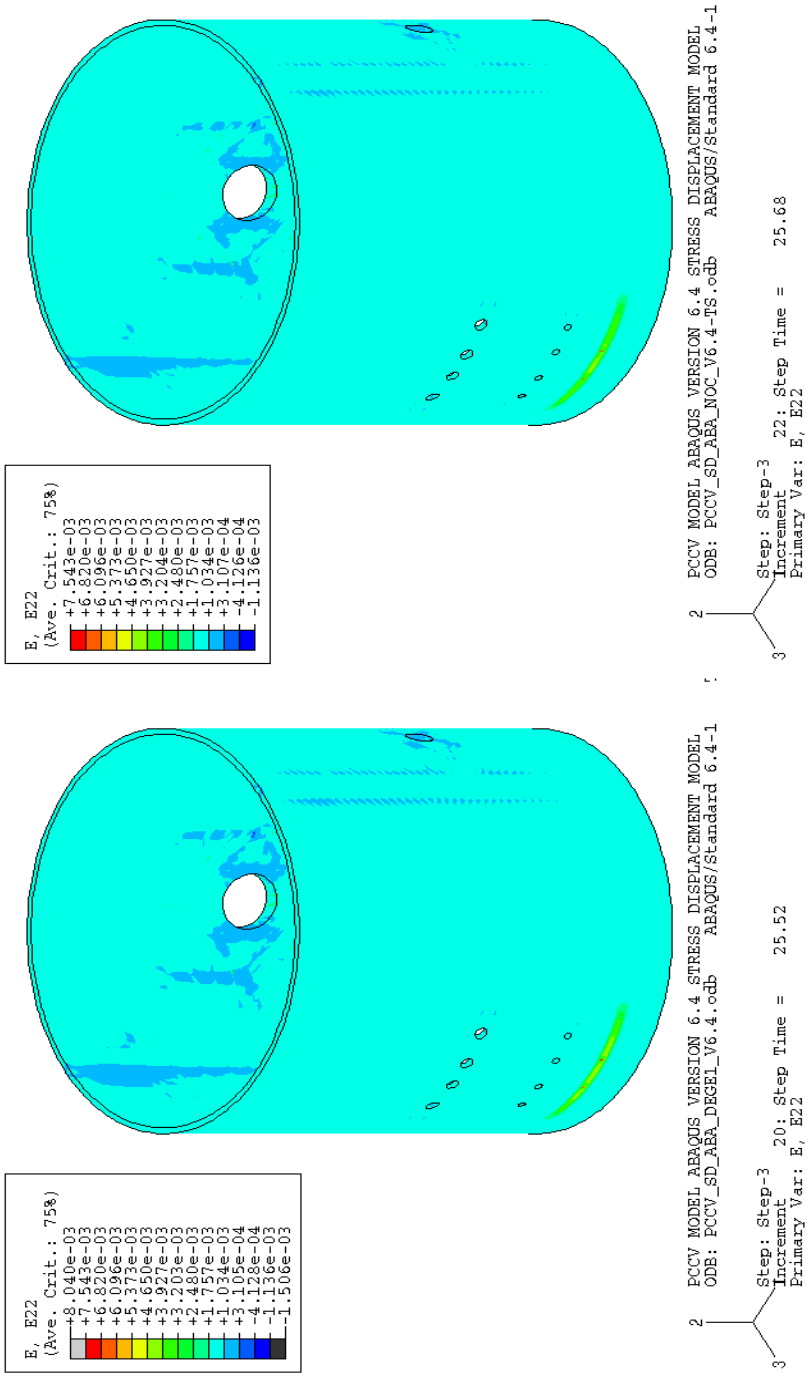

Thermal Transient Creep Not Simulated

Thermal Transient Creep Simulated

Figure 69 Deformation Comparison: E/H Elevation at 0.837 MPa Internal Pressure and 179^0 C Temperature

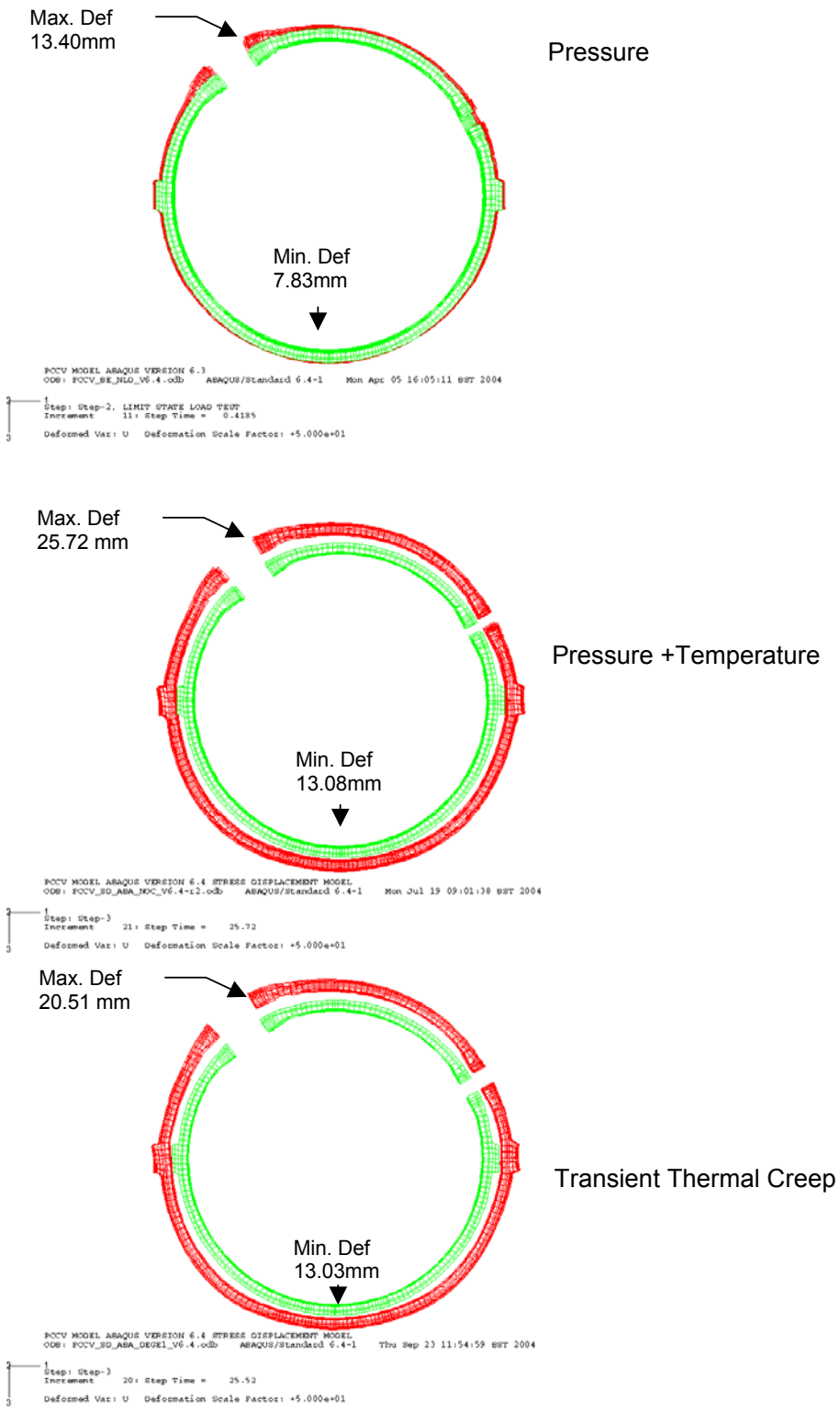

Figure 70 Deformation Comparison: 90-270^{O} Azimuth at 0.837 MPa Internal Pressure and 179^{o}C Temperature

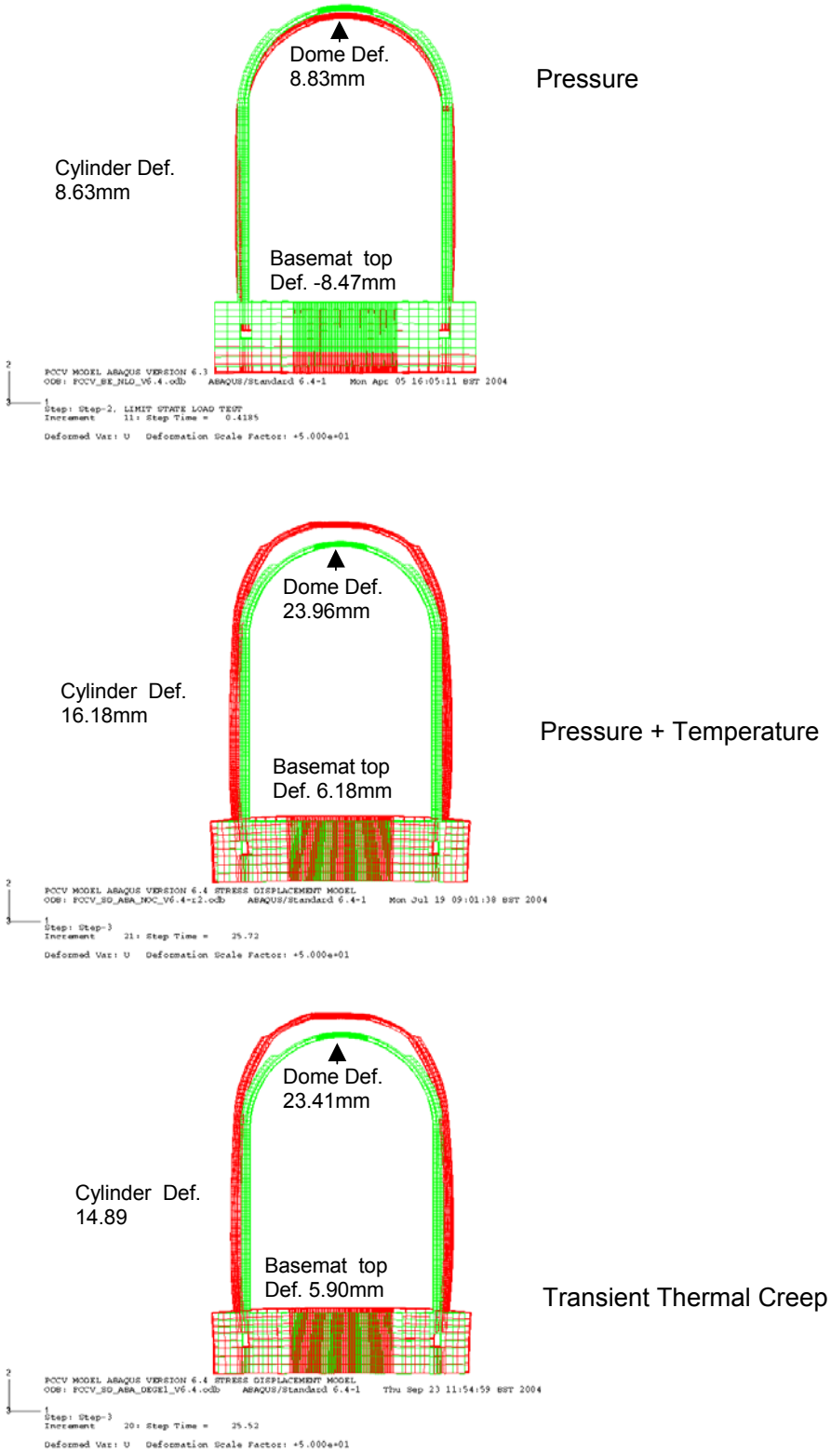

Figure 71 Deformation Comparison: 0-180° Azimuth at 0.837 MPa Internal Pressure and 179° C Temperature

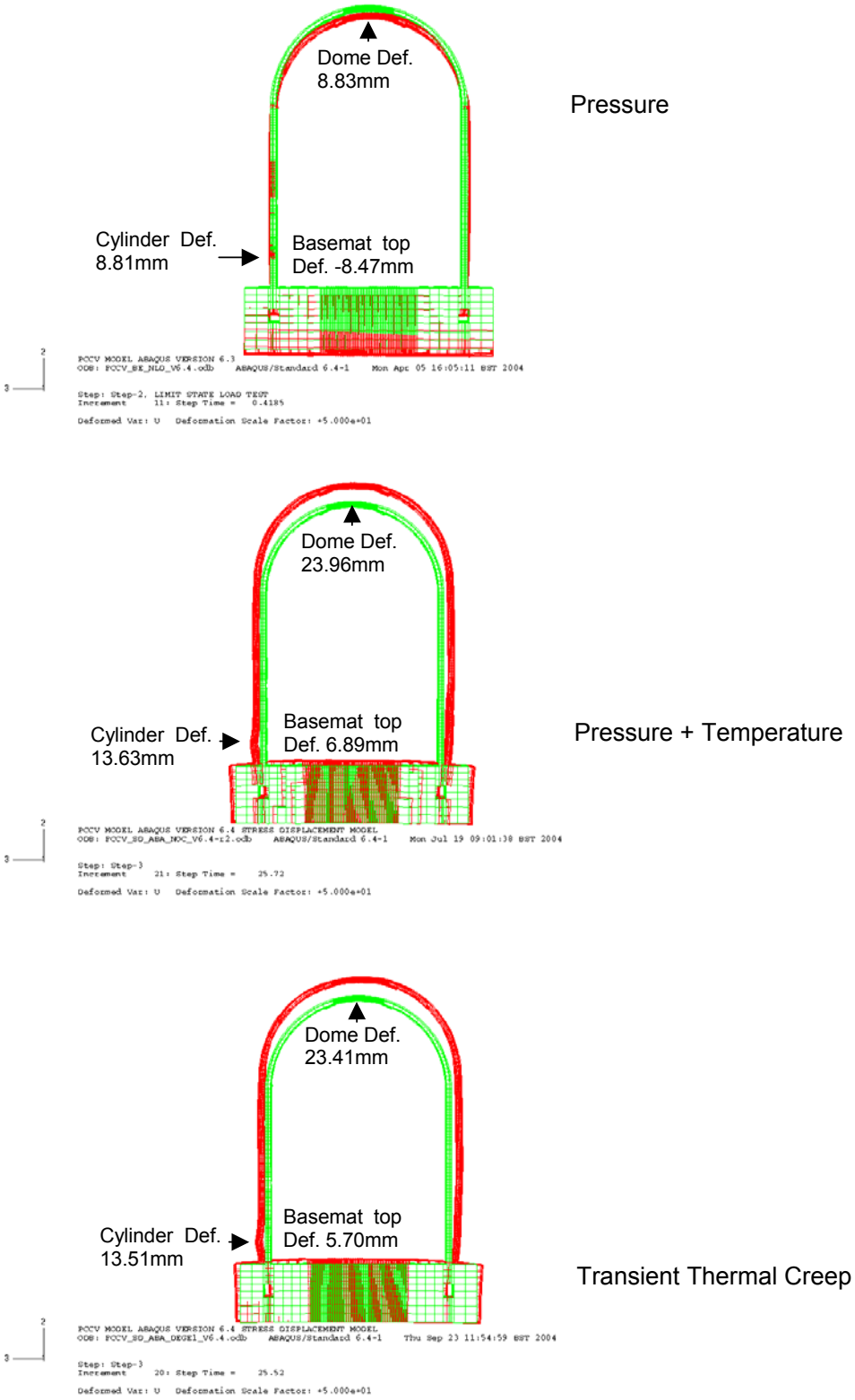

Figure 72 Liner Meridional Stress at Locations 36, 38 and 40

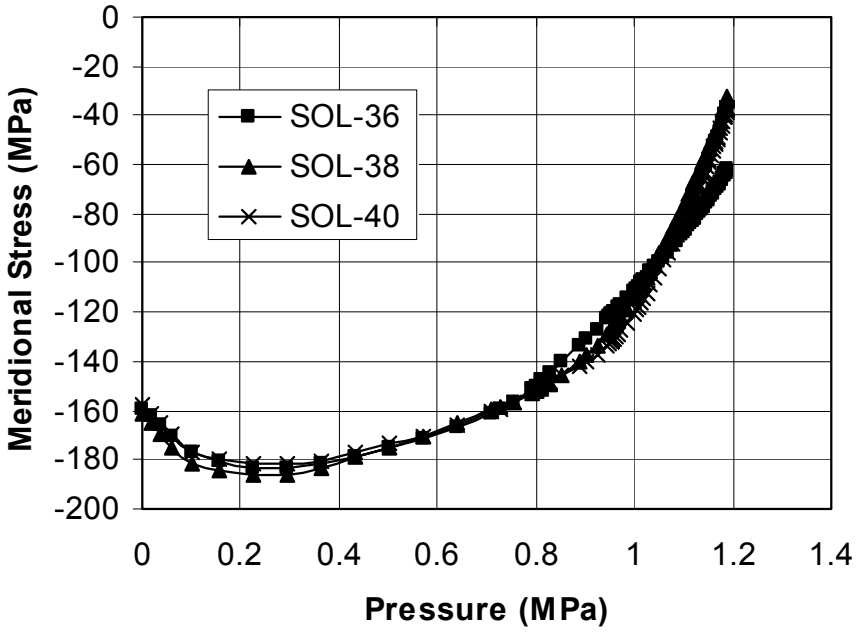

Figure 73 Hoop Stresses at Vessel Inner and Outer Surfaces, Wall Mid-Height

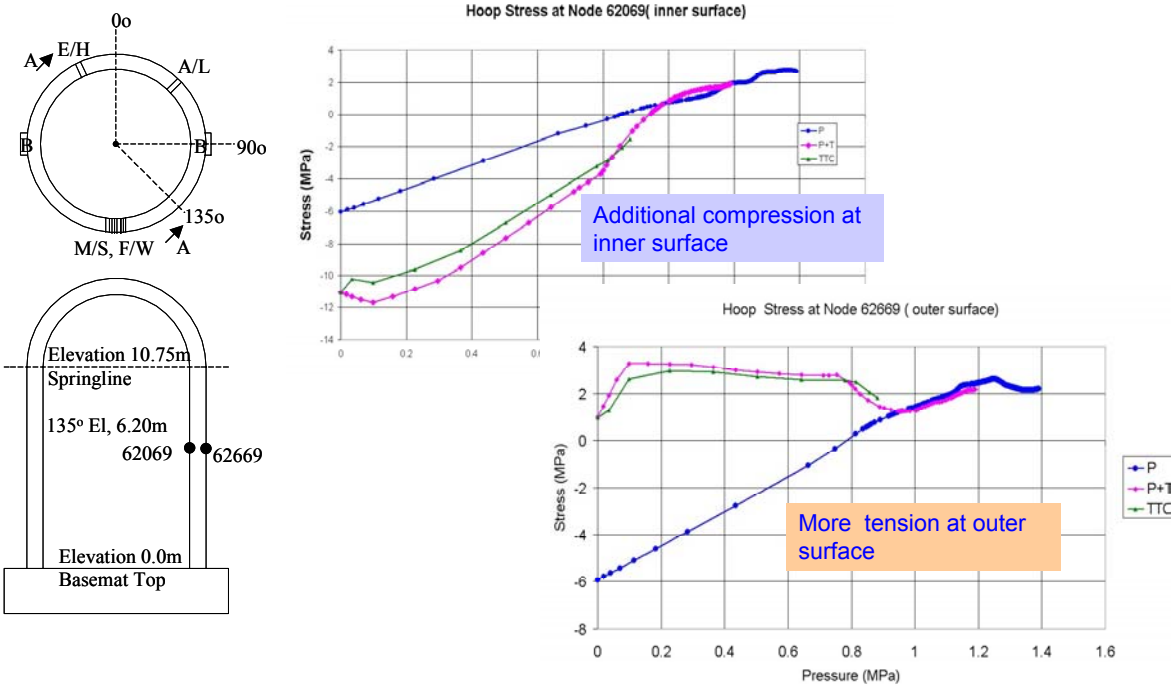

Figure 74 Meridional Stresses at Vessel Inner and Outer Surfaces, Wall Mid-Height

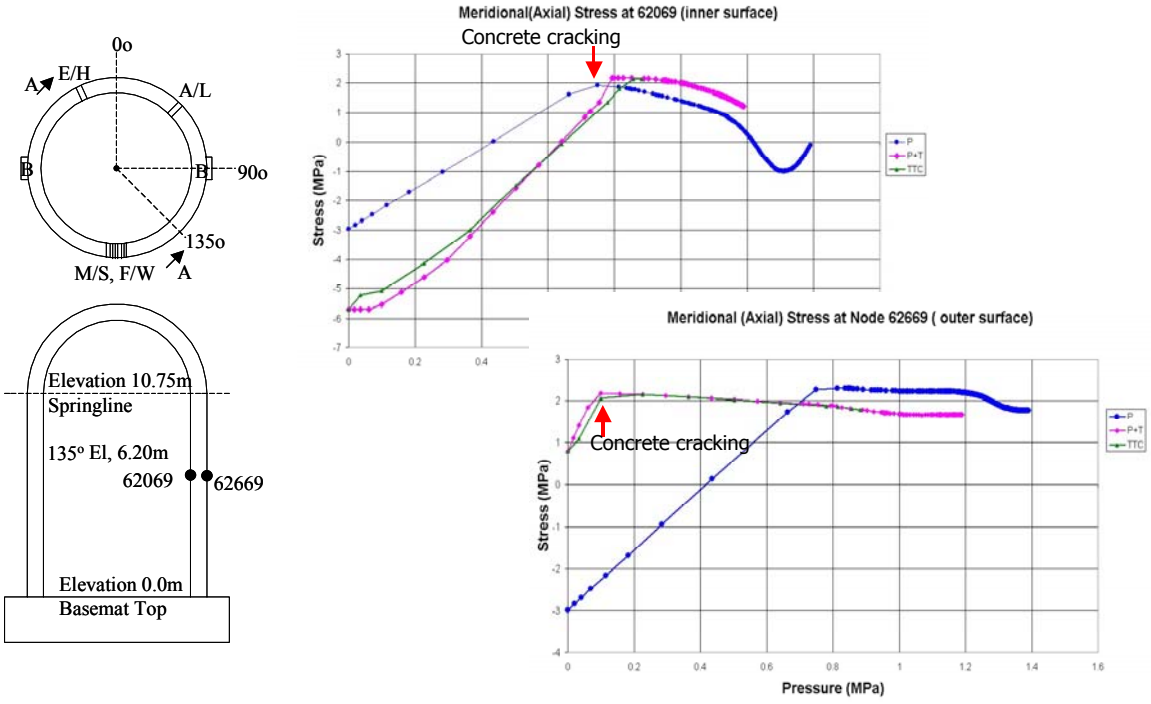

Figure 75 Hoop Stress Variation Thru Wall at 135^0 Azimuth and Cylinder Mid-Height

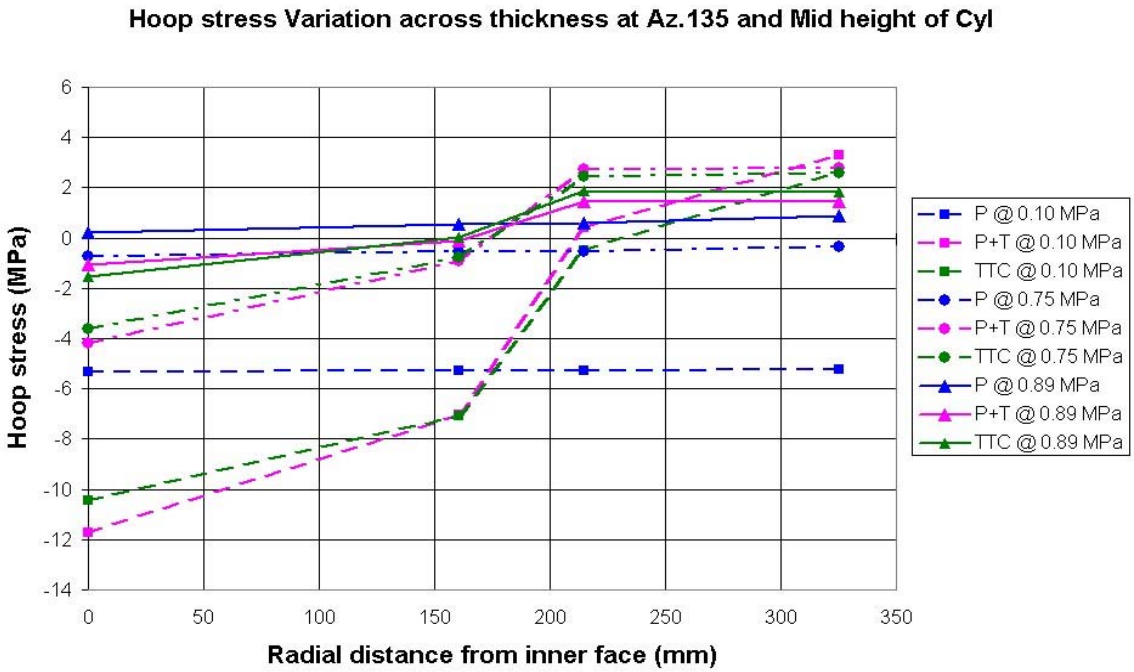

Figure 76 Meridional Stress Variation Thru Wall at 135^0 Azimuth and Cylinder Mid-Height

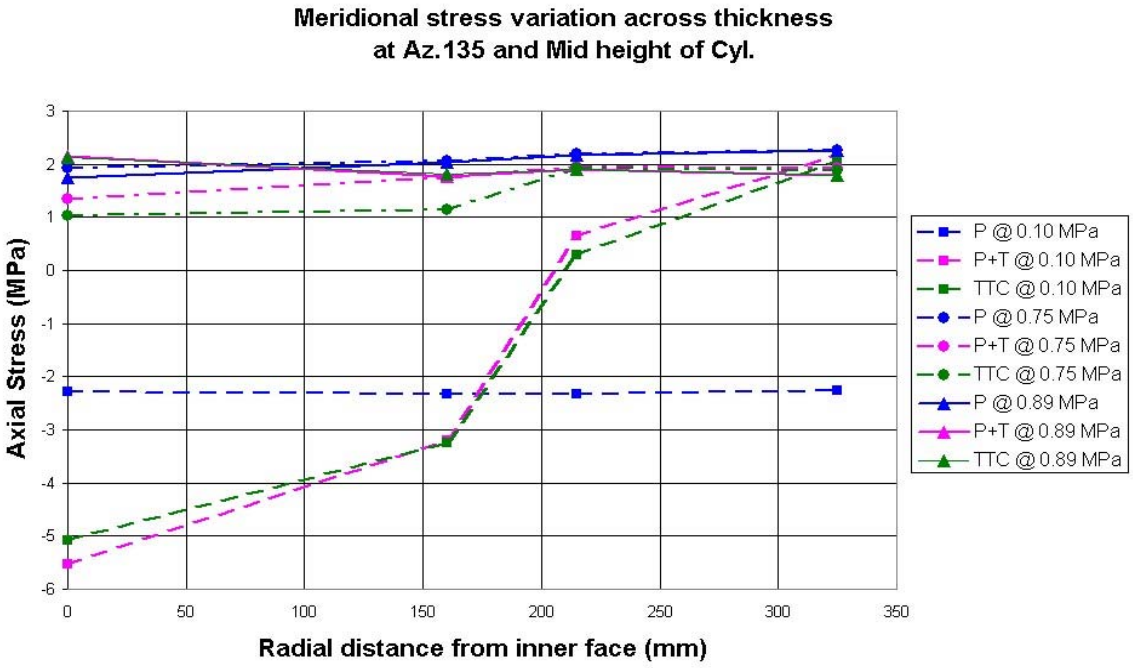

Appendix D: Energoprojekt Praha, UJV Rez. Div.
Phase 2: D-1 to D-18
Phase 3: D-19 to D-38

ISP48 Phase II Analysis Results

Jan Stepan, Jan Maly
UJV Rez div. Energoprojekt Praha

Analysis model

The analysis model is created in Abaqus general-purpose finite element program. The principal objective of the model was model behaviour of the whole structure including openings. The concrete is basic part of the model and is modeled by brick elements. Rod elements model rebars and prestressing tendons and they are embedded into concrete elements. Liner is modeled by plate elements connected on inner surface with concrete elements. Model includes EH and AL openings including change of wall thickness and changes in rebar and prestressing tendons. M/S openings weren't modeled because they have small impact on global response of structure and only added rebar rods were considered in model. The first version of model includes basement as well but due to limitations of model size (Abaqus error no. 3495 – regardless of size of installed memory is maximum available memory for Abaqus pre-processor about 1300MB under Windows systems) the size of model had to be decreased. Then the final version of model includes only cylindrical and dome part of the structure.

Basics characteristics and simplifications are abstracted into next points:

- The model includes concrete wall of cylindrical and dome part of structure. Basement wasn't modeled, its stiffness was neglected and connection between cylindrical wall and basement is modeled by external fix support, which eliminates displacements and rotations (effect of this simplification is small because the stiffness of basement is much more higher in comparison with the stiffness of remain parts of structure).
- Rebar and prestressing tendons were modeled by rod elements considering actual geometry around openings. Two simplifications were applied – the radial rebar wasn't modeled due to size limit of model and anchors of hoop cables were replaced by continual connections of elements due to elimination of cracks and instabilities in anchor area at buttress.
- Prestressing tendons were modeled as bonded tendons. Prestressing force along tendons was considered as uniform by mean value of measured force.
- Connection of liner and concrete doesn't respect actual design and is performed by common nodes of liner and concrete elements. So, results in liner corresponding of global behavior but there could be differences in places with local peak of stress (connection of liner to frame of openings, connection with basement).
- Starting state of analysis was unbroken structure. Cracking due to shrinkage was modeled by decreasing of modulus of elasticity along with lower tensile strength of concrete in tension.

Material characteristics were sets pursuant to results of tests. Abaqus Concrete damage plasticity model was used for modeling of non-linear behavior of concrete. The behavior of concrete in compression was assigned by Euro code 2, the behavior in tension was assigned by tensile strength and fracture energy. The non-linear behavior of rebar, presstresing tendons and liner was modeled by Abaqus Iron plasticity model. The basic values of material characteristics are in the following table:

Material	Modulus of elasticity	Strenght
Concrete	28 000 MPa	53 MPa in compression, 3.8 MPa in tension (decreased at 0.5 MPa)
Liner	210 000 MPa	yield stress 380 MPa, ultimate stress 450 MPa
Tendons	200 000 MPa	yield stress 1600 MPa, ultimate stress 1950 MPa
Rebar SD345	210 000 MPa	yield stress 360 MPa, ultimate stress 500 MPa
Rebar SD390	210 000 MPa	yield stress 470 MPa, ultimate stress 600 MPa

As indicated above, the prestressing tendons were modeled as bonded cables and their prestressing force was set by mean value of measured force. The prestressing force of hoop tendons is 30kN, the prestressing force of vertical tendons is 41kN.

Analysis was performed in two steps. The firs step was application of prestressing and dead load. The second step was application of internal overpressure. The presstresing was applied by initial conditions type stress. The internal overpressure was applied at liner elements. Forces in nodes at border of openings replaced the effect of internal ovepressure at locks. Response of structure at increasing overpressure was evaluated as sequence of static analysis at first. Due to decreasing of step time after beginning of cracks development and conjoin increasing of total analysis time, the Abaqus/Explicit quasi-static analysis was used. Change of overpressure in time was defined by linear function with the end at 1.6 MPa.

Analysis results

Results of the first analysis demonstrated higher stiffness of model, especially after cracks development, in comparison with response of real structure. Reevaluation was performed and tendon prestressing forces (due to higher prestressing forces the response of the model was below the response of structure) and tendon stress-strain curve (due to higher yield stress and ultimate stress the model had higher stiffness at high overpressure) were changed. Now the model shows quite good agreement with global structure response.

The global failure of structure and maximum internal overpressure is determined by bearing capacity of prestressing tendons. Theoretical, due to plastic capacity of liner, the tightness could be preserved till global failure. The results of real structure test shows that the tears of liner appear before the failure of structure (detailed inspections after LST revealed 26 discrete tears in the liner, all located at vertical field welds, and fabrication defects contributed to nearly all of the liner tears). Analogous, the breaking of tendons started at hoop strain approximately 1% although the tests of cables assign the breaking at strain 3.5%. So, question is how to set the limits of plastic strain of liner and tendons. For purpose of this analysis the strain at breaking of tendon was set at 1% and the onset of liner tearing was set at reaching of liner yield stress.

Figures 6-9 show total deformation at selected internal overpressures. Figure 10 shows comparison of test results and analysis results for radial displacements at 135°. History of deformation shows rapid increasing after 1.3MPa. It corresponds with reaching of yield stress in tendons at 1.25MPa. Figure 11 shows comparison of radial displacements at 90° (buttress) and at openings. Figure 12 shows comparison of vertical displacements. History of deformation shows higher model dome response to decreasing of stiffness of cylinder due to cracking in comparison with results of test.

Figures 13-14 shows liner strain in circumferential direction at 1.0MPa (stress in liner reaches the yield stress) and 1.25MPa (stress in tendons reaches the yield stress). In both cases the peak of strain is between openings next to E/H (approximately at 0°) due to change of curvature of the concrete wall. Additional concentrations of strain are at buttresses and at ending of additional rebar around openings.

Figures 15-16 shows tendon strain 1.25MPa (stress in tendons reaches the yield stress) and 1.52MPa (strain in tendons reaches 2%). Especially at overpressure 1.52MPa there is the expressive difference in distribution of strain along tendons due to rigid connection between tendons nodes and nodes of concrete wall. This type of connection doesn't make possible to correctly simulate tendon failure in case of structures prestressed by unbonded tendons. Despite it, the final failure mode during SFMT corresponds with state of stress detected by analysis. The comparison of tendons strain history in Figure 17 shows, that the collapse of structure happened when started the rapid increasing of tendons strain after reaching of the yield point.

The basic milestones of structure behaviour during overpressuration are summarized in the following table:

Pressure	Event
0.44 MPa	Beginning of cracking around E/H
0.60 MPa	Beginning of cracking of cylinder in circumferential direction
0.90 MPa	Continual horizontal cracks in cylinder
0.98 MPa	Yielding stress in liner
1.25 MPa	Yielding stress in tendons
1.30-1.50 MPa	Collapse of structure after breaking some tendons

Figure 1 FEM model

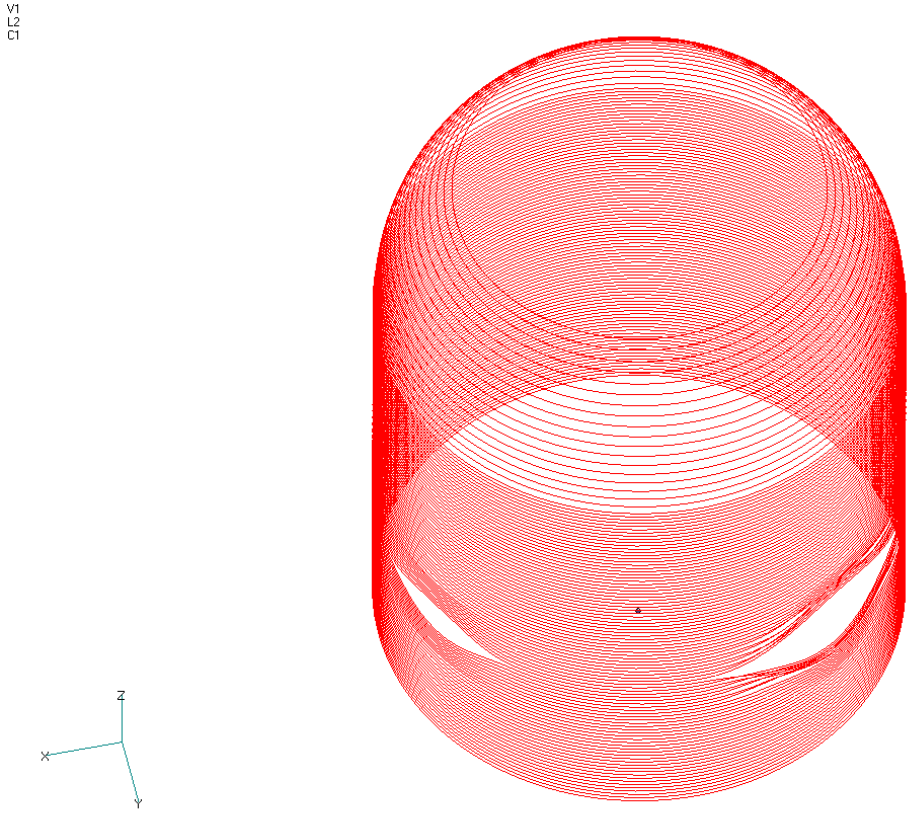

Figure 2 Prestressed tendons elements – hoop tendons

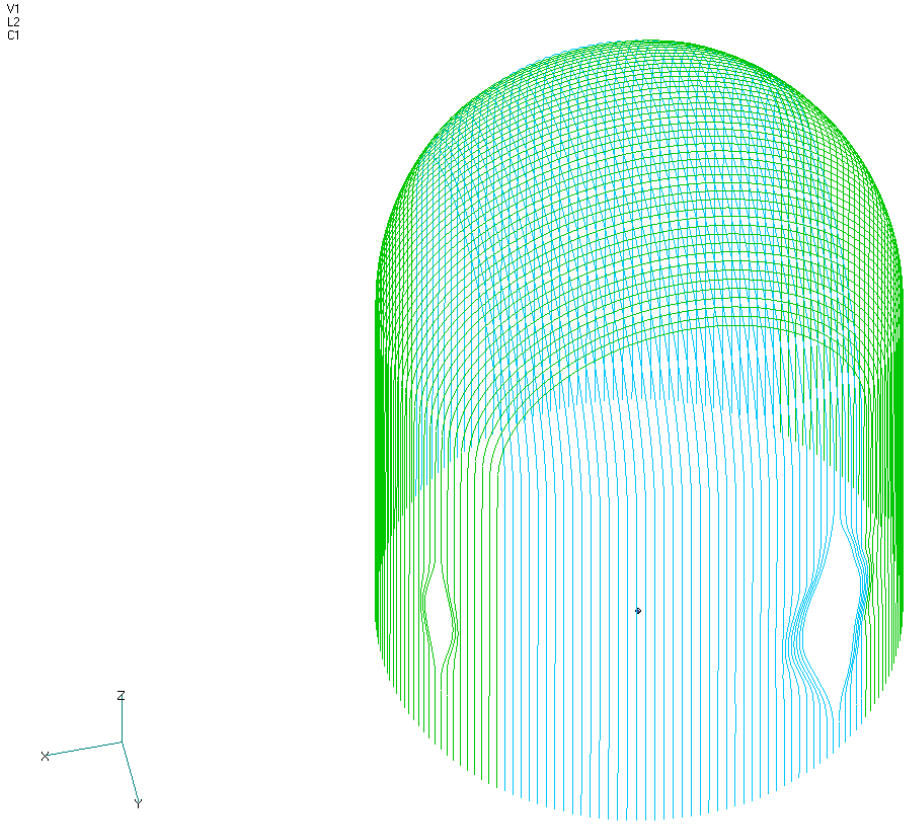

Figure 3 Prestressed tendons elements – vertical tendons

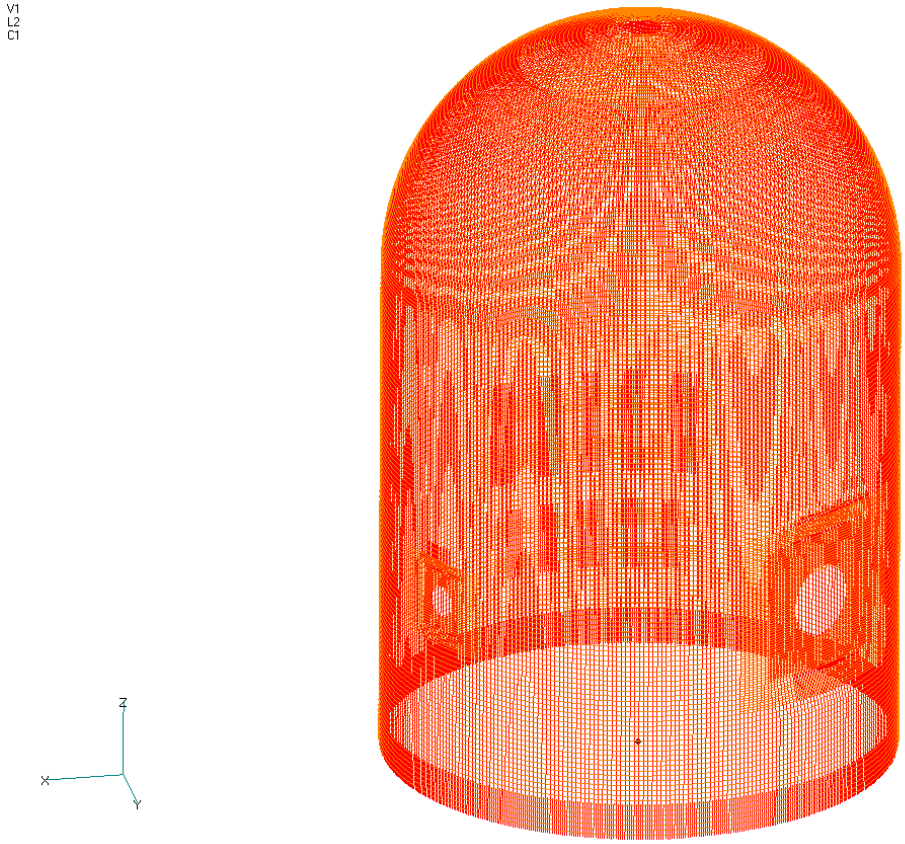

Figure 4 Rebar elements – inner row

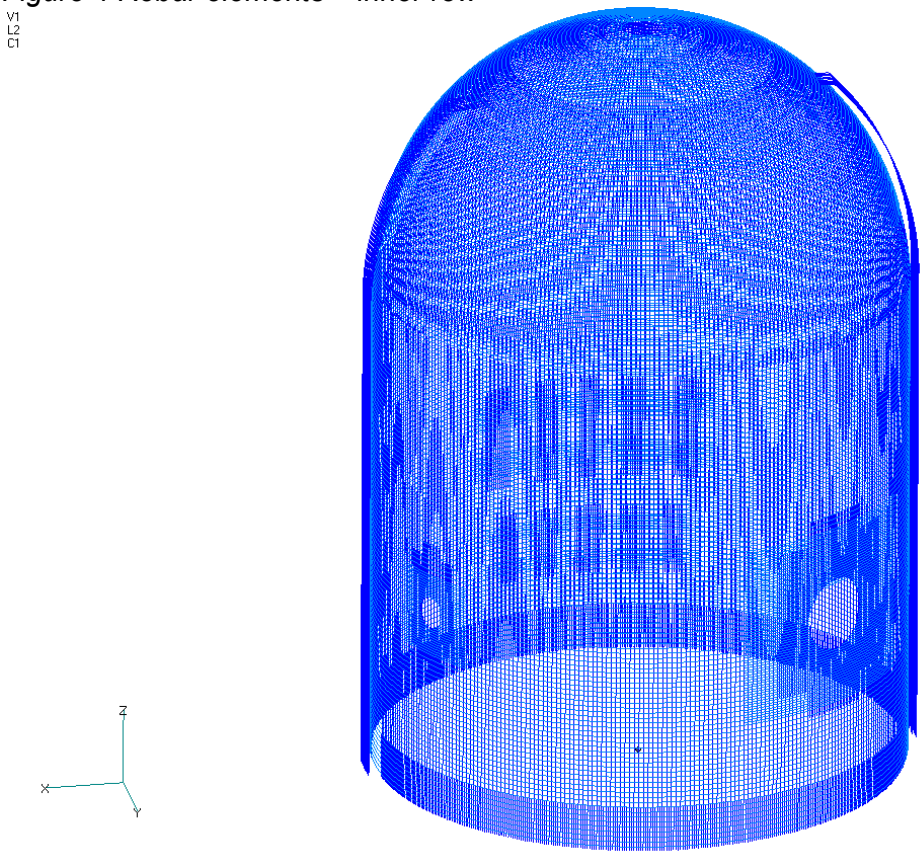

Figure 5 Rebar elements – outer row

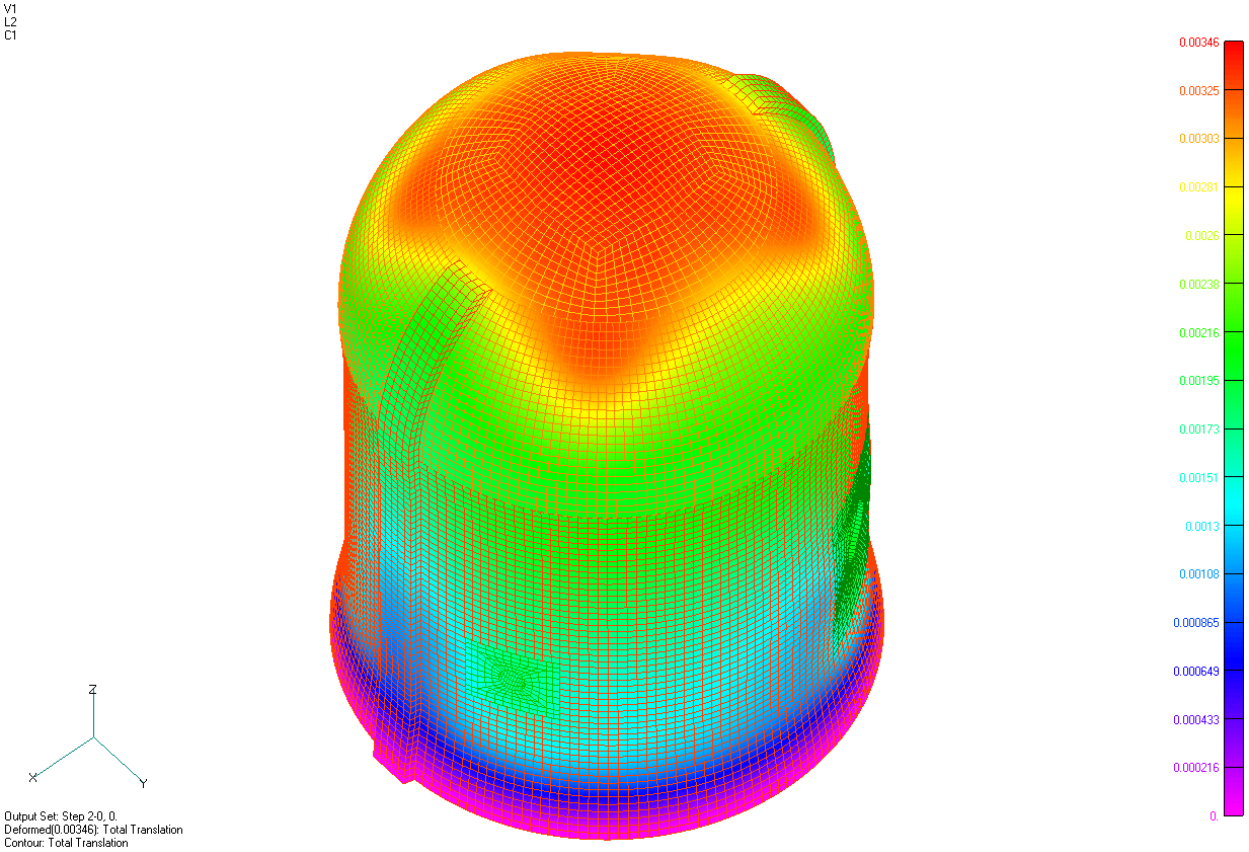

Figure 6 Total deformation (m) after loading by prestressing and dead load

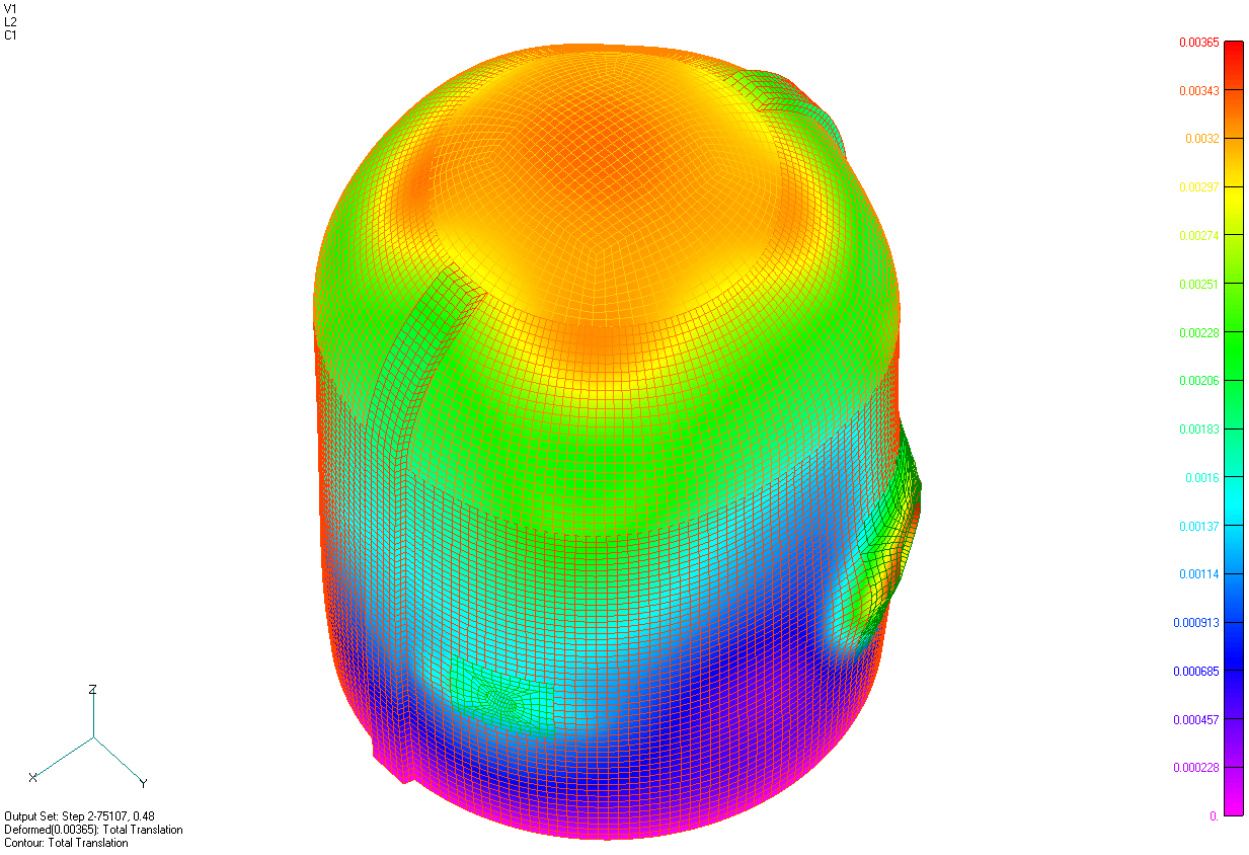

Figure 7 Total deformation (m) at 0.6MPa – concrete starts to crack in circumferential direction

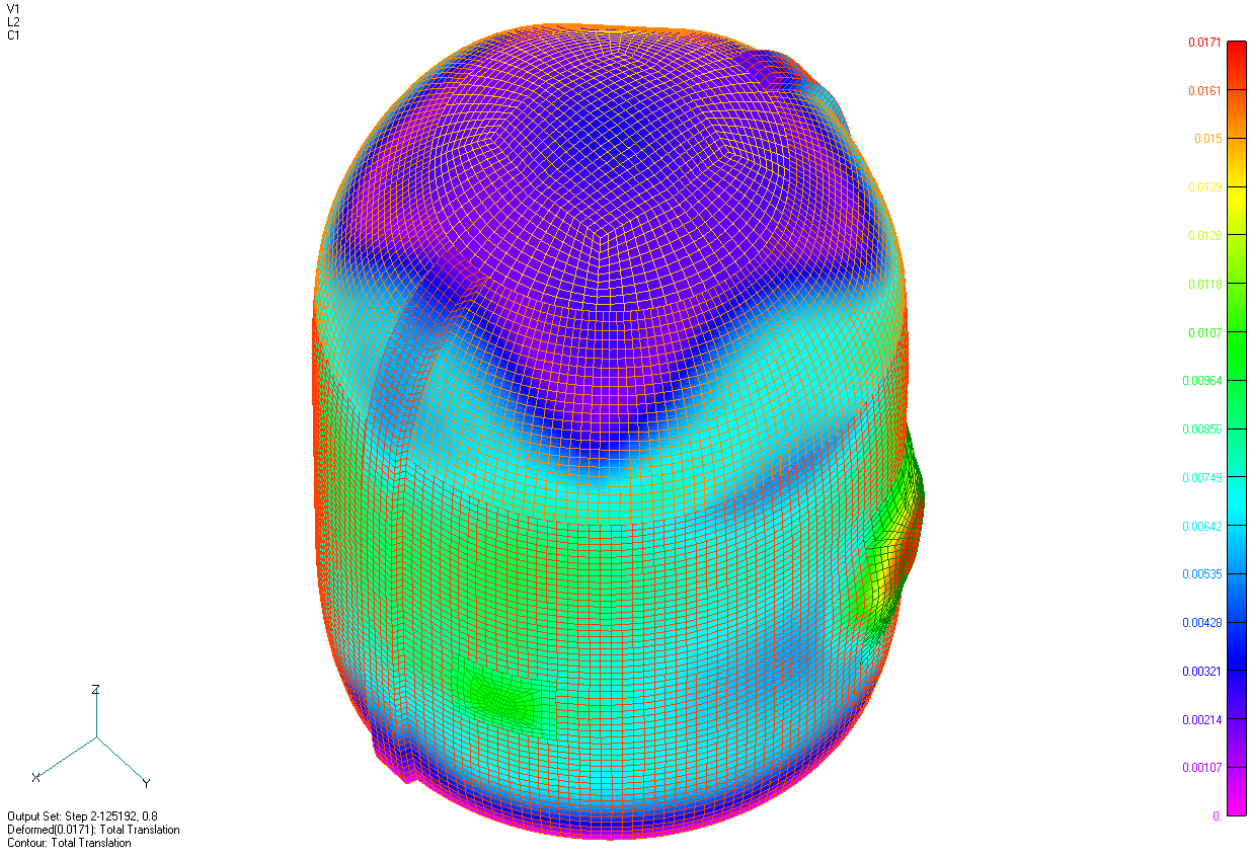

Figure 8 Total deformation (m) at 1.0MPa – continuous cracks in concrete in meridian direction

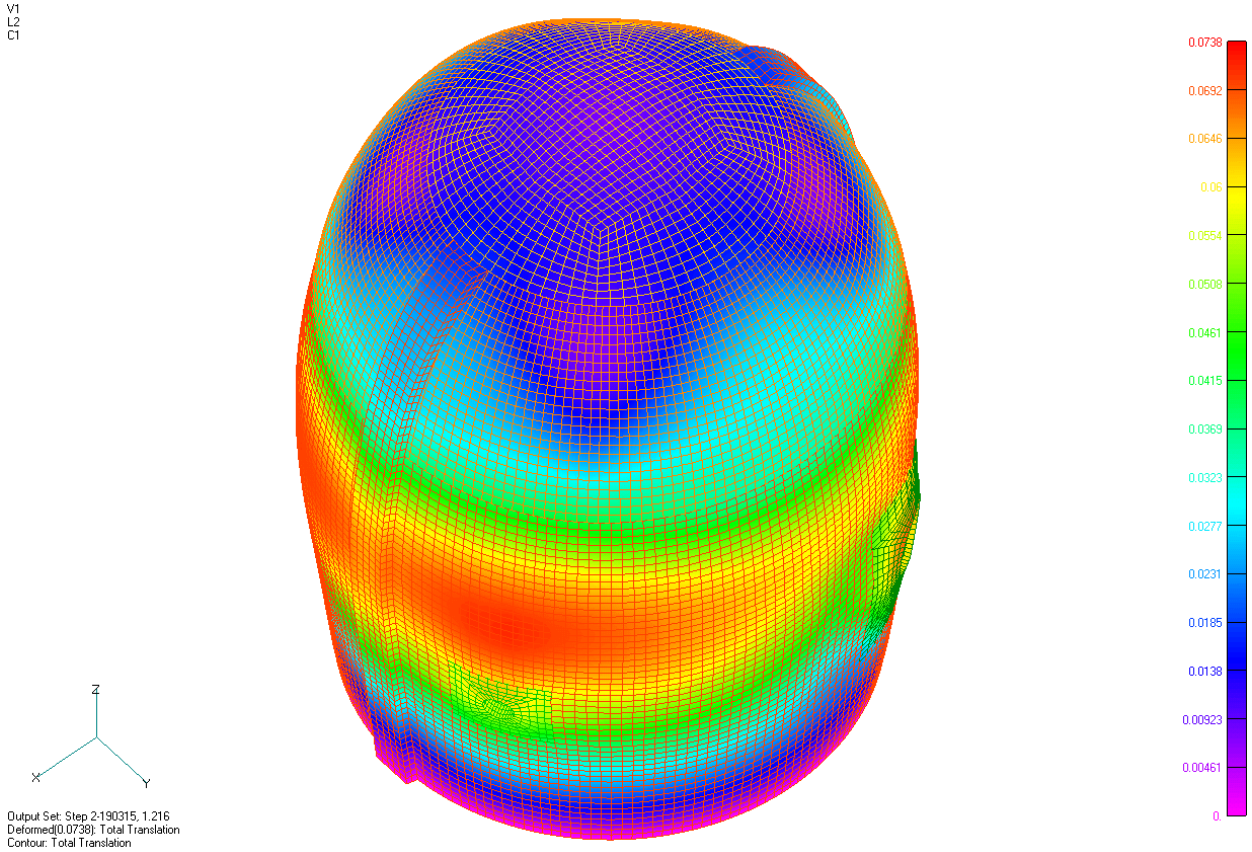

Figure 9 Total deformation (m) at 1.52MPa – strain of tendons reaches 2%

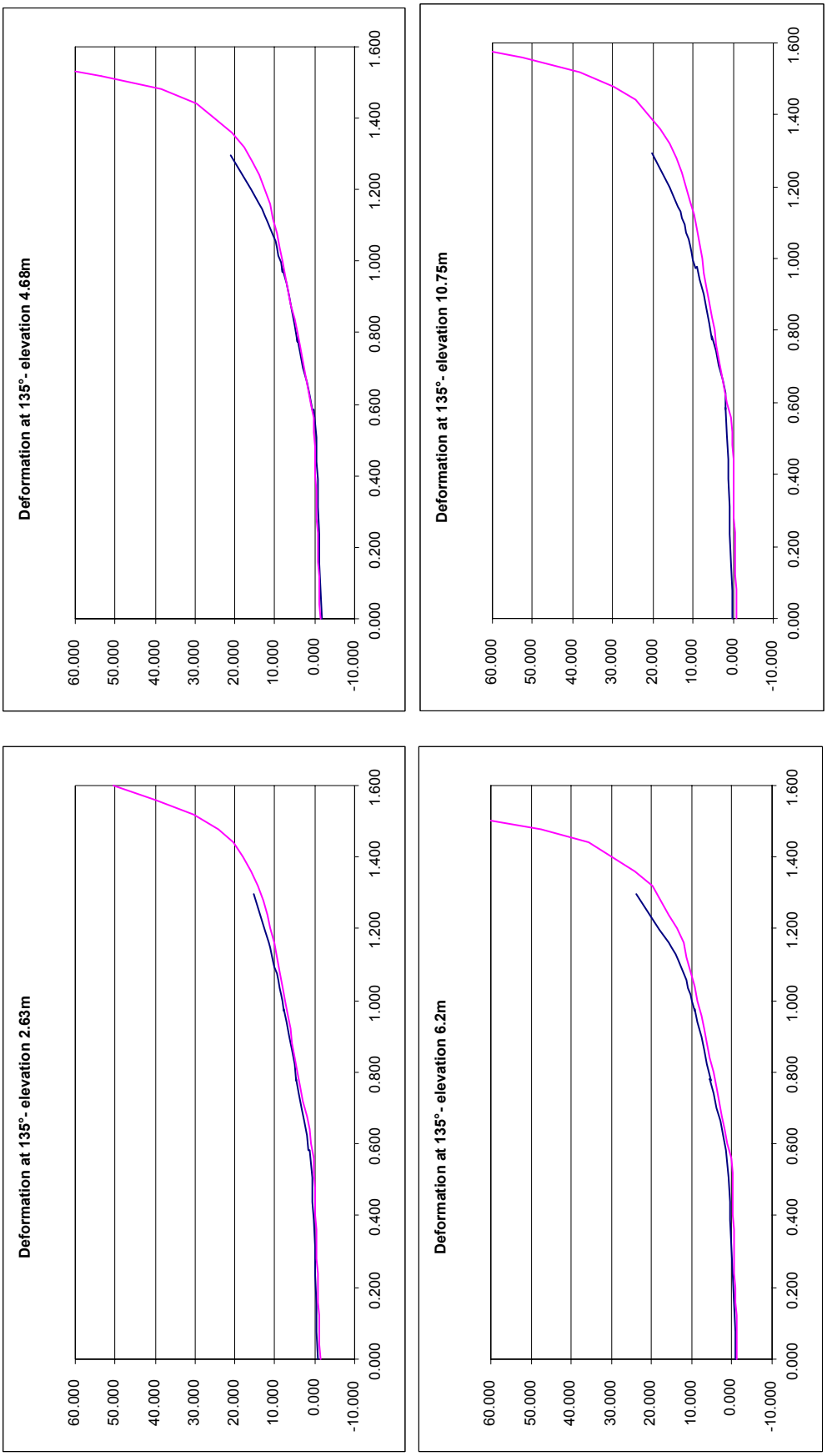

Figure 10 Comparison of radial displacements at 135 degrees (mm, MPa)

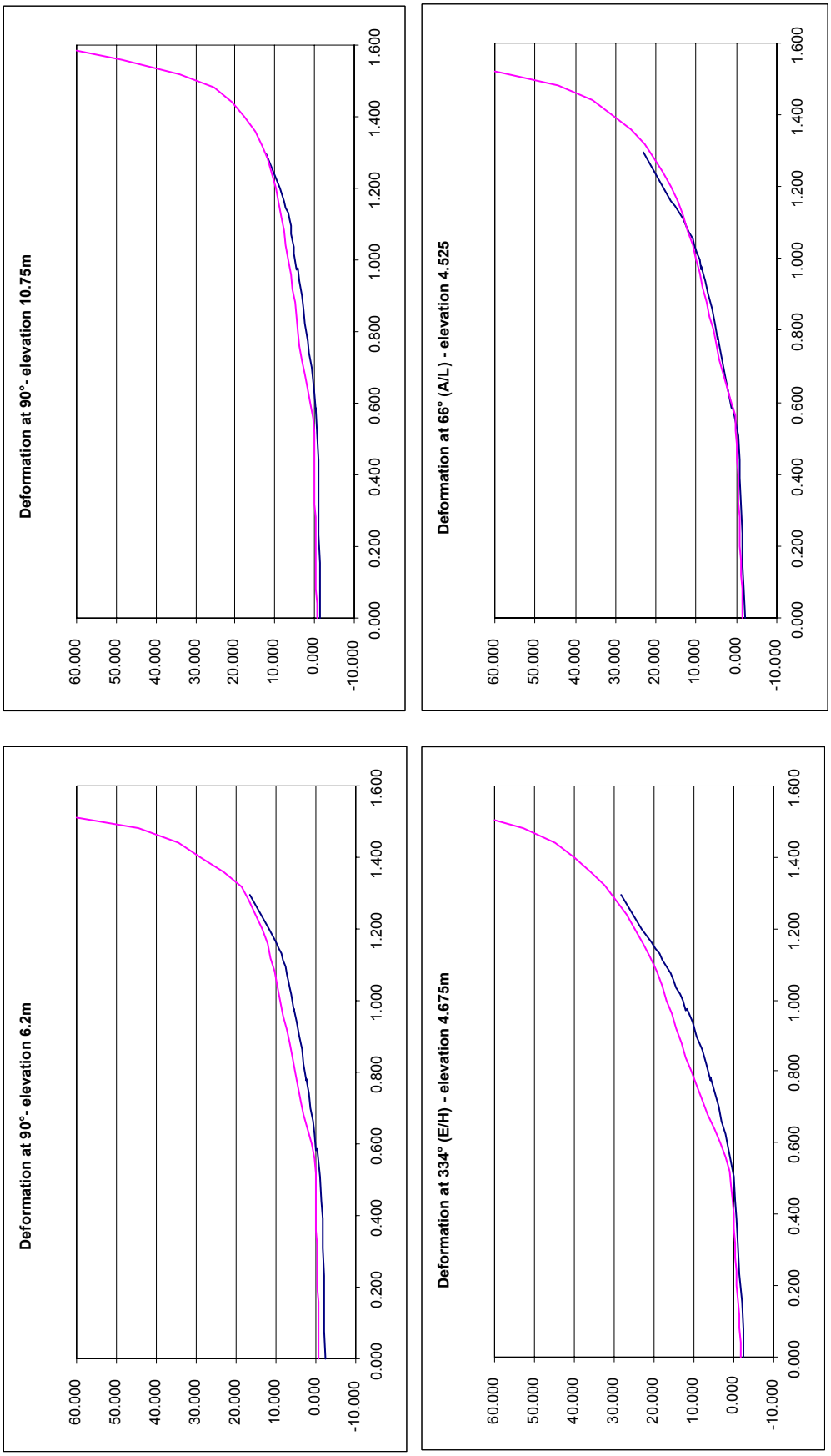

Figure 11 Comparison of radial displacements at 90 degrees and openings (mm, MPa)

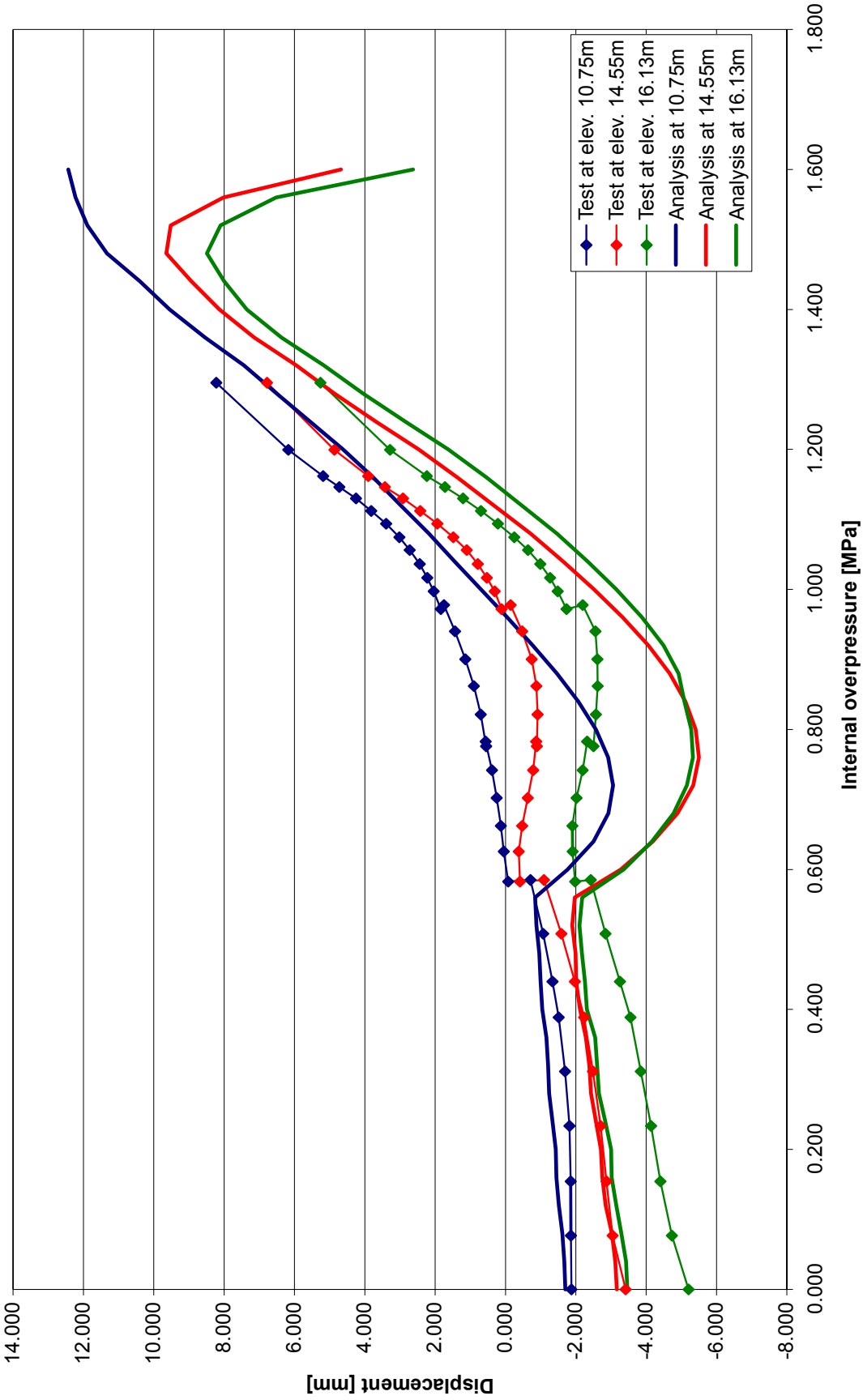

Figure 12 Comparison of vertical displacements

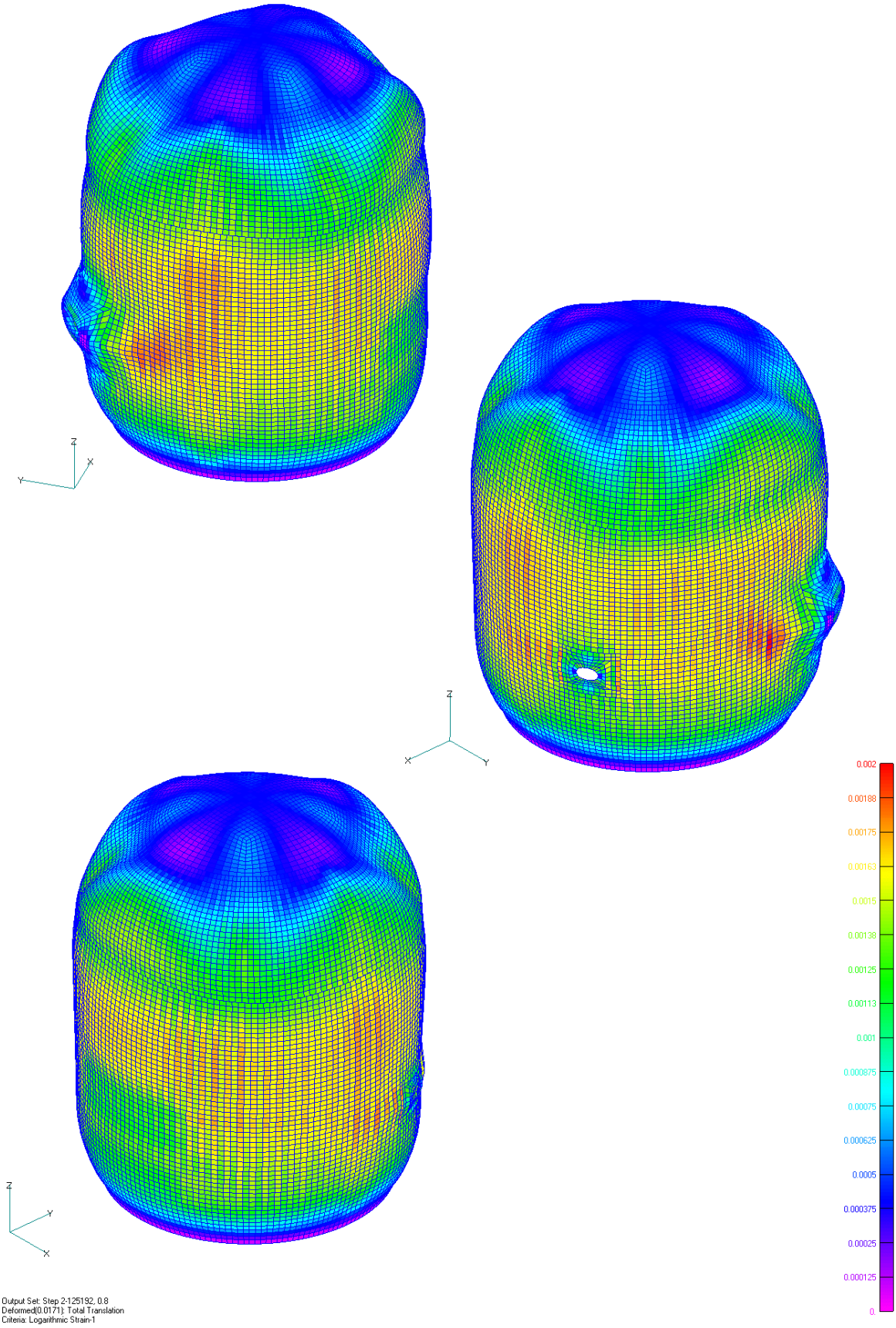

Figure 13 Liner strain in circumferential direction at 1.0MPa – stress in liner reaches yield stress

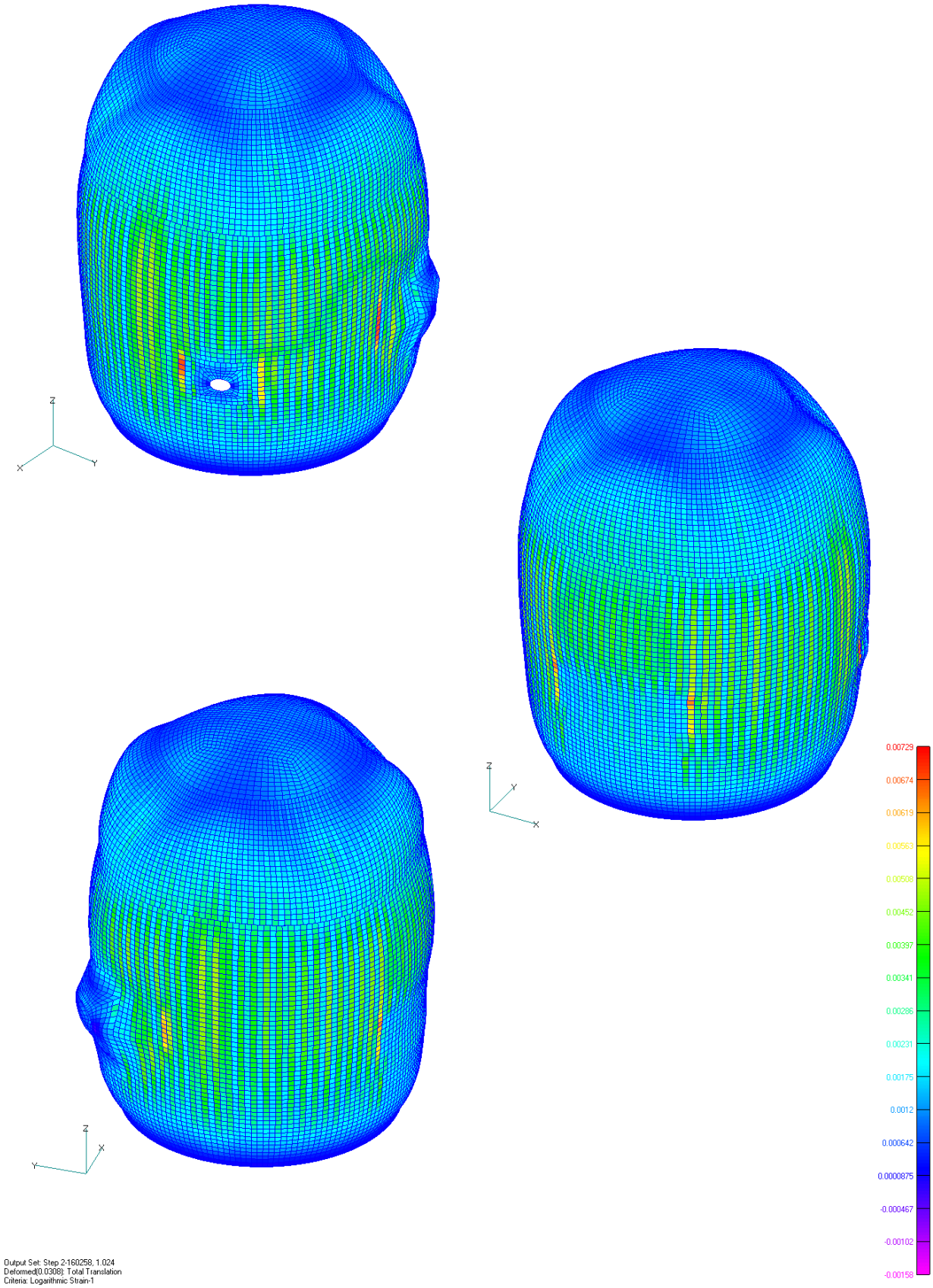

Figure 14 Liner strain in circumferential direction at 1.25MPa – stress in tendons reaches yield stress

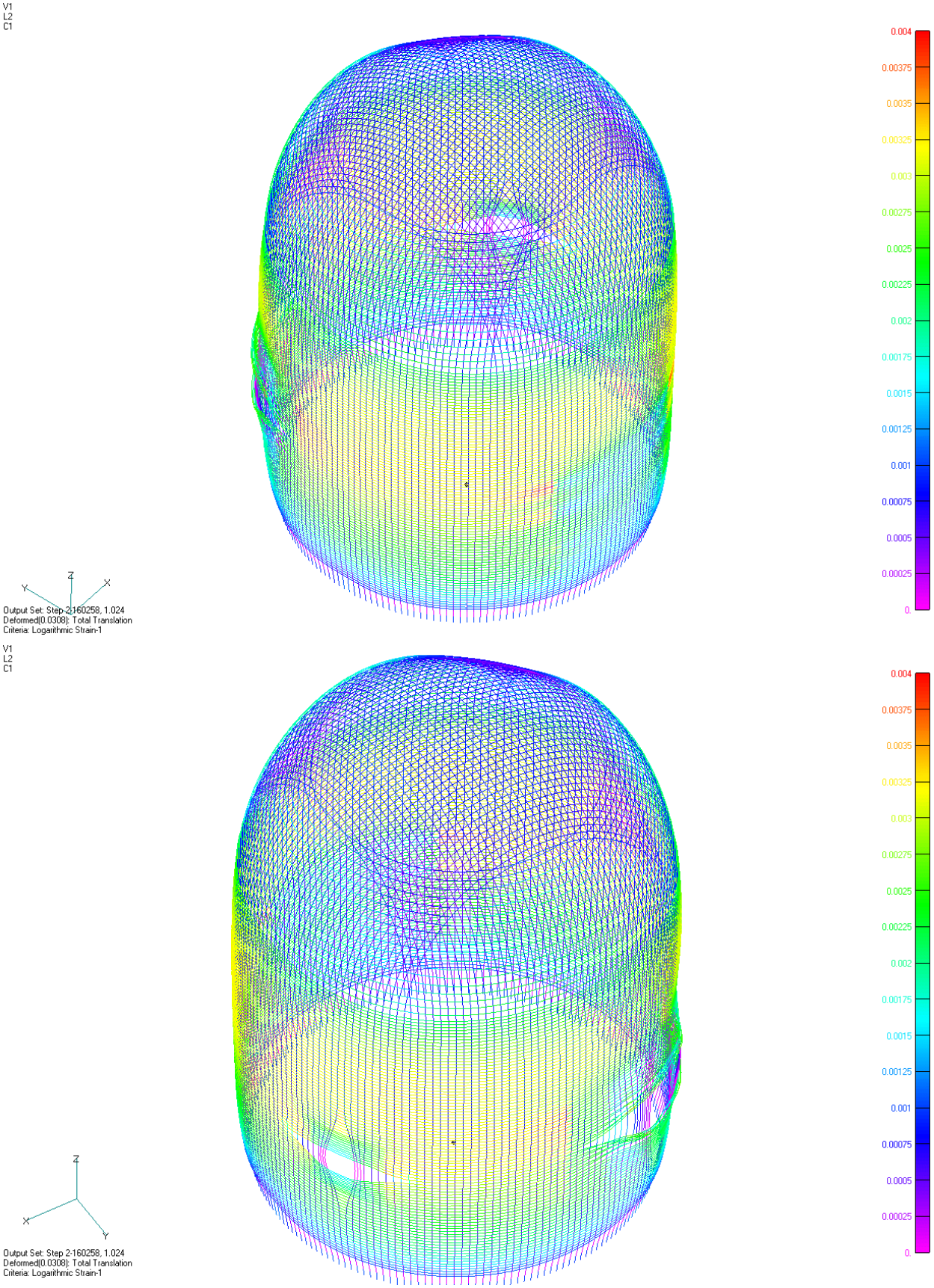

Figure 15 Tendon strain at 1.25MPa – stress in tendons reaches yield stress

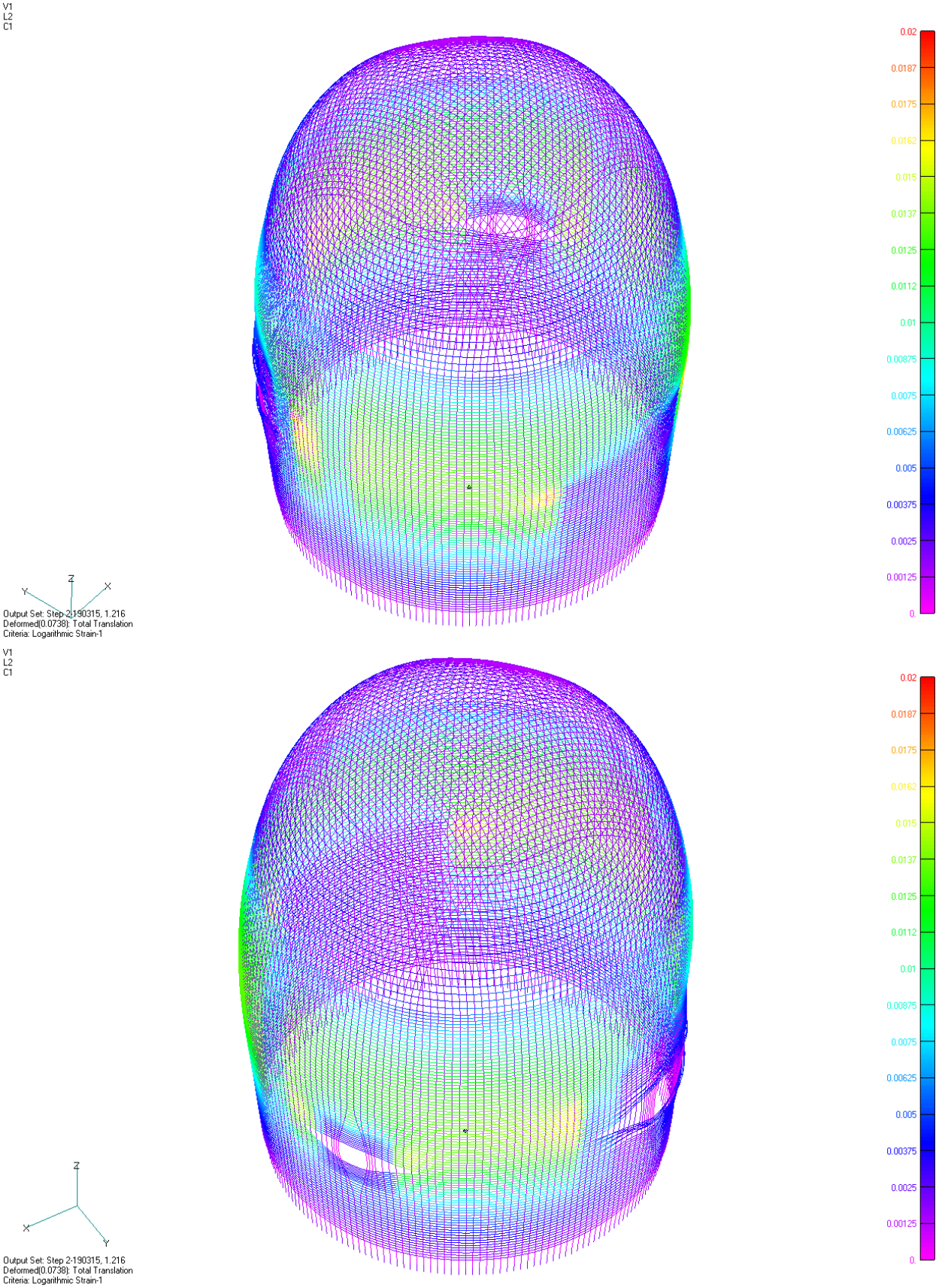

Figure 16 Tendon strain at 1.52MPa – strain in tendons reaches 2%

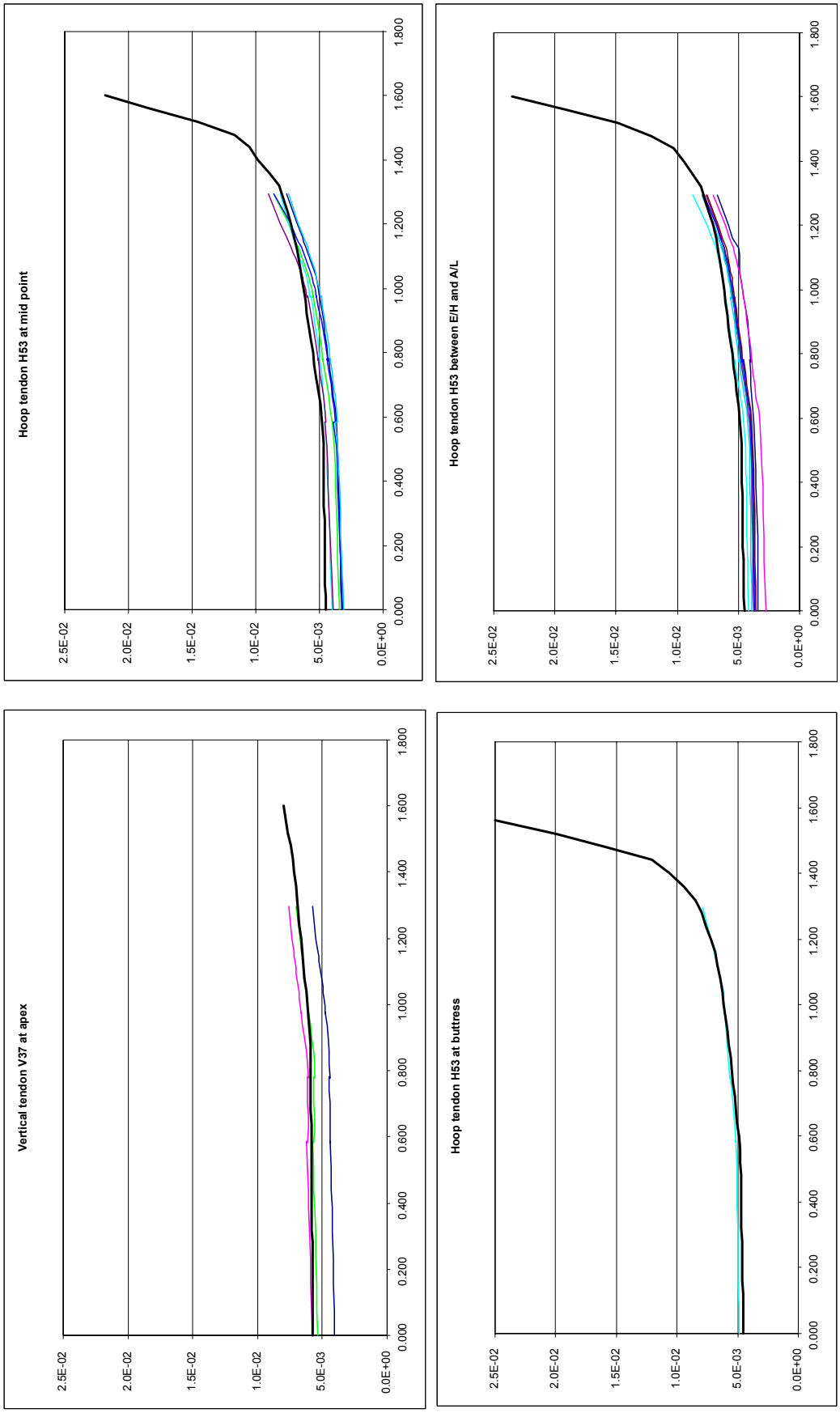

Figure 17 Comparison of tendons strain (m/m, MPa, analysis is black curve)

Page intentionally left blank

ISP48 PHASE III ANALYSIS RESULTS

Jan Stepan
Nuclear Research Institute Rez, div. Energoprojekt Praha, Prague, Czech republic

Analysis model and loadings

The analysis model used for Phase III calculations is the same as Phase II model. The difference is in the analysis type, in Phase II the response of structure was solved by Abaqus/Explicit and in Phase III the response of structure was solved by Abaqus/Standard. The change of the analysis type was forced by properties of Abaqus/Explicit which is not able to read temperature data along with restart from initial conditions. Using of Abaqus/Standard enabled to do analysis in the real time but due to higher sensitivity of calculation to the solving instabilities it is more difficult to solve the final failure mode of the structure.

The load cases corresponds to the case 1 and case 2 loading defined for Phase III included temperature gradients. The basic difference between these two cases is in the character of the temperature gradient across the wall section. In the case 1 loading, the temperature gradient corresponds with the steady state heat transfer – temperature gradient is closed to linear at every time step. In the case 2 loading, the temperature gradient corresponds to the time history of the thermal loading and material properties – temperature gradient isn't linear and is changing in time. This difference of loadings characters is evident in the tendon forces. During the case 1 loading the change of tendon temperature is similar to the change of concrete temperature and the impact of temperature changes to the tendon forces is small. On the contrary, during the case 2 loading there is considerable difference between the temperature of concrete and tendons and the tendon force history shows rise due to temperature loading.

Temperature degradation of concrete and steel (strength and modulus) could be considered in case of higher temperature loadings. For steel, there are interesting temperatures above 300°C, for concrete the boundary temperature is about 100°C. Due to parallel pressure loading, the PCCV structure acted mainly in tension and resistance is driven by properties of tendons and rebar. So, the temperature degradation is interesting especially for steel parts of structure. The case 1 temperature history shows that the temperature is under 300°C and therefore there is no need to consider temperature degradation of steel properties in this load case. In case 2 loading there is the temperature above 300°C twice. At first it is during hydrogen detonation when temperature rises above 600°C. Due to short time period of this loading is depth of wall temperature above 300°C aprox. 5% of total wall thickness and only liner is hits by temperature degradation. The second exceeding of temperature 300°C is at time aprox. 50 hours and then the temperature is continuously raising. In this case the increasing of temperature is long term and temperature degradation could affect rebar and tendon but due to higher pressure (close to the bearing capacity of the structure) the temperature couldn't be critical reason of structure failure. Following assumptions were considered in presented analysis: in case 1 analysis no temperature degradation was applied, in case 2 analysis the temperature degradation was applied only for liner.

Analysis results

Comparison of global deformation for pressure and pressure+temperature loadings is in Figure 1 to Figure 4 for case 1 and in Figure 13 to Figure 16 for case 2. Figure 7 and Figure 8 show comparison of case 1 deformation history at 135°, 90° and at openings. Comparison for case 2 is in Figure 17 and Figure 18. For case 1 there is a comparison for test, results of phase II analysis (Explicit), results of analysis for pressure loading and results of analysis for pressure and temperature loadings. For case 2 there is only a comparison for pressure loading and pressure+temperature loadings. The comparison of analysis results for only pressure loading (Explicit x Standard) shows that the results are very close to the pressure until the concrete cracking. At higher pressures there is a lower increase of deformation for Standard analysis due to an added small permanent stiffness of concrete elements which helps increase a stability of solution (this stiffness is imposed by duplicating of concrete elements - there is always one nonlinear concrete element along with one linear element with small stiffness at aprox. 1/10 of the original concrete stiffness). The influence of temperature loading on deformation of structure is favorable – increasing of inner temperature suppresses differences of deformation around openings (comparison of deformation history at elevation 4.68 for different azimuths is in Figure 9 and Figure 19).

The influence of heat rate on the structure state of stress is well demonstrated by force in tendons. The history of tendon forces is in Figure 10 for case 1 and Figure 20 for case 2. For case 1 loading, the force history for pressure and temperature loading is close to the force history for only pressure loading. On the other hand, there is big difference of tendons forces between pressure and pressure+temperature loading in case 2. Similar results are for the liner and rebar (Figure 11 and Figure 12 for case 1, Figure 21 and Figure 22 for case 2). In case of rebar and liner, when we compare strains, there is next curve added into the charts – due to temperature loading it is need to differentiate the strain corresponding to the deformation and the strain corresponding to the stress (this strain is marked as “true” in the charts). Especially in case 2 there is the strong dependence of strain in rebar and liner on the depth of elements in the wall from the inner surface. The extreme case is liner which temperature responses to the inner temperature of containment with no delay and in case of fast changes of temperature the strain reaches high values.

Results discussion

Commentary on model:

- the model used for the analysis describes global behaviour of the structure altogether well especially for case 1 loading. Results of case 1 analysis for only pressure loading show better fit at the lower pressure with the test results in comparison with the Phase II analysis results. Reason is using of Abaqus/Standard analysis type in real time (a pseudo time sets in previous Abaqus/Explicit analysis was short and the results were affected by dynamic effects). Disadvantage is worse fit of results at higher pressure due to added small permanent stiffness of concrete elements.
- for the case 2 loading analysis there would be better to change the element mesh and use more elements across the wall thickness. The four linear elements used in

current model are too coarse considering temperature gradient across the wall thickness.

- a global model is able to simulate beaviour of the structure from strength point of view. But there is need to create detail models to analyze liner behaviour and its tightness ability along with the liner anchors.

Commentary on results and results evaluation:

- comparison of the results of temperature-pressure loading analysis with the results of pressure loading analysis shows that temperature loading with the temperature gradient across the wall close to uniform is more favorable. On the other hand, long term high temperature loading causes temperature degradation into higher depth of wall. Rapid changes of temperature in containment are the most dangerous for liner, response of the rest of structure is suppressed by thermal capacity of structure material.
- the temperature degradation effects weren't too important in analyzed loading cases. Degradations of concrete have low effect due to tensile acting of concrete - pressure loading history corresponds to temperature loading history so there is high pressure at higher temperatures. Temperature degradation of steel has no effect in the case 1 loading due to low temperature. In case 2, there is considerable effect on liner during hydrogen detonation but due to relatively short time period of this loading there is no temperature degradation of rebar or tendons. Temperature degradation at final part of case 2 loading history could affect inner rebar row but the corresponding pressure loading is at the bearing capacity of the structure and likely there will be the structure failure before the temperature degradation could affect the rebar.
- beyond the direct influence of the temperature on degradation of material properties there are additional effects, e.g. thermal spalling of concrete at higher heating rates or redistribution and decrease of thermal stress in concrete. Simulation of these effects is more complicated (in global models) so it is difficult to include there direct into analysis. On the other hand, influence of thermal spalling of concrete is possible do decrease for example by applications of polypropylene fibres – higher temperature destroy the fibres and porosity of the concrete increases.
- the analysis results shows that the temperature couldn't change the failure mode of the structure significantly and, especially for long term thermal loading, the pressure will be the critical loading. On the other hand, thermal loading with fast changes of inner temperature is the critical loading for liner.

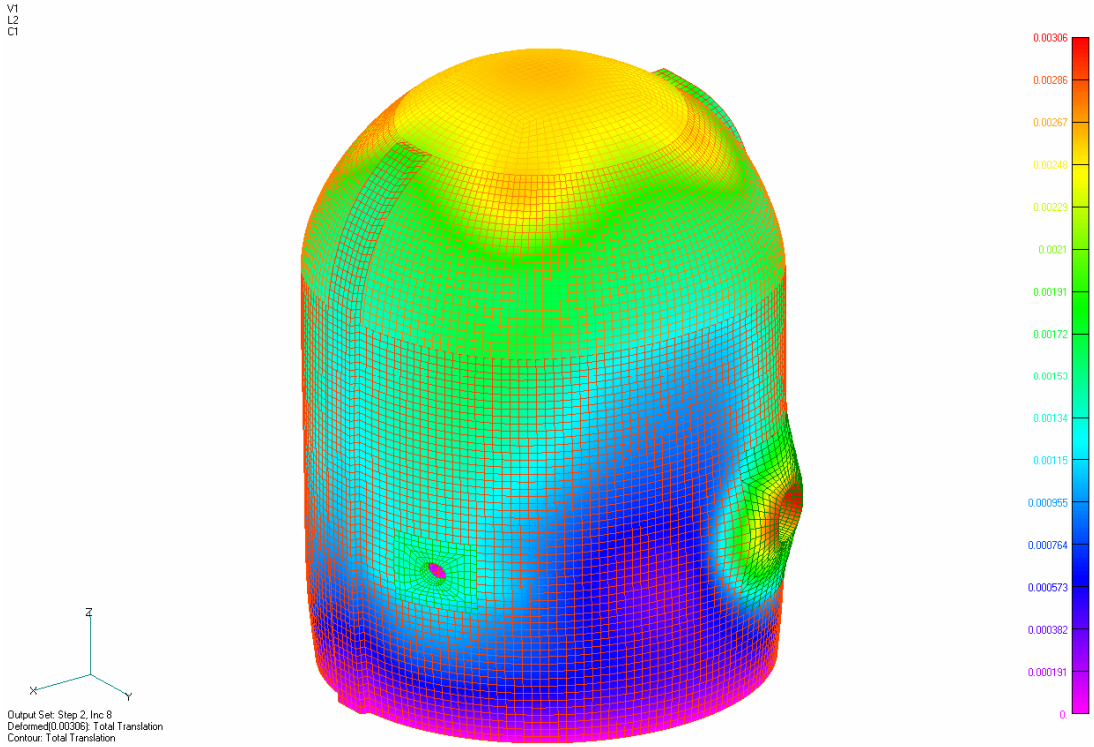

Figure 1 Case 1: Total deformation at 0.6MPa – loading by pressure

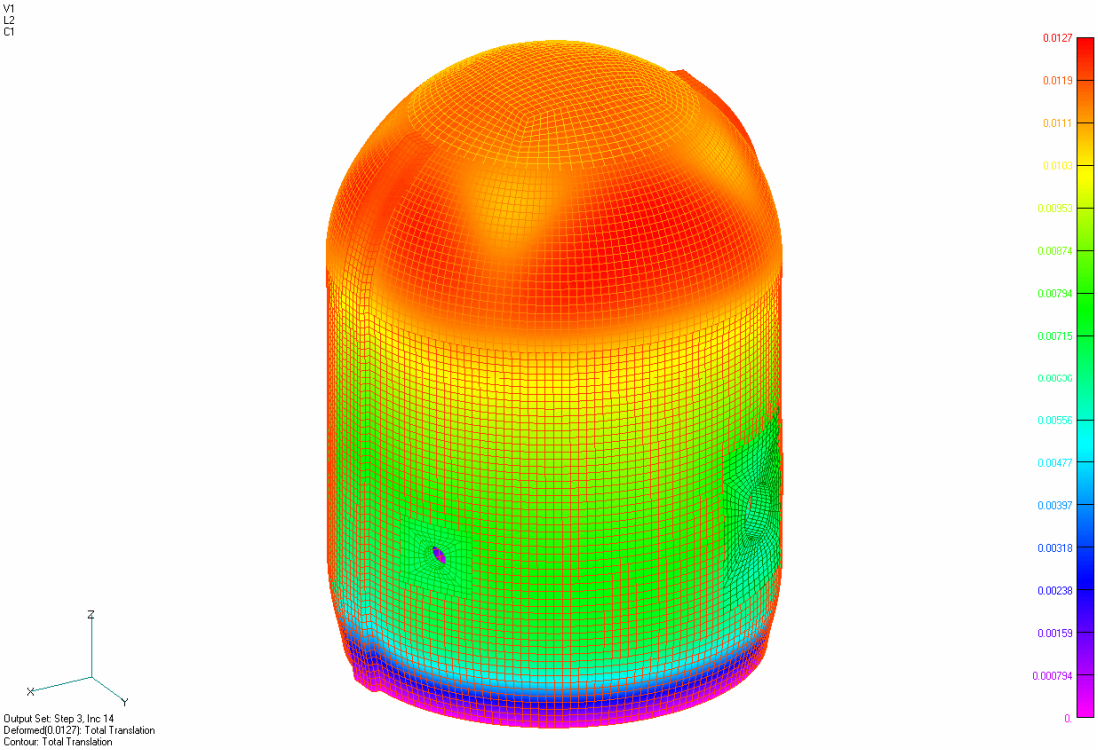

Figure 2 Case 1:Total deformation at 0.6MPa – loading by pressure and temperature

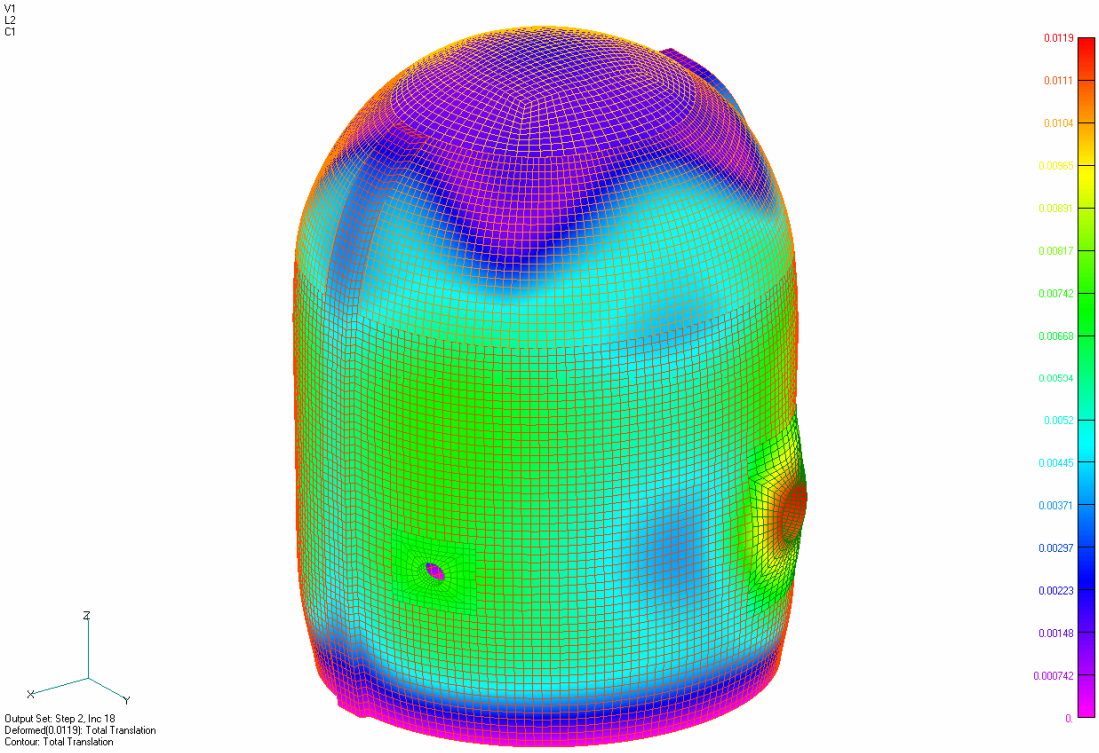

Figure 3 Case 1:Total deformation at 1.0MPa – loading by pressure

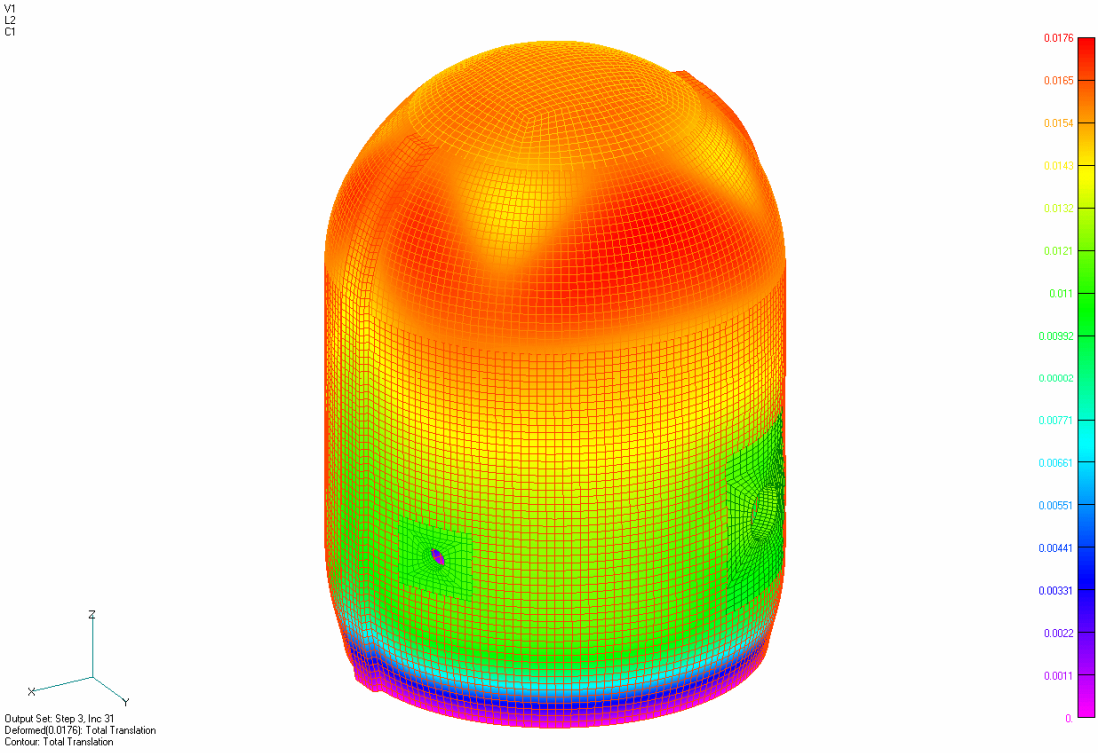

Figure 4 Case 1:Total deformation at 1.0MPa – loading by pressure and temperature

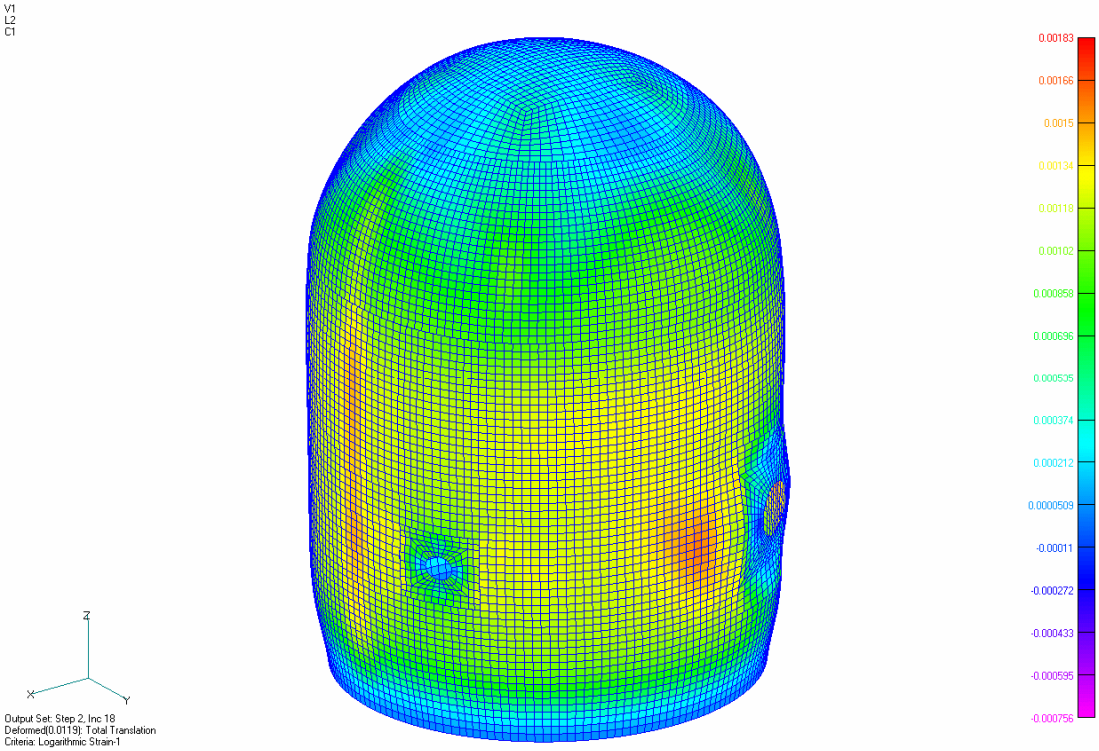

Figure 5 Case 1:Liner strain in circumferential direction at 1.0MPa – loading by pressure

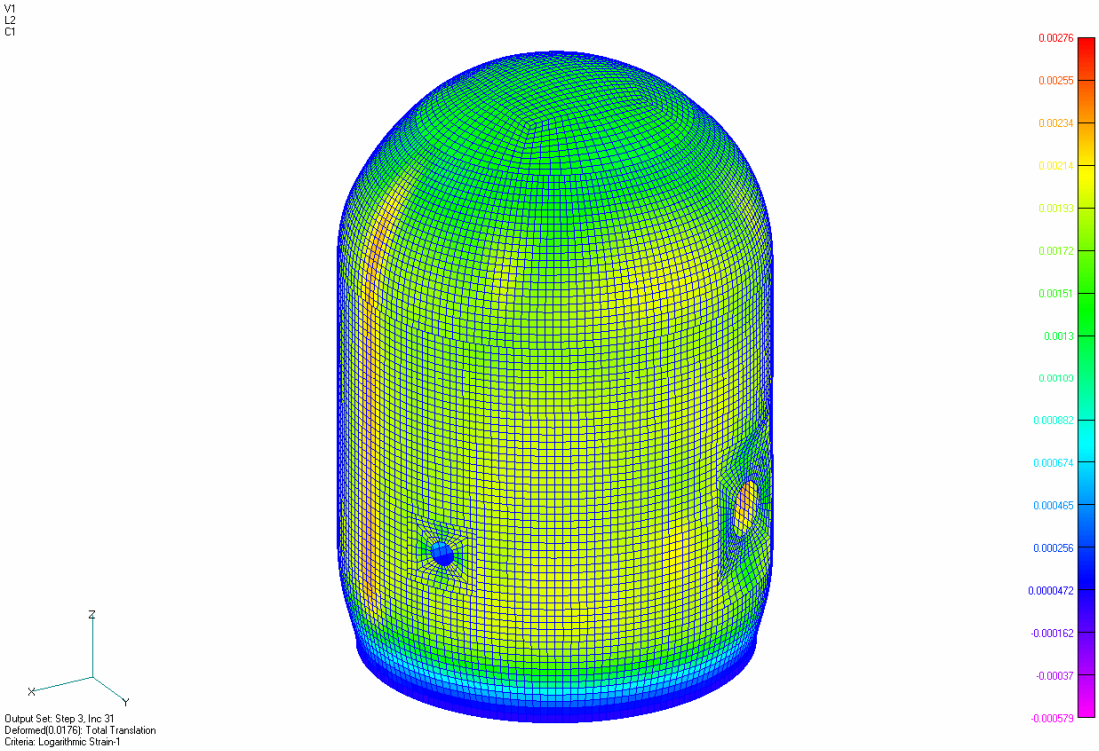

Figure 6 Case 1:Liner strain in circumferential direction at 1.0MPa – loading by pressure and temperature

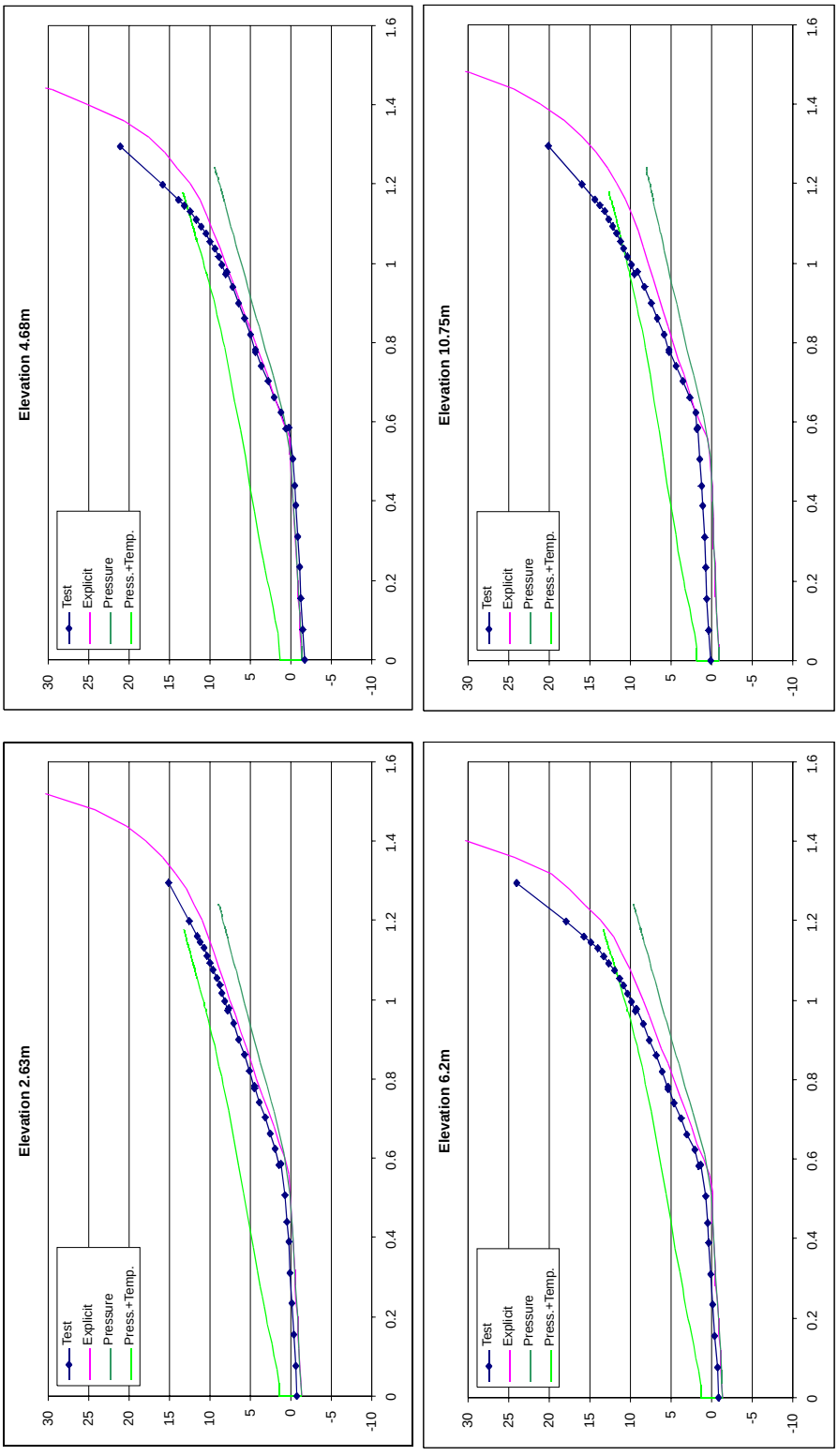

Figure 7 Case 1:Comparison of radial displacements at 135 degrees (mm, MPa)

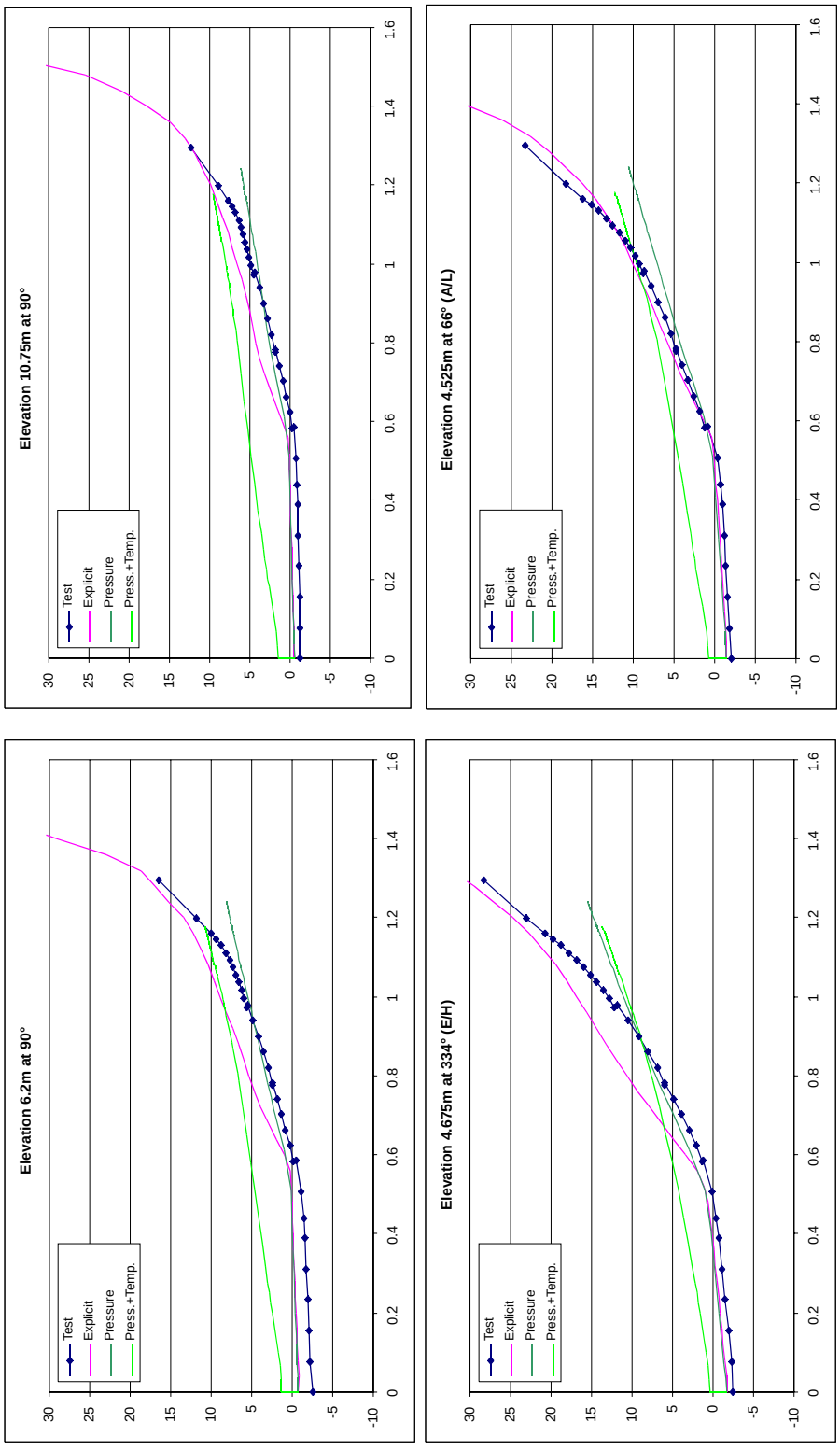

Figure 8 Case 1:Comparison of radial displacements at 90 degrees and openings (mm, MPa)

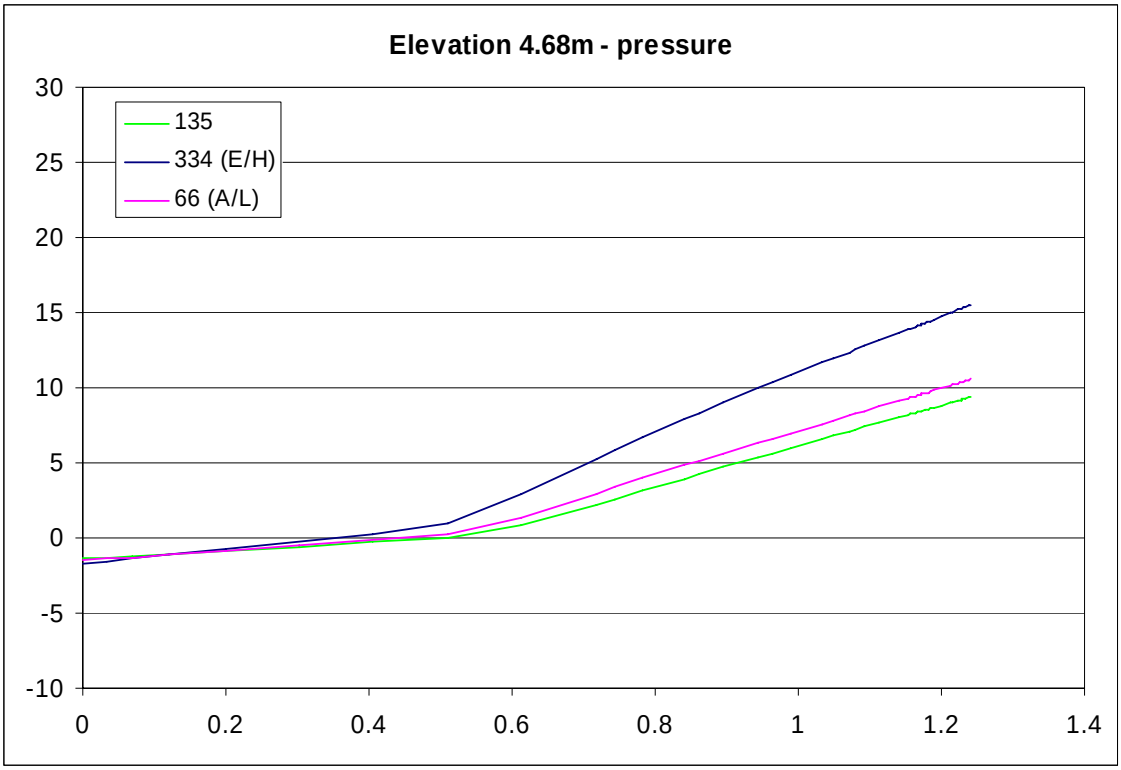

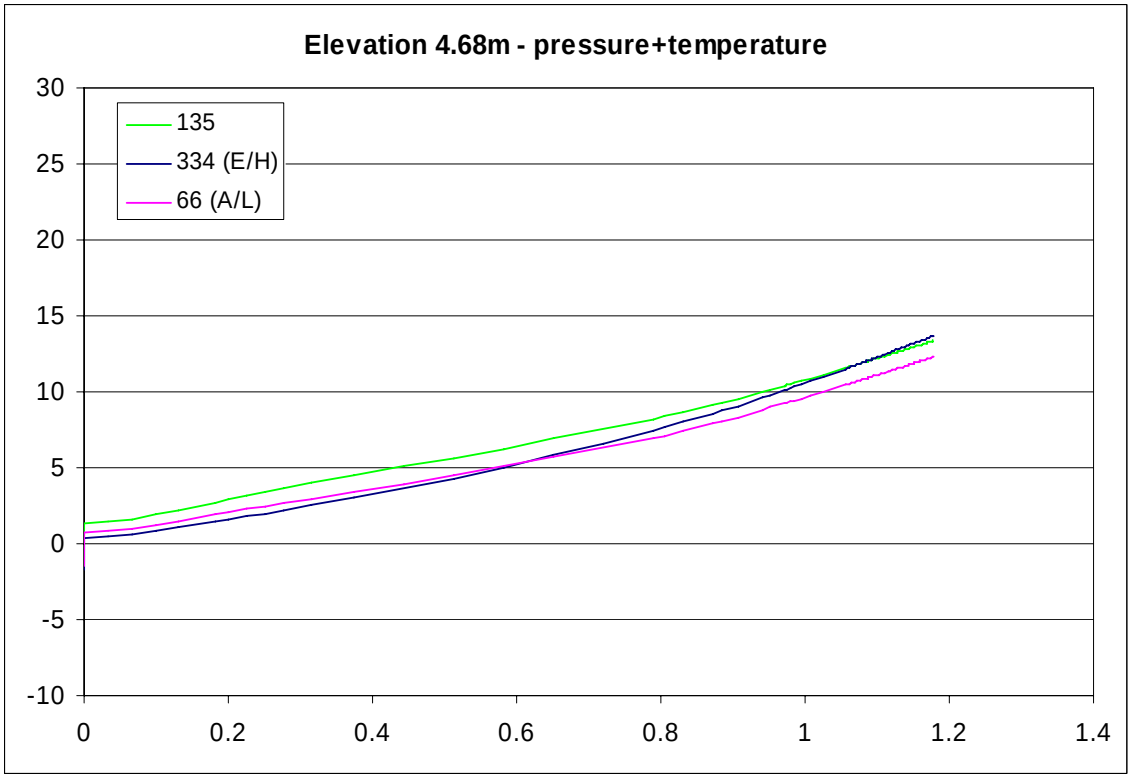

Figure 9 Case 1:Comparison of radial displacements at elevation 4.68 for different azimuths (mm, MPa)

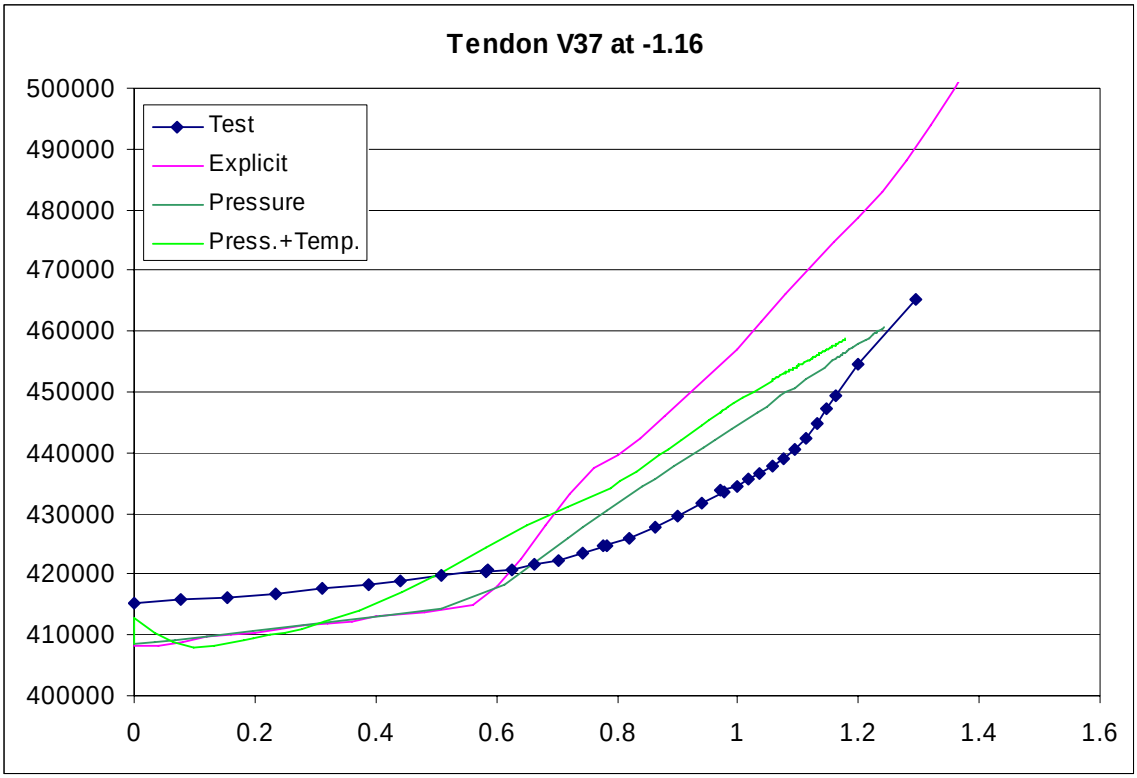

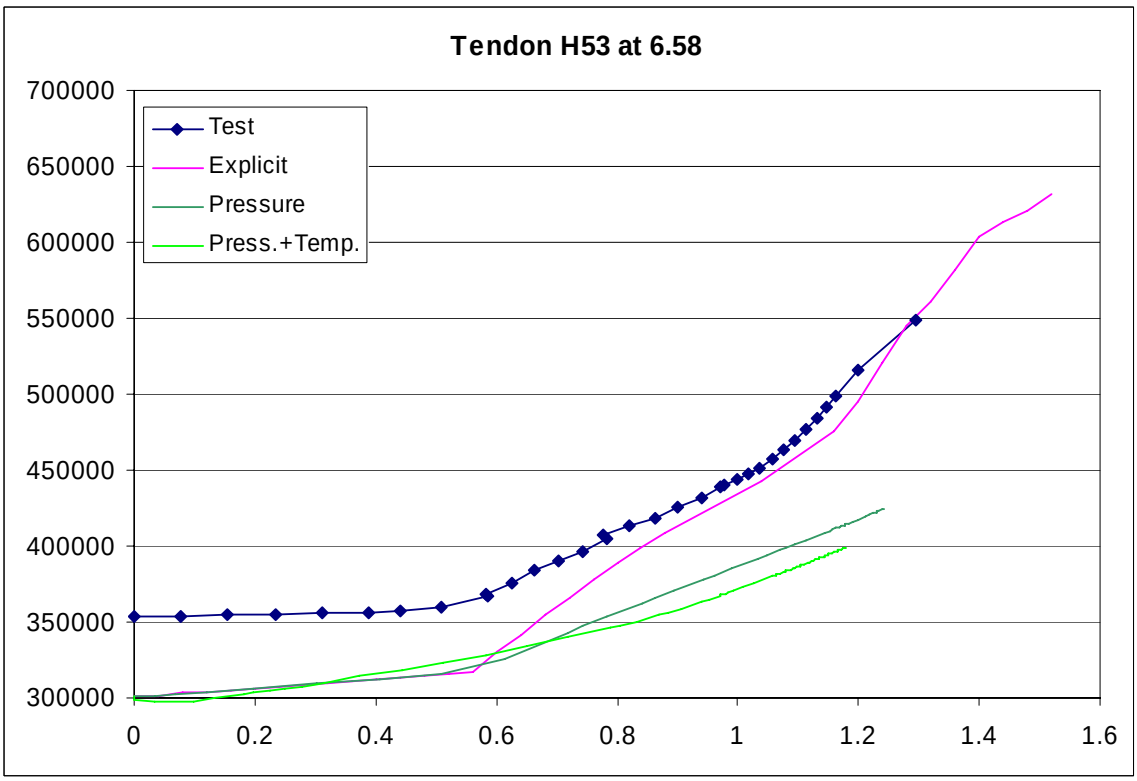

Figure 10 Case 1:Comparison of tendons strain and force (m/m or N, MPa)

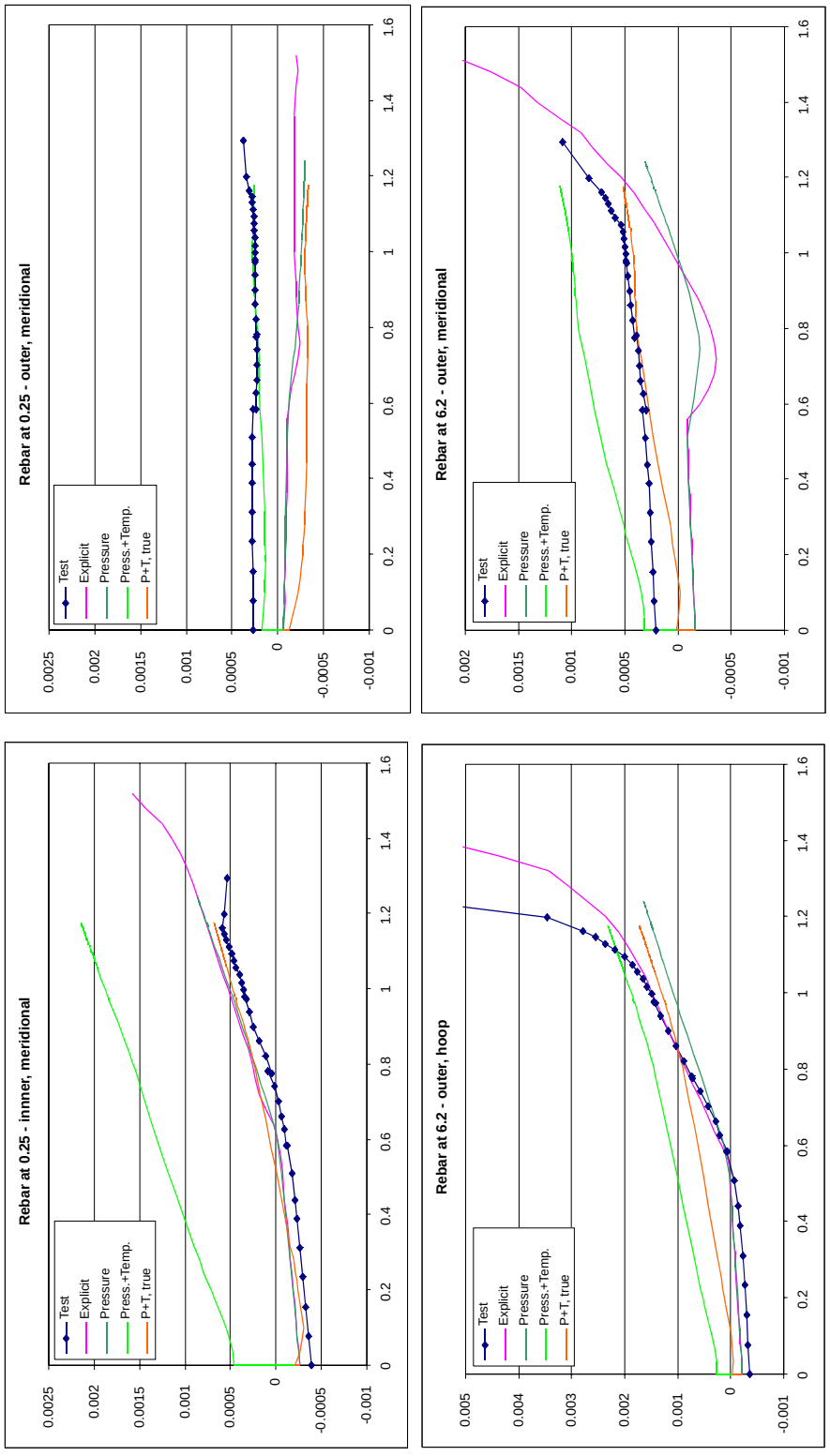

Figure 11 Case 1:Comparison of rebar strain (m/m, MPa)

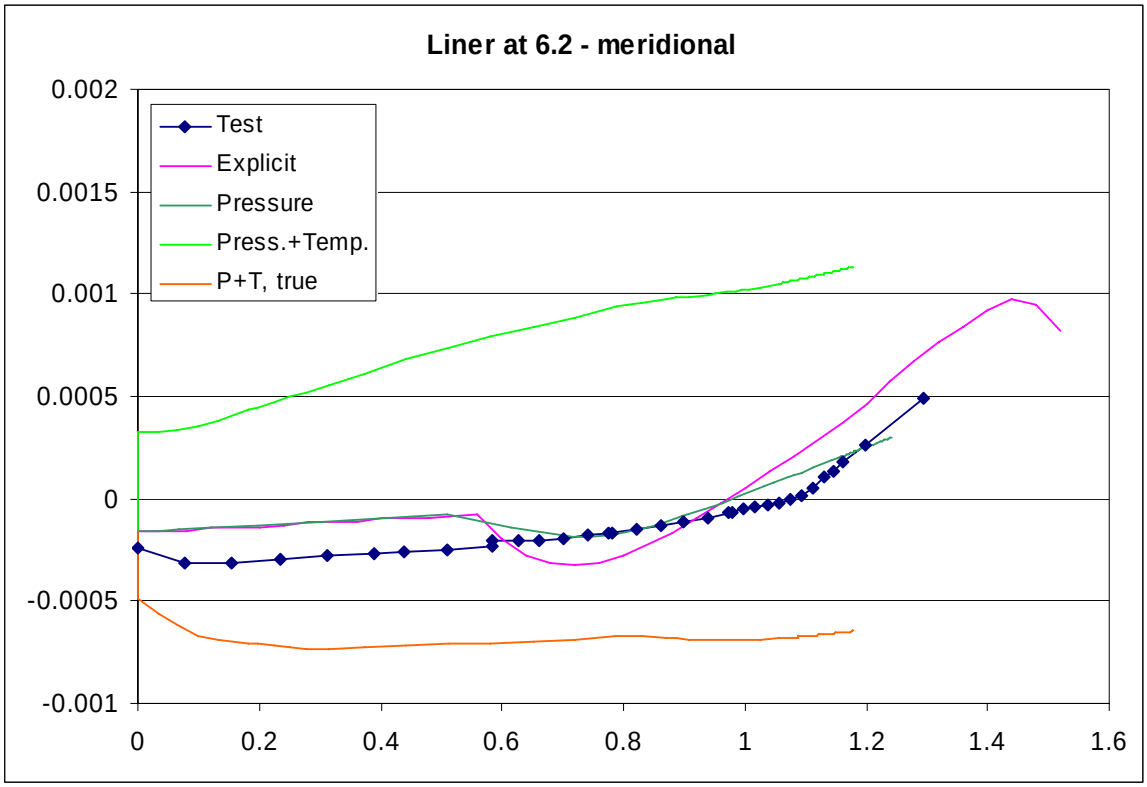

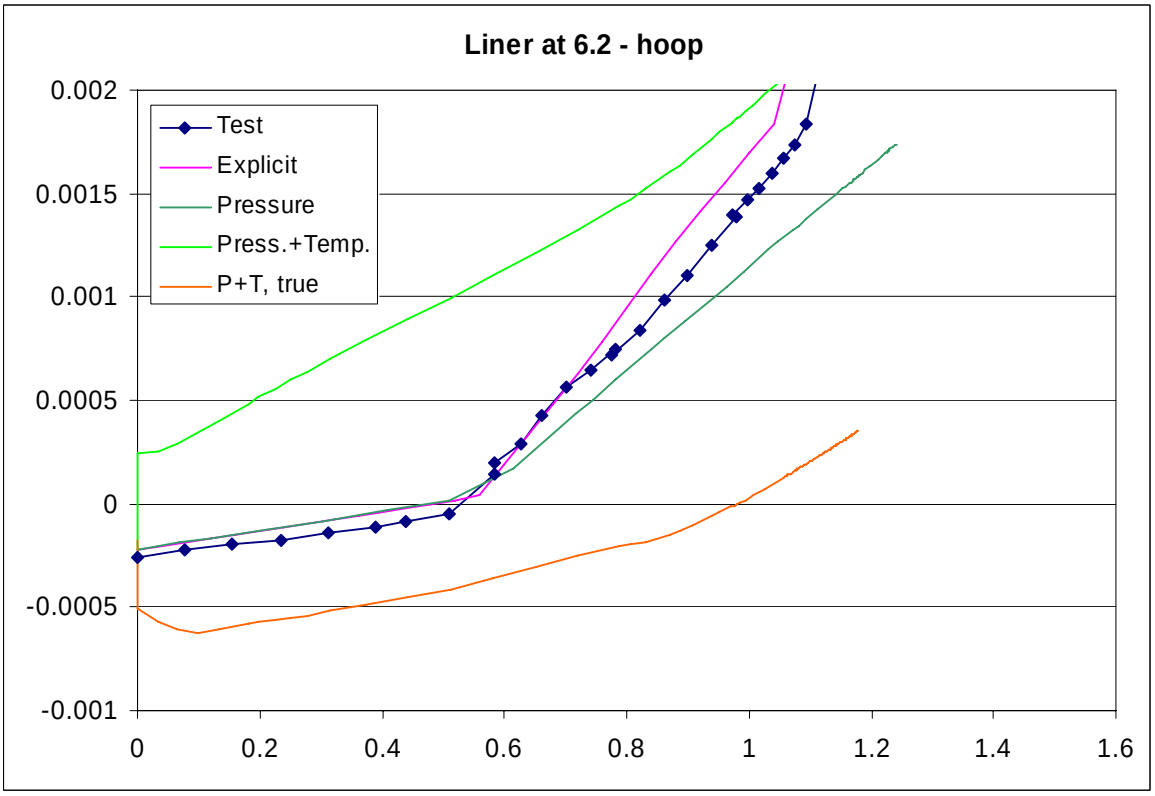

Figure 12 Case 1:Comparison of liner strain at 135° (m/m, MPa)

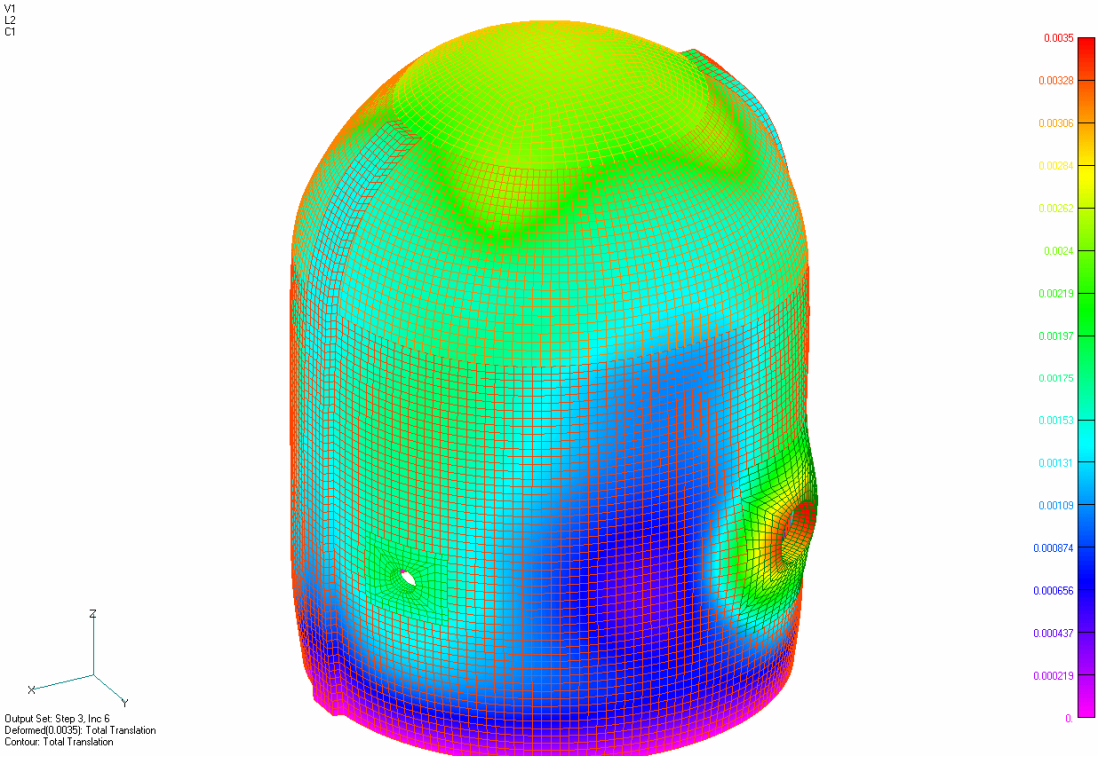

Figure 13 Case 2:Total deformation at time of hydrogen detonation – loading by pressure

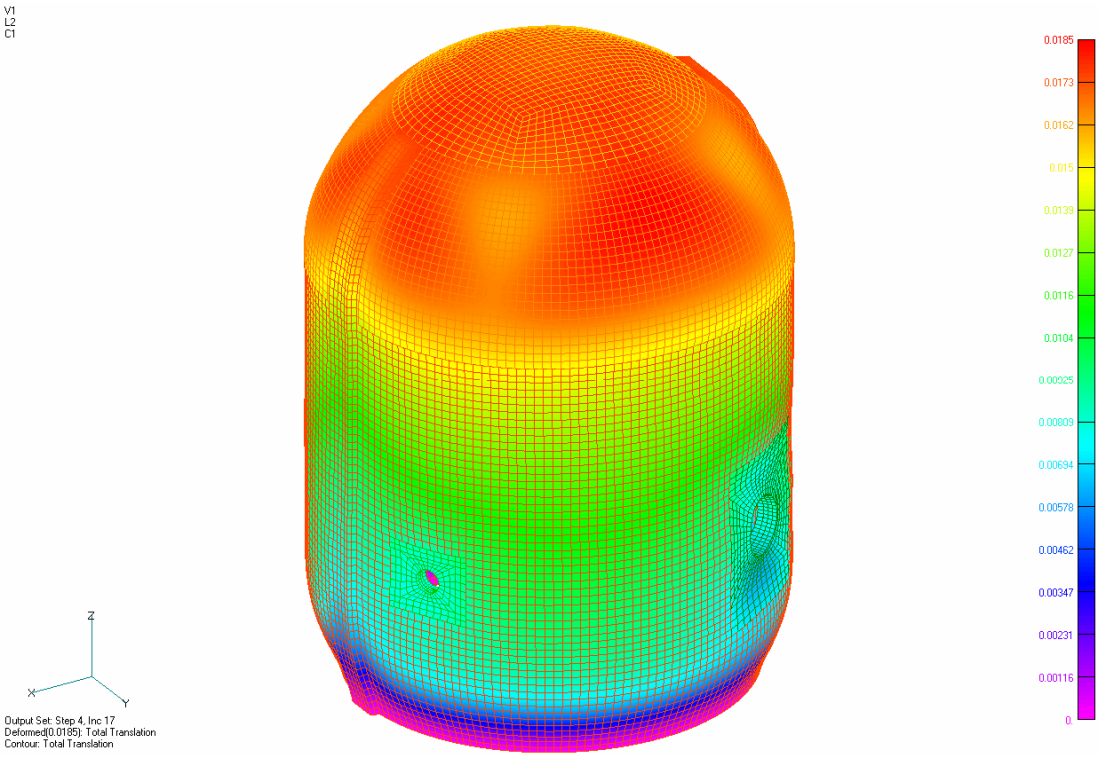

Figure 14 Case 2:Total deformation at time of hydrogen detonation – loading by pressure and temperature

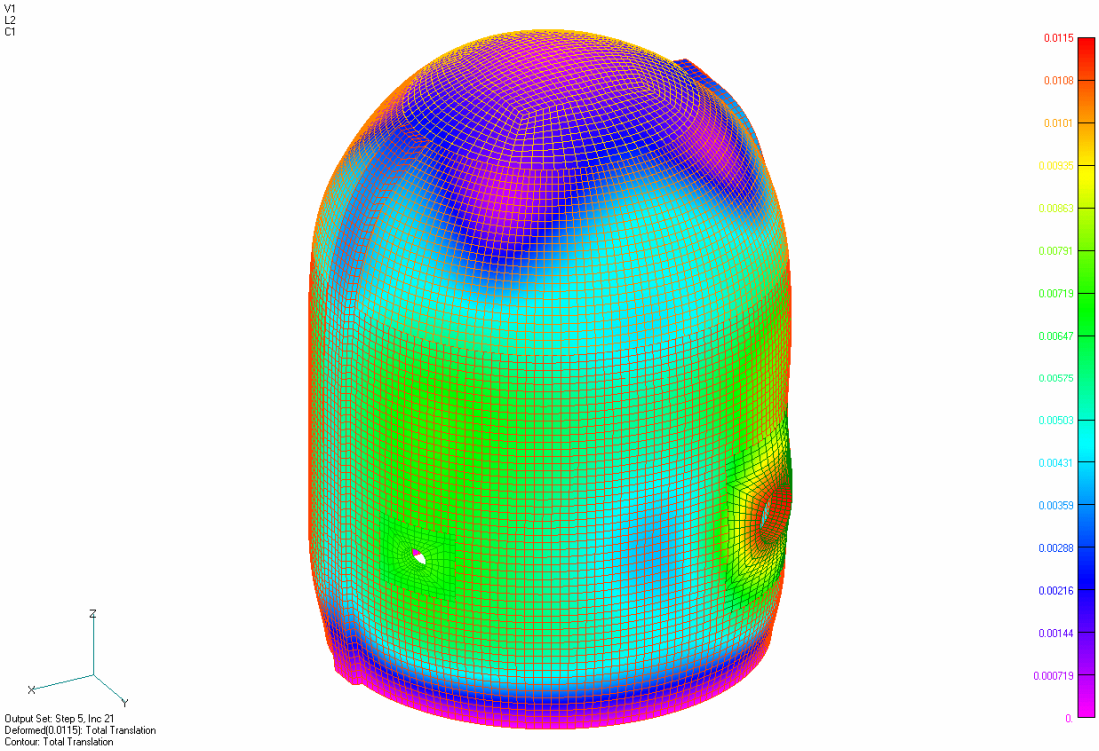

Figure 15 Case 2:Total deformation at time 3600 min. – loading by pressure

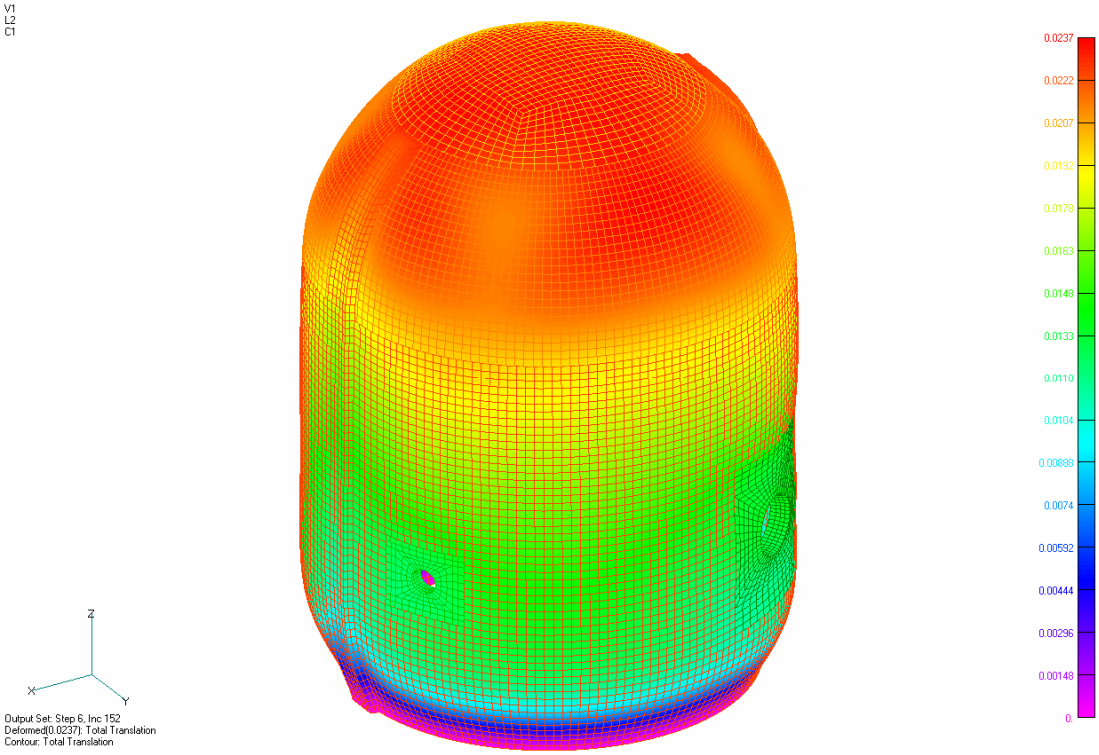

Figure 16 Case 2:Total deformation at time 3600 min. – loading by pressure and temperature

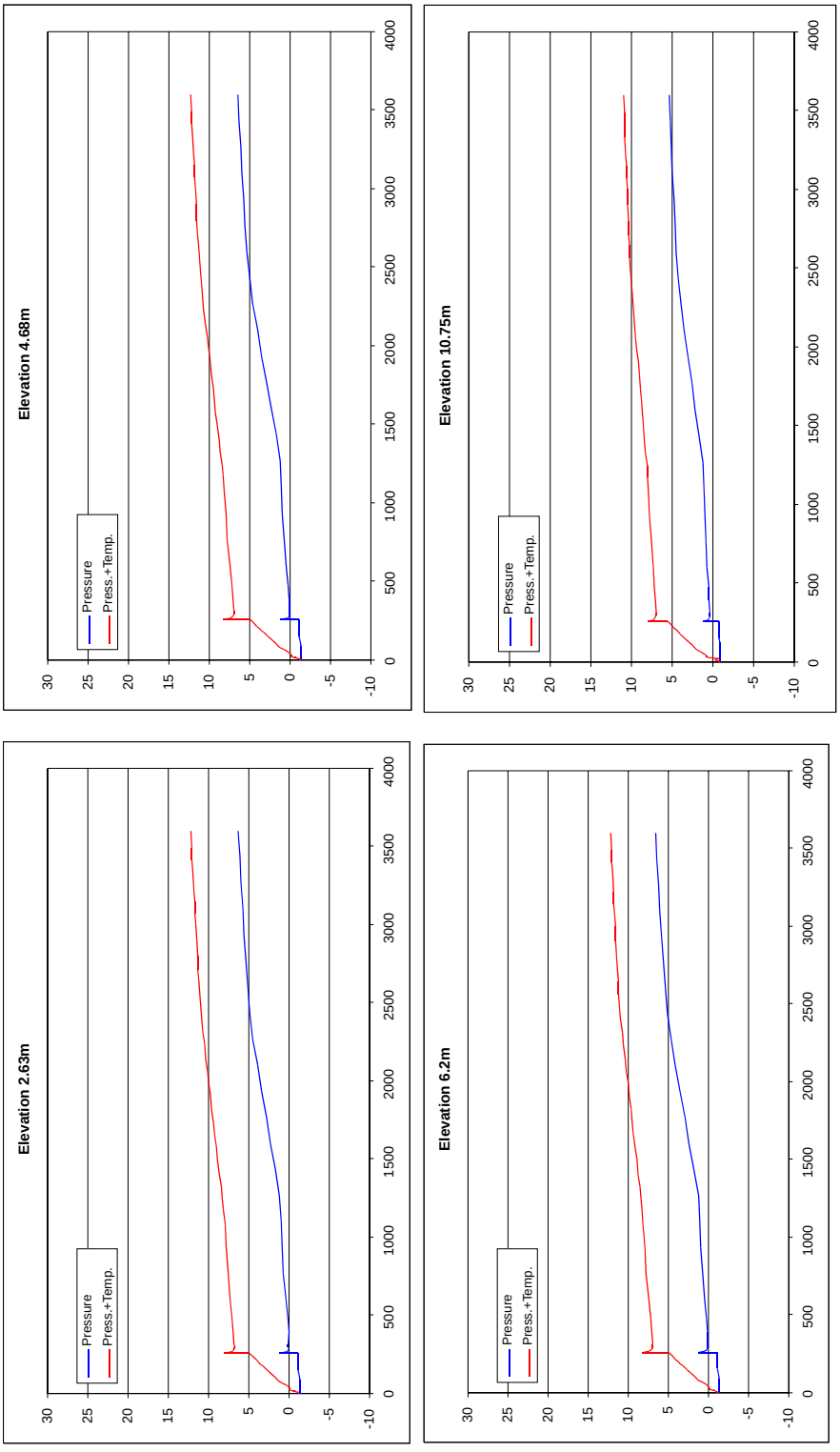

Figure 17 Case 2:Comparison of radial displacements at 135 degrees (mm, MPa)

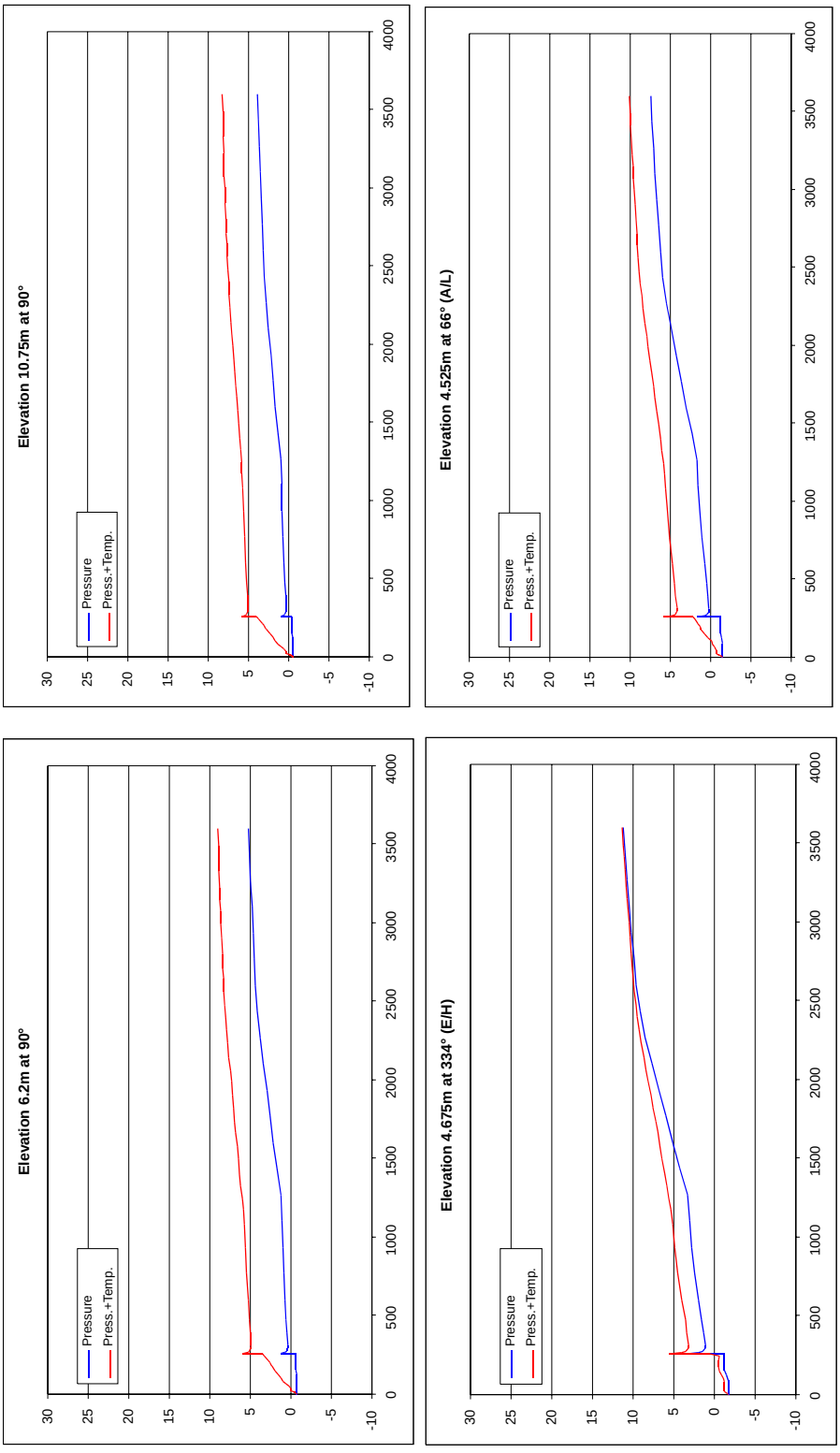

Figure 18 Case 2:Comparison of radial displacements at 90 degrees and openings (mm, MPa)

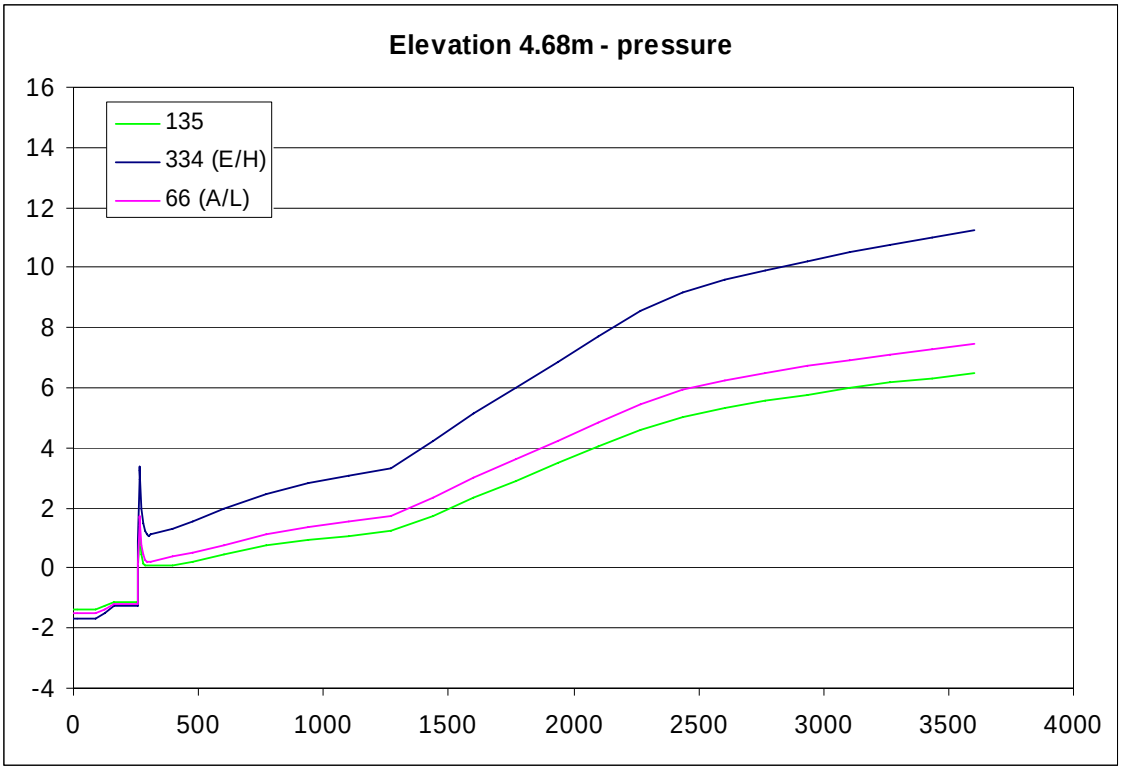

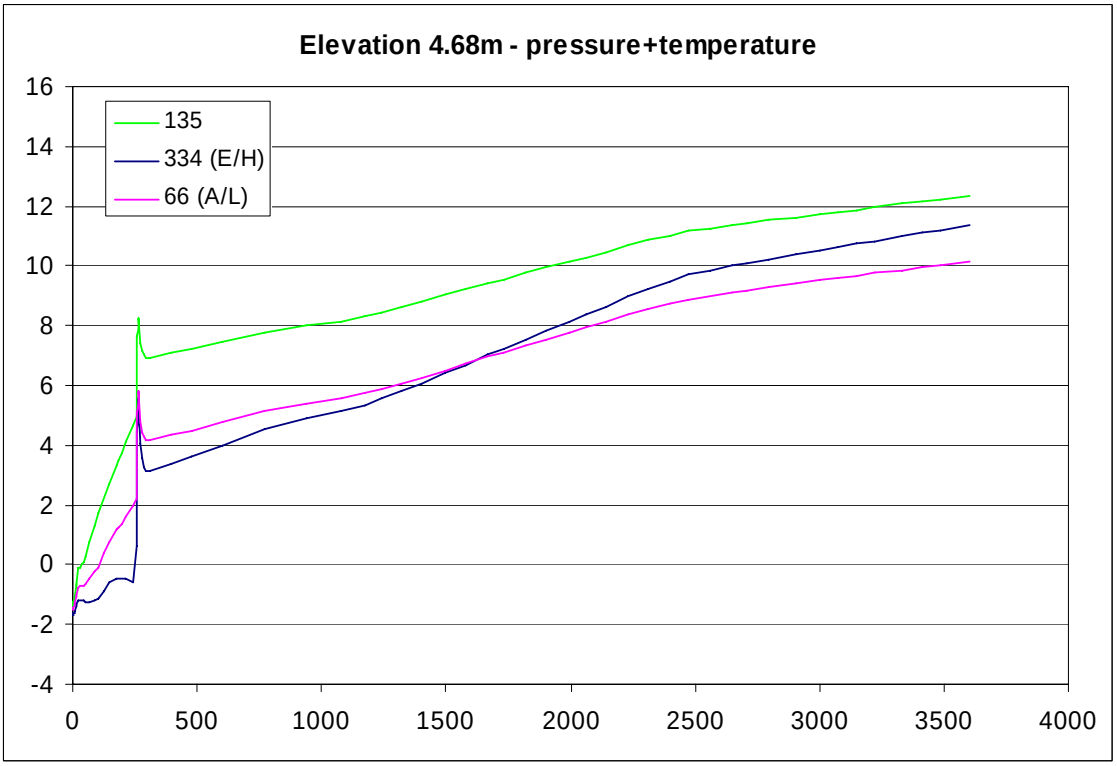

Figure 19 Case 2:Comparison of radial displacements at elevation 4.68 for different azimuths (mm, MPa)

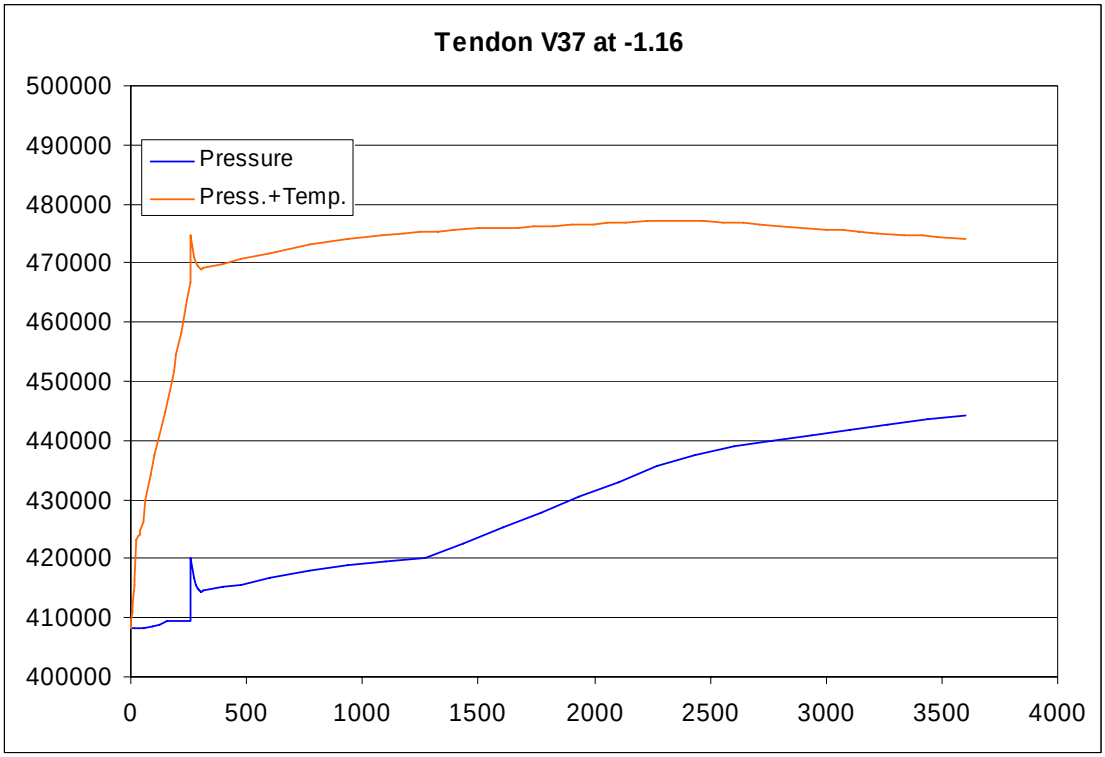

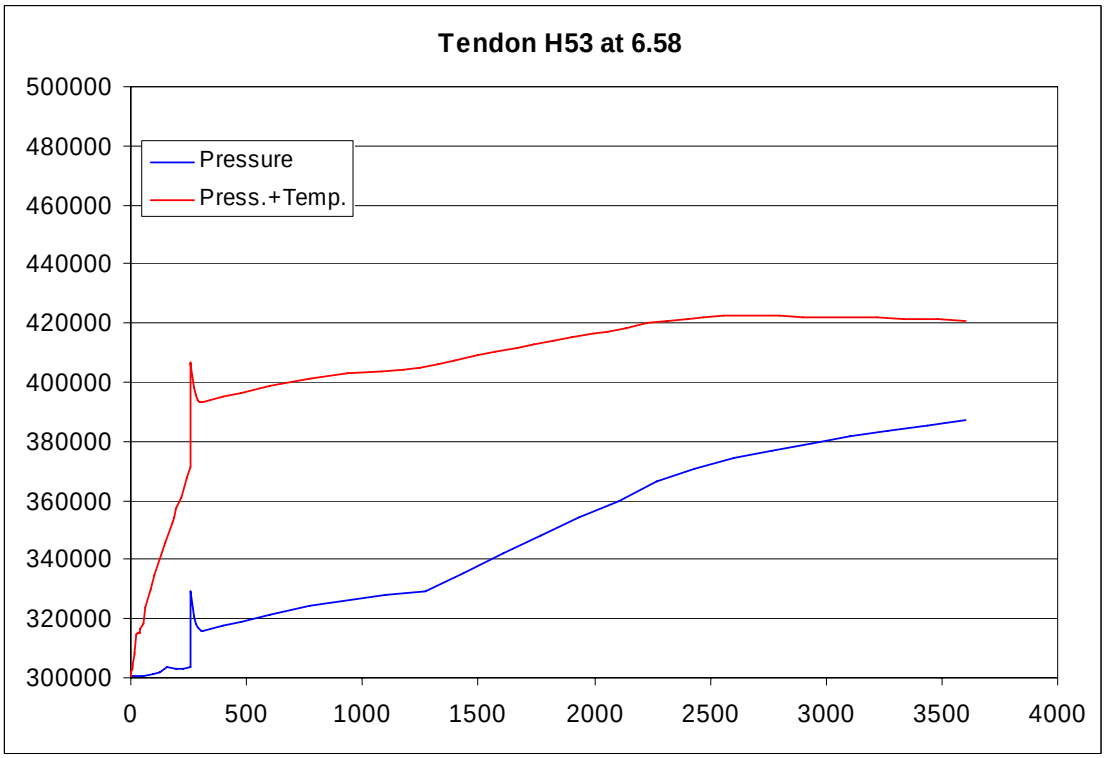

Figure 20 Case 2:Comparison of tendons strain and force (m/m or N, MPa)

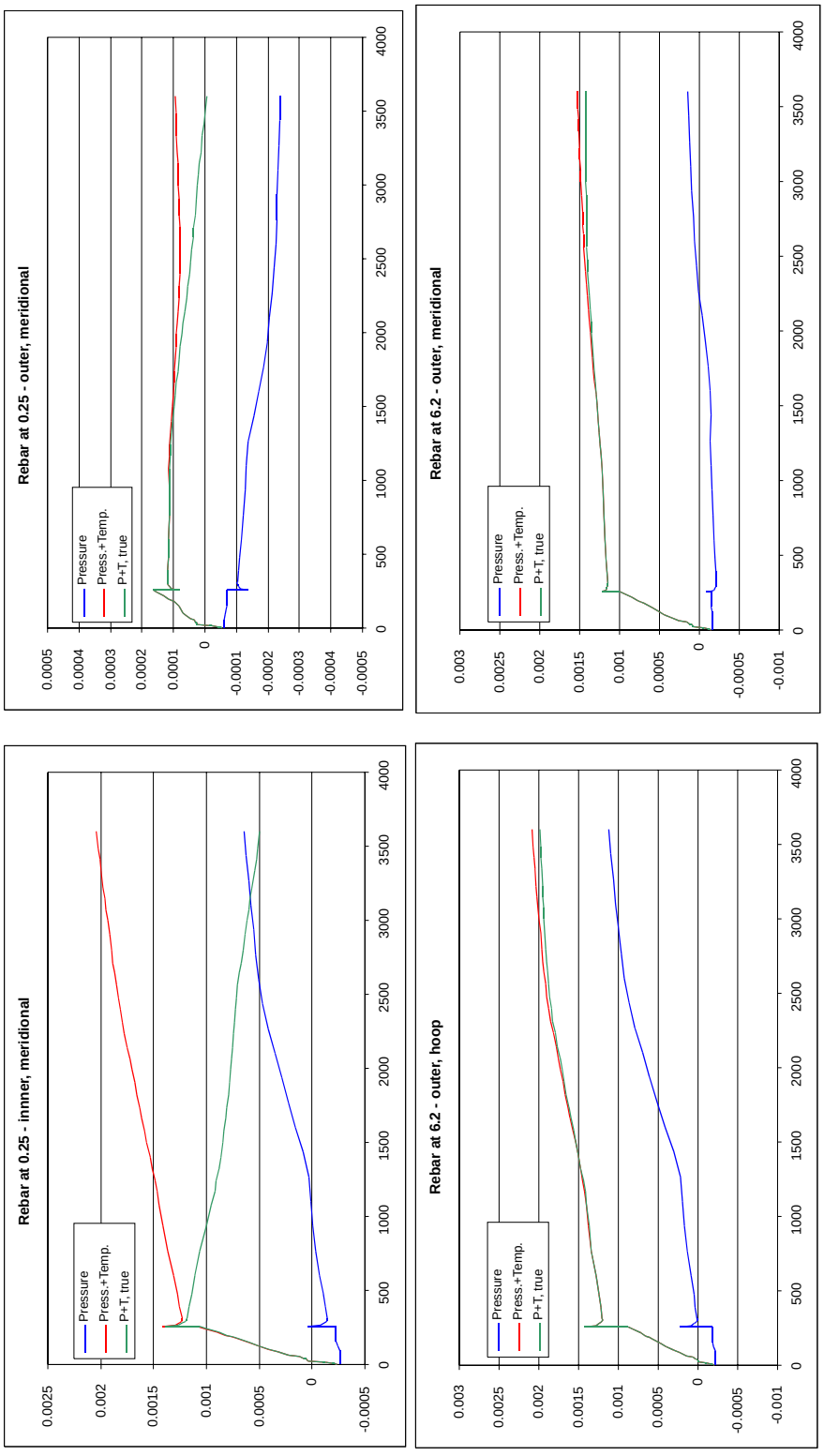

Figure 21 Case 2:Comparison of rebar strain (m/m, MPa)

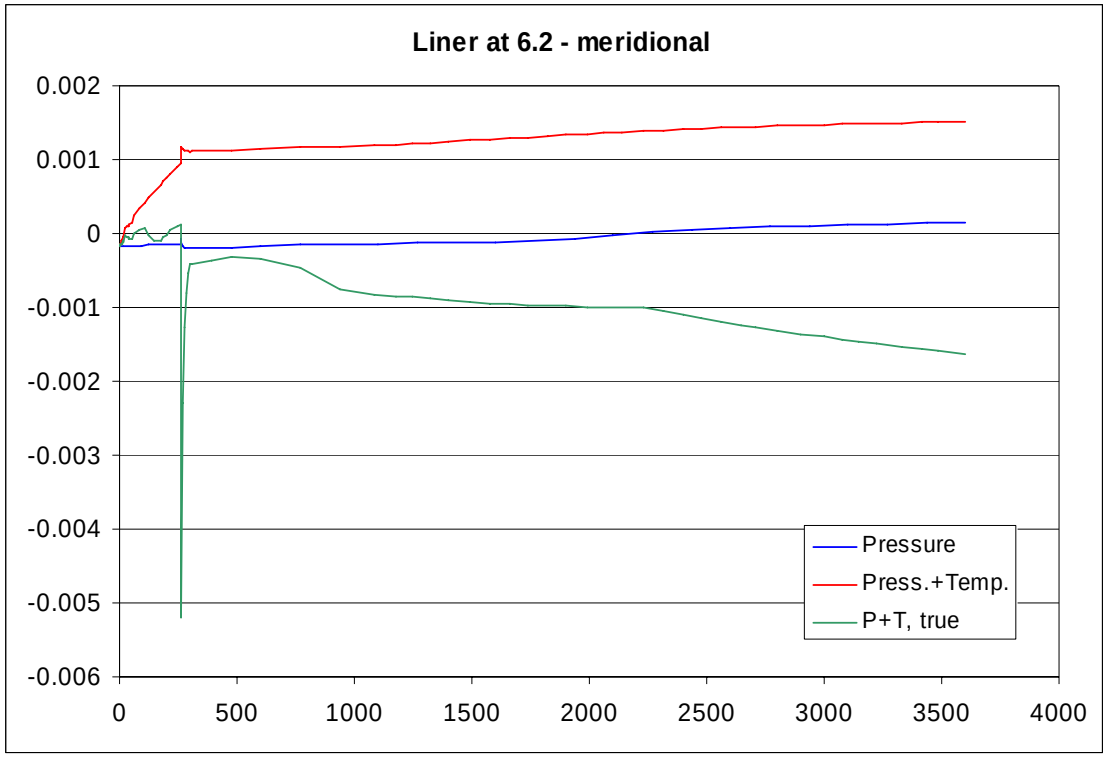

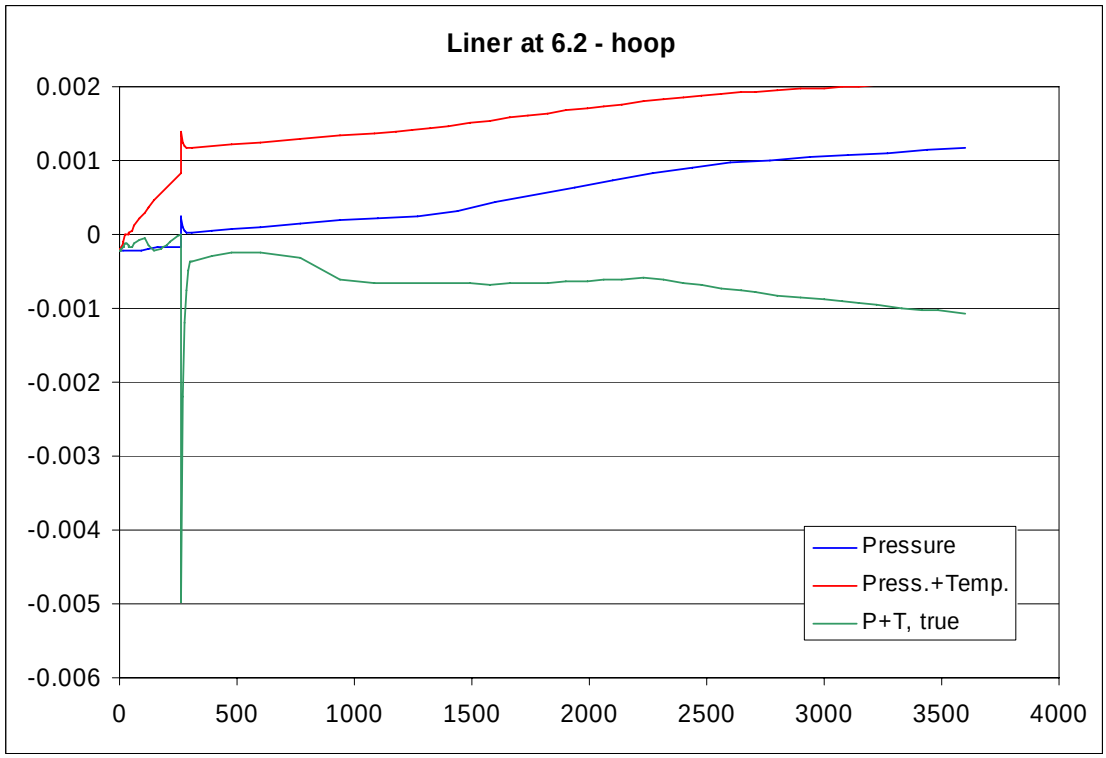

Figure 22 Case 2:Comparison of liner strain at 135° (m/m, MPa)

Appendix E: Fortum Nuclear Services Ltd.
Phase 2: No report available
Phase 3: E-1 to E-7

Page intentionally left blank

International Standard Problem #48 Containment Capacity Phase 3 Calculation of Response Under Both Mechanical and Thermal Loading Report of Fortum Contribution

Pentti Varpasuo – Fortum Nuclear Services- (FINLAND)

1. BACKGROUND

In Sandia 1:4 Scale containment test there was no results supporting this calculation. Anyhow, it was decided in ISP -48 research group that taking account the transient in temperature was more realistic than a constant temperature analysis assumption. Thus the proposal made by IRSN was approved and the pressure and thermal loadings as defined in WASH1400 as the basis of round-robin analysis effort.

2. MODELLING APPROACH

2.1 Finite Element Model

The numerical analyses of the Fortum contribution have been performed using the general purpose finite element programs MSC.Nastran and ABAQUS/Standard and ABAQUS/Explicit. To predict the inelastic response of the tested structure the finite element model of the structure was developed. Figure 1 shows the global 3-D finite element mesh of the scale model of the containment.
Four-node quadrilateral shell elements were used to represent the containment shell. A discrete modelling was adopted to represent the tendons in the containment wall through the use of two-node beam elements. Perfect bond between tendon elements and concrete was assumed in analysis.
Non-linear inelastic behaviour was assumed for the entire wall structure (concrete and steel elements).

The size of the finite element model is 22000 node points 65 000 elements and 130 000 degrees of freedom. All tendons in the model are modelled on individual basis. The rebars and the liner are not modelled explicitly. Their stiffness and strength are taken into account in the stress-strain curve of the concrete material.

At this stage of the analysis detailed post-tensioning losses and the their distribution along the tendons are not evaluated explicitly. The stress in tendons is applied based on average value of calculated losses in previous containment design and analysis projects.
The definition of thermal loads is as follows:
Case1: Monotonically increasing static pressure and temperature (saturated steam conditions). The gradients were provide provided by SNL (see Ref 1.).
Case2: Station Blackout Scenario (NRC/SNL/DEA proposal plus hydrogen detonation defined by IRSN). The gradients were provide provided by SNL (see Ref 1.).

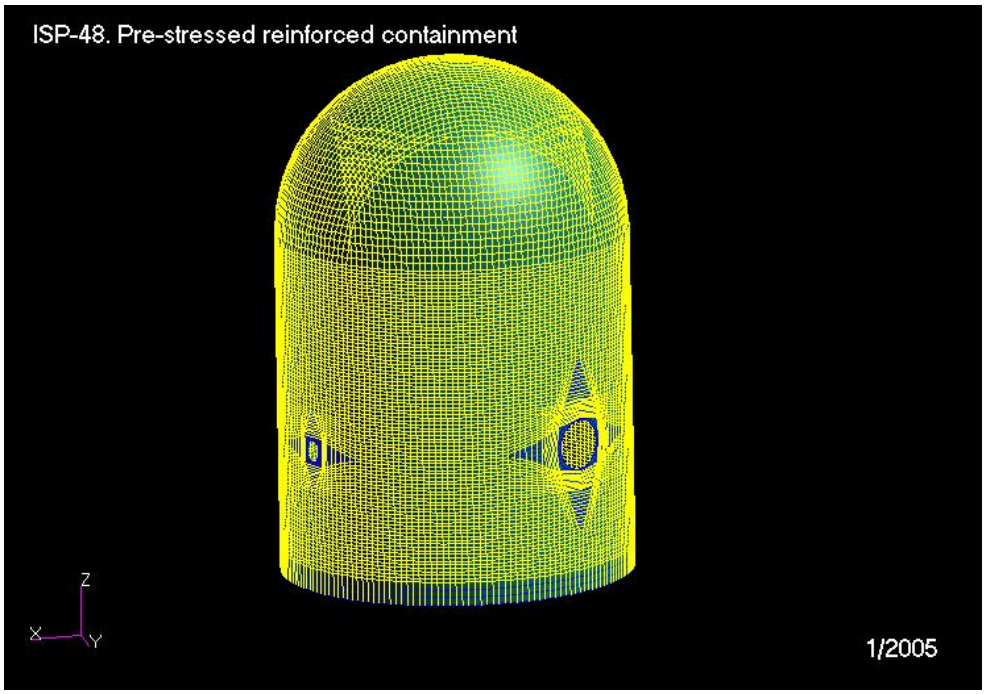

Figure 1: 3-D finite element mesh of the containment model

2.2 Material Constitutive Models

The concrete model that provides acceptable representation of the inelastic behavior of reinforced concrete under monotonous loading was adopted. The model is based on the nonlinear elasticity theory for un-cracked concrete. The concrete Young's modulus is 30000 MPa and the Poisson's ratio is 0.2. The non-linear stress strain relationship adopted for concrete material is depicted in Figure 2. For tendon steel the von Mises plasticity model was adopted. The parameter values were taken to be as follows: 1680 MPa for yield limit, 210 0000 MPa for Young's modulus and 0.3 for Poisson's ratio. The coefficient of thermal expansion for both steel and concrete was taken to be 1.E-5.

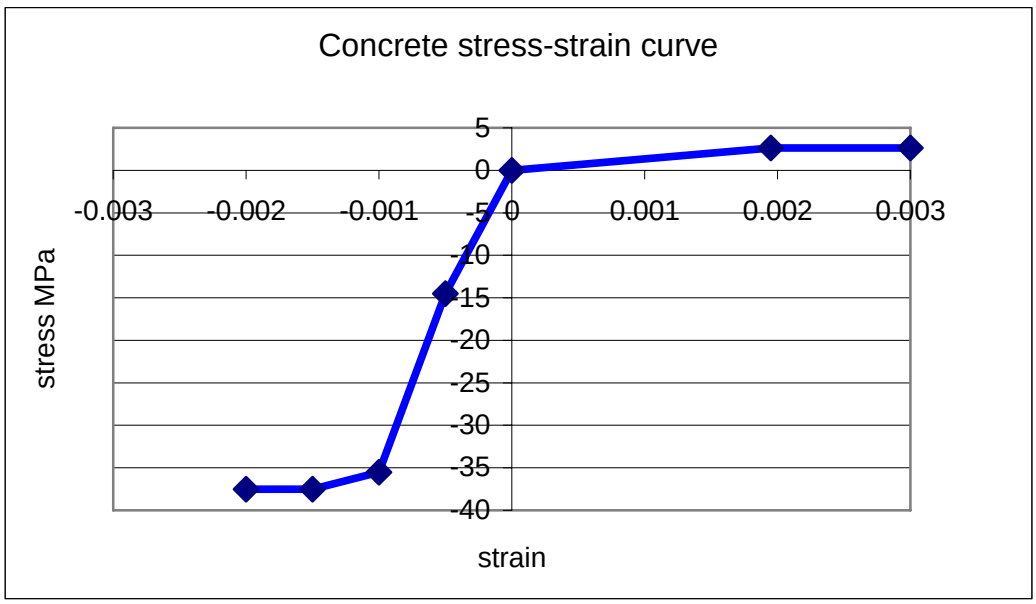

Figure 2 Concrete stress –strain curve

3. ANALYSIS AND RESULTS

All runs were performed as nonlinear static runs.

3.1 Transient without thermal load

The loads taken into account in this load case were the own weight, the post-tensioning load of tendons and the internal pressure transient up to failure.
In the following Figure 3 the radial displacement field is depicted at the Failure pressure of 1.71 MPa. The units of displacements are meters.

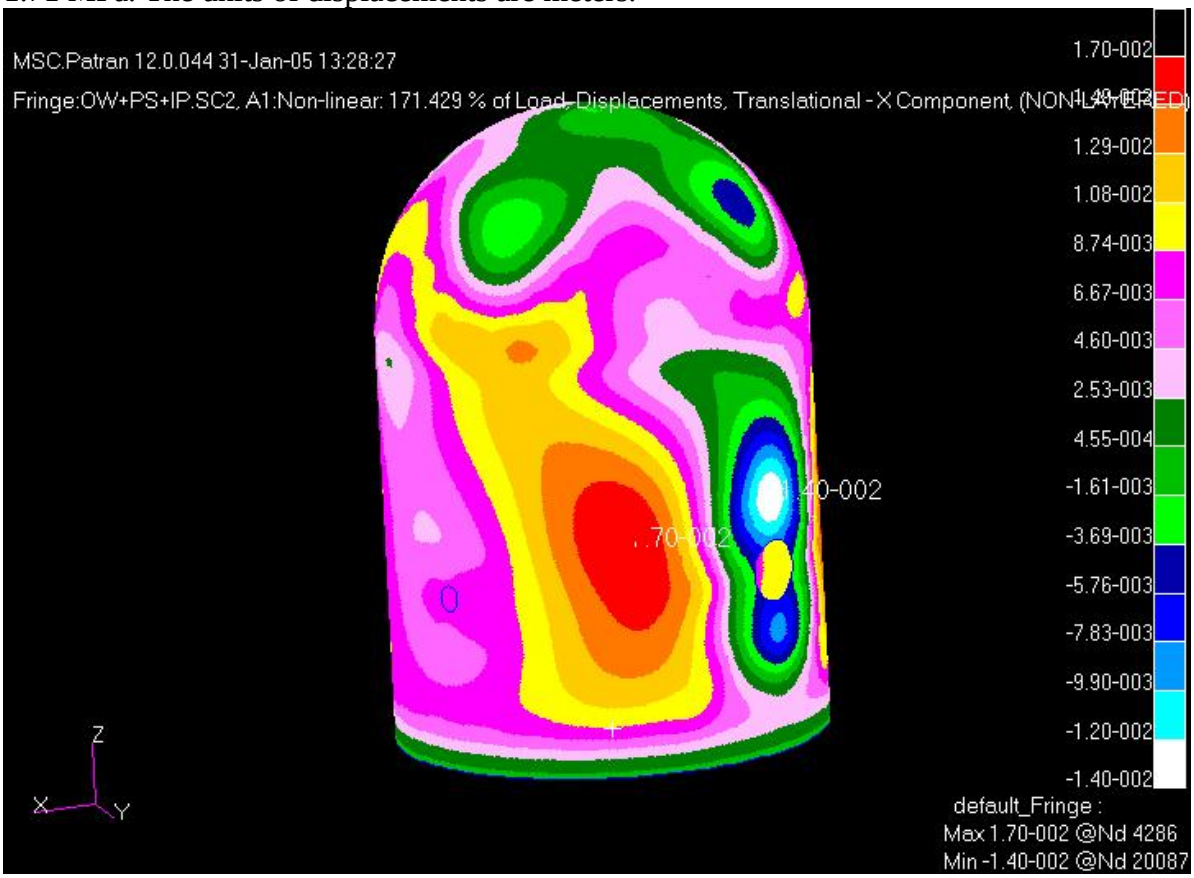

Figure 3 Radial displacement field at failure for load case without thermal gradient

3.2 Transient with thermal load of Case 1

The loads taken into account in this load case were the own weight, the post-tensioning load of tendons, the thermal load of Case 1 and the internal pressure transient up to failure.
In the following Figure 4 the radial displacement field is depicted at the Failure pressure of 1.78 MPa. The units of displacements are meters.

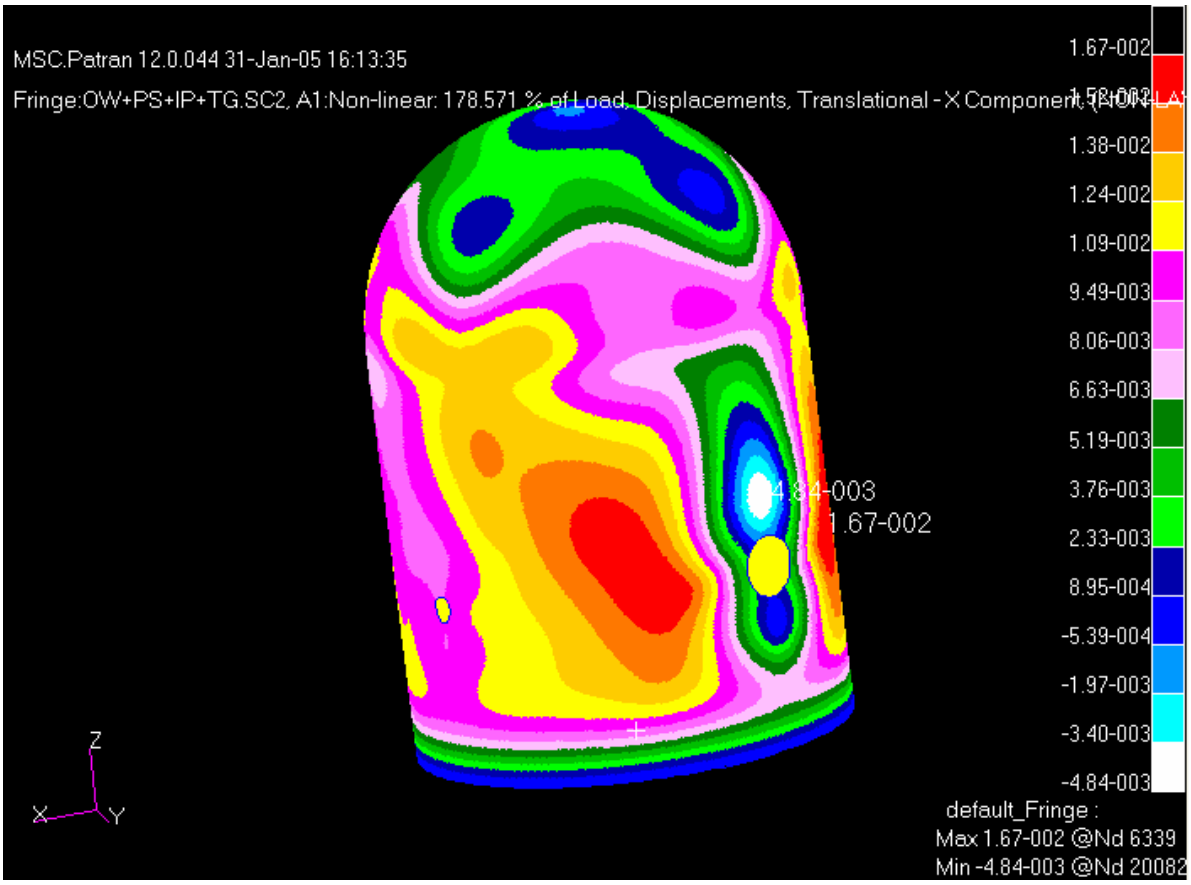

Figure 4 Radial displacement field at failure for load Case 1

3.3 Transient with thermal load of Case 2

The loads taken into account in this load case were the own weight, the post-tensioning load of tendons, the thermal load of Case 2 and the internal pressure transient up to failure.
In the following Figure 5 the radial displacement field is depicted at the Failure pressure of 1.78 MPa. The units of displacements are meters.

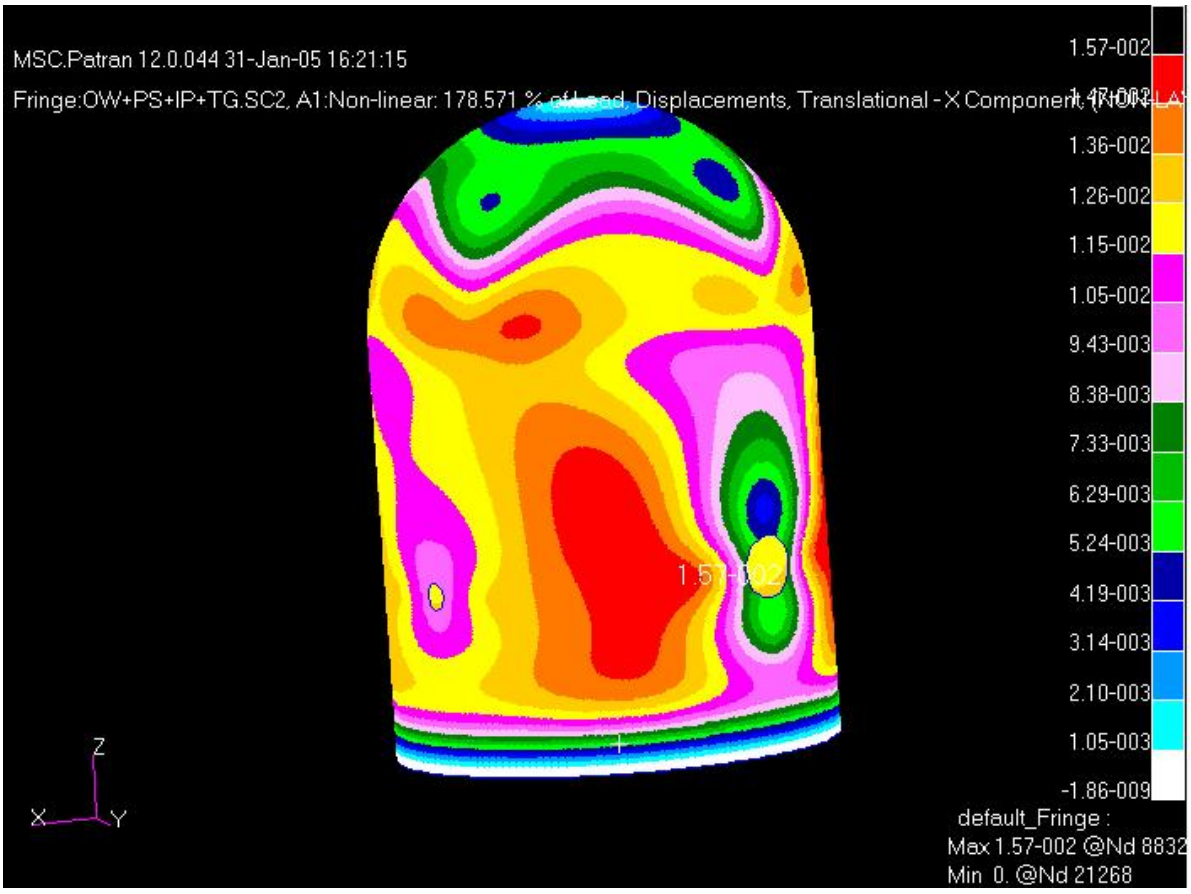

Figure 5 Radial displacement field at failure for load Case 2

4. CONCLUSION

This document gave the short brief of the Fortum approach and basic results of ISP-48 Phase 3 containment scale test model analysis effort.

REFERENCES

R. Dameron, M. Wolohan, B. Hansen, E. Kelley, M. Hessheimer, Analysis of Axisymmetric Prestressed Concrete Containment Vessel (PCCV) Including Thermal Effects A Summary of Temperature Section Results, Analytical Assumptions and Technical Approach for use by the ISP48, David Evans and Associates, Inc. and, Sandia National Laboratories, May 27, 2004, Revised August 19, 2004.

MacNeal-Schwendler Corp., MSC. Nastran ver. 70.1, User's manual, Los Angeles, CA, 2001.

Hibbit,Karlsson&Sorensen Inc., Abaqus/Standard, Abaqus/Explicit, User's manual, Boston, MA, 2003.

Appendix F: Gesellschaft für Anlagen und Reaktorsicherheit mbH
Phase 2: F-1 to F-24
Phase 3: F-25 to F-66

Gesellschaft für Anlagen-
und Reaktorsicherheit
(GRS) mbH

Structure mechanics analysis of the prestressed concrete model containment tested at Sandia National Laboratories – Contribution to International Standard Problem (ISP) 48

Technical Report

H. Grebner
J. Sievers

December 2003

BMWA-Project: RS 1154

Structure mechanics analysis of the prestressed concrete model containment tested at Sandia National Laboratories -

Contribution to International Standard Problem (ISP) 48

H. Grebner, J. Sievers
Gesellschaft für Anlagen- und Reaktorsicherheit (GRS) mbH, Köln, Germany

Introduction

Tests of the failure behaviour of a 1:4 scaled prestressed concrete containment vessel were performed at Sandia National Laboratories (Albuquerque, New Mexico) in the years 2000 and 2001. **Fig. 1** gives a schematic view of the containment model.

In combination with the tests calculations were carried out by several institutions. After completion of the tests the International Standard Problem ISP 48, supported by CSNI-IAGE working group, was defined to perform an international comparative study on the present state of analysis methods used for the assessment of prestressed concrete containments concerning load-carrying capacity and leaktightness. Especially the failure behaviour as well as the estimation of leak rates through cracks in the steel liner and the concrete are of interest. GRS participates in ISP 48. In the following preliminary analysis results are summarized.

Basis of the standard problem is the so-called limit state test [1] which was finished with an internal pressure of 1.3 MPa (about 3.3 times design pressure). At this pressure the leak rate through leaks in the steel liner and the concrete was higher than the amount which could be compensated by the nitrogen supply system.

GRS – Finite-Element-Model

Up to now an axisymmetric model is used without consideration of geometric inhomogenities due to penetrations in the wall. **Fig. 2** shows the model and its main components.The steel liner at the inner surface and the concrete parts are made of 8-node isoparametric elements with 4 integration points, while the rebar and tendon parts

are modelled as truss elements (with 3 nodes for the meridional and radial ones and one node for those in hoop direction). A stiff coupling between steel and concrete is simulated. Dimensions and material data are taken from [1].

For the liner and the rebar elements elastic-plastic material models with multi-linear stress-strain curves are used (see **Fig. 3**). The behaviour of the tendons is simulated by a nonlinear-elastic material model (also shown in **Fig. 3**). The end points of the curves correspond with the uniaxial rupture strains of the materials. As the rebar and tendon elements behave primarily uniaxial the end values of the curves in Fig. 3 may be used directly for the assessment of rebar and tendon elements. In the case of the liner a reduction by the stress multiaxiality has to be taken into account. The concrete material model includes the formation of micro-cracks for tensile stresses exceeding a critical value as well as crushing for high compressive stresses. **Fig. 4** shows schematically the uniaxial stress-strain curve used in the model. **Tables 1** to **4** show the material data used as input for the Finite-Element-Calculations. For the calculations the Finite-Element-Program ADINA [2] was used.

The prestressing of the tendons is simulated by initial strains in the respective truss-elements. The containment model is loaded by increasing internal pressure.

Analysis results

In the calculations small increments are used for the increase of the internal pressure (totally about 1200 time steps). Despite of this, convergence problems arise and above about 1.0 MPa internal pressure the calculation is performed without equilibrium iterations. As discussed in [3] the error caused by such a proceeding may be neglected.

Some typical results are presented in the **Figs. 5** to **28**.

Figs. 5 to **8** show the deformation of the complete model for different values of internal pressure.

The development of circumferential micro-cracks in the cylindrical part of the model is presented in **Fig. 9**. Only a small pressure increment (about 0.01 MPa) is necessary to get from only a few micro-cracks to a situation with micro-cracks at all integration points

through the wall at the section shown in Fig. 9. The formation of radial micro-cracks in the cylinder starts at a higher pressure level (about 0.9 MPa as shown in **Fig. 10**). Above 1.1 MPa also meridional micro-cracks are found.

Figs. 11 to **28** give a compilation of the results at the standard output locations contributed by GRS to ISP 48, especially displacements and strains of the liner, the rebars, the tendons and the concrete.

A few examples of comparisons between calculation and measurement are shown in **Figs. 14** to **16**, **19**, **20**, **24** and **26** to **28** for locations in the cylindrical part of the model. While **Figs. 14** and **15** present the radial displacement at the inner surface of the liner, **Fig. 16** shows the vertical displacement at the transition of cylindrical part to dome. The other figures show comparisons of the strain from measurement and calculation for the liner (**Figs. 19** and **20**), a hoop rebar (**Fig. 24**), 2 hoop tendons (**Figs. 26** and **27**) and the concrete (**Fig. 28**).

For pressure loading up to 0.6 MPa (about 1.5 times design pressure) the calculated results of displacements and strain in the liner, the rebars, the tendons and the concrete agree very well with measured data. Major differences between experiment and analysis are found in the pressure region of about 0.6 to 0.74 MPa. In this pressure region the deviations may be due to a too stiff coupling of concrete and steel in our Finite-Element-Model, which will be investigated by further studies.

In the pressure region 0.74 to 0.75 MPa the formation of micro-cracks predominantly in circumferential direction is calculated.

For the pressure region 0.75 to 1.0 MPa mostly a good coincidence of calculation and measurement is found. Above 1.0 MPa plastification starts in the hoop rebars and again larger differences between experiment and calculation are found. At maximum load (1.3 MPa) hoop tendon strains of nearly 1% are found, which is about 1/3 of the uniaxial rupture strain. The maximum strain values in the rebars and the liner lie below 1%. Thus a larger difference to the uniaxial rupture strain is found in this case.

The deformation behaviour of the dome part of the containment is not simulated very well by our Finite-Element-Model. This is partly due to the fact that an axisymmetric model is used which can not provide an adequate modelling of the hairpin tendons in the upper dome part. Furthermore the formation of micro-cracks and the post-cracking

stiffening behaviour have influence on the vertical deformation of the dome. Further investigations are in progress.

Summary

GRS participates in the International Standard Problem (ISP) 48 with Finite-Element-Calculations. An axisymmetric Finite-Element-Model was developed, in which the liner at the inner surface and the concrete parts are simulated by 8-node elements. Rebar and tendon parts are modelled by truss-elements. The necessary input-data for the nonlinear material models used are gained from Sandia-measurements. The model is loaded by the prestressing of the tendons and by increasing internal pressure (up to 1.3 MPa).

The analyses results in terms of displacements and strains in the liner, the rebars, the tendons and the concrete of the cylindrical part agree well with measured data up to about 0.6 MPa internal pressure (i.e. 1.5 times design pressure). First circumferential micro-cracks in the concrete are found at about 0.75 MPa. With increasing pressure micro-cracks are present through the whole wall. Above about 0.9 MPa the formation of micro-cracks in radial and meridional direction is calculated. At the maximum load (1.3 MPa) almost all concrete parts of the model have micro-cracks which may cause leaks.

Nevertheless the failure of the containment model is not expected for loads up to 1.3 MPa without consideration of geometric inhomogenities due to penetrations in the wall. Although the calculated strains in liner, rebars and tendons show some plastification, the maximum values are below the critical ones. The safety margin against failure is smallest in some hoop tendons.

At present parametric studies are performed to investigate the differences between calculations and measured data. Furthermore three-dimensional models are developed to simulate the wall penetrations in the Sandia containment model.

The work described in this Technical Report is sponsored by the German Ministry of Economics and Labor.

References

[1] Hessheimer, M. F., et al.: Overpressurization test of a 1:4 scale pre-stressed concrete containment model. NUREG/CR-6810 (2003).

[2] ADINA – A Finite-Element-Program for Automatic Dynamic Incremental Nonlinear Analysis, Version 8.1 – Theory and Modeling Guide, Volume I: ADINA. ADINA R&D, Inc. (2003).

[3] Bachmann, P., et al.: Analyse zur Bestimmung des Versagensdruckes und des Versagensverhaltens eines Stahlbetoncontainments im Maßstab 1:6 (Vorausberechnungen). GRS-A-1415 (1988).

Table 1: Material data of the liner steel (see Fig. 3)

General data		"True" stress-strain values for multilinear curve	
		Strain [-]	Stress [MPa]
		0.002	380
Young' modulus	219000 MPa	0.01	403
Poisson ratio	0.3	0.02	430
Density	7800 kg/m^3	0.03	452
		0.04	470
		0.05	480
		0.28	670

Table 2: Material data of the rebar steel

General data		"True" stress-strain values for multilinear curve	
		Strain [-]	Stress [MPa]
		0.002	420
Young' modulus	200000 MPa	0.01	455
Poisson ratio	0.3	0.03	520
Density	7800 kg/m^3	0.05	580
		0.075	620

Table 3: Material data of the tendon strands

General data		"True" stress-strain values for nonlinear-elastic curve	
		Strain [-]	Stress [MPa]
		0.0	0
Young's modulus	216200 MPa	0.0074	1600
Poisson ratio	0.3	0.0080	1650

Density	7800 kg/m^3	0.0092	1734
		0.0100	1760
		0.0200	1880
		0.0325	2000

Table 4: Material data of the concrete (see Fig. 3)

Density	2176 kg/m^3
Initial Youngs' modulus	27000 MPa
Poisson ratio	0.18
Maximum tensile stress	3.45 MPa
Strain at maximum tensile stress	0.000128
Parameter to describe post-cracking stiffening ξ	8
Maximum stress in compression	-47.3
Strain at maximum compressive stress	-0.00186
Strain at beginning of crushing	-0.0032
Stress at beginning of crushing	-30

Figures

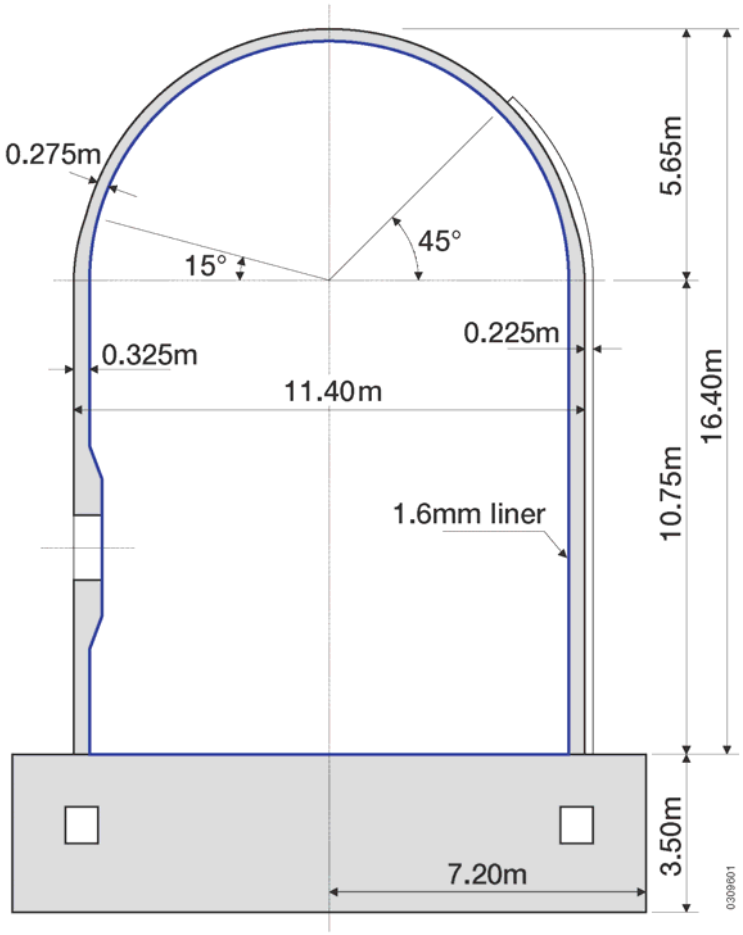

Fig. 1: Major dimensions of the containment model

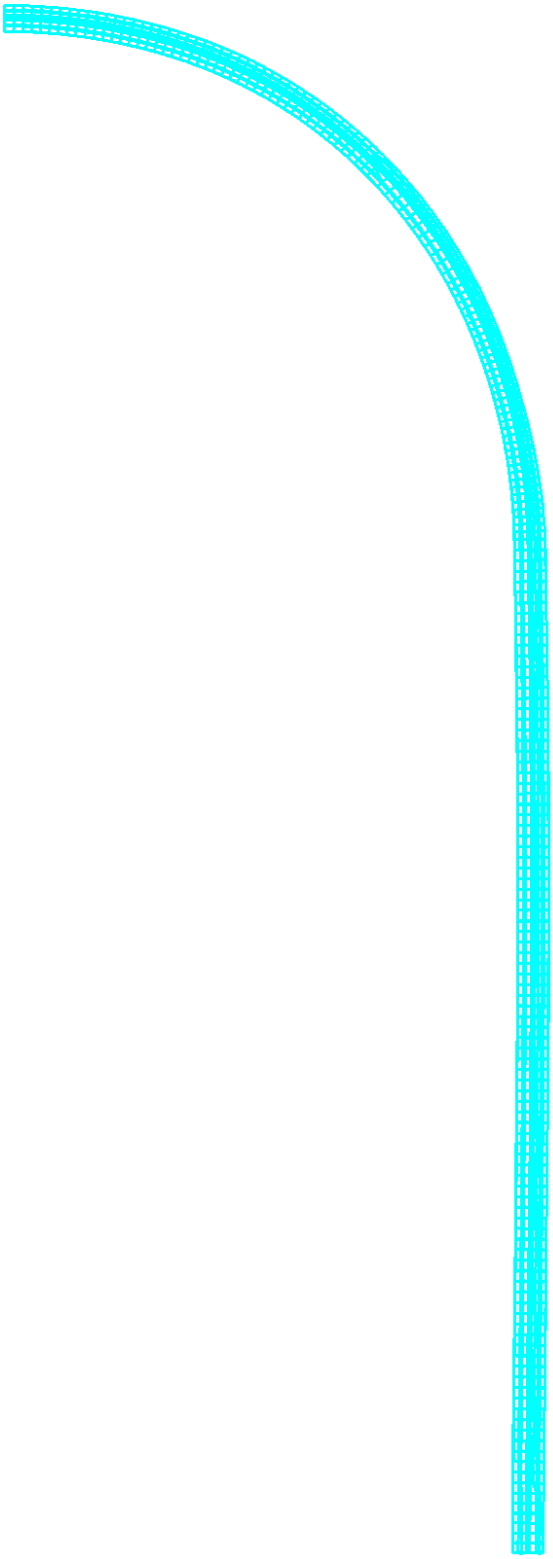

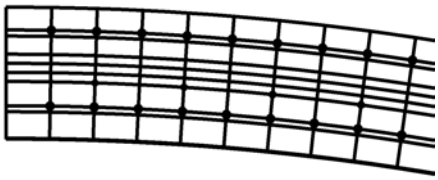

Part of the model (middle of dome, inner surface coated with metallic liner)

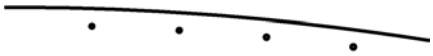

Tendons middle of dome

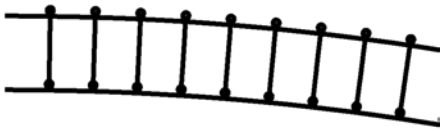

Rebar elements middle of dome

Axisymmetric model

Fig. 2: Finite element model of prestressed concrete model containment

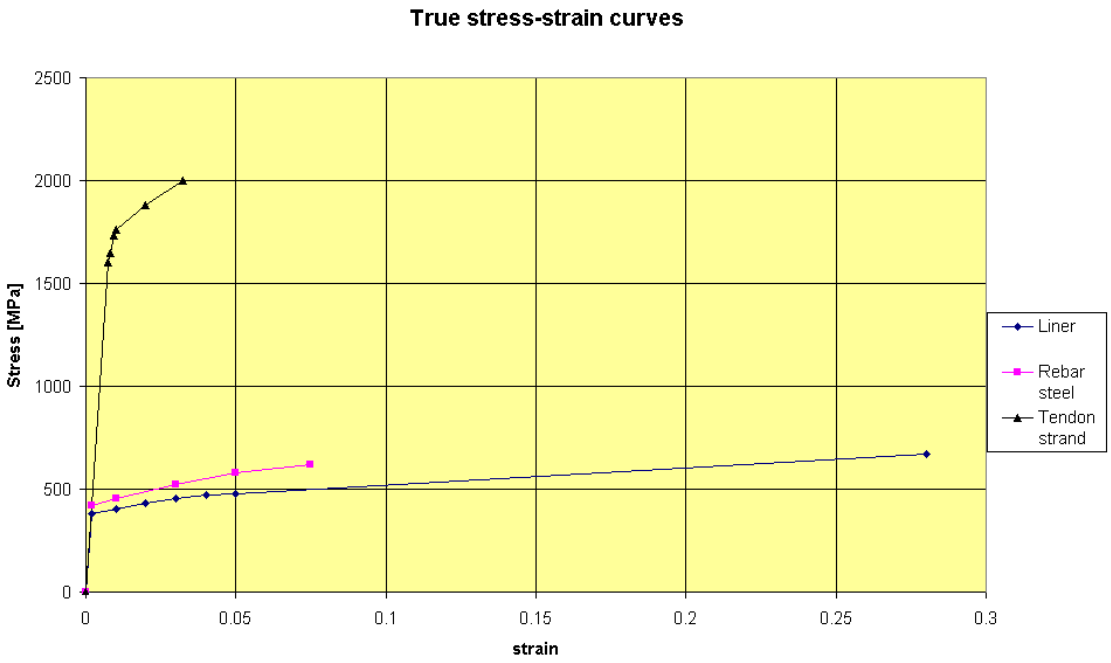

Fig. 3: True stress-strain curves of liner and rebar steel as well as tendon strand as used as input for the finite-element-calculations

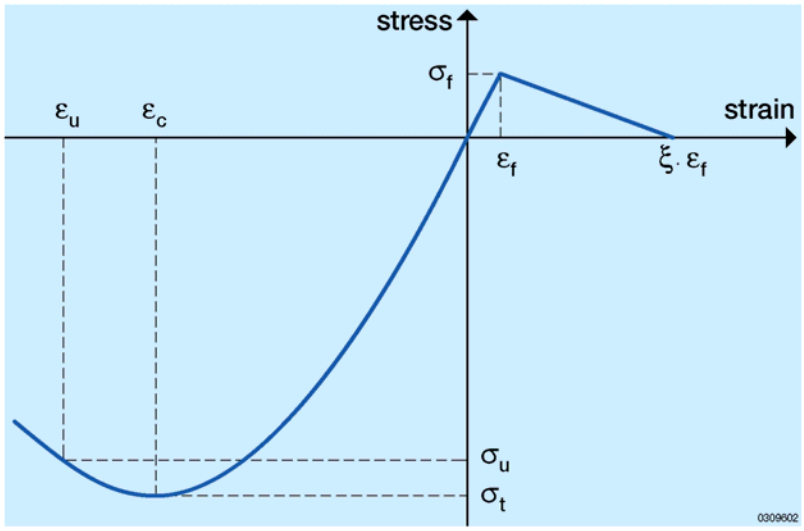

Fig. 4: Uniaxial stress-strain curve used in the concrete model

Fig. 5: Deformed model at 0.7 MPa (magnifcation of displacements = 50)

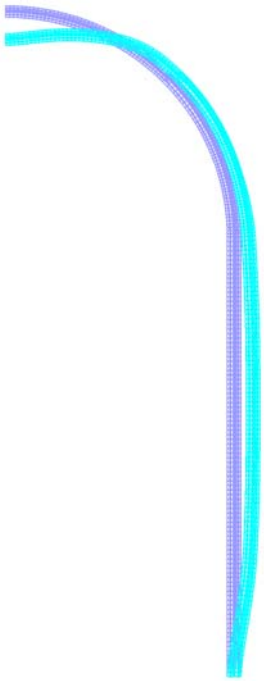

Fig. 6: Deformed model at 1.0 MPa (magnifcation of displacements = 50)

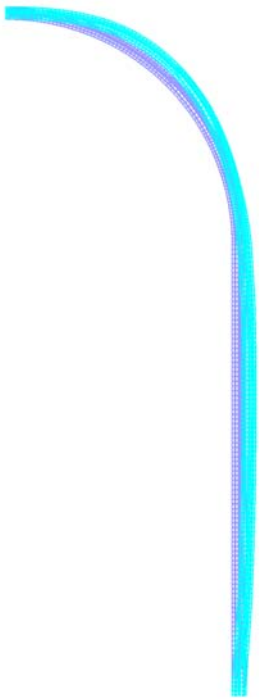

Fig. 7: Deformed model at 1.3 MPa (magnifcation of displacements = 10)

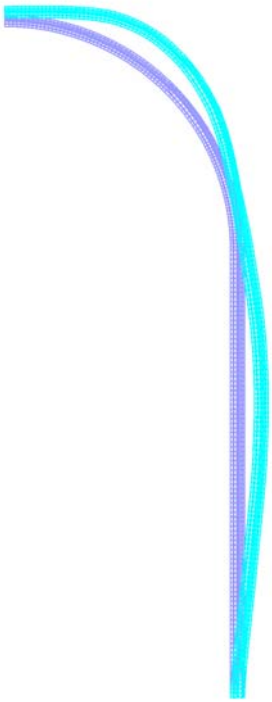

Fig. 8: Deformed model at 1.4 MPa (only in calculation, magnifcation of displacements = 10)

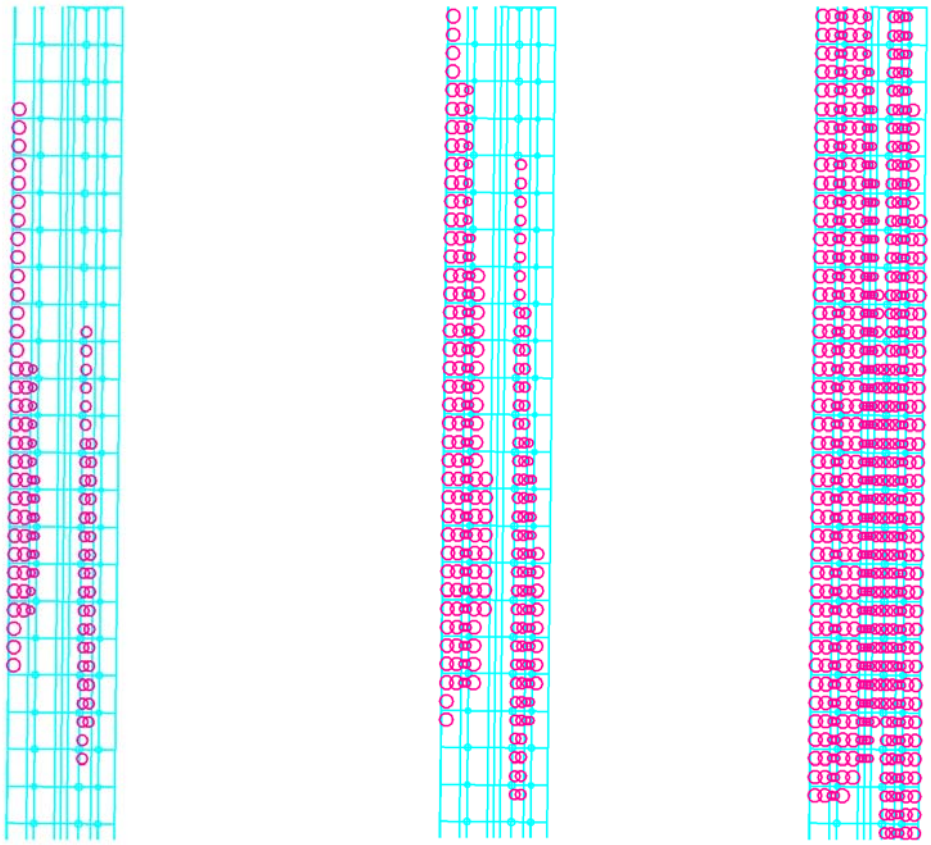

p = 0.740 MPa p = 0.742 MPa p = 0.745 MPa

Fig. 9: Development of circumferential micro-cracks (shown by red circles) in the cylindrical part of the model (height about 3 m)

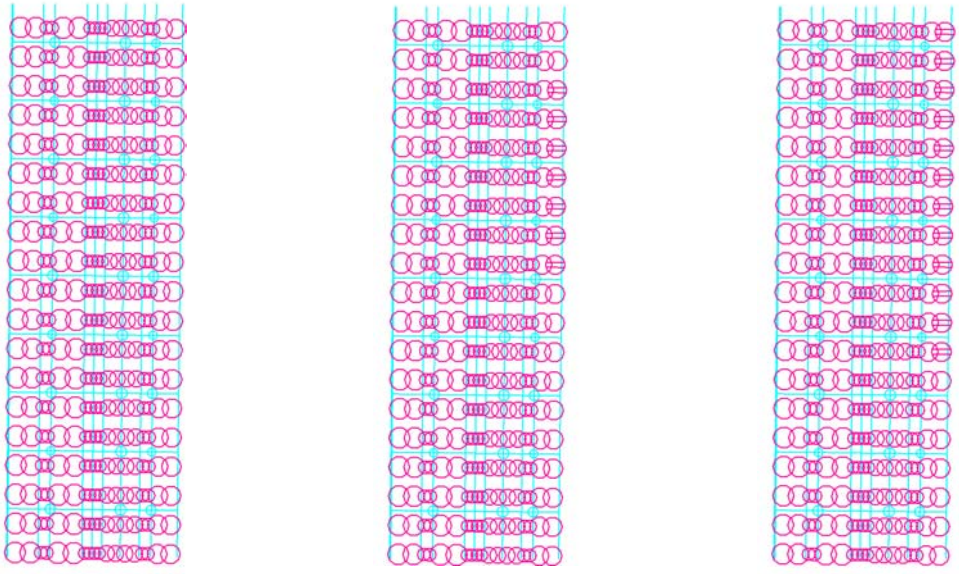

p = 0.910 MPa p = 0.915 MPa p = 0.920 MPa

Fig. 10: Development of circumferential and radial micro-cracks (parallel straight red lines) in the cylindrical part of the model (height about 3 m)

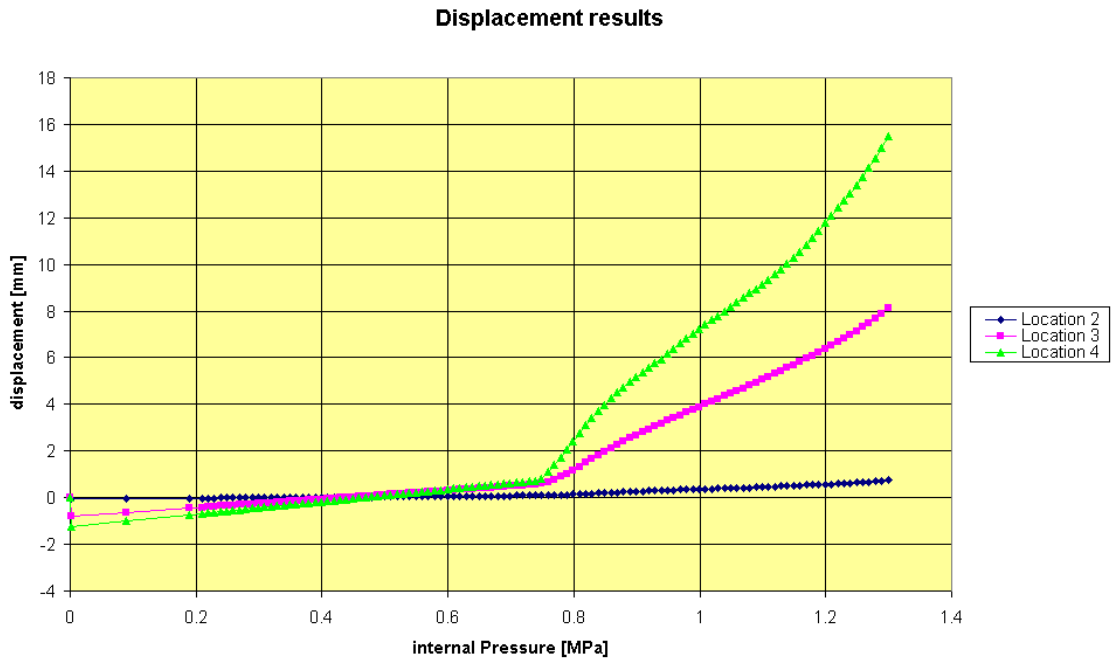

Fig. 11: Radial displacement results at inner surface of the liner (location 2: height 0.25 m, location 3: height 1.43 m, location 4: height 2.63 m)

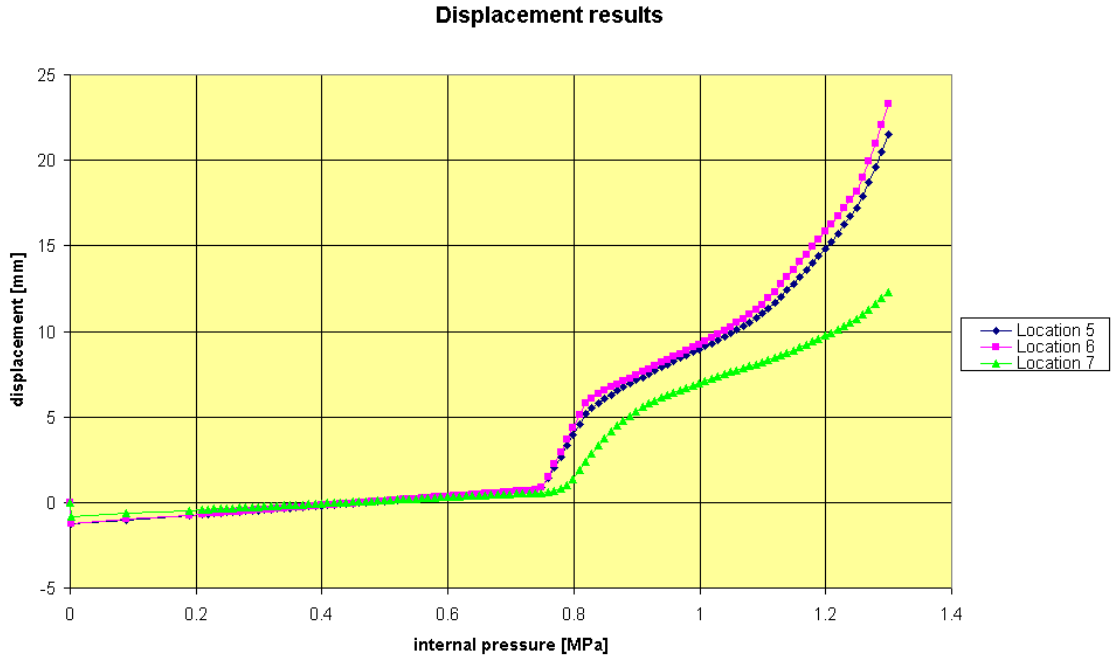

Fig. 12: Radial displacement results at inner surface of the liner (location 5: height 4.68 m, location 6: height 6.2 m, location 7: height 10.75 m)

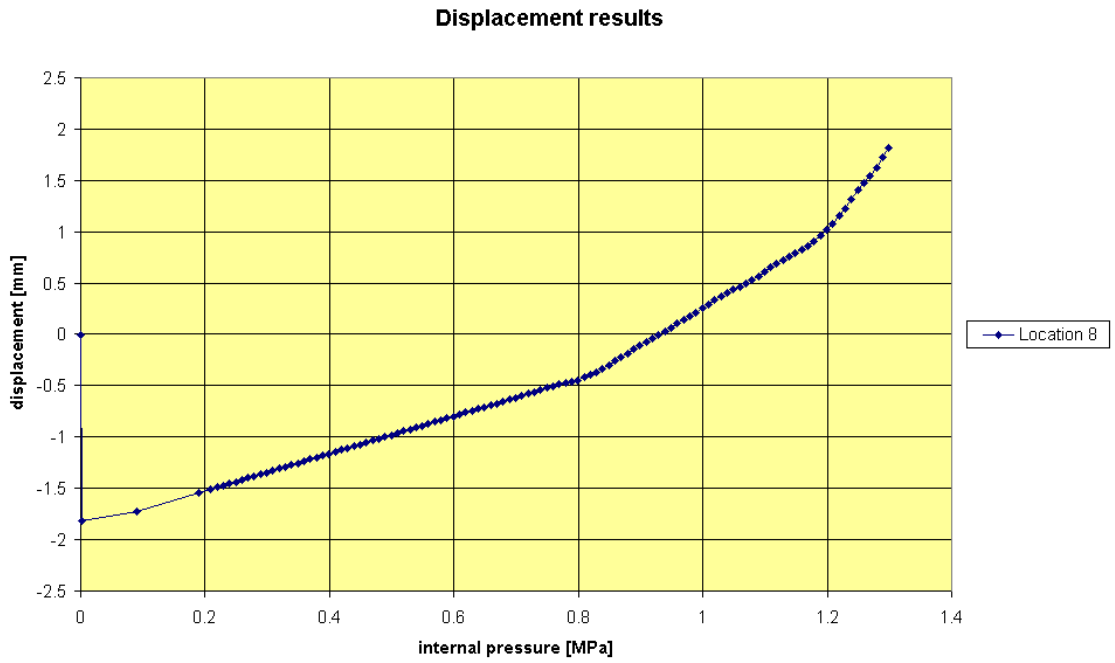

Fig. 13: Vertical displacement results at inner surface of the liner (location 8: height 10.75 m)

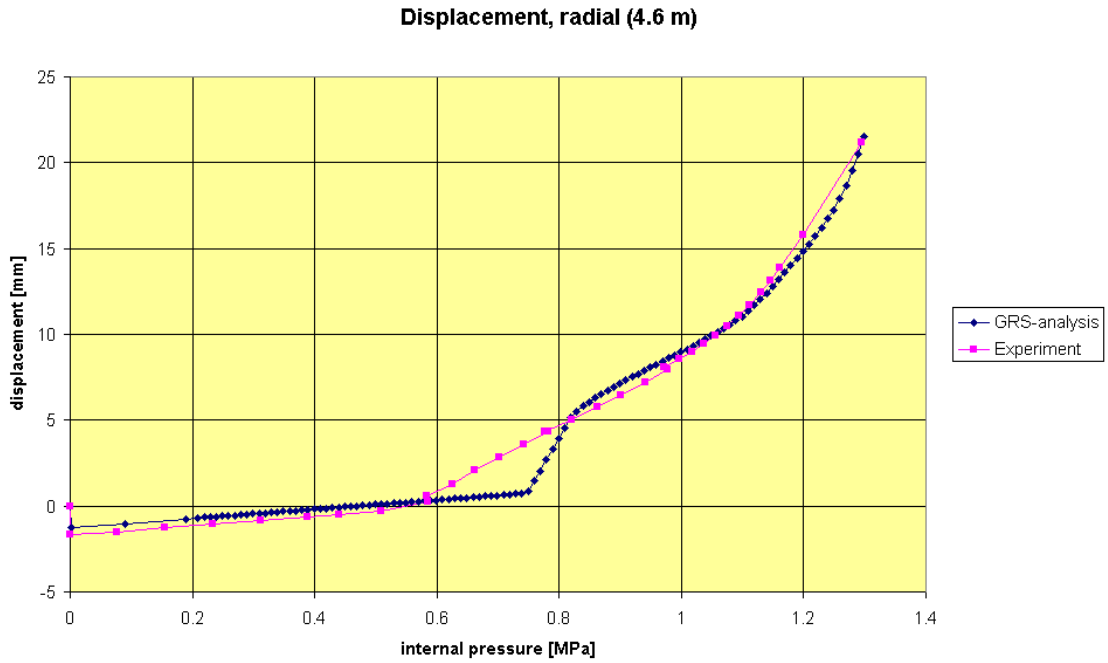

Fig. 14: Radial displacement at the inner surface of the liner (vertical position 4.6 m above top of basemat) from measurement and calculation

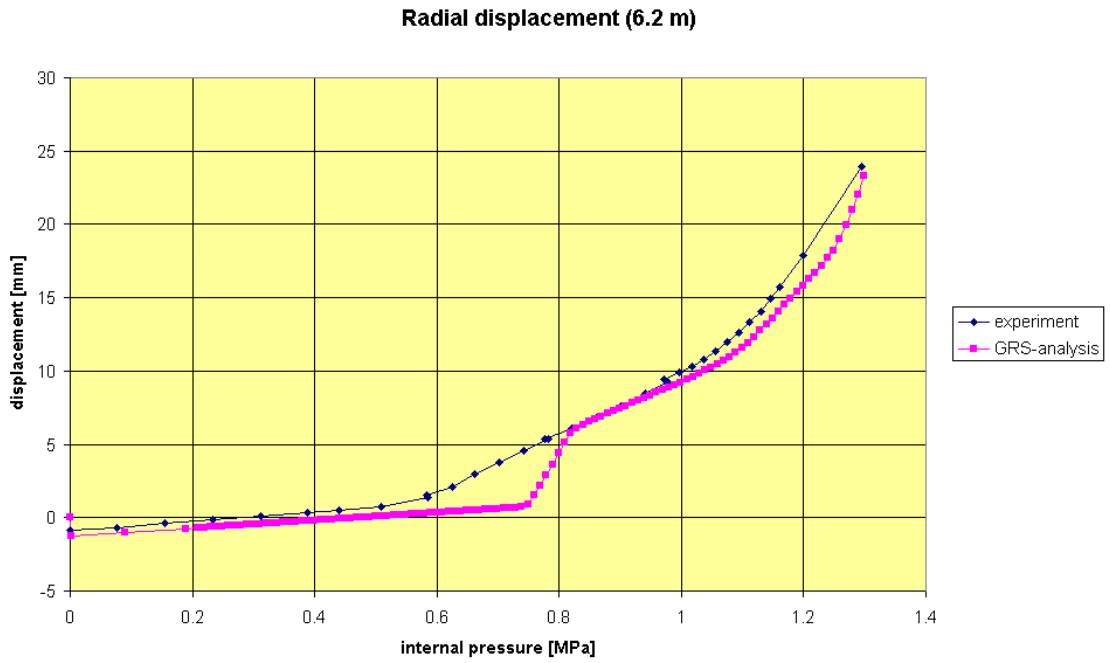

Fig. 15: Radial displacement at the inner surface of the liner (vertical position 6.2 m above top of basemat) from measurement and calculation

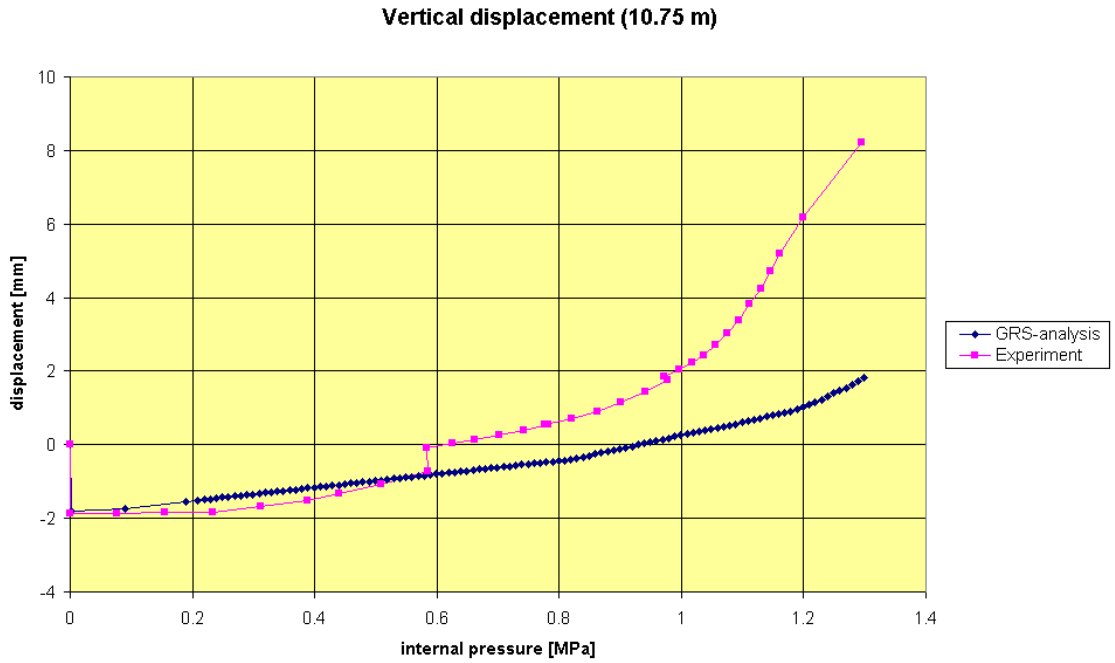

Fig. 16: Vertical displacement at the inner surface of the liner (vertical position 10.75 m above top of basemat) from measurement and calculation

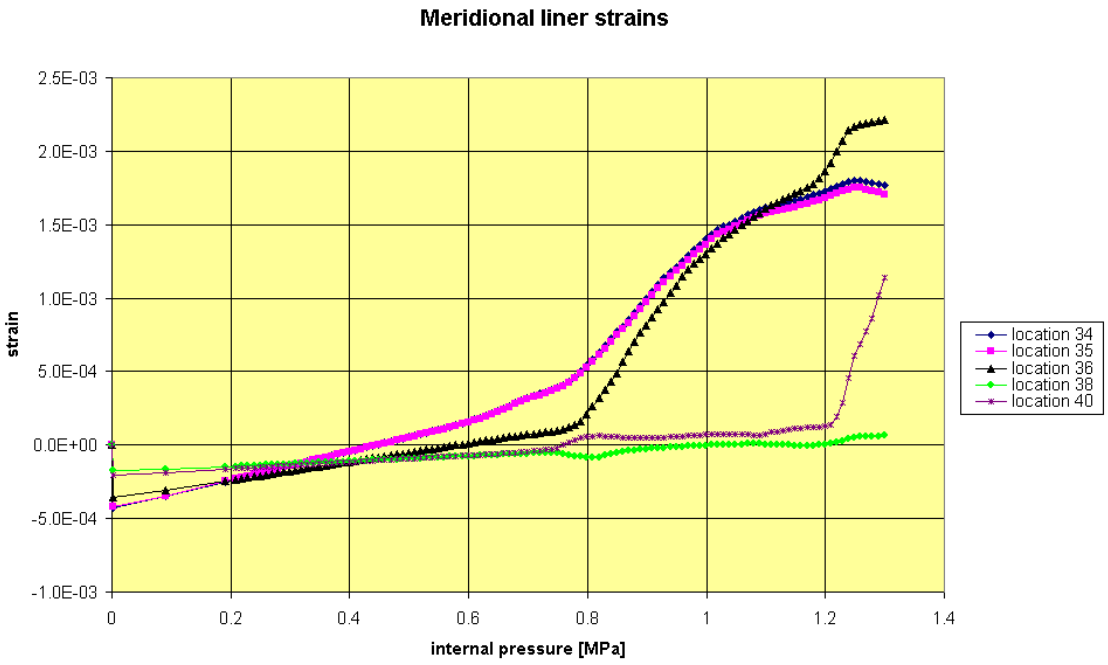

Fig. 17: Meridional liner strains at different standard output locations (location 34: height 0.01 m, location 35: height 0.01 m, location 36: height 0.25 m, location 38: height 6.2 m, location 40: height 10.75 m; all at inner liner surface except location 35, which is at outside liner surface)

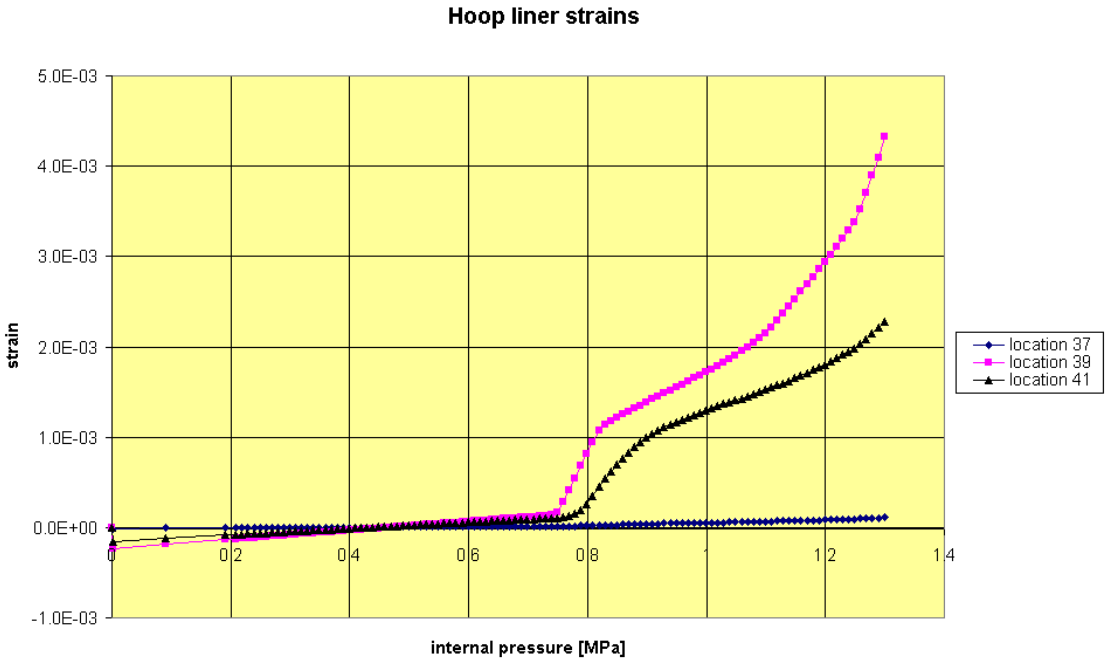

Fig. 18: Hoop liner strains at inner liner surface for different standard output locations (location 37: height 0.25 m, location 39: height 6.2 m, location 41: height 10.75 m)

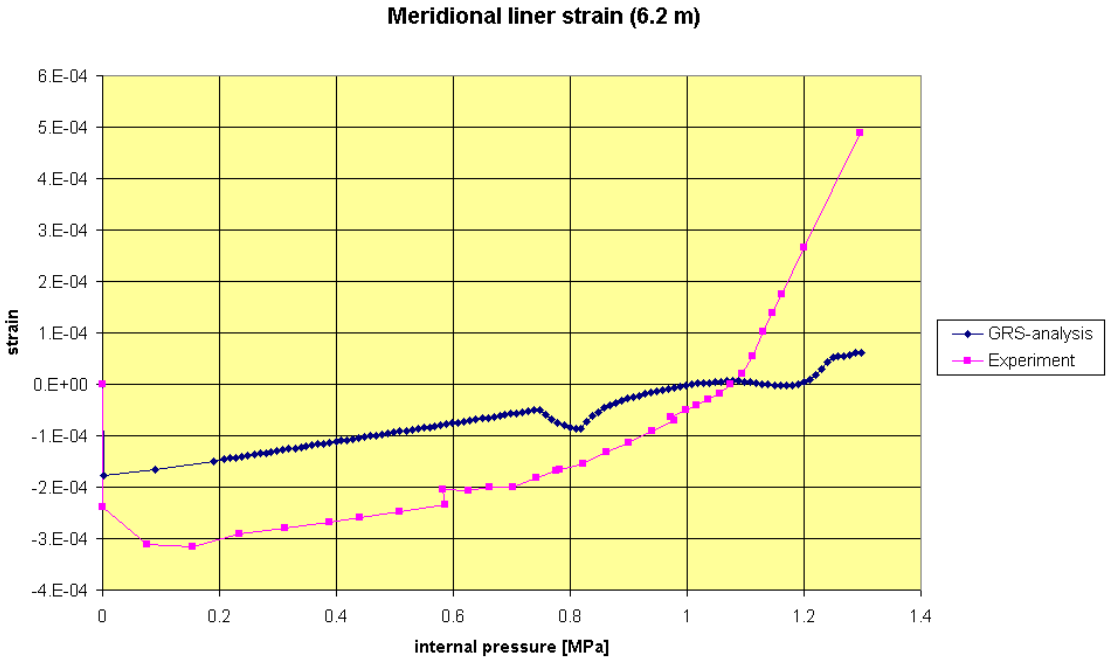

Fig. 19: Meridional strain in liner (vertical position 6.2 m above top of basemat) from measurement and calculation

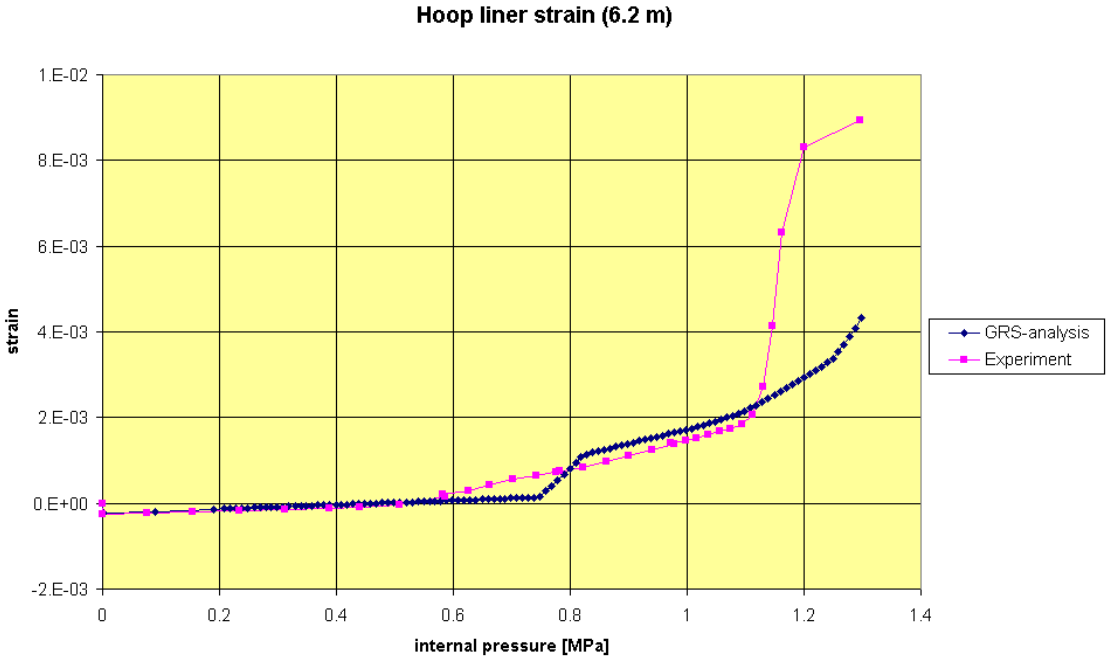

Fig. 20: Hoop strain in liner (vertical position 6.2 m above top of basemat) from measurement and calculation

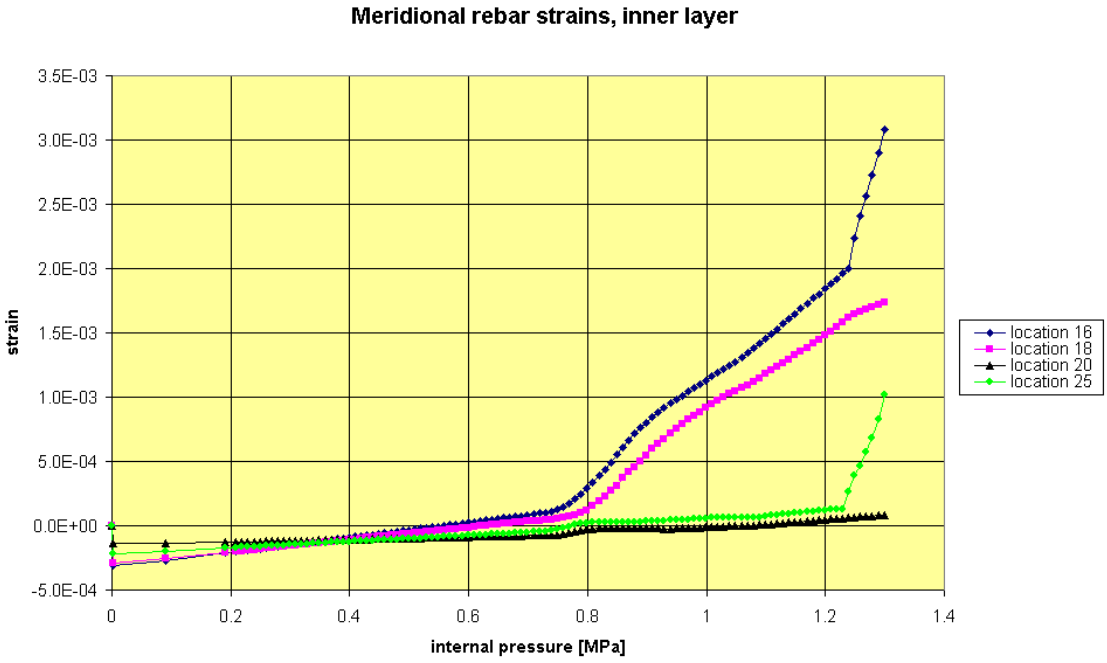

Fig. 21: Inner layer meridional rebar strains at different standard output locations (location 16: height 0.05 m, location 18: height 0.25 m, location 20: height 1.43 m, location 25: height 10.75 m)

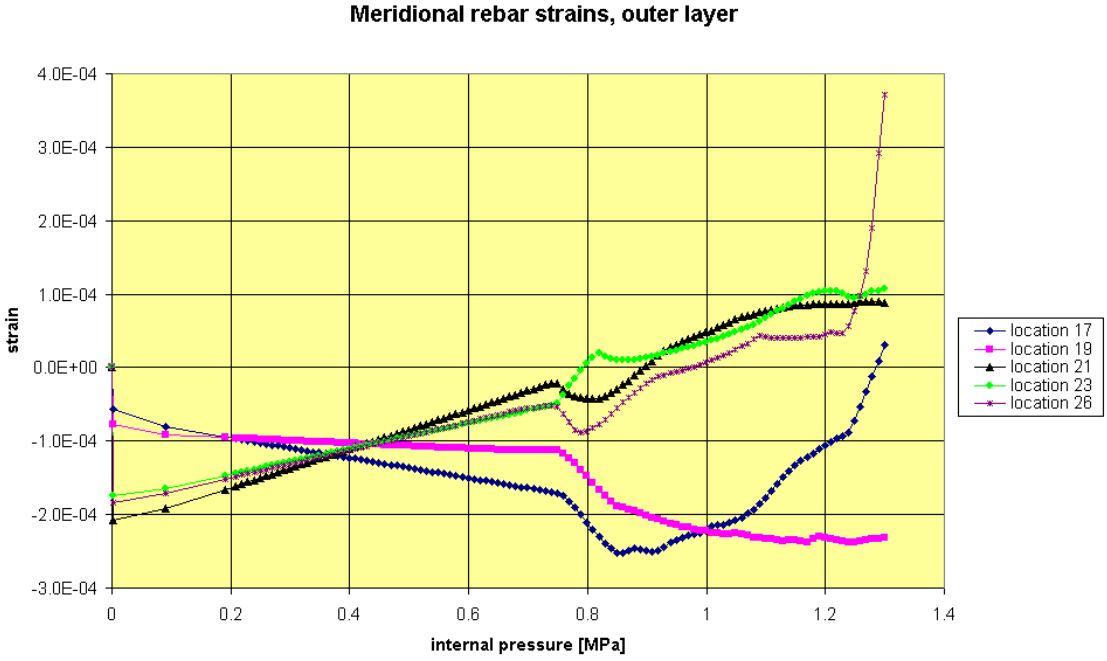

Fig. 22: Outer layer meridional rebar strains at different standard output locations (location 17: height 0.05 m, location 19: height 0.25 m, location 21: height 1.43 m, location 23: height 6.2 m, location 26: height 10.75 m)

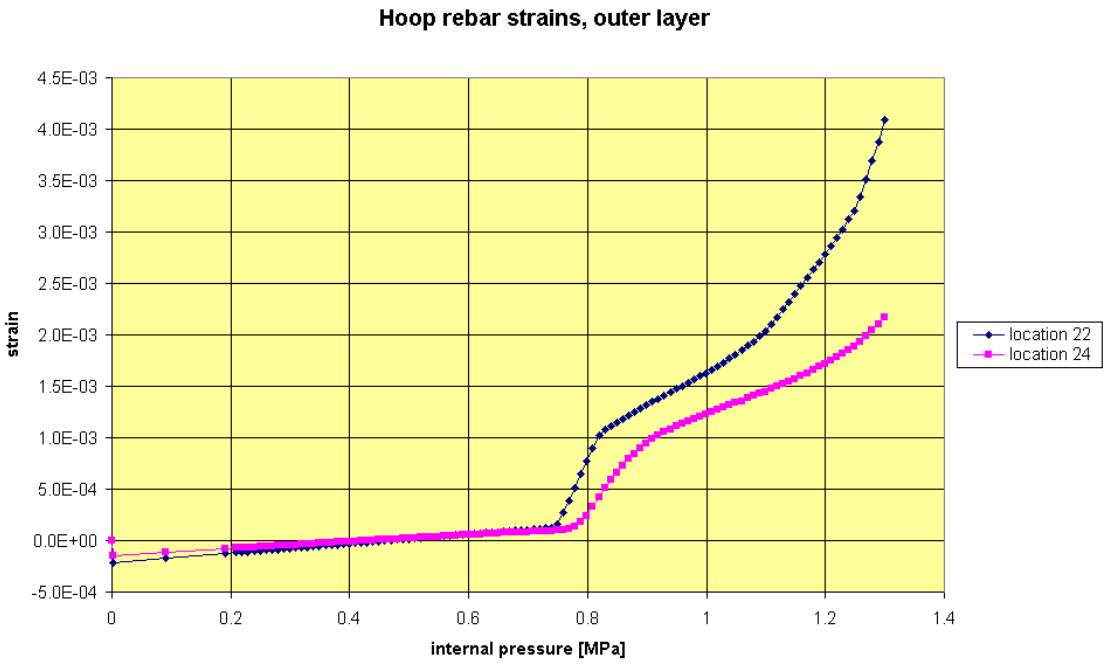

Fig. 23: Outer layer hoop rebar strains at different standard output locations (location 22: height 6.2 m, location 24: height 10.75 m)

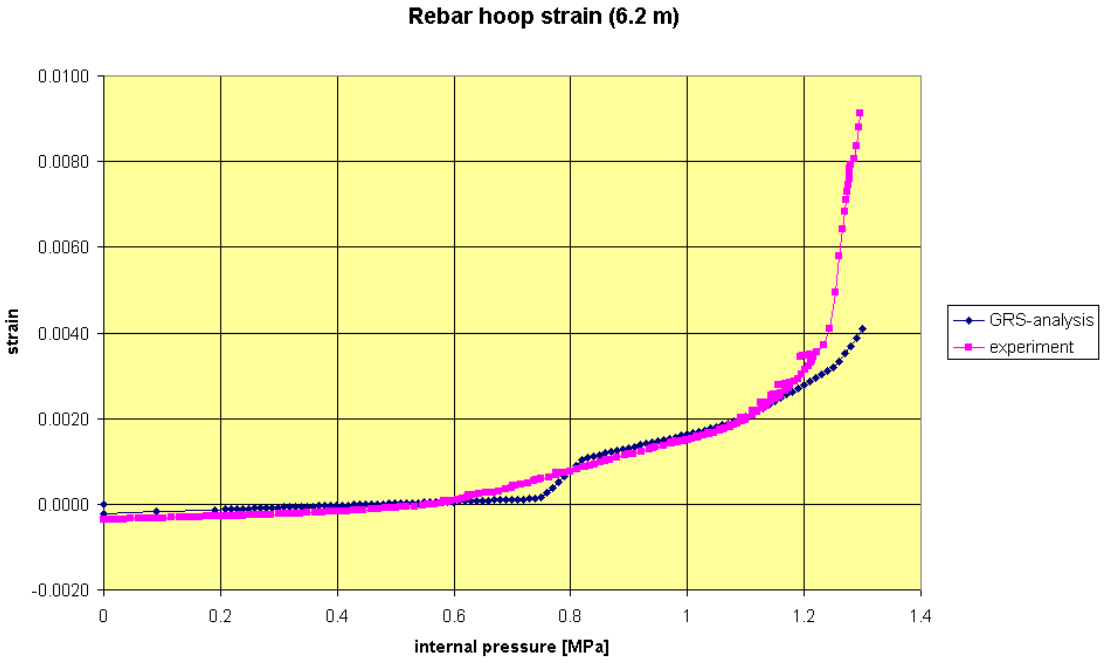

Fig. 24: Rebar hoop strain at outer hoop rebar (vertical position 6.2 m above top of basemat) from measurement and calculation

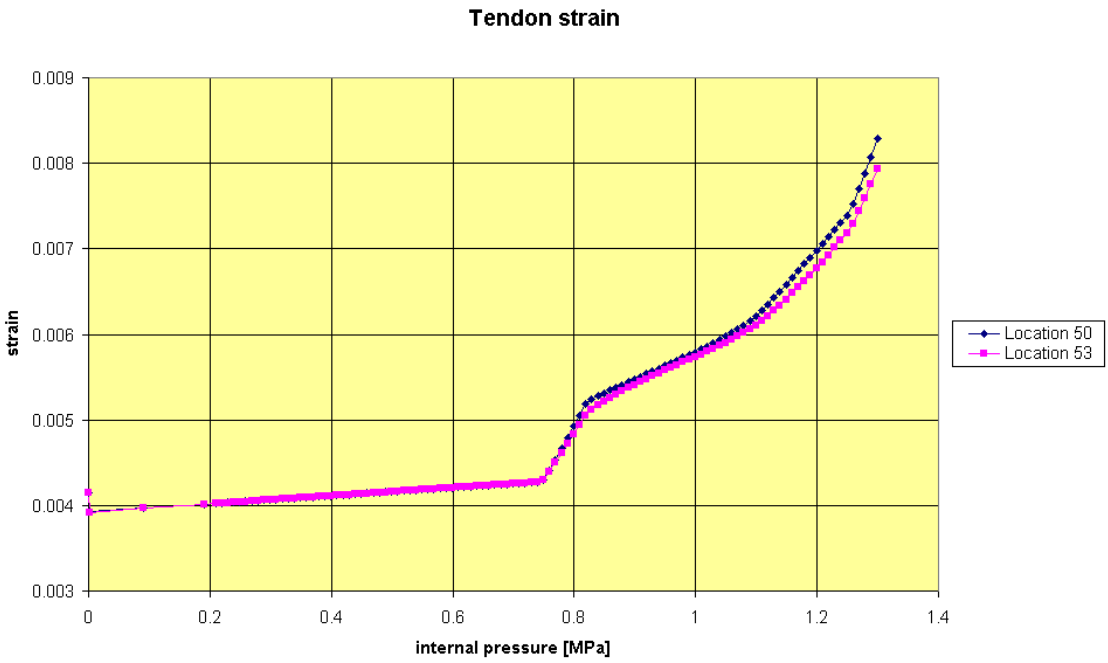

Fig. 25: Hoop tendon strains at different standard output locations (location 50: height 6.58 m, location 53: height 4.57 m)

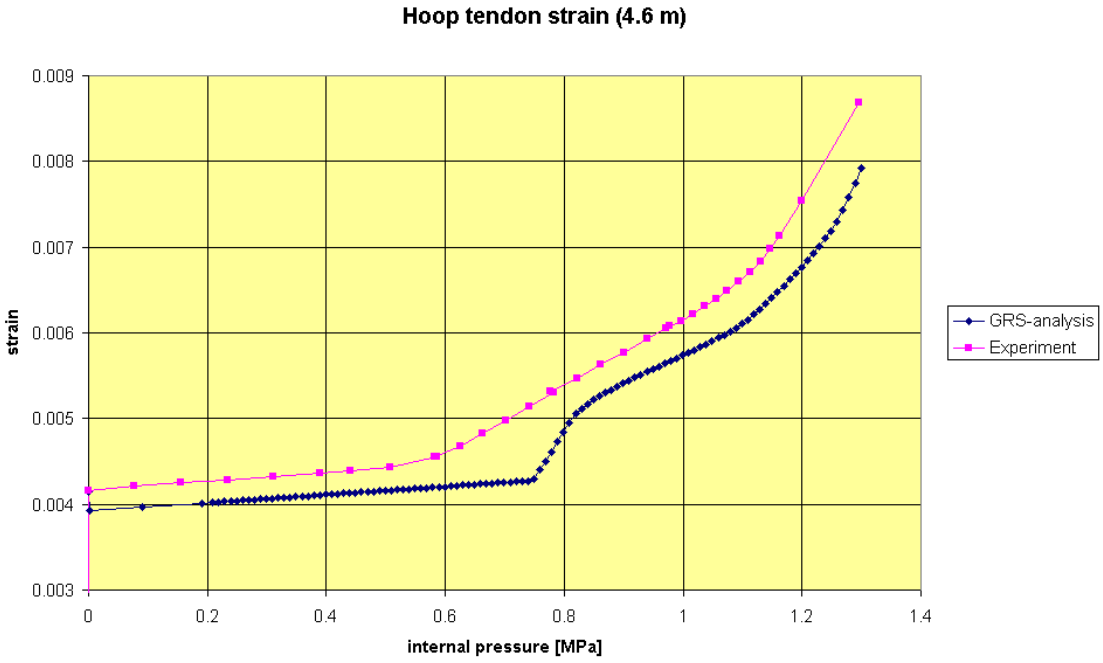

Fig. 26: Strain in hoop tendon (vertical position 4.6 m above top of basemat) from measurement and calculation

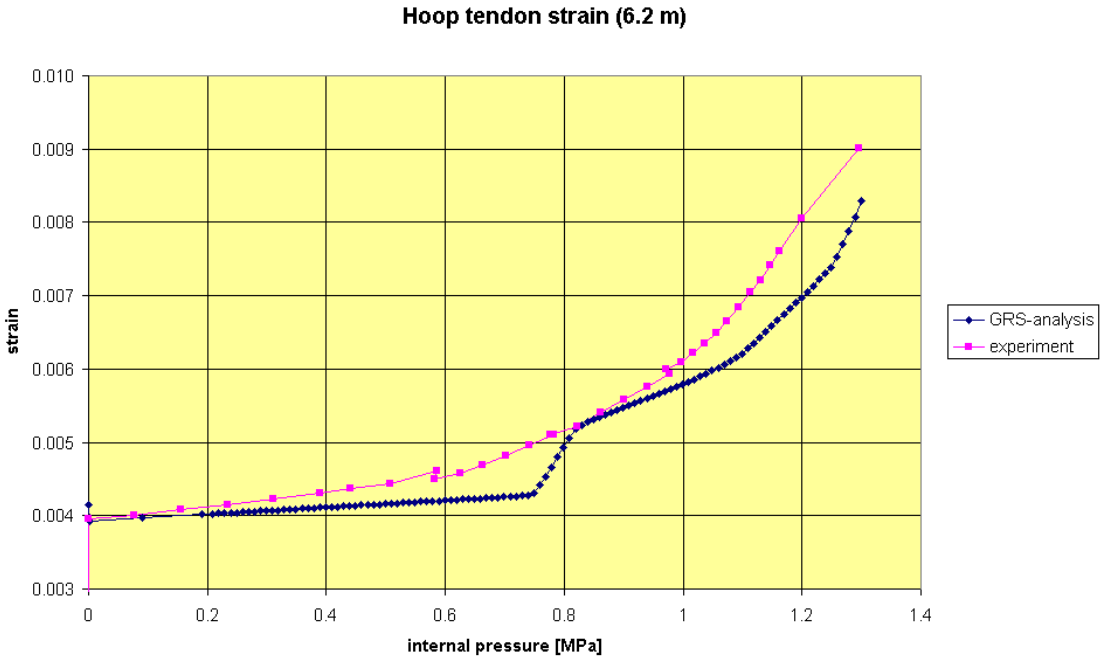

Fig. 27: Strain in hoop tendon (vertical position 6.2 m above top of basemat) from measurement and calculation

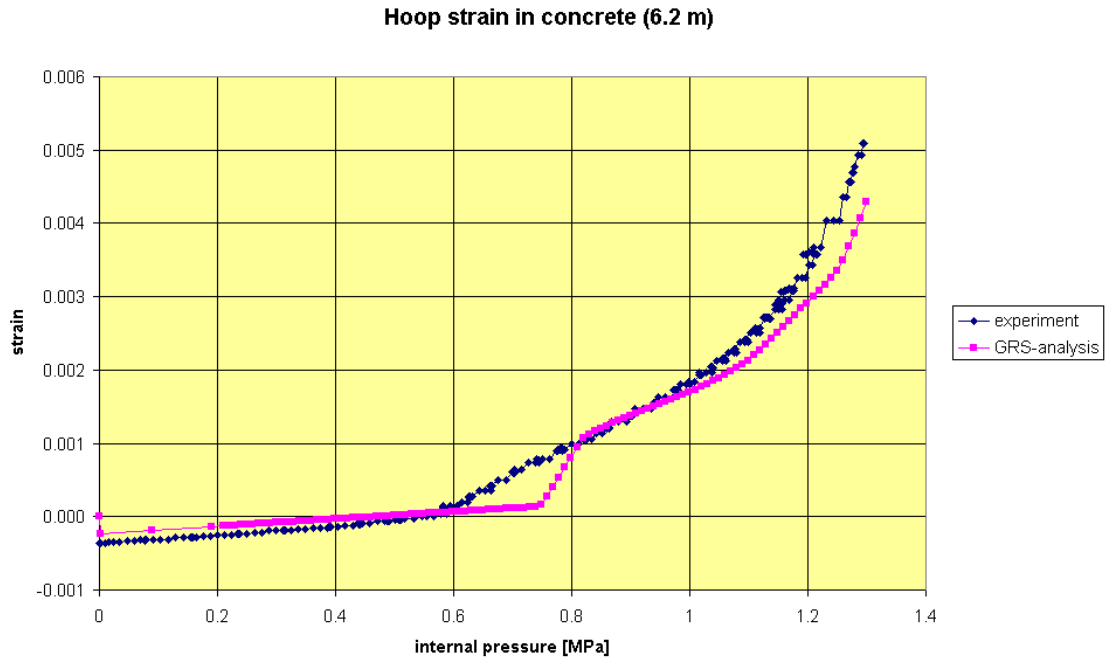

Fig. 28: Hoop strain in the concrete nearby the liner (vertical position 6.2 m above top of base-mat) from measurement and calculation

Gesellschaft für Anlagen- und Reaktorsicherheit (GRS) mbH

Structure mechanics analysis of the prestressed concrete model containment tested at Sandia National Laboratories – GRS-Contribution to International Standard Problem (ISP) 48, Phase 3

Technical Report

H. Grebner
J. Sievers

July 2005

BMWA-Project: RS 1154

Structure mechanics analysis of the prestressed concrete model containment tested at Sandia National Laboratories -

GRS-Contribution to International Standard Problem (ISP) 48, Phase 3, Extended Version

H. Grebner, J. Sievers
Gesellschaft für Anlagen- und Reaktorsicherheit (GRS) mbH, Köln, Germany
July 2005

Introduction

As agreed upon by the participants of the International Standard Problem (ISP) 48 the 1:4 scaled prestressed concrete containment vessel (as shown schematically in **Figs. 1** and **2**) tested at Sandia National Laboratories (SNL, Albuquerque, New Mexico) was also used as basis for calculations including thermal loading, planned as Phase 3 of ISP 48. During the meeting of the participants at Madrid in spring 2004 it was decided to analyse two loading cases with temperature, case 1 and 2, respectively. As case 1 a monotonically increasing pressure and temperature (saturated steam) loading should be considered, while a station blackout scenario including a peak loading due to hydrogen burning was proposed for case 2. The calculations to case 1 were planned to be obligatory for all participants, while the treatment of case 2 should be on a voluntary basis. For case 1 the participants had the choice either to perform heat transfer calculations by themselves or to use temperature gradients prepared by SNL.

In the next chapters the contribution of GRS to Phase 3 will be summarized.

GRS – Finite-Element-Models

In the first part of the studies the same axisymmetric model was used without consideration of geometric inhomogenities due to penetrations in the wall as already used in Phase 2 [1,2]. **Fig. 3** shows the model and its main components. The steel liner at the inner surface and the concrete parts are made of 8-node isoparametric elements with 4 integration points, while the rebar and tendon parts are modelled as truss

elements (with 3 nodes for the meridional and radial ones and one node for those in hoop direction). A stiff coupling between steel and concrete is simulated. As can be seen from the schematic presentation in **Figs. 4** and **5** the arrangement of tendons and rebars is modelled rather realistically. The model is loaded by internal pressure and temperature gradients, as will be described in the next chapter.

Our attempts to calculate case 2 with the model of Fig. 3 were not yet successful. To get some local information a very simple axisymmetric model consisting of a section (slice) of the cylindrical part of the containment was considered. The model is shown in **Fig. 6**. It contains all rebar and tendon elements as well as the liner located in the slice with the dimensions corresponding to a height position of 6.2 m above top of basemat. Further adequate boundary conditions for the deformation of the cutting surface are chosen.

Mechanical and thermal loading

As mentioned before a rather simple combination of mechanical and thermal loading is considered in Phase 3 case 1. **Fig. 7** shows the assumed time dependence of internal pressure and inner surface temperature, as given by [3]. With the axisymmetric model shown in **Fig. 8** heat transfer calculations were performed by David Evans and Associates (DEA) [4] with the temperature curve of Fig. 7 as boundary condition. The calculated temperature distributions at the cross sections 1 to 8 were made available to the participants by [3]. **Figs. 9** to **11** show the temperatures at the cross sections 1, 2 and 5 as provided by [3]. These temperatures were used by GRS together with interpolated values in the regions between the cross sections as temperature loading input for the structure mechanical calculations.

For case 2 (station blackout including peak loading due to hydrogen burning) the assumed time dependence of internal pressure and temperature at inner surface (from [3]) is shown in **Fig. 12**. Also in this case the temperature values calculated by [4] are used. **Fig. 13** gives an example of the temperature distributions over the wall.

Temperature dependent material data

For the liner elements a thermo-elastic-plastic material model with multi-linear stress-strain curves is used. As shown in **Fig. 14** the same stress-strain curve as in the GRS calculations of Phase 2 [1] is taken for the temperature region between room tem-

perature and 300°C. Stress-strain curves for temperatures above 300°C and further temperature dependent material data are presented in **Table 1a** and **1b**. Thereby the temperature dependency of the strenght values of steel proposed in [4] has been used to construct the values shown in Table 1a and 1b. For the truss elements simulating the rebar and tendon parts the use of the thermo-elastic-plastic material model with multi-linear stress-strain behaviour is not possible within the analysis code ADINA [5] used by GRS. In this case a thermo-elastic-plastic model with bilinear stress-strain curves is used. The curves used for the temperature region between room temperature and 300°C are also shown in Fig. 14. The temperature data of the rebar and tendon materials are summarized in the **Tables 2** and **3**. The concrete material model may also be used with temperature dependent data. **Table 4** presents the values used in the calculation. The reduction of strenght is again evaluated according to [4].

For case 1 loading conditions the temperature dependency of the material properties in the steel components is negligible because the structure temperatures do not exceed 200°C. As Fig. 13 shows for case 2 the high temperature values at the begin up to about 600°C after about 4 h of the transient occur only in a small region at the inner surface of the containment model. Thus the temperatures of the tendons (about in the middle of the wall) stay below 200°C during the whole transient.

Analysis results

The prestressing of the tendons is simulated by initial strains in the respective truss-elements. The calulations are performed using the program ADINA [5].

Results for case 1

In the calculations a fictitious time increment is added before the transient to raise the temperatures from room temperature to the values at begin of the pressure increase. About 80% of the transient could be analysed with the FE-model shown in Fig. 3, i.e. up to about 1.15 MPa internal pressure. Further pressure increase leads to numerical problems within the equilibrium iterations. The complete transient was analyzed with the simplified slice model (see Fig. 6) which is more robust from numerical point of view. **Figs. 15** to **18** show temperature distributions in the upper cylindrical part of the

model (height about 10 m) for different transient times as used as input for the mechanical analysis.

Selected results of the calculation are presented in the **Figs. 19** to **52**.

Figs. 19 to **26** show the deformation of the complete model for different steps of the calculation including the first step (mainly pre-stressing influence), the time step (p = 0), where the initial temperature distribution is applied, as well as several steps with combined pressure and temperature loading.

The development of micro-cracks in the complete model and in a section of the cylindrical part of the model is presented in **Figs. 27** to **34**. The temperature gradients effect compressive stresses near the inner surface and tensile stresses in the regions near the outer surface, as **Fig. 35** shows for integration points at 6.2 m above the top of the basemat. The development of micro-cracks starts near the outer surface (see Figs. 27 and 28). At a pressure value of about 0.66 MPa the first regions are formed, where axial micro-cracks are calculated in the whole wall (as shown at the section presented in Figs. 29 to 34).

Figs. 36 to **43** give a compilation of the results at the standard output locations contributed by GRS to ISP 48, especially displacements and strains of the liner, the rebars and the tendons. The strain results shown here are total strain values, i.e. the sum of mechanical and thermal strains.

A few examples of comparisons between calculations with temperature loading and results of Phase 2 calculations are shown in **Figs. 44** to **52** for the radial and vertical displacement at the inner surface of the liner at different positions of the cylindrical part of the model, as well as for strains of the two calculations for the liner, rebars and a hoop tendon.

For the displacement results due to the additional temperature load the values for the calculation with temperature loading are at equal pressure steps always higher than the corresponding values without temperature gradients in the wall (Figs. 44 to 46). Further Fig. 44 shows that the calculated results of the slice model (see Fig. 6) agree very well with the results of the more complex model shown in Fig. 3. Considering the strain results (Figs. 47-52) it should be noticed that the case 1 results are mechanical strains, i.e. total strain values minus thermal strains. This is of special importance for the liner

results where the temperature gradients cause negative strains for small pressure values in addition to the prestressing effect. When exceeding 1.3 MPa internal pressure a rapid increase of radial displacement and hoop strains is evaluated with the slice model reflecting the start of plastification in the hoop tendons. The maximum hoop tendon strain is nearly 3%, while from material tests a uniform elongation strain of 3.3% is found for the tendons.

As in the pressure only case some rebar elements show plastification at higher pressure values., The maximum hoop rebar strain calculated with the slice model (at 1.45 MPa) is nearly 2.5%, which is still away from the rebar fracture strain of about 7.5 percent.

Results for case 2

Due to numerical problems with the complete axisymmetric model the case 2 calculations were performed only with the section (slice) model. Thus only some localized information on a few standard output locations could be gained, i.e. the results shown are representative for a cylindrical section at 6.2 m above the basemat.

Some exemplary results are presented in the **Figs. 53** to **61** as function of transient time or of internal pressure.

Fig. 53 shows the time dependence of the radial displacement at the inner surface of the model, **Fig. 54** presents the same result as function of internal pressure. Comparisons of hoop strains of concrete positions near inside or outside of the wall are shown in **Fig. 55**. As at the inside integration point in the concrete high temperatures occur, in the first 30 hours of the transient compressive strains are found in this case. The differences between inside and outside at the end of the transient are again due to the thermal gradient through the wall. Concrete strains beyond the elastic limit shown in Fig. 14a characterise the damage of the concrete in terms of crack opening. **Figs. 56** and **57** show the behaviour of hoop and meridional liner strains, predominantly compressive strains, as function of time and of internal pressure. Hoop rebar strains for inner and outer rebars are given in **Fig. 58** and **59** again in dependence on time and pressure. Furthermore the tendon strains are presented in **Figs. 60** and **61**. During the peak loading after about 4 h the inner surface experiences temperature values up to

600°C for short times. Consequently the liner experiences some plastification in compression, but at the position of the tendons (at about 58% of the wall thickness) the temperature values remain below 80°C during the whole transient (see Fig. 13). Therefore the tendons remain elastic until the end of the transient, where the hoop tendon just reaches the yield stress.

The strains in total remain relatively low (due to the lower end pressure of 1.3 MPa in the calculation). For instance the maximum hoop tendon strain is below 1%. It is expected that critical strains in the tendons are reached if the transient, which is presently limited to 1.33 MPa at 60 h, is extrapolated with increasing pressure to further 25 h up to about 1.5 MPa.

Summary and assessment of the results

GRS participates in the International Standard Problem (ISP) 48 with finite-element-calculations. The axisymmetric finite-element-model which was developed for the phase 2 calculations is also used for phase 3 where combined pressure and temperature loading is considered. The model is loaded by the prestressing of the tendons, by increasing internal pressure (up to 1.3 MPa) and by thermal stresses due to temperature distributions provided by SNL. Due to numerical problems with this model a simplified axisymmetric section (slice) model of the cylindrical part of the containment, which is more robust from numerical point of view, was used in this case.

As expected the analyses results for case 1 and case 2 in terms of displacements show significant differences to the Phase 2 results (internal pressure only, see Figs. 44 to 46 and 54). Due to the temperature gradients in the wall the displacement results of Phase 3 case 1 are about 5-10 mm higher than the Phase 2 values almost independent of the pressure for the radial displacements and increasing (up to 20 mm) for the vertical displacement example.

First extended regions of axial micro-cracks in the concrete are found for case 1 at low pressure values, as e.g. shown in Fig. 28 for a pressure of 0.2 MPa, where a part of the wall thickness is cracked in the complete model starting from the outer surface. With increasing pressure micro-cracks penetrate the whole wall. At about 0.66 MPa the first formation of complete through wall arrangements of axial micro-cracks is calculated. At

the transient load step with 1.14 MPa internal pressure almost all concrete parts of the model have micro-cracks which may cause leaks.

Strains in the liner, the rebars and the concrete of the cylindrical part close to the inner and outer surface also show significant differences to the pressure only results (see Figs. 47-50 and 52), while the tendons near the middle of the wall show strains which are very similar to the pressure only values in the regions where comparison is possible (see **Fig. 62**). Fig. 62 presents a comparison of the evaluated hoop tendon strain (calculated with the slice model, mechanical strains only) as function of the internal pressure for the loadcases considered in Phase 2 and Phase 3 of the ISP 48. With the exception of the temperature and pressure peak of case 2 the tendon results are very similar to case 1 and the pressure only case. Obviously the tendons which are located about in the middle of the wall are not significantly influenced by the thermal gradients. This means that the containment failure in terms of rupturing of the tendons is not changed by the additional temperatures. On the other hand the additional compressive stresses near the inner wall and tensile stresses near the outer wall caused by the thermal gradients strongly influence the behaviour of the liner and the concrete cracking.

For the pressure only case and the temperature case 1 failure of the containment model due to rupture of circumferential tendons is predicted at an internal pressure of about 1.45-1.50 MPa without consideration of geometric inhomogenities due to penetrations in the wall. The calculated strains in some of the rebars show plastification, but the final values are below the critical ones with a sufficient margin.

The results of the case 2 calculations show that, although some plastification in the rebars occurs, the maximum strain values are sufficiently below critical values.

The work described in this Technical Report is sponsored by the German Ministry of Economics and Labor.

References

[1] Grebner, H., J. Sievers: Structure mechanics analysis of the prestressed concrete model containment tested at Sandia National Laboratories – Contribution to International Standard Problem (ISP) 48. GRS, Technical report, December 2003.

[2] Hessheimer, M. F.: International Standard Problem No. 48 Containment Capacity, Phase 2 Report, Results of Pressure Loading Analysis. NEA/CSNI/R(2004)11 (2004).

[3] Hessheimer, M. F.: E-Mail on Temperature Gradients dated August 24, 2004.

[4] Dameron, R., et al.: Analysis of Axisymmetric Prestressed Concrete Containment Vessel (PCCV) Including Thermal Gradients. Report David Evans & Associates (DEA), August 19, 2004.

[5] ADINA – A Finite-Element-Program for Automatic Dynamic Incremental Nonlinear Analysis, Version 8.1 – Theory and Modeling Guide, Volume I: ADINA. ADINA R&D, Inc. (2003).

Table 1a: Material data of the liner steel, part 1

T [°C]	E [MPa]	ν	α [1/K]	ε_0	σ_0 [MPa]
24	219000	0.3	$11.2 \cdot 10^{-6}$	0.002	380
300	219000	0.3	$11.2 \cdot 10^{-6}$	0.002	380
400	209000	0.3	$14.01 \cdot 10^{-6}$	0.002	363
600	102200	0.3	$14.59 \cdot 10^{-6}$	0.002	177.4
800	23020	0.3	$10.5 \cdot 10^{-6}$	0.002	39.9

Table 1b: Material data of the liner steel, part 2

ε	σ [MPa]				
	T = 24°C	T = 300°C	T = 400°C	T = 600°C	T = 800°C
0.01	403	403	384.5	188.1	42.3
0.02	430	430	410.3	200.7	45.2
0.03	452	452	431.3	211	47.5
0.04	470	470	448.4	219.4	49.4
0.05	480	480	458	224	50.5
0.28	670	670	639.2	312.7	70.4

Table 2: Material data of the rebar steel

T [°C]	E [MPa]	ν	σ_0 [MPa]	E_T [MPa]	α [1/K]
24	210000	0.3	420	5000	$11.2 \cdot 10^{-6}$
300	210000	0.3	420	5000	$11.2 \cdot 10^{-6}$
400	200360	0.3	400.7	4770	$14.01 \cdot 10^{-6}$
600	98020	0.3	196	2334	$14.59 \cdot 10^{-6}$
800	22070	0.3	44.1	525.5	$10.5 \cdot 10^{-6}$

Table 3: Material data of the tendon strands

T [°C]	E [MPa]	ν	σ_0 [MPa]	E_T [MPa]	α [1/K]
24	217670	0.3	1730	8500	$11.2 \cdot 10^{-6}$
300	217670	0.3	1730	8500	$11.2 \cdot 10^{-6}$
400	207680	0.3	1526	5560	$14.0 \cdot 10^{-6}$
600	101610	0.3	746.9	3968	$14.6 \cdot 10^{-6}$
800	22880	0.3	168.2	893.4	$10.5 \cdot 10^{-6}$

Table 4: Material data of the concrete

T [°C]	E_0 [MPa]	ν	α [1/K]	σ_t [MPa]	σ_c [MPa]	ε_c	σ_u [MPa]	ε_u
24	27000	0.18	$9 \cdot 10^{-6}$	3.45	-47.3	-0.00186	-30	-0.0032
200	25330	0.18	$10 \cdot 10^{-6}$	3.03	-41.6	-0.00186	-26.4	-0.0032
300	23690	0.18	$11.2 \cdot 10^{-6}$	2.66	-36.4	-0.00186	-23.1	-0.0032
400	21680	0.18	$11.2 \cdot 10^{-6}$	2.24	-30.5	-0.00186	-19.3	-0.0032
600	17080	0.18	$11.2 \cdot 10^{-6}$	1.38	-18.9	-0.00186	-12.0	-0.0032
800	12580	0.18	$11.2 \cdot 10^{-6}$	0.75	-10.3	-0.00186	-6.5	-0.0032

Table 5: Positions of standard output locations

Loca-tion	Height* [m]	Radial position	Loca-tion	Height* [m]	Radial position	Loca-tion	Height* [m]	Radial position
2	0.25	Inner surfa.	17	0.05	Outer rebar	28	14.55	Inner rebar
3	1.43	Inner surfa.	18	0.25	Inner rebar	29	14.55	Outer rebar
4	2.63	Inner surfa.	19	0.25	Outer rebar	34	0.01	Liner
5	4.68	Inner surfa.	20	1.43	Inner rebar	35	0.01	Liner
6	6.2	Inner surfa.	21	1.43	Outer rebar	36	0.25	Liner
7	10.75	Inner surfa.	22	6.2	Outer rebar	37	0.25	Liner
8	10.75	Inner surfa.	23	6.2	Outer rebar	38	6.2	Liner
9	14.55	Inner surfa.	24	10.75	Outer rebar	39	6.2	Liner
10	14.55	Inner surfa.	25	10.75	Inner rebar	40	10.75	Liner
11	16.13	Inner surfa.	26	10.75	Outer rebar	41	10.75	Liner
16	0.05	Inner rebar	27	14.55	Outer rebar	42	16.13	Liner
48	15.6	Meridional tendon	50	6.58	Hoop tendon			

*: Position above basemat

Figures

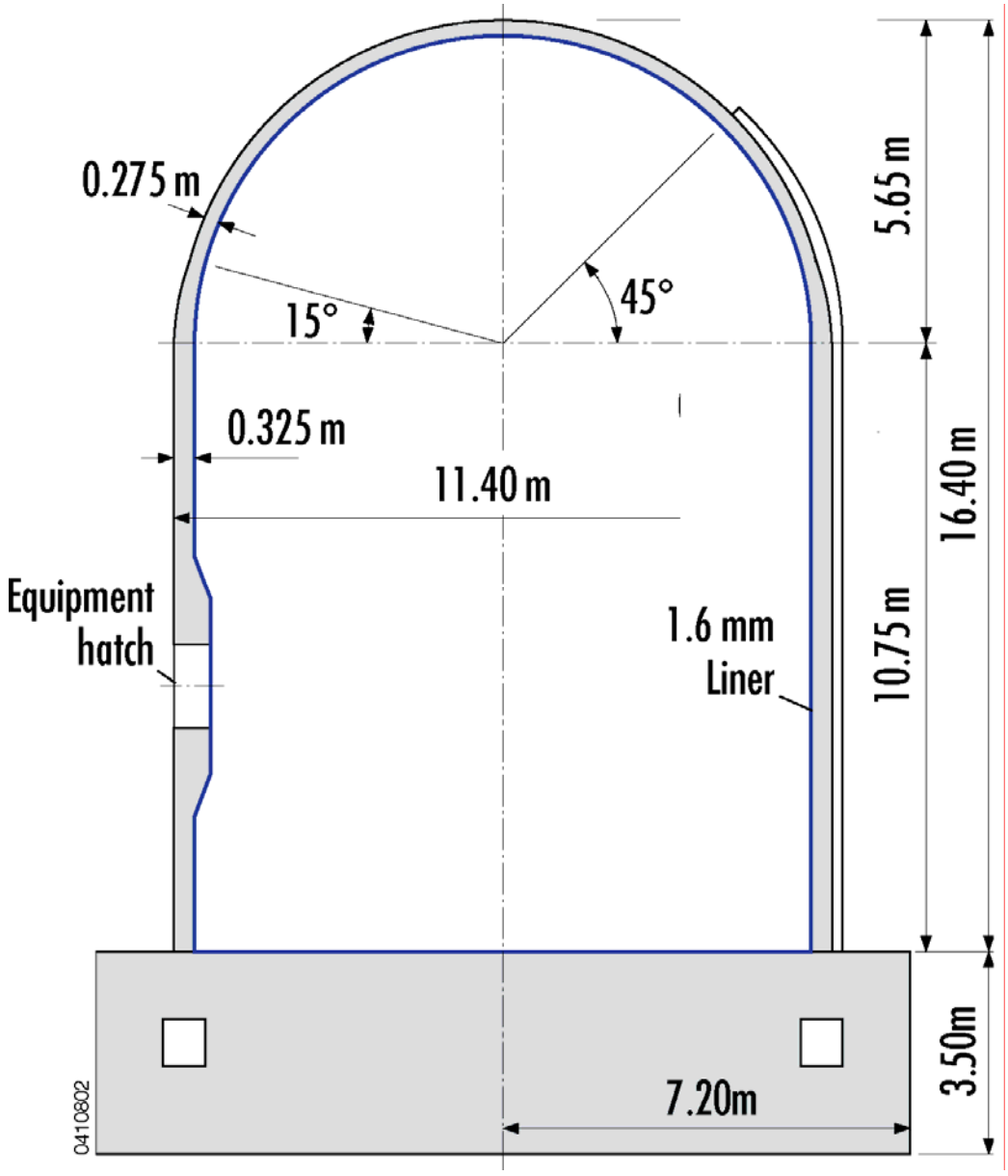

Fig. 1: Major dimensions of the containment model, vertical section

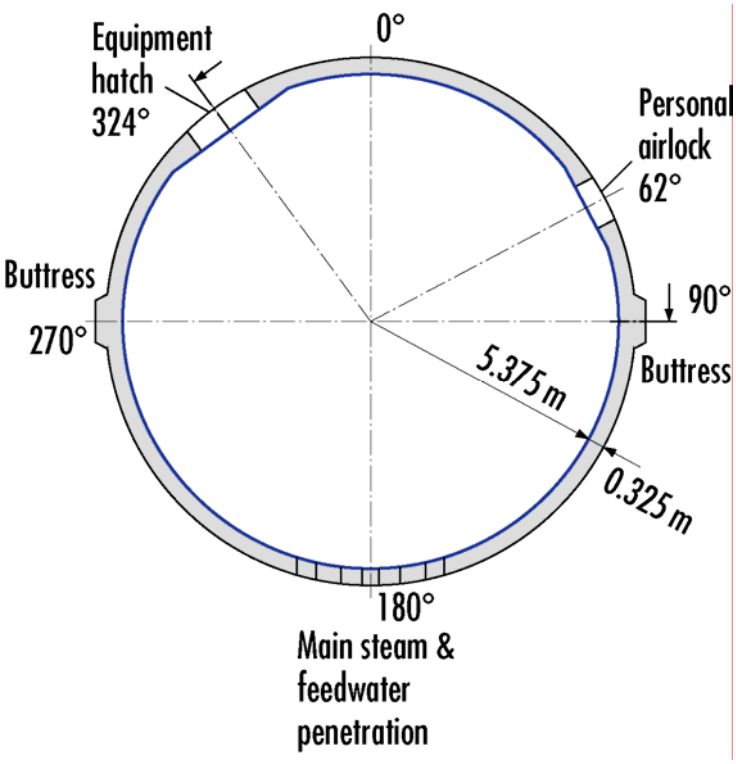

Fig. 2: Major dimensions of the containment model, horizontal section

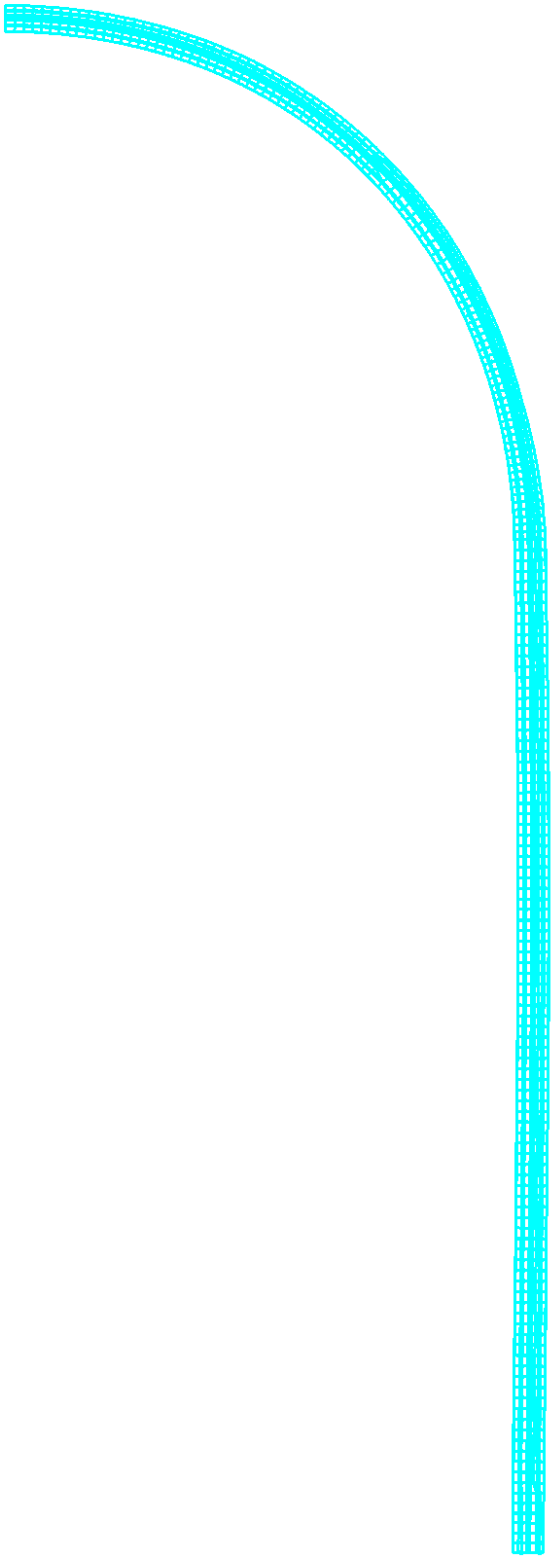

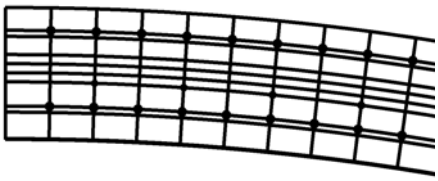

Part of the model (middle of dome, inner surface coated with metallic liner)

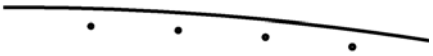

Tendons middle of dome

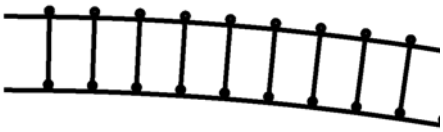

Rebar elements middle of dome

Axisymmetric model

Fig. 3: Finite element model of prestressed concrete model containment

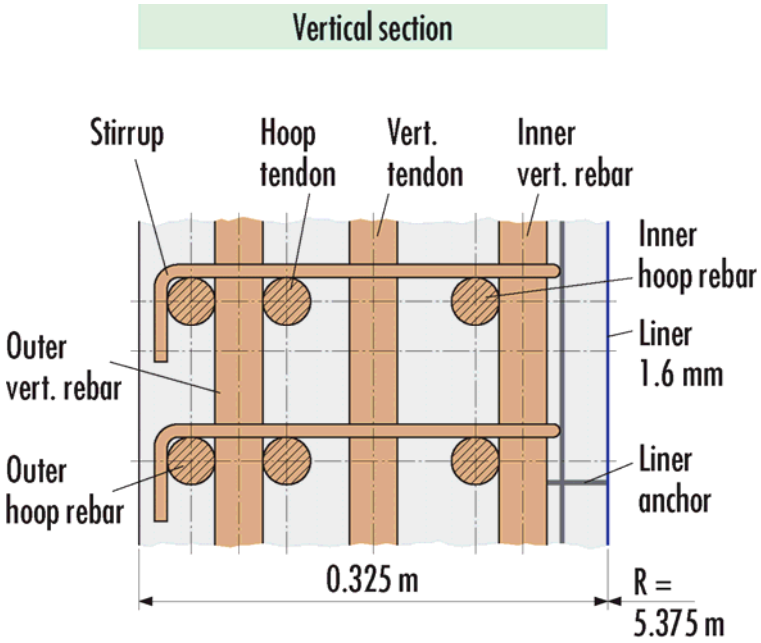

Fig. 4: Arrangement of tendons and rebars, vertical section

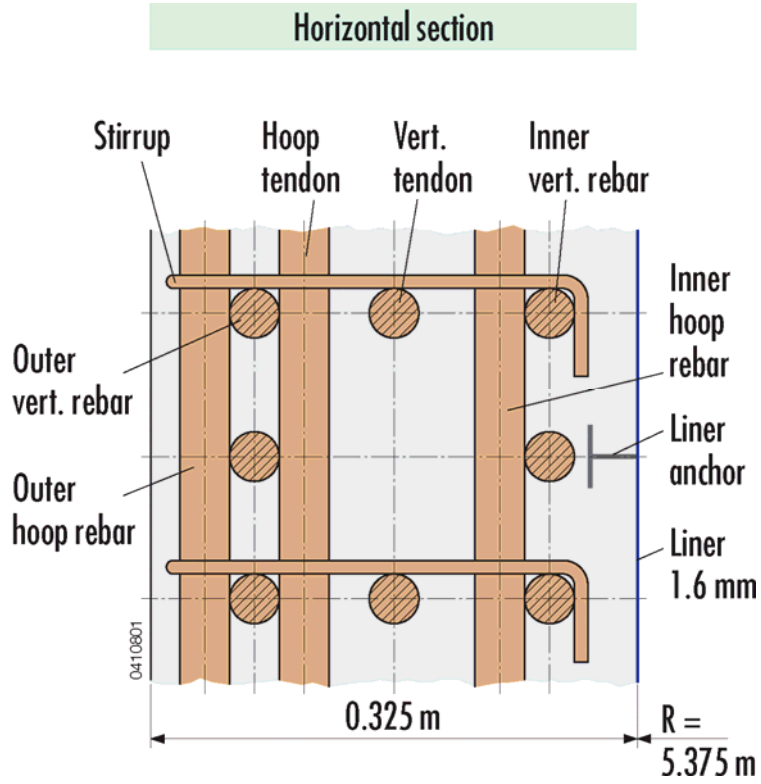

Fig. 5: Arrangement of tendons and rebars, horizontal section

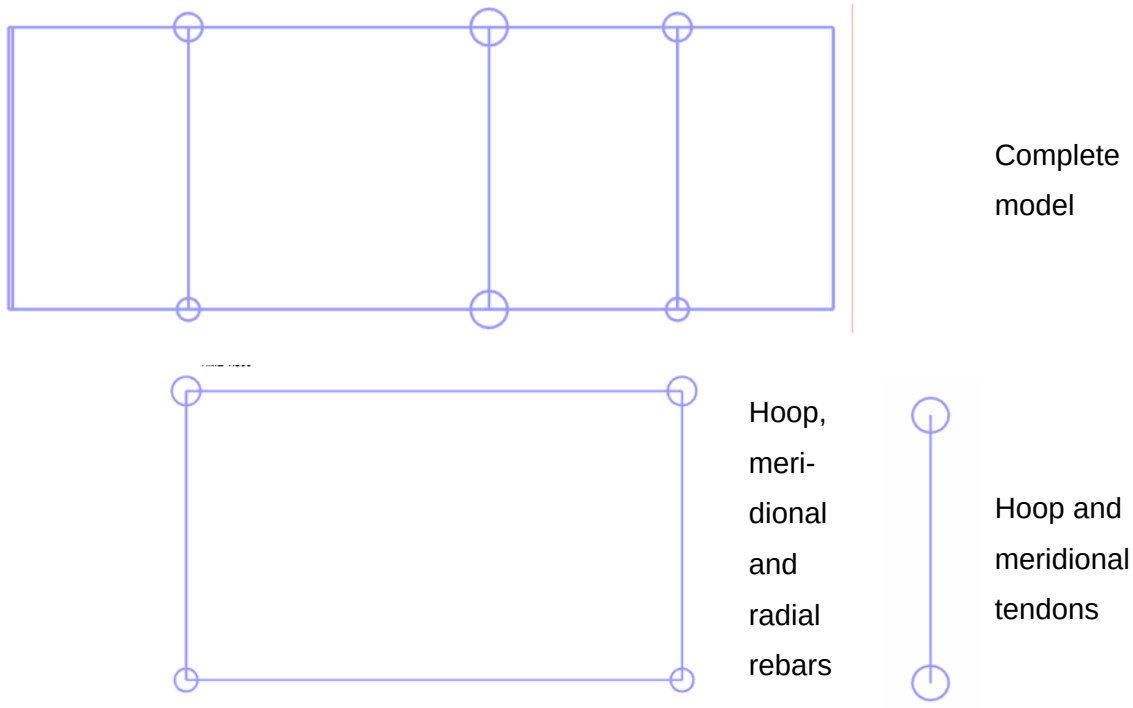

Fig. 6: Finite element section model (slice) of prestressed concrete model containment

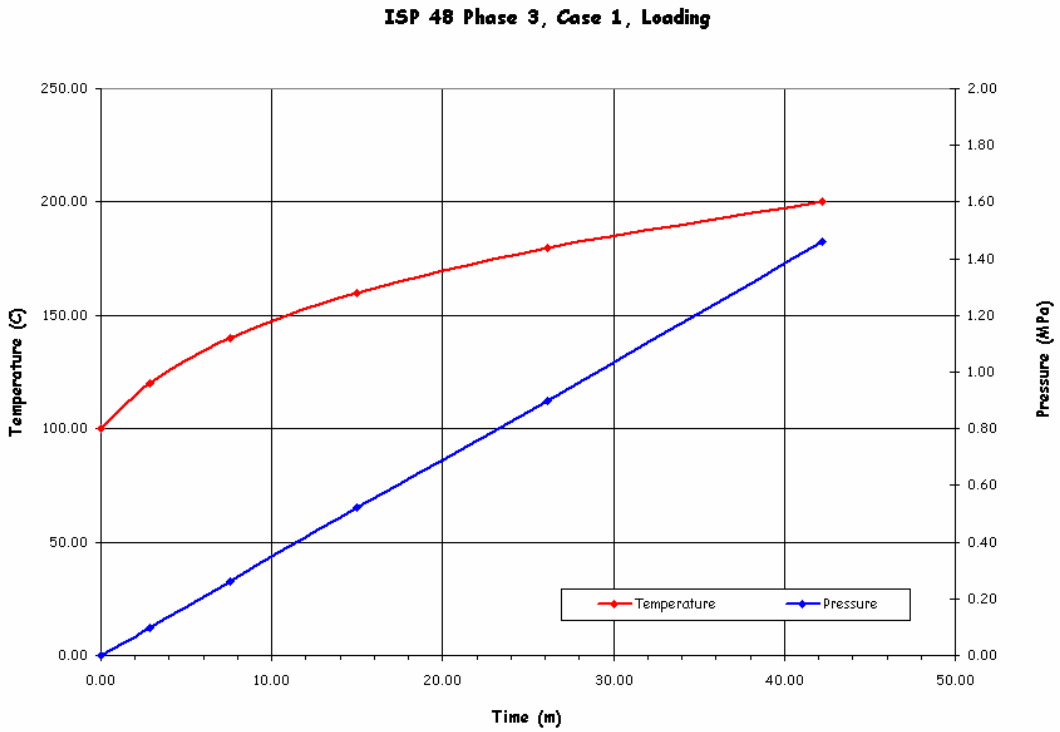

Fig. 7: Assumed time dependence of pressure and inner surface temperature for Phase 3 case 1 (from [3])

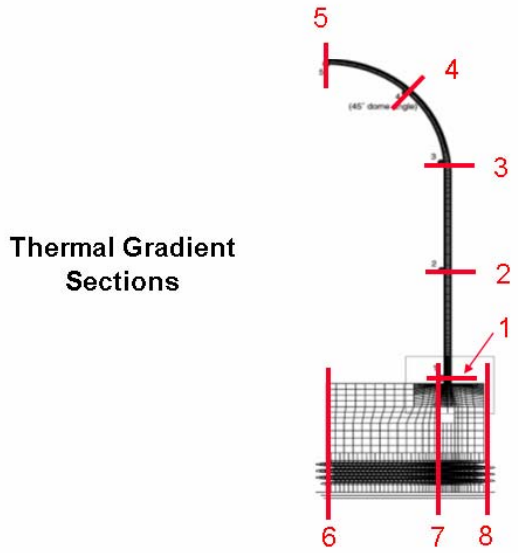

Fig. 8: Axisymmetric model used by DEA [3] for heat transfer calculations within Phase 3 and sections, where temperature results are provided

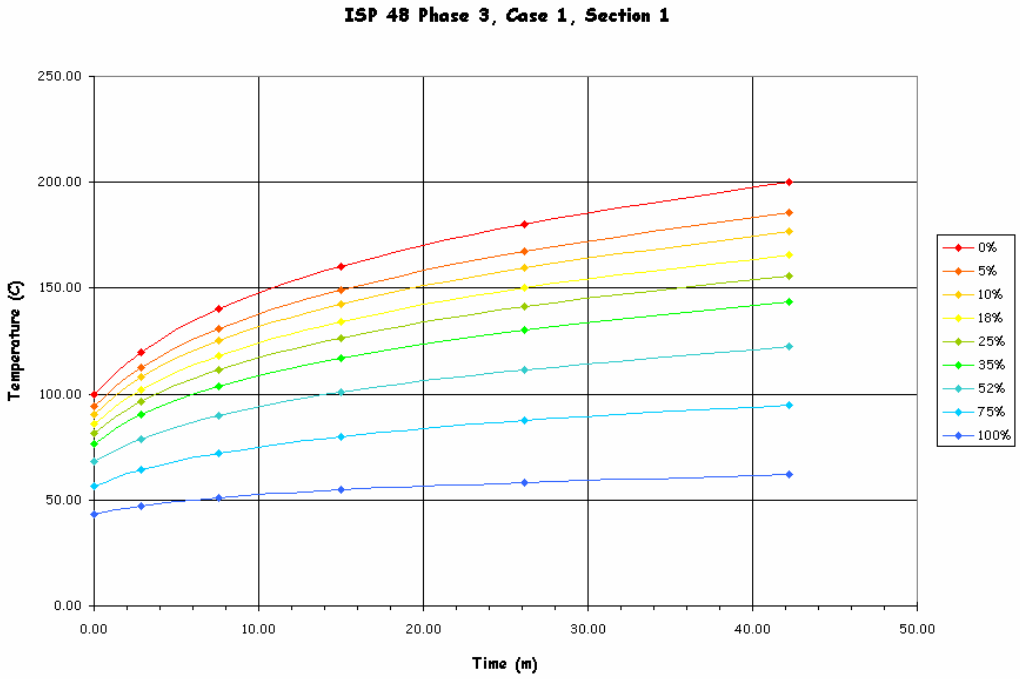

Fig. 9: Temperature results provided by DEA [3] for section 1 at different wall positions (in % of wall thickness) for Phase 3 case 1

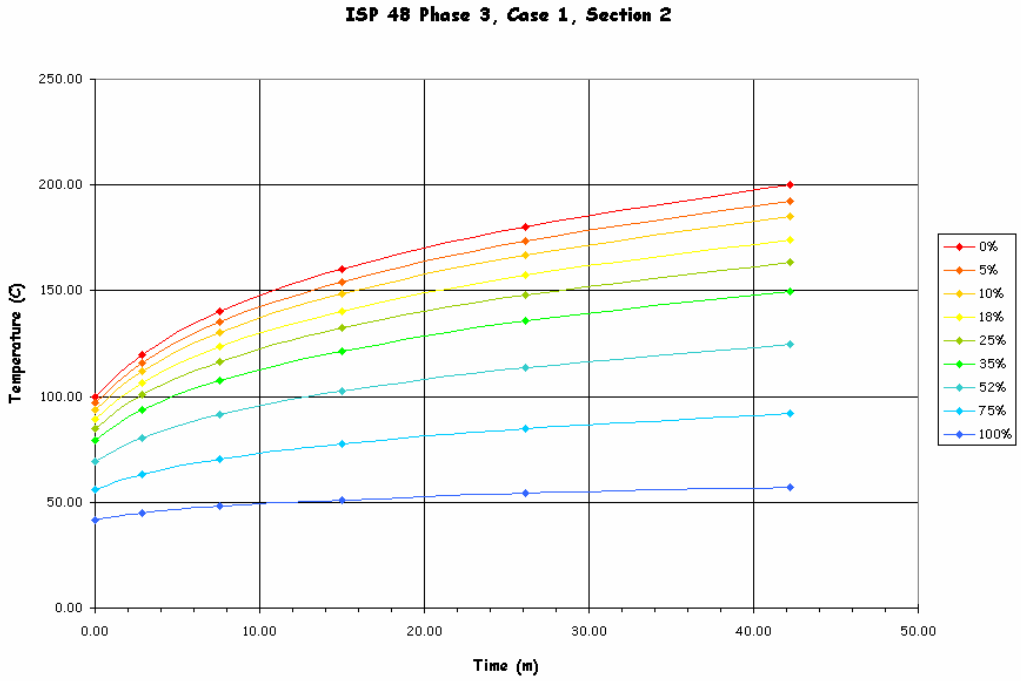

Fig. 10: Temperature results provided by DEA [3] for section 2 at different wall positions (in % of wall thickness) for Phase 3 case 1

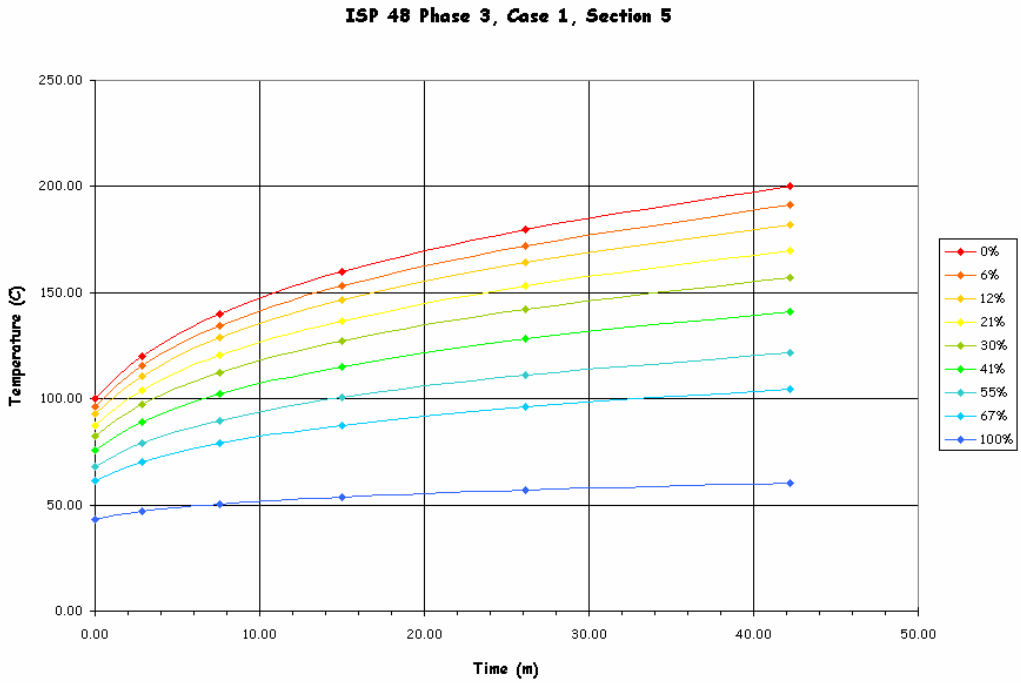

Fig. 11: Temperature results provided by DEA [3] for section 2 at different wall positions (in % of wall thickness) for Phase 3 case 1

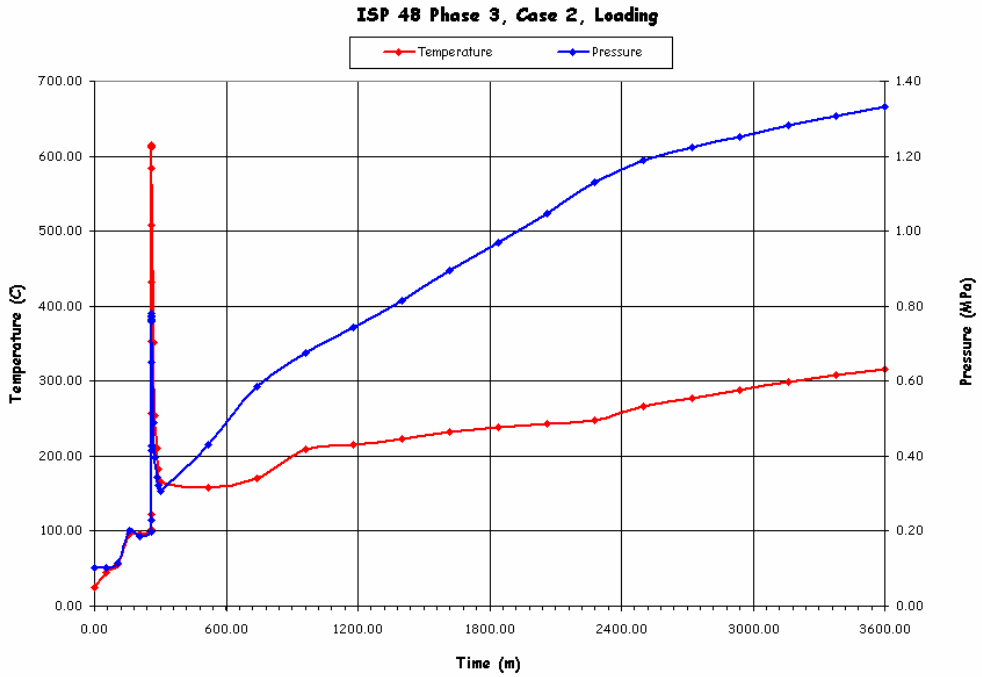

Fig. 12: Assumed time dependence of pressure and inner surface temperature for Phase 3 case 2 (from [3])

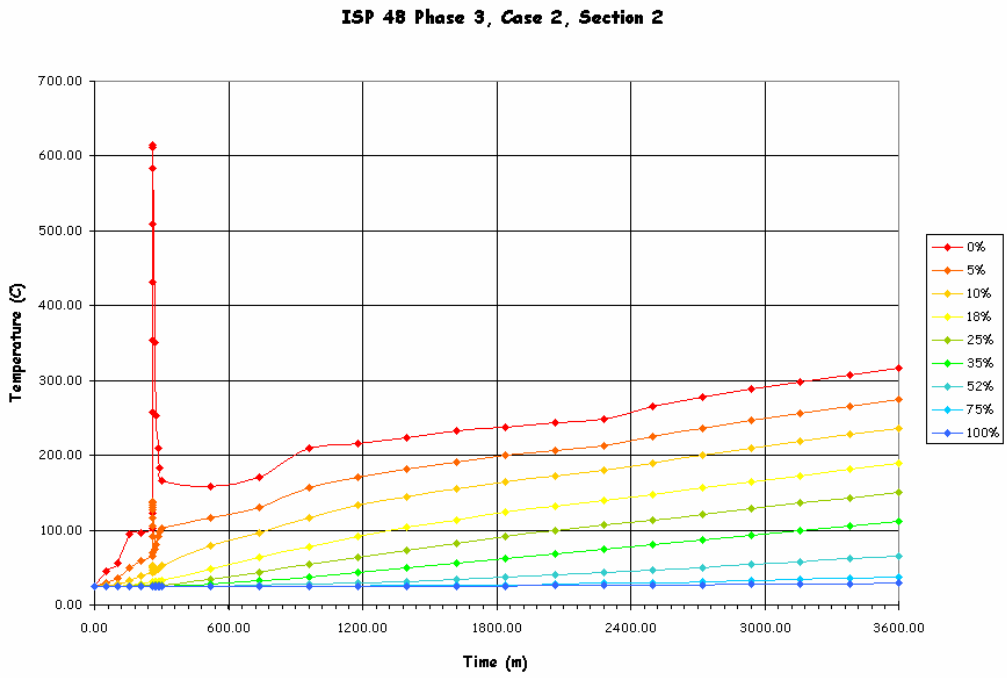

Fig. 13: Temperature results provided by DEA [3] for section 2 at different wall positions (in % of wall thickness) for Phase 3 case 2

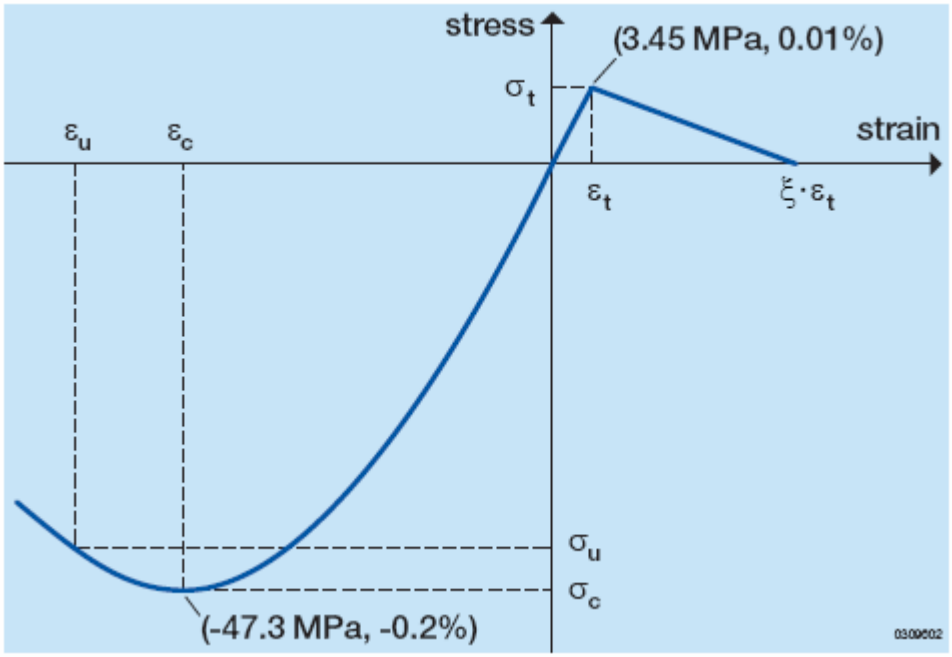

Fig. 14a: True stress-strain curve of concrete for room temperature as used as input for the finite-element-calculations with ADINA

Fig. 14b: True stress-strain curves of liner and rebar steel as well as tendon strand for the temperature region between room temperature and 300°C as used as input for the finite-element-calculations with ADINA

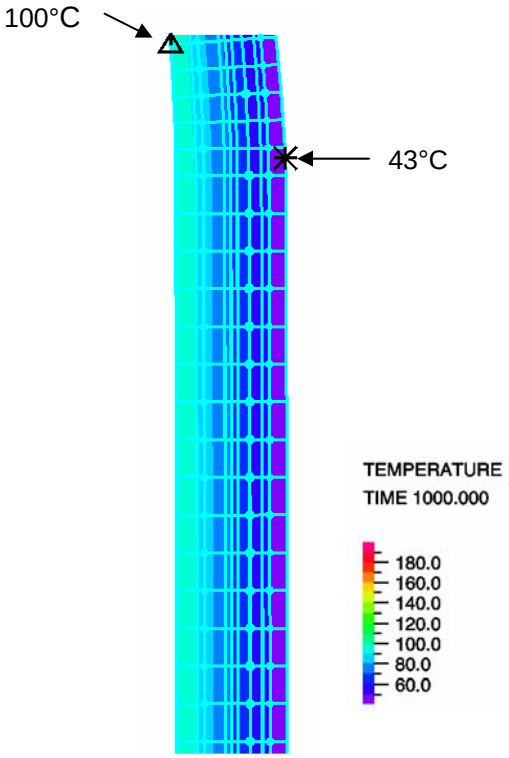

Fig. 15: Case 1, initial temperature distribution in the wall at about 10 m height, t =0 min, p = 0 MPa

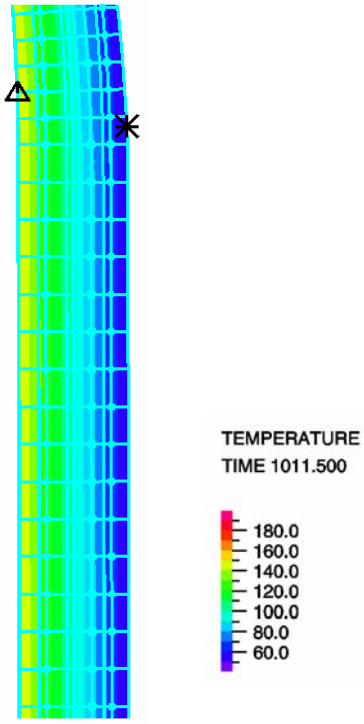

Fig. 16: Case 1, temperature distribution in the wall at about 10 m height, t = 11.5 min, p = 0.4 MPa

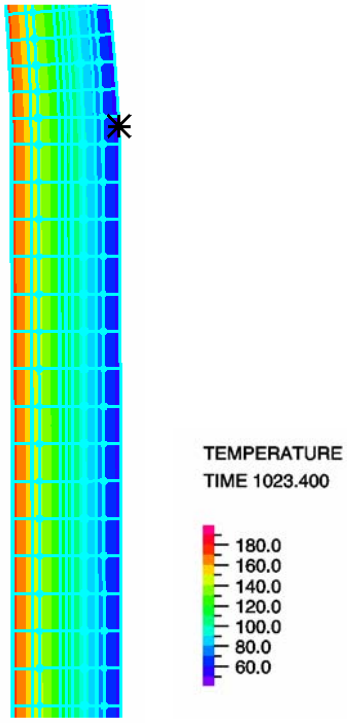

Fig. 17: Case 1, temperature distribution in the wall at about 10 m height, t = 23.4 min, p = 0.8 MPa

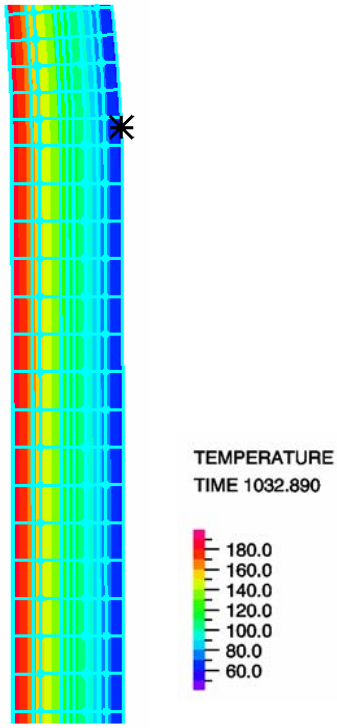

Fig. 18: Case 1, temperature distribution in the wall at about 10 m height, t = 32.9 min, p = 1.14 MPa

Fig. 19: Case 1, deformed model at first step of calculation (only pre-stressing, displacement magnification 200)

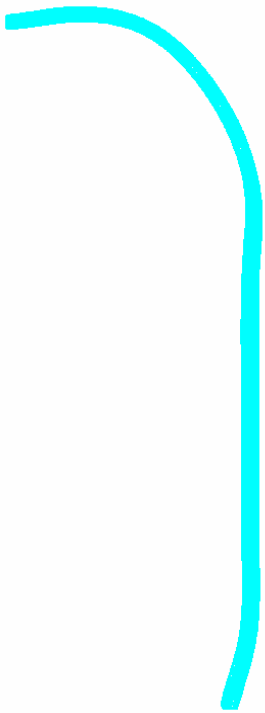

Fig. 20: Case 1, deformed model at t = 0, p = 0 (only initial temperature distribution, displacement magnification 200)

Fig. 21: Case 1, deformed model at t = 5.2 min, p = 0.2 MPa (with temperature load, displacement magnification 100)

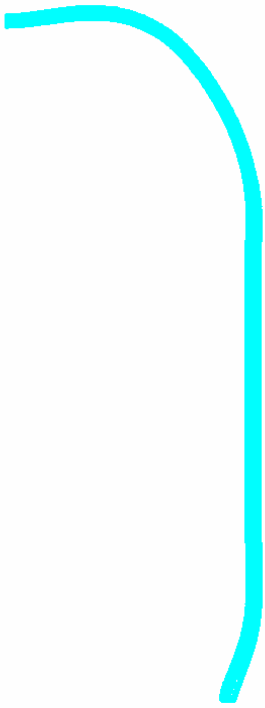

Fig. 22: Case 1,deformed model at t = 11.5 min, p = 0.4 MPa (with temperature load, displacement magnification 100)

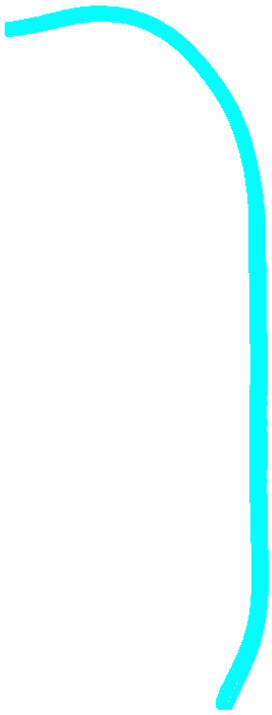

Fig. 23: Case 1, deformed model at t = 17.1 min, p = 0.6 MPa (with temperature load, displacement magnification 100)

Fig. 24: Case 1, deformed model at t = 23.4 min, p = 0.8 MPa (with temperature load, displacement magnification 100)

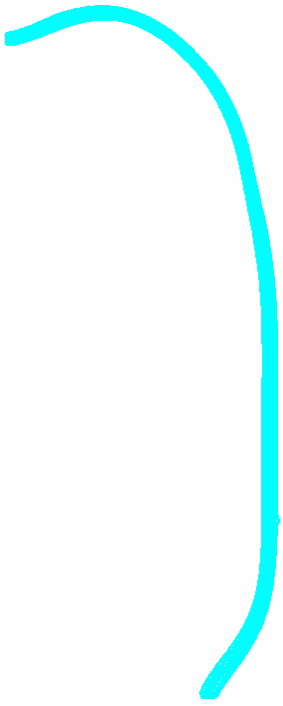

Fig. 25: Case 1, deformed model at t = 28.9 min, p = 1.0 MPa (with temperature load, displacement magnification 100)

Fig. 26: Case 1, deformed model at t = 32.9 min, p = 1.14 MPa (with temperature load, displacement magnification 100)

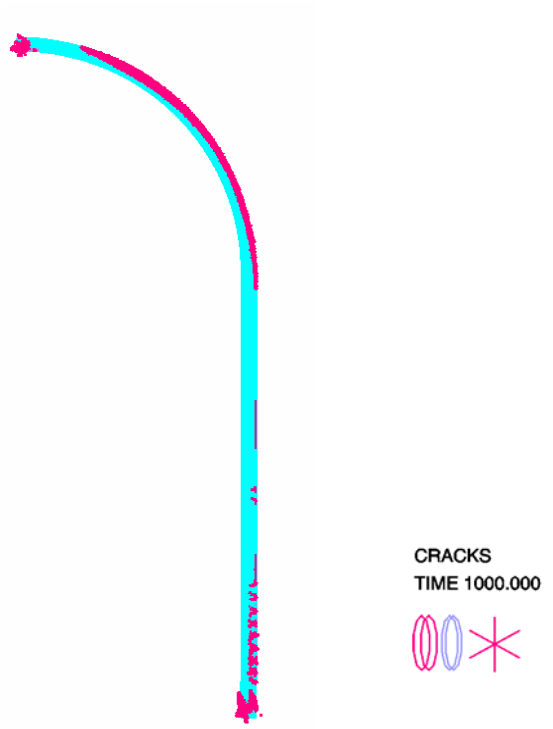

Fig. 27: Case 1, location of cracks at t = 0, p = 0.0 MPa (only temperature load)

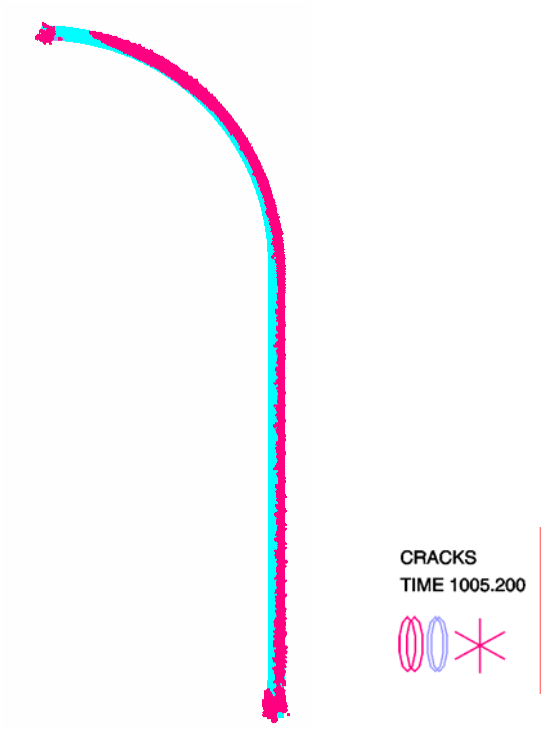

Fig. 28: Case 1, location of cracks at t = 5.2 min, p = 0.2 MPa (with temperature load)

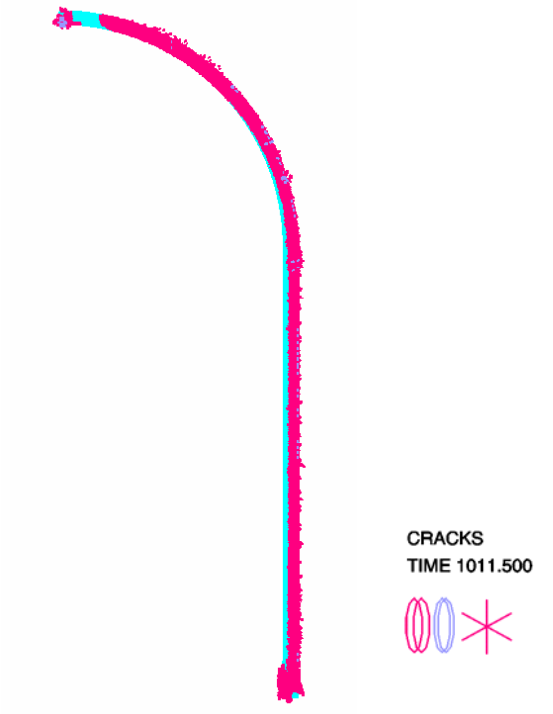

Fig. 29: Case 1, location of cracks at t = 11.5 min, p = 0.4 MPa (with temperature load)

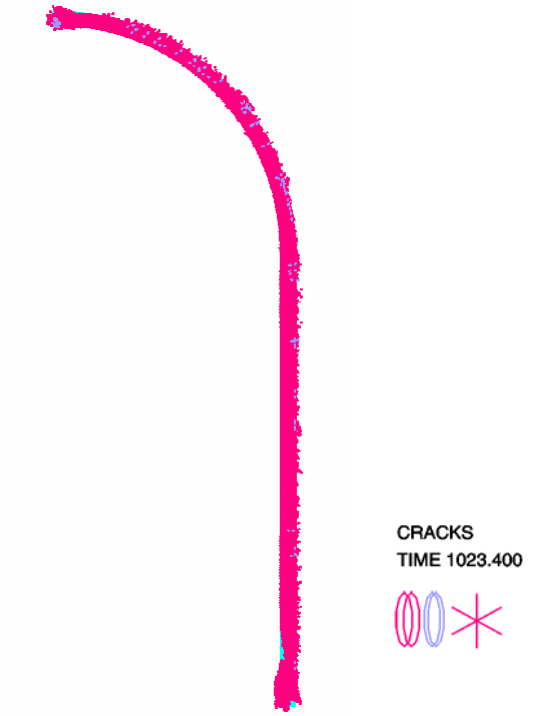

Fig. 30: Case 1, location of cracks at t = 23.4 min, p = 0.8 MPa (with temperature load)

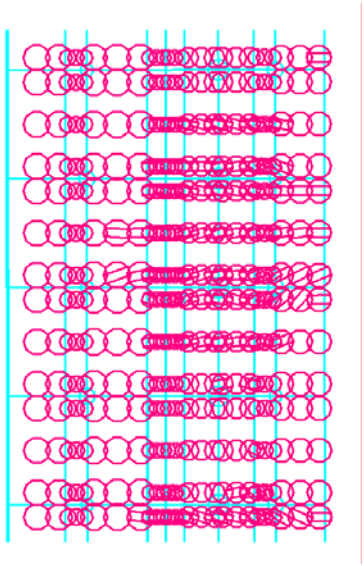

Fig. 31: Case 1, location of cracks at t = 18.7 min, p = 0.646 MPa (with temperature load), section of upper cylindrical part of the model

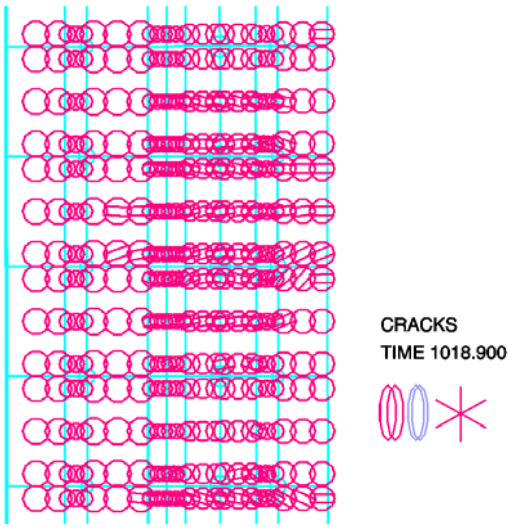

Fig. 32: Case 1, location of cracks at t = 18.9 min, p = 0.653 MPa (with temperature load), section of upper cylindrical part of the model

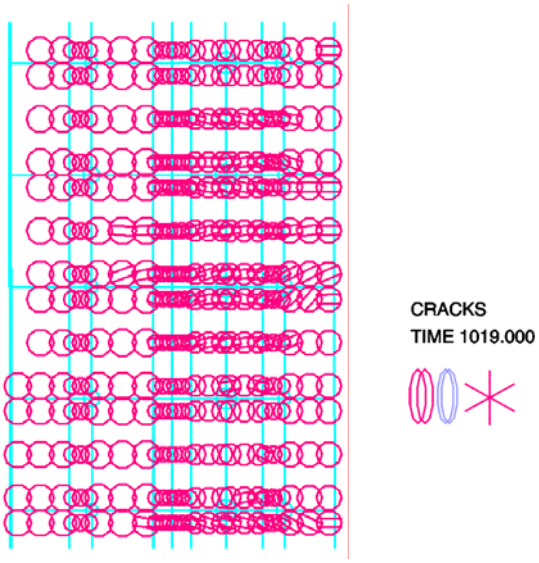

Fig. 33: Case 1, location of cracks at t = 19 min, p = 0.656 MPa (with temperature load), section of upper cylindrical part of the model

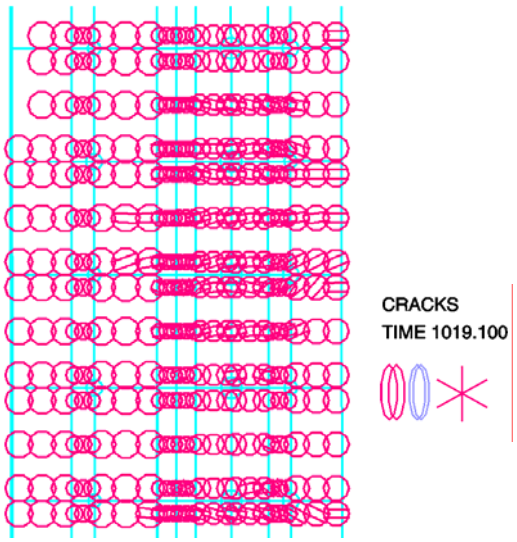

Fig. 34: Case 1, location of cracks at t = 19.1 min, p = 0.659 MPa (with temperature load), section of upper cylindrical part of the model

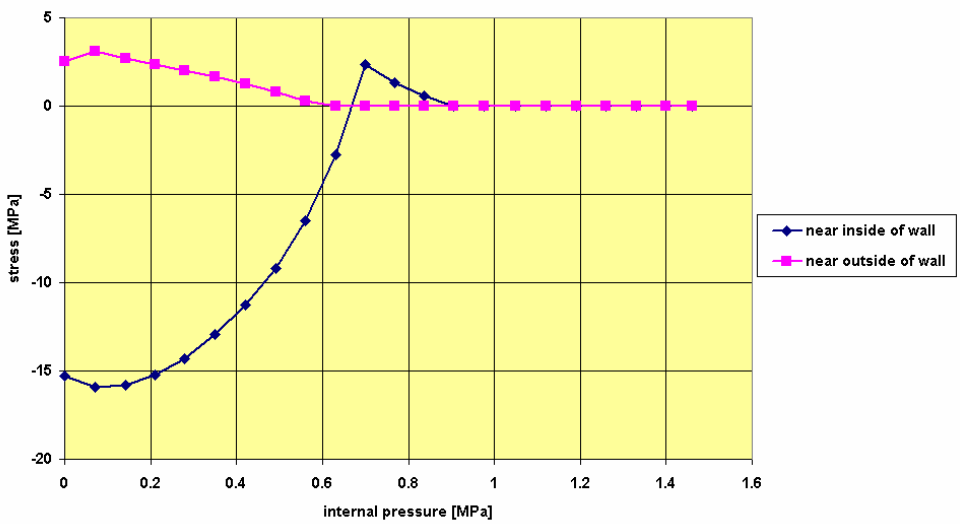

Fig. 35: Case 1, hoop stress in the concrete for the slice model at positions near inside and outside of the wall, case 1, position 6.2 m above top of basemat

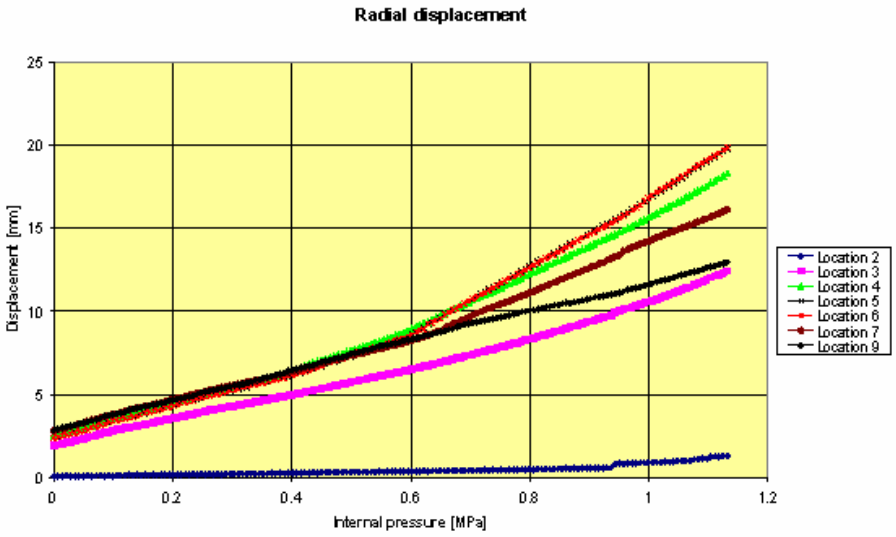

Fig. 36: Case 1, radial displacement at the inner surface of the liner (at different vertical positions above top of basemat, definitions of locations see Table 5)

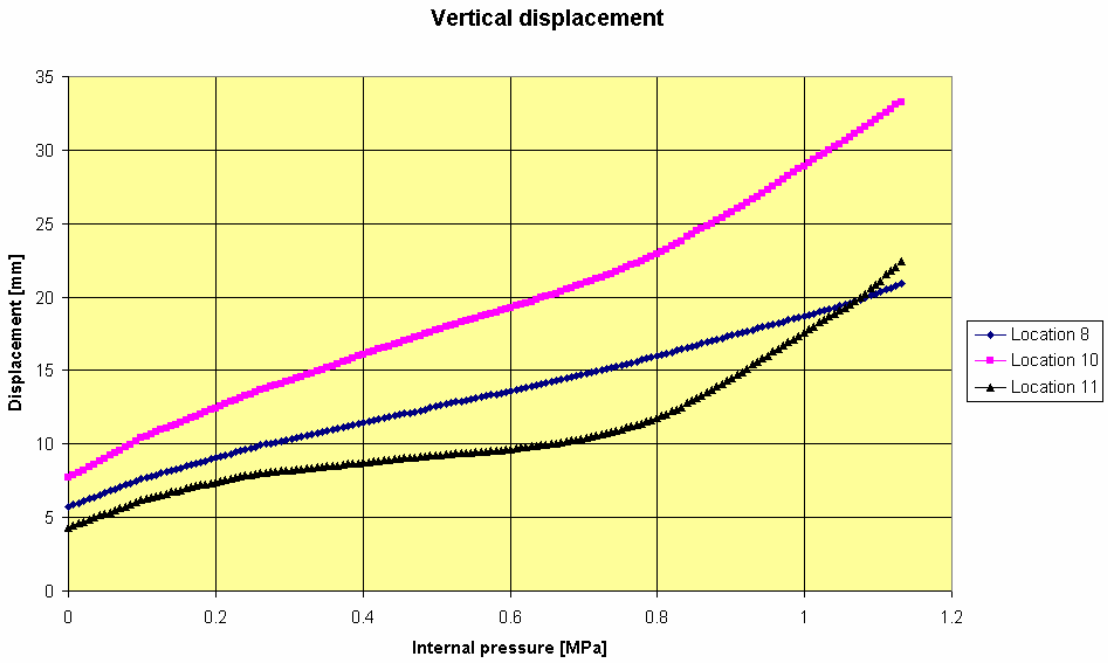

Fig. 37: Case 1, vertical displacement at the inner surface of the liner (at different vertical positions above top of basemat)

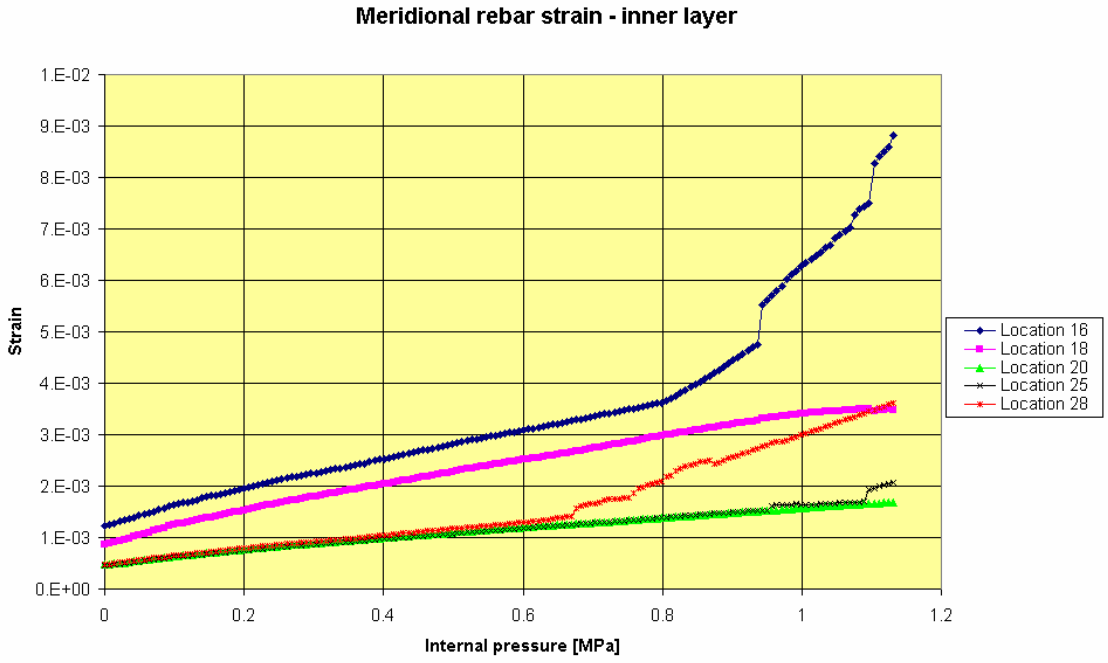

Fig. 38: Case 1, meridional rebar total strain at the inner rebar layer (at different vertical positions above top of basemat)

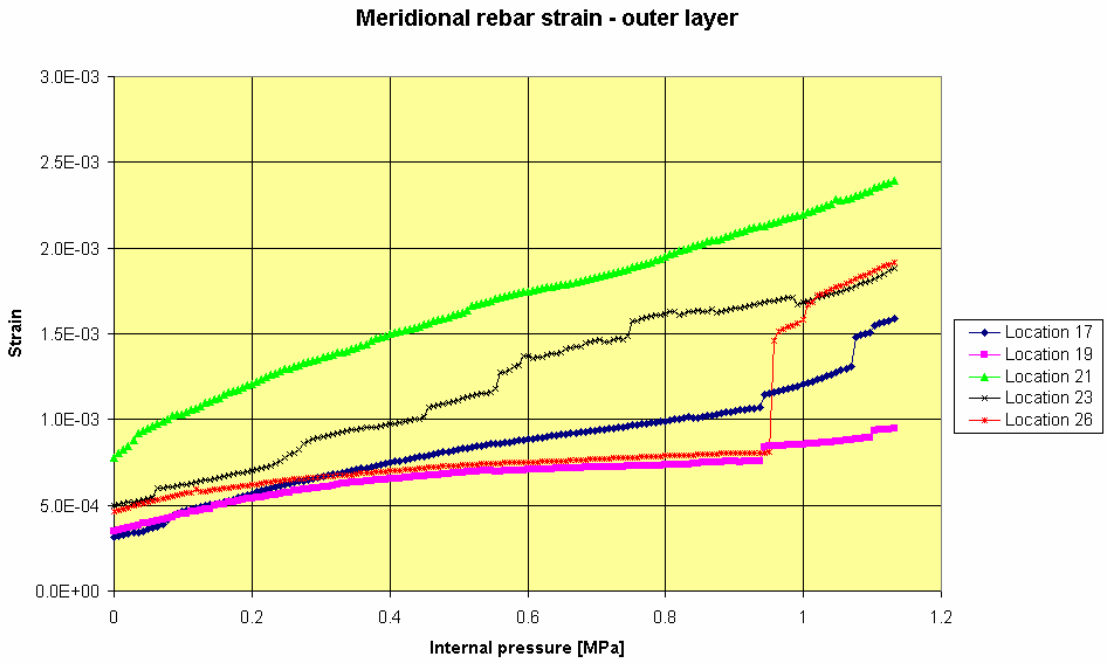

Fig. 39: Case 1, meridional rebar total strain at the outer rebar layer (at different vertical positions above top of basemat)

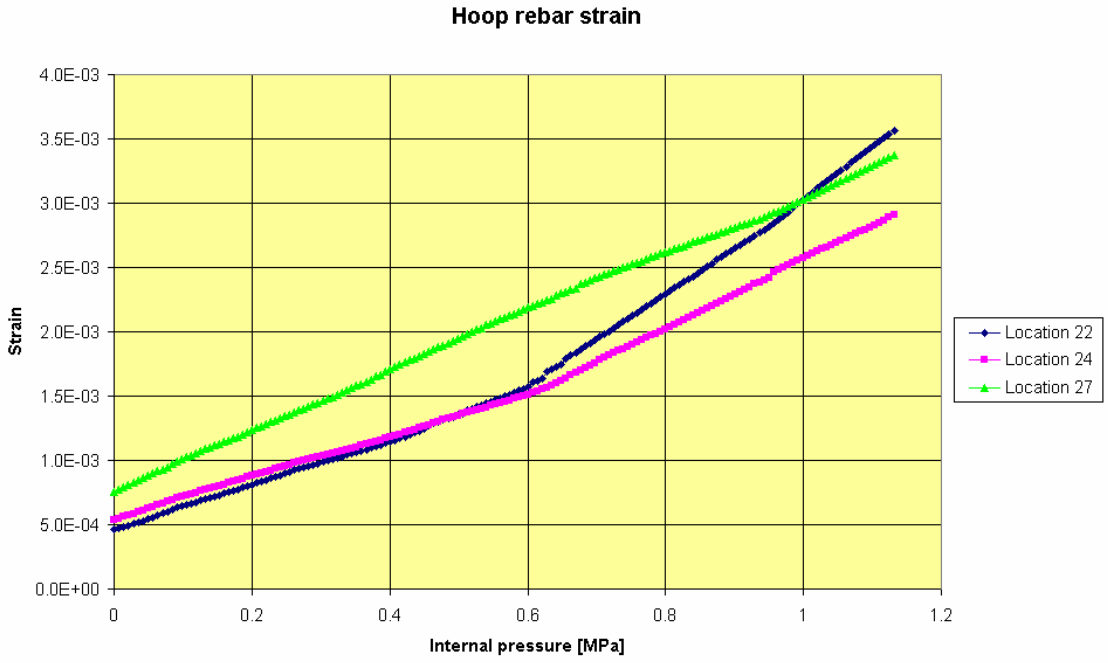

Fig. 40: Case 1, hoop rebar total strain (at different vertical positions above top of basemat)

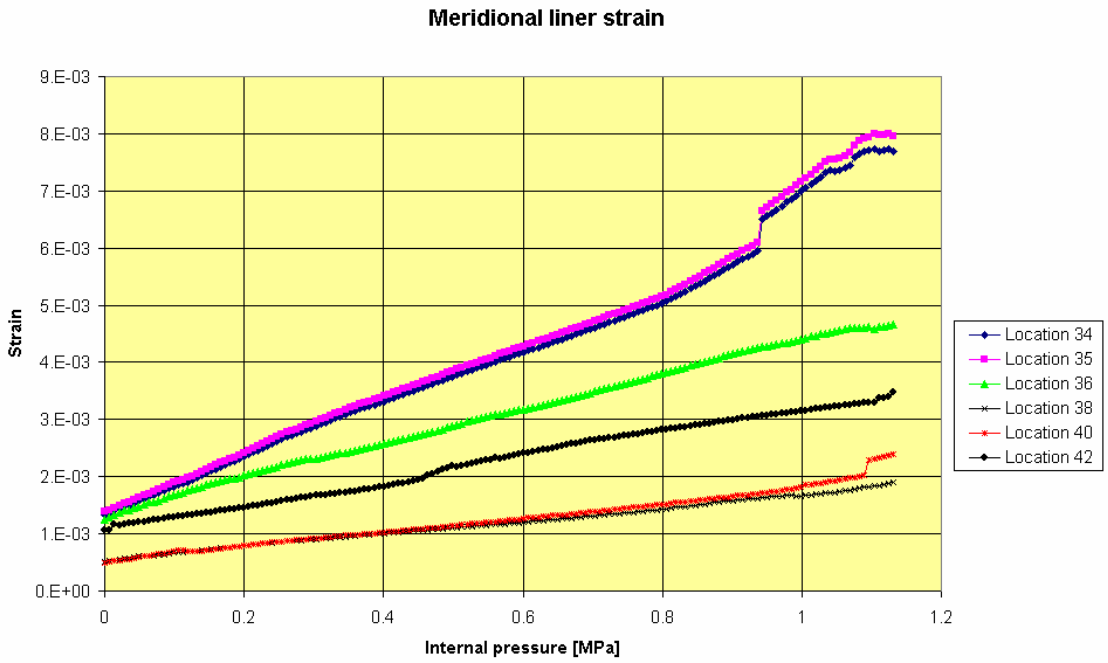

Fig. 41: Case 1, meridional total liner strain (at different vertical positions above top of basemat)

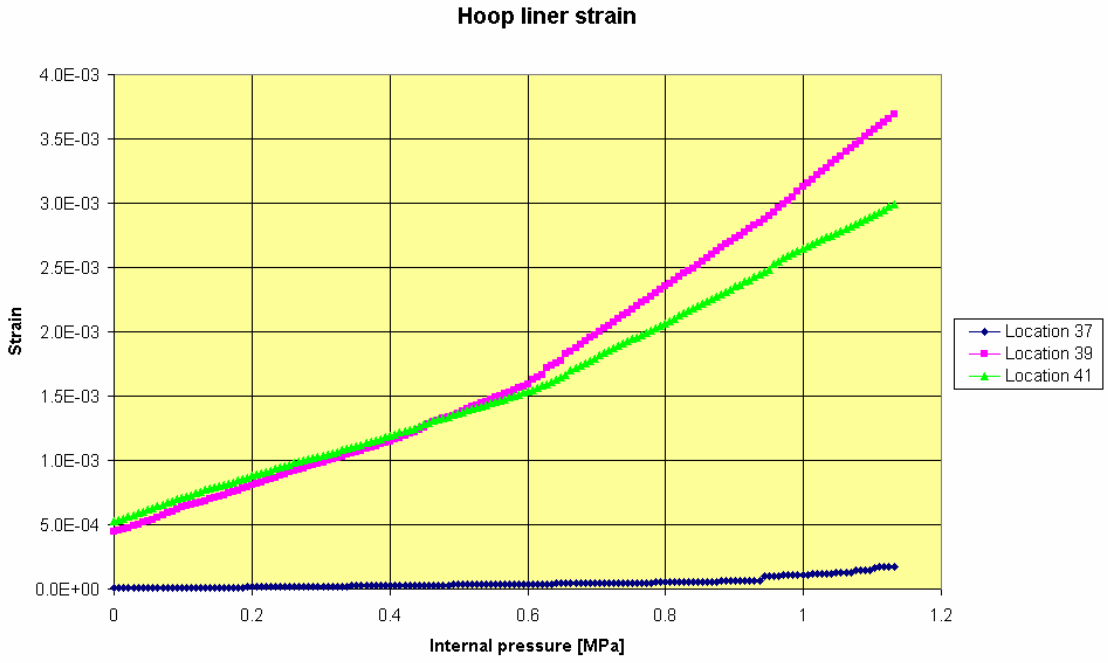

Fig. 42: Case 1, hoop total liner strain (at different vertical positions above top of basemat)

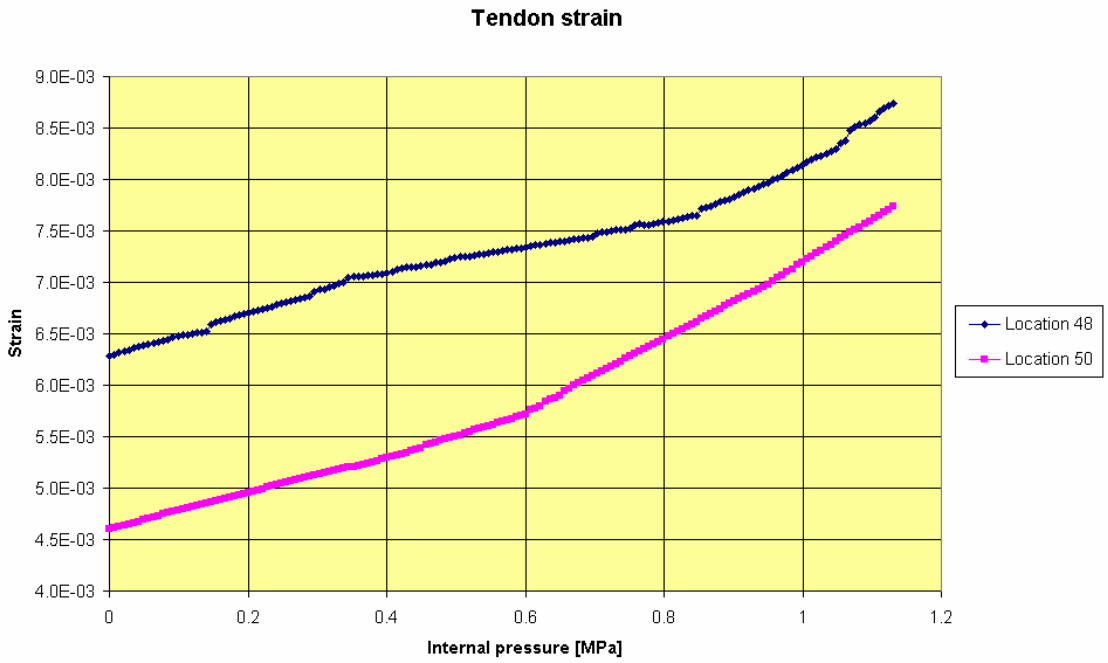

Fig. 43: Case 1, tendon total strain (at different vertical positions above top of basemat, location 48: meridional tendon, location 50: hoop tendon)

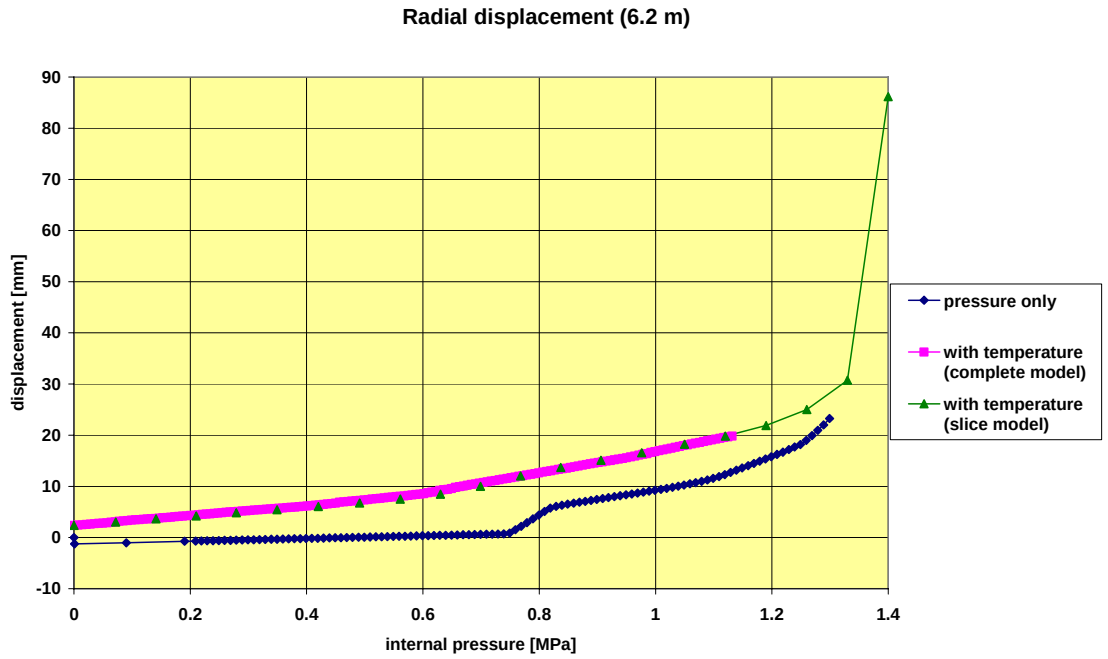

Fig. 44: Case 1, comparison of radial displacement from calculations with pressure only and with combined pressure and temperature loading (position 6.2 m above top of basemat)

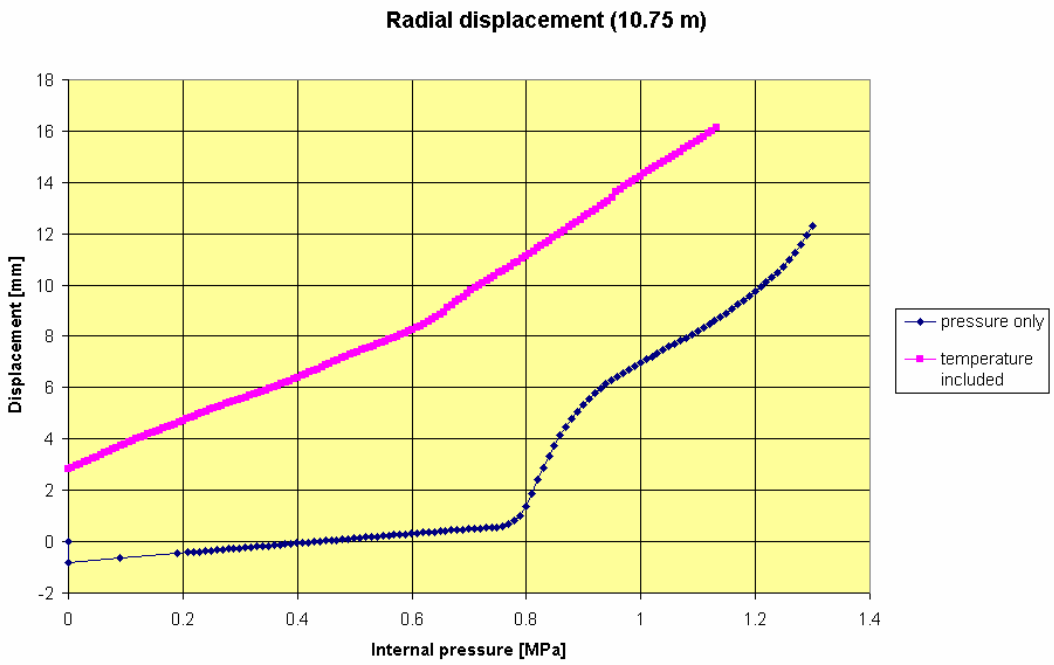

Fig. 45: Case 1, comparison of radial displacement from calculations with pressure only and with combined pressure and temperature loading (position 10.75 m above top of basemat)

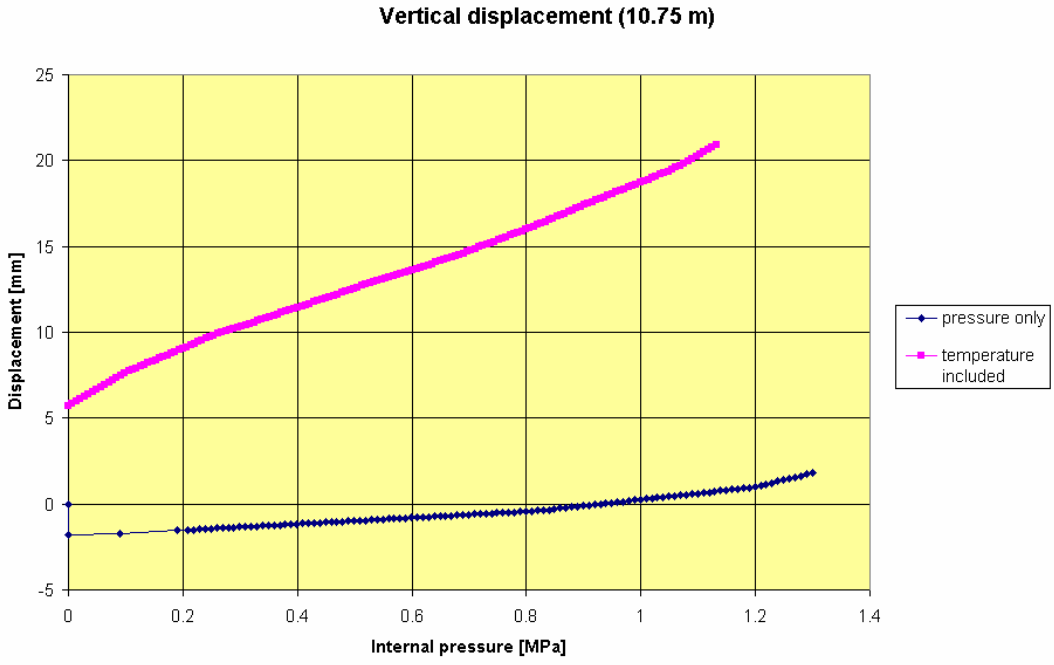

Fig. 46: Case 1, comparison of vertical displacement from calculations with pressure only and with combined pressure and temperature loading (position 10.75 m above top of basemat)

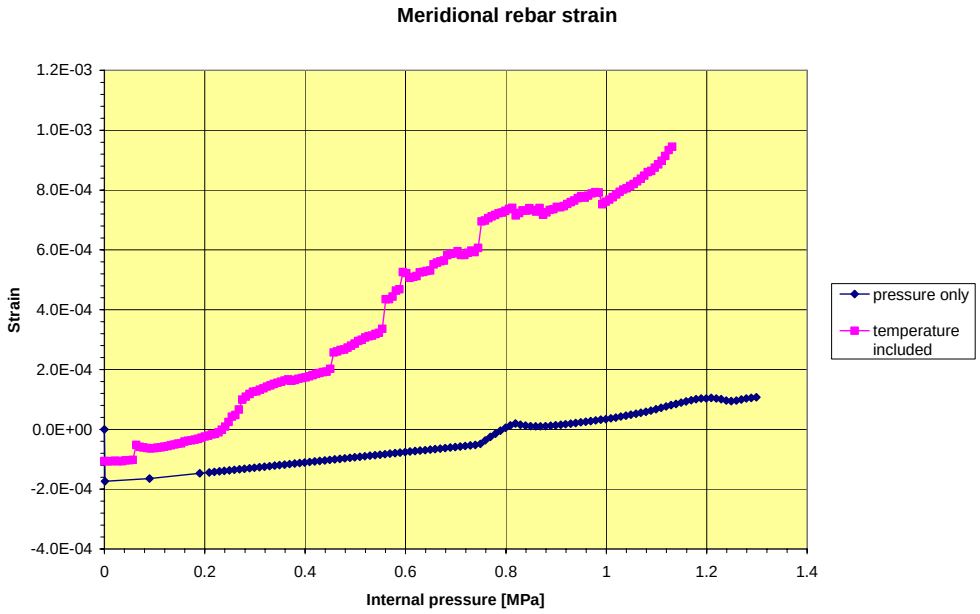

Fig. 47: Case 1, comparison of meridional rebar strain (outer rebar, mechanical strain) from calculations with pressure only and with combined pressure and temperature loading (position 6.2 m above top of basemat)

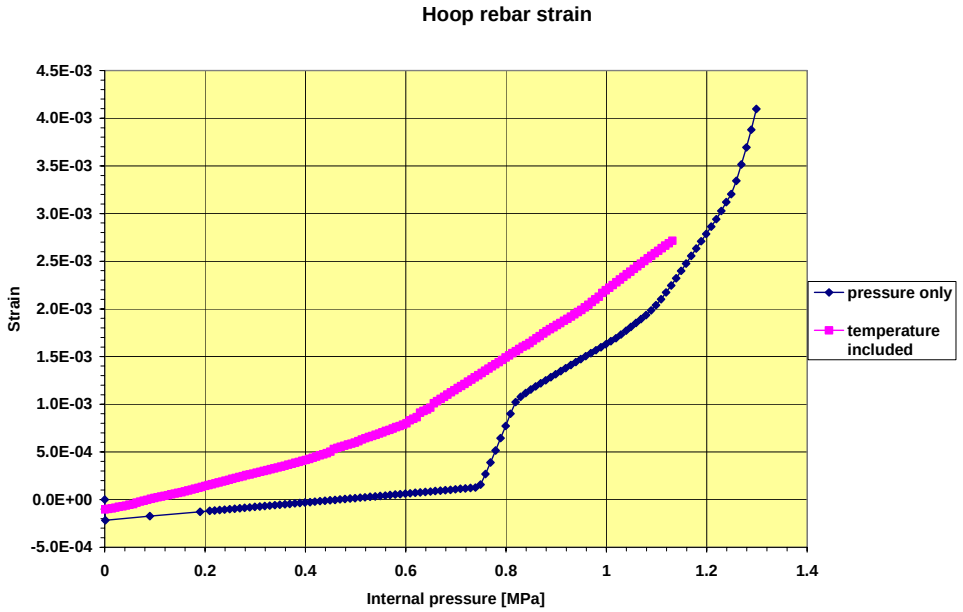

Fig. 48: Case 1, comparison of hoop rebar strain (outer rebar, mechanical strain) from calculations with pressure only and with combined pressure and temperature loading (position 6.2 m above top of basemat)

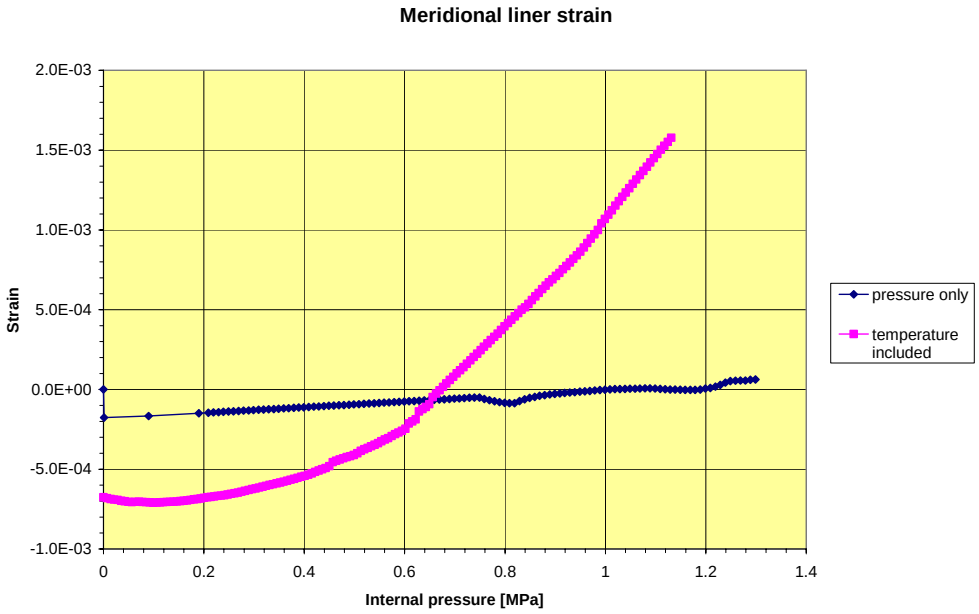

Fig. 49: Case 1, comparison of meridional liner strain (mechanical strain) from calculations with pressure only and with combined pressure and temperature loading (position 6.2 m above top of basemat)

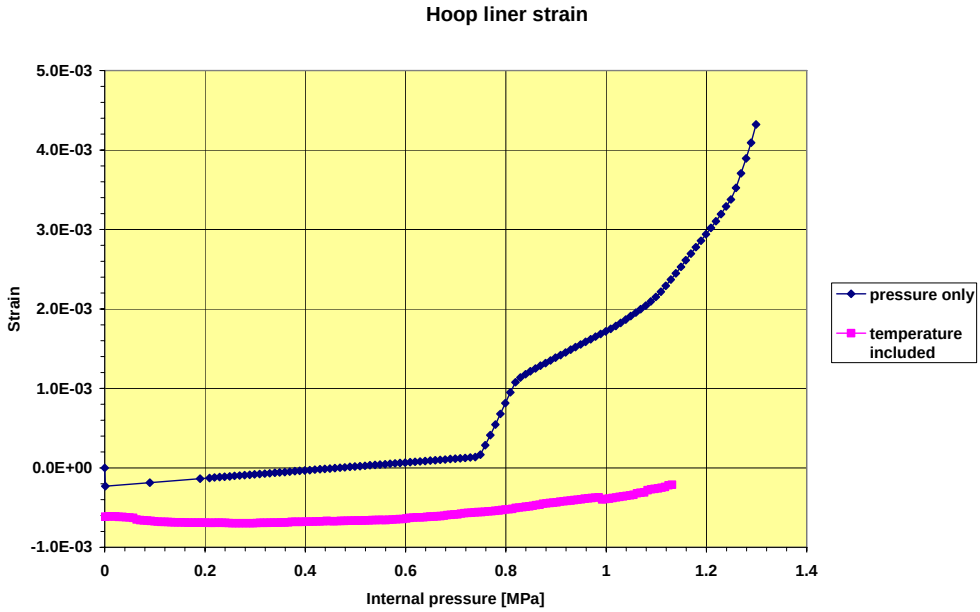

Fig. 50: Case 1, comparison of hoop liner strain (mechanical strain) from calculations with pressure only and with combined pressure and temperature loading (position 6.2 m above top of basemat)

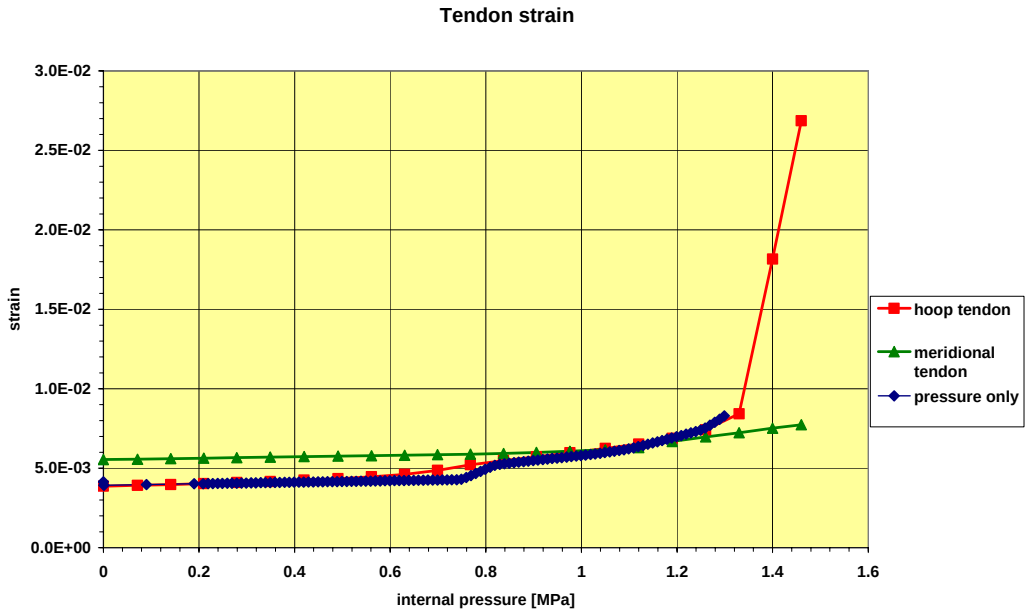

Fig. 51: Case 1, comparison of tendon strain (mechanical strain) from calculations with pressure only (hoop tendon, complete model, Fig. 3) and with combined pressure and temperature loading (hoop and meridional tendon) for slice model (position 6.6 m above top of basemat)

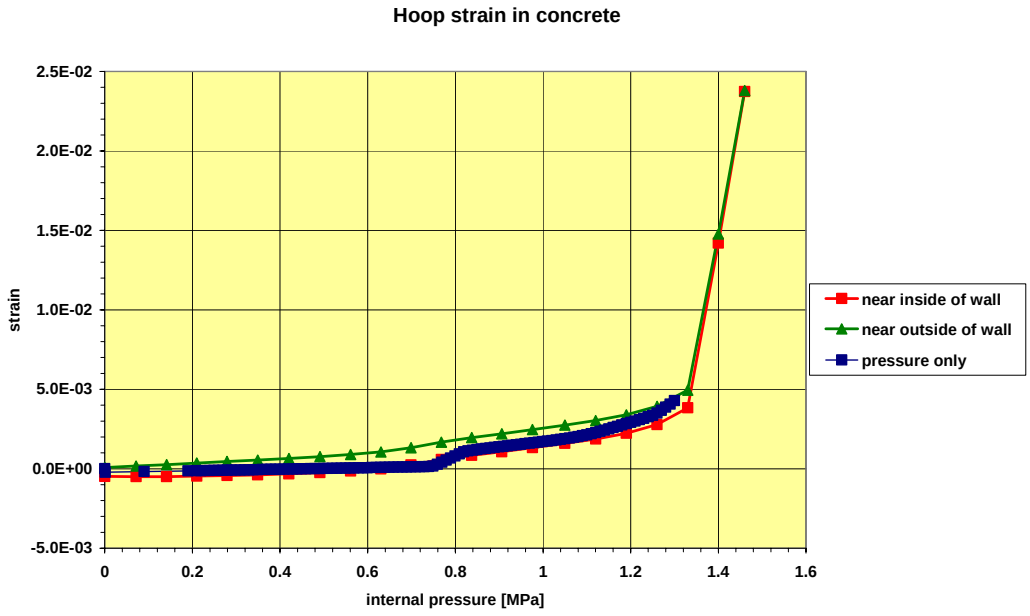

Fig. 52: Case 1, hoop strain in the concrete for the slice model (Fig. 6) at positions near inside and outside of the wall, combined pressure and temperature loading (mechanical strains) and for pressure only (complete model, Fig. 3)

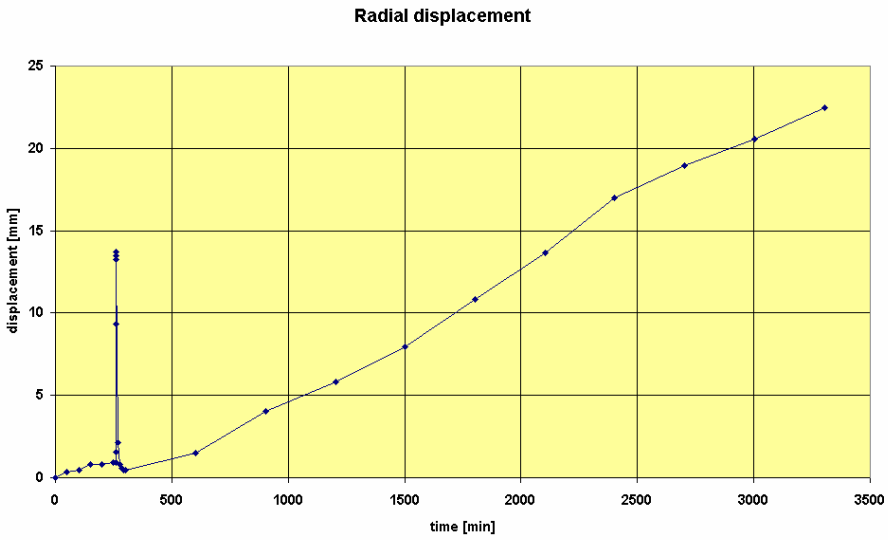

Fig. 53: Case 2, radial displacement, combined pressure and temperature loading (slice model), position 6.2 m above top of basemat

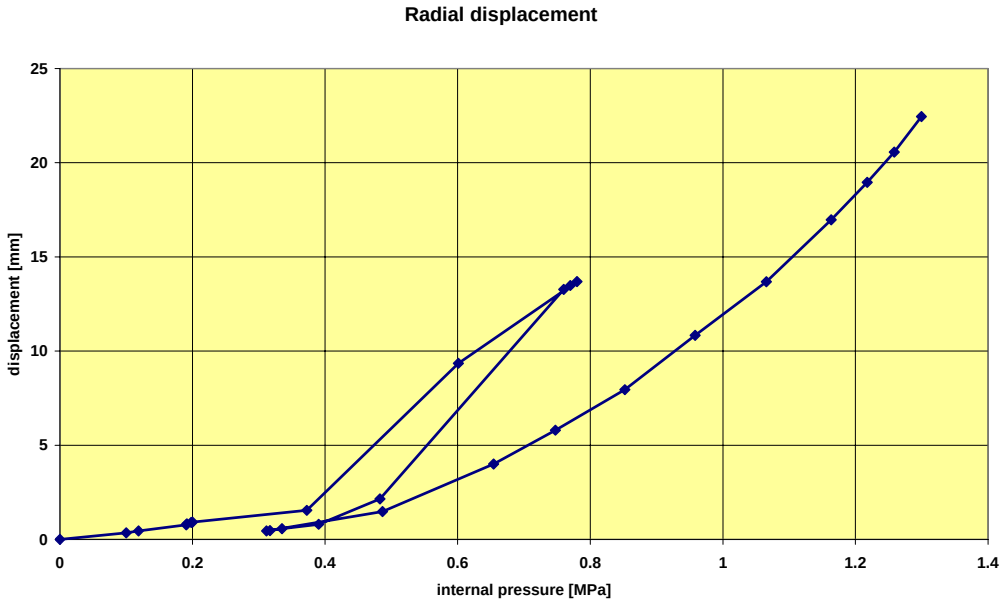

Fig. 54: Case 2, radial displacement, combined pressure and temperature loading (slice model), as function of pressure, position 6.2 m above top of basemat

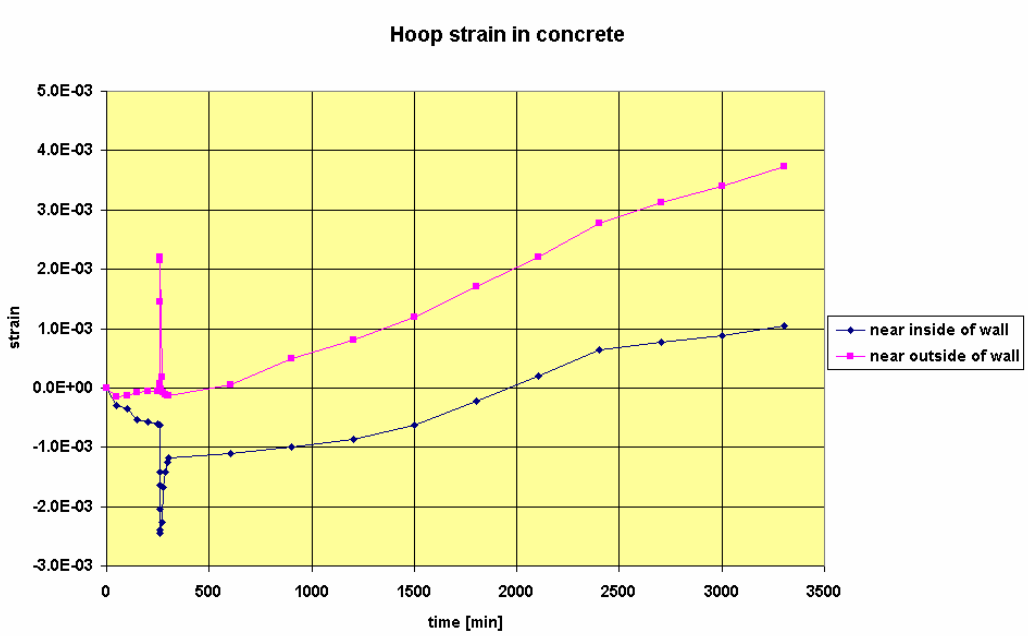

Fig. 55: Case 2, hoop strains (mechanical) in concrete for points near inner and outer surface, combined pressure and temperature loading (slice model) , position 6.2 m above top of basemat

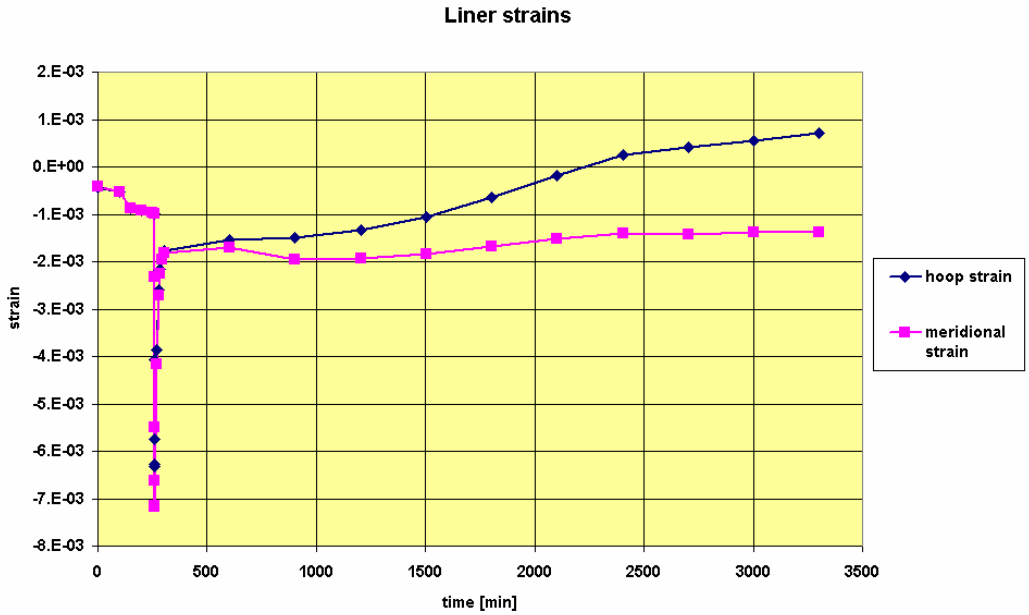

Fig. 56: Case 2, liner strains (mechanical), combined pressure and temperature loading (slice model) , position 6.2 m above top of basemat

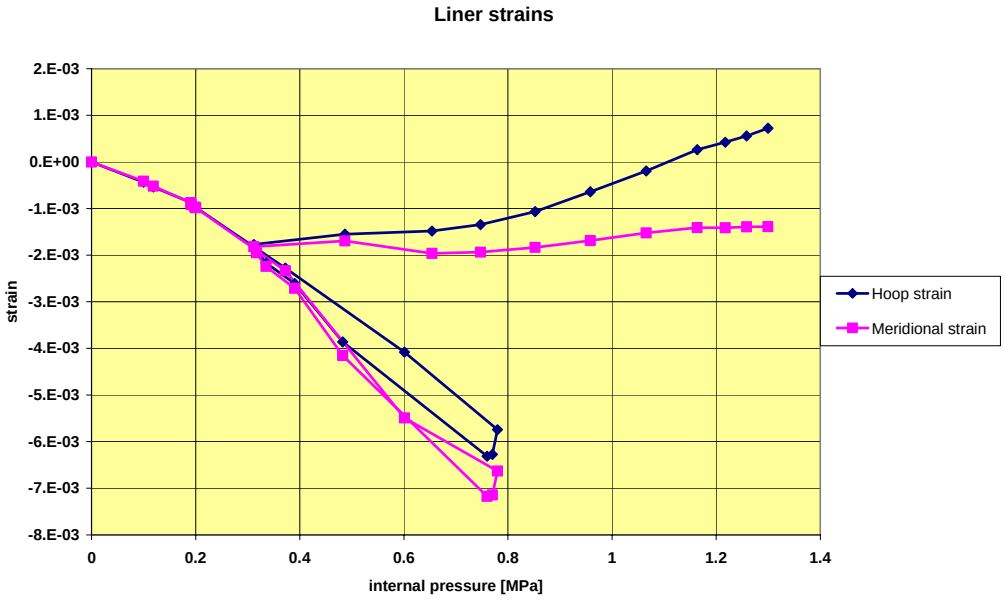

Fig. 57: Case 2, liner strains (mechanical), combined pressure and temperature loading (slice model), as functions of pressure, position 6.2 m above top of basemat

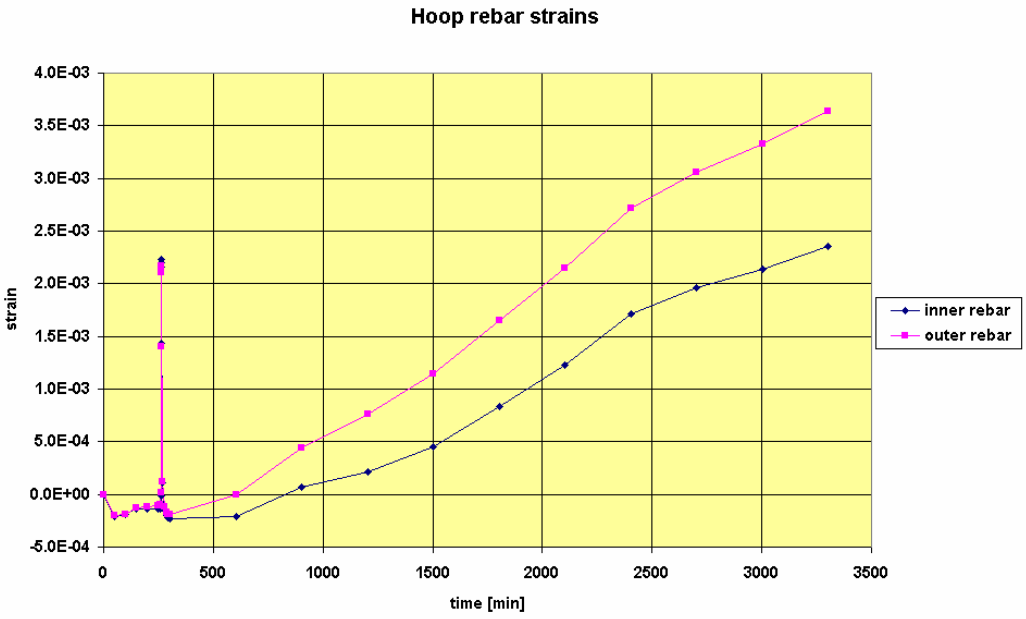

Fig. 58: Case 2, hoop rebar strains for inner and outer rebar, combined pressure and temperature loading (slice model) , position 6.2 m above top of basemat

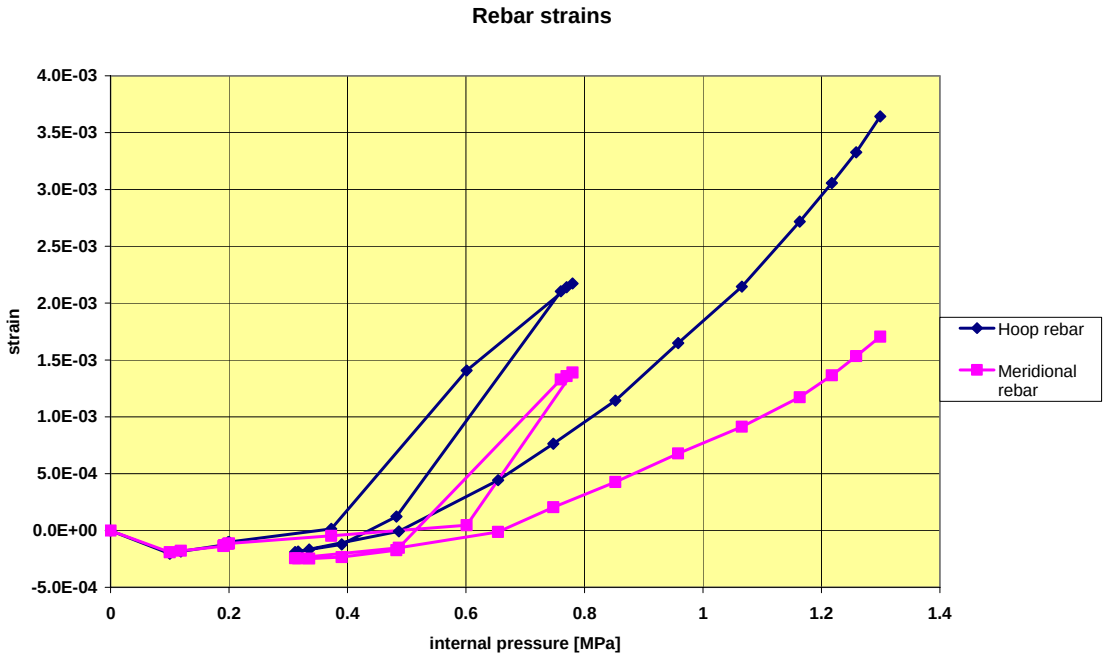

Fig. 59: Case 2, rebar strains (mechanical) for hoop and meridional rebar, combined pressure and temperature loading (slice model), as functions of internal pressure, position 6.2 m above top of basemat

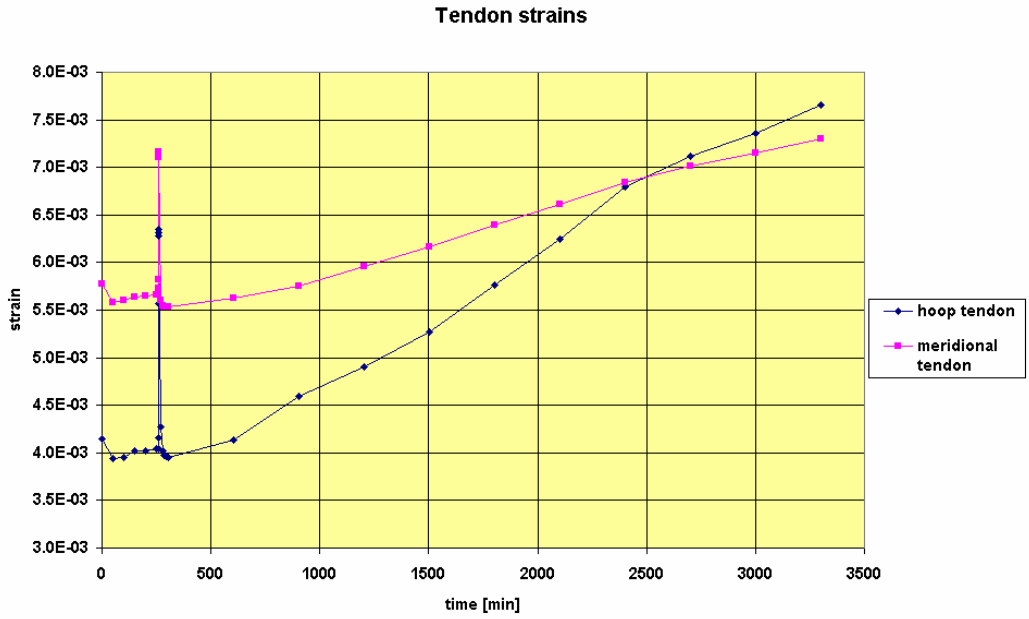

Fig. 60: Case 2, tendon strains (mechanical strains), combined pressure and temperature loading (slice model) , position 6.2 m above top of basemat

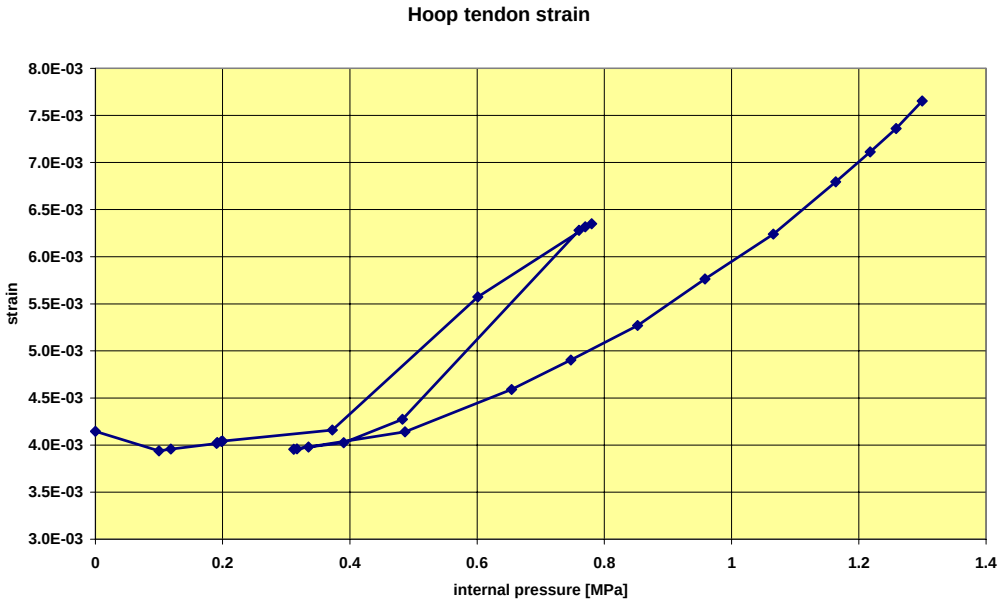

Fig. 61: Case 2, hoop tendon strain (mechanical strain), combined pressure and temperature loading (slice model), as function of internal pressure, position 6.2 m above top of basemat

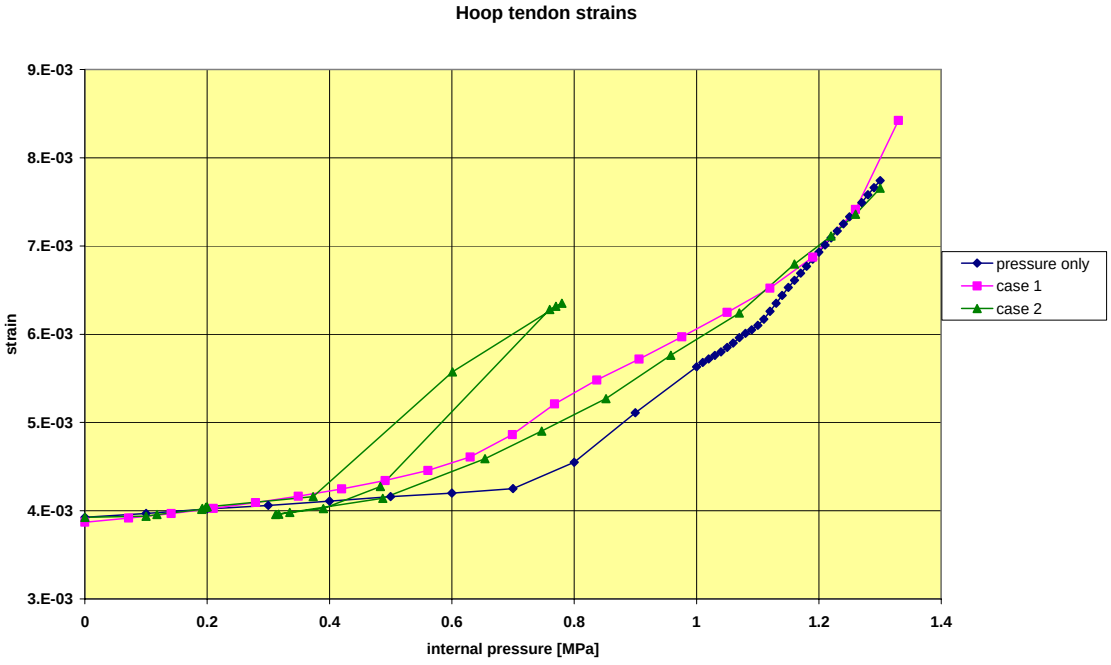

Fig. 62a: Hoop tendon strain (mechanical strain), for pressure only and combined pressure and temperature cases 1 and 2 (slice model), as function of internal pressure (up to about 1.3 MPa)**,** position 6.2 m above top of basemat

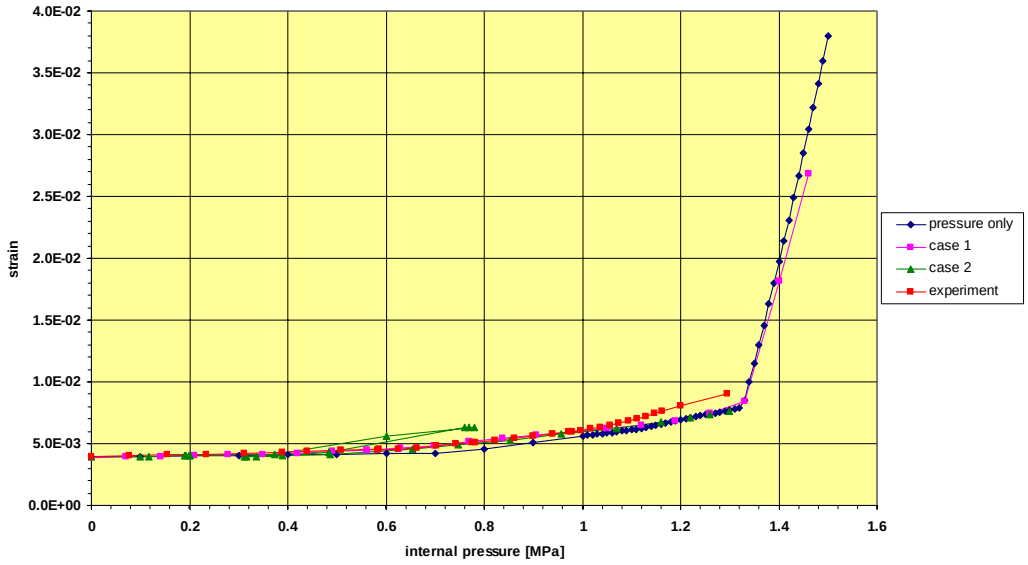

Fig. 62b: Hoop tendon strain (mechanical strain), for pressure only, combined pressure and temperature cases 1 and 2 (slice model) and from experiment, as function of internal pressure**,** position 6.2 m above top of basemat

Appendix G: Institut de Radioprotection et de Sûreté Nucléaire
Commissariat a l'Energie Atomique

Phase 2: G-1 to G-84
Phase 3: G-85 to G-86

ABSTRACT

Objective of this paper is to describe the modelling and the computation of the NRC/NUPEC Sandia test of a Prestressed Concrete Containment Vessel (PCCV) model. The model was a 1:4 scale of a Japanese nuclear power plant (ohi-3) The work is part of the ISP48 international benchmark. In this paper is described the finite element model, the prestressed stage and the computation of the Limit State Test (LST) which consists in increasing the internal pressure as much as possible.

1 Introduction

This work has been performed by IRSN (French Institut de Radioprotection et de Surete Nucleaire) and CEA (French Commissariat à l'Energie Atomique) in the frame of the ISP 48 (International Standard Problem).
The computation of the containment has been performed with the Cast3M finite element code of CEA. All input data has been collected in the ISP 48 PCCV Data Package edited by Mr Hessheimer.

2 Finite element model

2.1 Geometry

The finite element model is a 3-D model with the modelling of the Equipment hatch and of the Personal Air Lock penetrations. The two opposite buttress are also taken into account as well as the basemat and the tendon gallery.

The concrete part is represented by solid linear elements (hexahedron 8 nodes). Four elements in the thickness of the wall and the mean size of elements is 0,5 metre in the vertical direction and 0,4 metre in the hoop direction. 16834 elements and 19736 nodes compose the complete model, including basemat. (Fig 1)

The reinforcing steel is represented by linear 2 nodes elements. The mean size of elements is 0,5 metre as well as for the wall as for the basemat. There are 130556 elements and 112532 nodes representing reinforcing steels. Meshes of concrete and of reinforcing steel are independent. Nodes of reinforcing steels will be attached to concrete by means of relations between displacements unknowns. Reinforcing steel are well meshed in the basemat and in the cylindrical wall but simplifications are made around penetrations and dome (fig 2)

The 198 tendons are also meshed with their deviations around penetrations. Size of elements is around 0,5 metre and there are 15174 elements with 15372 nodes. Figures 3 to 14 represent tendons by group.

Liner is meshed by 3 or 4 nodes shell elements. There are 2694 elements with 2672 nodes (Fig 15).

The whole mesh including attach relations between unknowns represented a total of 700.000 degrees of freedom.

2.2 Material characteristics

2.2.1 Concrete

The Concrete is modelled by the OTTOSEN model, which is a smeared cracks model. There are two different concrete. The first is for the basemat and characteristics are:

- Young modulus E = 29030 MPa

- Poisson ratio $\nu = 0,2$
- Voluminal mass $\rho=2250\ kg/m^3$
- U T S $\sigma_{traction} = 3,93\ MPa$
- GFTR GFTR=135 J/ m^2

The second concrete is for the wall of the containment, characteristics are:

- Young modulus E = 31970 MPa
- Poisson ratio $\nu = 0,2$
- Voluminal mass $\rho=2500\ kg/m^3$
- U T S $\sigma_{traction} = 4,21\ MPa$
- GFTR GFTR=135 J/ m^2

For the prestressing part of the computation concrete is supposed to remain elastic.

2.2.2 Reinforcing steel

The general behaviour of steel is elastoplastic. Characteristics depend on the size of diameter of irons. Elastic modulus of steel is extract from tensile curves.

Figure 16 to 21 give tensile curves for irons depending on irons diameter.

- Young modulus E = 183600 MPa
- Poisson ratio $\nu = 0,3$
- Voluminal mass $\rho = 7850\ kg/m^3$

2.2.3 Tendons

The general behaviour of tendon is elastoplastic. Characteristics are:

- Young modulus E = 200 000 MPa
- Poisson ratio $\nu = 0,3$
- Voluminal mass $\rho=7800\ kg/m^3$
- Yield limit $\sigma_e = 1400\ MPa$
- Ultimate strength $\sigma_u = 1900\ MPa$

The tensile curve is given Fig 22

2.2.4 Liner

The general behaviour of the liner is elastoplastic. Characteristics are

- Young modulus E = 156 500 MPa
- Poisson ratio $\nu = 0,3$

- Voluminal mass ρ=7800 kg/m^3
- Yield limit σ_e = 375 MPa
- Ultimate strength σ_u = 450 MPa

The tensile curve is given Fig 23

2.3 Prestressing

The prestressing of the containment represents the real sequence of physical prestressing of the mock-up. There are 12 steps in the prestressing loading. The following table gives details on each step.

Prestressing steps	
Step	Tendons
1	H91 H92 H95 H96 H99 H100 H103 H104 H107 H108
2	V1 V3 V5 V7 V39 V41 V43 V45 V46 V48 V50 V52 V84 V86 V88 V90
3	V21 V32 V25 V66 V68 V70
4	V9 V11 V13 V15 V17 V19 V27 V29 V31 V33 V35 V37 V54 V56 V58 V60 V62 V64 V72 V74 V76 V78 V80 V82
5	H3 H4 H7 H8 H11 H12 H15 H16 H19 H20 H23 H24 H27 H28 H31 H32 H35 H36 H39 H40 H43 H44 H47 H48 H51 H52 H59 H60 H63 H64 H67 H68
6	H93 H94 H97 H98 H101 H102 H105 H106
7	H71 H72 H75 H76 H79 H80 H83 H84 H87 H88
8	V2 V4 V6 V8 V38 V40 V42 V44 V47 V49 V51 V53 V83 V85 V87 V89
9	V20 V22 V24 V26 V65 V67 V69 V71
10	V10 V12 V14 V16 V18 V28 V30 V32 V34 V36 V55 V57 V59 V61 V63 V73 V75 V79 V81
11	H1 H2 H5 H6 H9 H10 H13 H14 H17 H18 H21 H22 H25 H26 H29 H30 H33 H34 H37 H38 H41 H42 H45 H46 H49 H50 H53 H54 H57 H58 H61 H62 H65 H66 H69 H70
12	H77 H78 H73 H74 H81 H82 H85 H86 H89 H90

The effective loads are different for hoop tendons and vertical tendons. For the hoop tendons the tension applied to the end of the tendon is F_h = 453300 N. For the vertical tendon the applied tension at the end of the tendon is F_v = 503100 N.

All formulas to describe shrink of concrete, creep of concrete and lost of tension along a tendon are coming from the French standard BPEL99. Coefficients used for these formulas are the following:

Ff = 0,18	coefficient of angular friction
Phif = 0,002	coefficient of linear friction
Ganc = 0,008 m	seating loss
Rmu0 = 0,43	relaxation coefficient of irons
Fprg = 1978 MPa	ultimate strenght of tendon
Rh10 = 1,5	relaxation at 1000 hours in %

The prestressing of the containment starts 180 days after the end of the building of the containment. Tensioning of group of tendons takes place every 5 days and the containment can creep for another period of 125 days before the Limit state Test. We will use " this last date as the "end of the prestressing period".

3 Results of prestressing state

Displacements, loads in tendons and stresses in concrete and in the liner are shown hereafter.

3.1 Displacements after prestressing

The following figure presents the measured values of radial displacements during the building of the mock-up at elevation 4.860 meter from the top of the basemat.

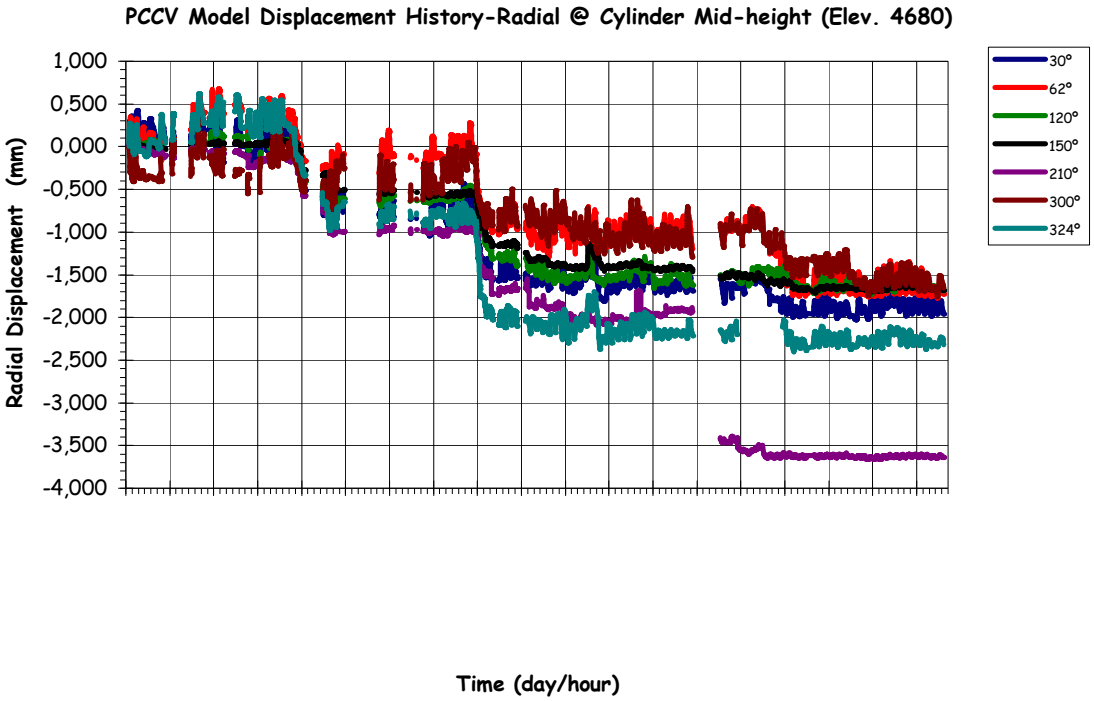

If we consider the maximum values for displacements measured on the mock-up, we obtain:

30°	**62°**	**120°**	**150°**	**210°**	**300°**	**324°**
4680	**4680**	**4680**	**4680**	**4680**	**4680**	**4680**
-2,030E+00	-1,770E+00	-1,730E+00	-1,710E+00	-3,660E+00	-1,760E+00	-2,400E+00

As it can be seen from figure 25 the computation leads to the same profile of distribution along azimuth and values are of the same order. Computation leads to a maximum value of 4mm for radial displacement at this elevation in front of 3.66mm. The Fig 24 presents the initial mesh and the deformed one after prestressing. The figure 25 is an isovalue of computed radial displacements for the containment after prestressing.

3.2 Tensions along tendons

The following tables give maximum, mean and minimum computed load for each tendon. The three first tables are for vertical tendons and next ones are for hoop tendons.

Group	tendon	Minimum tension(N)	Mean tension (N)	Maximum tension(N)	**Group**	tendon	Minimum tension(N)	Mean tension (N)	Maximum tension (N)
2	1	300019	376556	434065	3	1	334755	403216	430225
	2	320414	391775	433236		2	334798	403290	429818
	3	328655	396079	434309		3	333882	403205	430203
	4	323287	387681	424530		4	310250	383593	431428
	5	332137	400990	430912		5	333034	398572	431503
	6	341750	401109	433760		6	323485	391522	431452
	7	343291	402597	432672		**moye**	**328367**	**397233**	**430772**
	8	334169	403391	433717		**mini**	**310250**	**383593**	**429818**
	9	338722	404181	431166		**maxi**	**334798**	**403290**	**431503**

10	344444	402557	431118
11	343969	401524	431041
12	333732	400700	430956
13	284743	370825	430825
14	280585	371020	430849
15	282583	372585	430857
16	289537	375929	430918
moye	**312289**	**387415**	**430966**
mini	**280585**	**370825**	**424530**
maxi	**344444**	**404181**	**434309**

Prestressing of groups 2 and 3 for vertical tendons

Group	tendon	Minimum tension(N)	Mean tension (N)	Maximum tension (N)	**Group**	tendon	Minimum tension(N)	Mean tension (N)	Maximum tension (N)
4	1	306891	383075	437933	8	1	320244	396468	451811
	2	315723	389293	432213		2	333767	407313	452011
	3	338587	404562	436420		3	339977	408768	444691
	4	344453	407189	432556		4	314643	390796	443919
	5	344130	406977	432526		5	345184	415314	434529
	6	343614	407104	432099		6	346147	415899	434589
	7	343369	407069	432034		7	357836	416344	451980
	8	344182	406900	432370		8	358924	417654	451662
	9	344088	407019	432466		9	349733	417766	440686
	10	343595	406715	432520		10	357442	416531	440340
	11	343749	406499	432505		11	356295	415790	439761
	12	335243	406206	432457		12	345490	414976	439854
	13	336046	406071	432367		13	303706	384992	439970
	14	335735	406175	432430		14	298685	384746	439771
	15	334307	402328	432411		15	301218	386389	439958
	16	325098	394111	432458		16	299019	386669	440500
	17	306344	382433	432468		**moye**	**326449**	**400982**	**440105**
	18	333120	401129	432432		**mini**	**298685**	**384746**	**434529**
	19	324445	392948	427724		**maxi**	**358924**	**417766**	**452011**
	20	335680	400843	428112					
	21	310392	381780	421832					
	22	314682	386563	425942					
	23	293700	379181	432430					
	24	289187	374851	432307					
	moye	**313444**	**387466**	**429156**					
	mini	**289187**	**374851**	**421832**					
	maxi	**344453**	**407189**	**437933**					

Prestressing of groups 4 and 8 for vertical tendons

Group	tendon	Minimun tension(N)	Mean tension (N)	Maximum tension (N)	**Group**	tendon	Minimum tension(N)	Mean tension (N)	Maximum tension (N)
9	1	353411	417069	439631	10	1	326593	400438	443527
	2	346753	417454	440971		2	339235	412382	444767
	3	346531	417447	440864		3	358758	422470	445221
	4	353387	417062	439485		4	358687	422432	445376
	5	336337	404555	440013		5	358567	422001	445392
	6	336138	406133	440383		6	358457	421996	445465
	7	345651	413288	440585		7	358612	422403	445243
	8	322049	397460	440560		8	358569	422386	444914
	moye	**342532**	**411309**	**440312**		9	358909	422460	444581
	mini	**322049**	**397460**	**439485**		10	349988	422419	443113
	maxi	**353411**	**417454**	**440971**		11	350107	422478	450005
						12	349844	422325	450264
						13	340857	414374	446551
						14	327198	403651	446646
						15	353438	419766	446650
						16	346289	413700	449120
						17	312727	391875	440900
						18	328412	402921	437344
						19	321368	396070	441376
						20	311444	393223	449975
						moye	**330217**	**404448**	**444820**
						mini	**311444**	**391875**	**437344**
						maxi	**358909**	**422478**	**450264**

Prestressing of groups 9 and 10 for vertical tendons

Group	tendon	Minimum tension(N)	Mean tension (N)	Maximum tension (N)	**Group**	tendon	Minimum tension(N)	Mean tension(N)	Maximum tension (N)
1	1	243656	306874	367344	5	1	249771	316371	377433
	2	244379	308034	368960		2	248599	315397	376776
	3	246895	308544	358041		3	244796	310879	371480
	4	247270	308166	358135		4	244109	309963	370921
	5	245568	303982	356254		5	239005	306254	367209
	6	242061	302523	355487		6	240162	305549	366613
	7	245020	299969	357464		7	231870	301011	364606
	8	245496	297731	355804		8	231791	299799	365157
	9	238609	290025	342464		9	234067	301847	363253
	10	239121	288198	334459		10	235704	300671	354342
	moye	**243755**	**299892**	**352264**		11	228603	300604	363031
	mini	**238609**	**288198**	**334459**		12	231554	297463	360902
	maxi	**247270**	**308544**	**368960**		13	218865	295365	360374
						14	222375	287934	360601
						15	211400	288456	359740
						16	222186	289635	349982
						17	188711	277083	356206
						18	213737	287716	357490

19	211017	285120	356242
20	210154	284596	357694
21	217381	293386	356662
22	226640	294444	358029
23	230298	299703	362388
24	236154	298283	360488
25	236430	301270	361565
26	236482	301142	363198
27	236121	300739	360883
28	236174	300634	363621
29	235844	300197	360222
30	235849	300082	362545
31	235437	299613	359534
32	235356	299486	361769
33	234972	299037	358890
34	234723	298952	360994
moye	**235560**	**299843**	**361057**
mini	**188711**	**277083**	**349982**
maxi	**249771**	**316371**	**377433**

Prestressing of groups 1 and 5 for hoop tendons

Group	tendon	Minimum tension(N)	Mean tension (N)	Maximum tension (N)	**Group**	tendon	Minimum tension(N)	Mean tension (N)	Maximum tension (N)
6	1	250278	313425	374316	7	1	240012	304566	364797
	2	250639	314255	375858		2	239894	304699	366640
	3	252470	314714	365149		3	240569	305257	365549
	4	252261	314155	365518		4	240568	305370	367320
	5	252271	310174	367845		5	241401	306335	366720
	6	250255	309638	363504		6	241519	306546	368489
	7	251280	305185	364801		7	242669	307870	368354
	8	249328	302996	359101		8	243032	308240	370164
	moye	**251098**	**310568**	**367012**		9	245088	310265	370811
	mini	**249328**	**302996**	**359101**		10	245687	310769	372556
	maxi	**252470**	**314714**	**375858**		**moye**	**242567**	**307582**	**368745**
						mini	**239894**	**304566**	**364797**
						maxi	**245687**	**310769**	**372556**

Prestressing of groups 6 and 7 for hoop tendons

Group	tendon	Minimum tension(N)	Mean tension (N)	Maximum tension (N)	**Group**	tendon	Minimum tension(N)	Mean tension (N)	Maximum tension (N)
11	1	258229	324538	386023	12	1	254456	320246	381470
	2	257681	324135	385835		2	254388	320267	382217
	3	255856	322209	383578		3	254547	320388	381634

	4	255541	321863	383474
	5	254218	320342	381557
	6	254036	320102	381626
	7	247418	317515	380222
	8	252526	317061	380465
	9	245406	315593	379474
	10	251840	316936	380463
	11	251811	317009	379331
	12	251637	314761	378619
	13	242292	314520	378426
	14	244663	311923	378461
	15	225902	307735	378234
	16	234774	305609	378403
	17	220341	301836	367722
	18	229677	305639	375646
	19	222362	299325	375146
	20	224152	300939	375698
	21	228052	304931	375238
	22	229075	301931	375792
	23	243096	314492	368489
	24	245010	313502	375968
	25	245410	315864	379027
	26	251505	315922	378331
	27	251615	317476	378613
	28	251630	317406	379925
	29	251304	317007	378078
	30	251262	316909	379375
	31	250883	316383	377387
	32	250744	316241	378536
	33	250228	315551	376465
	34	250061	315397	377503
	35	249362	314554	375385
	36	249014	314396	376372
	moye	**250357**	**315805**	**377388**
	mini	**220341**	**299325**	**367722**
	maxi	**258229**	**324538**	**386023**

4	254542	320443	382371
5	254780	320707	381991
6	254813	320771	382679
7	255299	321292	382618
8	255420	321398	383278
9	256336	322203	383584
10	256502	322365	384165
moye	**255280**	**321196**	**382790**
mini	**254388**	**320246**	**381470**
maxi	**256502**	**322365**	**384165**

Prestressing of groups 11 and 12 for hoop tendons

From all these values we can see that there is a good homogeneity in the tension of all tendons. Figures 27 to 34 present tensions along tendons H11, H35, H53, H67, H68, V37, V46 and V85.

3.3 Stresses in concrete

Results show a good uniform state of stresses in the concrete as expected.

The following table present a summary of maximum and minimum computed values of stresses at the end of prestressing period.

	Minimum value (MPa)	Maximum value (MPa)
Radial stresses	-7,4	2,0
Hoop stresses	-14	0,1
Meridional stresses	-8,85	2,5
Principal stress 1	-2,9	4,2
Principal stress 2	-6,25	1,0
Principal stress 3	-13,2	2,5

Summary table for stresses in the concrete

Values obtained in normal zones are in agreement with the value of the tension of tendons. Figures 35 to 36 present a visualisation of the stresses state in the concrete.

3.4 Stresses in the liner

The following table presents a summary of the computed stresses in the liner.

	Minimum value (MPa)	Maximum value (MPa)
Principal stress 1	-147	-12,5
Principal stress 2	-250	-28

It appears that the liner is everywhere in a compressive state.

3.5 Conclusion for prestressing computation

The computed prestressed state has displacements a bit higher than in experiment and tensions of tendons a bit smaller than in experiment. Stresses are also a little too small. All this may be explained by the use of the French BPEL99 rules for creep and shrink. The quality of concrete in front of creep and shrink has been taken from French rules and this seems to over estimate the creep and the shrink of the concrete.

Another difference in the computation in front of experiment is that the computation considers that as soon as a tendon is in tension it is sealed in the concrete.

Nevertheless the computed prestressed state of the containment seams to be in a good agreement with the experiment. This state will be used, as an initial state, to perform the Limit State Test.

4 Limit State Test computation

The already computed prestressed state of the containment is used as initial state at the beginning of the increasing of pressure.

4.1 Loads

Starting from the initial state computed after the prestressing of the concrete, an inside pressure, given by air pressure, increase up to 1,295 MPa as in the experimental test. Looking at results, and especially at curve 14 giving radial displacement just nearby the Equipment Hatch, we have noticed that we have applied the pressure on the surface of the hatch in the wrong way. This affects the local results but is not important for global results.

4.2 Analysis of results

The beginning of the cracking of concrete is around 0,67 MPa, which is in a good agreement with experiment. First cracks appear at the junction of the cylindrical wall and the basemat.

After this level of pressure it seems that the response of the structure is more or less the response of tendons and irons.

At a level of 1,2 MPa a new type of behaviour takes place. In the experiment this appears at a level of 1,05 MPa.

We can notice that the change of behaviour in the experiment is slow while it seems to be sharper in the computation. This may come from the perfect connection between irons and concrete in the computation while in the reality this connection breaks here and there for high level of pressure.

In the computation, the extremity of a tendon is not well represented because the end node is attached in the concrete and it creates local stresses that do not exist. Then results, in the concrete along buttress are not workable.

Results are plotted for two different pressure levels, after the beginning of cracking and at the end of the computation for a pressure of 1,295 MPa (Figures 43 to 59).

A series of curves (displacements, deformations, loads) comparing computation and experiment are also given.

4.2.1 Displacements

Looking at curves 1 to 15 we can notice that displacements for node, which are near the basemat, are not very good. This is because the computation considers that all nodes at the bottom of the basemat have a zero displacement in the axial direction. For that reason all results for nodes too close to basemat are not very good. In another hand, values of displacements are not very large and this may not influence the global behaviour of the structure. Starting with curve 3 at an elevation of 1,43 metre results have the same shape than experimental ones.
For most of the curves displacements at the starting of loading are higher than experimental ones. This can be explaining by the fact that the creep given by French rules BPEL99 with French coefficients taken for south of France are not valid for Sandia experiment.

Looking at curve 10 we can see that computation follows pretty well the general behaviour of the dome.
Curve 14 which gives radial displacements at nodes just by Equipment hatch, shows clearly that in the computation, pressure was not applied in the rigth direction.

4.2.2 Deformations

Again all results concerning rebars too close to the basemat are not easy to compare. For others rebars, by example curve 24 for a rebar at an elevation of 10,75 metre results are in a good agreement with experimental results. In this curve it can be seen that creep during prestressing is too important.

It must be pointed here that, in the computation, rebars are perfectly clamped in the concrete. This fact in conjunction with the fact that the cracking concrete behaviour is a smeared one induced that results along a rebar can be very different for one point to another one.

For the curves giving deformations in the hoop direction we find the type of curve giving radial displacements which is obvious and which is not so clear for experimental results.

4.2.3 Tensions in tendons

In the computation tendons are perfectly clamped in the concrete and therefore no redistribution of tensions occurs in the computation. This explains the oscillations observed in curves (Fig 55 - 56 - 57).
At the beginning of the LST the general level of tensions of tendons are a little too small. This is also due to the excessive creep during prestressing of the concrete.

4.2.4 Cracks

The first change of response of the structure can be observed around 0,67 MPa, this is due to the first cracks in the concrete. As we have taken the OTTOSEN model for concrete, which is a smeared one, we can observe that cracks concern often one row of elements out of two.

At a level of 0,71 MPa we can clearly observed vertical cracks due to excessive hoop stresses, especially in the region between the two penetrations (Fig 50)

If we do not consider results around buttress, the main crack, even at a level of pressure of 0,71MPa, is between the two penetrations which is the failure point during experimental test. The computation is able to predict where the failure will occur.

5 Conclusion

The computation of a prestressed concrete containment vessel has been conducted through a pressure of 1,295 MPa. The mesh is 3D with very little simplifications of concrete part or irons part. There are 700 000 degrees of freedoms in the structure and the computation with

Cast3m has been possible because of all improvments made these three last years under the direction of IRSN .
First, the prestressing is computed using French regulatory rules for creep and shrinkage. For this part, the prestressing has been applied in twelve steps and results are in a good agreement with experimental data's.
Then the limit state test, consisting in increasing internal pressure, is computed up to the end of the experiment. After a long computation (1 000 000 seconds CPU) results are in a good range in front of experimental results. The prediction of the failure mode seems to be possible from the computation.

LIST OF FIGURES

Fig 1: mesh of the concrete of the containment without basemat
Fig 2: mesh of the irons!
Fig 3: mesh of first group of tendons
Fig 4: second group of tendons
Fig 5: Third group of tendons
Fig 6: Fourth group of tendons
Fig 7: Fifth group of tendons
Fig 8: Sixth group of tendons
Fig 9: Seventh group of tendons
Fig 10: Eighth group of tendons
Fig 11: Ninth group of tendons
Fig 12: Tenth group of tendons
Fig 13: Eleventh group of tendons
Fig 14: Twelfth group of tendons
Fig 15: Mesh of the liner
Fig 16: Tensile curve for 6mm diameter irons
Fig 17: Tensile curve for 10mm diameter irons
Fig 18: Tensile curve for 13mm diameter irons
Fig 19: Tensile curve for 16mm diameter irons
Fig 20: Tensile curve for 19mm diameter irons
Fig 21: Tensile curve for 22mm diameter irons
Fig 22: Tensile curve for tendons
Fig 23: Tensile curve for liner
Fig 24: End of prestressing – initial mesh and final mesh
Fig 25: End of prestressing – radial displacements (mm)
Fig 26: End of prestressing – Radial stresses in the concrete vessel
Fig 27: End of prestressing – tension of tendon H11 (N)
Fig 28: End of prestressing – Tension of tendon H35 (N)
Fig 29: End of prestressing – Tension of tendon H53 (N)
Fig 30: End of prestressing – Tension of tendon H67 (N)
Fig 31: End of prestressing - Tension of tendon H68 (N)
Fig 32: End of prestressing – tension of tendon V37 (N)
Fig 33: End of prestressing – Tension of tendon V46 (N)
Fig 34: End of prestressing - Tension of tendon V85 (N)
Fig 35: End of prestressing – Hoop stresses in the concrete vessel (MPa)
Fig 36: End of prestressing – vertical stresses in the concrete vessel (MPa)
Fig 37: Pressure 0,71 MPa – Radial stresses in the wall (MPa)
Fig 38: Pressure 0,71 MPa – Hoop stresses in the wall (MPa)
Fig 39: Pressure 0,71 MPa – vertical stresses in the wall (MPa)
Fig 40: Pressure 0,71 MPa – Von Mises stresses in the liner (MPa)
Fig 41: Pressure 0,71 MPa – Tensions in tendons H11, H35, H53 (N)
Fig 42: Pressure 0,71 MPa – tensions of tendons H67, H68, V37 (N)
Fig 43: Pressure 0,71 MPa – tensions of tendons V46, V85
Fig 44: Pressure 0,71 MPa – First opening cracks in the wall (Metre)

Fig 45: Pressure 1,295 MPa – radial stresses in the wall (MPa)
Fig 46: Pressure 1,295 MPa – Hoop stresses in the wall (MPa)
Fig 47: Pressure 1,295 MPa – Vertical stresses in the wall (MPa)
Fig 48: Pressure 1,295 MPa – Von Mises stresses in the liner (MPa)
Fig 49: Pressure 1,295 MPa – Tensions of tendons H11, H35, H53 (N)
Fig 50: Pressure 1,295 MPa – Tensions of tendons H67, H68, V37 (N)
Fig 51: Pressure 1,295 MPa – tensions of tendons V46, V85 (N)
Fig 52: Pressure 1,295 MPa – Hoop crack opening (metre)
Fig 53: Pressure 1,295 MPa – Vertical crack opening (metre)

LIST OF COMPARISONS EXPERIMENT / COMPUTATION

Curve 1	Displacement vertical	AZ 135	el	0,0	m	outside cylinder
Curve 2	Displacement radial	Az 135	el	0,25	m	inside liner surface
Curve 3	Displacement radial	Az 135	el	1,43	m	inside liner surface
Curve 4	Displacement radial	Az 135	el	2,63	m	inside liner surface
Curve 5	Displacement radial	Az 135	el	4,68	m	inside liner surface
Curve 6	Displacement radial	Az 135	el	6,2	m	inside liner surface
Curve 7	Displacement radial	Az 135	el	10,75	m	inside liner surface
Curve 8	Displacement vertical	Az 135	el	10,75	m	inside liner surface
Curve 9	Displacement radial	Az 135	el	14,55	m	inside liner surface
Curve 10	Displacement vertical	Az 135	el	14,55	m	inside liner surface
Curve 11	Displacement vertical	Az 135	el	16,13	m	inside liner surface
Curve 12	Displacement radial	Az 90	el	6,2	m	inside liner surface
Curve 13	Displacement radial	Az 90	el	10,75	m	inside liner surface
Curve 14	Displacement radial	Az 334	el	4,675	m	inside liner surface
Curve 15	Displacement radial	Az 66	el	4,525	m	inside liner surface
Curve 16	Rebar strain meridional	Az 135	el	0,05	m	inner rebar layer
Curve 17	Rebar strain meridional	Az 135	el	0,05	m	outer rebar layer
Curve 18	Rebar strain meridional	Az 135	el	0,25	m	inner rebar layer
Curve 19	Rebar strain meridional	Az 135	el	0,25	m	outer rebar layer
Curve 20	Rebar strain meridional	Az 135	el	1,43	m	inner rebar layer
Curve 21	Rebar strain meridional	Az 135	el	1,43	m	outer rebar layer
Curve 22	Rebar strain hoop	Az 135	el	6,2	m	outer rebar layer
Curve 23	Rebar strain meridional	Az 135	el	6,2	m	outer rebar layer
Curve 24	Rebar strain hoop	Az 135	el	10,75	m	outer rebar layer
Curve 25	Rebar strain meridional	Az 135	el	10,75	m	inner rebar layer
Curve 26	Rebar strain meridional	Az 135	el	10,75	m	outer rebar layer
Curve 27	Rebar strain hoop	Az 135	el	14,55	m	outer rebar layer
Curve 28	Rebar strain meridional	Az 135	el	14,55	m	inner rebar layer
Curve 29	Rebar strain meridional	Az 135	el	14,55	m	outer rebar layer
Curve 30	Rebar strain hoop	Az 90	el	0,05	m	inner rebar layer
Curve 31	Rebar strain meridional	Az 90	el	0,05	m	outer rebar layer
Curve 32	Rebar strain hoop	Az 90	el	6,2	m	outer rebar layer
Curve 33	Rebar strain meridional	Az 90	el	6,2	m	outer rebar layer
Curve 34	Liner strain meridional	Az 0	el	0,01	m	inside liner surface
Curve 35	Liner strain meridional	Az 0	el	0,01	m	outside liner surface
Curve 36	Liner strain meridional	Az 135	el	0,25	m	inside liner surface
Curve 37	Liner strain hoop	Az 135	el	0,25	m	inside liner surface
Curve 38	Liner strain meridional	Az 135	el	6,2	m	inside liner surface
Curve 39	Liner strain hoop	Az 135	el	6,2	m	inside liner surface
Curve 40	Liner strain meridional	Az 135	el	10,75	m	inside liner surface
Curve 41	Liner strain hoop	Az 135	el	10,75	m	inside liner surface
Curve 42	Liner strain meridional	Az 135	el	16,13	m	inside liner surface
Curve 43	Liner strain meridional	Az 90	el	6,2	m	inside liner surface
Curve 44	Liner strain hoop	Az 90	el	6,2	m	inside liner surface

Curve 45	Liner strain hoop	Az 334	el	4,675	m inside liner surface
Curve 46	Liner strain hoop	Az 58	el	4,525	m inside liner surface
Curve 47	base liner radial	Az 135	el	0,	100 mm inside cylinder
Curve 48	Tendon strain hairpin	Az 180	el	15,6	m tendon V37
Curve 49	Tendon strain hairpin	Az 135	el	10,75	m tendon V46
Curve 50	Tendon strain hoop	Az 90	el	6,58	m tendon H53
Curve 51	Tendon strain hoop	Az 180	el	6,58	m tendon H53
Curve 52	Tendon strain hoop	Az 280	el	6,58	m tendon H53
Curve 53	Tendon strain hoop	Az 0	el	4,57	m tendon H35
Curve 54	Tendon force hairpin	Az 241	el	-1,16	m tendon V37
Curve 55	Tendon force hoop	Az 275	el	6,58	m tendon H53

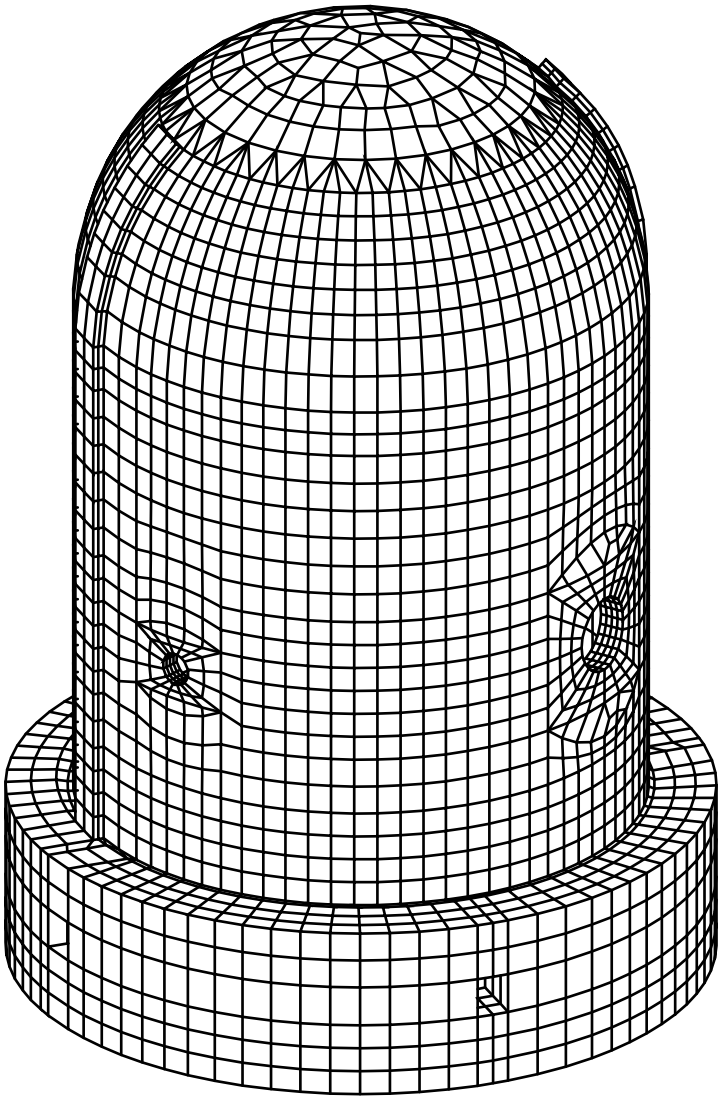

maillage beton 16384 elements 19736 noeuds

Fig 1: mesh of the concrete of the containment with basemat

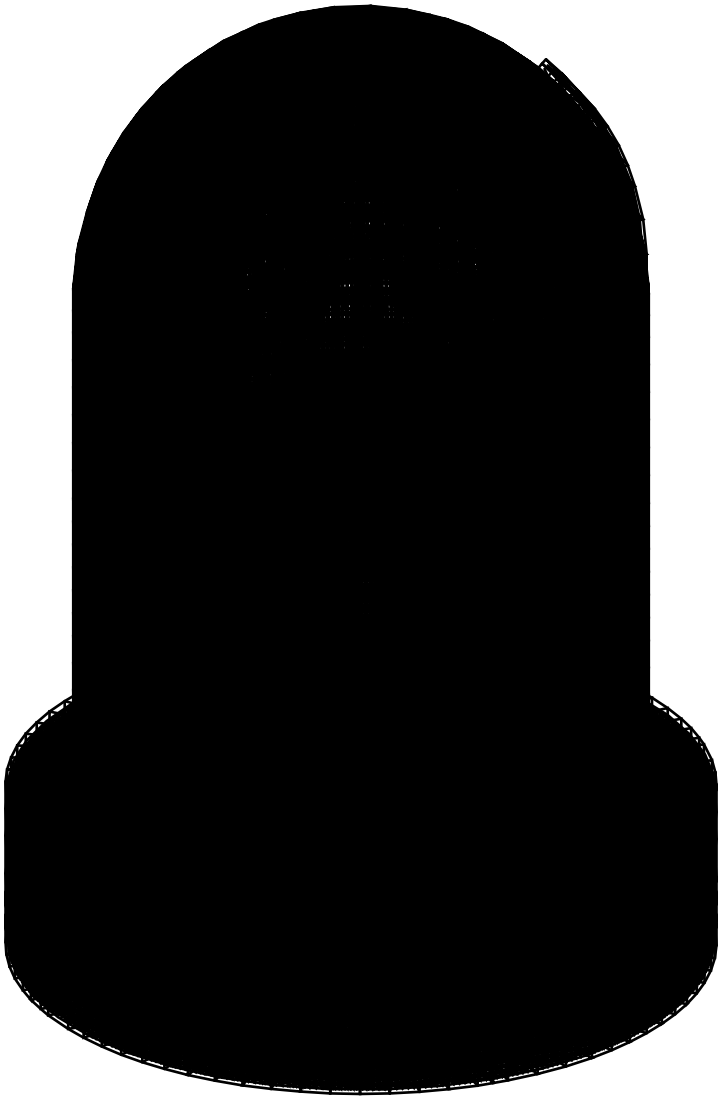

maillage des fers passifs 118556 elements 130525 noeuds

Fig 2: mesh of the irons!

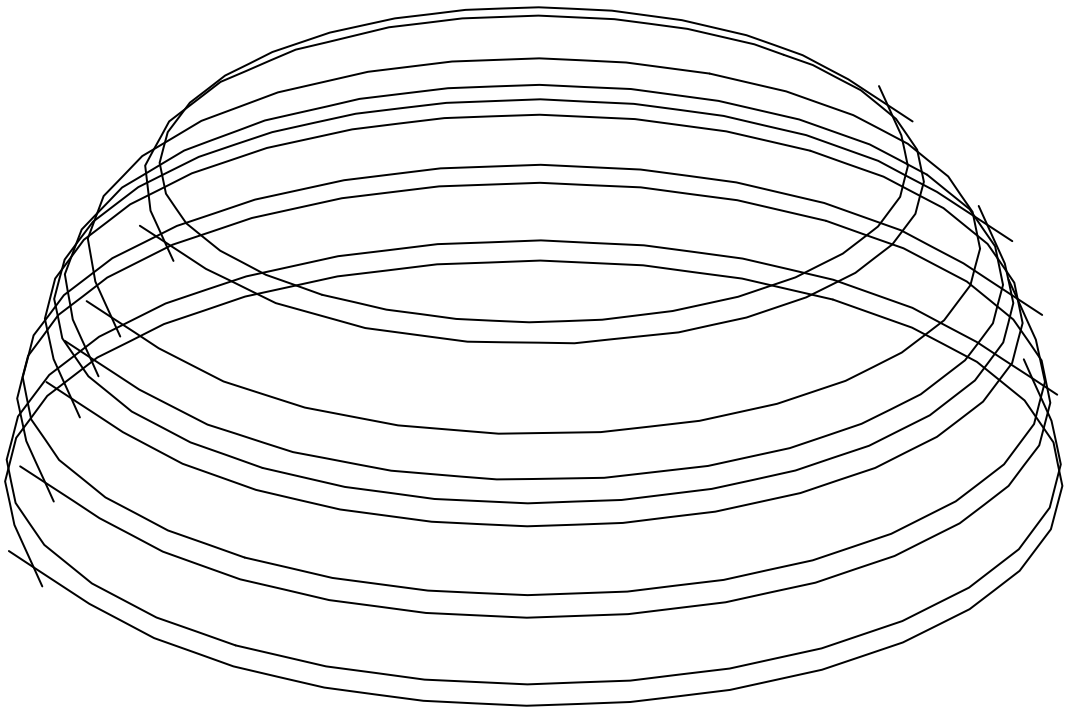

cables groupe 1,   666 elements 676 noeuds

Fig 3: mesh of first group of tendons

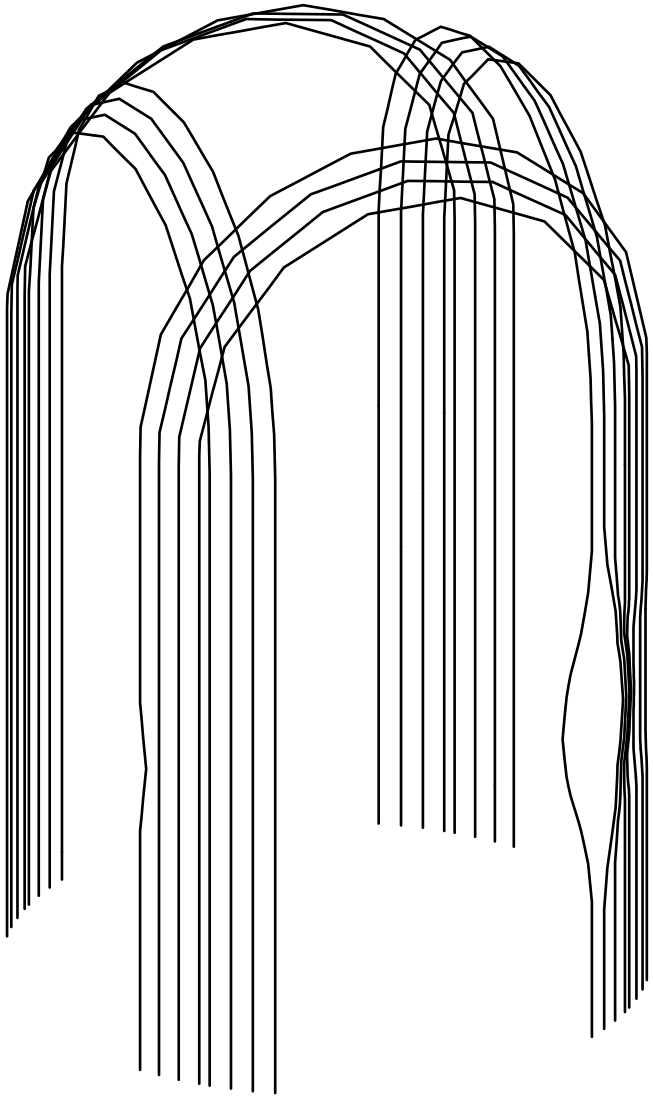

cables groupe 2,   1340 elements 1356 noeuds

Fig 4: second group of tendons

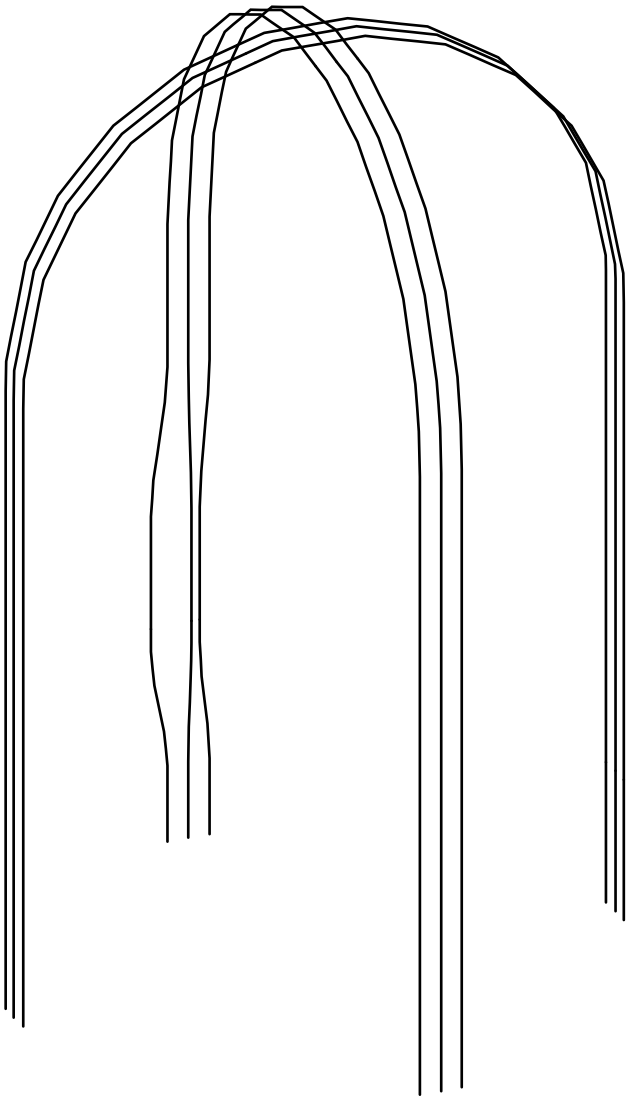

cables groupe 3,   513 elements 519 noeuds

Fig 5: Third group of tendons

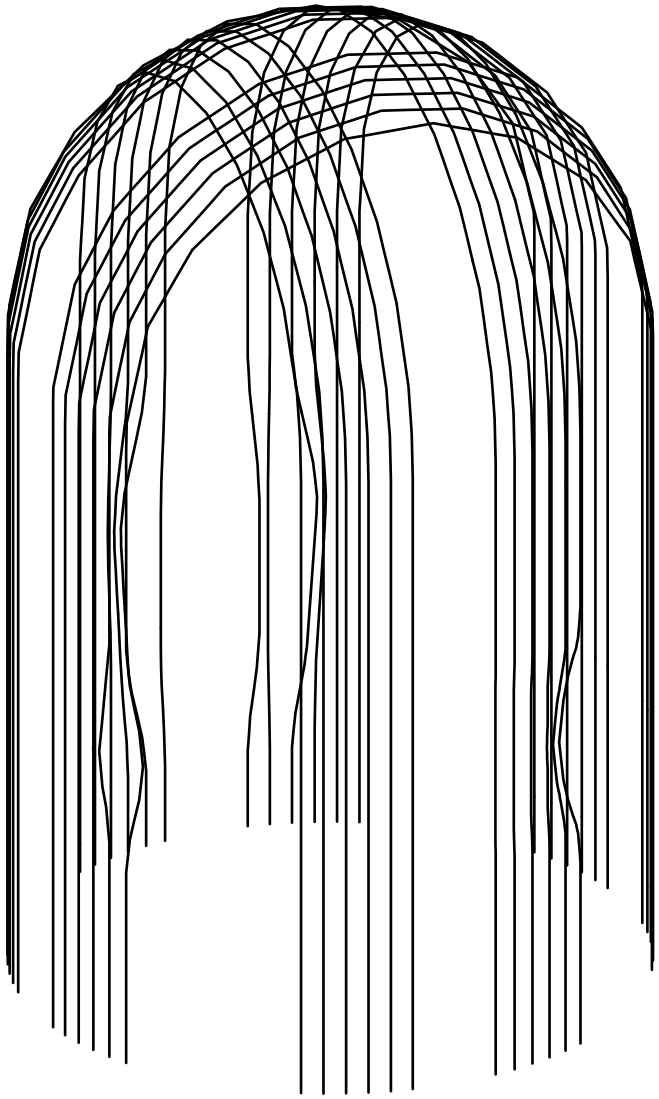

cables groupe 4,   2124 elements 2148 noeuds

Fig 6: Fourth group of tendons

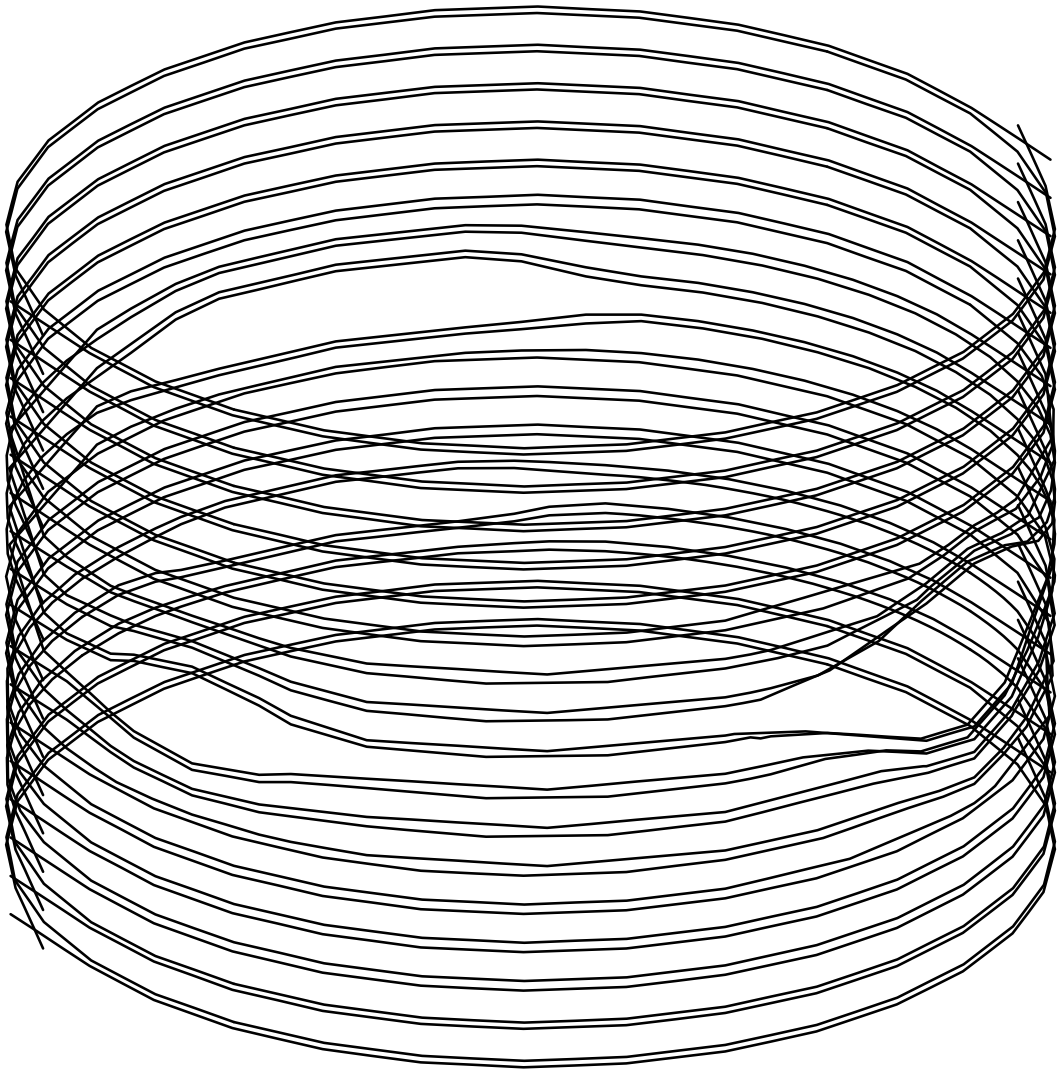

```
cables groupe 5,   2399 elements 2433 noeuds
```

Fig 7: Fifth group of tendons

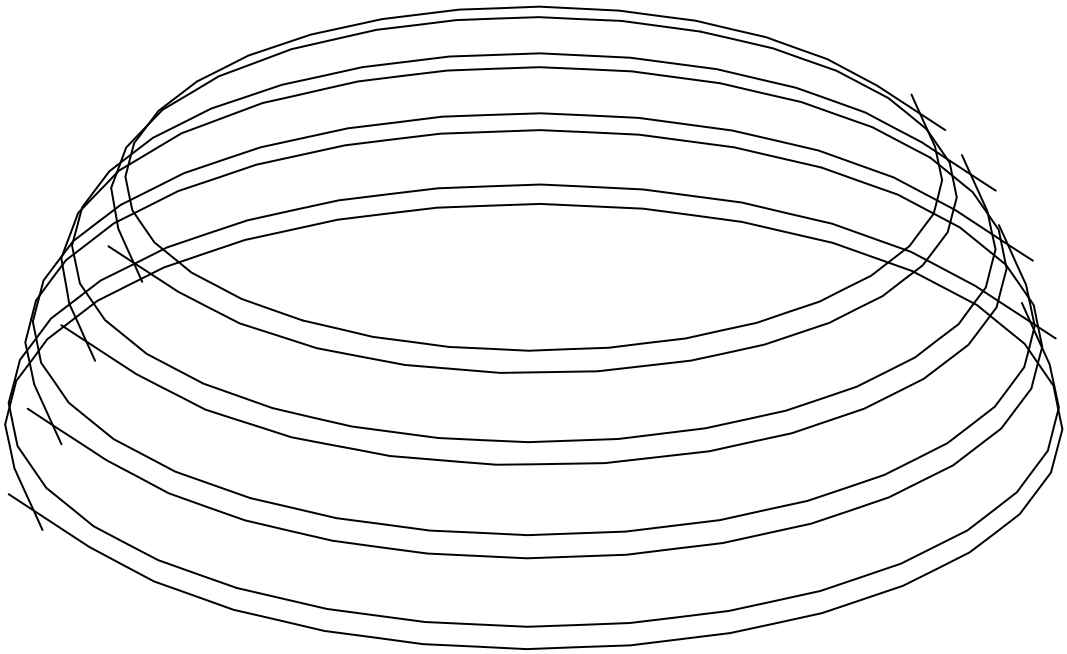

cables groupe 6,   532 elements 540 noeuds

Fig 8: Sixth group of tendons

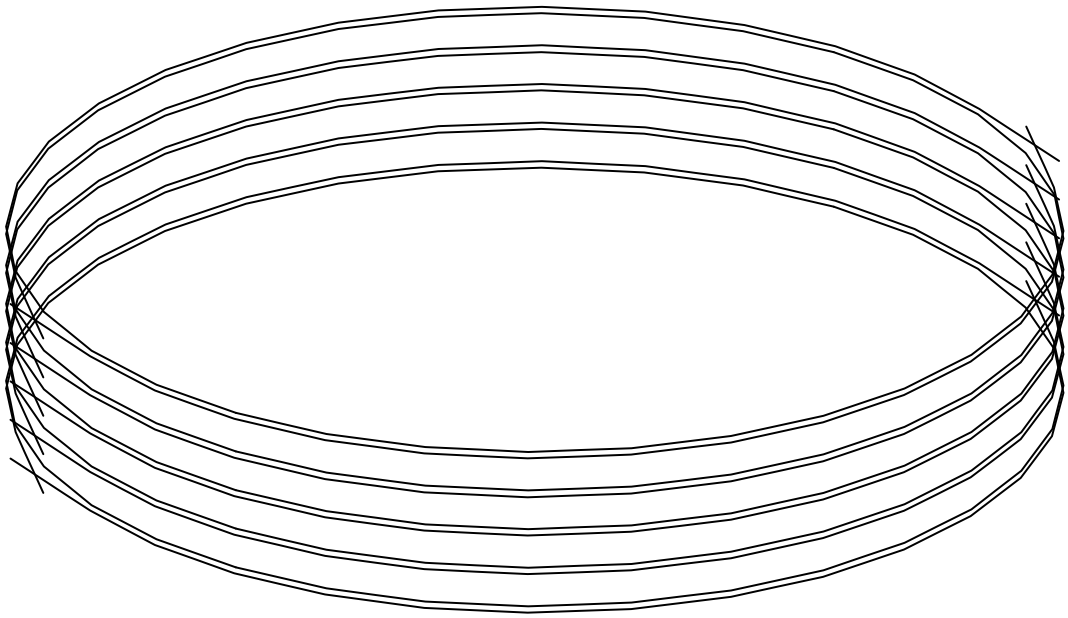

cables groupe 7,   660 elements 670 noeuds

Fig 9: Seventh group of tendons

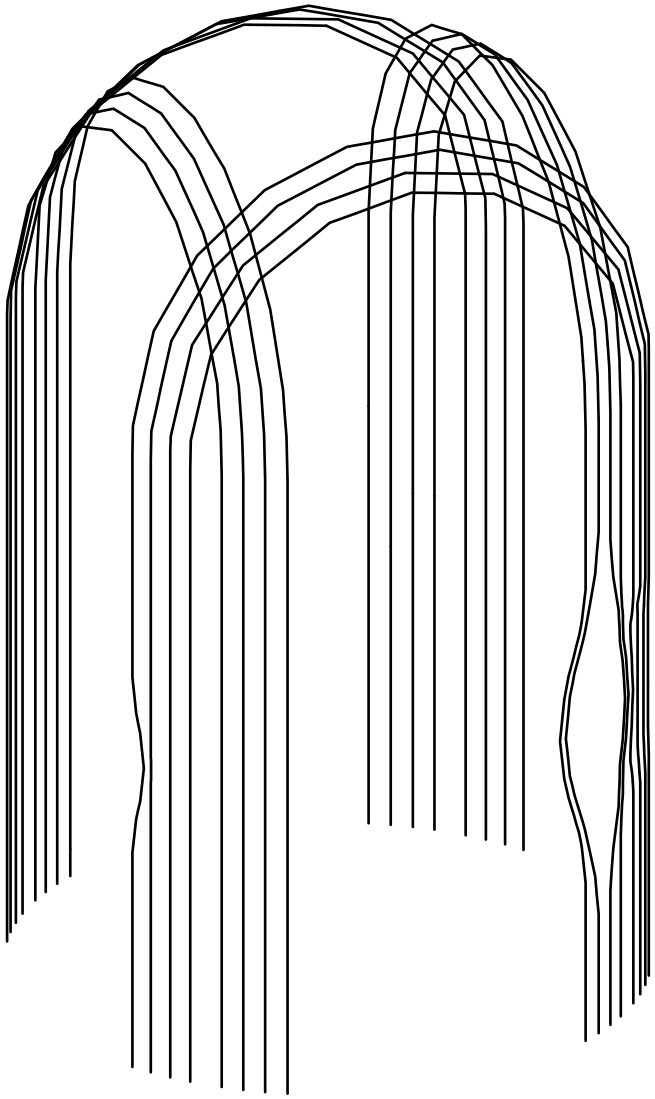

cables groupe 8,   1332 elements 1348 noeuds

Fig 10: Eighth group of tendons

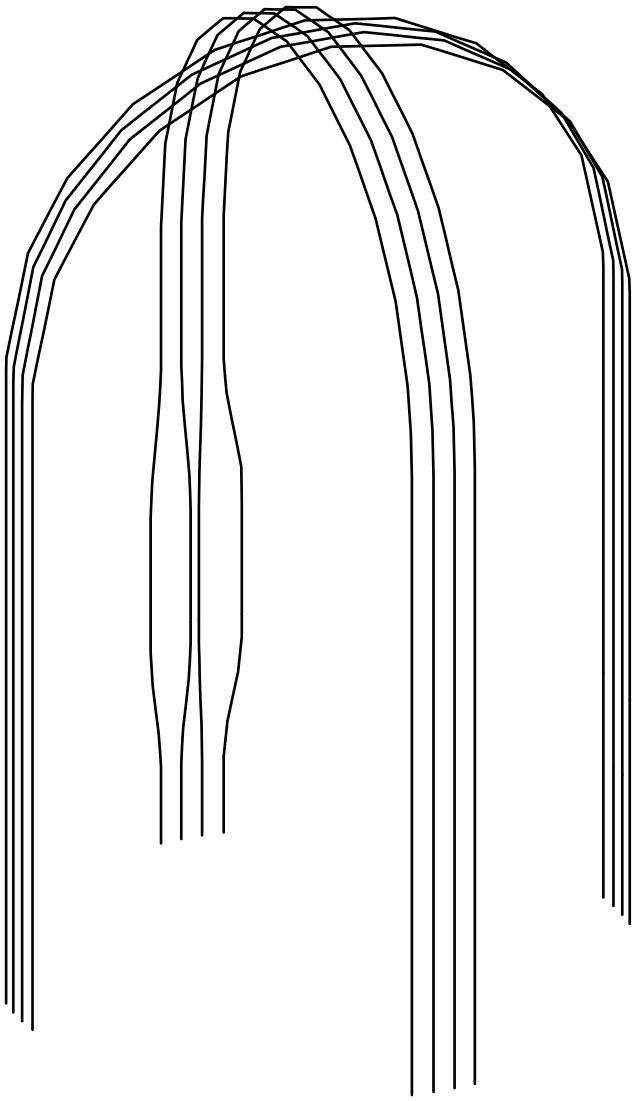

cables groupe 9,   690 elements 698 noeuds

Fig 11: Ninth group of tendons

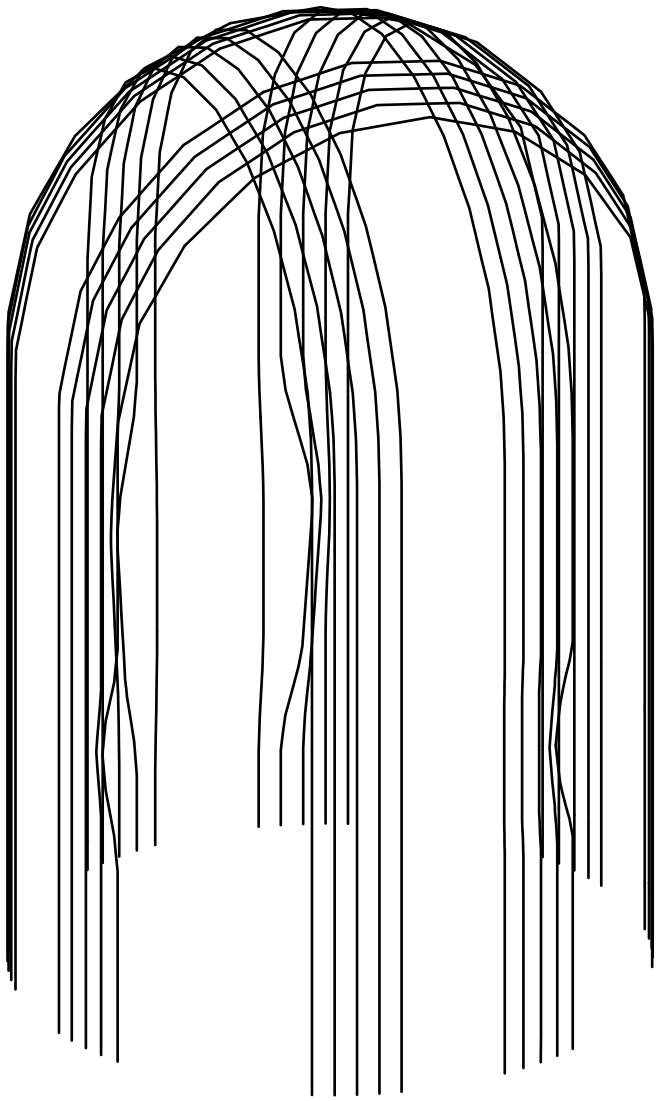

cables groupe 10,   1753 elements 1773 noeuds

Fig 12: Tenth group of tendons

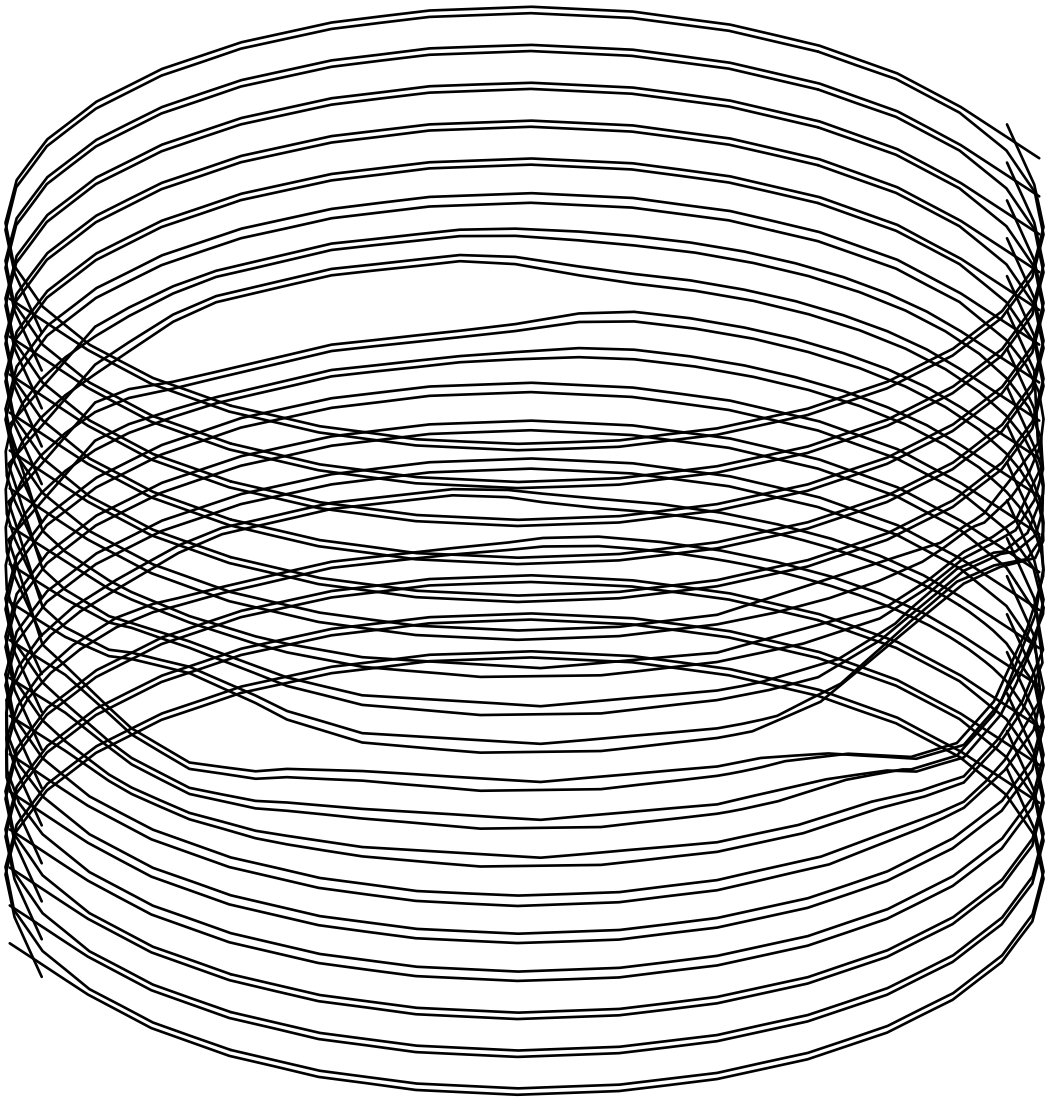

cables groupe 11,   2505 elements 2541 noeuds

Fig 13: Eleventh group of tendons

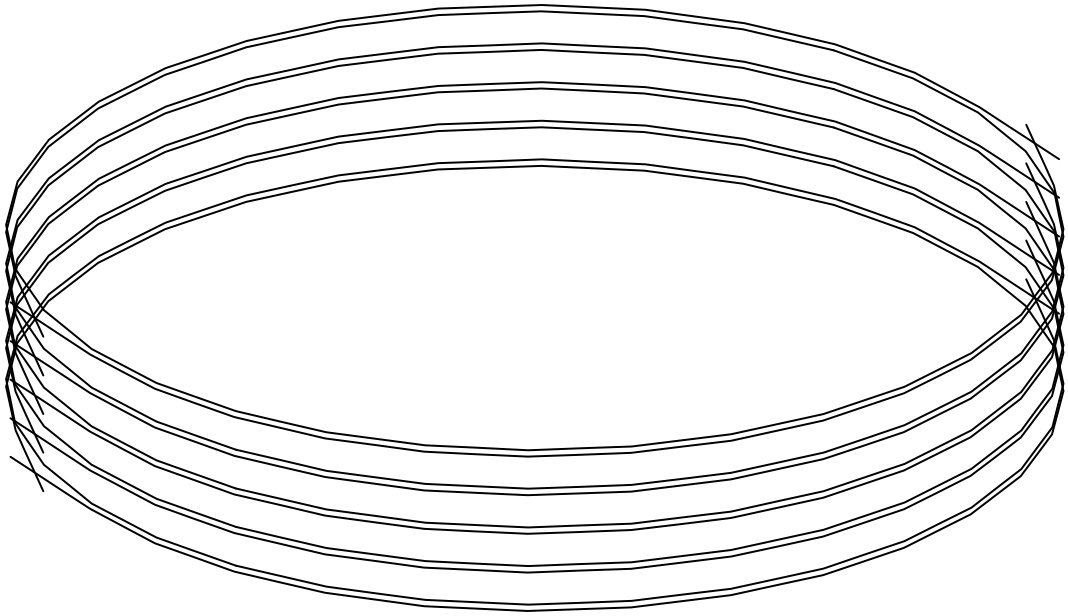

cables groupe 12,   660 elements 670 noeuds

Fig 14: Twelfth group of tendons

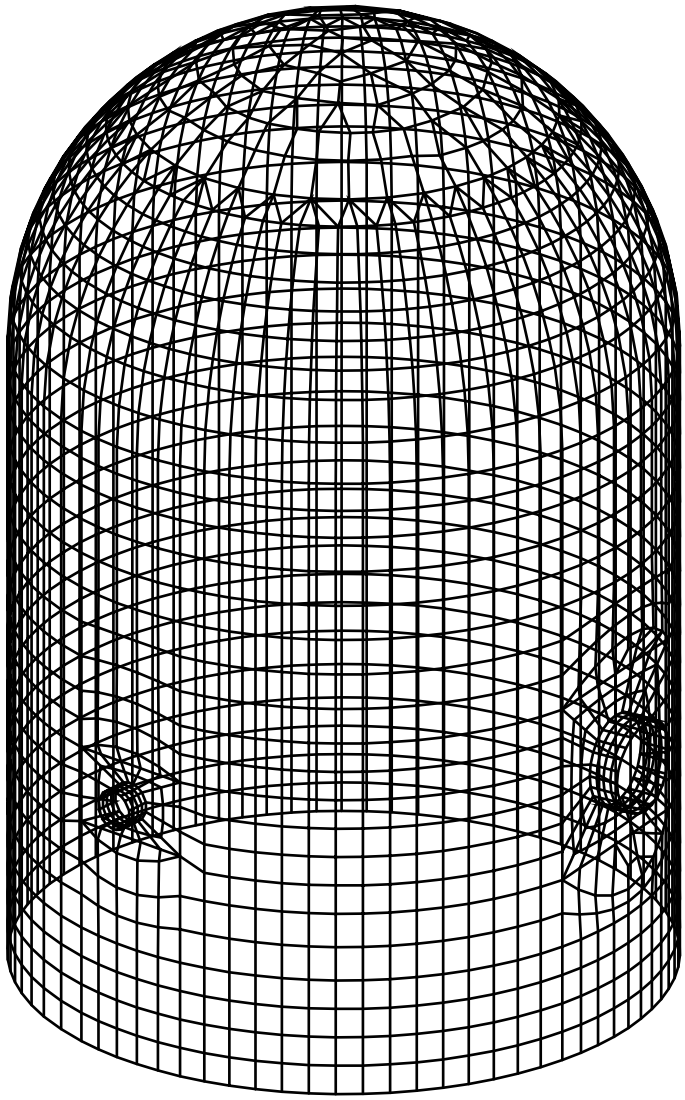

maillage de la peau 2694 elements 2672 noeuds

Fig 15: Mesh of the liner

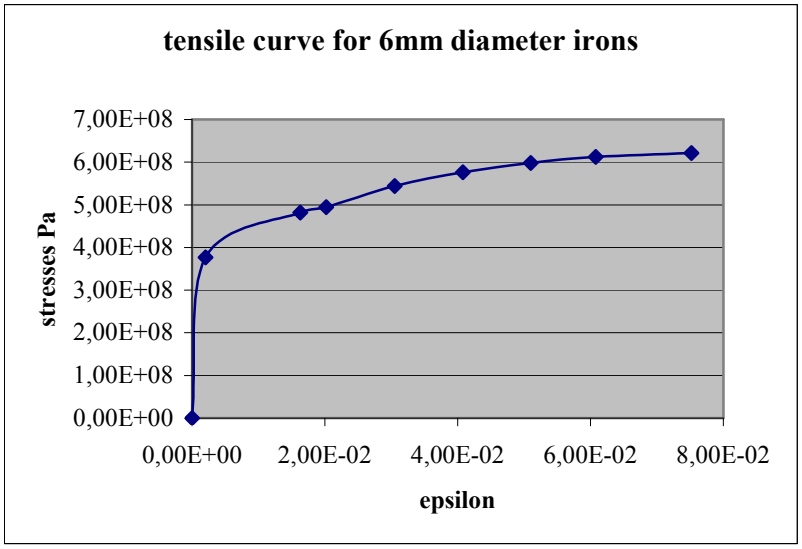

Fig 16: tensile curve for 6mm diameter irons

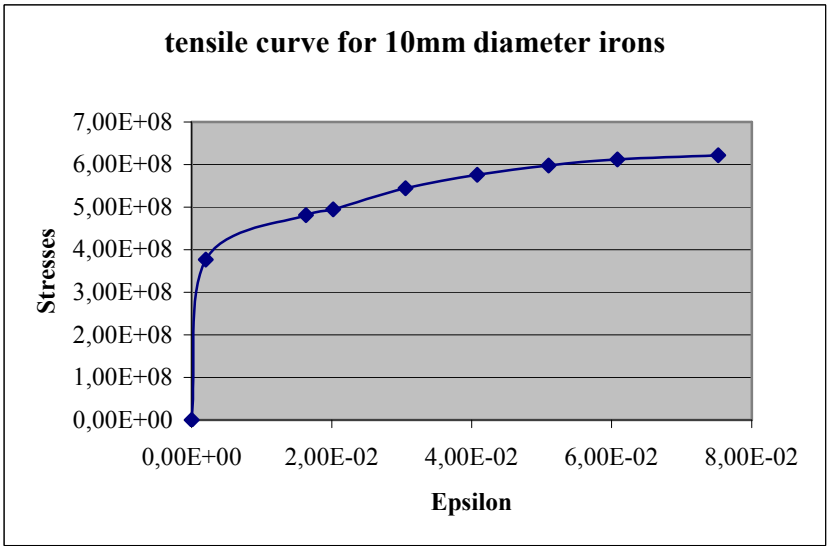

Fig 17: tensile curve for 10mm diameter irons

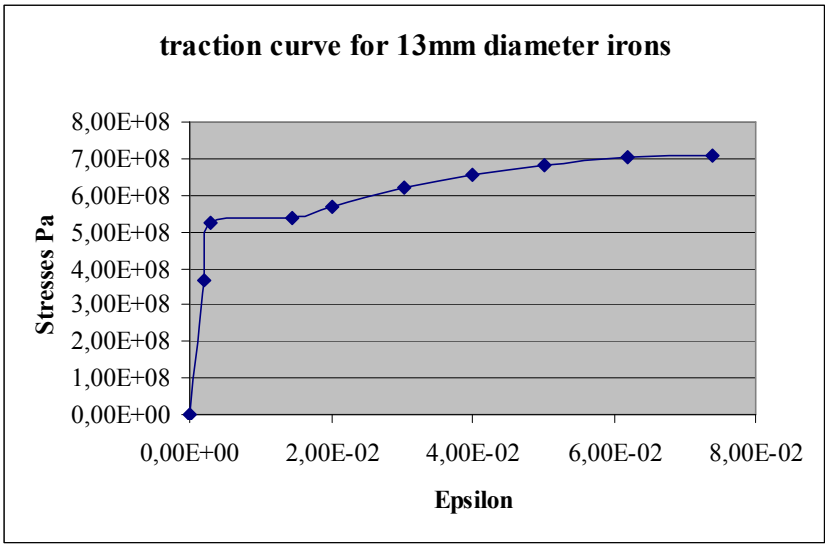

Fig 18: tensile curve for 13mm diameter irons

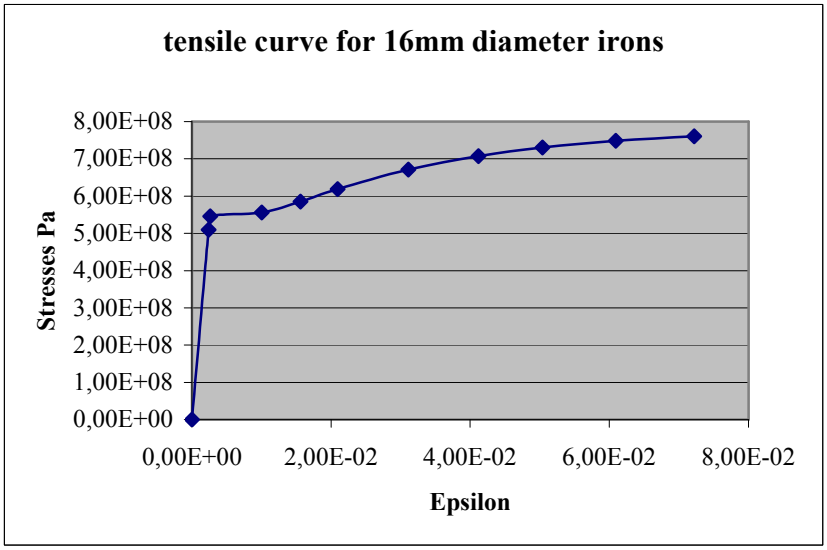

Fig 19: tensile curve for 16mm diameter irons

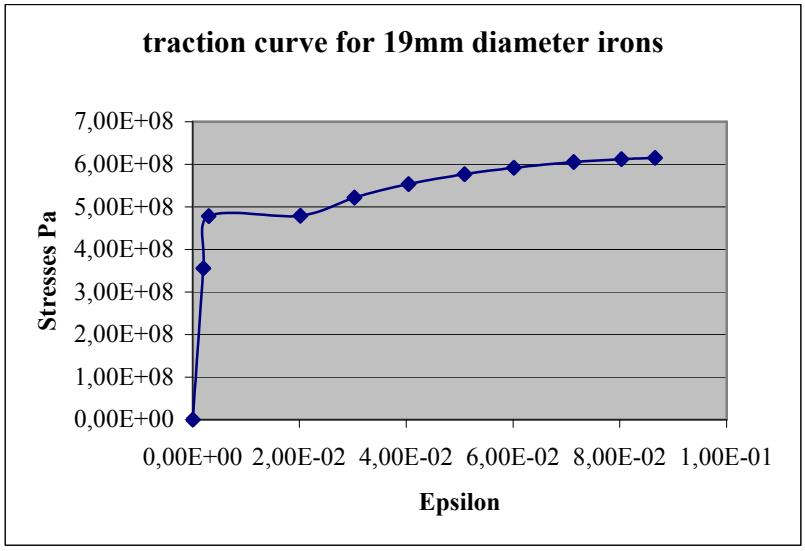

Fig 20: tensile curve for 19mm diameter irons

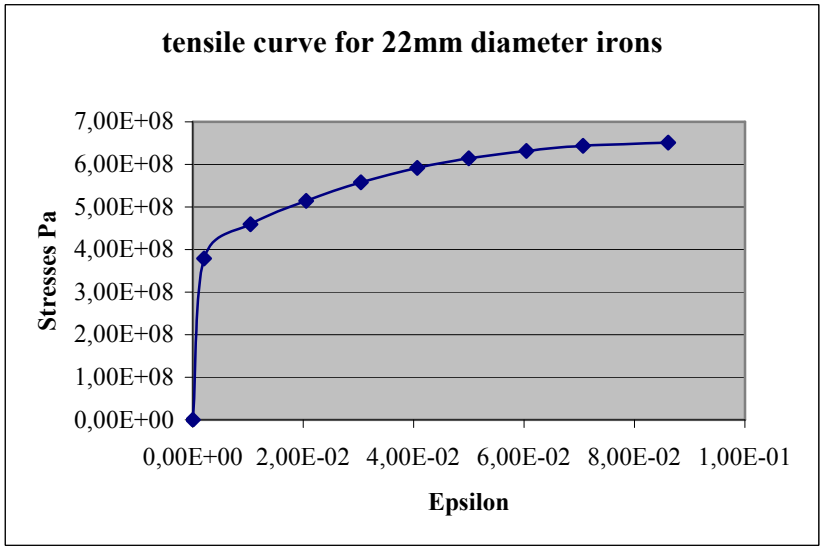

Fig 21: tensile curve for 22mm diameter irons

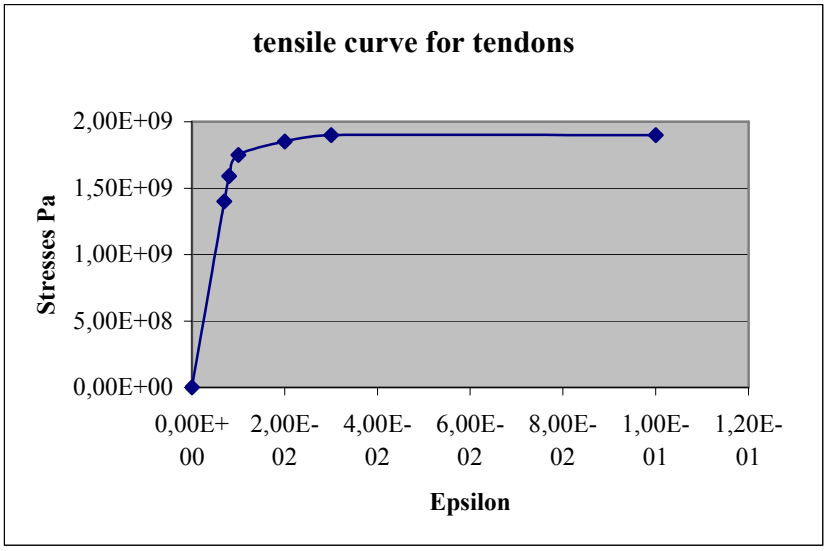

Fig 22: tensile curve for tendons

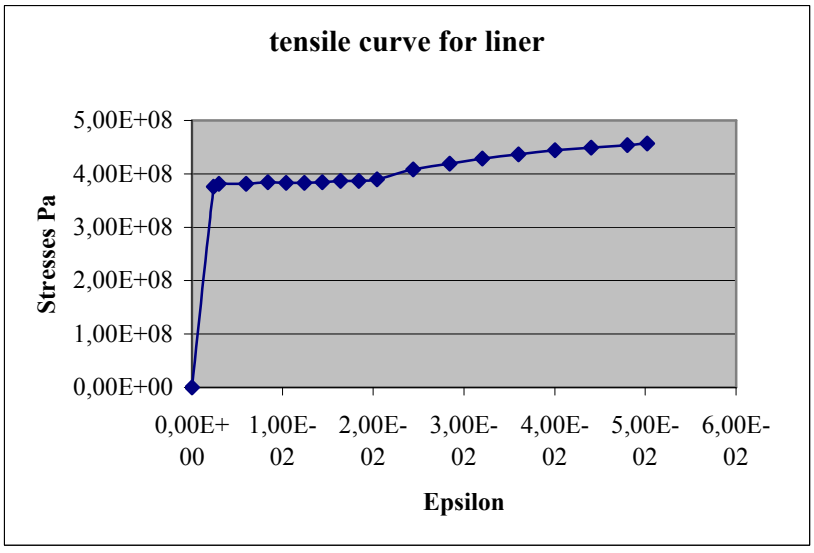

Fig 23: tensile curve for liner

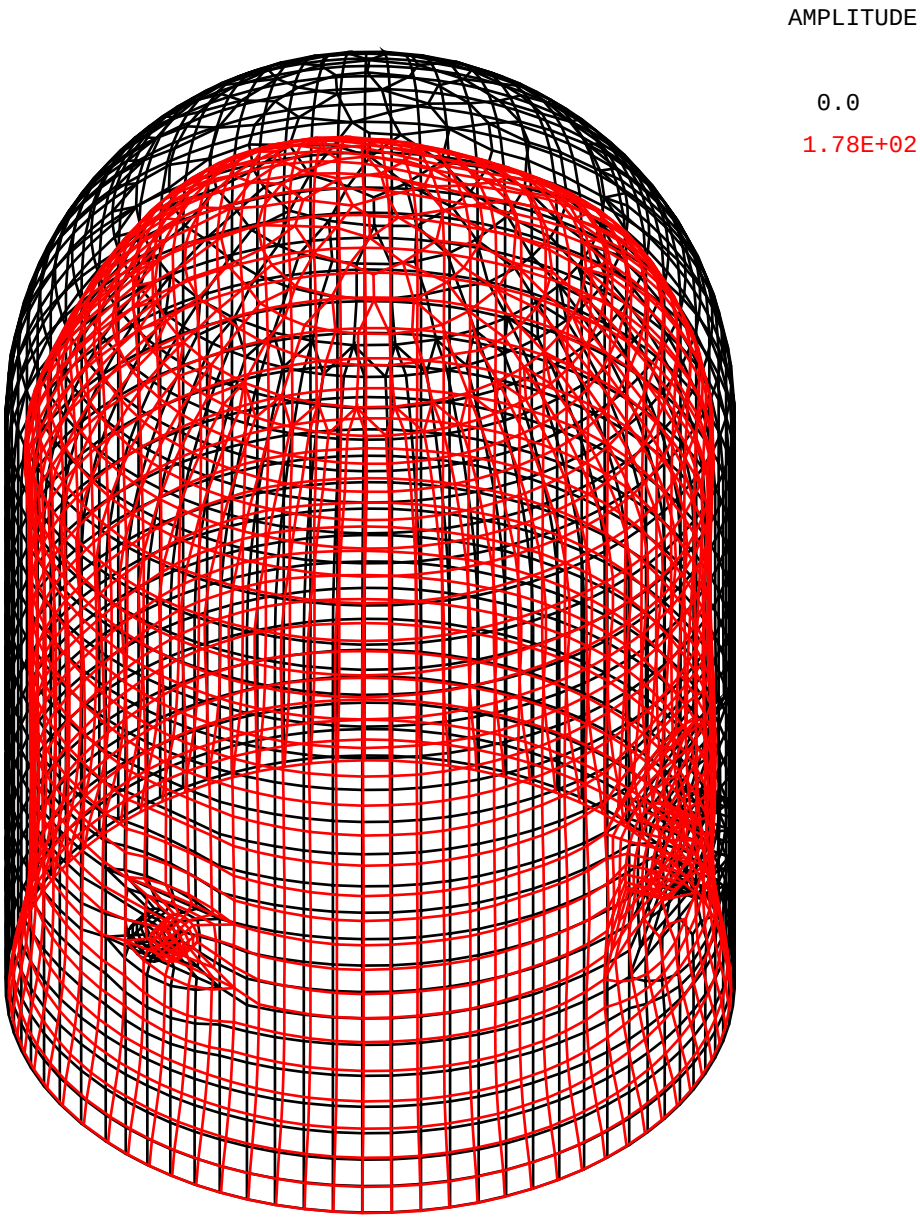

Fig 24: End of prestressing – initial mesh and final mesh

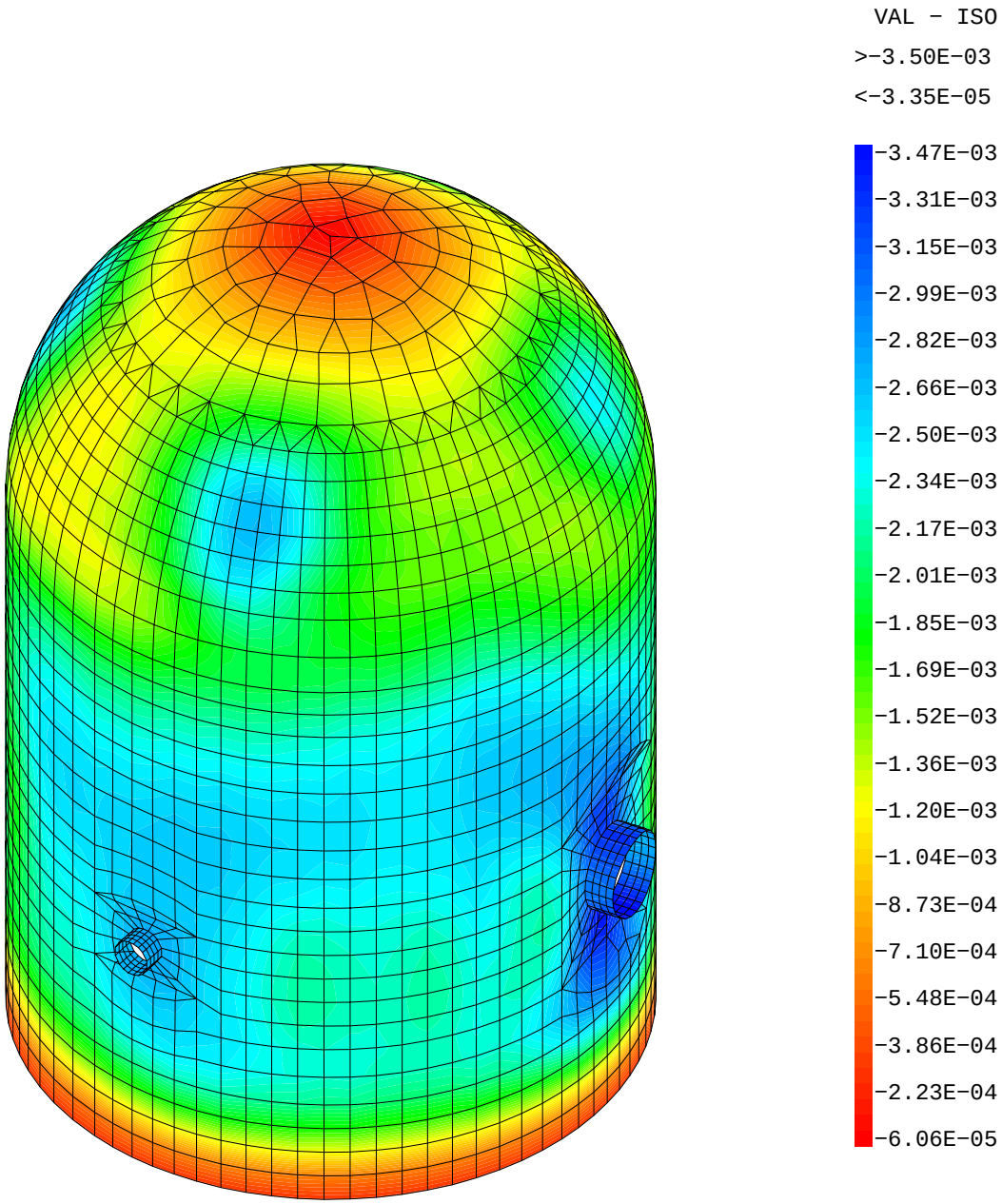

FIN PRECONTRAINTE – ISOVALEURS DE DEPLACEMENTS RADIAUX POUR LA PEAU

Fig 25: End of prestressing – radial displacements (mm)

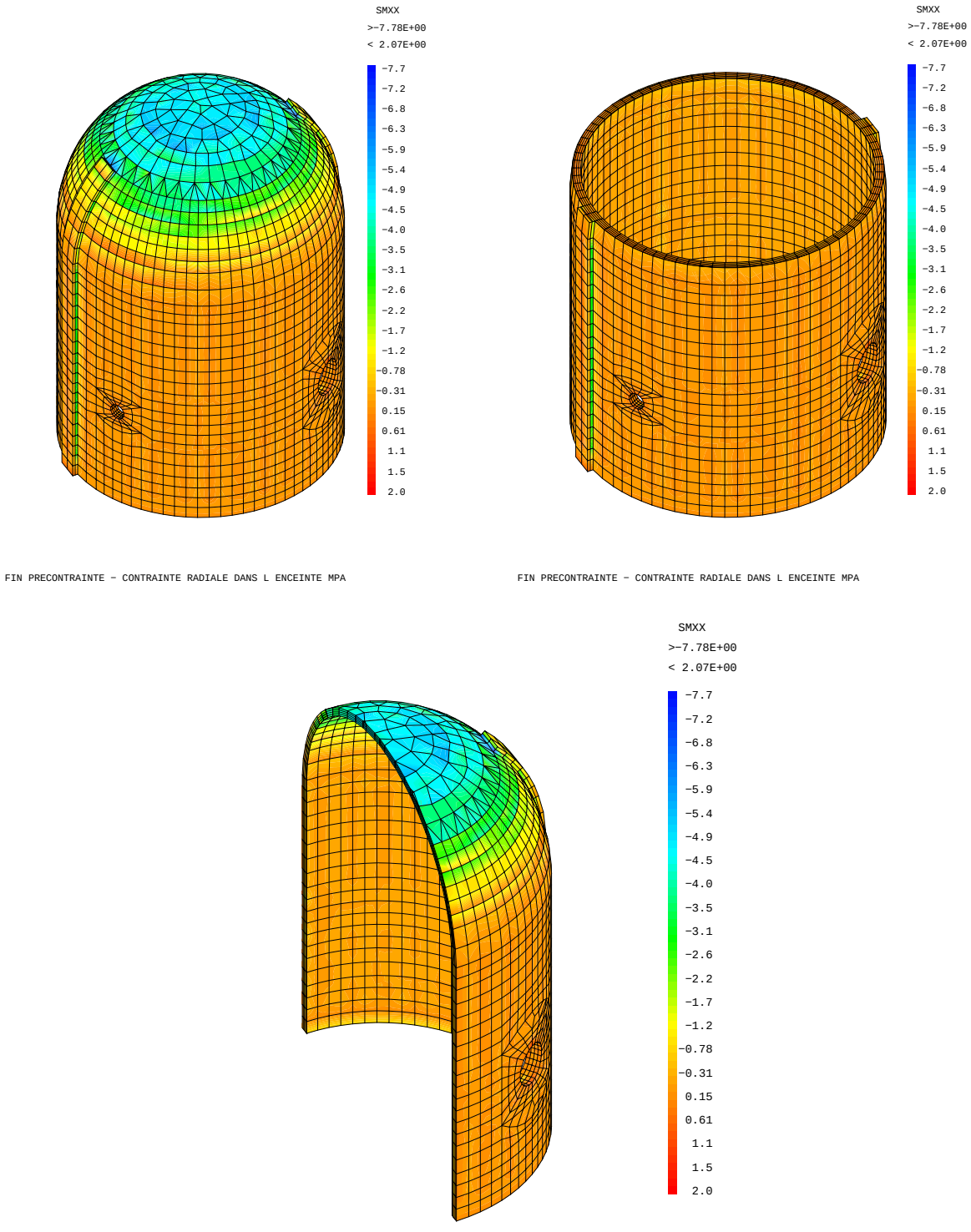

Fig 26: End of prestressing – Radial stresses in the concrete vessel

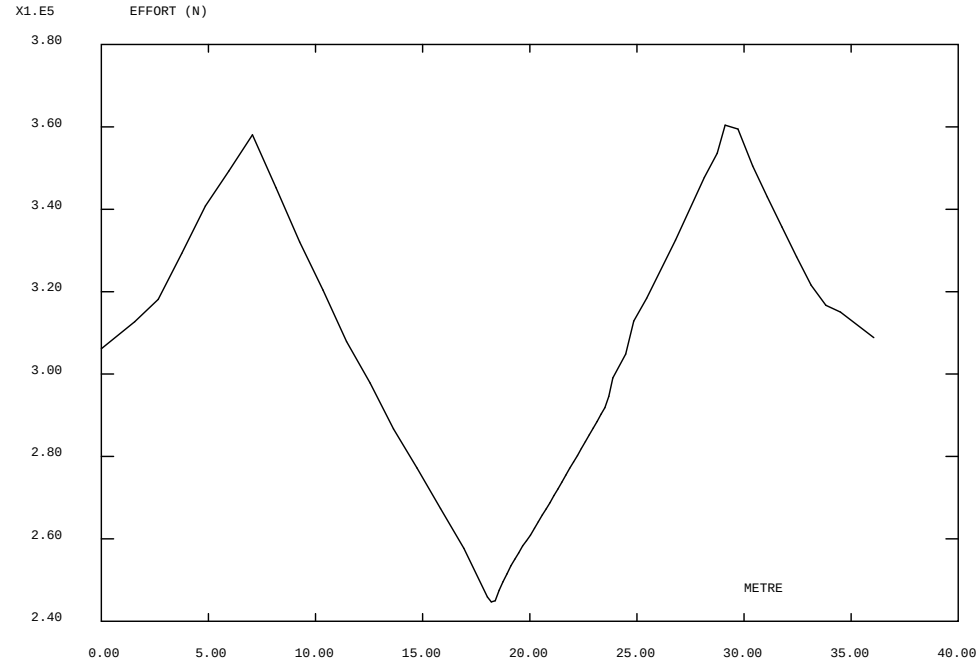

Fig 27: End of prestressing – tension of tendon H11 (N)

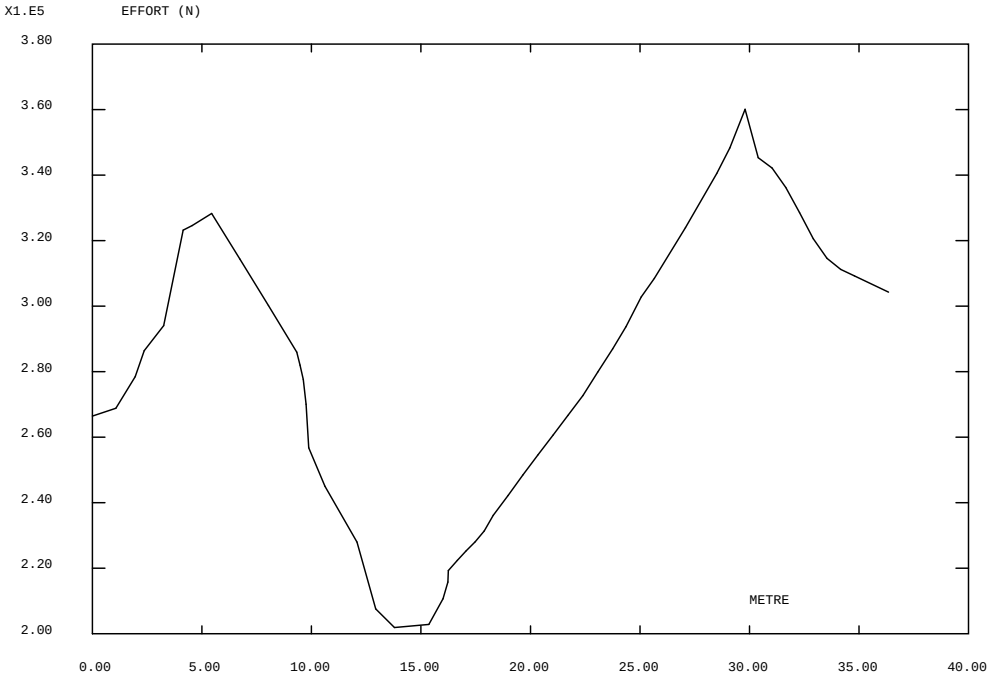

Fig 28: End of prestressing – Tension of tendon H35 (N)

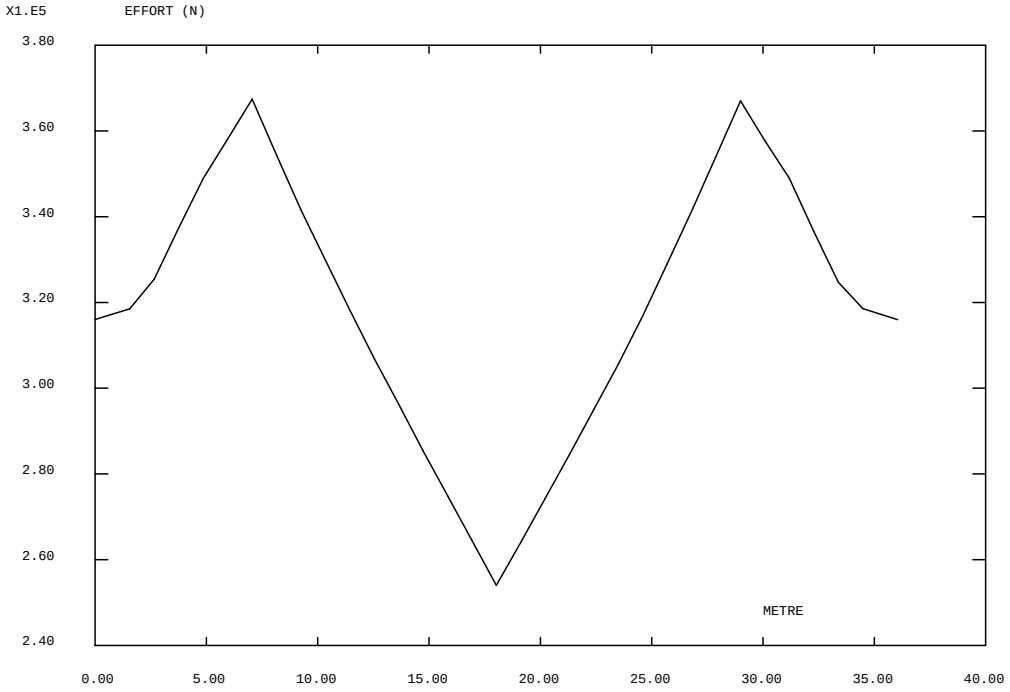

Fig 29: End of prestressing – Tension of tendon H53 (N)

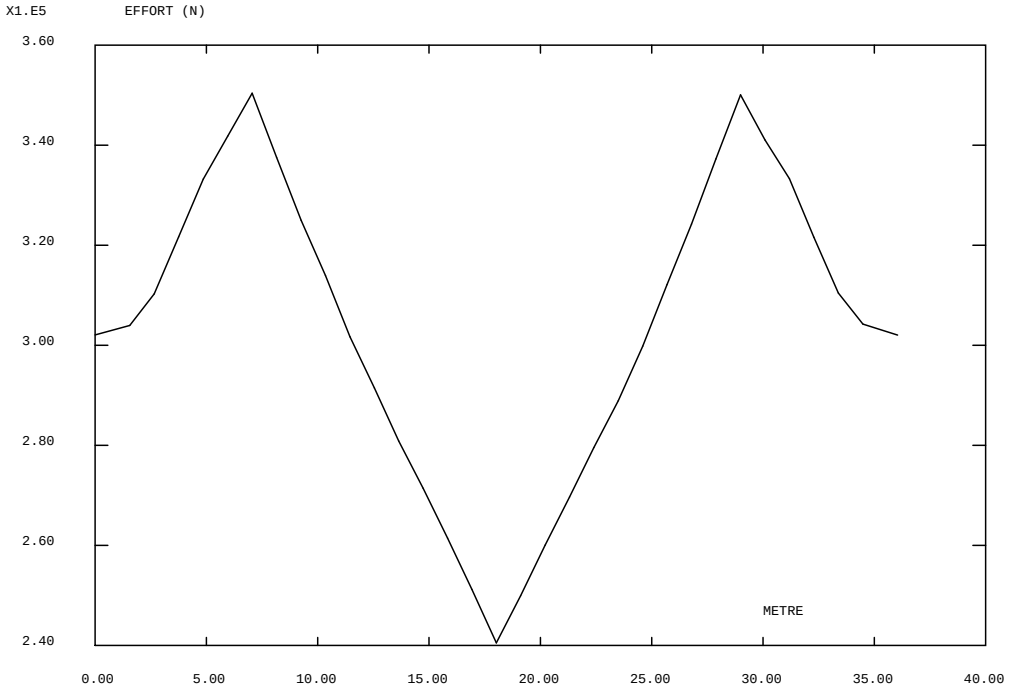

Fig 30: End of prestressing – Tension of tendon H67 (N)

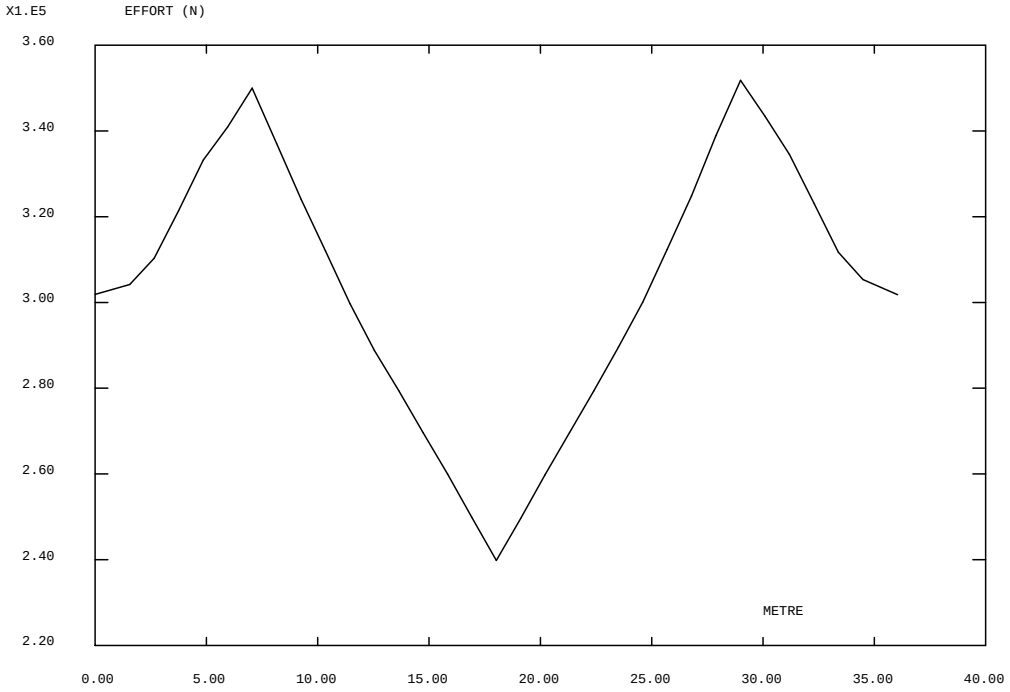

Fig 31: End of prestressing - Tension of tendon H68 (N)

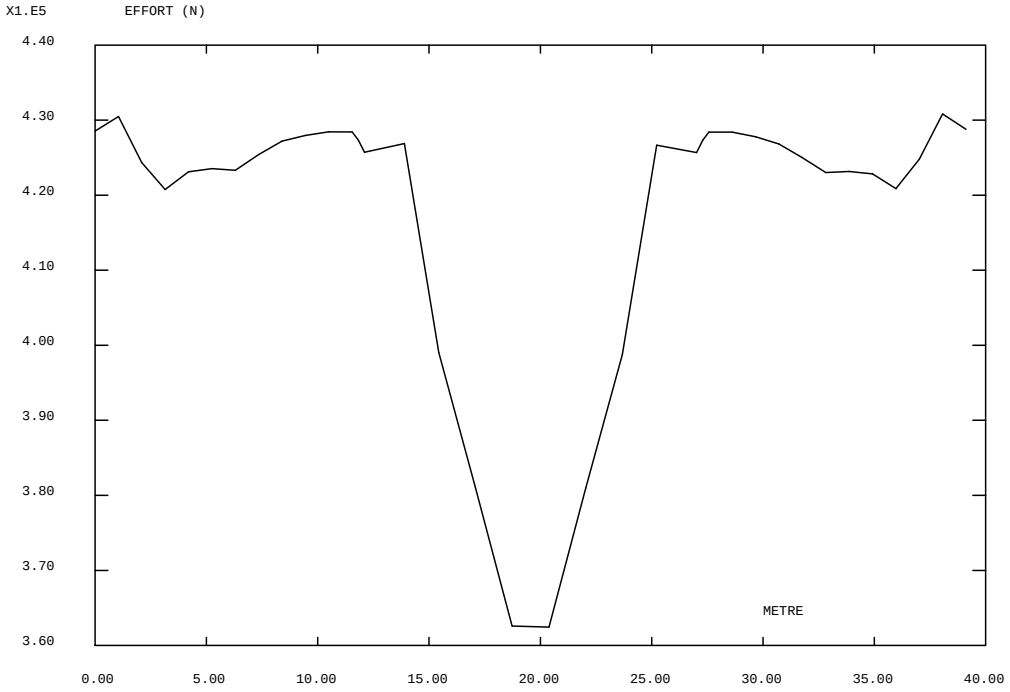

Fig 32: End of prestressing – tension of tendon V37 (N)

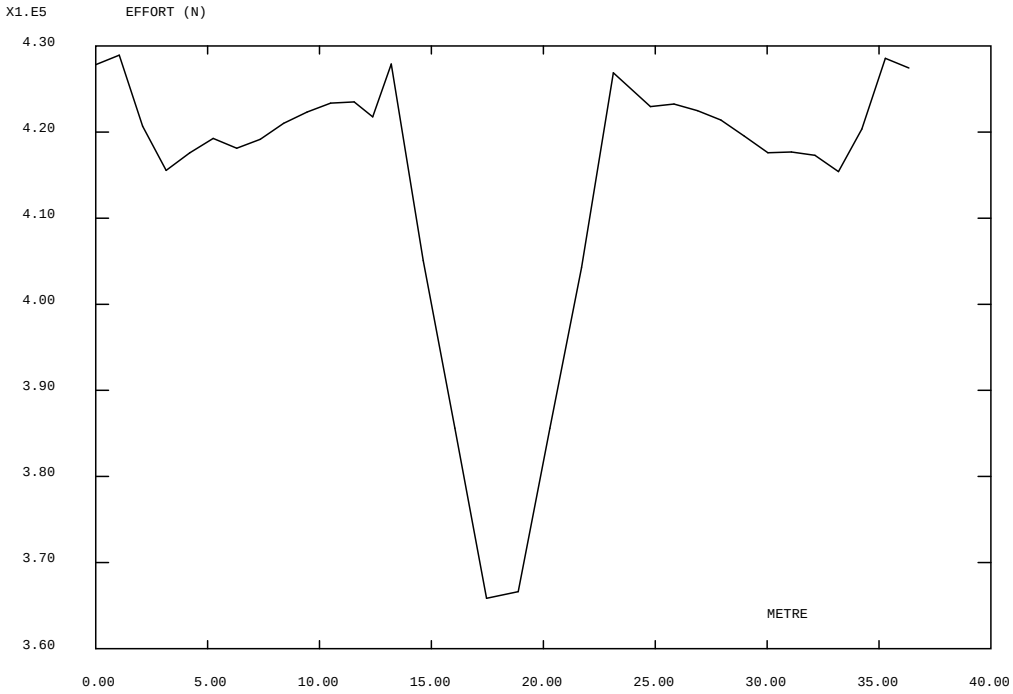

Fig 33: End of prestressing – Tension of tendon V46 (N)

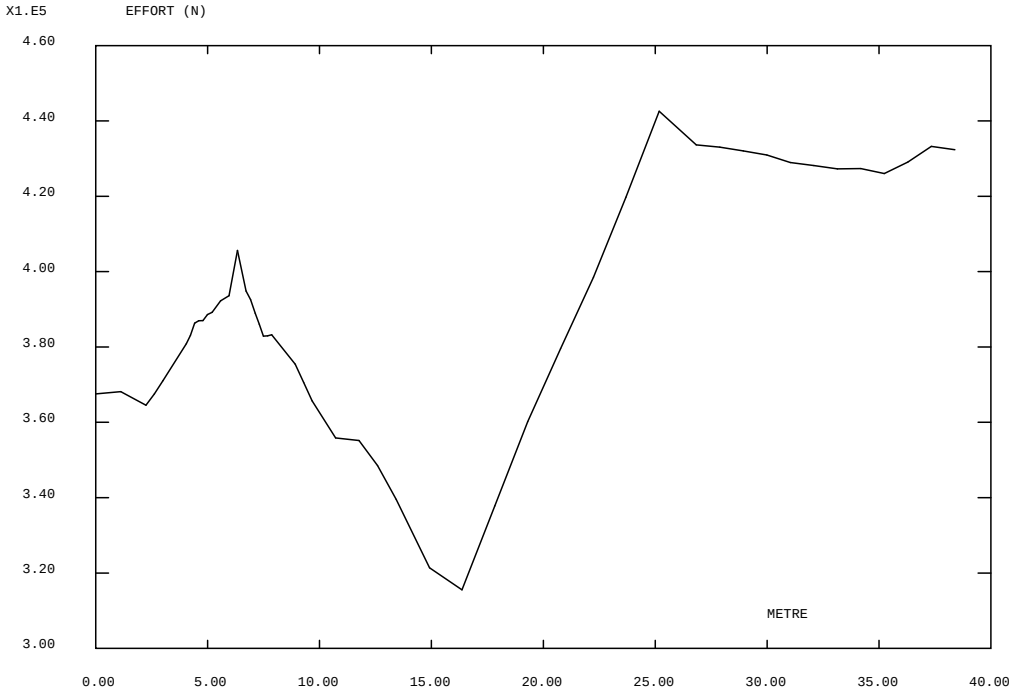

Fig 34: End of prestressing - Tension of tendon V85 (N)

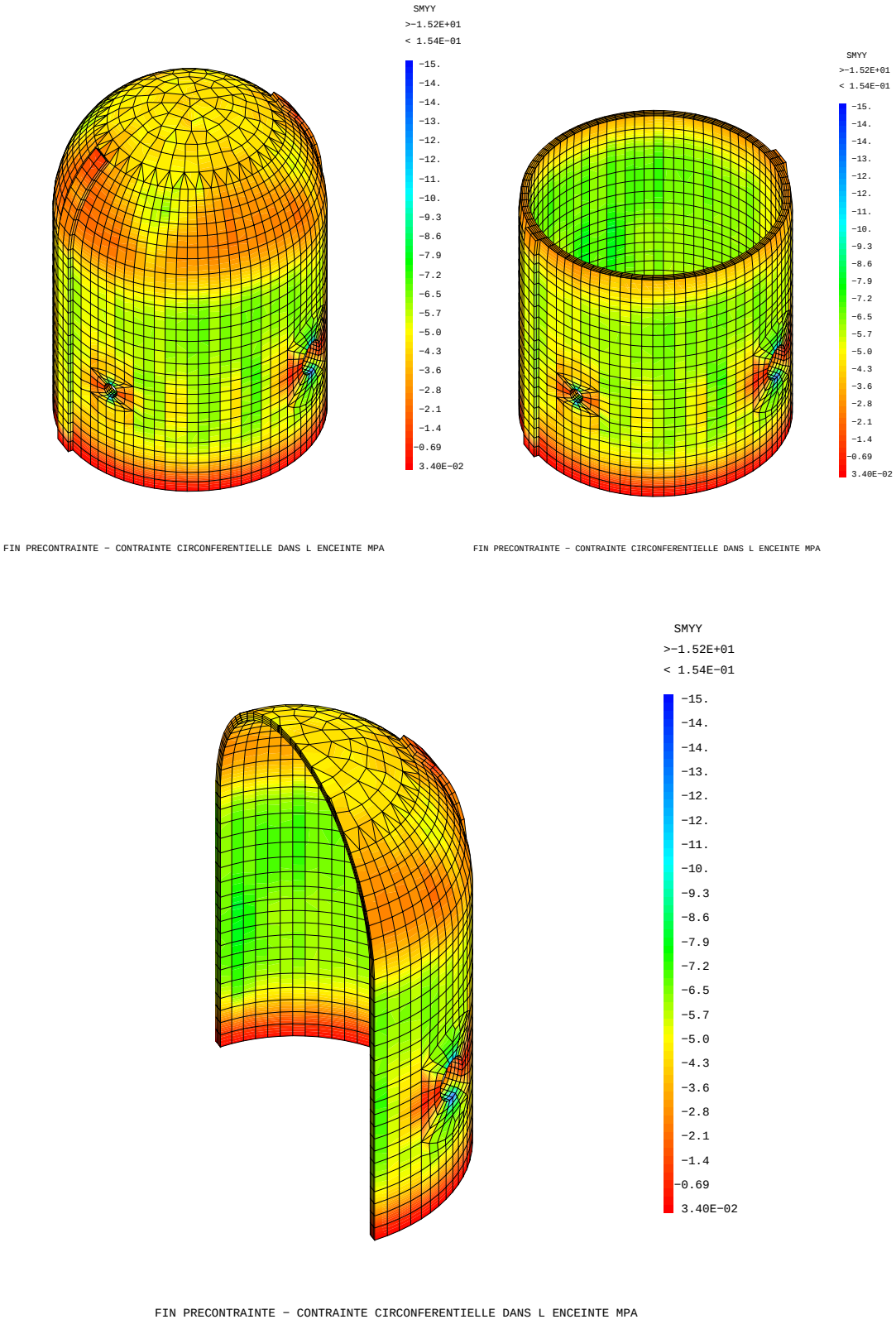

Fig 35: End of prestressing – Hoop stresses in the concrete vessel (MPa)

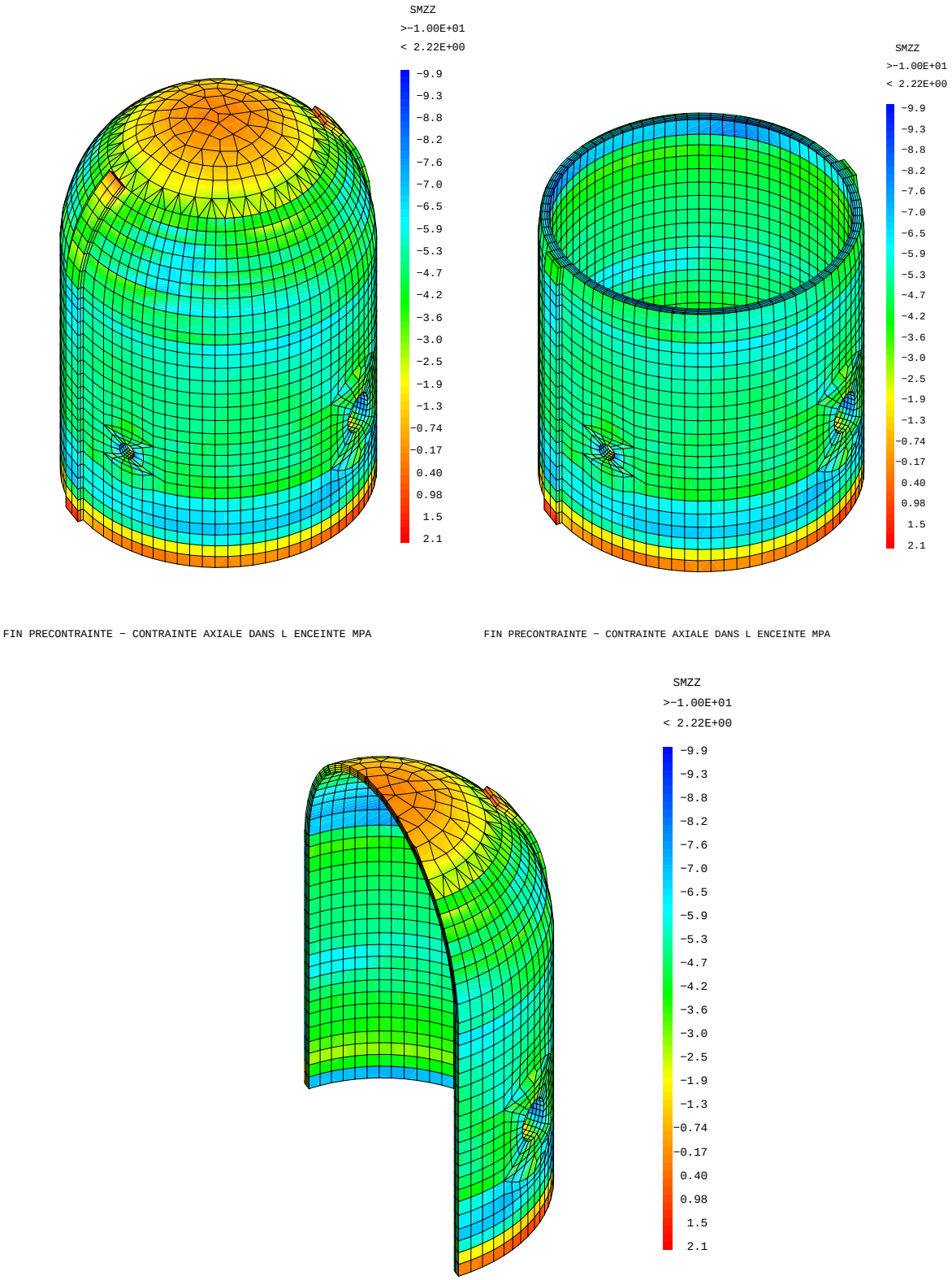

Fig 36: End of prestressing – vertical stresses in the concrete vessel (MPa)

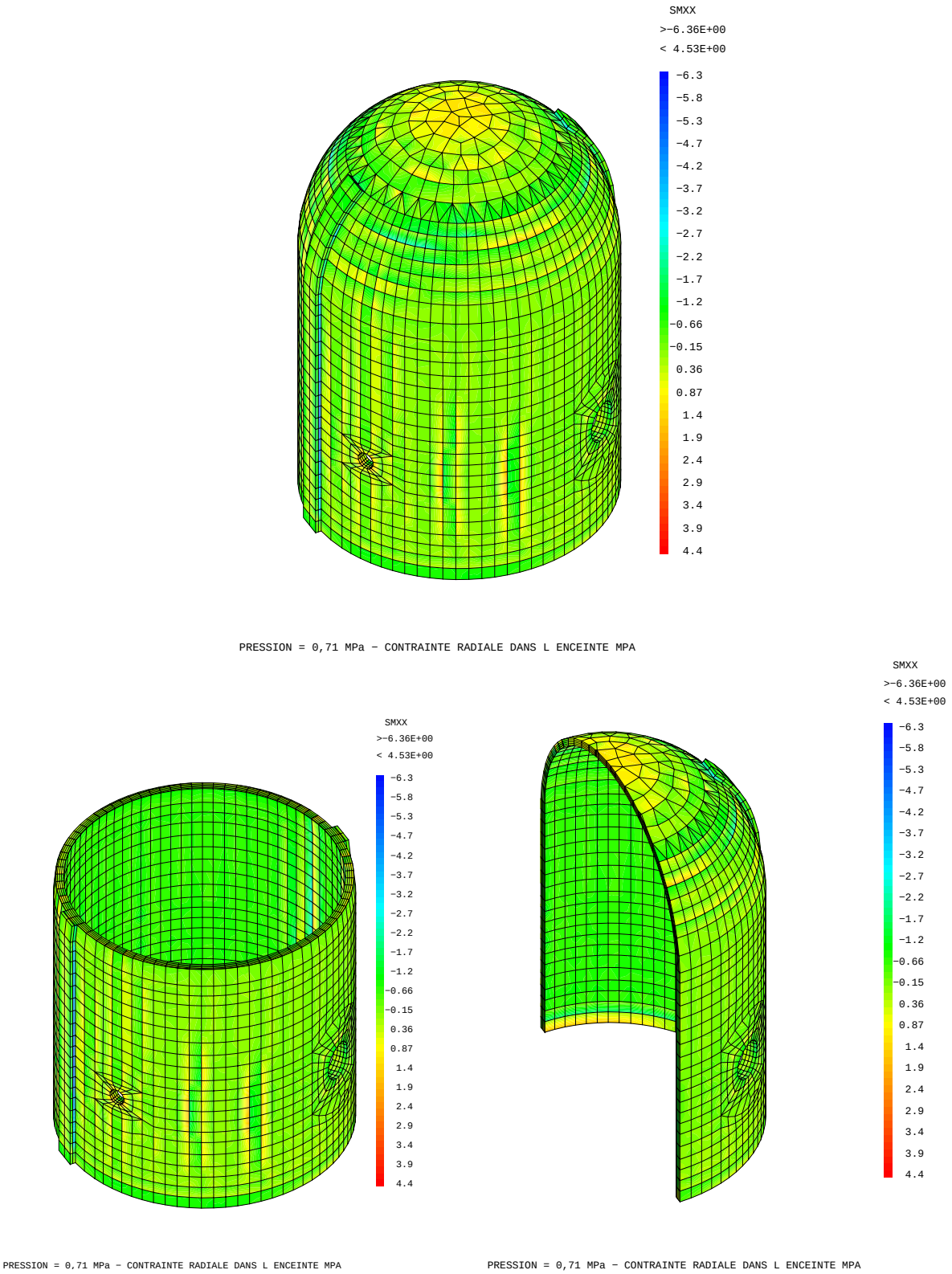

Fig 37: Pressure 0,71 MPa – Radial stresses in the wall (MPa)

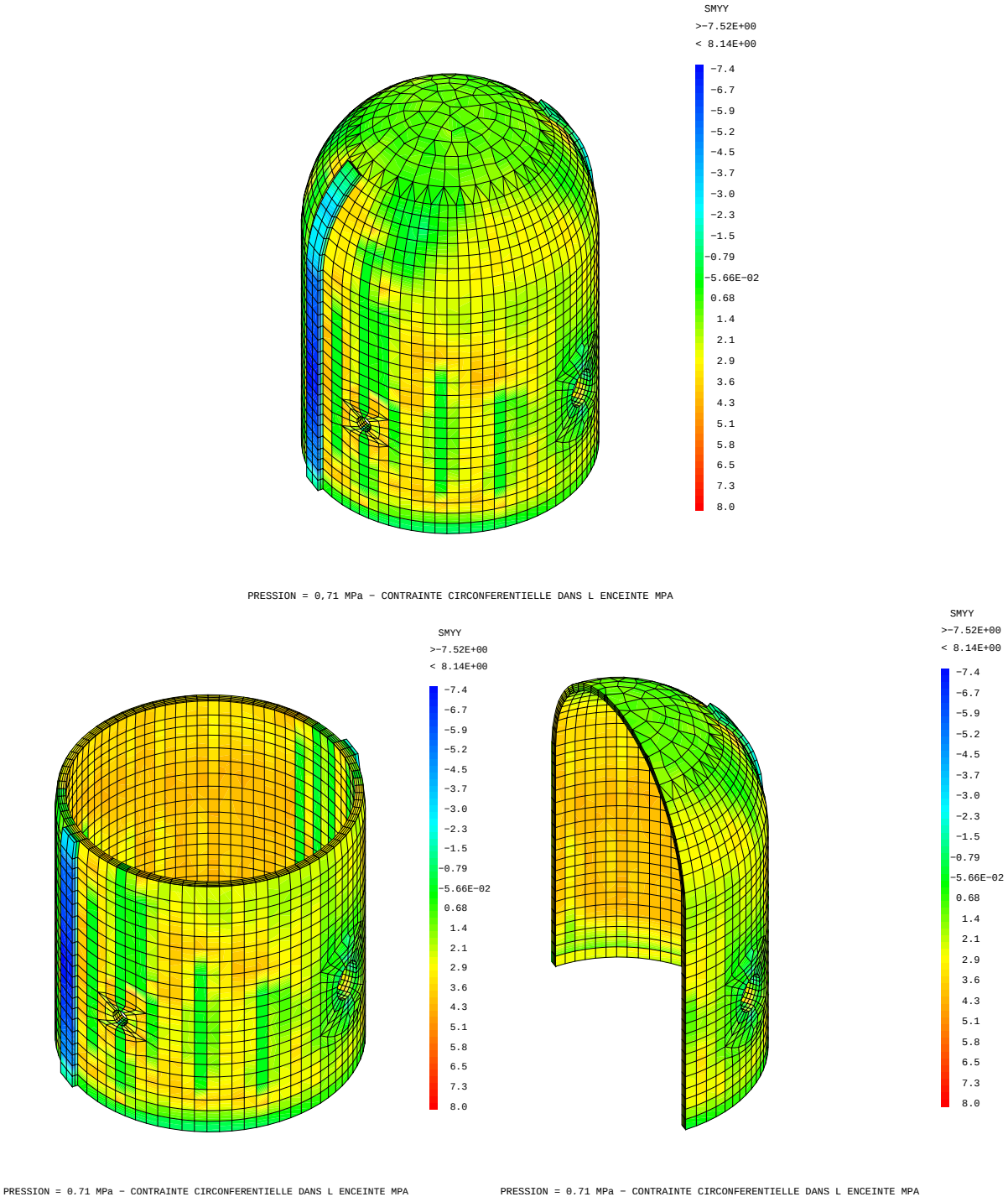

Fig 38: Pressure 0,71 MPa – Hoop stresses in the wall (MPa)

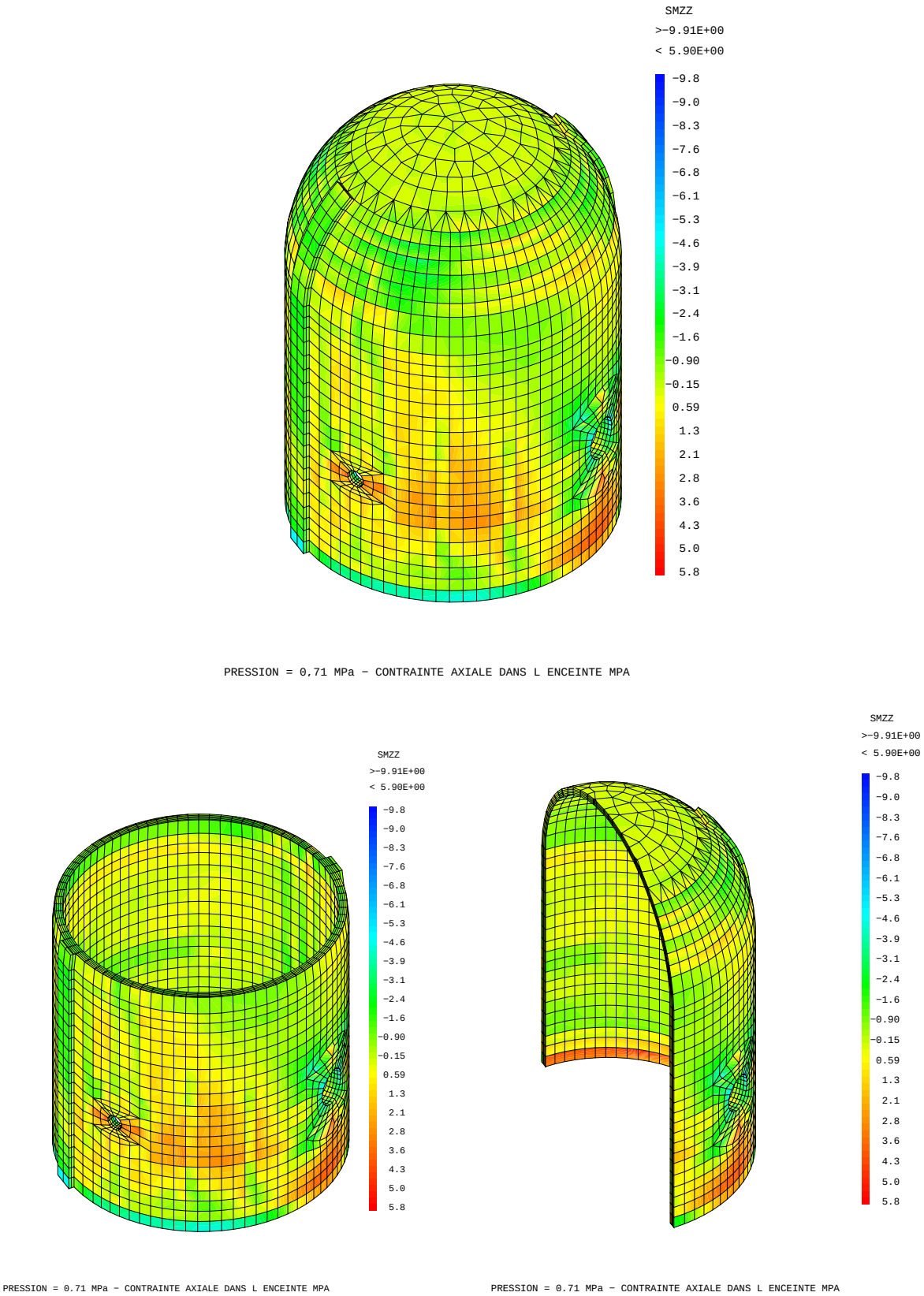

Fig 39: Pressure 0,71 MPa – vertical stresses in the wall (MPa)

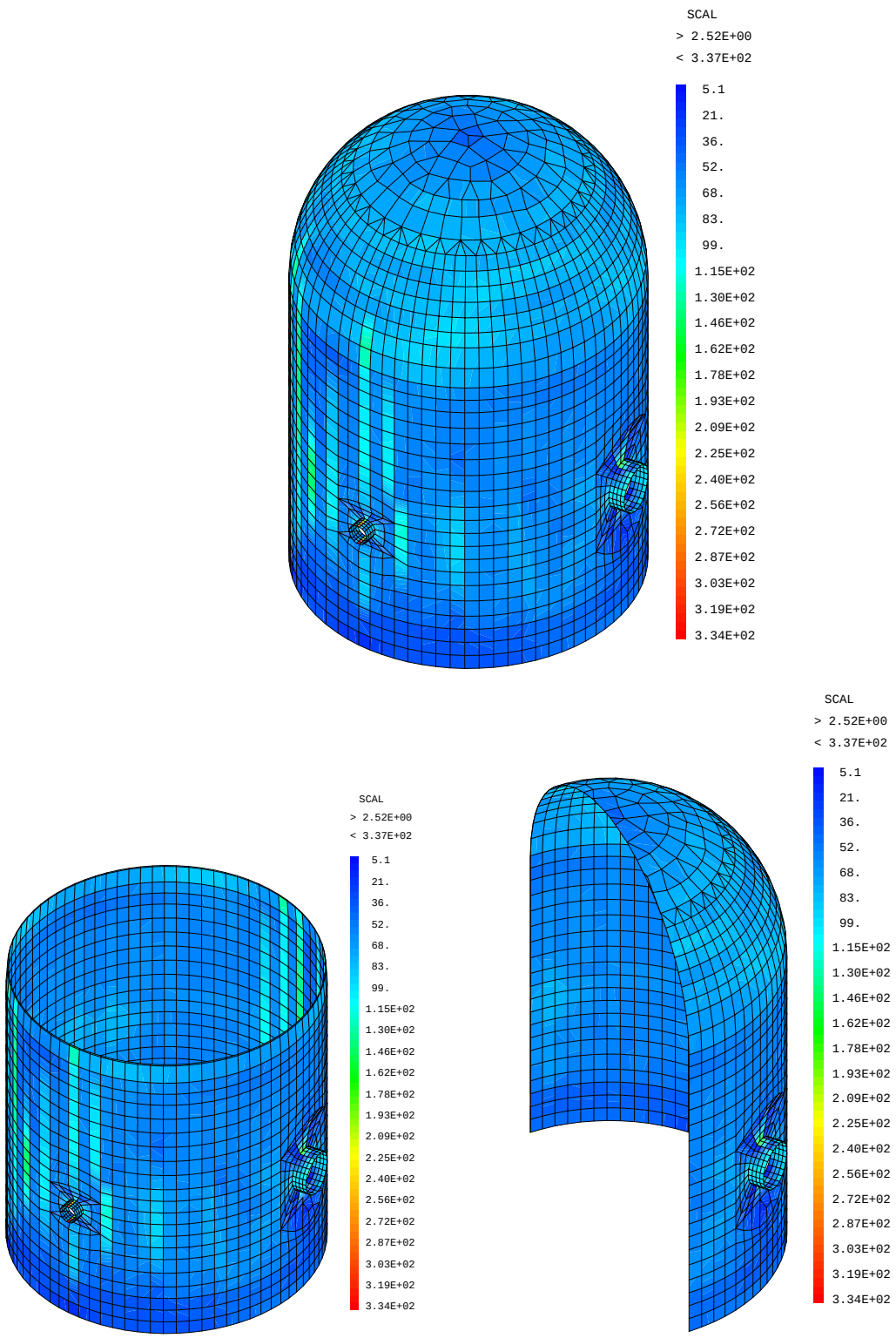

Fig 40: Pressure 0,71 MPa – Von Mises stresses in the liner (MPa)

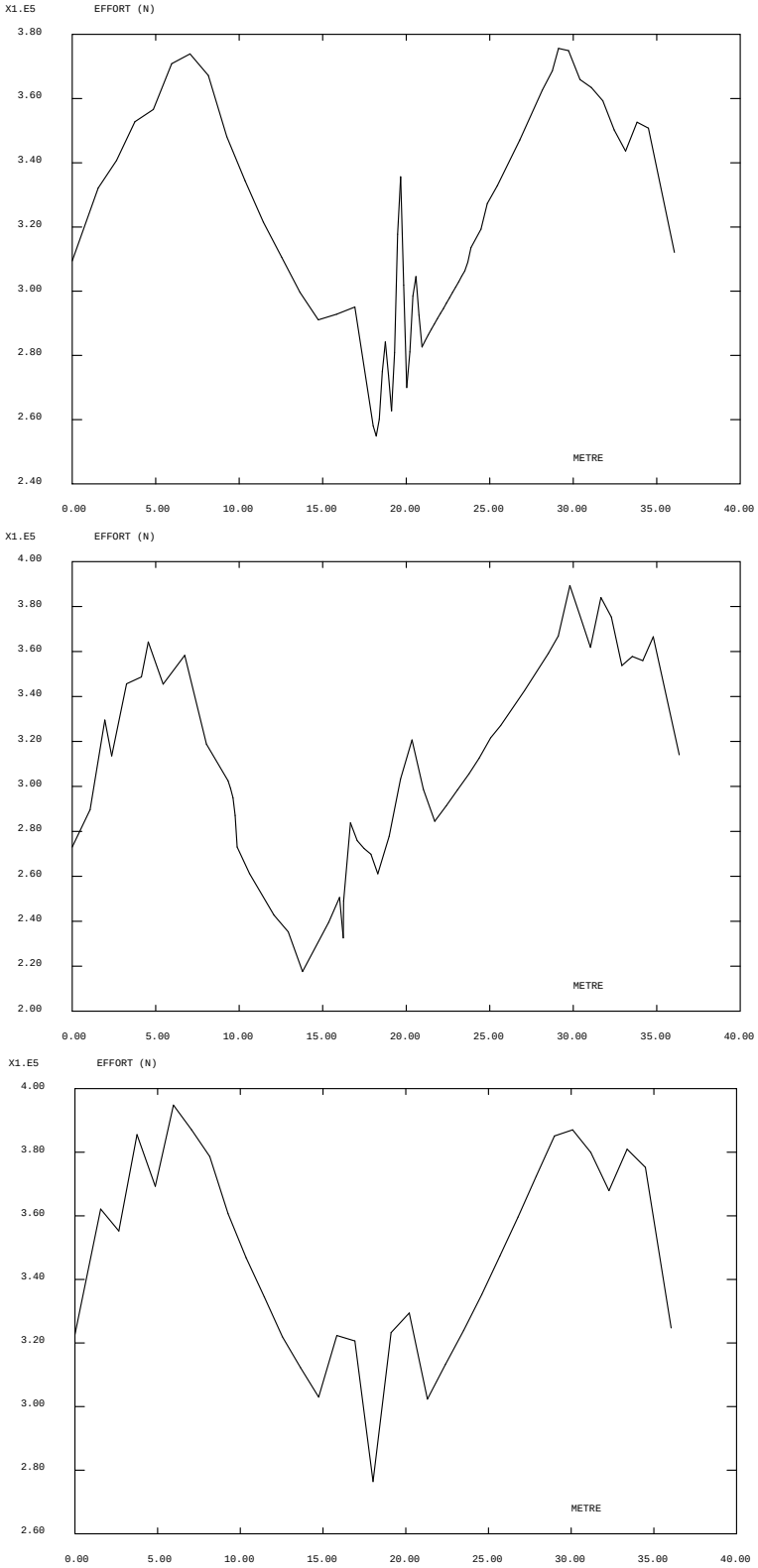

Fig 41: Pressure 0,71 MPa – Tensions in tendons H11, H35, H53 (N)

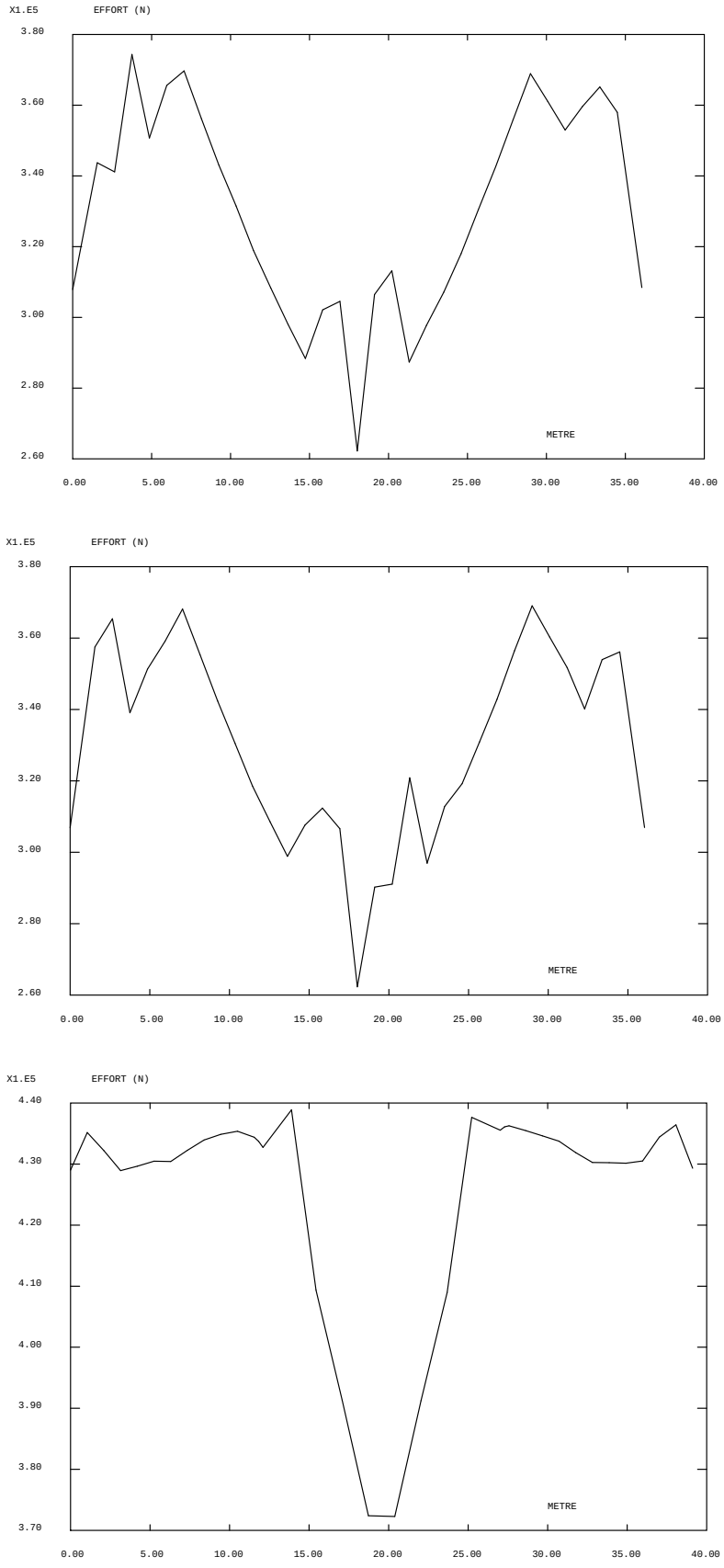

Fig 42: Pressure 0,71 MPa – tensions of tendons H67, H68, V37 (N)

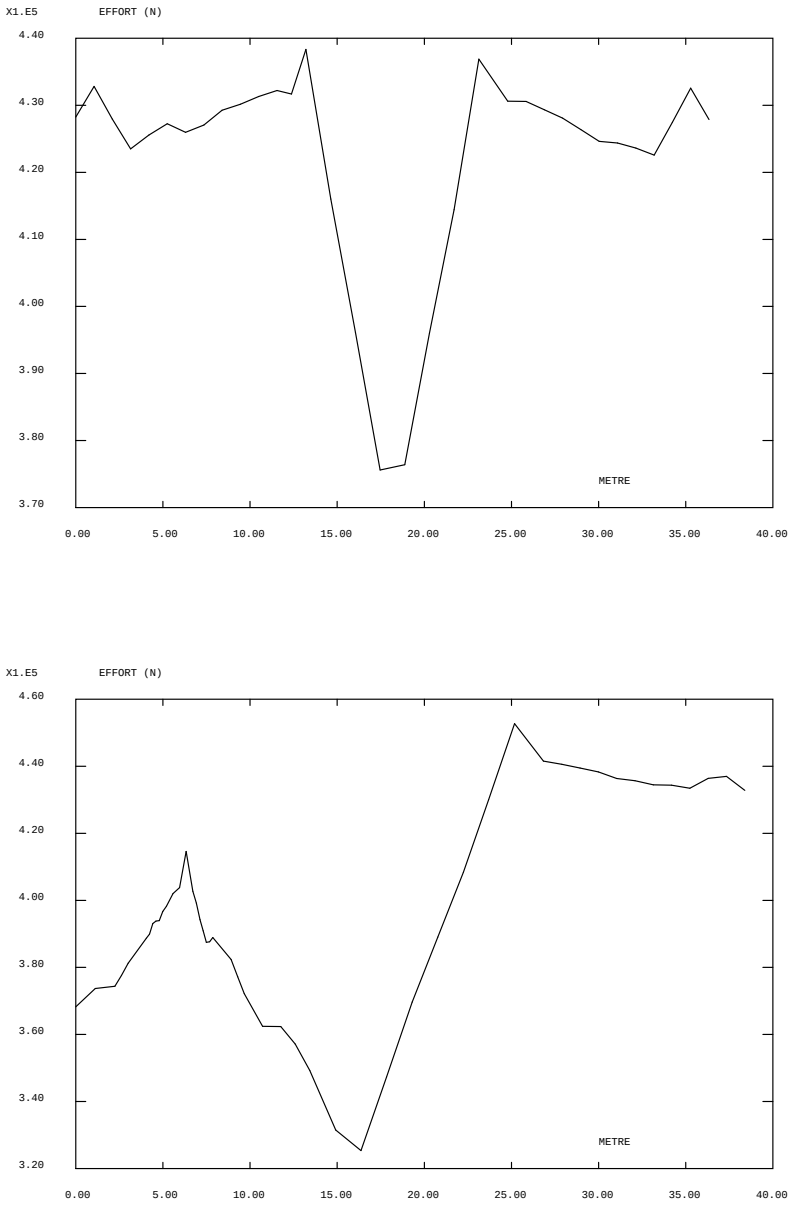

Fig 43: Pressure 0,71 MPa – tensions of tendons V46, V85

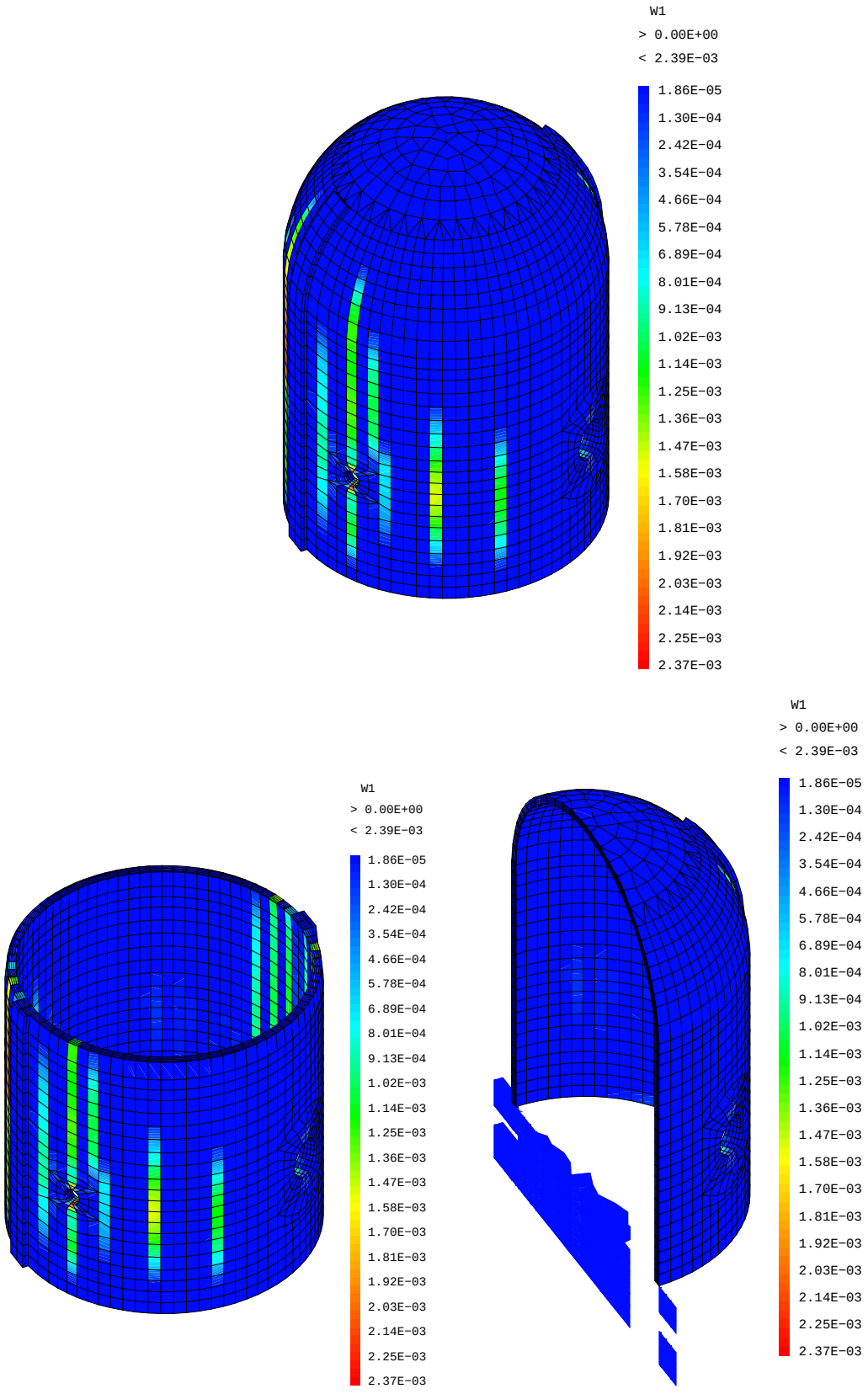

Fig 44 : Pressure 0,71 MPa – First opening cracks in the wall (Metre)

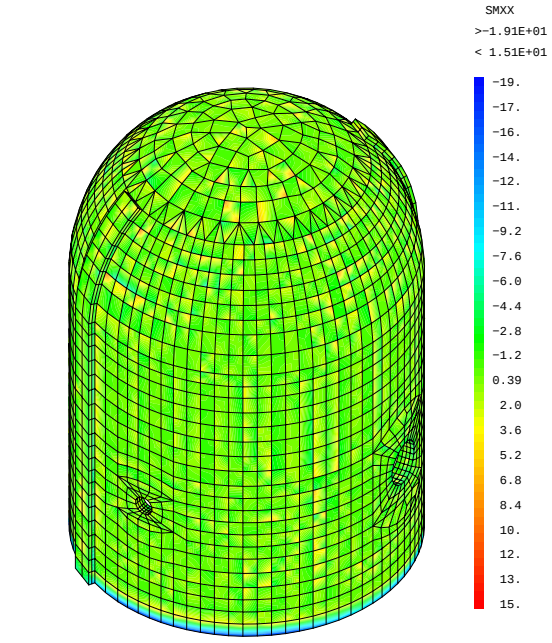

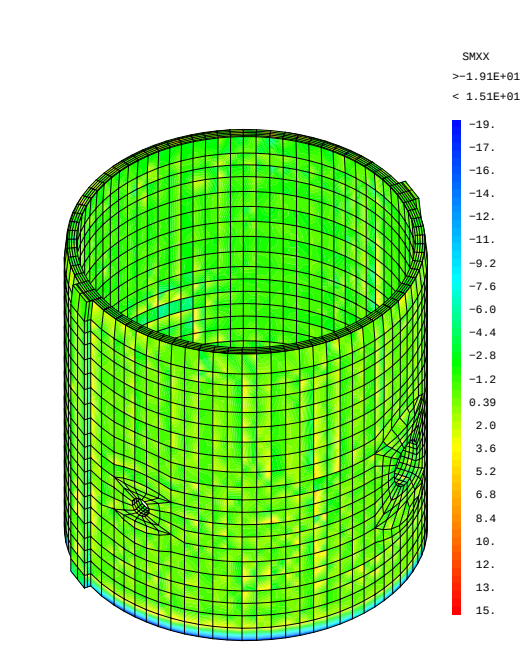

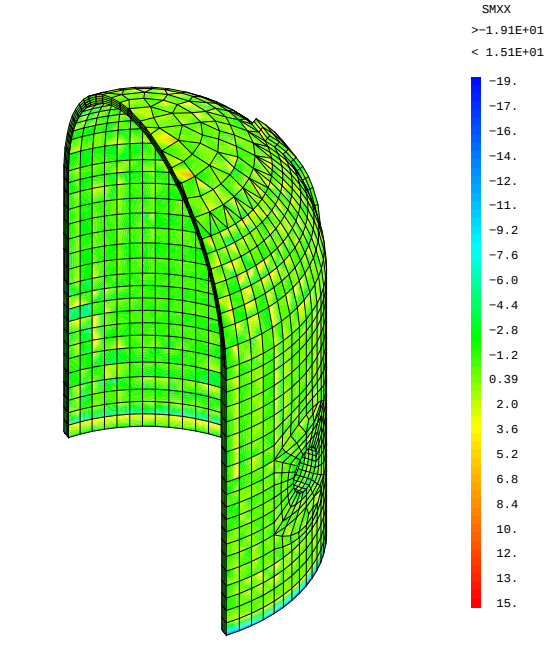

Fig 46 : Pressure 1,295 MPa – radial stresses in the wall (MPa)

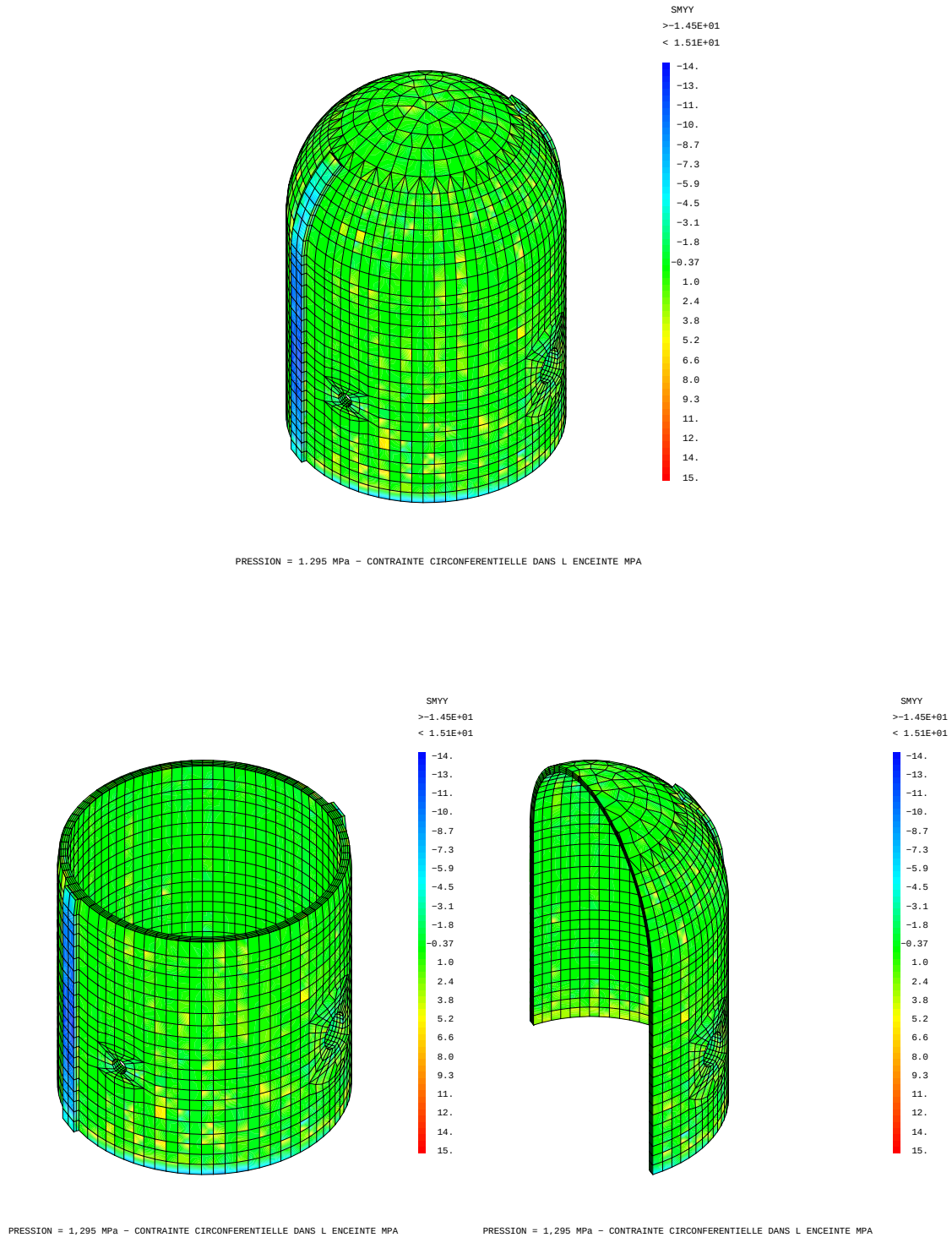

Fig 46: Pressure 1,295 MPa – Hoop stresses in the wall (MPa)

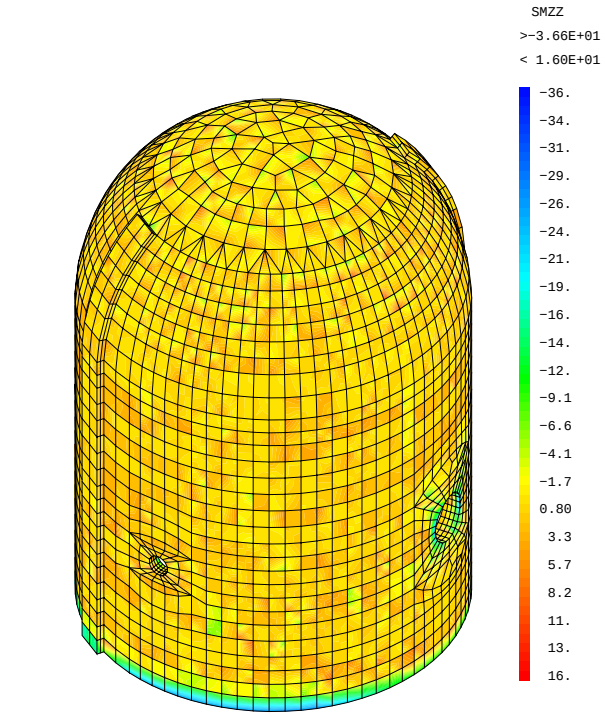

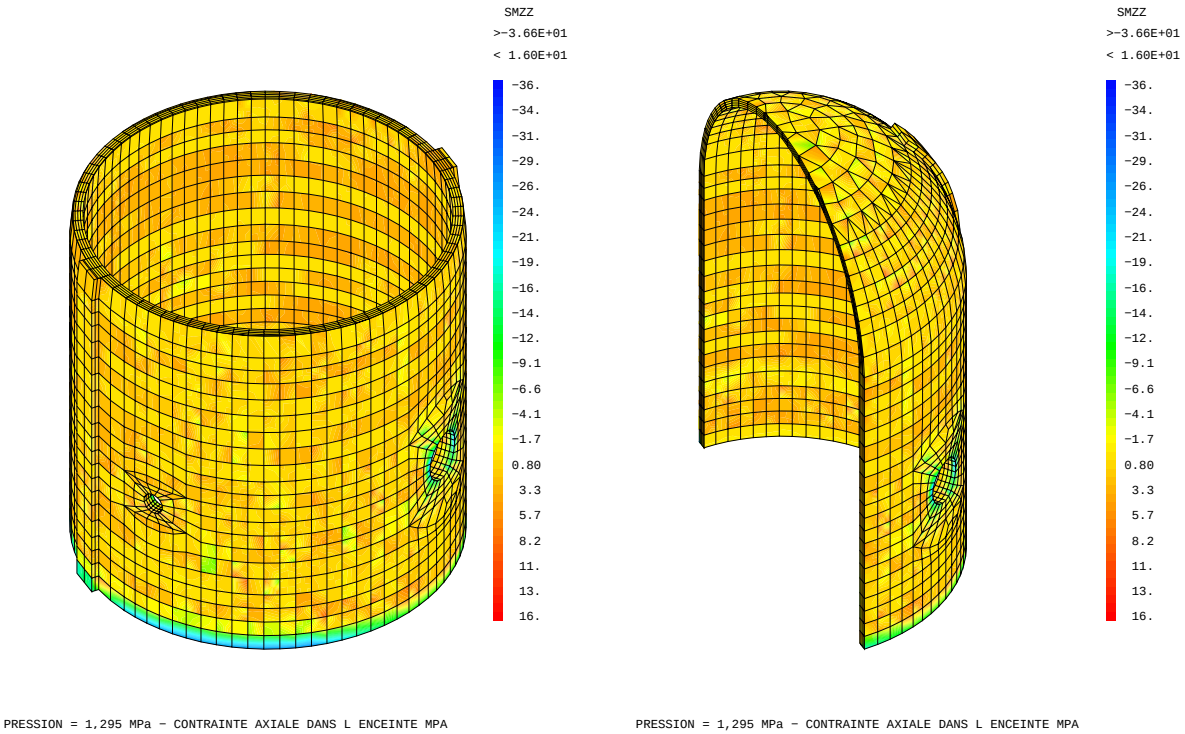

Fig 47 : Pressure 1,295 MPa – Vertical stresses in the wall (MPa)

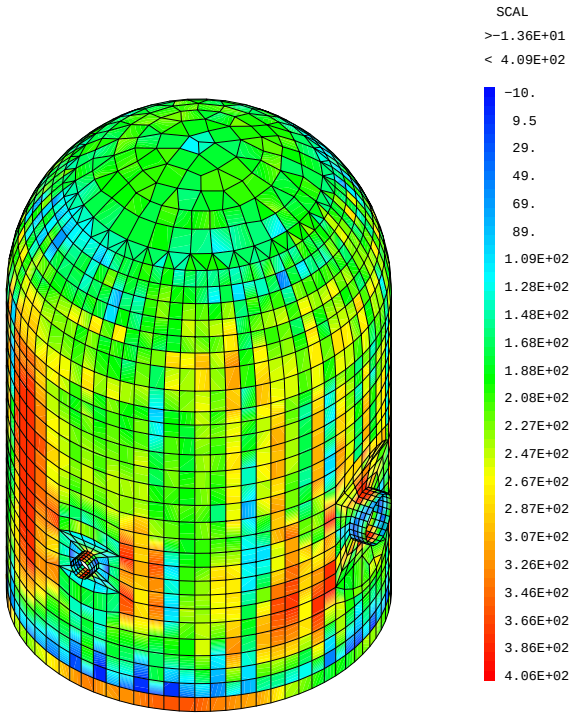

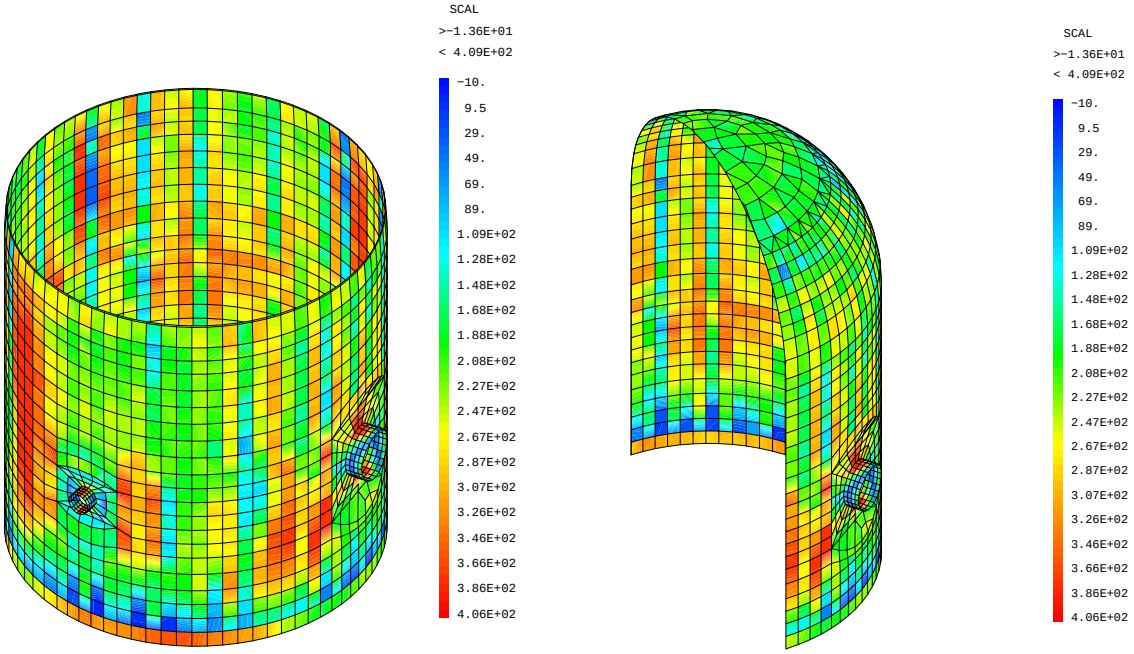

Fig 48 : Pressure 1,295 MPa – Von Mises stresses in the liner (MPa)

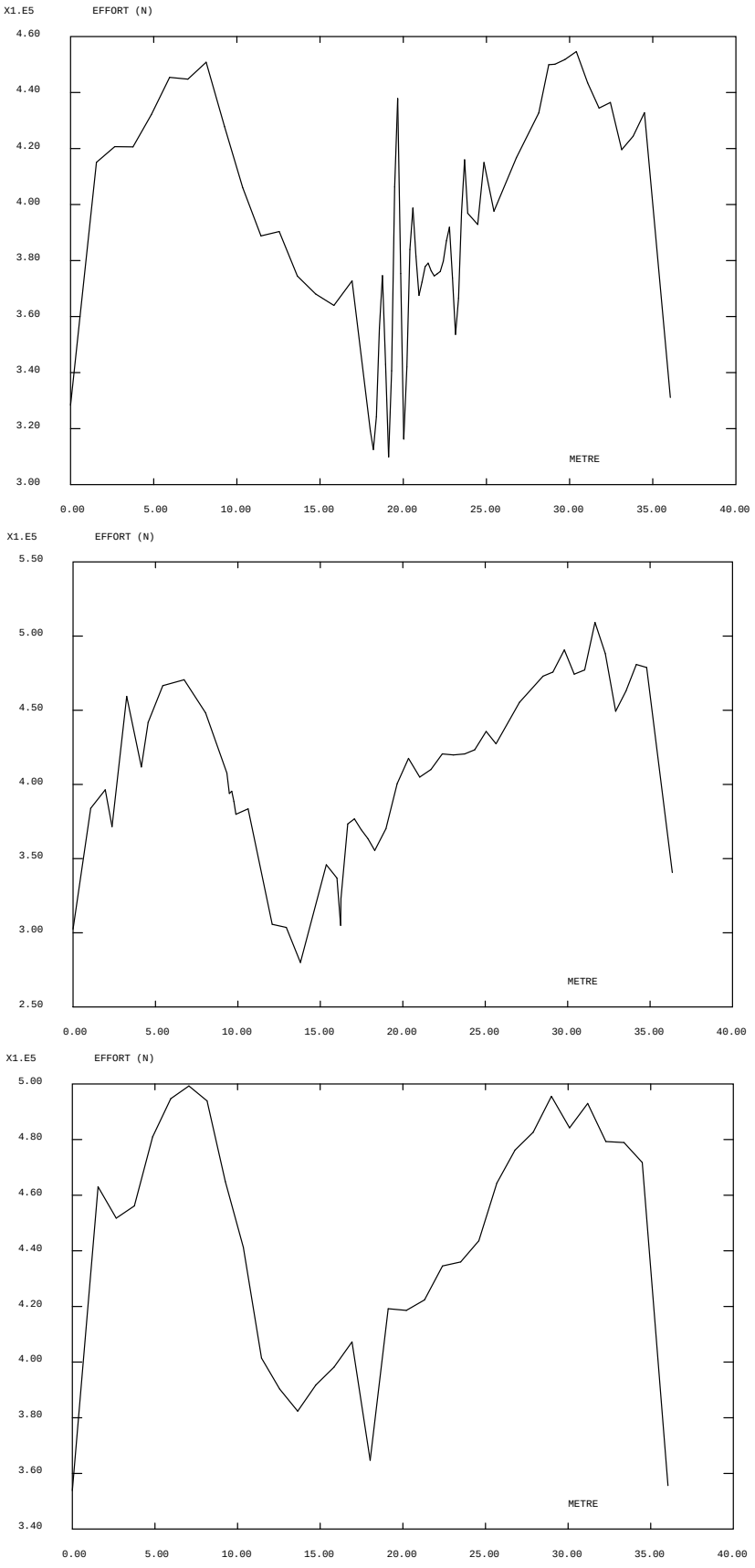

Fig 49 : Pressure 1,295 MPa – Tensions of tendons H11, H35, H53 (N)

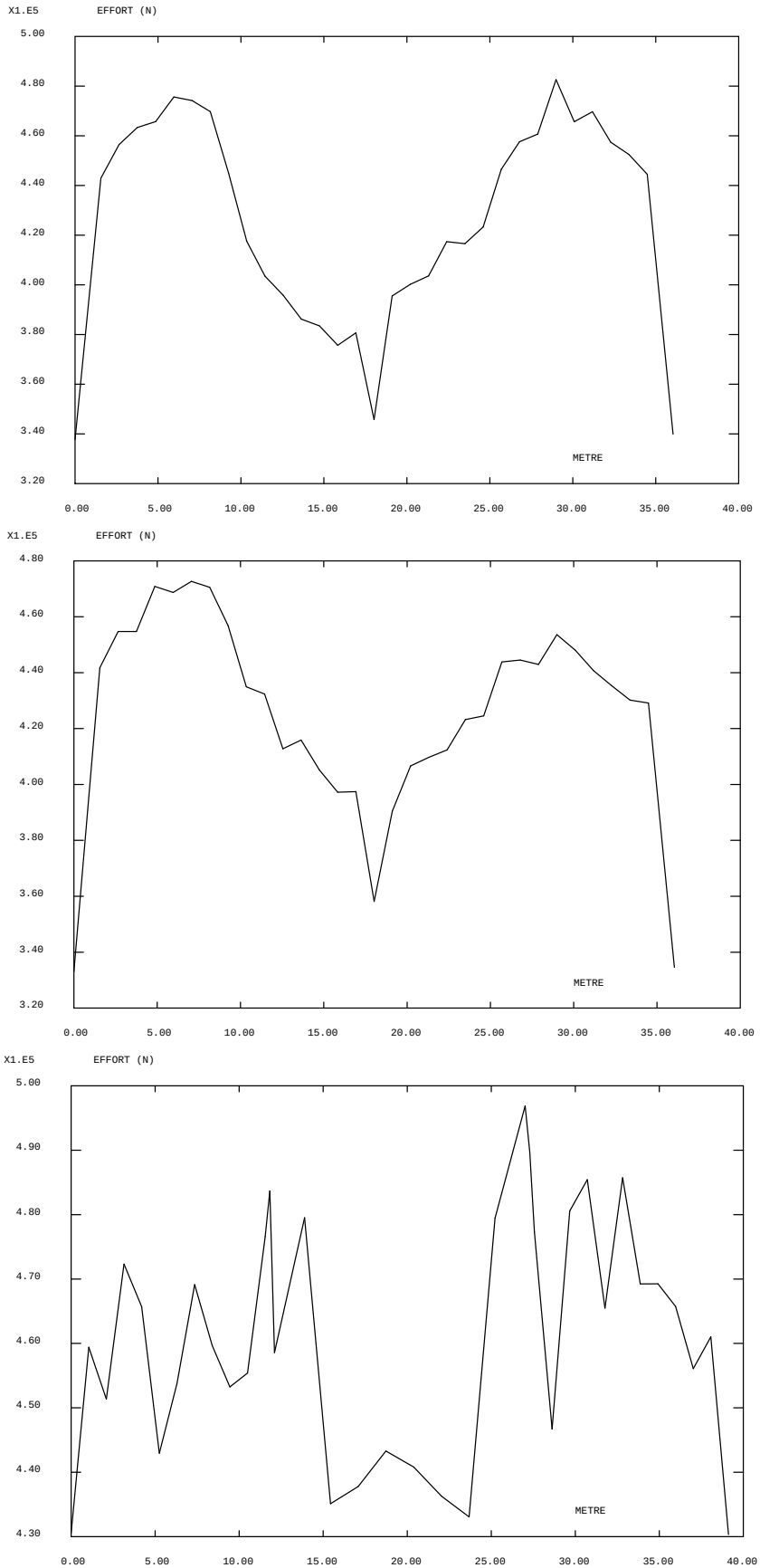

Fig 50 : Pressure 1,295 MPa – Tensions of tendons H67, H68, V37 (N)

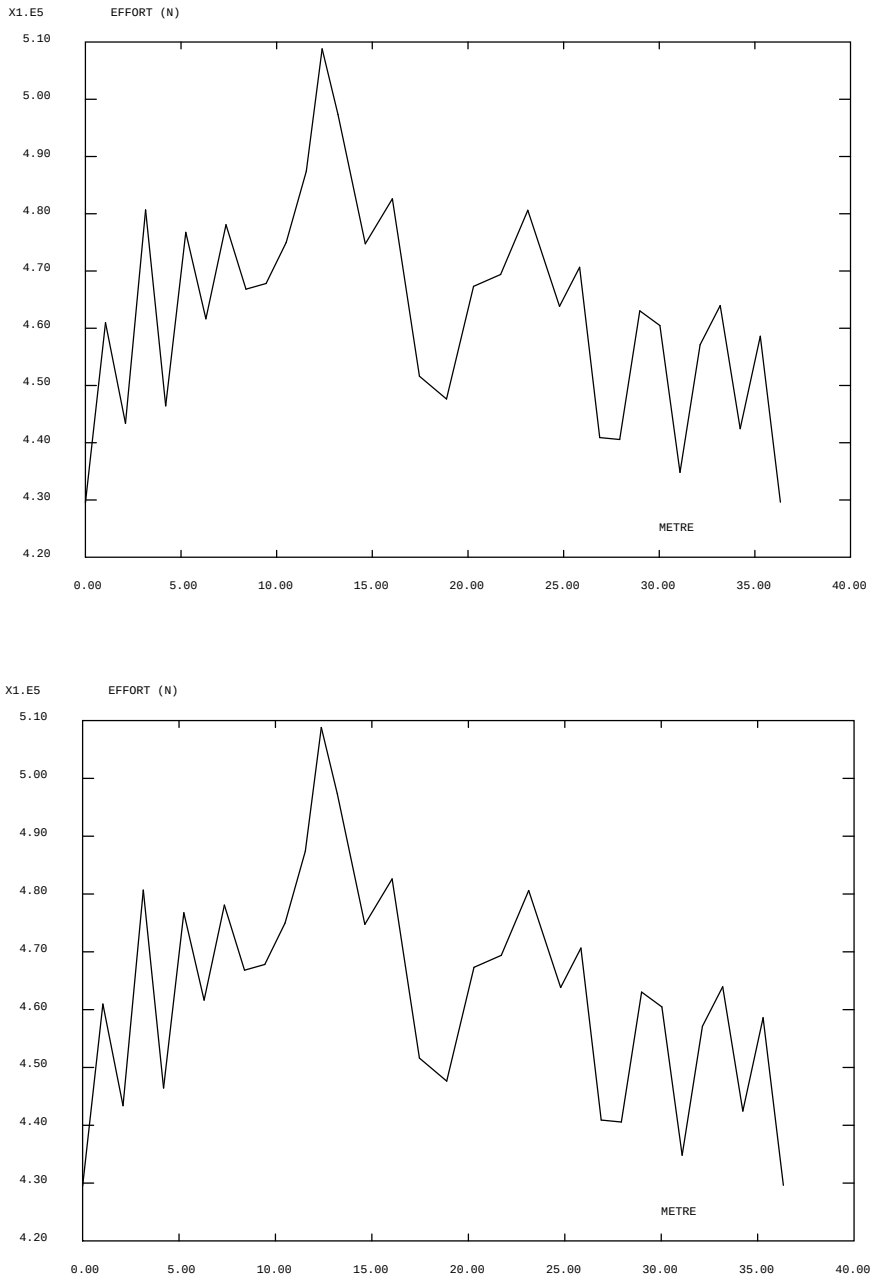

Fig 51 : Pressure 1,295 MPa – tensions of tendons V46, V85 (N)

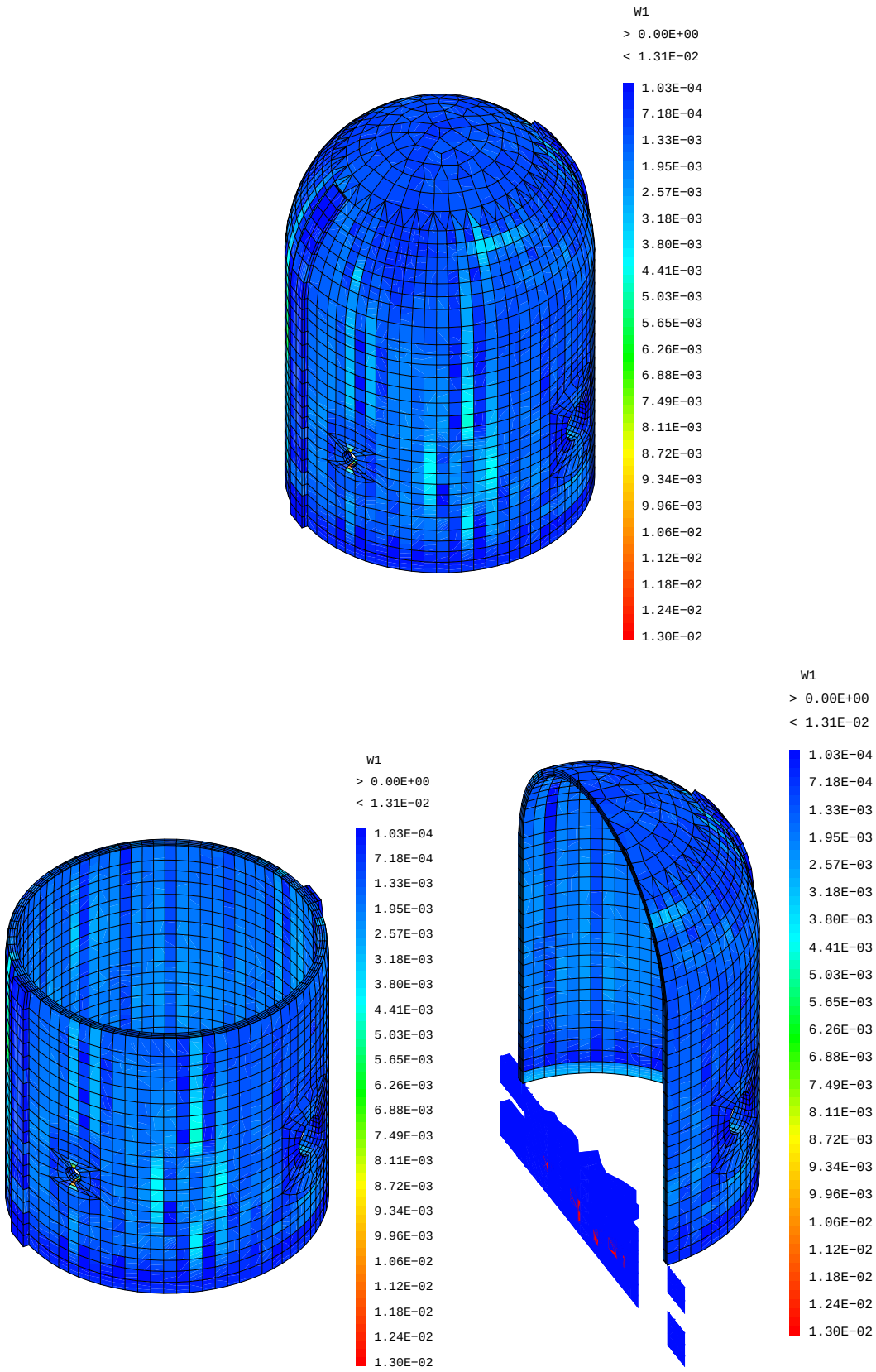

Fig 52 : Pressure 1,295 MPa – Hoop crack opening (metre)

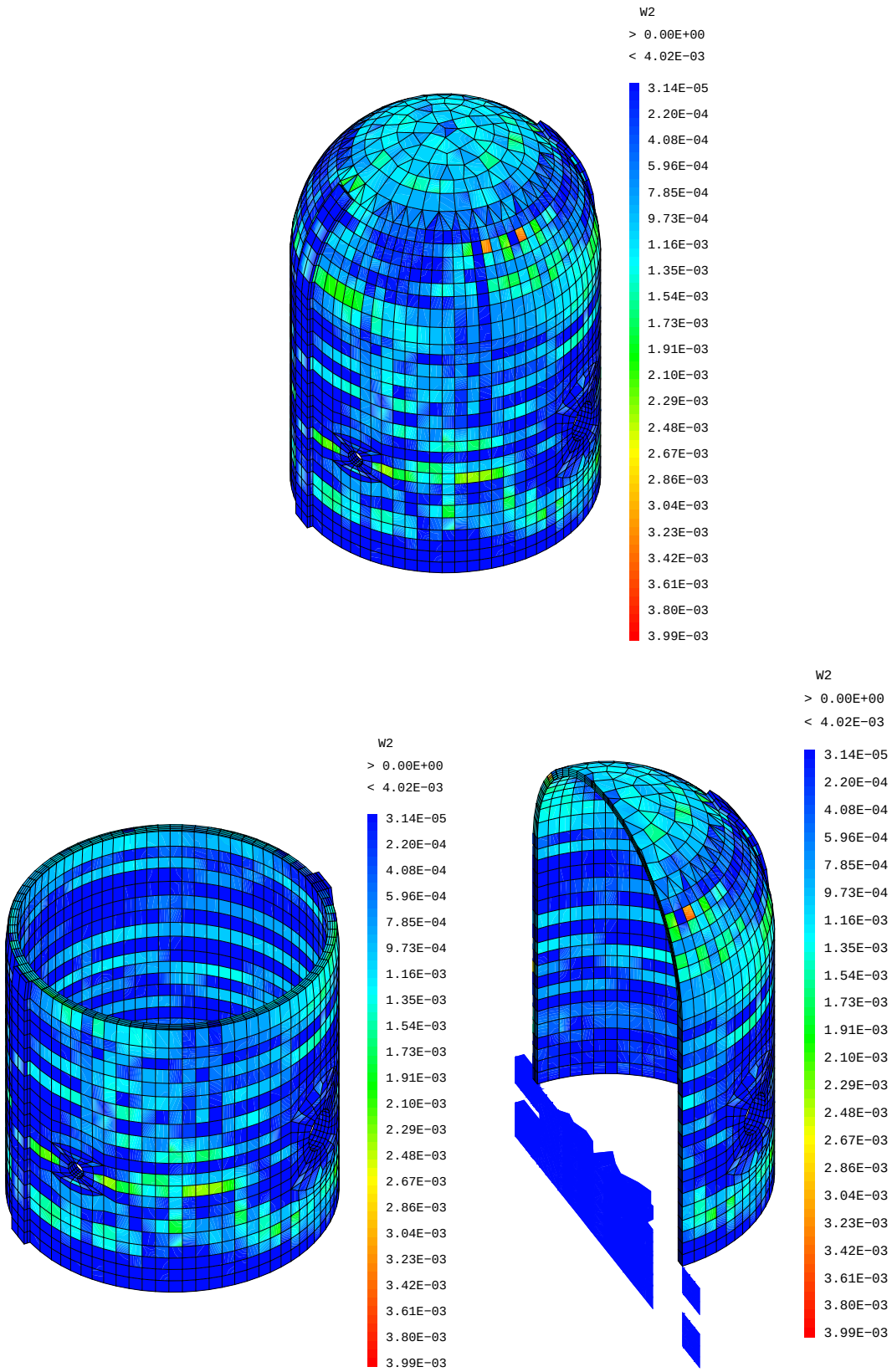

Fig 53 : Pressure 1,295 MPa – Vertical crack opening (metre)

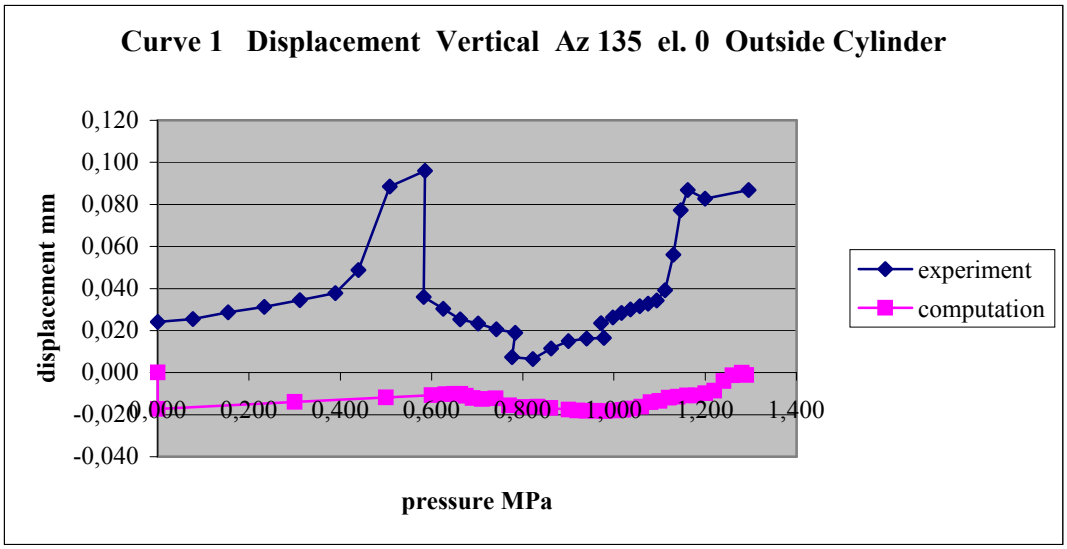
Curve 1 Displacement Vertical Az 135 el. 0 Outside Cylinder
displacement mm
0,120
0,100
0,080
0,060
0,040
0,020
0,000
-0,020
-0,040
0,000
0,200
0,400
0,600
0,800
1,000
1,200
1,400
pressure MPa
experiment
computation

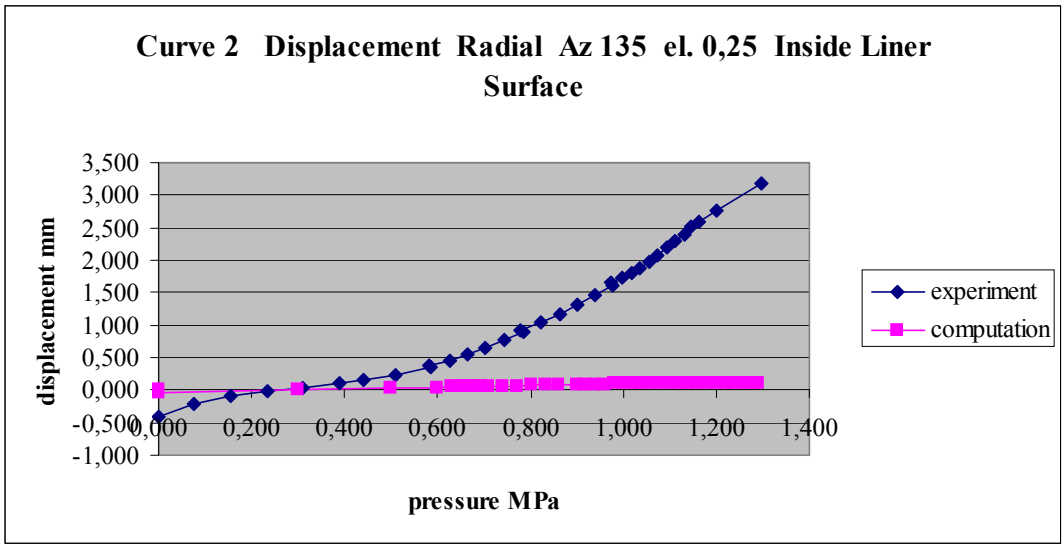
Curve 2 Displacement Radial Az 135 el. 0,25 Inside Liner Surface
displacement mm
3,500
3,000
2,500
2,000
1,500
1,000
0,500
0,000
-0,500
-1,000
0,000
0,200
0,400
0,600
0,800
1,000
1,200
1,400
pressure MPa
experiment
computation

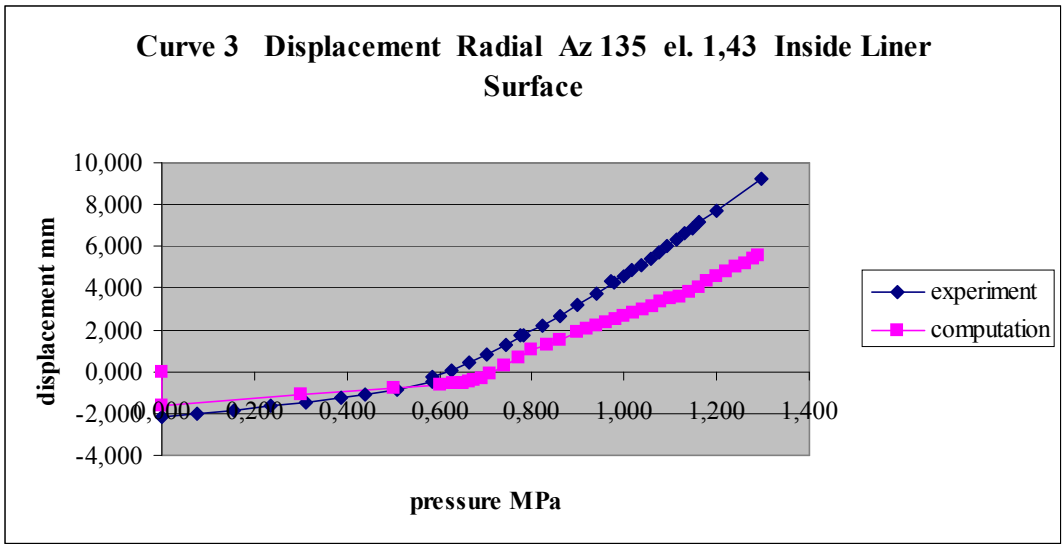
Curve 3 Displacement Radial Az 135 el. 1,43 Inside Liner Surface
displacement mm
10,000
8,000
6,000
4,000
2,000
0,000
-2,000
-4,000
0,000
0,200
0,400
0,600
0,800
1,000
1,200
1,400
pressure MPa
experiment
computation

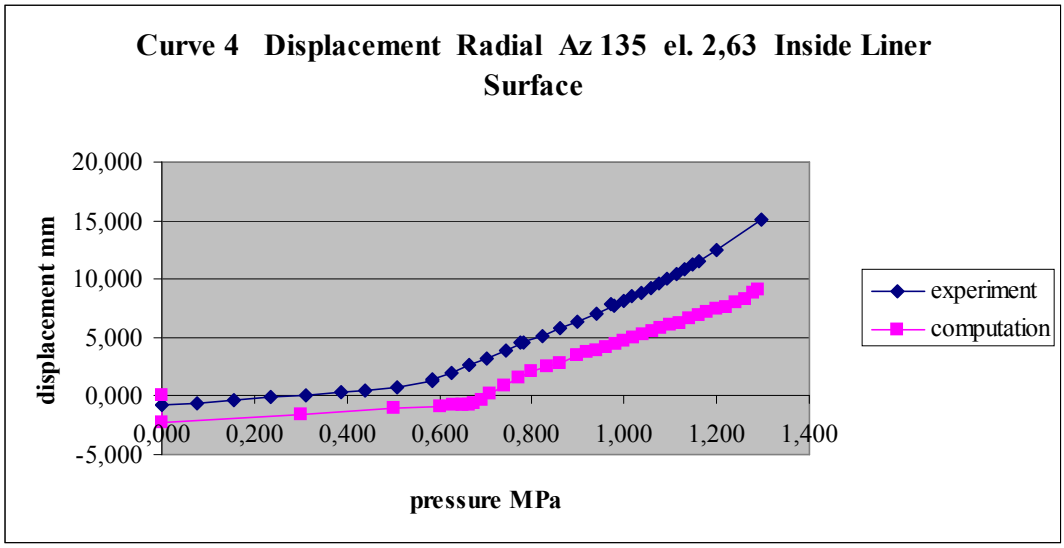
Curve 4 Displacement Radial Az 135 el. 2,63 Inside Liner Surface
displacement mm
20,000
15,000
10,000
5,000
0,000
-5,000
0,000
0,200
0,400
0,600
0,800
1,000
1,200
1,400
pressure MPa
experiment
computation

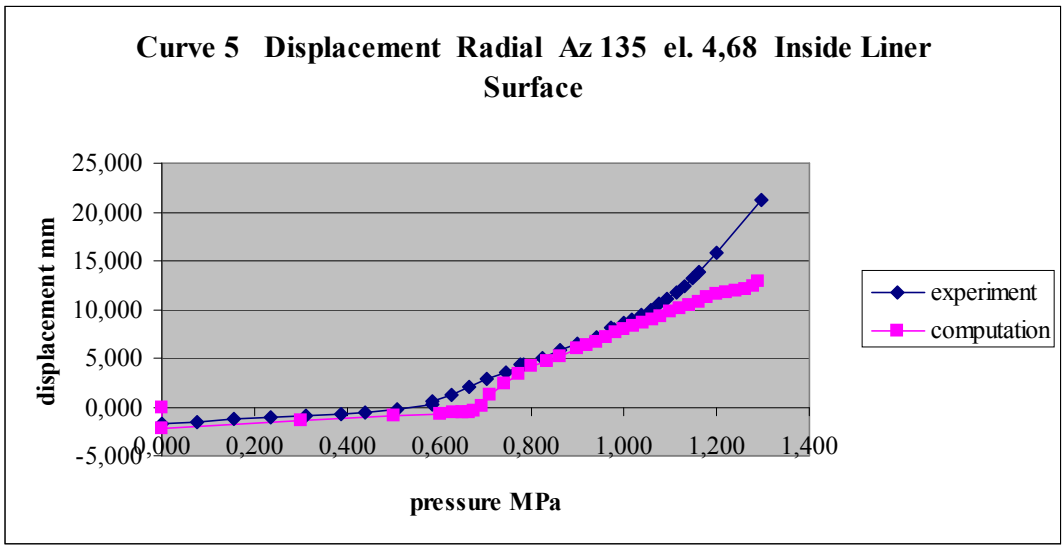
Curve 5 Displacement Radial Az 135 el. 4,68 Inside Liner Surface
displacement mm
25,000
20,000
15,000
10,000
5,000
0,000
-5,000
0,000
0,200
0,400
0,600
0,800
1,000
1,200
1,400
pressure MPa
experiment
computation

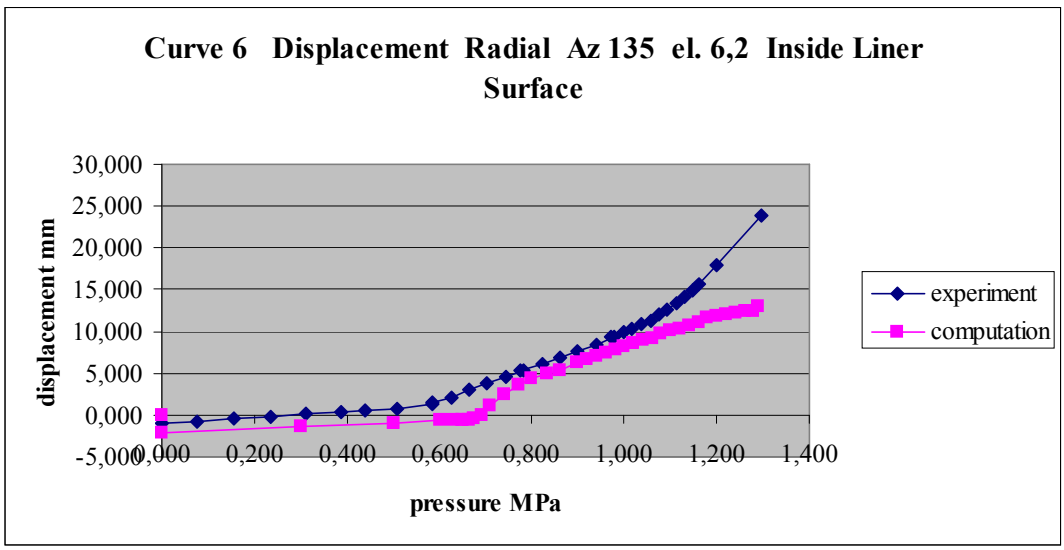
Curve 6 Displacement Radial Az 135 el. 6,2 Inside Liner Surface
displacement mm
30,000
25,000
20,000
15,000
10,000
5,000
0,000
-5,000
0,000
0,200
0,400
0,600
0,800
1,000
1,200
1,400
pressure MPa
experiment
computation

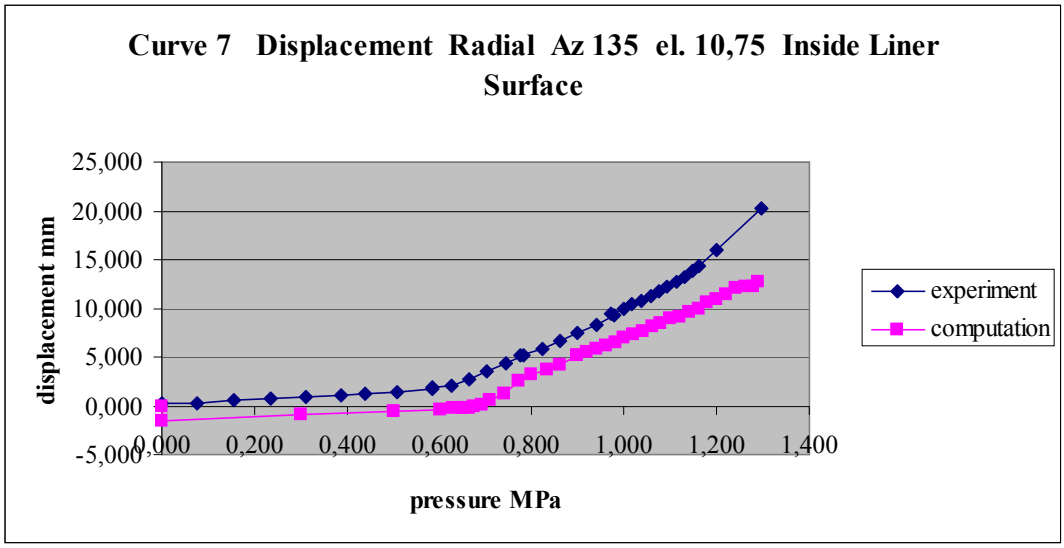
Curve 7 Displacement Radial Az 135 el. 10,75 Inside Liner Surface
displacement mm
25,000
20,000
15,000
10,000
5,000
0,000
-5,000
0,000
0,200
0,400
0,600
0,800
1,000
1,200
1,400
pressure MPa
experiment
computation

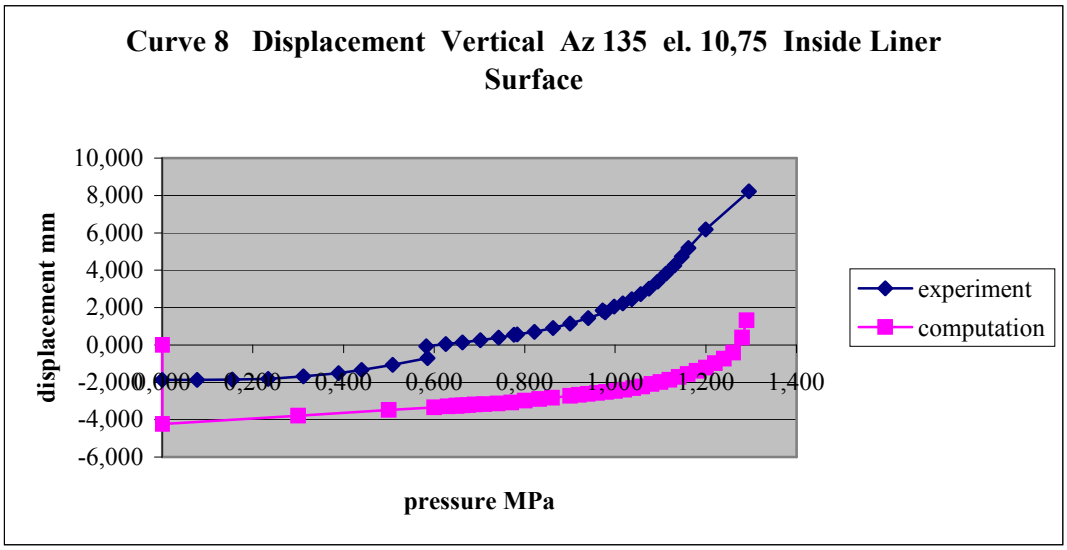
Curve 8 Displacement Vertical Az 135 el. 10,75 Inside Liner Surface
displacement mm
10,000
8,000
6,000
4,000
2,000
0,000
-2,000
-4,000
-6,000
0,000
0,200
0,400
0,600
0,800
1,000
1,200
1,400
pressure MPa
experiment
computation

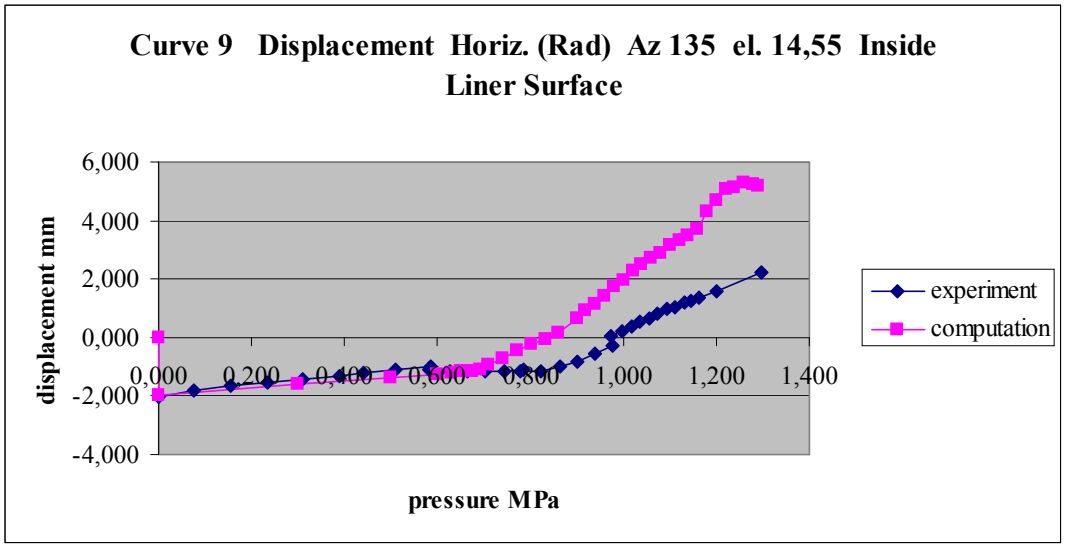
Curve 9 Displacement Horiz. (Rad) Az 135 el. 14,55 Inside Liner Surface
displacement mm
6,000
4,000
2,000
0,000
-2,000
-4,000
0,000
0,200
0,400
0,600
0,800
1,000
1,200
1,400
pressure MPa
experiment
computation

Curve 10 Displacement Vertical Az 135 el. 14,55 Inside Liner Surface

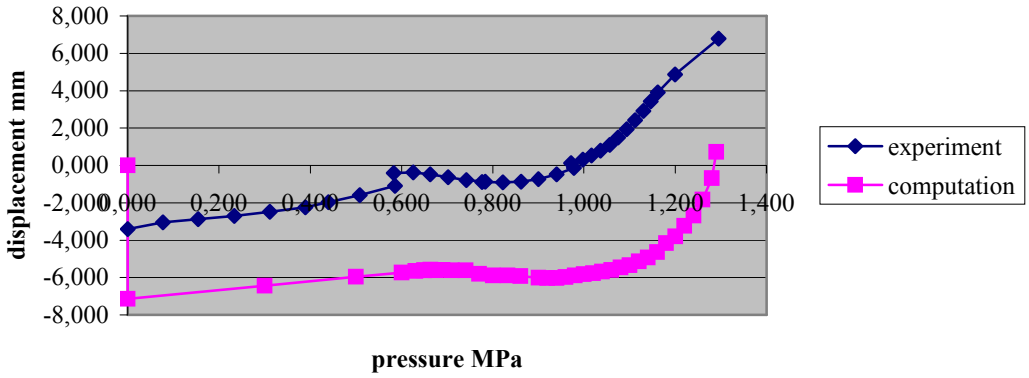

Curve 11 Displacement Vertical Az 135 el. 16,13 Inside Liner Surface

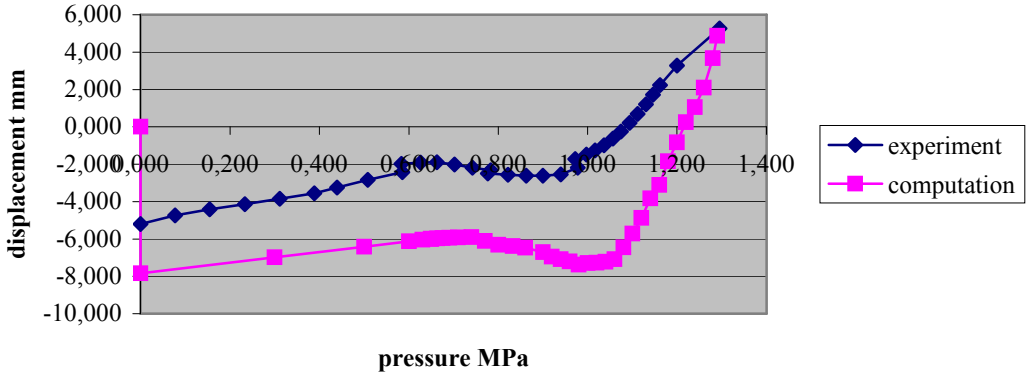

Curve 12 Displacement Radial Az 90 el. 6,2 Inside Liner Surface

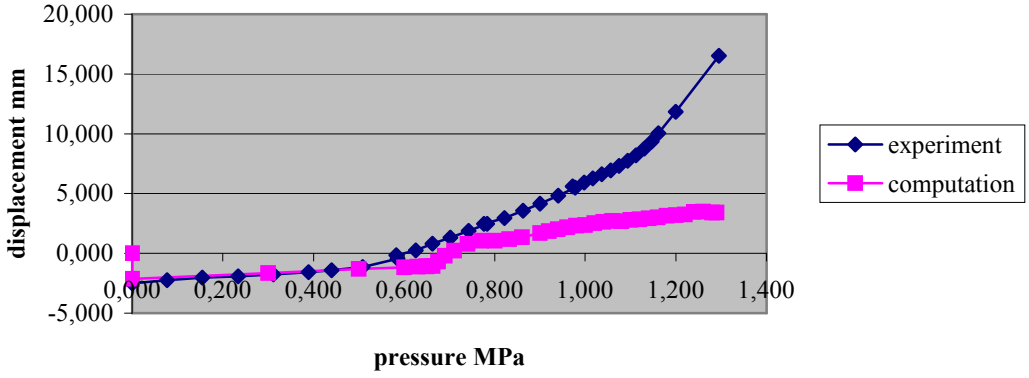

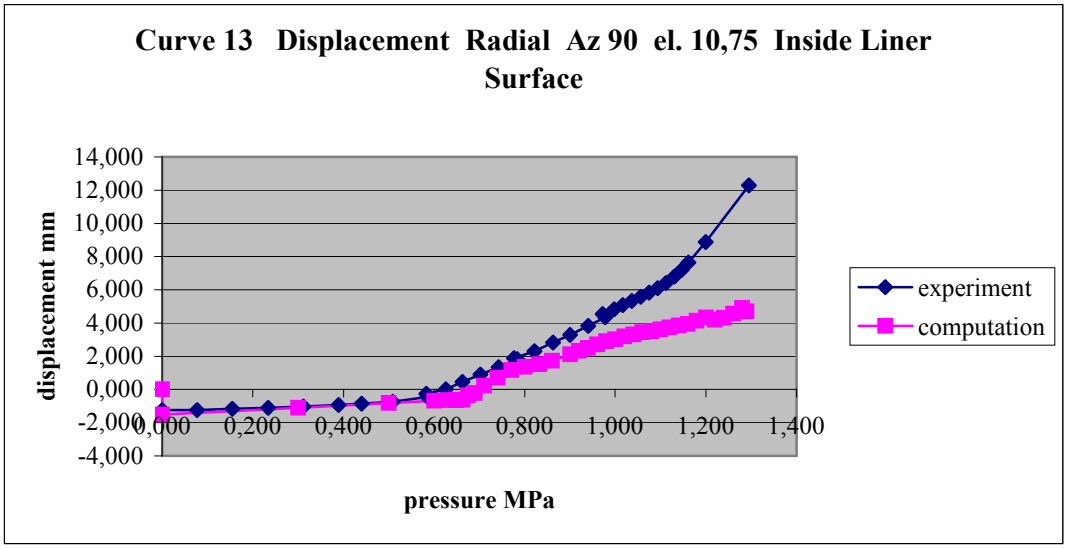
Curve 13 Displacement Radial Az 90 el. 10,75 Inside Liner Surface
displacement mm
14,000
12,000
10,000
8,000
6,000
4,000
2,000
0,000
-2,000
-4,000
0,000
0,200
0,400
0,600
0,800
1,000
1,200
1,400
pressure MPa
experiment
computation

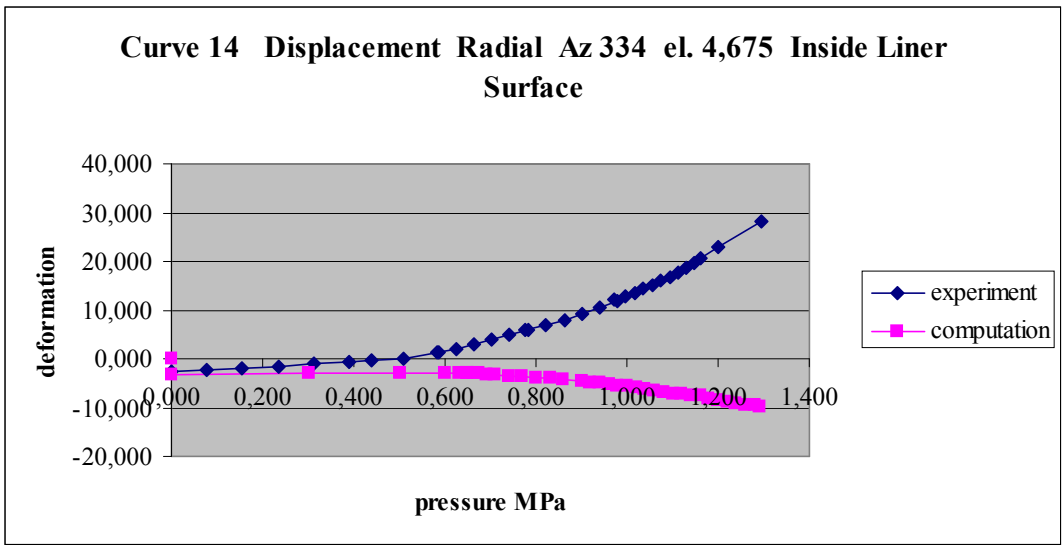
Curve 14 Displacement Radial Az 334 el. 4,675 Inside Liner Surface
deformation
40,000
30,000
20,000
10,000
0,000
-10,000
-20,000
0,000
0,200
0,400
0,600
0,800
1,000
1,200
1,400
pressure MPa
experiment
computation

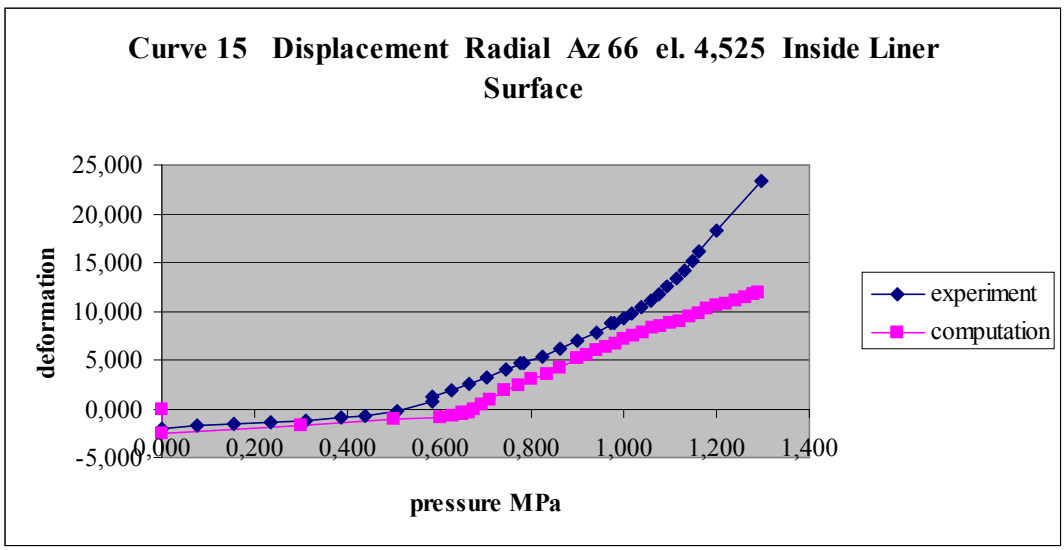
Curve 15 Displacement Radial Az 66 el. 4,525 Inside Liner Surface
deformation
25,000
20,000
15,000
10,000
5,000
0,000
-5,000
0,000
0,200
0,400
0,600
0,800
1,000
1,200
1,400
pressure MPa
experiment
computation

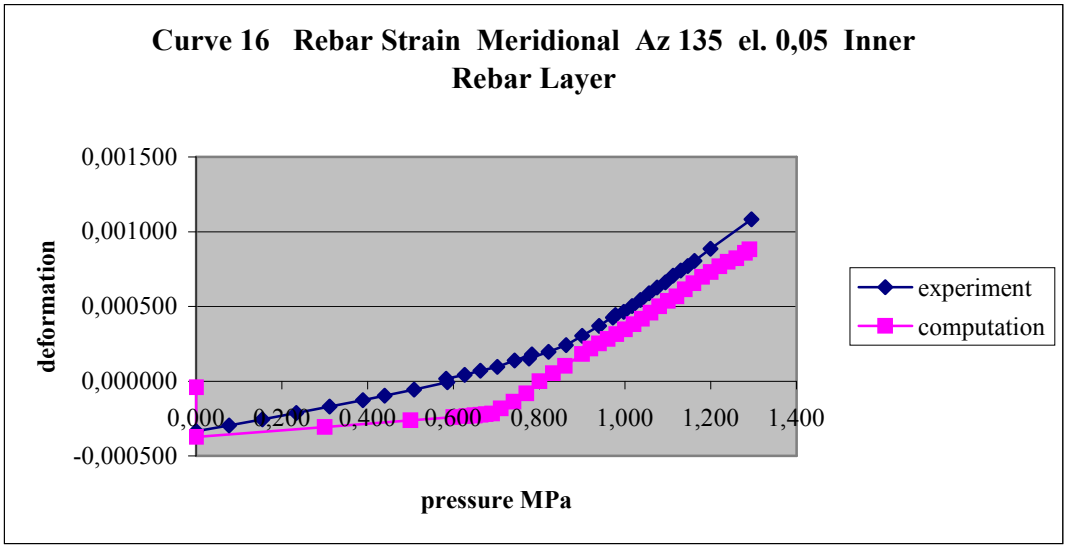
Curve 16 Rebar Strain Meridional Az 135 el. 0,05 Inner Rebar Layer
0,001500
0,001000
0,000500
0,000000
-0,000500
deformation
0,000
0,200
0,400
0,600
0,800
1,000
1,200
1,400
pressure MPa
experiment
computation

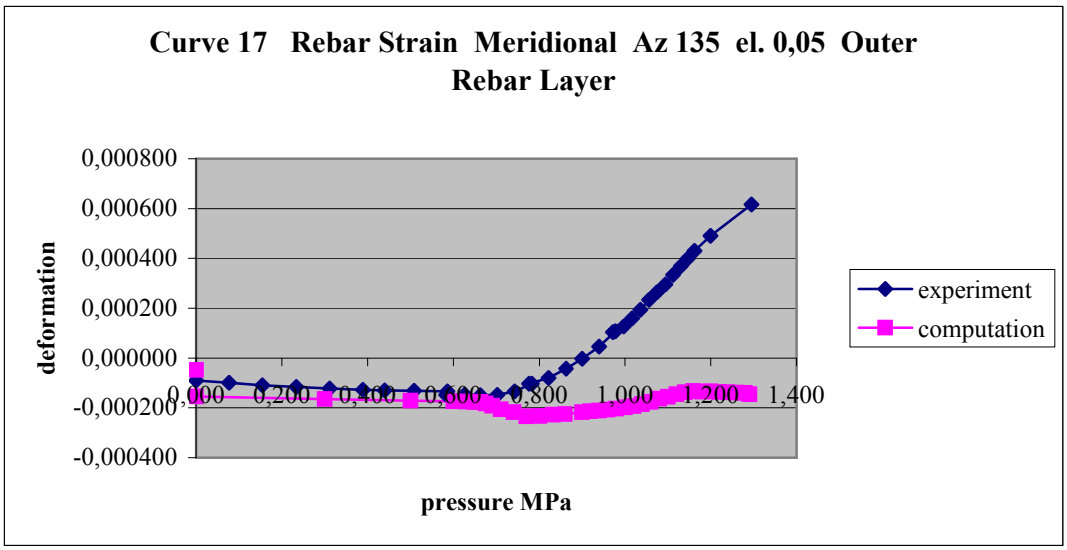
Curve 17 Rebar Strain Meridional Az 135 el. 0,05 Outer Rebar Layer
0,000800
0,000600
0,000400
0,000200
0,000000
-0,000200
-0,000400
deformation
0,000
0,200
0,400
0,600
0,800
1,000
1,200
1,400
pressure MPa
experiment
computation

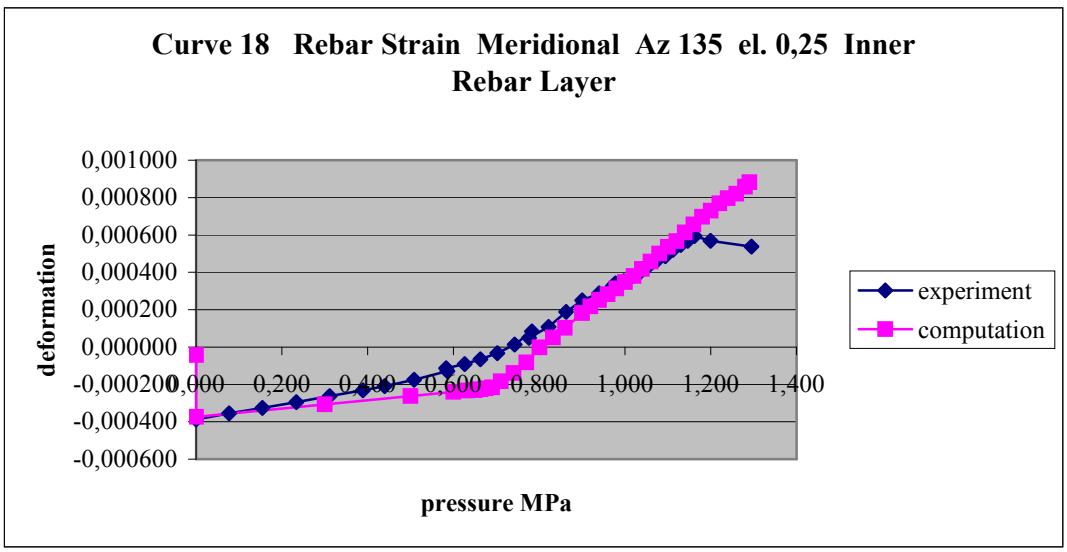
Curve 18 Rebar Strain Meridional Az 135 el. 0,25 Inner Rebar Layer
0,001000
0,000800
0,000600
0,000400
0,000200
0,000000
-0,000200
-0,000400
-0,000600
deformation
0,000
0,200
0,400
0,600
0,800
1,000
1,200
1,400
pressure MPa
experiment
computation

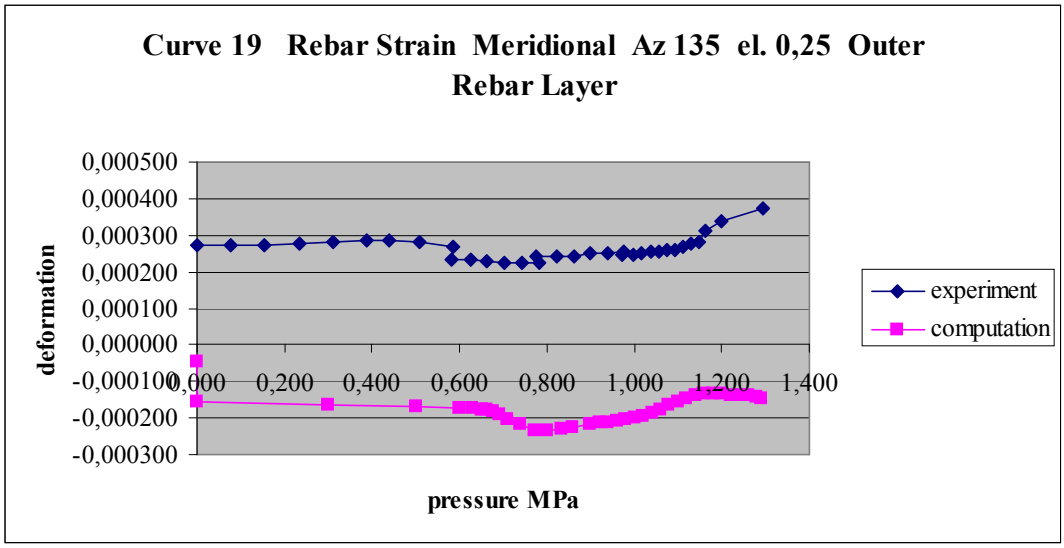
Curve 19 Rebar Strain Meridional Az 135 el. 0,25 Outer Rebar Layer
0,000500
0,000400
0,000300
0,000200
0,000100
0,000000
-0,000100
-0,000200
-0,000300
deformation
0,000
0,200
0,400
0,600
0,800
1,000
1,200
1,400
pressure MPa
experiment
computation

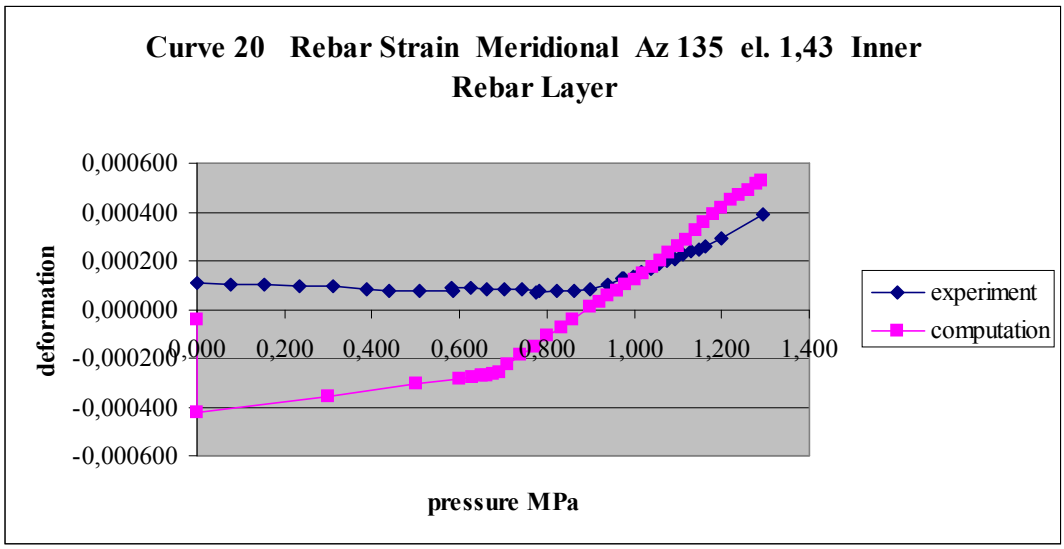
Curve 20 Rebar Strain Meridional Az 135 el. 1,43 Inner Rebar Layer
0,000600
0,000400
0,000200
0,000000
-0,000200
-0,000400
-0,000600
deformation
0,000
0,200
0,400
0,600
0,800
1,000
1,200
1,400
pressure MPa
experiment
computation

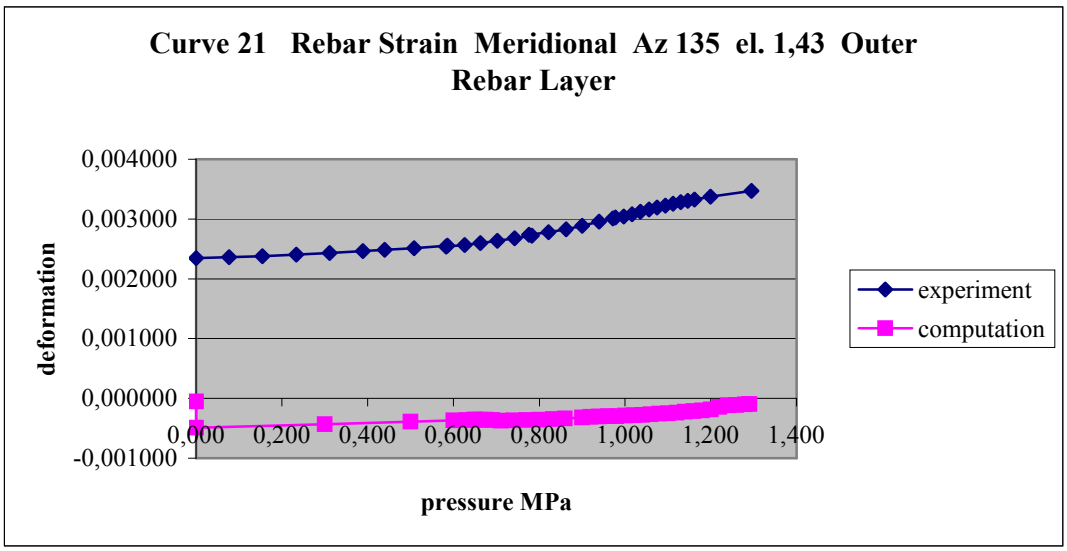
Curve 21 Rebar Strain Meridional Az 135 el. 1,43 Outer Rebar Layer
0,004000
0,003000
0,002000
0,001000
0,000000
-0,001000
deformation
0,000
0,200
0,400
0,600
0,800
1,000
1,200
1,400
pressure MPa
experiment
computation

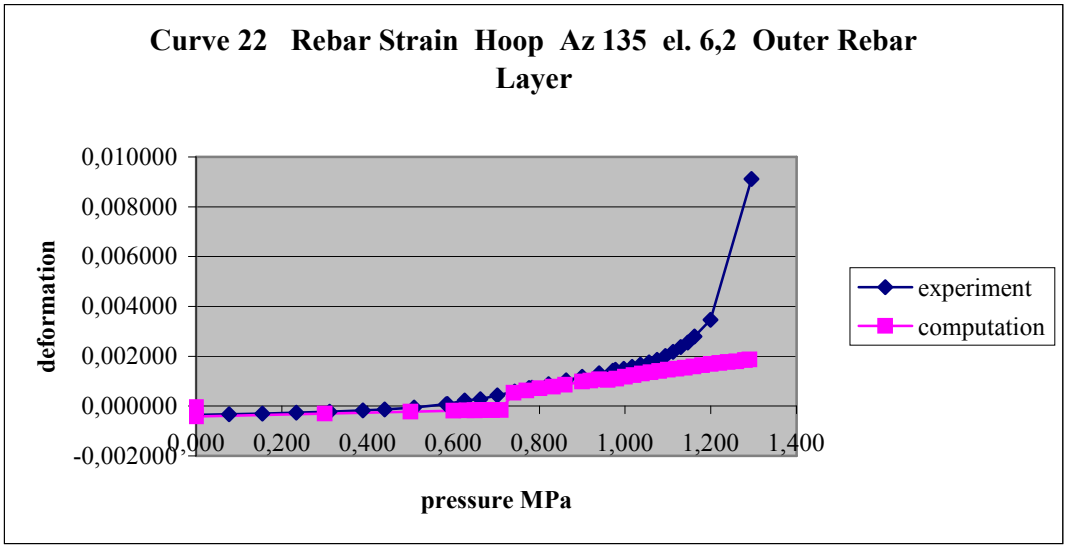
Curve 22 Rebar Strain Hoop Az 135 el. 6,2 Outer Rebar Layer
0,010000
0,008000
0,006000
0,004000
0,002000
0,000000
-0,002000
deformation
0,000
0,200
0,400
0,600
0,800
1,000
1,200
1,400
pressure MPa
experiment
computation

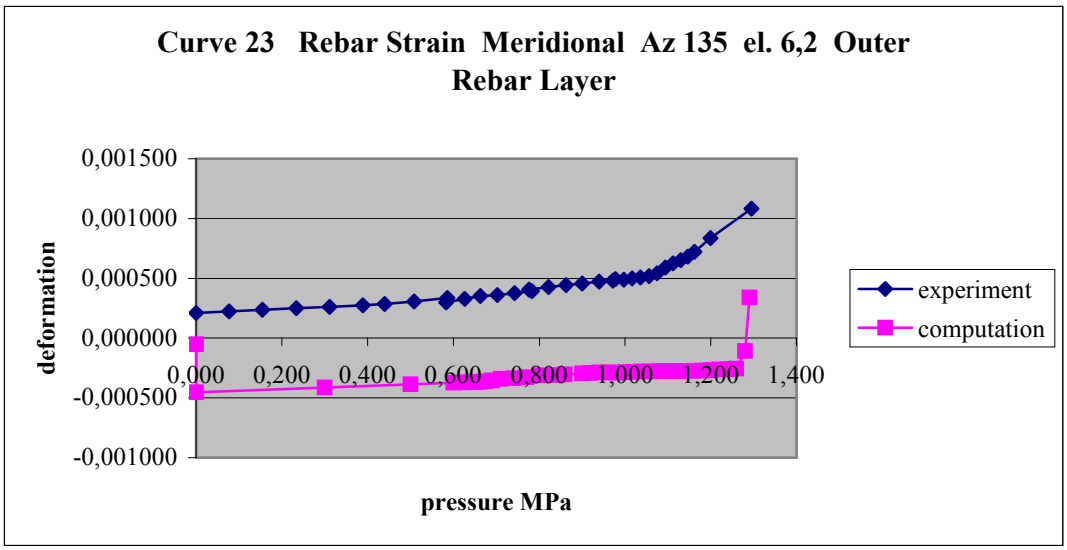
Curve 23 Rebar Strain Meridional Az 135 el. 6,2 Outer Rebar Layer
0,001500
0,001000
0,000500
0,000000
-0,000500
-0,001000
deformation
0,000
0,200
0,400
0,600
0,800
1,000
1,200
1,400
pressure MPa
experiment
computation

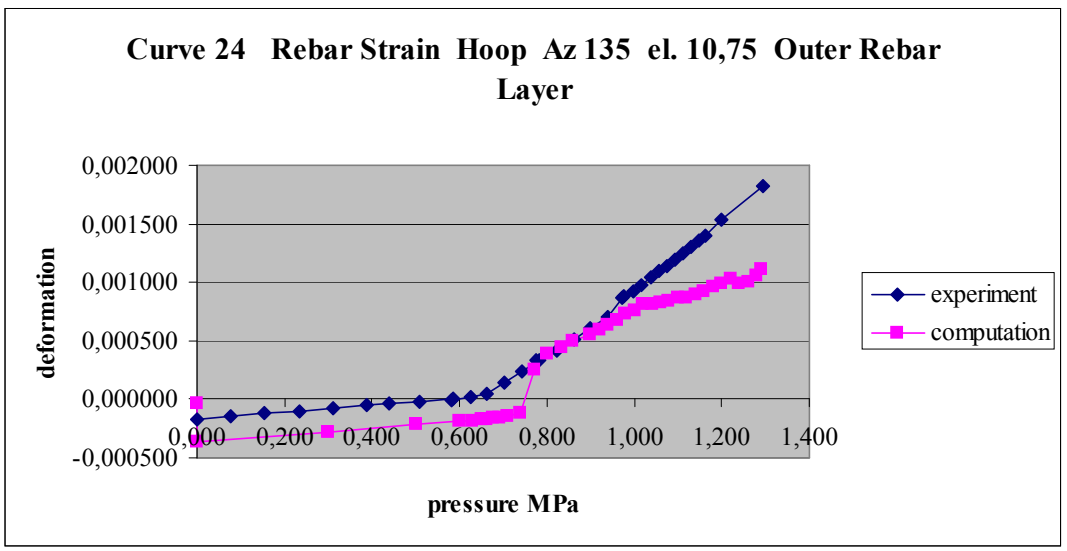
Curve 24 Rebar Strain Hoop Az 135 el. 10,75 Outer Rebar Layer
0,002000
0,001500
0,001000
0,000500
0,000000
-0,000500
deformation
0,000
0,200
0,400
0,600
0,800
1,000
1,200
1,400
pressure MPa
experiment
computation

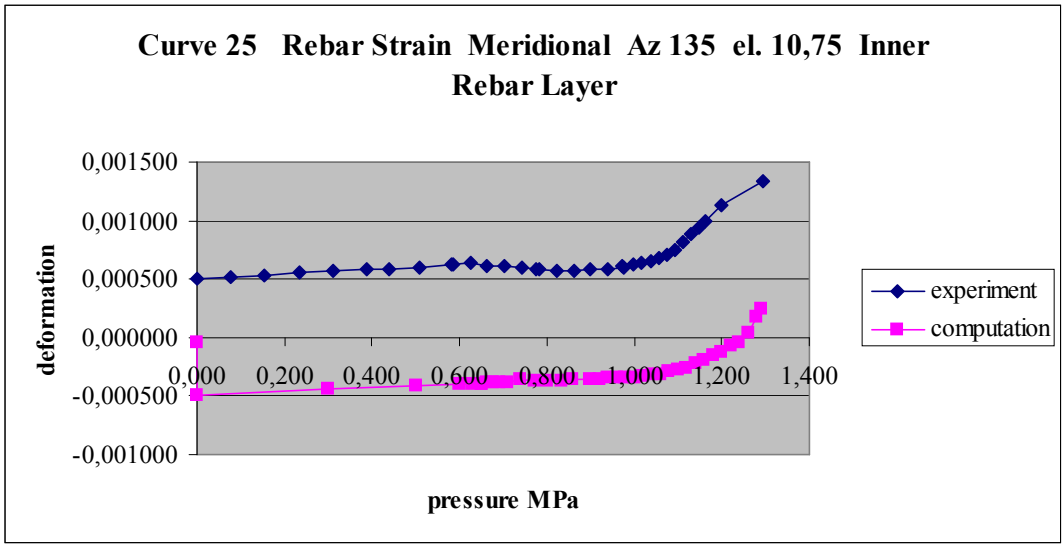
Curve 25 Rebar Strain Meridional Az 135 el. 10,75 Inner Rebar Layer
0,001500
0,001000
0,000500
0,000000
-0,000500
-0,001000
deformation
0,000
0,200
0,400
0,600
0,800
1,000
1,200
1,400
pressure MPa
experiment
computation

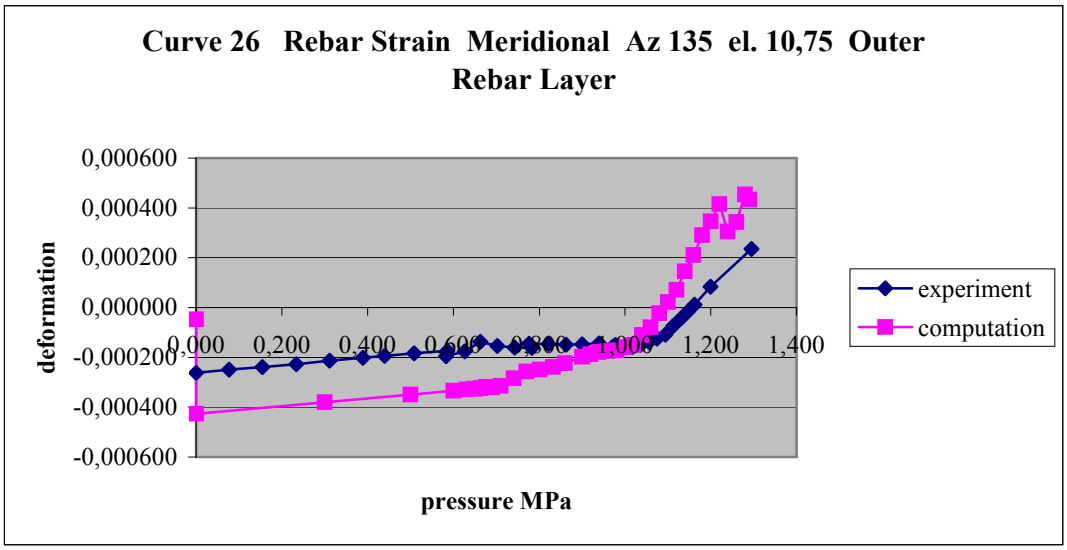
Curve 26 Rebar Strain Meridional Az 135 el. 10,75 Outer Rebar Layer
0,000600
0,000400
0,000200
0,000000
-0,000200
-0,000400
-0,000600
deformation
0,000
0,200
0,400
0,600
0,800
1,000
1,200
1,400
pressure MPa
experiment
computation

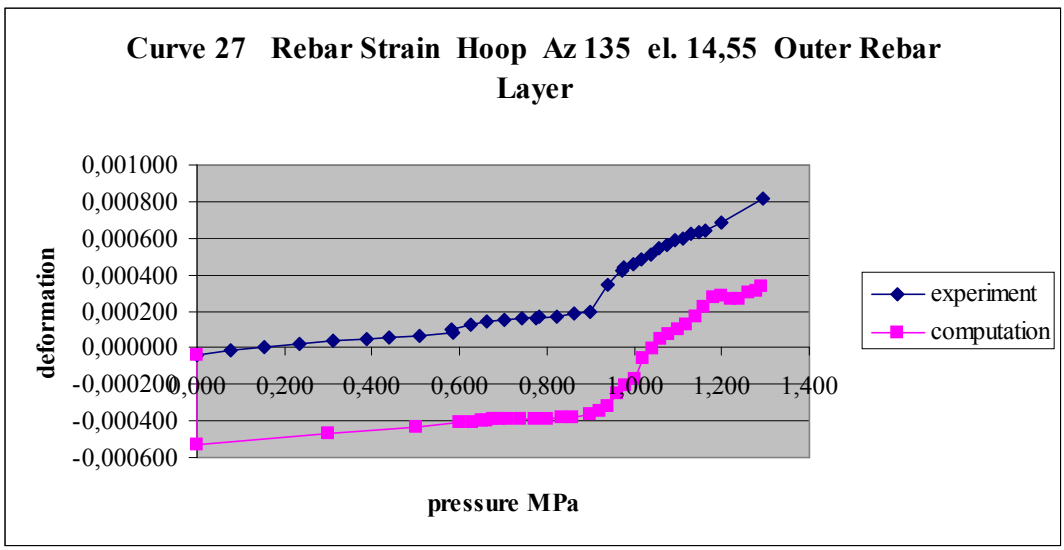
Curve 27 Rebar Strain Hoop Az 135 el. 14,55 Outer Rebar Layer
0,001000
0,000800
0,000600
0,000400
0,000200
0,000000
-0,000200
-0,000400
-0,000600
deformation
0,000
0,200
0,400
0,600
0,800
1,000
1,200
1,400
pressure MPa
experiment
computation

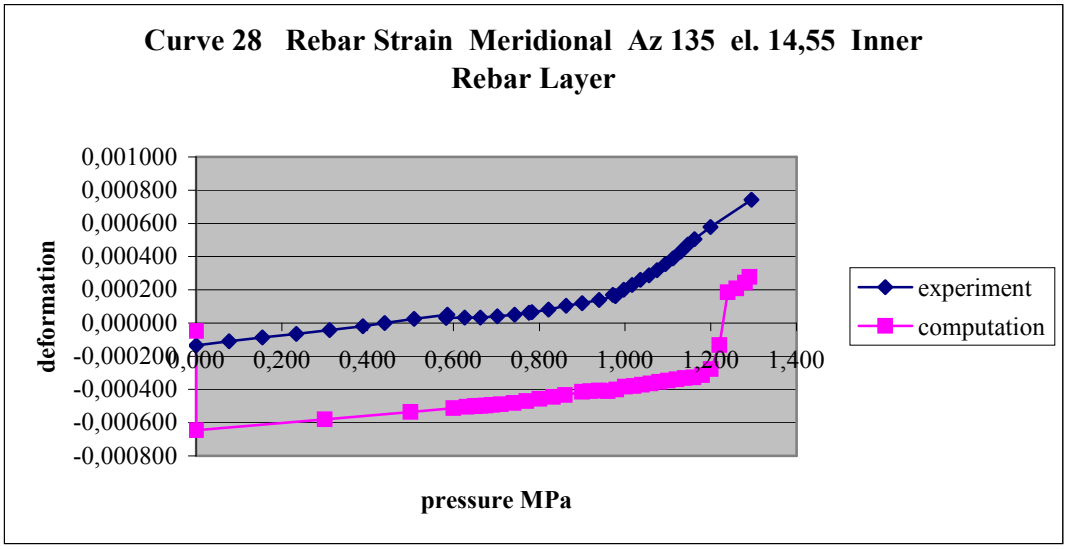
Curve 28 Rebar Strain Meridional Az 135 el. 14,55 Inner Rebar Layer
0,001000
0,000800
0,000600
0,000400
0,000200
0,000000
-0,000200
-0,000400
-0,000600
-0,000800
0,000
0,200
0,400
0,600
0,800
1,000
1,200
1,400
deformation
pressure MPa
experiment
computation

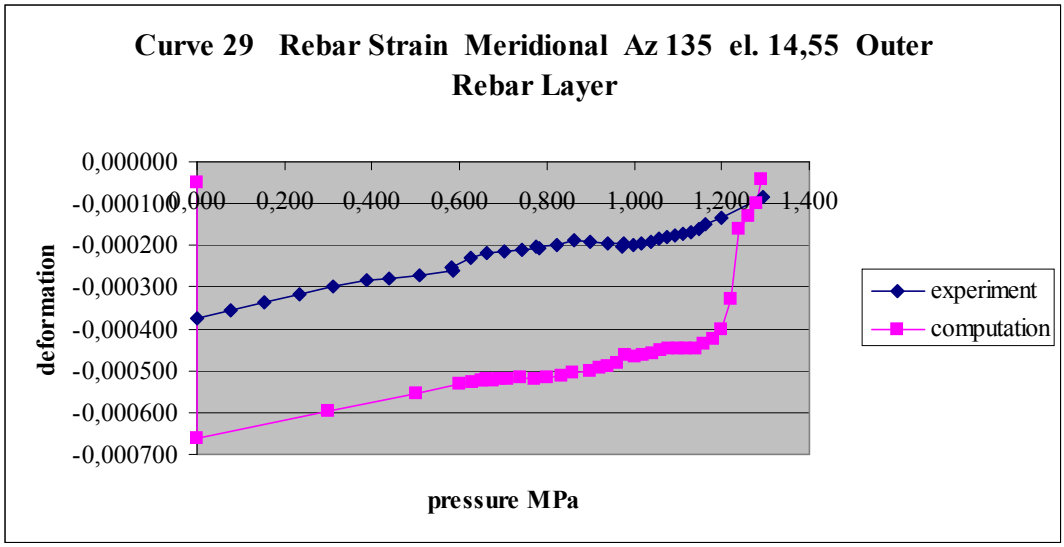
Curve 29 Rebar Strain Meridional Az 135 el. 14,55 Outer Rebar Layer
0,000000
-0,000100
-0,000200
-0,000300
-0,000400
-0,000500
-0,000600
-0,000700
0,000
0,200
0,400
0,600
0,800
1,000
1,200
1,400
deformation
pressure MPa
experiment
computation

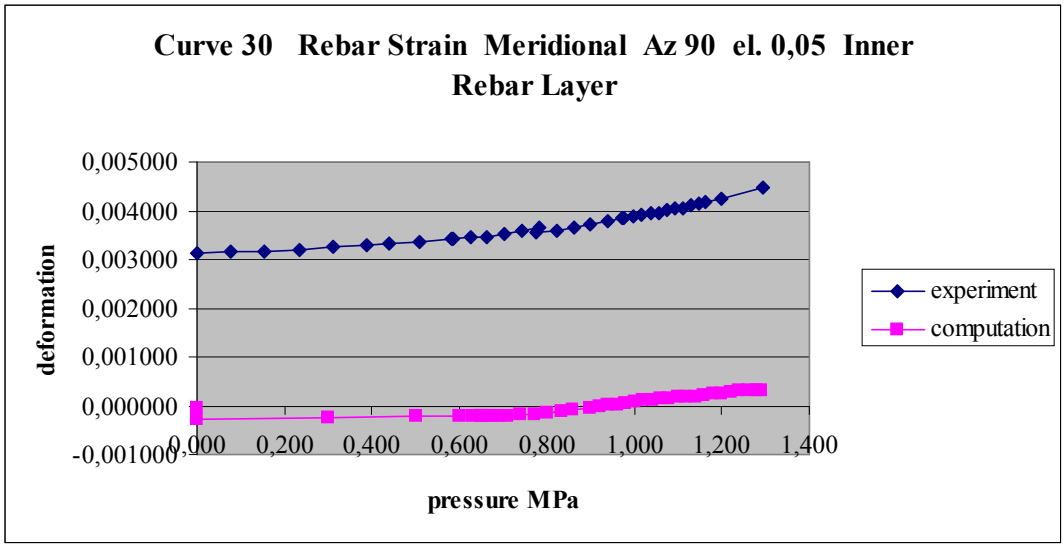
Curve 30 Rebar Strain Meridional Az 90 el. 0,05 Inner Rebar Layer
0,005000
0,004000
0,003000
0,002000
0,001000
0,000000
-0,001000
0,000
0,200
0,400
0,600
0,800
1,000
1,200
1,400
deformation
pressure MPa
experiment
computation

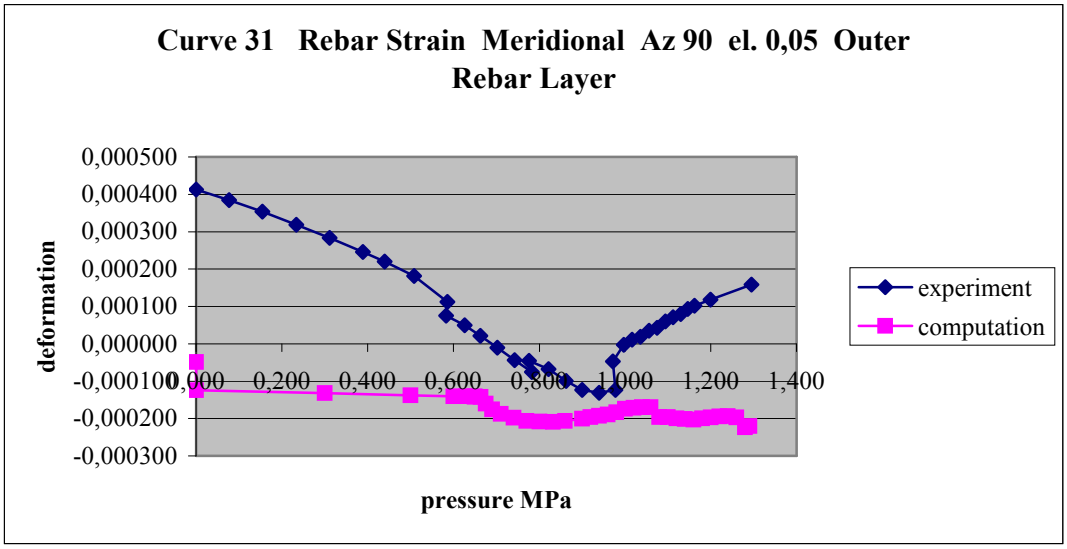
Curve 31 Rebar Strain Meridional Az 90 el. 0,05 Outer Rebar Layer
0,000500
0,000400
0,000300
0,000200
0,000100
0,000000
-0,000100
-0,000200
-0,000300
0,000
0,200
0,400
0,600
0,800
1,000
1,200
1,400
deformation
pressure MPa
experiment
computation

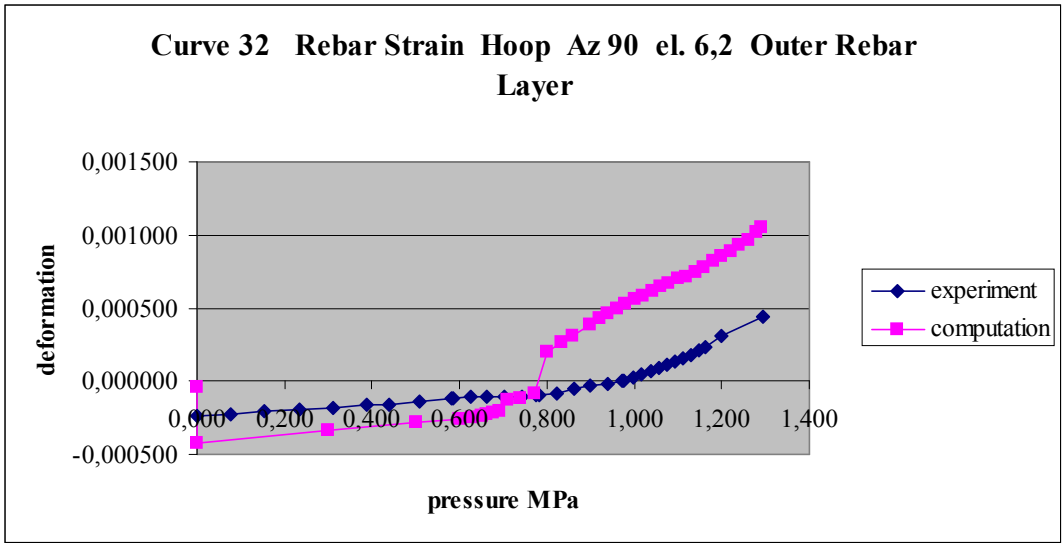
Curve 32 Rebar Strain Hoop Az 90 el. 6,2 Outer Rebar Layer
0,001500
0,001000
0,000500
0,000000
-0,000500
0,000
0,200
0,400
0,600
0,800
1,000
1,200
1,400
deformation
pressure MPa
experiment
computation

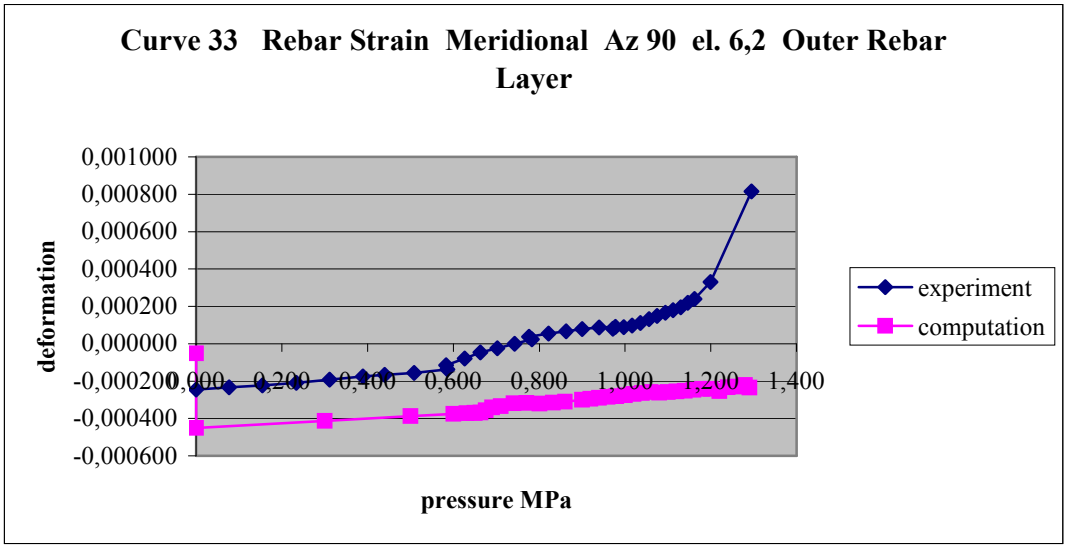
Curve 33 Rebar Strain Meridional Az 90 el. 6,2 Outer Rebar Layer
0,001000
0,000800
0,000600
0,000400
0,000200
0,000000
-0,000200
-0,000400
-0,000600
0,000
0,200
0,400
0,600
0,800
1,000
1,200
1,400
deformation
pressure MPa
experiment
computation

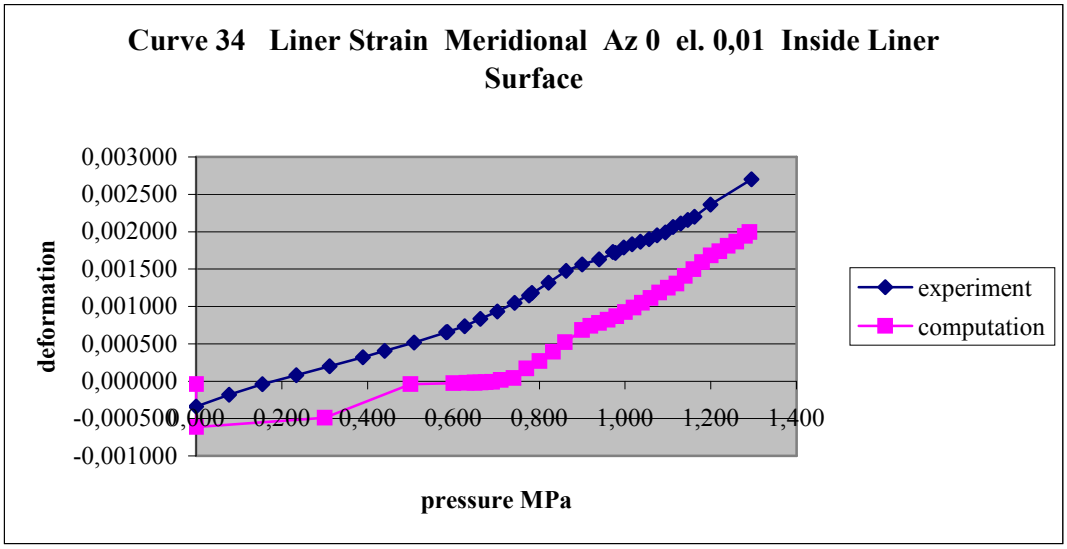
Curve 34 Liner Strain Meridional Az 0 el. 0,01 Inside Liner Surface
deformation
0,003000
0,002500
0,002000
0,001500
0,001000
0,000500
0,000000
-0,000500
-0,001000
0,000
0,200
0,400
0,600
0,800
1,000
1,200
1,400
pressure MPa
experiment
computation

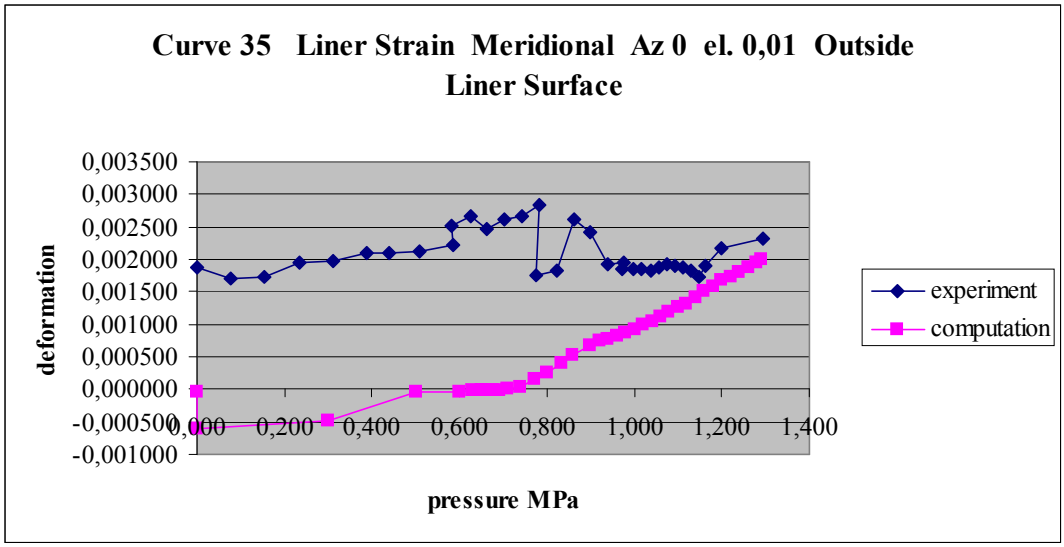
Curve 35 Liner Strain Meridional Az 0 el. 0,01 Outside Liner Surface
deformation
0,003500
0,003000
0,002500
0,002000
0,001500
0,001000
0,000500
0,000000
-0,000500
-0,001000
0,000
0,200
0,400
0,600
0,800
1,000
1,200
1,400
pressure MPa
experiment
computation

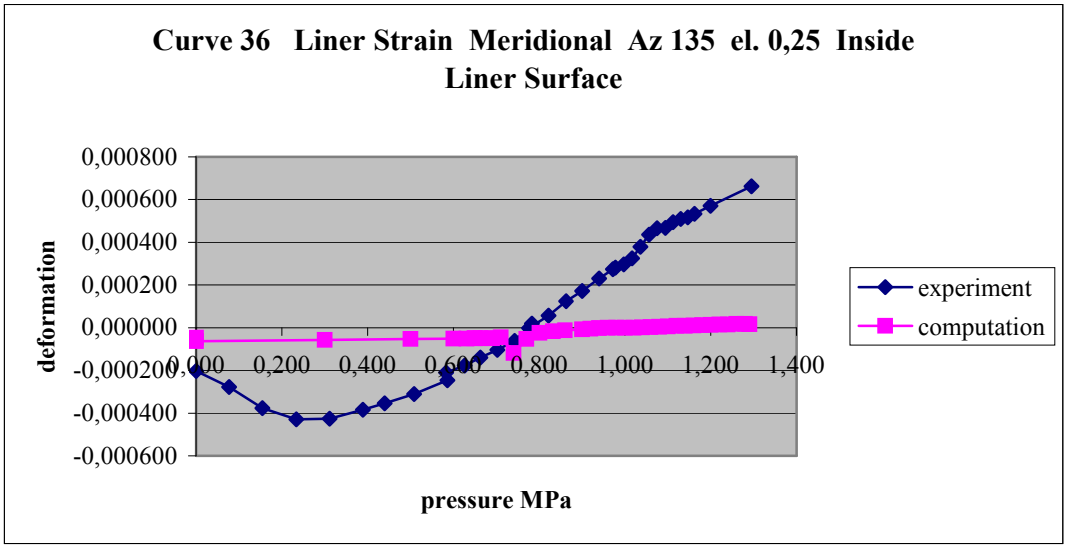
Curve 36 Liner Strain Meridional Az 135 el. 0,25 Inside Liner Surface
deformation
0,000800
0,000600
0,000400
0,000200
0,000000
-0,000200
-0,000400
-0,000600
0,000
0,200
0,400
0,600
0,800
1,000
1,200
1,400
pressure MPa
experiment
computation

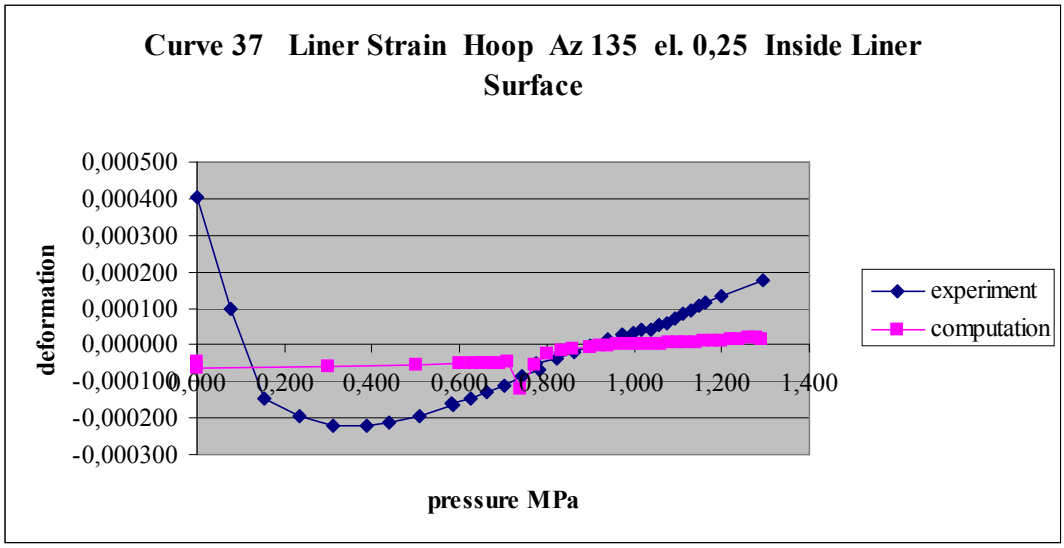
Curve 37 Liner Strain Hoop Az 135 el. 0,25 Inside Liner Surface
0,000500
0,000400
0,000300
0,000200
0,000100
0,000000
-0,000100
-0,000200
-0,000300
0,000
0,200
0,400
0,600
0,800
1,000
1,200
1,400
deformation
pressure MPa
experiment
computation

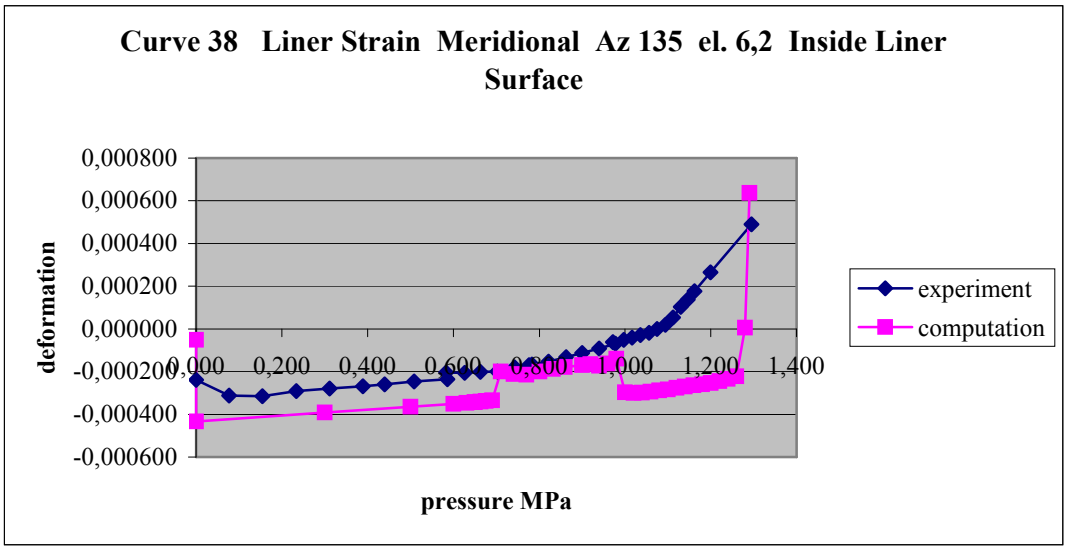
Curve 38 Liner Strain Meridional Az 135 el. 6,2 Inside Liner Surface
0,000800
0,000600
0,000400
0,000200
0,000000
-0,000200
-0,000400
-0,000600
0,000
0,200
0,400
0,600
0,800
1,000
1,200
1,400
deformation
pressure MPa
experiment
computation

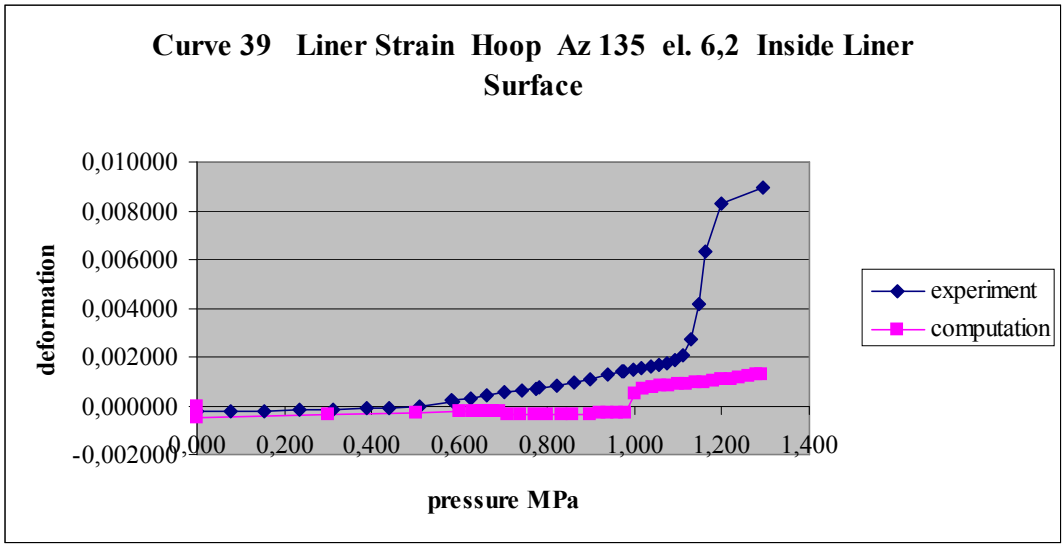
Curve 39 Liner Strain Hoop Az 135 el. 6,2 Inside Liner Surface
0,010000
0,008000
0,006000
0,004000
0,002000
0,000000
-0,002000
0,000
0,200
0,400
0,600
0,800
1,000
1,200
1,400
deformation
pressure MPa
experiment
computation

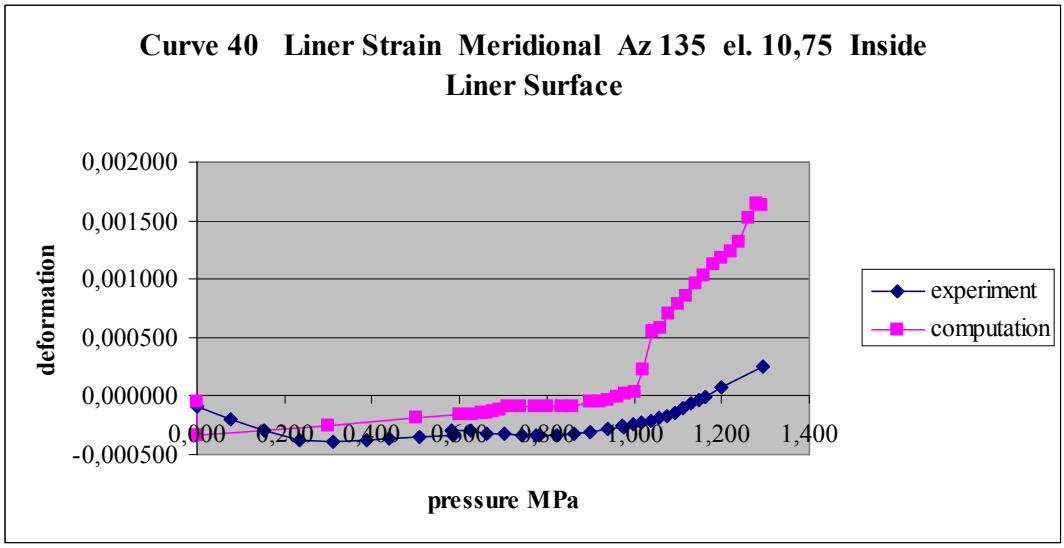
Curve 40 Liner Strain Meridional Az 135 el. 10,75 Inside Liner Surface
0,002000
0,001500
0,001000
0,000500
0,000000
-0,000500
deformation
0,000
0,200
0,400
0,600
0,800
1,000
1,200
1,400
pressure MPa
experiment
computation

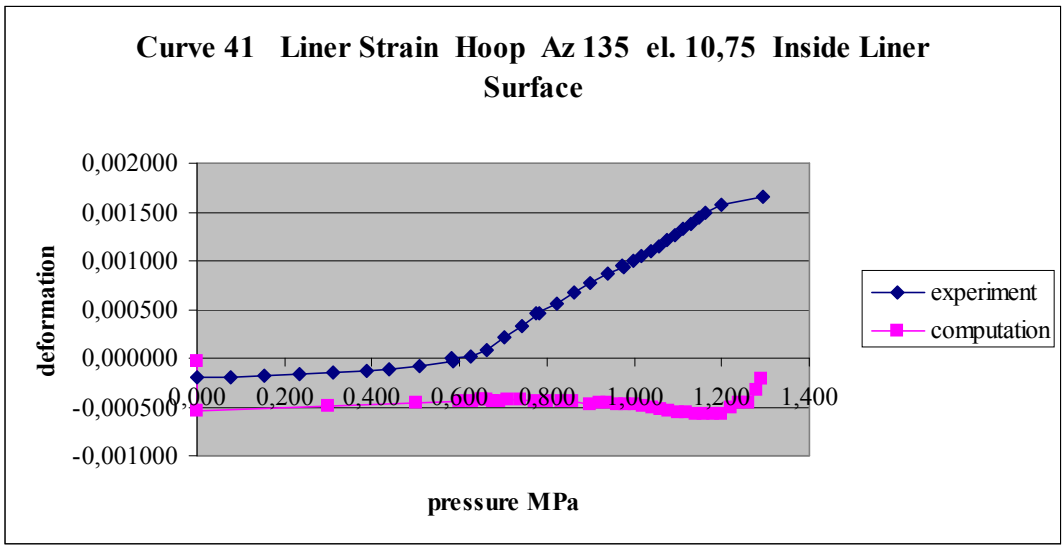
Curve 41 Liner Strain Hoop Az 135 el. 10,75 Inside Liner Surface
0,002000
0,001500
0,001000
0,000500
0,000000
-0,000500
-0,001000
deformation
0,000
0,200
0,400
0,600
0,800
1,000
1,200
1,400
pressure MPa
experiment
computation

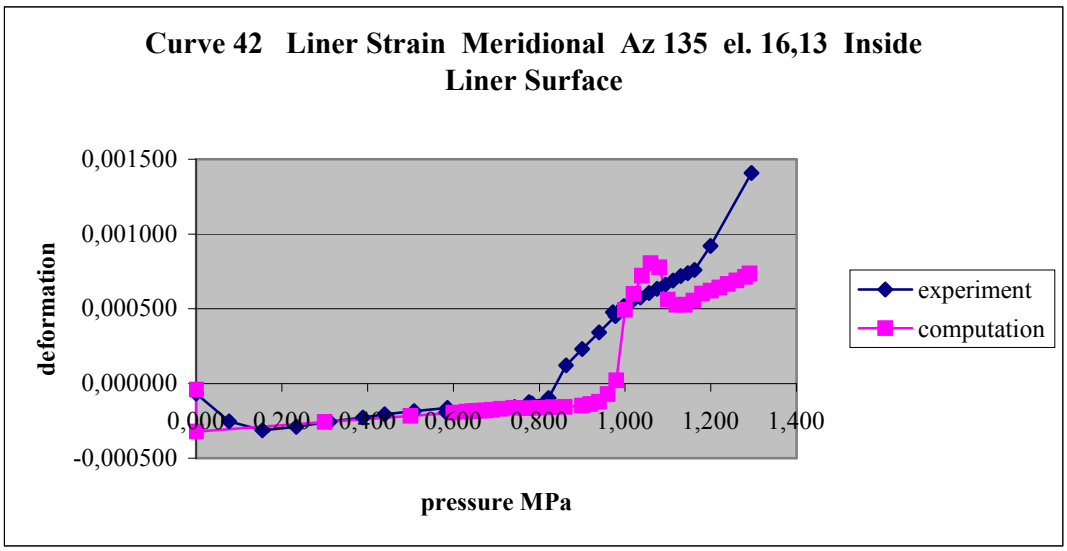
Curve 42 Liner Strain Meridional Az 135 el. 16,13 Inside Liner Surface
0,001500
0,001000
0,000500
0,000000
-0,000500
deformation
0,000
0,200
0,400
0,600
0,800
1,000
1,200
1,400
pressure MPa
experiment
computation

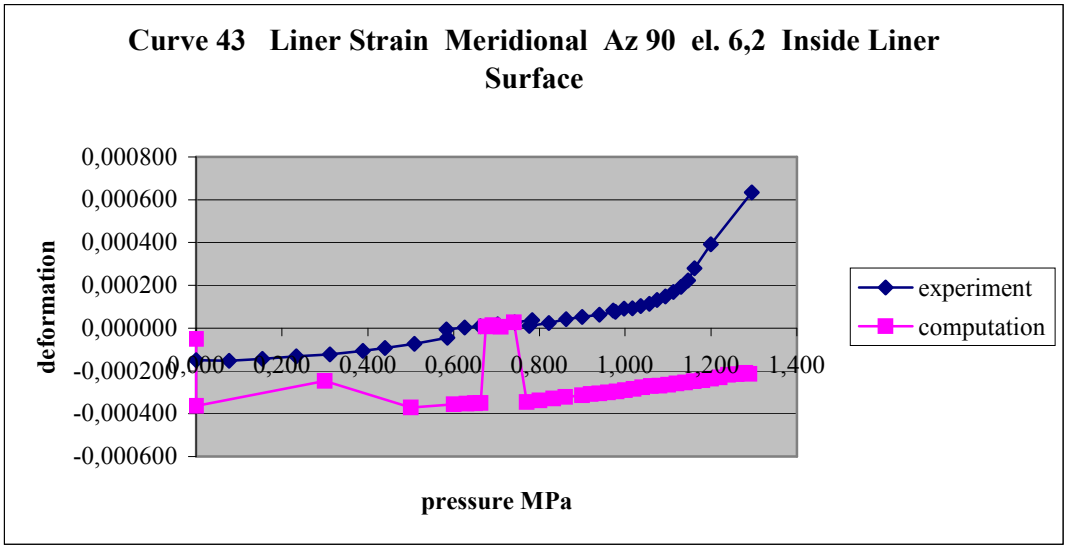
Curve 43 Liner Strain Meridional Az 90 el. 6,2 Inside Liner Surface
0,000800
0,000600
0,000400
0,000200
0,000000
-0,000200
-0,000400
-0,000600
0,000
0,200
0,400
0,600
0,800
1,000
1,200
1,400
deformation
pressure MPa
experiment
computation

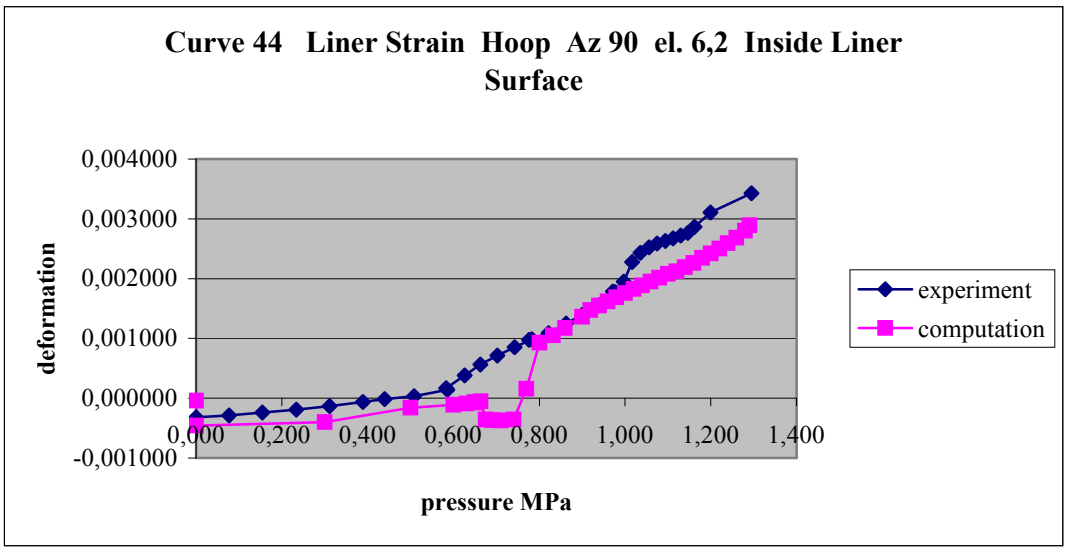
Curve 44 Liner Strain Hoop Az 90 el. 6,2 Inside Liner Surface
0,004000
0,003000
0,002000
0,001000
0,000000
-0,001000
0,000
0,200
0,400
0,600
0,800
1,000
1,200
1,400
deformation
pressure MPa
experiment
computation

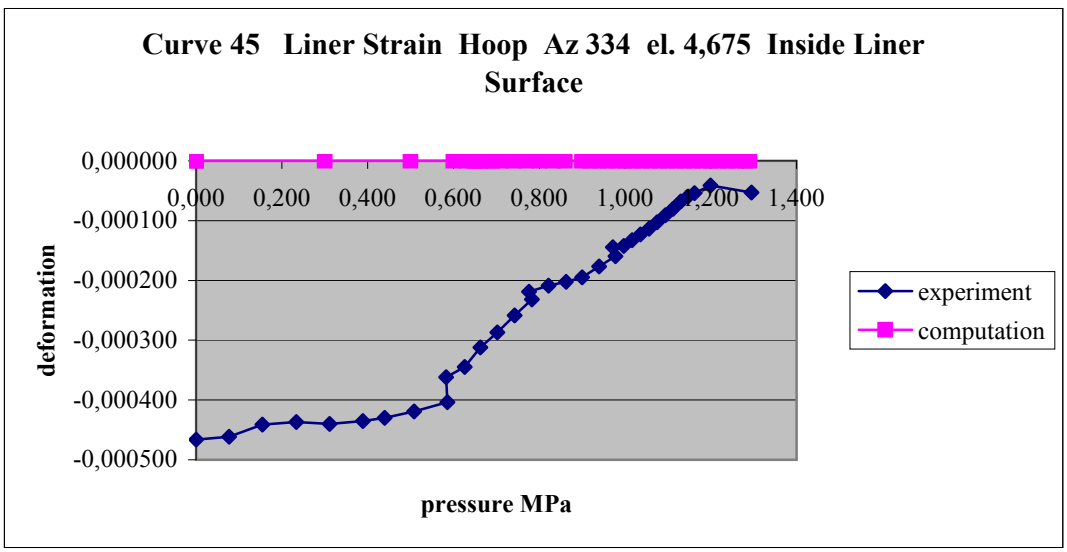
Curve 45 Liner Strain Hoop Az 334 el. 4,675 Inside Liner Surface
0,000000
-0,000100
-0,000200
-0,000300
-0,000400
-0,000500
0,000
0,200
0,400
0,600
0,800
1,000
1,200
1,400
deformation
pressure MPa
experiment
computation

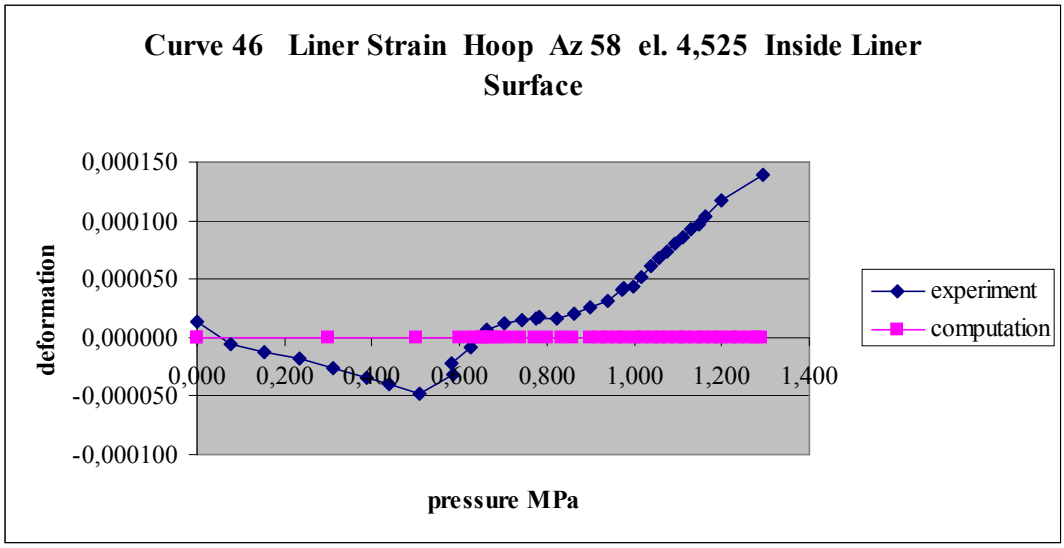
Curve 46 Liner Strain Hoop Az 58 el. 4,525 Inside Liner Surface
0,000150
0,000100
0,000050
0,000000
-0,000050
-0,000100
deformation
0,000
0,200
0,400
0,600
0,800
1,000
1,200
1,400
pressure MPa
experiment
computation

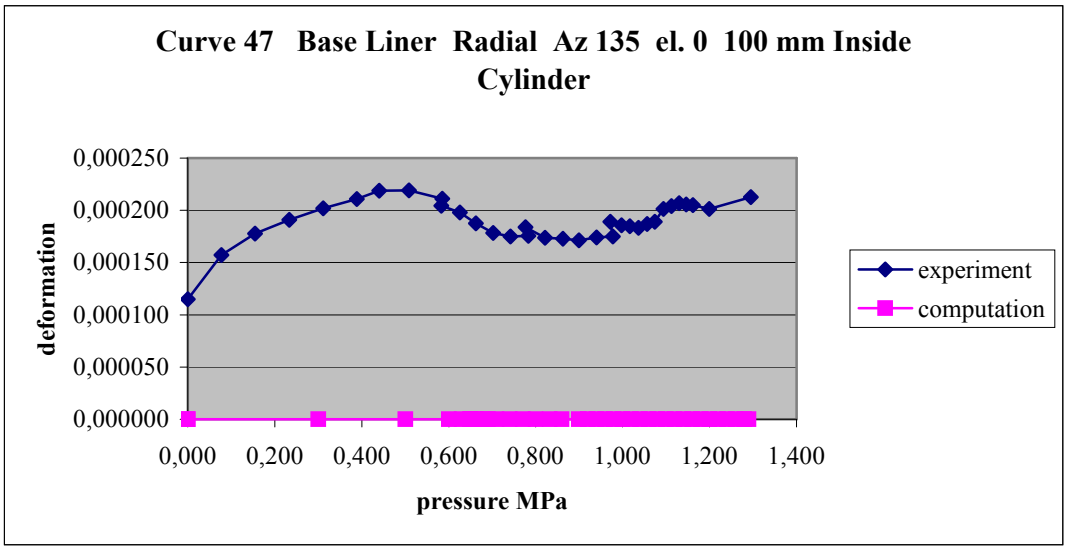
Curve 47 Base Liner Radial Az 135 el. 0 100 mm Inside Cylinder
0,000250
0,000200
0,000150
0,000100
0,000050
0,000000
deformation
0,000
0,200
0,400
0,600
0,800
1,000
1,200
1,400
pressure MPa
experiment
computation

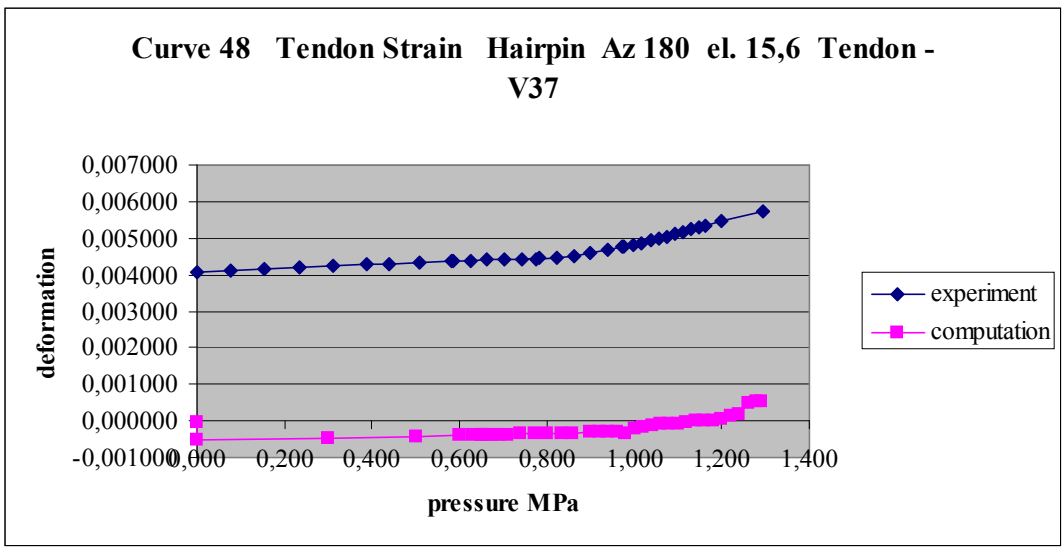
Curve 48 Tendon Strain Hairpin Az 180 el. 15,6 Tendon - V37
0,007000
0,006000
0,005000
0,004000
0,003000
0,002000
0,001000
0,000000
-0,001000
deformation
0,000
0,200
0,400
0,600
0,800
1,000
1,200
1,400
pressure MPa
experiment
computation

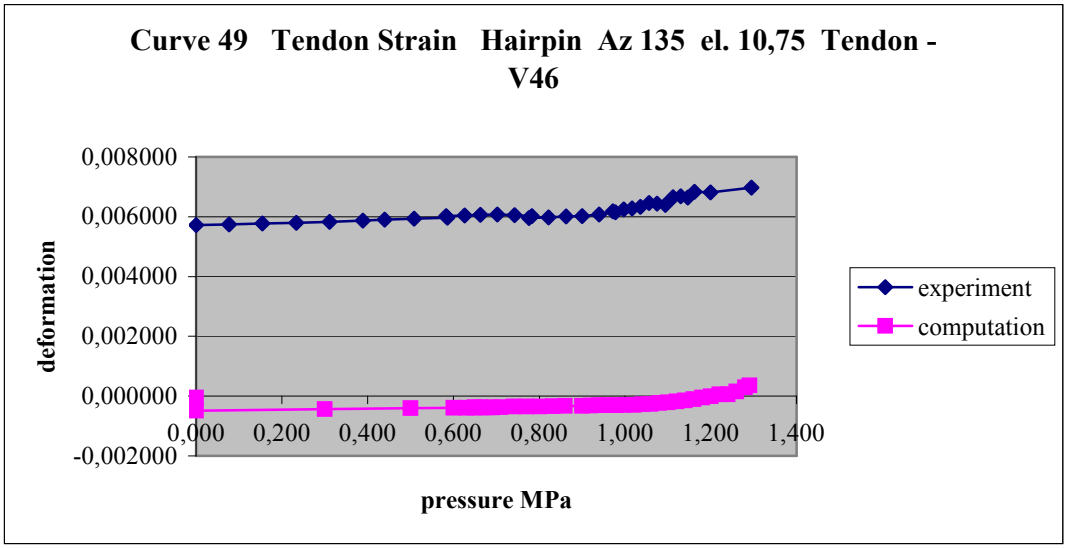
Curve 49 Tendon Strain Hairpin Az 135 el. 10,75 Tendon - V46
0,008000
0,006000
0,004000
0,002000
0,000000
-0,002000
deformation
0,000
0,200
0,400
0,600
0,800
1,000
1,200
1,400
pressure MPa
experiment
computation

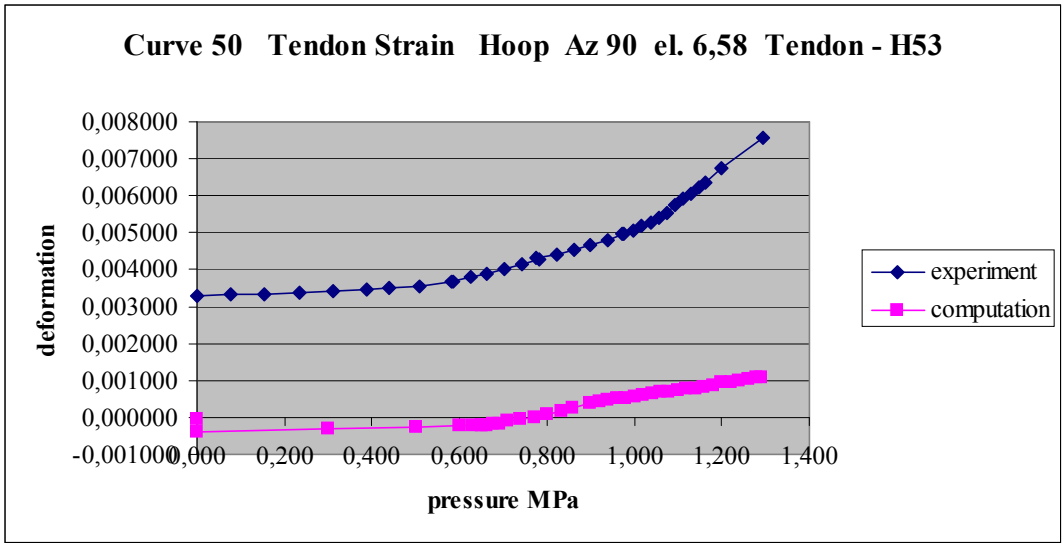
Curve 50 Tendon Strain Hoop Az 90 el. 6,58 Tendon - H53
0,008000
0,007000
0,006000
0,005000
0,004000
0,003000
0,002000
0,001000
0,000000
-0,001000
deformation
0,000
0,200
0,400
0,600
0,800
1,000
1,200
1,400
pressure MPa
experiment
computation

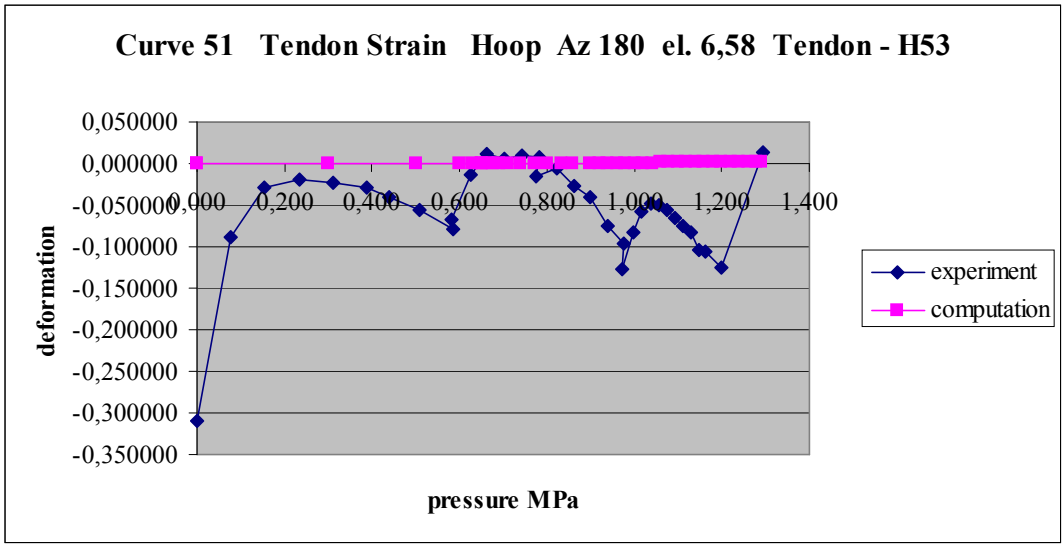
Curve 51 Tendon Strain Hoop Az 180 el. 6,58 Tendon - H53
0,050000
0,000000
-0,050000
-0,100000
-0,150000
-0,200000
-0,250000
-0,300000
-0,350000
deformation
0,000
0,200
0,400
0,600
0,800
1,000
1,200
1,400
pressure MPa
experiment
computation

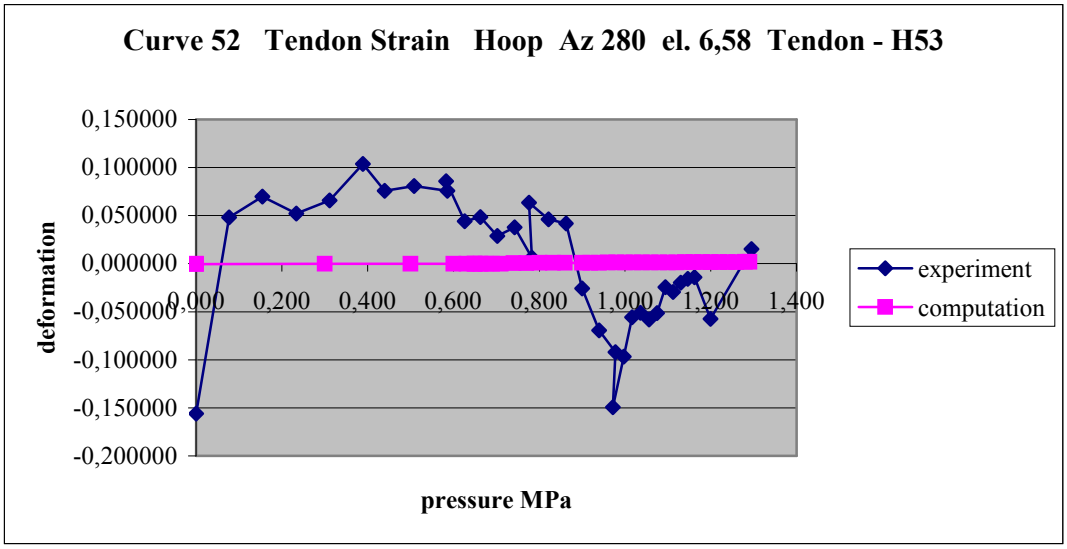
Curve 52 Tendon Strain Hoop Az 280 el. 6,58 Tendon - H53
0,150000
0,100000
0,050000
0,000000
-0,050000
-0,100000
-0,150000
-0,200000
deformation
0,000
0,200
0,400
0,600
0,800
1,000
1,200
1,400
pressure MPa
experiment
computation

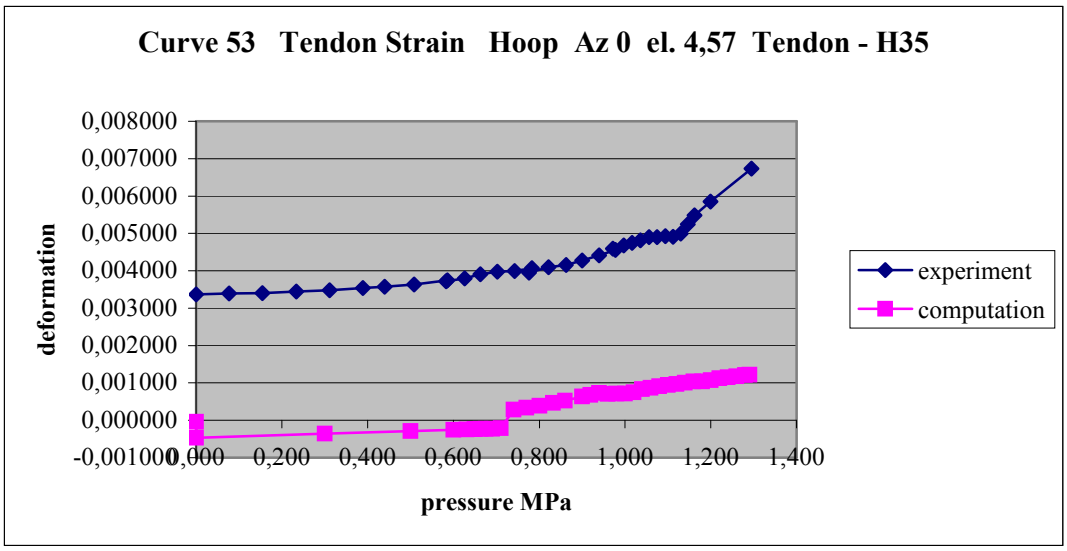
Curve 53 Tendon Strain Hoop Az 0 el. 4,57 Tendon - H35
0,008000
0,007000
0,006000
0,005000
0,004000
0,003000
0,002000
0,001000
0,000000
-0,001000
deformation
0,000
0,200
0,400
0,600
0,800
1,000
1,200
1,400
pressure MPa
experiment
computation

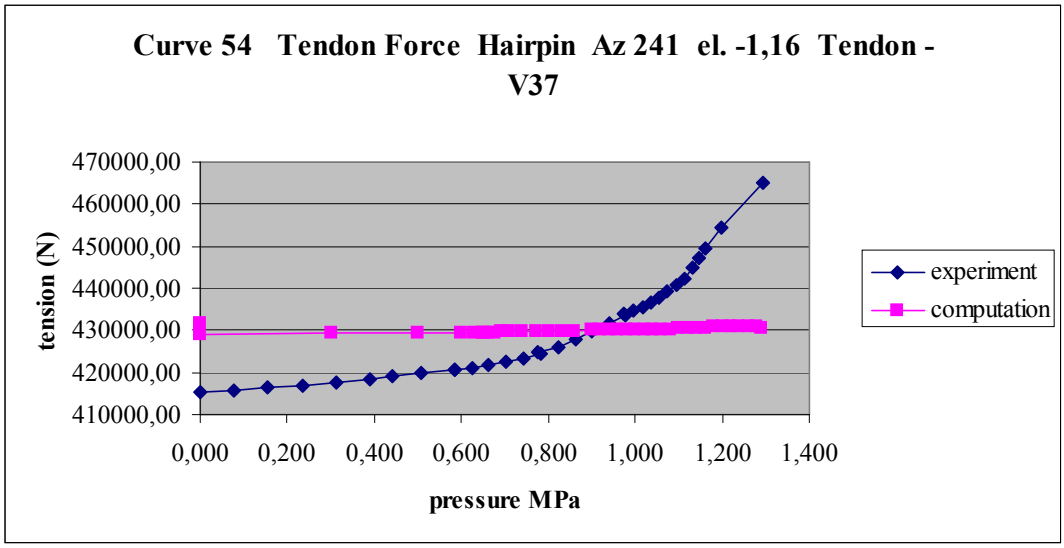
Curve 54 Tendon Force Hairpin Az 241 el. -1,16 Tendon - V37
470000,00
460000,00
450000,00
440000,00
430000,00
420000,00
410000,00
tension (N)
0,000
0,200
0,400
0,600
0,800
1,000
1,200
1,400
pressure MPa
experiment
computation

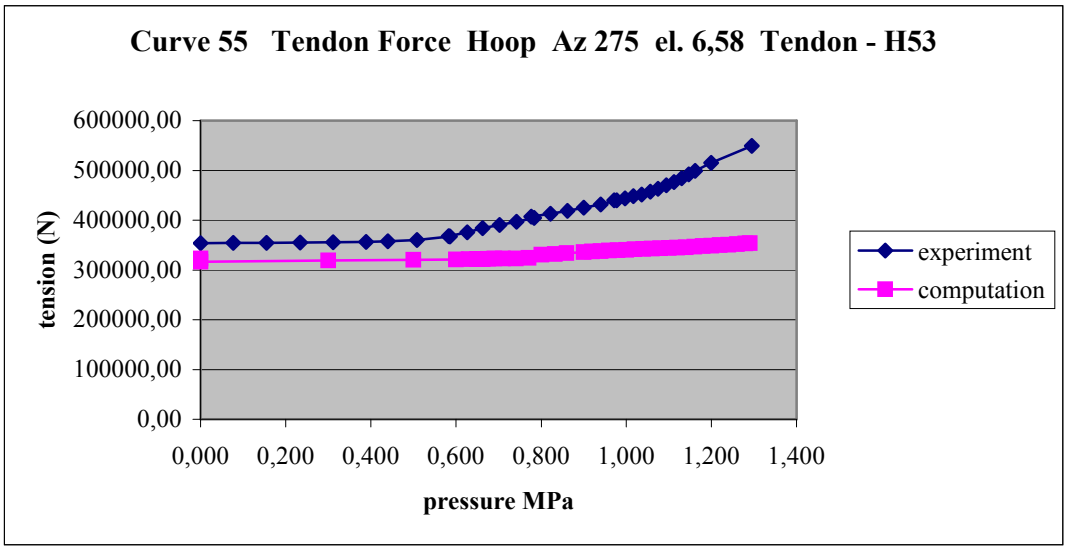
Curve 55 Tendon Force Hoop Az 275 el. 6,58 Tendon - H53
600000,00
500000,00
400000,00
300000,00
200000,00
100000,00
0,00
tension (N)
0,000
0,200
0,400
0,600
0,800
1,000
1,200
1,400
pressure MPa
experiment
computation

IRSN/CEA results of ISP48 phase 3.

IRSN-CEA conducts only Case 1. In fact, we believe that running Case 2 would have entailed changing the mesh in order to use more elements in the thickness of the wall to be able to capture the consequences of the thermal gradient. As the thermal gradient is more important than in case 1, this would have led to a longer computation.

The analysis of the results showed concrete cracking at 6 bars and a quasi linear behaviour up to 15 bars (radial displacement versus pressure). Other participants in the benchmark find that reinforcement exhibited a plastic behaviour at about 12 bars and that the structure failed at about 15 bars.

The following reasons could be considered to explain why our model does not exhibit plastic behaviour before 15 bars:

- First of all, in order to simplify our computation, we decided to maintain constant the material properties versus temperature. According to us, this simplification does not have a significant effect on the results.

- We considered in the calculation that the tendons are embedded in a concrete element despite their ability to slide inside their conduct.

- We finally found that the rebar yield limit that we consider in our computation is the first data given at the beginning of the ISP48 benchmark and is higher by 10 to 20% to the actual yield limit. This can be a good explanation for the general linear behaviour of the structure during our computation.

General conclusion of phase 3 case 1 is that thermal loading does not reduce the structure performance and even plays a positive role in the structural resistance to failure despite concrete cracking of the inner surface of the containment.

Concerning containment performance, one has to distinguish structural integrity loss from leak tightness loss. The former may be assessed using a burst criterion linked to the tendon failure: in this case, there is a good agreement between experimental data and F. E. computation results, even by simple hand calculation. Leak tightness loss refers to liner tearing and the agreement is far less obvious between experimental data (mock-up air leakage, tearing of liner coupon in laboratory) and strain evaluation of liner in the calculation model: there are two decades between the deformation at rupture of the liner coupon (rupture deformation of about 30%) and the deformation at rupture of the liner of the mock-up (maximum deformation less than 1%, while air leakage occurs).

Our opinion on this point is:

- The tear of the liner is a very local phenomenon; to capture it, the calculation model must be sufficiently refined up to welding size (while current calculations are carried out on a global scale, the size of the finite element varies from one meter to a few decimetres). The model should take into consideration singularities of each welding and of each liner anchor as well as the cracks in the concrete. It then ultimately should be able to determine the localization of the strain in the structure. This approach is very complicated and very difficult to realize.

- It is convenient to use a global criterion for liner tearing drawn from the experience feedback and mock-up tests results. The tests carried out at SANDIA on the PCCV model showed the existence of tears in the liner with significant leak rates for values of relative pressure of about 1 MPa, with an average strain of the liner of about 0.3 to 0.5%.

The transposition of the results of PCCV tests to the calculations led to the following global criterion: the maximum plastic strain obtained by nonlinear calculations in the current zone must be lower than a value of 0.30 % ± 0.15 %. Beyond this value, a risk of a local tear of the liner is very likely.
This criterion may be able to take into account the assumptions and uncertainties of modeling (size of the F.E. and liner homogenized)

- Another point to be highlighted: the containment leak tightness is the result of liner leak tightness but also of the leak tightness of all penetration closing devices. These closing devices are to be considered so as to verify that they do not control the tightness of the containment.